ISSN 1520-295X

Analytical Development and Experimental Validation of a Structural-Fuse Bridge Pier Concept

by
Samer El-Bahey and Michel Bruneau


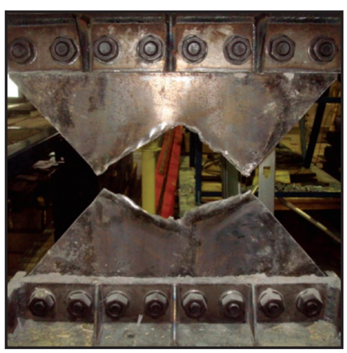

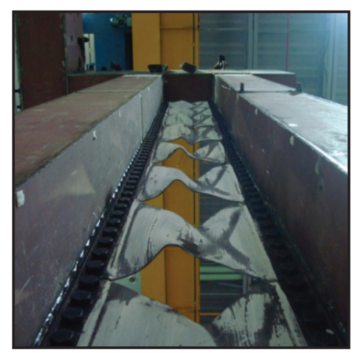

Technical Report MCEER-10-0005

October 1, 2010

This research was conducted at the University at Buffalo, State University of New York and was supported by the Federal Highway Administration under contract number DTFH61-07-C-00020.

Analytical Development and Experimental Validation of a Structural-Fuse Bridge Pier Concept

by

Samer El-Bahey[1] and Michel Bruneau[2]

Publication Date: October 1, 2010
Submittal Date: August 12, 2010

Technical Report MCEER-10-0005

Task Number 020-3.4

FHWA Contract Number DTFH61-07-C-00020

1 Graduate Student, Department of Civil, Structural and Environmental Engineering, University at Buffalo, State University of New York
2 Professor, Department of Civil, Structural and Environmental Engineering, University at Buffalo, State University of New York

MCEER
University at Buffalo, State University of New York
Red Jacket Quadrangle, Buffalo, NY 14261
Phone: (716) 645-3391; Fax (716) 645-3399
E-mail: *mceer@buffalo.edu*; WWW Site: *http://mceer.buffalo.edu*

Preface

MCEER is a national center of excellence dedicated to the discovery and development of new knowledge, tools and technologies that equip communities to become more disaster resilient in the face of earthquakes and other extreme events. MCEER accomplishes this through a system of multidisciplinary, multi-hazard research, in tandem with complimentary education and outreach initiatives.

Headquartered at the University at Buffalo, The State University of New York, MCEER was originally established by the National Science Foundation in 1986, as the first National Center for Earthquake Engineering Research (NCEER). In 1998, it became known as the Multidisciplinary Center for Earthquake Engineering Research (MCEER), from which the current name, MCEER, evolved.

Comprising a consortium of researchers and industry partners from numerous disciplines and institutions throughout the United States, MCEER's mission has expanded from its original focus on earthquake engineering to one which addresses the technical and socio-economic impacts of a variety of hazards, both natural and man-made, on critical infrastructure, facilities, and society.

The Center derives support from several Federal agencies, including the National Science Foundation, Federal Highway Administration (FHWA), and the Department of Homeland Security/Federal Emergency Management Agency, State of New York, other state governments, academic institutions, foreign governments and private industry.

The Center's Highway Project, primarily funded by the FHWA since 1992, focuses on the development of improved seismic design, evaluation, and retrofit methodologies and strategies for new and existing bridges and other highway structures. Over the years, MCEER has produced a new seismic retrofitting manual, consisting of two parts (bridges and other highway structures), as well as research products on the seismic retrofitting of truss bridges, seismic isolation manual and Risks from Earthquake Damage to Roadway System (REDARS).

In 2007, MCEER was awarded a new contract, "Innovative Technologies and Their Applications to Enhance the Seismic Performance of Highway Bridges." The major focus of the research program is on the development of detailed technology to apply accelerated bridge construction (ABC) in seismic regions, and the development of innovative seismic protection technologies that can enhance the seismic performances of precast reinforced concrete bridges with an emphasis on ABC.

This report describes an experimental and analytical study of a structural fuse concept where structural steel elements are added to a bridge bent to increase its strength and stiffness. The structural fuse is designed to sustain the seismic demand and dissipate seismic energy through

hysteretic behavior of the fuses while keeping the gravity-resisting structural elements of the bridge bent elastic. A parametric study is first carried out to investigate the effect of adding structural fuses to a RC bridge bent. Second, an experimental program for two large-scale twin-column segmental bridge bent specimens in an accelerated bridge construction application is developed to investigate the impact of the fuses on the behavior of the bridge system. The experimental work is followed by an analytical study to replicate the experimental results and to assess the adequacy of the design recommendations. Two types of structural fuses are used in this research: Buckling Restrained Braces (BRBs) for short length applications, and Steel Plate Shear Links (SPSLs) that are designed and detailed to dissipate energy through shear yielding. Both types of fuses resulted in increased stiffness and strength of the test system.

ABSTRACT

In this research, a structural fuse concept is proposed in which structural steel elements are added to a bridge bent to increase its strength and stiffness, and also designed to sustain the seismic demand and dissipate all the seismic energy through hysteretic behavior of the fuses, while keeping the gravity-resisting structural elements of the bridge bent elastic.

A parametric study to investigate the effect of adding structural fuses to a RC bridge bent is first conducted. Trends in behavior as a function of key parameters defining the proposed structural fuse system are presented, followed by a proposed systematic design procedure.

Then, an experimental program is developed for two large-scale twin-column segmental bridge bent specimens in an accelerated bridge construction application, having a series of structural fuses between the columns, and subjected to quasi-static cyclic tests to investigate the effect of adding these fuses on the total behavior of the system compared to the bare bents behavior.

The experimental work is then followed by analytical work to replicate the experimental results obtained and to assess the adequacy of the design recommendations as well as the effectiveness of adding structural fuses to bridge bents for seismic energy dissipation, providing an insight into the general behavior of the structural fuse system.

Two types of structural fuses are used in this second phase of work and implemented in this research; one is a newly proposed Buckling Restrained Braces (BRBs) concept for short length applications. The other is a special Steel Plate Shear Link (SPSL), which is a steel plate restrained against lateral buckling and designed and detailed to dissipate energy through shear yielding. Equations are developed to determine some critical design parameters of the SPSLs.

Uniaxial cyclic tests are then performed on the individual BRBs that have been used as structural fuses in the large specimens, as the axial force resisted by each individual BRB could not be measured during the bridge pier tests. Also quasi-static cyclic testing is performed on individual SPSLs to investigate the behavior of these newly proposed links having different dimensions and lateral restraining conditions.

ACKNOWLEDGMENTS

Sincere thanks to the staff of the Structural Engineering and Earthquake Simulation Laboratory at the University at Buffalo, Mark Pitman, Duane Kozlowski, Robert Staniszewski, Scot Weinreber, Christopher Budden, and Goran Josipovic for sharing their collective expertise. The experimental part of this research could not have been accomplished without your valuable collaboration.

This research was supported in part by the Federal Highway Administration under contract number DTFH61-07-C-00020 to the Multidisciplinary Center for Earthquake Engineering Research and is greatly appreciated. Also special thanks to the managers of Corus Bi-Steel and Star Seismic for their generous donations.

TABLE OF CONTENTS

TABLE OF CONTENTS (CONT'D)

TABLE OF CONTENTS (CONT'D)

TABLE OF CONTENTS (CONT'D)

TABLE OF CONTENTS (CONT'D)

TABLE OF CONTENTS (CONT'D)

LIST OF FIGURES

LIST OF FIGURES (CONT'D)

LIST OF FIGURES (CONT'D)

LIST OF FIGURES (CONT'D)

LIST OF FIGURES (CONT'D)

LIST OF FIGURES (CONT'D)

LIST OF FIGURES (CONT'D)

LIST OF FIGURES (CONT'D)

LIST OF FIGURES (CONT'D)

LIST OF FIGURES (CONT'D)

LIST OF FIGURES (CONT'D)

FIGURE **TITLE** **PAGE**

LIST OF TABLES

NOTATIONS

e^*= Balanced steel plate shear link angle

E= Modulus of Elasticity

G= Shear modulus

R_y= Ratio of expected yield strength to specified minimum yield strength

V_{yf} = Yield strength of the bare frame

V_{yb} = Yield strength of the BRB

V_{Df} =Maximum strength of the bare frame

V_{Dt}= Maxumum strength of total system

V_{Ds}= Lateral strength contribution of fuse system

V_{y1} =Total system yield strength

V_{y2} =Strength of the total system at the point of RC frame yielding

V_p =Lateral strength of the total system at the onset of column failure

V_e =Seismic demand on the total system if the system behaved elastically

V_i = Shear strength of the frame columns

V_n = Nominal flexural shear strength of the frame columns

K_{eff} = Elastic lateral stiffness of the bare frame

K_b = Elastic lateral stiffness of the fuses

K_{tot} = Elastic lateral stiffness of the total system

M_p= Full Plastic Moment

M_{pr}= Reduced Plastic Moment

y_o= Depth at mid length of the steel plate shear link

y_1= Depth of wedged part of the steel plate shear link

Δ_{yb} = BRB yield displacement

Δ_{yf} = Bare frame yield displacement

Δ_{Df} =Lateral displacement at the onset of bare frame damage

Δ_{bm}= Brace deformation at desigh story drift

Δ_{by}= Yield displacement of brace

δ_t=expected displacement after frame retrofit (also called target displacement).

β =Post-yield strain hardening stiffness ratio of the bare frame

ω= Strain hardening factor for buckling restrained braces

μ_{max} = maximum displacement ductility that the total system can withstand

NOTATIONS (CONTINUED)

μ_f= Bare frame displacement ductility

μ_b = BRB displacement ductility

μ_D is the maximum local member displacement ductility demand

ε_b = BRB maximum strain demand

γ= Steel plate shear link total rotation

Ω= Overstrength factor

L_b = Total length of BRB

L_{ysc} = Yielding length of BRB

c = yielding ratio of the BRB

θ_b = Balanced steel plate shear link edge angle

H_{tot} = Frame height

L= Frame width

D = Column diameter

n = Number of fuses

m = Mass of bent

ρ = Column reinforcement ratio

ξ = Frame strength ratio

η = BRB strength ratio

α = The ratio between the lateral stiffness of the BRB and the lateral stiffness of the bare frame

f_{yBRB} = BRB yield Strength

$f_c^{/}$ =Concrete compressive strength

C_1 = Modification factor to account for the influence of inelastic behavior on the response of the system

R_d = Displacement magnification factor for short periods

T_{eff} = Effective period of the total system

T_s = Period at the end of constant design spectral acceleration plateau

A_b = BRB Cross sectional area

E_s = BRB elasticity modulus

S_a = Spectral acceleration demand

ABBREBIATIONS

AASHTO	American Association of State Highway and Transportation Officials
AISC	American Institute of Steel Construction
ASTM	American Society for Testing and Materials
BRB	Buckling Restrained Brace
CB	Cap Beam
FB	Foundation Base
FEM	Finite Element Model
LB	Loading Beam
MCEER	Multidisciplinary Center for Earthquake Engineering Research
NEHERP	National Earthquake Hazard Rerduction Program
SPSL	Steel Plate Shear Link

SECTION 1
INTRODUCTION

1.1 General

Great strides have been made in earthquake engineering in the past decades with respect to the design of bridges to resist earthquakes. Nevertheless, most of the existing design procedures, while superior to what existed in the past, still to a large degree rely on detailing for ductile response structural elements that serve both purposes of providing lateral load resistance and providing the gravity load resisting systems. Although existing bridge design specifications aim to prevent total collapse of bridges, the damage to structural elements after an earthquake would often require temporary closure of the bridge for days or weeks to repair these elements, which in many cases are the bridge columns. Note that for a geographical area where all the bridges are designed to be in compliance to this design philosophy, it is conceivable that most of the bridges subjected to strong ground shaking in this area could be disabled after an earthquake. This could put an inordinate demand on the affected departments of transportation, as they would be required to simultaneously and rapidly repair multiple bridges – an expensive time consuming activity.

This raises questions as to whether it might be possible to design conventional bridges per a different design philosophy; in such alternative design concepts, reparability would have to be done following an earthquake while keeping the bridges in service for gravity loads, and to preserve the lateral load resistance by being able to replace rapidly the damaged lateral load resisting structural elements. While seismic isolation and mechanical damping are relatively mature technologies that have been promoted as ways to achieve no damage during earthquakes, the focus of the work described here is to achieve the stated objectives with structural systems using steel and concrete whose long term durability and performance at various temperatures is well understood, and without the need to accommodate the large displacements required for isolation systems and maintenance requirements for mechanical damping systems.

One design philosophy for which the stated objectives could be potentially achieved consists of introducing a disposable and replaceable structural element into the system that has adequate strength to resist lateral loads and that can also work as a metallic-hysteretic energy dissipation device, designing the whole system to sustain the seismic demand while preserving the integrity of the gravity-resisting bridge components by keeping them elastic during an earthquake. This design philosophy is known as the structural fuse concept.

The structural fuse concept was investigated in building applications by a number of investigators in recent years; however it has not been investigated for bridge applications to the same degree, particularly for short- and medium-span bridges. The concept is advantageous, as replacing fuse elements after an earthquake could be done without affecting the serviceability of the bridge being repaired. To make this concept more appealing, it would also be desirable to implement it in structural systems that would also provide benefits in the perspective of accelerated bridge construction (ABC). The work presented in this research will also investigate how this could be done.

Note that while structural fuses could be a useful concept for new bridges, it could also be useful for the seismic retrofit of existing bridges. Recent earthquakes in the United States, Japan and several other countries have demonstrated the seismic vulnerability of bridges, particularly as typical bridge piers designed prior to the 1970's where not designed to sustain plastic deformations for energy dissipation and were not detailed for ductile response. Many of these non-ductile bridges still exist. Adding structural fuses to the columns of existing bridges could mitigate damage to those bridges by keeping the gravity supporting elements intact and concentrating the damage throughout the easily replaceable and disposable fuses. Therefore, possible retrofit scenarios were also investigated throughout this research as a secondary benefit for the structural fuses.

1.2 Scope and Objectives

In this research, a structural fuse concept is proposed in which structural steel elements are added to a bridge bent to increase its strength and stiffness, and also designed to sustain the seismic demand and dissipate all the seismic energy through hysteretic behavior of the fuses while keeping the gravity-resisting structural elements of the bridge bent elastic. In addition, using easily replaceable and specially detailed disposable ductile structural elements can help achieve a fast return of the bridge to service. To achieve these objectives:

First, a parametric study to investigate the effect of adding structural fuses to a RC bridge bent is conducted. Trends in behavior as a function of key parameters defining the proposed structural fuse system are presented, followed by a proposed systematic design procedure.

Second, an experimental program is developed for two large-scale twin-column segmental bridge bent specimens in an accelerated bridge construction application, having a series of structural fuses between the columns, and subjected to quasi-static cyclic tests to investigate the effect of adding these fuses on the total behavior of the system compared to the bare bents behavior.

The experimental work is then followed by analytical work to replicate the experimental results obtained and to assess the adequacy of the design recommendations as well as the effectiveness of adding structural fuses to bridge bents for seismic energy dissipation, providing an insight into the general behavior of the structural fuse system.

Two types of structural fuses are used in this second phase of work and implemented in this research; one is a newly proposed Buckling Restrained Braces (BRBs) concept for short length applications. The other is a special Steel Plate Shear Link (SPSL), which is a steel plate restrained against lateral buckling and designed and detailed to dissipate energy through shear yielding. Equations are developed to determine some critical design parameters of the SPSLs.

Uniaxial cyclic tests are then performed on the individual BRBs that have been used as structural fuses in the large specimens, as the axial force resisted by each individual BRB could not be measured during the bridge pier tests. Also quasi-static cyclic testing is performed on individual SPSLs to investigate the behavior of these newly proposed links having different dimensions and lateral restraining conditions.

1.3 Outline of Report

Section 2 contains a brief overview of past experimental and analytical research related to the structural fuse concept as applied in building applications, as well as a summary of research conducted on buckling restrained braces.

Section 3 describes a parametric study for a prototype RC bridge bent retrofitted using BRBs to investigate trends in behavior as a function of key parameters defining the proposed structural fuse system, while using BRBs of different stiffnesses and strengths as the energy dissipating fuses. Nonlinear dynamic analyses validating the proposed static procedure are also presented, followed by a design example. Finally, a general retrofit procedure is presented, with emphasis on how to select suitable values for the various parameters to achieve a satisfactory structural fuse system.

Section 4 describes an innovative Steel Plate Shear Link (SPSL) used as a structural fuse. Equations are developed to determine some critical design parameters of the SPSL, link ductility, lateral stiffness, and strength. Finally, a preliminary finite element model is then presented to verify the proposed SPSL concept.

Section 5 describes the design and detailing of two large-scale twin-column segmental bridge bent specimens, having either Steel Plate Shear Links (SPSLs) or Buckling Restrained Braces (BRBs) as a series of structural fuses between the columns, and subjected to a series of quasi-static cyclic tests. Coupon testing of the steel being used in the experiment as well as cylinder tests of the infill concrete is then presented. Finally the instrumentation layout is described.

Section 6 describes the results and observations of the testing program. Testing of each specimen is described in detail, and observations made regarding the behavior of each specimen are given through the steps of the applied displacement protocol. Force versus displacement hysteretic curves, photos of specimens condition during and after testing, and related descriptions are then presented.

Section 7 describes the analytical investigation conducted to replicate the experimental results, as finite element analyses were conducted to replicate the full range of results obtained from the experiments. Finally all results are compared to highlight the difference in behavior between all tested specimens.

Section 8 describes uniaxial tests conducted on the newly proposed short length BRB concept used in the bridge pier testing. Two BRB test series were conducted to investigate the effect of changing the cross section on the overall behavior. The BRBs assembly description is presented, followed by the testing setup, instrumentations, and loading protocol. Finally, the testing observations are presented with hysteretic curves and photos of the specimen during and after testing.

Section 9 describes design and detailing of SPSLs for quasi-static cyclic testing, the design of a setup to carry out the testing, and the instrumentation used to capture results. The loading protocol used and observations made during the quasi-static testing are then described. Specimen link shear versus total rotation hysteresis curves are then presented with photos and a description of observations made during the cyclic history for each SPSL being tested. Finite element models are then generated to replicate the observed hysteretic behavior of the SPSLs being tested, and provide insight into the general behavior of the SPSLs.

Section 10 summarizes the work and presents conclusions for this research project, and some recommendations for future work.

SECTION 2
LITERATURE REVIEW

2.1 Introduction

Many existing bridges, particularly those built before the mid-1970's, are particularly vulnerable to strong ground motions as they do not meet current standards for earthquake resistant construction. In recent earthquakes in California, Japan, and Central and South America, bridges constructed in reinforced or prestressed concrete have collapsed or have been severely damaged when subjected to strong earthquakes. This poor performance can be attributed to the design philosophies adopted at the time of their construction in addition to a lack of attention to design details. In many seismic regions, California in particular, there was a great expansion of the freeway and highway systems in the 1950's and 1960's before modern bridge seismic design codes had been developed; as a result, now over 40% of the nation's bridges are in need of repair or replacement.

As mentioned in section 1, many design philosophies have been developed for the seismic design of bridges. Nevertheless, a lot of those design procedures rely on detailing the bridge columns and piers for ductile response, while these elements also serve as gravity load resisting systems. As a consequence, the damage to these elements after an earthquake would often require temporary closure of the bridge for repairs.

To achieve a more stringent seismic performance for buildings and bridges, one alternative design approach that was proposed in the past aimed at concentrating damage in certain structural elements, while the main structure would be designed to remain elastic or with minor inelastic deformations following a damaging earthquake. This concept was further developed to make these elements disposable and easily replaced, in what was known thereafter as the structural fuse concept. A more detailed review on the development of the structural fuse concept and its state of the art is presented in section 2.2.

Achieving the structural fuse concept requires introducing a dedicated lateral load resisting system that serves as a passive energy dissipation device to the system to improve its seismic performance by dissipating most of the seismic induced energy. A fair number of devices can be used as passive energy dissipation systems; one type of particular contemporary interest is the Buckling Restrained Brace (BRB), which has been manufactured and marketed by a number of suppliers in North American, such as the Nippon Steel Corporation, Star Seismic, and Core Brace. BRB technology is fairly mature and has been widely investigated in recent decades. BRBs are becoming widely used in steel building in the United States, but there still has been only a few applications in concrete buildings and yet no applications in concrete bridges. Other passive energy dissipation devices also exist, such as the added damping and stiffness (ADAS) flexural beam damper (e.g. Steimer et al. 1981), and the steel yielding dampers (e.g. Kelly et al. 1972) to name a few, but they are beyond the scope of the current study.

In this research two hysteretic energy devices are considered, as mentioned in section 1. The first is the BRB, because it is a fairly mature technology with a well known behavior. The second is a newly proposed device called a Steel Plate Shear Link (SPSL) and developed as part of this research project to explore an alternative design to dissipate the seismic energy using a configuration that could be esthetically pleasing to bridge owners such as departments of transportation. Section 2.3 will focus on reviewing the state of the art on BRBs.

As mentioned in section 1, since there is an aspect of the application of the structural fuse concept in bridges that could be relevant for the retrofit of concrete bridges, a brief overview of the state of the art on the brittle behavior of concrete bridge columns is presented in section 2.4. Finally, a brief description of the coupled shear walls is presented in section 2.5 to state the similarity between their behavior and the behavior of the bridge bent system with passive energy dissipation devices as structural fuses.

2.2 The Structural Fuse Concept

2.2.1 General

In seismic design, loads resulting from an earthquake are reduced by a response modification factor, which allows the structure to undergo inelastic deformations while most of the energy is dissipated through hysteretic behavior. Designs have always (implicitly or explicitly) relied on this reduction in the design forces. However, this methodology relies on the ability of the structural elements to accommodate inelastic deformations, without compromising the stability of the structure. Furthermore, inelastic behavior translates into some level of damage in these elements. This damage leads to permanent system deformations following an earthquake, leading to high cost for repair works, in the cases when repairs are possible. In fact, it is frequently the case following earthquakes that damage is so extensive that repairs are not viable, even though the structure has not collapsed, and that the building must be demolished.

2.2.2 Development and Implementation of the Structural Fuse Concept in Buildings

The structural "ductile" fuse concept has been mentioned often in the literature, going back at least as far as Roeder and Popov (1977) when they introduced the eccentrically braced frame concept to increase the hysteretic energy capacity of steel frames. In that work, the beam segment yielding in shear was called the link as well as the ductile fuse because of its energy dissipation capacity. While this system was considered to have a good seismic behavior due to its energy dissipation capacity, the concept of a disposable or removable element was not yet considered. Also beyond difficulties of link replacement, large plastic deformations of the link could cause significant damage to the floors and slabs.

Many others, such as Fintel and Ghosh (1981) used the capacity design concept originally developed in New Zealand (Park and Paulay 1975) to design beams to be intentionally weaker members that yields by plastic hinging, to protect other members like columns from potential damage as they are considered more crucial members for the structure. In moment resisting frames, the intent was for columns to remain elastic under seismic loading and energy was to be dissipated by plastic hinging of the beams which were considered structural fuses. However, as was the case with the work done by Roeder and Popov, these beams cannot be considered to be disposable elements.

Wada et al. (1994) proposed the concept of "damage-controlled" or "damage tolerant" structures. The approach stated that the structure should have two separate components, the first being the main structure, which is composed of a moment frame designed to resist 80% of the lateral loads (Akira Wada, Tokyo Institute of Technology, personal communication to M. Bruneau, 2010). The second is a system of passive energy dissipation elements designed to resist loads resulting from strong ground motions. Due to the high cost to repair conventionally designed structures the idea of implementing disposable elements which are easy to replace and can dissipate energy became very attractive.

The damage controlled structures concept was further investigated and improved following the 1995 Northridge and 1995 Hyogoken-Nabu earthquakes by Conner et al. (1997), by stating that the effectiveness of the damage controlled structures proposed by Wada et al. (1994) depends on the energy dissipation capacity of the braces and the ability of the primary structure to remain elastic during a major seismic event, which would require very high strength material for the primary structure and very low strength material for the bracing system. Experimental studies were performed on typical structural panels for a set of steel structures with strength ranging up to 800MPa for the primary structure and as low as 100 MPa for the braces. The study demonstrated that by adjusting the distribution of stiffness and hysteretic damping, it is possible to control the seismic response of a building. An optimal stiffness distribution was proposed and applied to a set of building cases, design guidelines for the magnitude and variation of the hysteretic damper properties throughout the height of the building were established and verified through numerical simulation. The study showed that the effective damping ratio of 5% can be obtained with a brace yield force distribution having a maximum value of 1~2% of the total building weight, and varying over the height in the same way as the stiffness.

Further developments were proposed by Shimizu et al. (1998), Wada and Haung (1999), Haung et al. (2000). Wada and Haung (1995) implemented an approach based on balance of energy to design tall building structures having either hysteretic dampers or viscous dampers.

A comprehensive study of damage controlled structures in Japan was presented by Wada et al. (2000). That paper presented some research work done on the development of the damage controlled structures concept and it’s potential to design new constructions and retrofit existing structures. A dynamic analysis method was proposed for three dimensional frames with elements used to develop the structural fuse concept. Experimental studies were performed on a number of moment resisting frames with and without Buckling Restrained Braces working as a structural fuse. The experiments was used to validate the concept of damage controlled structures as the Buckling Restrained Braces were used to dissipate energy through hysteretic behavior, protecting beams and columns from yielding, thus ensuring that the primary structure remains elastic.

Vargas and Bruneau (2009) studied the implementation of the structural fuse concept using metallic dampers to improve the structural behavior of systems under seismic loads. A detailed design process was presented, as well as the modifications necessary to the process for retrofitting applications. The structural fuse concept was described in this study in a parametric formulation, considering the behavior of nonlinear single degree of freedom (SDOF) systems subjected to synthetic ground motions. Nonlinear dynamic response was presented in dimensionless charts normalized with respect to key parameters. Allowable story drift was introduced as an upper bound limit to the charts, which produces ranges of admissible solutions. A generic retrofit case study was also presented to illustrate the benefits of adding metallic fuse elements to an existing frame. A comparative analysis was made between a bare frame (i.e., without metallic dampers), and the same frame retrofitted using metallic fuse elements, to improve the behavior of the existing structure. In the process of attempting to implement the structural fuse concept into actual designs. A systematic design procedure was proposed for designing and retrofitting purposes. Figure 2-1 shows a comparison between the energy dissipated by the bare frame and the frame with the structural fuse, figure 2-2 shows regions of admissible solutions in terms of frame ductility and story drifts.

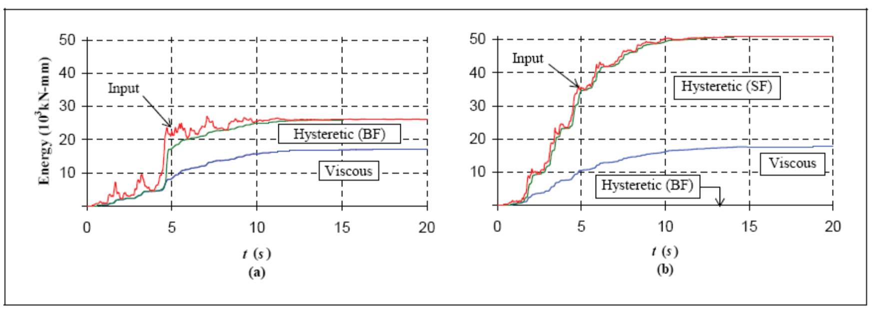

FIGURE 2-1 Comparison between the Energy Dissipated by the Bare Frame and the Frame with the Structural Fuse (Vargas and Bruneau 2009)

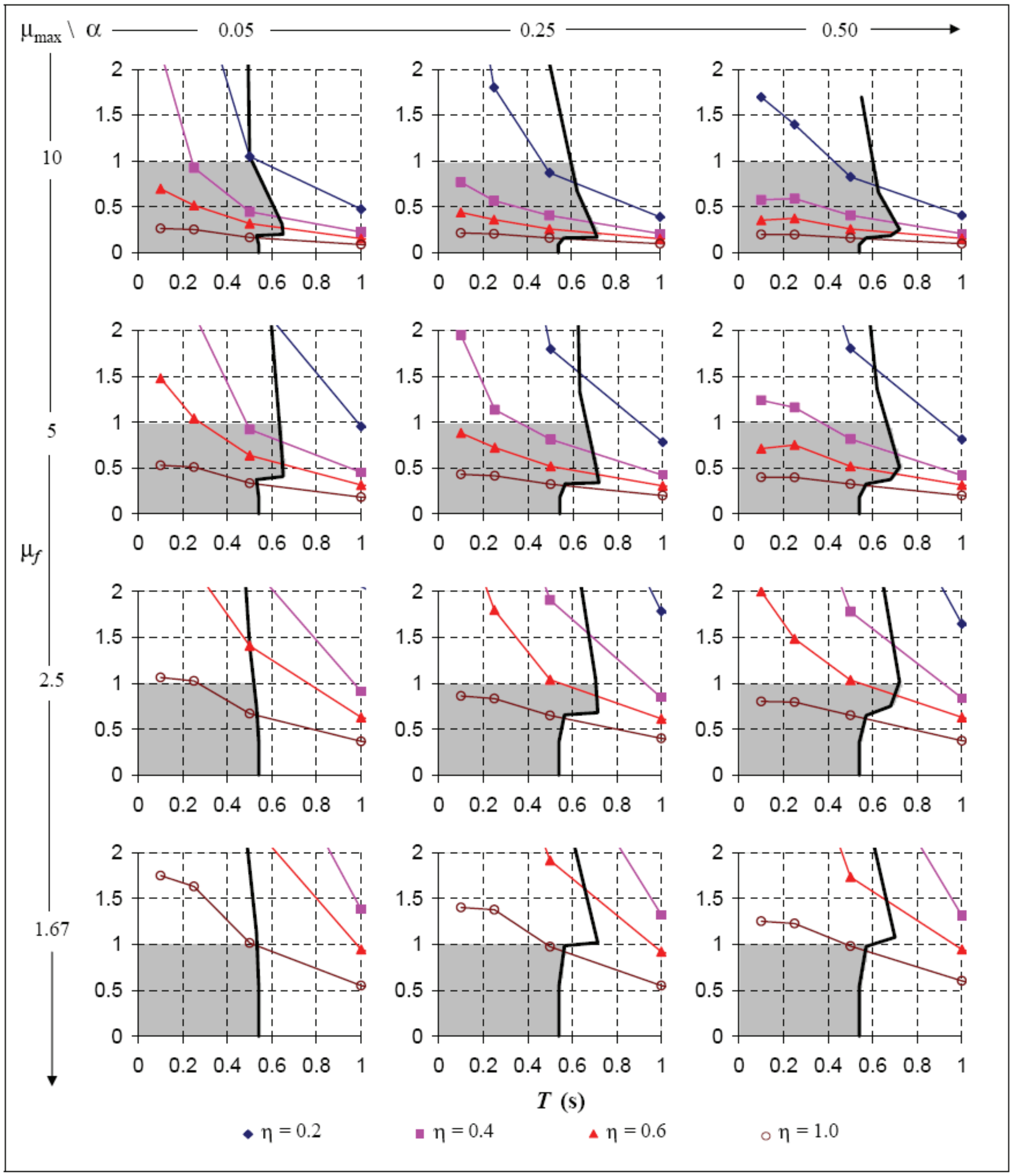

FIGURE 2-2 Admissible Solutions Regions in Terms of Frame Ductility and Story Drifts (Vargas and Bruneau 2009)

2.2.3 Implementation of the Structural Fuse Concept in Bridges

The structural fuse concept has not been implemented in bridges as extensively as in buildings. The only application that is known to date is the new design of the San Francisco-

Oakland bay bridge self-anchored suspension span, that in intended to replace the east span on the bridge.

The main tower structural system shown in figure 2-3 consists of four closely spaced reinforced concrete columns connected by a series of steel shear links. Each column is made up of a hollow, semi-elliptical cross section with an interior steel liner that tapers from the tower head to the base. The links and concrete tower shafts form a transverse structural frame system with a greater number of redundant ductile elements than a traditional portal system. The shear links are designed to be damaged in the Safety Evaluation Earthquake (SEE) event, dissipating all the seismic energy, and at the same time limiting the damage of the tower shafts. The stiffness of the concrete columns and shear links are tuned such that shear link ductility demand increases progressively, while maintaining almost elastic action in the concrete elements throughout the SSE event.

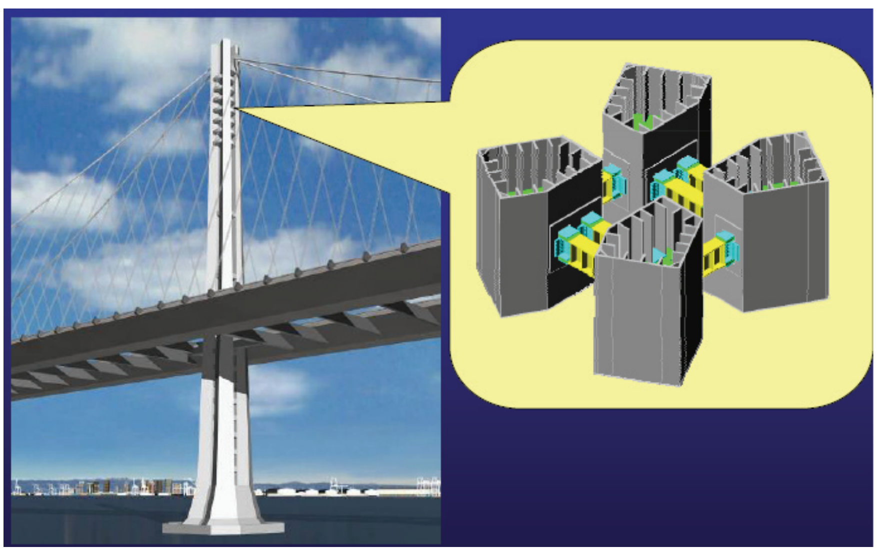

FIGURE 2-3 Bay Bridge Tower with Shear Links

Goodyear and Sun (2003) presented the preliminary design process for the state-of-the-art single-tower, cable-stayed solution for the San Francisco-Oakland Bay Bridge East Span replacement project. The lateral displacement ductility demand was established through non-linear analysis using the program ADINA, and the capacity of the tower was established by nonlinear pushover analysis. Comparison pushover curves of the tower with and without the links are presented in figure 2-4. The pushover curve of the tower without the links showed first yield of the concrete portal frame at less than 0.5 meter drift, which would require post-earthquake repair to the structure at approximately 1/2 the demand displacement for the SEE. The pushover curve of the tower with shear links showed no inelastic demand in the concrete tower elements until well beyond the SEE demand displacement. All inelastic demand for the single tower was confined to the steel links. Dimensions of the shear links are shown in figure 2-5.

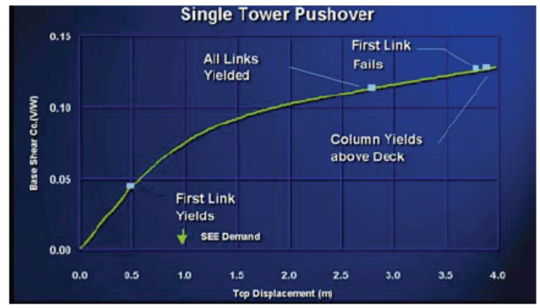

(a) (b)

FIGURE 2-4 Pushover Curves for the Tower; (a) With Shear Links, (b) Without Shear Links (Goodyear and Sun 2003)

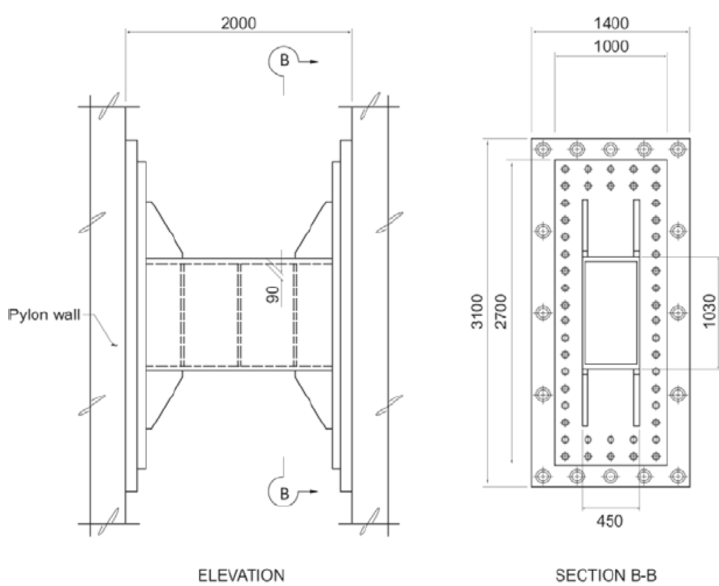

FIGURE 2-5 Shear Link Dimensions (Goodyear and Sun 2003)

2.3 Buckling Restrained Braces (BRB) as Passive Energy Dissipation Devices

2.3.1 General

A Buckling Restrained Brace (BRB), a.k.a. an Unbonded Brace, is a steel element that offers strength and energy dissipation while at the same time exhibiting well-distributed yielding in the buckling-restrained brace. Most commercially available BRBs consist of a steel core encased in a steel tube filled with concrete (although other concepts have also been developed and experimentally validated to achieve the same behavior). For the sake of this research, a brief overview on the work that has been developed for the BRB will be presented. A more detailed description of the mechanics of the BRBs with fully detailed design examples are presented in López and Sabelli (2004).

In this section, a brief description of the mechanics of the BRB is presented in section 2.3.2, and a summary of much of the early development of the BRB and the state of the art with respect to research and project validation testing is presented in sections 2.3.3 and 2.3.4, respectively. Some existing application of BRB to real building retrofit projects are then presented in section 2.3.5, followed by some seismic retrofit proposals for existing buildings using BRBs in section 2.3.6. Finally, as stated before, some applications of BRBs have been done developed for bridges; these are presented in section 2.3.7.

2.3.2 Mechanism of Buckling Restrained Braces

The basic principle in the construction of a BRB (Unbonded Brace) is to prevent Euler buckling of the steel core by encasing it over its length. This could be done in many ways; one such approach is to encase the steel core in a steel tube filled with concrete or mortar. The term "Unbonded Brace" derives from the need to provide a slip surface or unbonding layer between the steel core and the surrounding material, such that axial loads are only carried by the steel core. The materials and geometry in this slip layer should be designed to allow relative movement between the steel element and the concrete due to shearing and Poisson's effect, while at the same time preventing local buckling of the steel as it yields in compression. The concrete and steel tube encasement should provide sufficient flexural strength and stiffness to prevent global buckling of the brace, allowing the core to undergo fully-reversed axial yield cycles without loss of stiffness or strength. The concrete and steel tube also helps to resist local buckling. Figure 2-6 shows a schematic mechanism of the BRB.

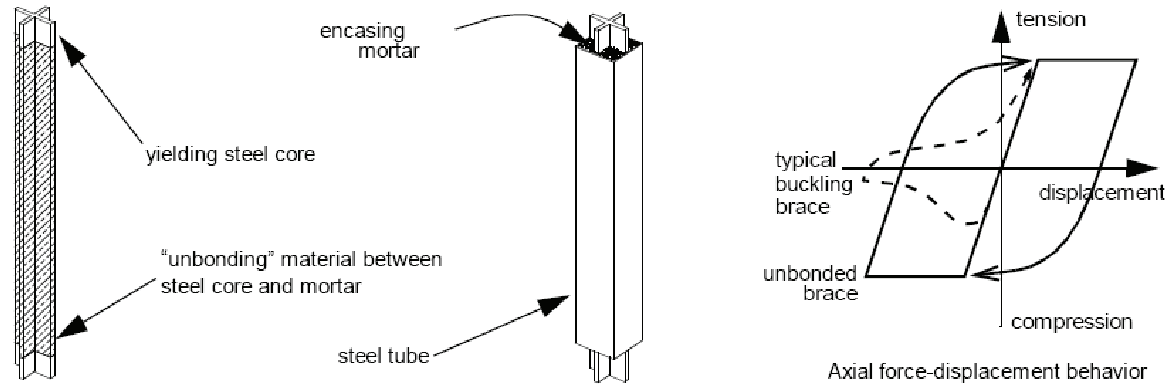

FIGURE 2-6 Schematic Mechanism of the Unbonded Brace (Clark et al. 2000)

2.3.3 Research Validation Testing

A variety of BRBs having various materials and geometries have been proposed and studied extensively over the last decade. A summary of much of the early development of unbonded braces which use a steel core inside a concrete filled steel tube is provided in Watanabe, et al., 1988. Since the 1995 Kobe Earthquake, these elements have been used in numerous major structures in Japan (e.g., Reina, and Normile, 1997).

Watanabe et al. (1988), Wada et al. (1989) and Watanabe et al. (1992) studied the effect of the outer tube confinement on the performance of the BRB. Series of tests have been performed with identical inner steel cores. The outer buckling strength p_e varied such that the ratio $\frac{p_e}{p_y}$ ranged from 3.5 to 0.55 (where p_y is the steel core's yield portion). It was observed that the ratio $\frac{p_e}{p_y}$ >1.5 resulted in a stable hysteretic behavior.

The first BRB tests in the United States were apparently conducted in 1999 (Aiken et al. 2000) for a project that is claimed to be the first building in the U.S. to use BRBs. Uniaxial component testing have been performed on three different brace sizes with capacities ranging from 1,217 kN to 2,155 kN.

Another set of tests were conducted for representative braces designed for a new hospital constructed in the San Francisco Bay Area (Ko et al. 2002). Two identical braces with a capacity of 2,033 kN were tested in that case.

Hasegawa et al. (1999) performed shake table testing on a BRB using the 1995 Kobe record and the 1940 El-Centro record. Stable hysteretic behavior was reported during the tests and the brace was subjected to a maximum axial strain of 7.2%

Clark et al. (2000) performed a series of large-scale tests on BRBs having yield forces of 1200, 1600, and 2100 kN. The BRBs were subjected to a cyclic loading protocol consistent with that used for testing steel beam-to-column connections. Additional tests studied the behavior of the BRBs under a near-field loading history, a displacement time history derived from a seismic analysis of an idealized 5-story building, and a low-cycle fatigue test. The BRBs exhibited stable cycle behavior with no degradation of strength or stiffness for all of the loading cycles up to failure, with a fracture failure of the core plate occurring inside the confining tube. The BRBs forces in compression was found to be slightly higher than that in tension; the difference between the peak tension load and the peak compression load ranged between 7.3 and 9.5 percent for the three specimens. Figure 2-7 shows the force vs. displacement curve of one of the BRBs being tested during basic loading history; figure 2-8 shows the hysteretic behavior of the same BRB during the low cycle fatigue test.

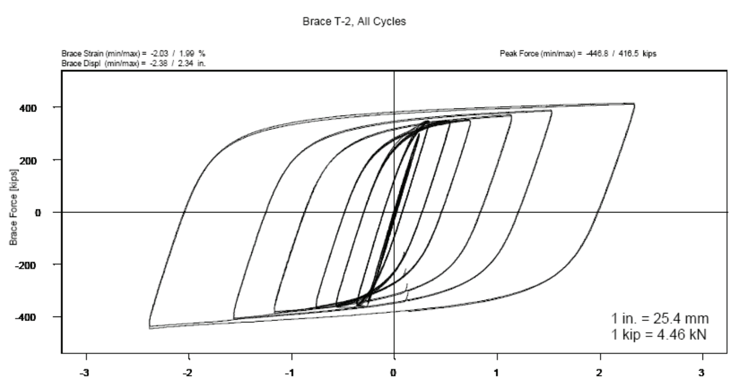

FIGURE 2-7 Force-Displacement Behavior of Brace Specimen T-2 during Basic Loading History (Clark et al. 2000)

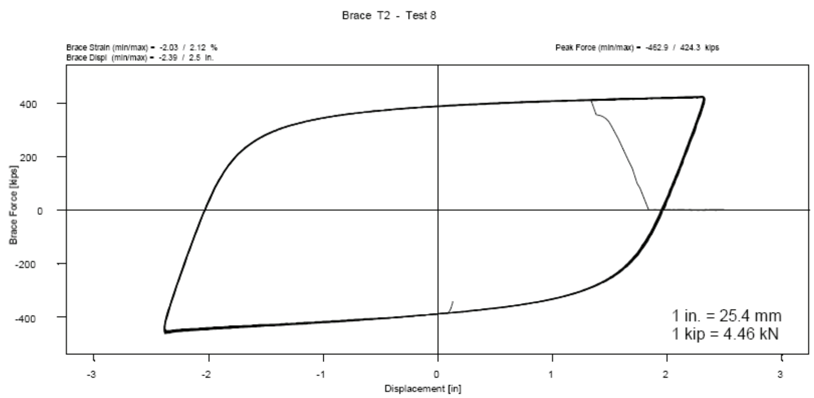

FIGURE 2-8 Hysteretic Behavior of Brace Specimen T-2 during Low Cycle Fatigue Tests (Clark et al. 2000)

For the sake of considering various possible BRB concepts, Iwata et al. (2000) performed tests on four types of specimens; three of them had a cross section composed of a plate of dimensions 16mm x167mm, while the fourth had a cross section composed of a built-up W section with dimensions 136mmx136mmx9mmx6mm. All core plates where designed to have the same cross area. Yield stress measured during the tests where 262.6 MPa for specimens 1, 2 and 3 and 289.1 MPa for specimen 4. The core plate of the first specimen was restrained by a rectangular hollow section filled with mortar; a soft rubber sheet was used for unbonding of the core plate to the mortar. The second specimen was the same as the first but without the rubber sheet and mortar. The core plate of the third was covered by joining together 2 channels and 2 plates with high strength bolts with an unbounded rubber sheet provided between the core and the restraining parts. The core plate of the fourth specimen was a built-up wide flange beam covered by a rectangular hollow section with no mortar in between. Figure 2-9 shows the cross sections of the 4 specimens. Stable hysteresis was observed up to a 1.0% strain in all specimens except for the second specimen in which a slight drop in strength started to occur. Specimens 2 and 4, having no unbounded material, fractured in tension as a result of cyclic degradation due low cycle fatigue precipitated by cyclic local buckling. Figure 2-10 shows the hysteretic behavior of all 4 specimens.

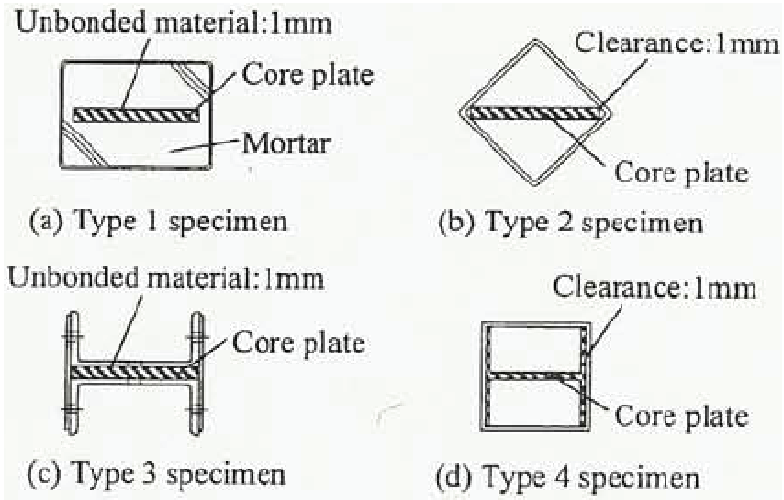

FIGURE 2-9 Experimentally Tested Cross Sections of the Unbonded Braces (Iwata et al. 2000)

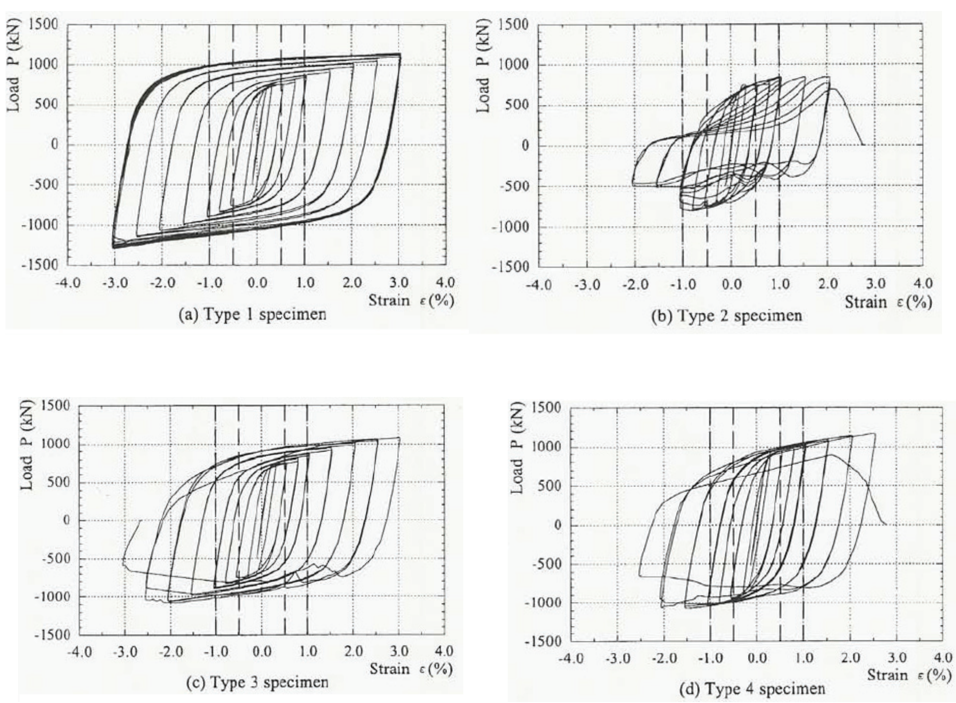

FIGURE 2-10 Hysteretic Behavior of Tested Unbonded Braces (Iwata et al. 2000)

2.3.4 Project Validation Testing

Black et al. (2004) tested the axial behavior of BRBs for a large retrofit project. Five specimens were tested with properties of existing braces implemented in two seismic retrofit projects in California. Each specimen had core lengths of approximately 3400mm and yield strengths ranging between 1217kN and 2155kN. Testing protocols consisted of two phases. First, the BRBs were subjected to an OSHPD loading protocol followed by additional tests which included large deformation, low cycle fatigue tests and simulated earthquake displacement tests. Ductile and stable hysteretic behavior was observed by the tested BRBs. The BRBs behaviors were modeled using a Bouc-Wen model (Wen 1976).

Lopez et al. (2002) presented a series of tests that were carried out in support of a new laboratory building. In these tests, the braces were tested in a subassembly to confirm the behavior of the BRB under frame loading conditions. This study focused on the behavior of the braces under frame-induced axial and rotational deformations, the appropriateness of assuming brace performance for frame conditions as determined from uniaxial component tests, and also the behavior of connections under frame lateral deformations. The subassembly tests demonstrated good hysteretic behavior of the BRBs. Their hysteretic and elongation behavior were proven not to be influenced by the combined axial and flexural demands associated with loading in a frame configuration.

2.3.5 Applications of Buckling Restrained Braces in RC Buildings

2.3.5.1 General

BRBS are well established in Japan, and have been used in more than 250 buildings there. Since 1999, they have also been implemented in the U.S. By 2010, there were apparently over 30 buildings in the United States, new or retrofitted, that were constructed with BRBs, with at least four implementations in reinforced concrete buildings. These four known implementations are reviewed below. However, the seismic performance of the details used to connect the BRBs to the RC frames has not been investigated experimentally.

2.3.5.2 Martin County Hall of Justice

The Martin County Civic Center is located in San Rafael California. It is a long and narrow building with dimensions of approximately 880 ft. long and 110 ft. wide. The original lateral load resisting system was comprised of concrete diaphragms, collectors and shear walls. Several deficiencies were discovered during a seismic vulnerability assessment; in particular, in the transverse direction, the stairs and elevator walls were found to be insufficiently reinforced to carry the seismic force demand. It was also found out that without retrofit, the diaphragm and the collectors would not be able to transfer seismic forces to the existing lateral resisting elements due to weak connections. In general, the existing lateral-load resisting elements were too weak to resist the seismic demands.

Shaw et al. (2000) presented the BRBs and shear walls concept that was chosen as a retrofit scheme for this historic building: thirteen locations were chosen for the lateral resisting elements (BRBs and shear walls) in the transverse direction, and nine locations in the longitudinal direction. Figure 2-11 shows a section in the building with the new BRBs and shear walls; figure 2-12 shows the BRB's connection detail used.

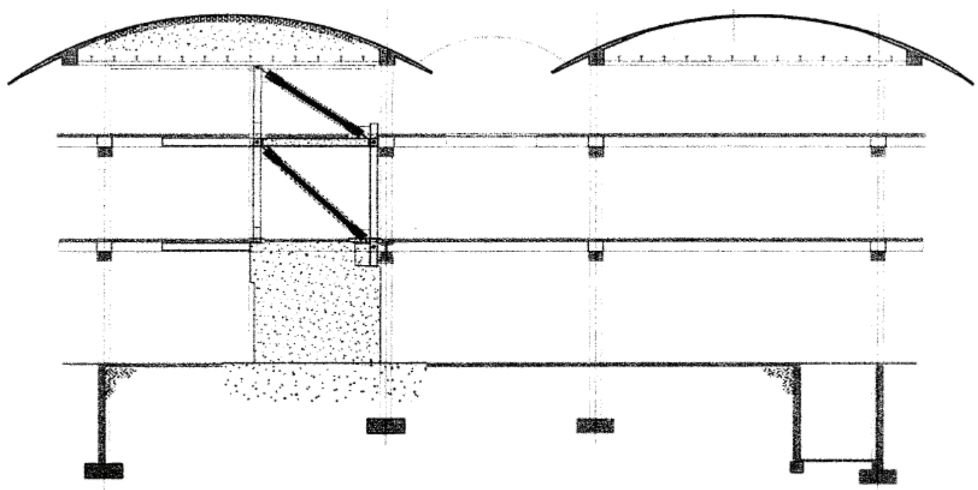

FIGURE 2-11 Martin County Hall of Justice Building Cross Section with Buckling Restrained Braces and Shear Walls (Shaw et al. 2000)

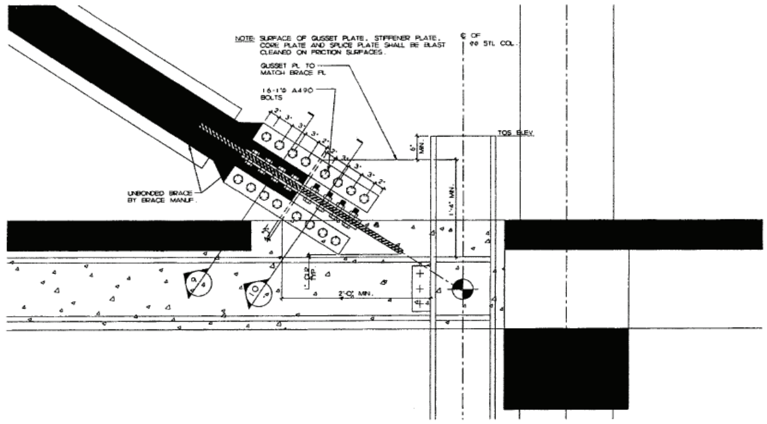

FIGURE 2-12 Buckling Restrained Brace Connection Detail Used in Martin County Hall of Justice (Shaw et al. 2000)

2.3.5.3 Wallace F. Bennett Federal Building

The Wallace F. Bennett Federal Building is located in downtown Salt Lake City, Utah. This is an 8-story; 300,000 sq. ft. office building that was constructed in the early 1960s. The reinforced concrete structure is constructed of eight-inch thick two-way flat plate floors, spirally-reinforced rectangular columns and pile foundations. It was well designed and constructed for its time, and has been carefully maintained over its life. Nonetheless, the Bennett Building lacked the many advances in seismic resistant design that have been incorporated into building codes since the time of its design and construction, and would not have been capable of resisting the large magnitude earthquake that the nearby Wasatch Fault is capable of generating.

Aiken et al. (2001) presented the structural steel framework that was constructed to interconnect the diagonal braces to form the seismic lateral force resisting system for the upgraded building. This framework was constructed of vertical and horizontal steel wide-flange members attached to the exterior of the building. The structural steel framework, to which the BRBs connect, was designed to remain safely below the yield stress level for the maximum forces deliverable by the BRBs, thus ensuring that yielding will be limited to the braces and not occur in the structural steel framework. Because the "damage tolerant" BRB system has predictable and ductile behavior with a large capacity for plastic deformation in both tension and compression, large amounts of seismic energy can be absorbed by the structure. This is important, because, although the building may sustain significant damage during an earthquake, it is expected to remain stable and capable of withstanding large aftershocks or possibly additional earthquakes without collapse, figure 2-13 shows a photograph of the building prior to rehabilitation and an architectural rendering of the upgraded building. Figure 2-14 shows two brace connection details assembled in the upgraded building.

FIGURE 2-13 Wallace F. Bennett Building Prior and Post Rehabilitation (Aiken et al. 2001)

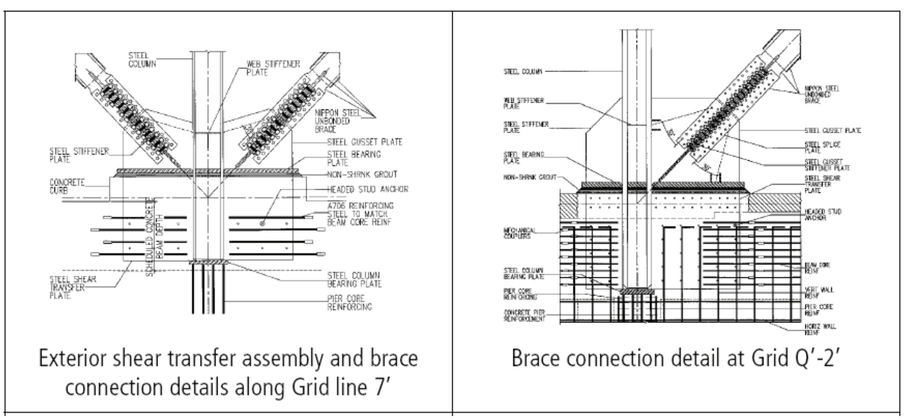

FIGURE 2-14 Buckling Restrained Braces Connection Details used in Wallace F. Bennett Building (Aiken et al. 2001)

2.3.5.4 Hildebrand Hall University of California, Berkeley, California

Morgan et al. (2004) presented the rehabilitation of the Hildebrand Hall with BRBs. This laboratory building was constructed in 1963 and is composed of a three-story tower structure atop an expanded two-story basement, and has overall plan dimensions of approximately 172 ft by 215 ft. Story heights are 15 ft and 17 ft for the first two basement levels, 18 ft for the first level, and 12 ft for the upper two levels. The building is shown in figure 2-15 prior and post rehabilitation. The tower structure roof and floor framing systems are post-tensioned lightweight concrete slabs supported directly on concrete columns and bearing walls. There are no beams, column capitals, or drop panels beneath the slab. The lateral force resisting system is composed of the floor slabs, which act as diaphragms, and transfer loads to the stair and elevator core concrete walls, and four large concrete box columns located at the corners of the structure. The walls are typically 10 in. thick and act as shear walls, transferring lateral forces down the structure to their foundations. The columns and slabs were not detailed to act in frame-action, and therefore provided negligible lateral strength. The retrofit scheme chosen included BRBF at the north and south ends of the building. The frames were detailed such that the columns do not pass through the slabs so as not to disrupt the existing post-tensioning tendons. The existing concrete box columns adjacent to the steel braces were thickened to provide the frames with continuous chord action for seismic overturning considerations. The capacity curve for the braced frame direction is shown in figure 2-16.

FIGURE 2-15 Hildebrand Hall University of California Prior and Post Rehabilitation (Morgan et al. 2004)

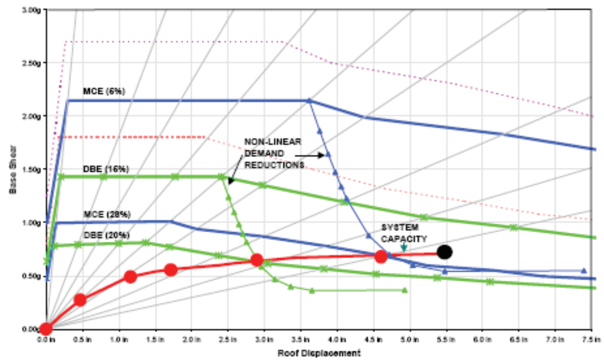

FIGURE 2-16 Capacity Curve for the Braced Frame Direction (Morgan et al. 2004)

2.3.5.5 Connections of BRBs to Concrete Columns

It appears in reviewing the literature that BRBs were generally not directly connected to RC columns. In fact, all the implementation examples described above used a secondary steel framing system itself attached to the RC frame or columns. However, evidence exists showing that conventional steel braces can be connected directly to RC columns, as shown for example in figure 2-17. Therefore, this suggests that BRB's gussets could also be modified to be directly connected to RC columns. However, experimental research investigating the performance of steel braces connected to RC columns could not be found.

FIGURE 2-17 Conventional Steel Braces Directly Connected to RC Columns (Professor Tena-Colunga, Universidad Autonoma Metropolitana, Mexico City, personal communications, 2008)

2.3.6 Seismic Retrofit Proposals for RC buildings

This section focuses on a few reported instances for which BRB were proposed to be used for the retrofit of RC buildings, not knowing at the time of this writing if these were actually implemented.

2.3.6.1 Webb Tower in University of Southern California in Los Angeles

Islam et al. (2006) presented the retrofit of the existing 14-story residential structure that was constructed in 1972 using lightweight concrete and has a rectangular floor plate with plan dimensions of approximately 75 ft x 105 ft. The gravity system of the building consists of a post tensioned concrete flat slab supported by rectangular concrete columns. The existing lateral system of the building consists of perimeter post-tensioned concrete moment frames with non-ductile detailing of the beams and columns. Several seismic deficiencies were discovered in the building including non-ductile detailing, excessive building deflection and joint shear overstress. The retrofit scheme developed used a single bay of BRBs having a design axial capacity of between 230 kips and 700 kips in combination with a reinforced concrete beam column frame on each side of the building. Figure 2-18 shows interstory drift demand in the east-west direction prior and post retrofitting; figure 2-19 shows the maximum beam plastic rotation demands in east-west direction prior and post retrofitting. Figure 2-20 shows a photograph of the existing building and an architectural rendering of the building with the proposed retrofit scheme.

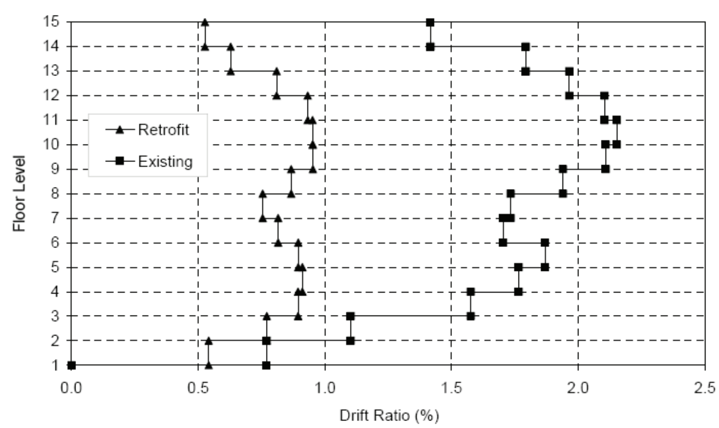

FIGURE 2-18 Interstory Drift Demand in East-West Direction for EQ- III Prior and Post Retrofitting for the Webb Tower (Islam et al. 2006)

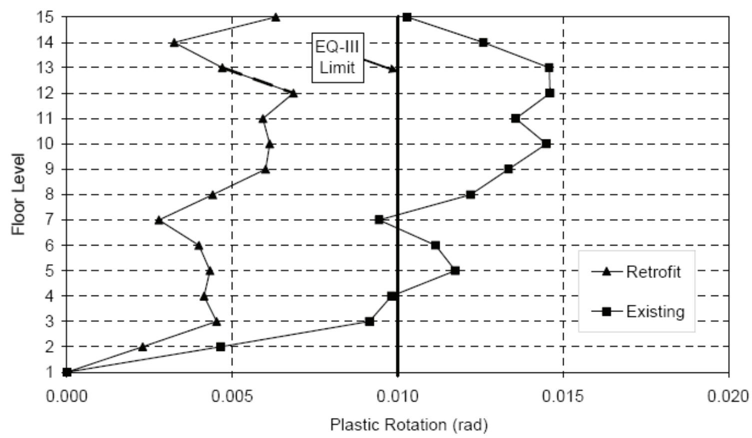

FIGURE 2-19 Maximum Beam Plastic Rotation Demand in East-West Direction for EQ- III Prior and Post Retrofitting for the Webb Tower (Islam et al. 2006)

FIGURE 2-20 Webb Tower in University of Southern California Prior and Post Rehabilitation (Islam et al. 2006)

2.3.6.2 RC Building in Avellino South of Italy

Di Sarno et al. (2007) proposed a seismic retrofit scheme using BRBs for a RC building located in Avellino in the south of Italy. The building was designed in the 1970's using only gravity loads. The lateral resisting system consists of a multi-storey RC frame with deep beams. Figure 2-21 shows a photograph of the existing building. BRBs were chosen to be installed along the perimeter of the structure to minimize the interruption of the building functionality and occupancy, as shown in Figure 2-22. Elastic static and dynamic (response spectrum) analyses were carried out with respect to the national and European standards for earthquake resistant structures. Capacity curves and nonlinear response history analyses were also carried out to assess the actual strength and ductility of the sample structures. A suite of seven natural spectrum-compatible records were selected to perform the nonlinear time-history analyses and to compute the mean values of the response parameters, either force-based or deformation-based. The response curves of the existing and retrofitted building are provided in figure 2-23.

FIGURE 2-21 Existing RC Building in Avellino South of Italy (Di Sarno et al. 2007)

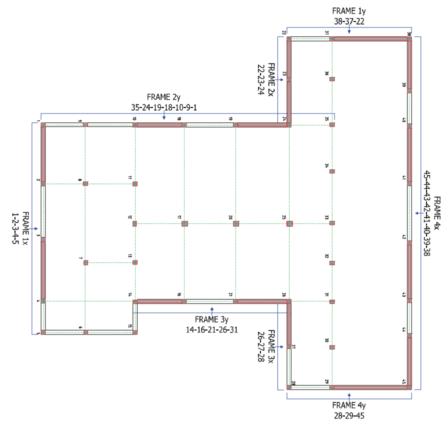

FIGURE 2-22 Proposed Layout of Buckling Restrained Bracing in the Avellino Building (Di Sarno et al. 2007)

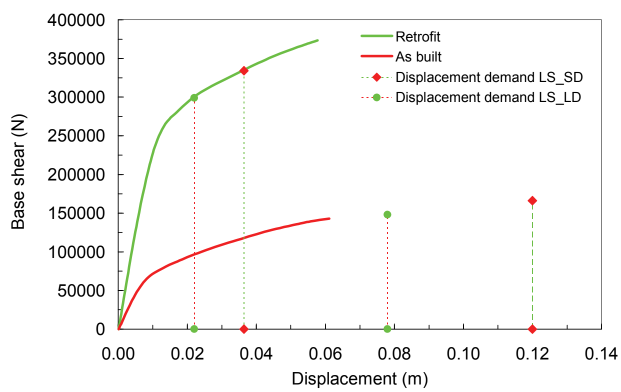

FIGURE 2-23 Response Curves for the Existing and Retrofitted Building in Avellino Italy (Di Sarno et al. 2007)

2.3.7 Implementation of Buckling Restrained Braces in Bridges

Implementations of BRBs in bridges have been recently contemplated; a few researchers have investigated the addition of BRBs to bridges to improve their seismic performance. Examples of these implementations are shown below.

Carden et al. (2006) studied the behavior of ductile end cross frames with BRBs in an 18 m long single span model of a two-girder bridge scaled down from a prototype by a factor of 0.4. The BRBs used Japanese LYP-225 steel with specified expected yield strength of 225 MPa. Each BRB had a core cross sectional area of 25 mm x 16 mm. The geometry of the end region and connection details is shown in figure 2-24. Experiments were performed on four BRBs identical to those used in the bridge model to determine their axial properties when subject to cyclic axial loads. Bolted connections were used to attach the BRBs to the grips of the load frame. The BRBs were subjected to different loading histories, including increasing amplitude, decreasing amplitude, reversed static, and dynamic loading.

Two cases were studied; first the BRBs were designed with a single bolt connection to provide an ideal pin-ended connection and then welded to provide a moment resisting, fixed-end connection as significant flexural actions in the braces were expected due to the fact that braces in the bridge model were relatively short compared to those used in building applications. The BRBs were designed with slip critical connections to provide optimal hysteretic behavior and prevent any negative effects from slippage of the connections on the cumulative plastic capacity of the brace. The bridge model with a BRB in the cross frame at each end was subjected to increasing amplitudes of transverse excitation using the 1940 El-Centro earthquake ground motion, scaled from 0.25 to 2.0 times the recorded level. For the pin ended connection model, figure 2-25 shows the transverse shear force plotted against the displacement of the deck slab, relative to the transverse bearing displacement adjacent to the bottom of the brace, at each end. Slight pinching was observed in the hysteretic loops due to slippage in the connections. For the fixed ended connection model, figure 2-26 shows the transverse bearing force displacement curve adjacent to the bottom of the brace, at each end. It was observed that the maximum force at the ends of the bridge increased while the overall displacements at the ends remained similar.

The axial deformations measured across the deformable length of the brace increased to about 60% of the expected maximum axial brace deformation based on the maximum horizontal end displacement. Therefore around 40% of the deformation is attributed to deformations outside the core of the brace, including relative displacements between the deck slab and the girders and deformations in the connections. Thus the efficiency of the braces was increased by prevention of slippage in the brace connections.

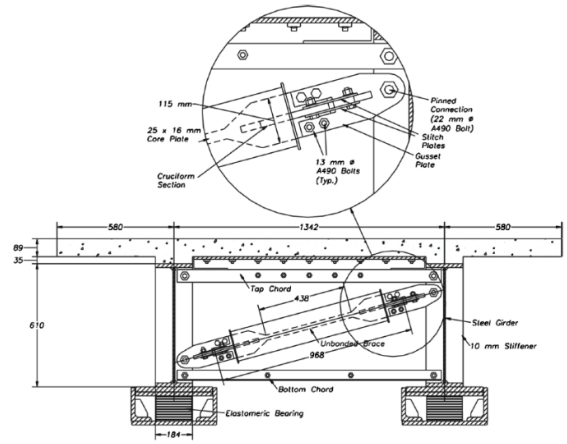

FIGURE 2-24 End Region Connection Detail (Carden et al. 2006)

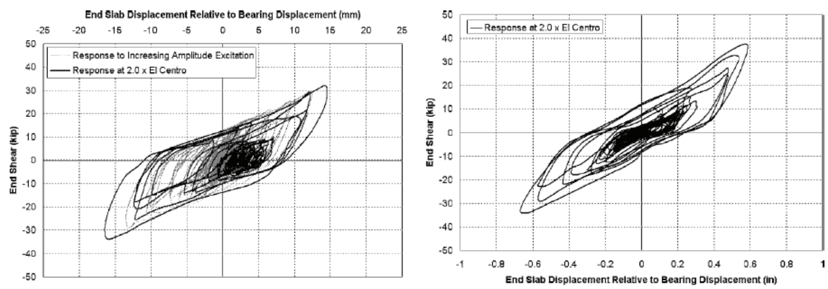

FIGURE 2-25 Transverse Shear Force Displacement Curves of the Deck Slab (Carden et al. 2006)

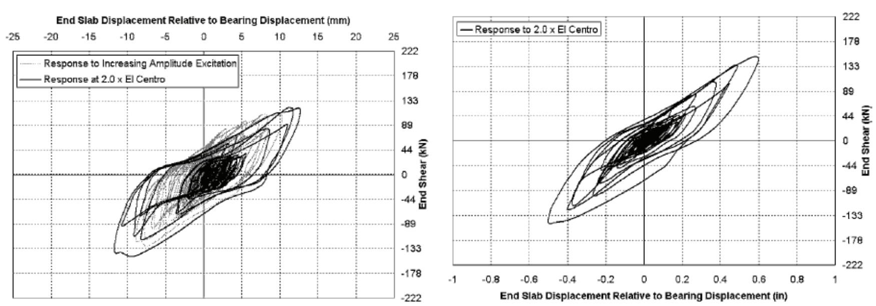

FIGURE 2-26 Transverse Bearing Force Displacement Curves of the Deck Slab (Carden et al. 2006)

Usami et al. (2005) studied the implementation of BRBs on steel arch bridges for seismic upgrading; the cross section of the BRB used is shown in figure 2-27. Experiments were performed using the experimental set-up is shown in figure 2-28. Deformations showing small amplitude of local buckling with a higher mode shape along the length of the steel plate were observed when taken out of the specimen after testing, as shown in figure 2-29. The BRB showed stable hysteretic behavior, as shown in figure 2-30.

The studied steel arch bridge was composed of reinforced concrete deck slab, steel girders and arch ribs as shown in figure 2-31 Cross-sections and dimensions of the bridge members are shown in figure 2-32. Nonlinear time-history analysis of the bridge showed that its seismic performance in the transverse direction was not sufficient. Retrofit to improve seismic response in the transverse direction considered replacing some lateral members and diagonals by BRBs; the two schemes shown in figure 2-33 were considered. In figure 2-33(a), lateral braces of the piers were replaced to reduce the strain demand in the side piers. In figure 2-33(b), in addition to BRB members installed in the side pier part, a total of twelve diagonals near two arch rib bases were replaced by BRBs. Nonlinear analysis of the two upgraded models predicted a maximum transverse displacement of the original bridge of about 50 cm, while the two upgraded bridges scenarios showed larger displacement demand of about 60 cm. Vertical displacements were almost similar in all cases. The transverse and vertical displacement demands at the mid-point of the steel girder are shown in figure 2-34.

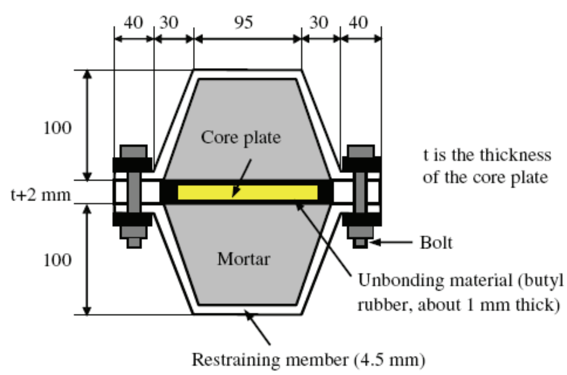

FIGURE 2-27 Experimentally Tested Cross Sections of the Unbounded Braces (Usami et al. 2005)

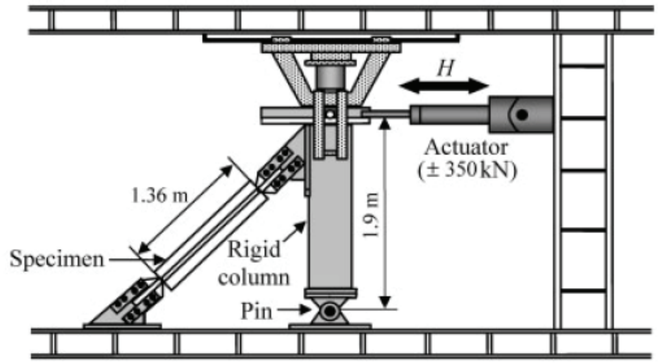

FIGURE 2-28 Experimental Set-Up for Buckling Restrained Bracing Tested by (Usami et al. 2005)

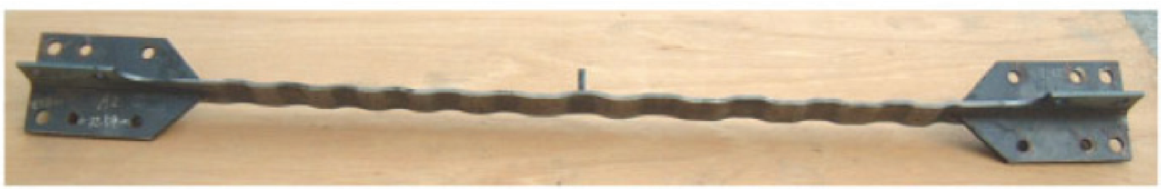

FIGURE 2-29 Higher Mode Shape Deformation of the Tested Specimen (Usami et al. 2005)

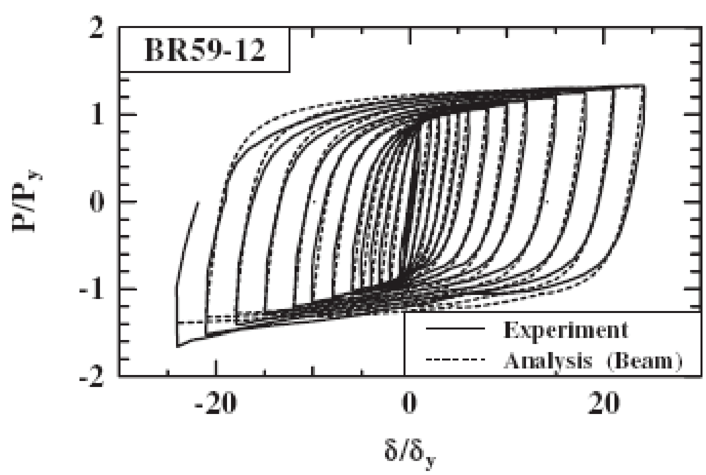

FIGURE 2-30 Hysteretic Behavior of the Tested Specimen (Usami et al. 2005)

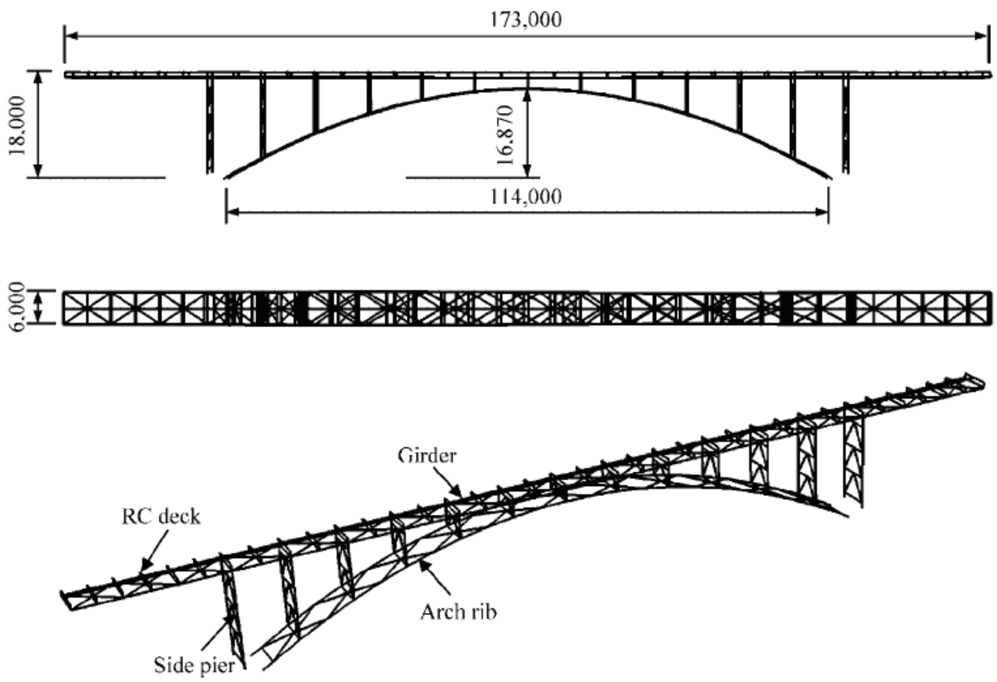

FIGURE 2-31 Layout of the Studied Arch Bridge (Usami et al. 2005)

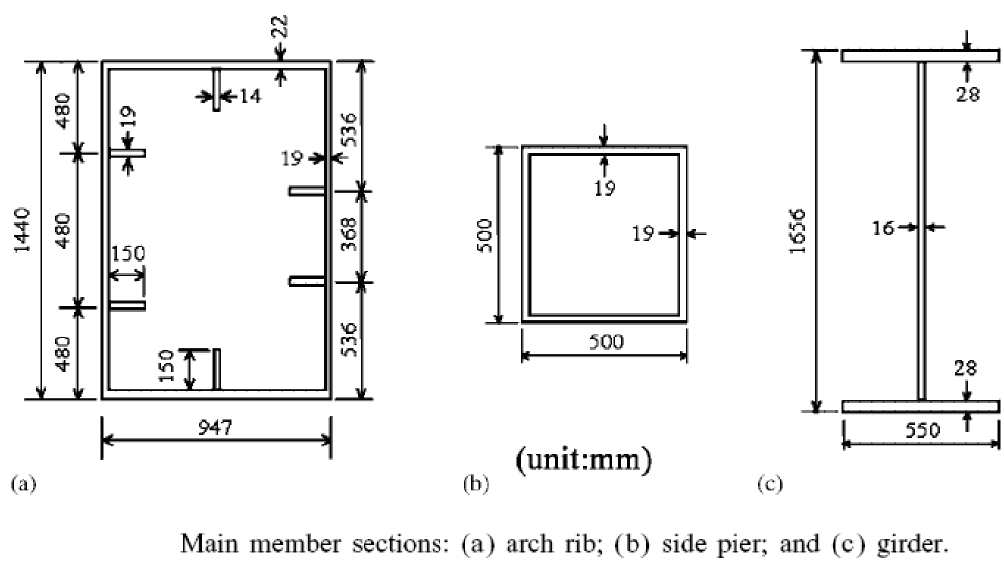

FIGURE 2-32 Cross Sections and Dimensions of the Main Members of the Arch (Usami et al. 2005)

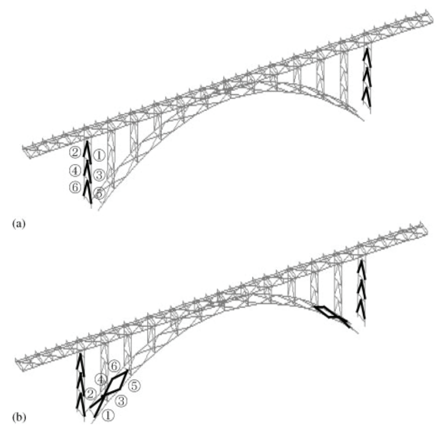

FIGURE 2-33 Locations of Buckling Restrained Braces for the two Retrofit Proposals (Usami et al. 2005)

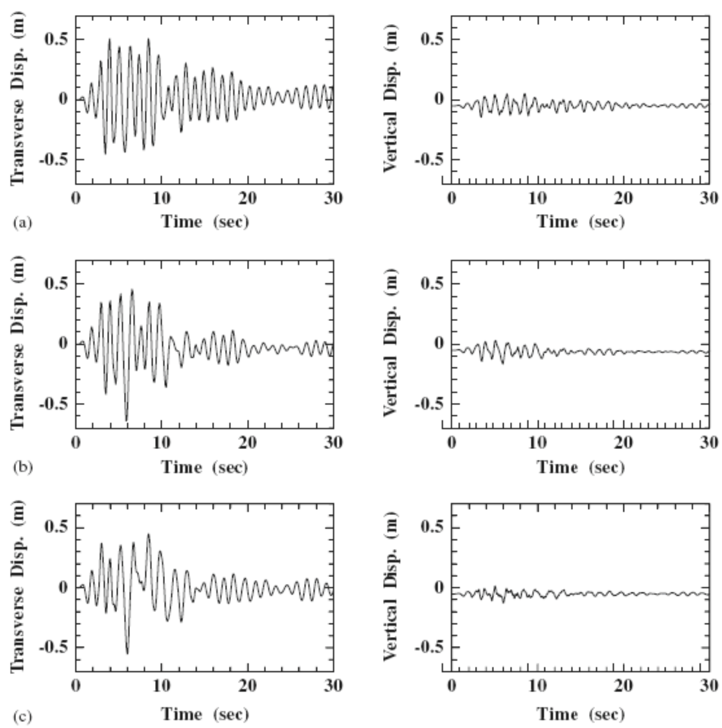

FIGURE 2-34 Transverse and Vertical Displacement Demands at the Mid-Point of the Steel Girder (Usami et al. 2005)

(a) Original Model, (b) First Upgrade, (c) Second Upgrade

Gray et al. (2006) proposed retrofitting the Alaskan Way Viaduct with a shoring system comprised of auxiliary structural steel frames and dampers. The Alaskan Way Viaduct is a 2.2 mile long double-decked, reinforced concrete viaduct carrying State Route 99 along the shoreline of Elliot Bay and past downtown Seattle. The viaduct consists of independent structural units comprising three bays each. The unit consists of four transverse frames that support longitudinal edge girders and stringers on two levels. Transverse sub-floor beams connect the girders and the stringers on each level. Several structural deficiencies were found including inadequate flexural capacity of the longitudinal reinforcement of the columns, inadequate lap splices, and joints were found to be vulnerable to degradation from high diagonal tensile stresses. Inadequate confining reinforcement in the columns was also observed. The seismic retrofit scheme proposed included two longitudinal structural steel frames and two transverse structural steel frames per three-bay unit of the structure. Steel jackets around the bases of the columns were also proposed to prevent degradation of the splices of the main column reinforcing bars located immediately above the footings. BRBs between adjacent units of the viaduct were also proposed to minimize pounding between them during an earthquake. Pushover analysis was performed verified by a nonlinear time history analysis to evaluate the response of the existing and retrofitted bridge. Figure 2-35 shows a rendering of the bridge with the proposed retrofit scheme.

FIGURE 2-35 Render of the Retrofit Scheme (Gray et al. 2006)

2.4 Seismic Vulnerability in Reinforced Concrete Bridges

The problems of non-ductile concrete structures is well knows and have been summarized by Park and Paulay (1975), Xiao et al. (1986), Ang. et al. (1989), Watanabe and Ichinose (1992), Wong et al. (1993), Buckle et al. (1994), and many other researchers. An overview of some of the factors responsible for seismically-induced damage to bridges is summarized by Priestley et al. (1996). Among those, many are beyond the scope of this study, such as underestimated seismic displacements (as a consequence of using elastic analysis or for other reasons) that can lead to span failure due to unseating at movement joints, or such as abutment slumping related to soft soils and consolidated abutment fill. Of interest here are column failures which may result from a number of deficiencies. Some of these deficiencies are reviewed below, as they must be appreciated if the structural fuse philosophy is to be implemented in otherwise non-ductile concrete bridges.

2.4.1 Flexural Strength and Deformation Capacity

In the past, prior to the enactment of ductile detailing in bridge specifications, column longitudinal reinforcement has often been lap spliced immediately above the foundation, with a splice length inadequate to develop the flexural strength of the column. Furthermore, because termination of the column longitudinal reinforcement was based on the design moment envelope obtained from by elastic analysis, without accounting for the effect of tension shift due to diagonal shear cracking, bridge columns could develop unintended flexural hinges at mid-height during a severe earthquake.

Research has been conducted by Priestley et al. (1996) and limit state parameters for the flexural strength of RC columns were defined as shown in figure 2-36 . Some key parameters required for the seismic assessment are labeled on that figure, and are described below.

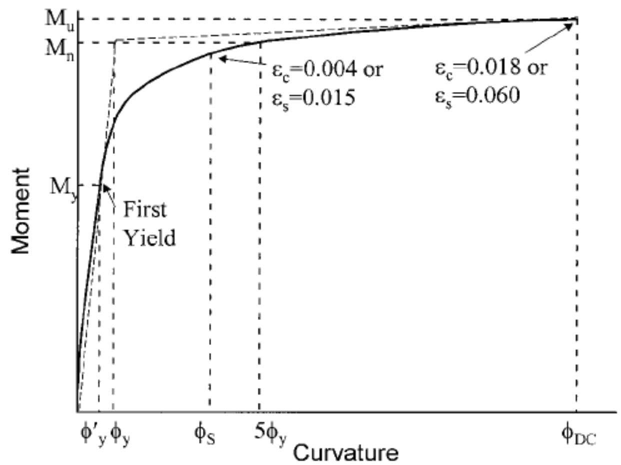

FIGURE 2-36 Definition of Limit State Parameters and Idealized Moment-Curvature Response (Priestley et al. 1996)

The parameters shown in the figure where defined as:

$$EI_{cr} = \frac{M_n}{\phi_y} \tag{2-1}$$

$$\phi_y D = 2.45\varepsilon_y \pm 15\% \tag{2-2}$$

$$\phi_s D = 0.015 - 0.02\left[\frac{P}{f_c^{/} A_g}\right] \pm 15\% \tag{2-3}$$

$$\phi_{DC} D = 0.068 - 0.068\left[\frac{P}{f_c^{/} A_g}\right] \pm 15\% \tag{2-4}$$

where φ_y is the Idealized yield curvature, $\varphi_y{}'$ is the curvature at first yield, φ_s is the curvature at first yield of the steel bars, φ_{DC} is the damage curvature, D is the column diameter, and I_{cr} is the cracked moment of inertia of the column.

Flexural Strength of RC columns has been also studied by various researchers. In particular, a commonly used plastic hinge method was proposed by Priestley and Park (1987) to identify the flexural strength of RC columns. Figure 2-37 shows a typical RC column ductility (flexural) capacity.

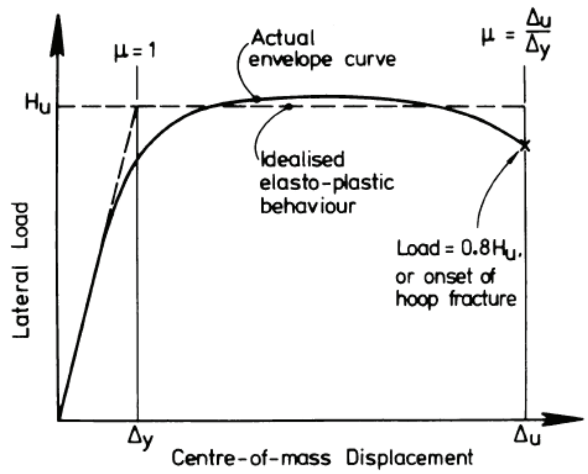

FIGURE 2-37 Ideal RC Column Ductility Capacity Curve (Priestley and Park 1987)

The idealized yield displacement could be calculated as:

$$\Delta_y = \frac{C\phi_y L^2}{3} \tag{2-5}$$

$$\phi_y = \frac{M_y}{E_c I_{cr}} \tag{2-6}$$

where: ϕ_y = Yield Curvature at column base; M_y = Yield moment; I_{cr} =Cracked moment of inertia and usually a value ranging from 0.5-0.75 I_g; L= Distance from point of maximum moment to point of contra-flexure; C=Factor to take into account the additional displacement due to foundation.

The maximum (damage) displacement can be calculated as:

$$\Delta_{\max} = \Delta_y + \theta_p \left(L - 0.5L_p\right) \tag{2-7}$$

$$\theta_p = (\phi_{\max} - \phi_y)L_p \tag{2-8}$$

where: $\phi_{\max} = \dfrac{\varepsilon_c}{c}$ or $\phi_{\max} = \dfrac{\varepsilon_s}{D' - c}$ whichever is less

and ε_c and ε_s are the damage limit state strains for concrete and steel respectively.

Figure 2-38 shows the CALTRANS specifications for column local displacement capacity for cantilever and fixed columns.

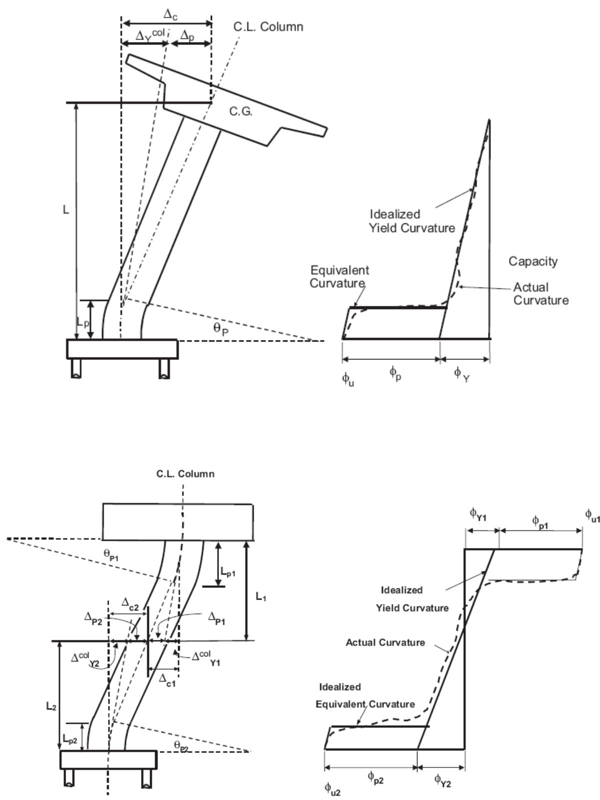

FIGURE 2-38 Local Displacement Capacity for Cantilever and Fixed Columns (CALTRANS)

2.4.2 Shear Strength of RC Columns

Inelastic shear deformation is unsuitable for ductile seismic response as shear failure is a brittle failure and involves rapid strength degradation; when the transverse reinforcement yields, the width of flexural-shear cracks increases, rapidly reducing the concrete shear resisting strength and leading to a brittle failure. Shear design was not considered to be a critical issue in bridges prior to 1970 as transverse reinforcement in older bridge columns were taken as No. 4 bars spaced at 12 in regardless the column size or the design shear force.

Priestley et al. (1994) studied the shear behavior of RC columns built prior 1970, and, on the basis of their experimental results, proposed a model modifying equations by Ang. et al. (1989).

That model, proposed that shear strength is composed of three independent components. The first component is from the concrete, V_c, and its strength depends on the ductility level achieved as it decreases with increasing ductility; this is because, when the plastic rotation increases, flexural-shear cracks increases which results in reducing the contribution on the concrete in resisting the shear force as shown in figure 2-39.

The second component is the truss component, V_s, and is a result of the contribution of the transverse reinforcement in the column; this component does not vary with ductility.

The third component is the axial load component, V_p, and depends on the column aspect ratio; it also does not vary with ductility, as is illustrated in figure 2-40.

The proposed model is expressed by:

$$V_n = V_c + V_s + V_p \qquad (2\text{-}9)$$

For Circular Columns:

$$V_c = k\sqrt{f_c^{/}}A_e \qquad (2\text{-}10)$$

$$V_p = P\tan\alpha = \left(\frac{D-c}{2a}\right)P \qquad (2\text{-}11)$$

$$V_s = \frac{\pi A_{sh} f_{yh} D^{/}}{2S}\cot 30^{\circ} \qquad (2\text{-}12)$$

where: k=Factor depending on column ductility; A_e= effective area of column and is taken as equal to $0.8A_g$; D= Overall section depth; D' = Distance between the centers of the peripheral hoop or spiral; c= Depth of compression zone; a= total column length for cantilever columns and half the column length for reversed bending columns; A_{sh} = Area of transverse reinforcement bar; f_{sh} = Yield strength of transverse steel.

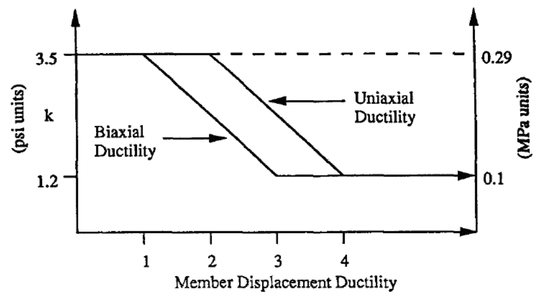

FIGURE 2-39 Degradation of Concrete Strength with Ductility (Priestley et al. 1994)

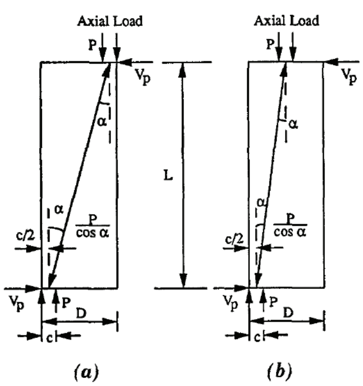

FIGURE 2-40 Contribution of Axial Force to Shear Strength of Columns (Priestley et al. 1994); (a) Reversed Bending (b) Single Bending

Experimental evidence has been presented to justify the accuracy of the model compared to previously introduced models, as shown in figure 2-41.

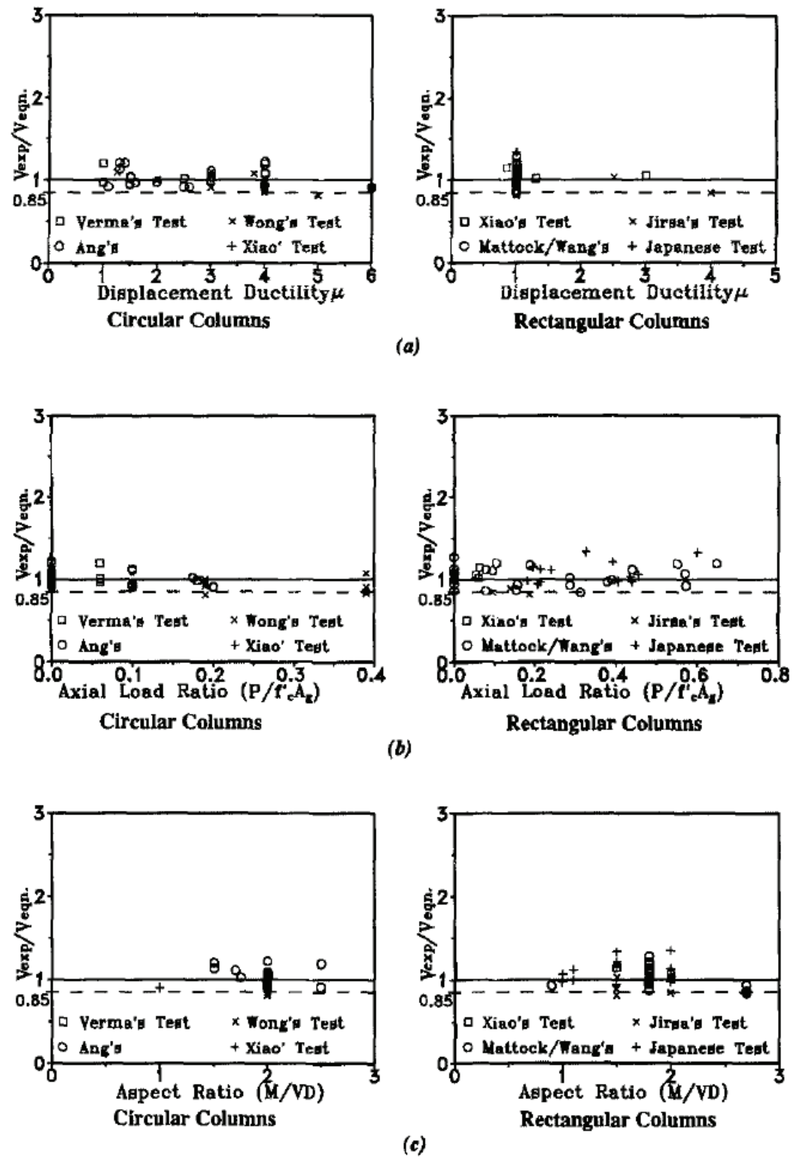

FIGURE 2-41 Experimental Comparison (Priestley et al. 1994); (a) Displacement Ductility (b) Axial Load Ratio (c) Aspect Ratio

2.4.3 Types of Failure in RC columns

In order to obtain satisfactory seismic response of RC structures, brittle failure modes are undesirable and it is common practice to rely on ductile inelastic response of plastic hinges to dissipate the seismic energy of an earthquake. In fact, it is deemed necessary to prevent these brittle failure modes, which include, for the case at hand, shear failure modes. This could be done by ensuring that the shear strength of a column exceeds the shear demand corresponding to the development of the maximum possible flexural strength (Ang et al. 1989).

Shear strength is a function of the flexural ductility, as when plastic-hinge rotations increase, the widening of flexure-shear cracks reduces the capacity for shear transfer by aggregate interlock, and the shear strength reduces. If the shear force demand corresponding to the development of flexural strength is less than the residual shear strength, V_r, ductile flexural response will occur. While if the shear force demand is greater than the initial shear strength, V_i, a brittle shear failure will occur. Finally, if the shear force is between the initial and residual shear strength, then shear failure will occur at a ductility corresponding to the intersection of the strength and force-deformation characteristics, as shown in figure 2-42 (Priestley et al. 1994).

That being said, caution should be made when designing or retrofitting RC bridge bents using a structural fuse concept. As ignoring the shear failure mode could result in a brittle failure of the columns before flexural yielding occurs. Taking the brittle shear failure more into account is further investigated in section 3.

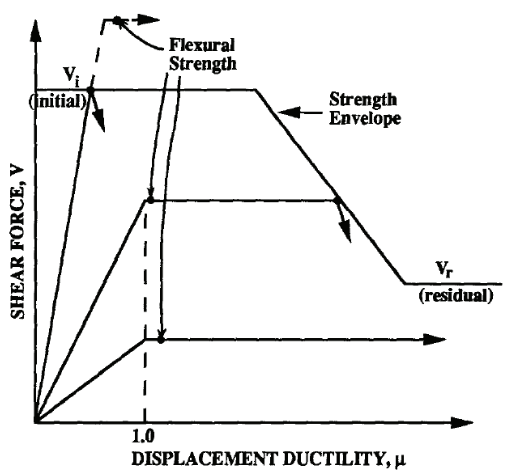

FIGURE 2-42 Interaction between Shear Strength and Ductility (Priestley et al. 1994)

2.5 Coupled Shear Walls

Coupled shear walls (CSWs) can provide an efficient structural system that can resist horizontal forces due to wind and seismic effects in multistory RC buildings. CSWs are usually built over the entire height of the building and are laid out either as a series of walls coupled by beams and/or slabs or as a central core structure with openings. Adding passive energy dissipation devices in between bridge columns could result in a system behavior similar to that of CSWs. Extensive analytical and experimental studies have been conducted on CSWs (e.g. Schnobrich 1977; Wight 1988; Paulay 1971; Kabeyasawa et al. 1982, 1984; and Chaallal, O. et al. 1996). These studies established valuable recommendations for the design and detailing of CSW buildings. They also demonstrate that the structural behavior of reinforced concrete CSWs is greatly influenced by the behavior of their coupling system, which in turn depends on the geometry and strength of the coupling beams relative to the walls. Figure 2-43 shows a schematic of the behavior of CSWs with different degrees of coupling, namely the ratio of the stiffness of the coupling beam relative to the walls. Depending on the degree of coupling, CSWs falls into one of the following three categories: a series of linked isolated walls (low coupling), CSWs with effective coupling (intermediate coupling), and walls with openings (pierced walls, high coupling).

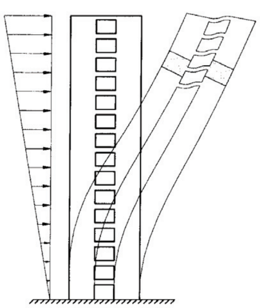

2-43 Behavior of CSW with Different Degrees of Coupling (Chaallal, O. et al. 1996)

2.6 Summary

This section described the state-of-the-art with respect to the structural fuse concept and its implementation in buildings. Past developments of on BRBs and their implementation in buildings and bridges was then described, followed by a brief summary of the key failure mechanisms in RC columns.

It has been shown that the more restrictive definition and implementation of the structural fuse concept is relatively recent; it is a seismic design philosophy that has been recently implemented in building, but not as frequently in bridges, and not so in the substructures of short- and medium-span bridges. As a result, it is worthwhile to investigate possible ways to introduce a structural fuse system into bridge bents that would include lateral load resisting disposable and replaceable elements to increase the seismic performance of bridges.

BRBs were shown to be a fairly mature technology, with well known hysteretic behavior and already implemented successfully in many buildings and a few bridges. For that reason, BRBs appear to be a desirable device to consider implementing a structural fuse retrofit strategy. This could be done for reinforced concrete bridges in need of seismic retrofit, but also as part of an integrated design procedure for accelerated bridge construction (ABC). However, bridge columns could also be fitted with different types of fuses, and other types are also worthy of consideration. Any of the concepts considered would have to be validated experimentally and analytically.

SECTION 3
STRUCTURAL FUSE STRATEGY FOR SEISMIC RETROFIT OF REINFORCED CONCRETE BRIDGE BENTS

3.1 Introduction

Recent earthquakes in the United States, Japan and several other countries have demonstrated the vulnerability of reinforced concrete bridges to seismic damage. These vulnerabilities have varied from total collapse, such as in the 1995 Kobe earthquake (Schiff 1998), to minor cracking and concrete spalling, such as in the 2001 Nisqually earthquake (Ranf et al. 2007). Typical RC bridge piers designed prior to the 1970's where not detailed to prevent shear failure due to seismic excitation nor detailed for ductile response. For example, 13mm (No. 4) ties or hoops spaced at 300mm (12") where typically used irrespective of column size, longitudinal reinforcement, or seismic demands. Also, short lap splices where used in column hoops and ties; as a result, these would open-up after concrete cover spalling during a severe earthquake that brought these structures into the inelastic range.

Providing reliable mechanisms for dissipation of the destructive earthquake energy is key for the safety of structures against intense earthquakes. Since these bridges where not designed to sustain plastic deformations for energy dissipation, and even the ones that are designed for that would require significant amount of repair after a seismic attack. It was thought about introducing a new element to the system to sustain the seismic demand while preserving the integrity of the bridge main components (structural fuse).

Here, a structural fuse concept is proposed in which structural steel elements are added to an RC bridge bent to increase its strength and stiffness, and also designed to sustain the seismic demand and dissipate all the seismic energy through hysteretic behavior of the fuses, while keeping the RC bridge piers elastic. Several types of structural fuses can be used and implemented in bridges; the focus in this section will be on using Buckling Restrained Braces (BRB) for the retrofit of RC bridge bents. The characteristics and seismic performance of

BRBs have been described in section 2. Other types of structural fuses will be discussed in later sections with different types of bridge bents.

A parametric study for a prototype RC bridge bent retrofitted using BRBs is presented in section 3.2. That study was conducted to investigate trends in behavior as a function of key parameters defining the proposed structural fuse system, while using BRBs of different stiffnesses and strengths as the energy dissipating fuses.

A general parametric study in section 3.3 is introduced in two dimensional charts; a close form solution is also developed as an alternative to the charts.

The results of nonlinear dynamic analyses conducted to validate the proposed static procedure are presented in section 3.4, followed by a design example.

Finally, a general retrofit procedure is presented in section 3.5, with emphasis on how to select suitable values for the various parameters presented earlier to achieve a satisfactory structural fuse system.

3.2 Parametric Study of an RC Bridge Bent with BRB

3.2.1 Idealized Model and Definitions

A parametric study has been conducted to develop an understanding of the impact of various factors on helping to achieve the desired structural fuse behavior described earlier in section 2. For this purpose, an analytical model for a general RC bent with a BRB system inserted as a structural fuse has been developed. An equivalent elasto-plastic model with strain hardening was used for the RC columns and an elastic perfectly plastic model was used for the BRB.

Figure 3-1 schematically shows a simple two column RC bridge bent retrofitted using an inverted V (chevron) BRB system.

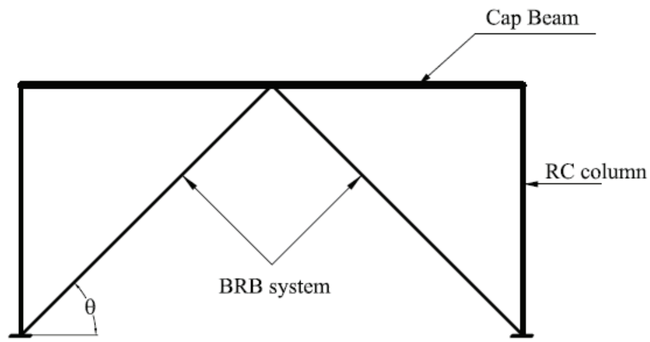

FIGURE 3-1 Layout of Studied Retrofit Scheme

The general pushover curves corresponding to this idealized structural system and some of the important parameters used in this study are shown in figure 3-2,

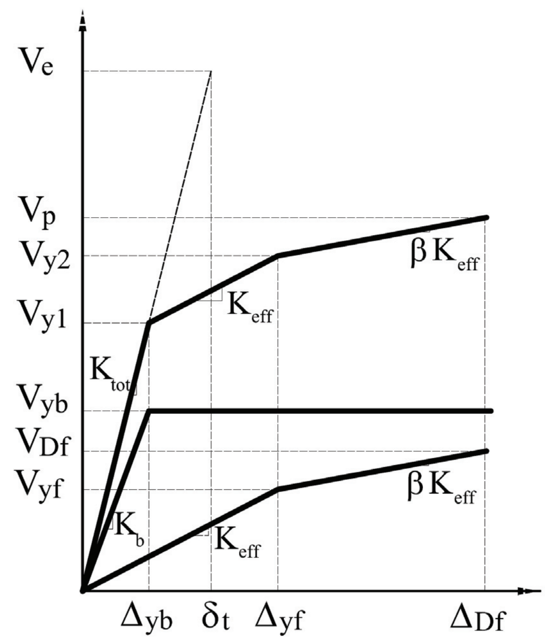

FIGURE 3-2 General Pushover curve

where k_{eff}=Effective lateral stiffness of the RC frame obtained from the cracked moment of inertia; β =Post-yield strain hardening stiffness ratio of the RC frame; k_b =Lateral stiffness of the BRB system; Δ_{yb}=Lateral yield displacement of the BRB system; Δ_{yf} =Lateral yield displacement of the RC frame; Δ_{Df} =Lateral displacement at the onset of RC frame damage (i.e. column shear or flexural failure); V_{yf} =Yield strength of the RC frame; V_{Df} =Maximum strength of the RC frame; V_{yb} =Yield strength of the BRB; V_{y1} =Total system yield strength; V_{y2} =Strength of the total system at the point of RC frame yielding; V_p =Lateral strength of the total system at the onset of column failure; V_e =Seismic demand on the total system if the system behaved elastically; δ_t=expected displacement after frame retrofit (also called target displacement).

For the studied system, the cap beam is conservatively assumed to be rigid; such a large difference in stiffness between the cap beam and the columns is typical in many bridge applications. Also columns here are assumed to be rigidly connected to the base and foundation.

For the current assumptions, the RC bridge bent can be considered as a single degree of freedom system with lumped mass at the superstructure level and whose effective lateral stiffness is equal to:

$$K_{eff} = 2\left[\frac{12E_c I_{cr}}{H^3}\right] \tag{3-1}$$

where H=total column height; I_{cr}=Cracked moment of inertia; E_c=Concrete modulus of elasticity.

Lateral stiffness of the added BRB system can be calculated as follows:

$$K_b = \frac{2E_s A_b \cos\theta}{cL_b} \tag{3-2}$$

where L_b=BRB total length; c=Yielding portion of the BRB; A_b=Cross sectional area of a single BRB.

Adding the BRB system increases the lateral stiffness of the bare frame and the resulting total system stiffness is equal to:

$$K_{tot} = K_{eff} + K_b \tag{3-3}$$

This decreases the effective period of the primary structure, changing it from:

$$T_{frame} = 2\pi\sqrt{\frac{m}{K_{eff}}} \tag{3-4}$$

for the bare RC bridge bent to:

$$T_{eff} = 2\pi\sqrt{\frac{m}{K_{tot}}} \tag{3-5}$$

for the retrofitted structure.

Decreasing the effective period reduces the displacement demand on the retrofitted structure and the target displacement, δ_t, (as per the NEHRP 2003 Recommended Provisions) becomes:

$$\delta_t = C_0 C_1 \frac{S_a T_{eff}^2 g}{4\pi^2} \tag{3-6}$$

where C_0 is a modification factor to relate the displacement of the control point to the displacement of a relative single-degree-of-freedom system and determined as:

$$C_0 = \frac{\sum_{i=1}^{n} w_i \phi_i}{\sum_{i=1}^{n} w_i \phi_i^2} \tag{3-7}$$

and C_1 is a modification factor to account for the influence of inelastic behavior on the response of the system, and calculated as:

$$C_1 = \left(1 + \left(\frac{S_a}{V_y/W} - 1\right)\frac{T_s}{T_{eff}}\right)\left(\frac{V_y/W}{S_a}\right) \tag{3-8}$$

where V_y is the effective yield strength of the equivalent bilinear system.

The target displacement can also be calculated (as per AASHTO 2009 Guide Specifications for LRFD Seismic Bridge Design) as:

$$\delta_t = R_d \frac{S_a T_{eff}^2 g}{4\pi^2} \tag{3-9}$$

where R_d is a displacement magnification factor for short periods (less than $1.25\,T_s$) and is calculated as:

$$R_d = \left(1 - \frac{1}{\mu_D}\right)\frac{1.25 T_s}{T_{eff}} + \frac{1}{\mu_D} \tag{3-10}$$

where T_s is the period at the end of constant design spectral acceleration plateau, μ_D is the maximum local member displacement ductility demand (less than 6 for multiple column bents).

The value of the yield displacements of the BRB can be calculated as follows:

$$\Delta_{y_b} = \frac{f_{y_{BRB}} c L_b}{E_s \cos\theta} \tag{3-11}$$

where c is defined as the ratio of the yielding length of the BRB, L_{ysc}, to the total BRB length, L_b.

The yield displacement of the RC frame is defined using the equations adopted in the CALTRANS-Seismic Design Criteria (SDC) and originally introduced by Priestley et al. (1987):

$$\Delta_{yf} = \frac{2\varphi_y (L_m)^2}{3} \tag{3-12}$$

where L_m =is the distance from point of maximum moment to point of contra-flexure, and φ_y =Yield curvature of the bare frame, calculated as:

$$\phi_y = \frac{M_y}{E_c I_{cr}} \tag{3-13}$$

For the structural fuse concept, it is required that the BRB yield displacement, Δ_{yb}, be less that the yielding displacement of the frame, Δ_{yf}. As a result, the BRB stiffness and strength must be chosen to limit the demand on the structure such that the system displacement reached for the maximum credible earthquake is less than Δ_{yf}, concentrating energy dissipation in the BRB yielding, keeping the bare frame elastic. In this concept, a parameter , μ_{max}, is defined as the maximum displacement ductility that the system can withstand to ensure that the BRB acts as a structural fuse without yielding the RC bare frame, and calculated as the ratio between the yield displacement of the RC frame, Δ_{yf}, and the yield displacement of the BRB, Δ_{yb}, such that:

$$\mu_{\max} = \frac{\Delta_{yf}}{\Delta_{yb}} \tag{3-14}$$

Note that exceeding μ_{max} is not necessarily a system failure limit state, because in some instances, if this limit is exceeded, ductile yielding in the RC bent columns would occur.

However, in such a case, after removal of the BRB, the yielded RC frame would not return to its original undamaged position. In other instances though, yielding in the RC columns is not desirable and exceeding μ_{max} could be more problematic. This could be the case in non-ductile bridge columns that either cannot sustain large plastic deformations to ensure energy dissipation, or that lack adequate transverse reinforcement and could suffer sudden shear failure.

To ensure that the BRB behaves as a structural fuse, dissipating all the seismic energy while the bridge columns remain elastic, another parameter, μ_f, is defined as the maximum displacement ductility that the frame can withstand, and calculated as the ratio between the yield displacement of the column and the system displacement reached for the maximum credible earthquake (target displacement):

$$\mu_f = \frac{\delta_t}{\Delta_{yf}} \tag{3-15}$$

If shear failure is ignored and only flexural failure is considered, frame ductility must always be less than 1 to ensure that yielding in the RC column does not take place. Further constrains will be added to this parameter later in this section for the case when brittle shear failure is considered.

Another parameter, μ_b, is defined as the BRB displacement ductility and is calculated as the ratio between the system displacement reached for the maximum desired earthquake (target displacement) and the yield displacement of the BRB, Δ_{yb}:

$$\mu_b = \frac{\delta_t}{\Delta_{yb}} \tag{3-16}$$

It is effectively the global displacement ductility (or the displacement ductility) of the retrofitted structure, and should not exceed the maximum displacement ductility, μ_{max}, to insure that the BRB acts as a structural fuse.

Another parameter that affects the choice of the BRB stiffness is the BRB strain which can be calculated as:

$$\varepsilon_b = \frac{\Delta_e \cos\theta}{cL_b} = \frac{\delta_t \cos\theta}{cL_b} \tag{3-17}$$

That strain, in compliance with the AISC seismic provisions, is conservatively taken here to not exceed 1.5%, although it is known that a BRB could extend up to 3% before fracture occurs under repeated cyclic inelastic loading (Iwata et al. 2000).

From the above equations, the following relationship between $\mu_{\max}, \mu_f, \mu_b$ can be established:

$$\delta_t = \mu_f \Delta_{yf} = \mu_b \Delta_{yb} \tag{3-18}$$

$$\therefore \frac{\Delta_{yf}}{\Delta_{yb}} = \frac{\mu_b}{\mu_f} = \mu_{\max} \tag{3-19}$$

ensuring that μ_f is always less than 1 ensures that μ_b remains less than μ_{max}.

As mentioned earlier, shear failure is a brittle failure mode that must also be considered. It can occur when inadequate transverse reinforcement is provided such that shear failure would precede or prevent full development of ductile flexural hinging. To take into account the possibility of shear failure as a part of the structural fuse concept, the shear strength of the frame columns, V_i, must first be calculated and compared to the nominal flexural shear strength, V_n. Shear failure will occur if $V_i < V_n$, while flexural failure will occur if $V_i > V_n$; figure 3-3 schematically shows the relationship between shear and flexural failure. Given that a frame displacement ductility of 1 corresponds to the nominal flexural failure, if brittle shear failure is the governing failure mode, then the limited displacement frame ductility at which the column remains elastic, μ_{freq}, would be less than 1. From similar triangles, a simple relationship between the limited displacement frame ductility and the shear and flexural shear strength is calculated as:

$$\mu_{freq} = \frac{V_i}{V_n} \tag{3-20}$$

Figure 3-4 shows the limited frame ductility with respect to $\frac{V_i}{V_n}$

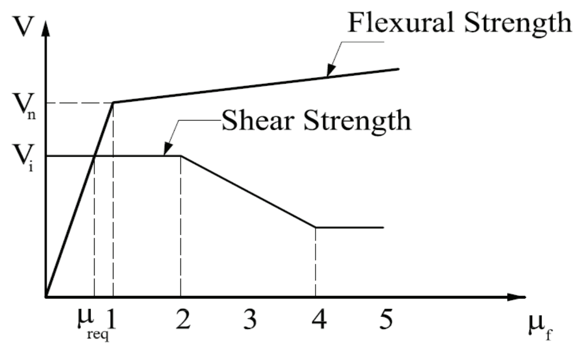

FIGURE 3-3 Relation between Shear and Flexural Failure

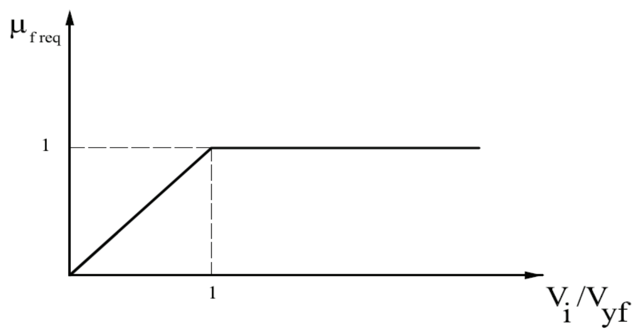

FIGURE 3-4 Desired Frame Ductility ($\mu_{f_{req}}$)

3.2.2 Case Study

A parametric case study was conducted to study the trends in behavior of a RC bent retrofitted using a BRB. A response spectrum was constructed based on the American Association of State Highway and Transportation Officials (AASHTO 2009 Guide Specifications for LRFD Seismic Bridge Design), and the National Earthquake Hazard Reduction Program Recommended Provisions (NEHRP 2003), for a region exposed to severe ground shaking, with a maximum credible design earthquake having S_S=2.1g and S_1=0.8g, for site soil-type class B and a 2% probability of exceedance in 50 years. The corresponding elastic response spectrum is shown in figure 3-5.

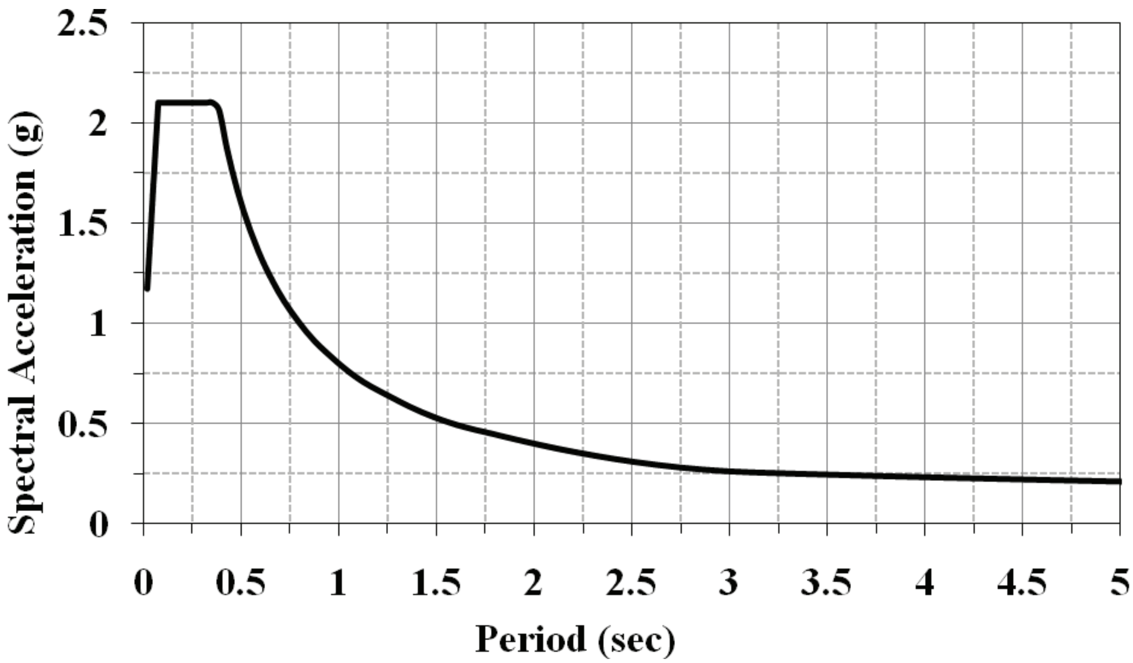

FIGURE 3-5 Elastic Response Spectra (ξ=5%)

A typical RC bridge bent has been chosen for this case study from a three span continuous Prototype Bridge having bents spaced at 36m (120') from each other and circular concrete columns of 1250 mm (50") diameter, *D,* fixed at the base. The width, *L*, of the typical bent is equal to 12.5 m (500") and its height, *H*, is 6.25 m (250"), with BRBs introduced in a chevron configuration at an angle, θ, of 45° between the braces and the horizontal, as shown in figure 3-6.The columns longitudinal reinforcement ratio, ρ, is considered to be 2% and their typical transverse reinforcement consists of, #4 bar spaced at 300 mm (12") center-to-center. The effective deck weight (girders + concrete slab + guard rails) was taken as 6.9 kPa (1 psi) for simplicity which, considering the tributary area of the bent resulted in concentrated lumped mass, *m*, at the superstructure level equal to 0.33 kN.sec^2/mm (1.86 kips.sec^2/in). The stiffness of the selected frame calculated using equation (3-1) was found to be 166 kN/mm (934 kip/in). The frame yield displacement, calculated using equation (3-12), was 23.5 mm (0.94").

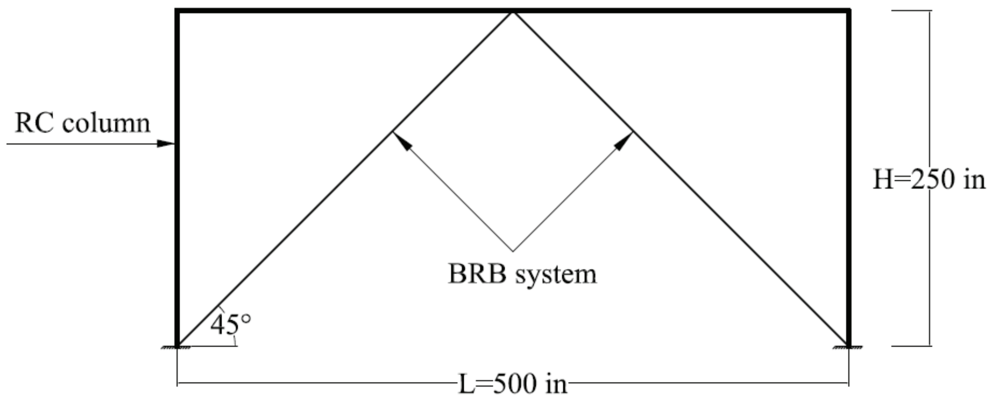

FIGURE 3-6 Chosen Retrofit Scheme

Two dimensional graphs were constructed to investigate the sensitivity of selected key parameters as a function of different BRB cross sectional areas, A_b, and yielding lengths of BRB, c, expressed as a function of the total BRB length. Note that these two parameters, together, directly define BRB strength and stiffness. For the specified design earthquake spectral demands, the value of the frame ductility is calculated for several BRB cross section area and ratio of the yielding length of the BRB to the total BRB length. Substituting equation (3-5) into (3-6), a relation between the target displacement, δ_t, and the total stiffness, K_{tot}, can be rewritten as:

$$\delta_t = R_d \frac{S_a mg}{K_{tot}} \tag{3-21}$$

Substituting equation (3-21) into (3-15), the total system stiffness, K_{tot}, required to achieve specified frame ductility, μ_f, can be rewritten as:

$$K_{tot} = R_d \frac{S_a mg}{\mu_f \Delta_{y_f}} \tag{3-22}$$

For the studied case, the value R_d will be taken as 1. Constant values of frame ductility, μ_f , are chosen from which the total system stiffness required to achieve the desired frame ductility is calculated, using equation (3-22). The calculated stiffness is then translated into BRB required area and yielding length ratio using equations (3-3) and (3-2). Figure 3-7 shows the variation in frame ductility, μ_f , for different values of BRB areas and yielding length ratios, each line representing a fixed value of μ_f less than 1 to ensure elastic response of the RC frame.

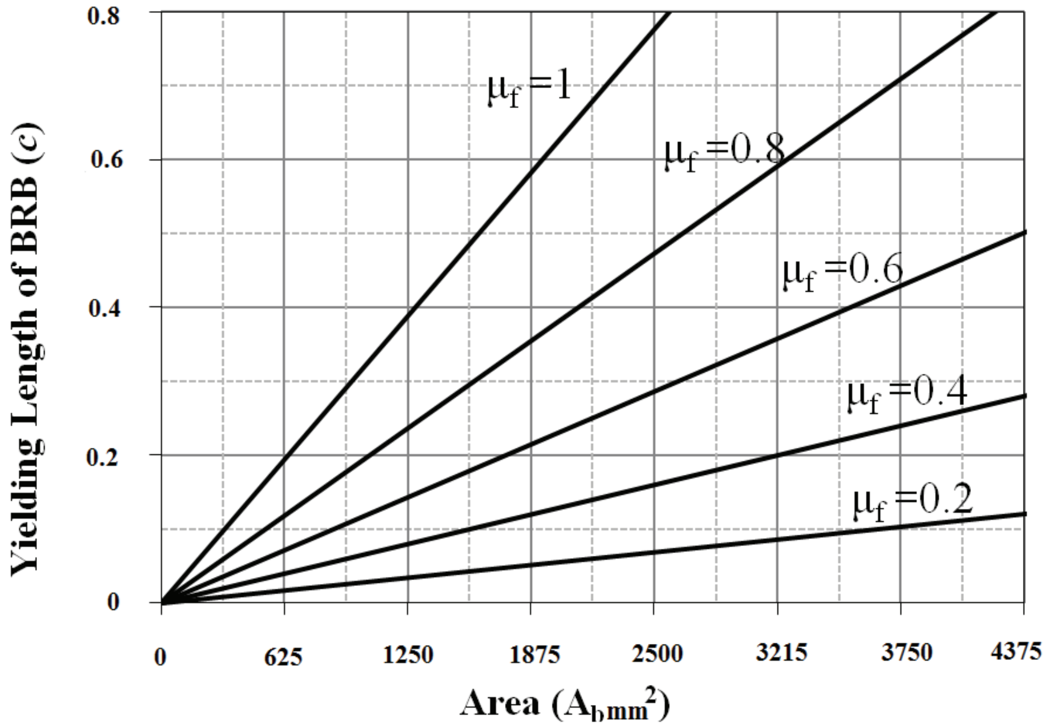

FIGURE 3-7 Frame Ductility Values for different BRB Areas and Yielding Length Ratios

For example, if A_b= 1875 mm^2 (3in^2) and c=0.6, the frame ductility, μ_f, corresponding to the chosen bent configuration and the chosen spectral acceleration from figure 3-7 will be equal to 1.

Substituting equation (3-21) into equation (3-16), and rewriting:

$$K_{tot} = R_d \frac{S_a mg}{\mu_b \Delta_{y_b}} \tag{3-23}$$

Substituting equation (3-23) into equation (3-11), the value of the total stiffness can be rewritten as:

$$K_{tot} = R_d \frac{S_a mgE_s \cos\theta}{\mu_b f_{y_{BRB}} cL_b} \tag{3-24}$$

again, R_d will be taken as 1.

Constant values of BRB ductilities, μ_b, are chosen, from which the required total system stiffness is then calculated from equation (3-24) to achieve that ductility, the calculated stiffness is then translated into BRB required area and yielding length ratio using equations (3-3) and (3-2). Figure 3-8 shows the variation in BRB ductility, μ_b, for different BRB areas and yielding length ratios, each curve representing a constant value of μ_b. Here, a minimum required value of BRB ductility of 4 is arbitrary chosen before μ_f reaches 1, to make sure that sufficient ductility is present in the structural fuse system to dissipate the seismic energy before yielding in the columns occur. For the same example above, the value of the BRB ductility, μ_b, from figure 3-8 is equal to 5.

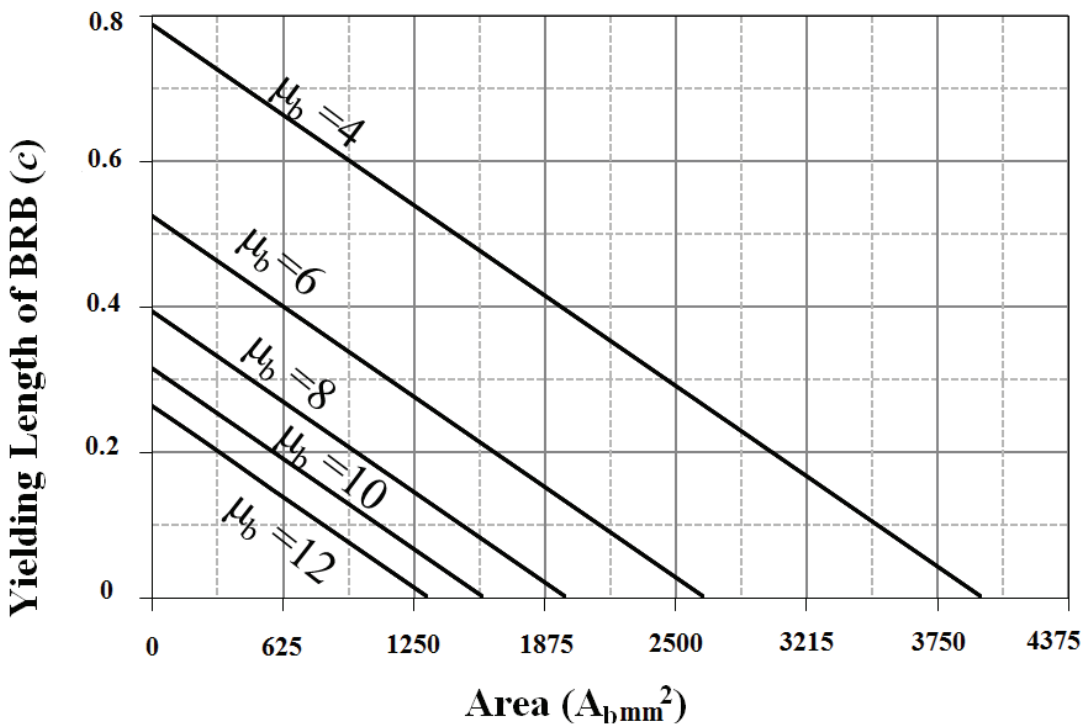

FIGURE 3-8 BRB Ductility Values for different BRB Areas and Yielding Length Ratios

Substituting equation (3-21) into (3-17), the value of the total stiffness can be rewritten as:

$$K_{tot} = R_d \frac{S_a mg \cos\theta}{\varepsilon_b c L_b} \tag{3-25}$$

Figure 3-9 shows the variation in BRB strain, ε_b, for different BRB areas and yielding length ratios for the 3 values of BRB strains of 1%, 1.5% and 3%.

It is observed from the previous figures that for a given yielding length of BRB, increasing the BRB area reduces μ_f, μ_b, and ε_b, as expected since the structure becomes stiffer and the spectral target drift reduces. Likewise, for a given BRB area, decreasing c has the same effect.

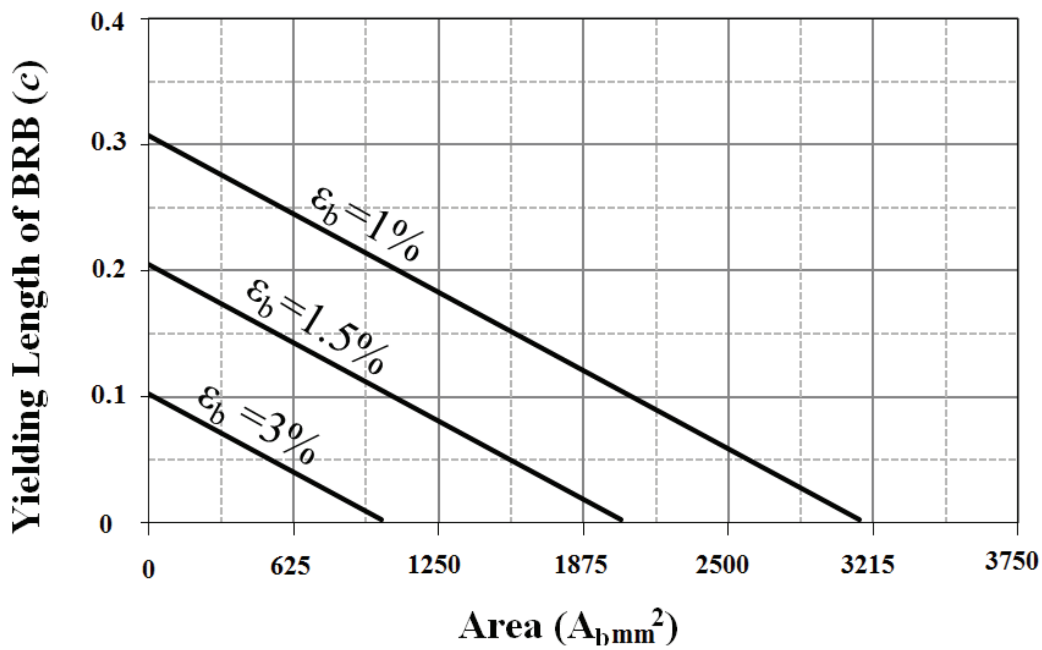

FIGURE 3-9 BRB Strain Values for different BRB Areas and Yielding Length Ratios

A plot combining the results from figures 3-7 to 3-9 is presented for the typical RC bent mentioned above. The region of admissible solution is shown in the shaded area of figure 3-10. It's boundaries are defined as follows: A maximum value of μ_f equal to 1 is chosen so that the RC frame remain elastic (assuming that no brittle shear failure will occur in this case); a minimum value of μ_b equal to 4 is chosen to ensure sufficient ductility in the system, and; a conservative constrain of ε_b<1.5% is chosen to comply with the AISC seismic provisions and to ensure that no fracture occurs in the BRB. If brittle shear failure was to be the governing failure mode, the region of admissible solution would simply be modified for a lesser value of μ_f as mentioned before.

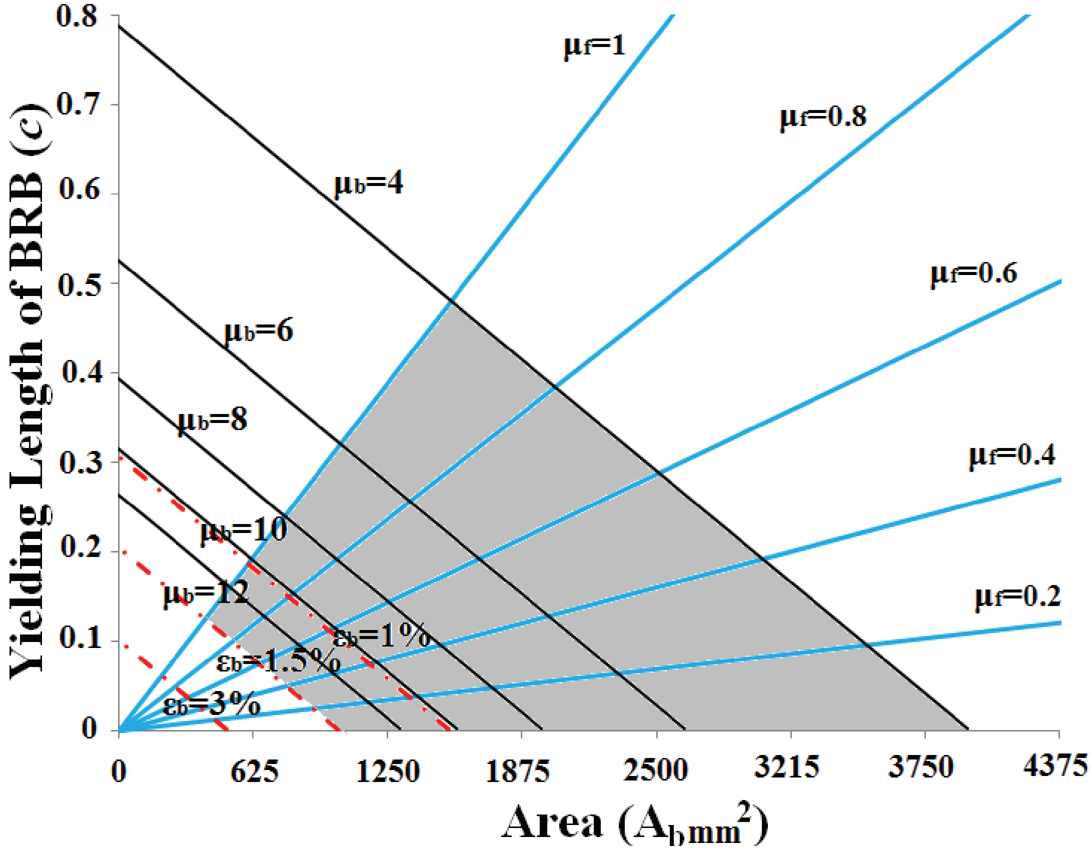

FIGURE 3-10 Region of Admissible Solution for the Typical Studied RC Bent

Similar plots were constructed for various columns diameters and various BRB angles to investigate the effect of changing these parameters on the region of admissible solutions. Figures 3-11 to 3-13 are matrices of plots that present results for the same set range of values for D and θ, where D increases horizontally and θ increases vertically. These figures respectively show the variation in frame ductility, the variation of BRB ductility and the variation of BRB strain, with respect to different BRB areas and yielding length ratios for different column diameters and different BRB angles.

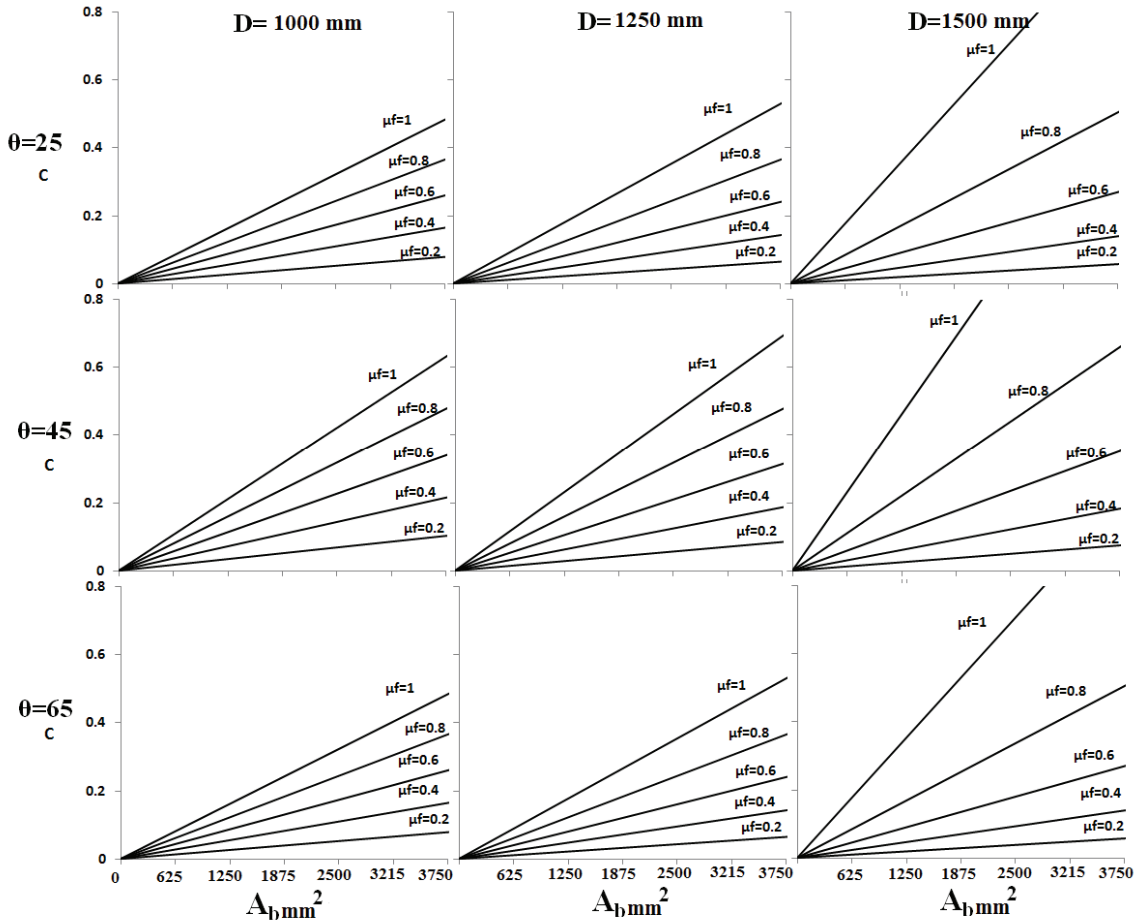

FIGURE 3-11 Frame Ductility Values for different Column Diameters and BRB Angles

Note, as shown in equations (3-22) and (3-25), that μ_f is a parameter that depends on spectral acceleration. Yet, both μ_f and ε_b always appear in the plots as straight lines. This is because each frame ductility value and each BRB strain value corresponds to a single value of spectral acceleration, regardless of its location on the spectrum, itself corresponding to a given value of period (i.e. total stiffness).

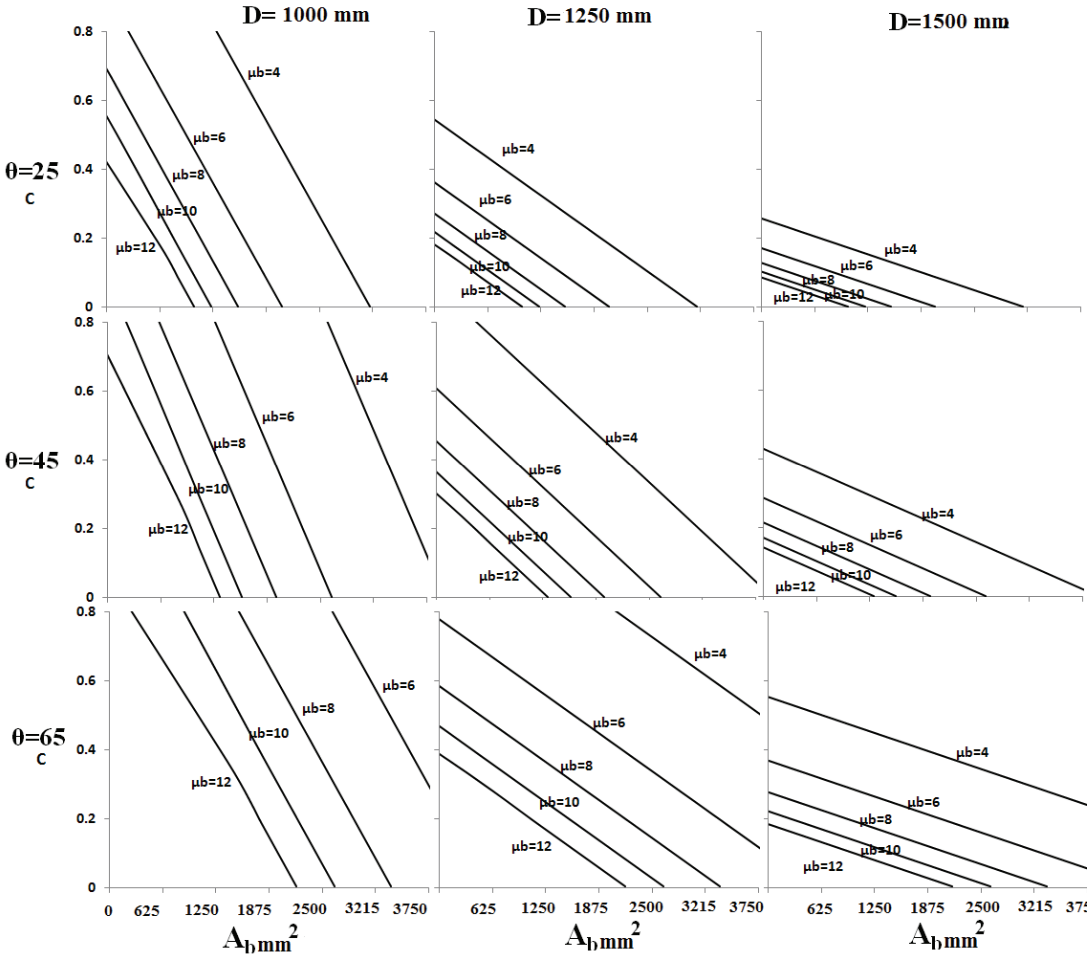

FIGURE 3-12 BRB Ductility Values for different Column Diameters and BRB Angles

Note from equation (3-24) that μ_b is also an acceleration dependant parameter. Yet, here, changing the values of the yielding BRB length ratio, *c,* will affect the value of the total stiffness, and accordingly, of the fundamental period and the spectral acceleration. That means that a specified value of BRB ductility could be achieved by different values of total stiffnesses according to the chosen value of *c* and A_b. In this case, when μ_b is drawn as straight lines, it is because the fundamental period of the total system lies in the constant acceleration zone of the spectra. As shown in some cases in figure 3-12, the line curves at small BRB areas and long yielding length ratios which corresponds to cases outside of the constant acceleration region of the spectra.

The effect of changing column height was also investigated for a typical RC bridge bent with columns of 50 in diameter. It is observed in figure 3-14 that for a given yielding length ratio and BRB area, increasing the column height would increase μ_b, and ε_b, while it would decrease μ_f as expected, since increasing the column height would increase the target displacement, resulting in increasing the value of the BRB ductility as well as the BRB strain. Also increasing the column height would result in decreasing both of the stiffness and strength of the bare frame while at the same time increase its yielding displacement, this will result in decreasing the value of the frame ductility for a fixed period of the retrofitted frame.

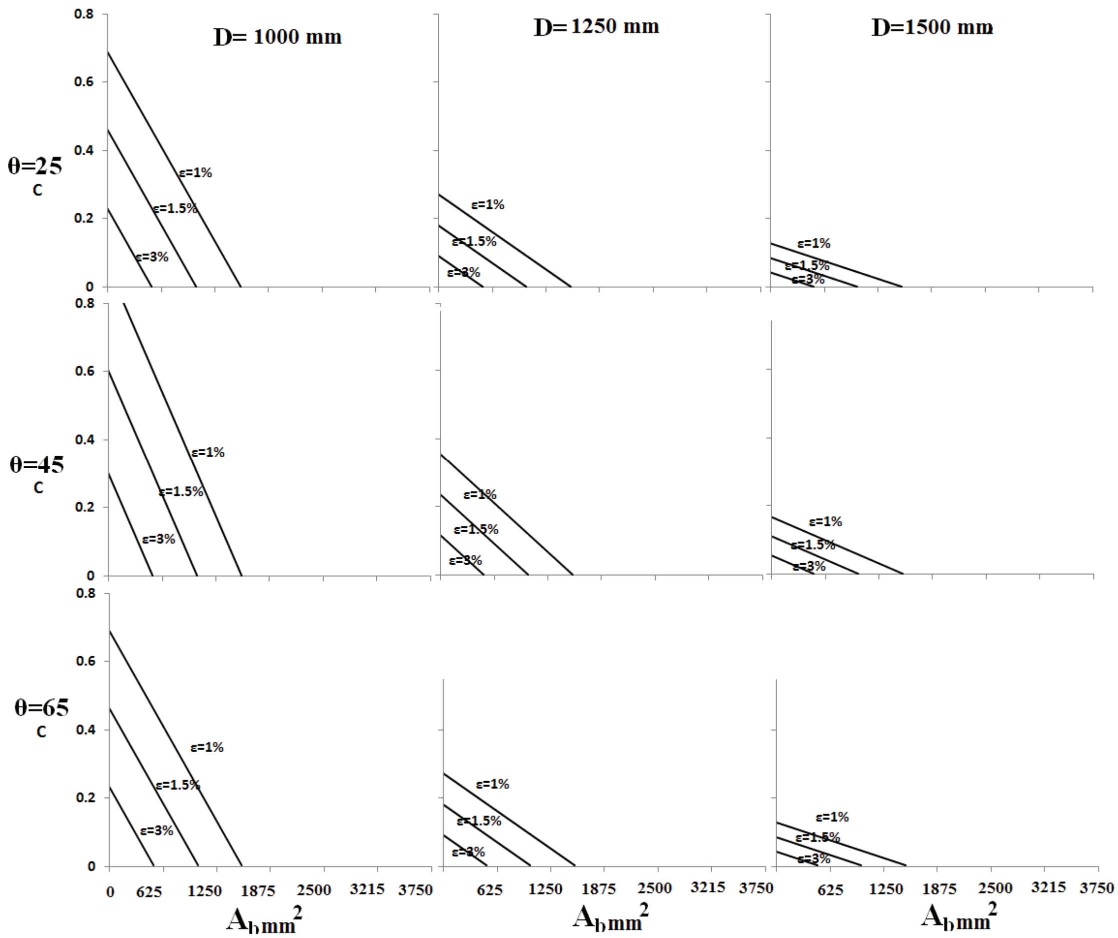

FIGURE 3-13 BRB Strain Values for different Column Diameters and BRB Angles

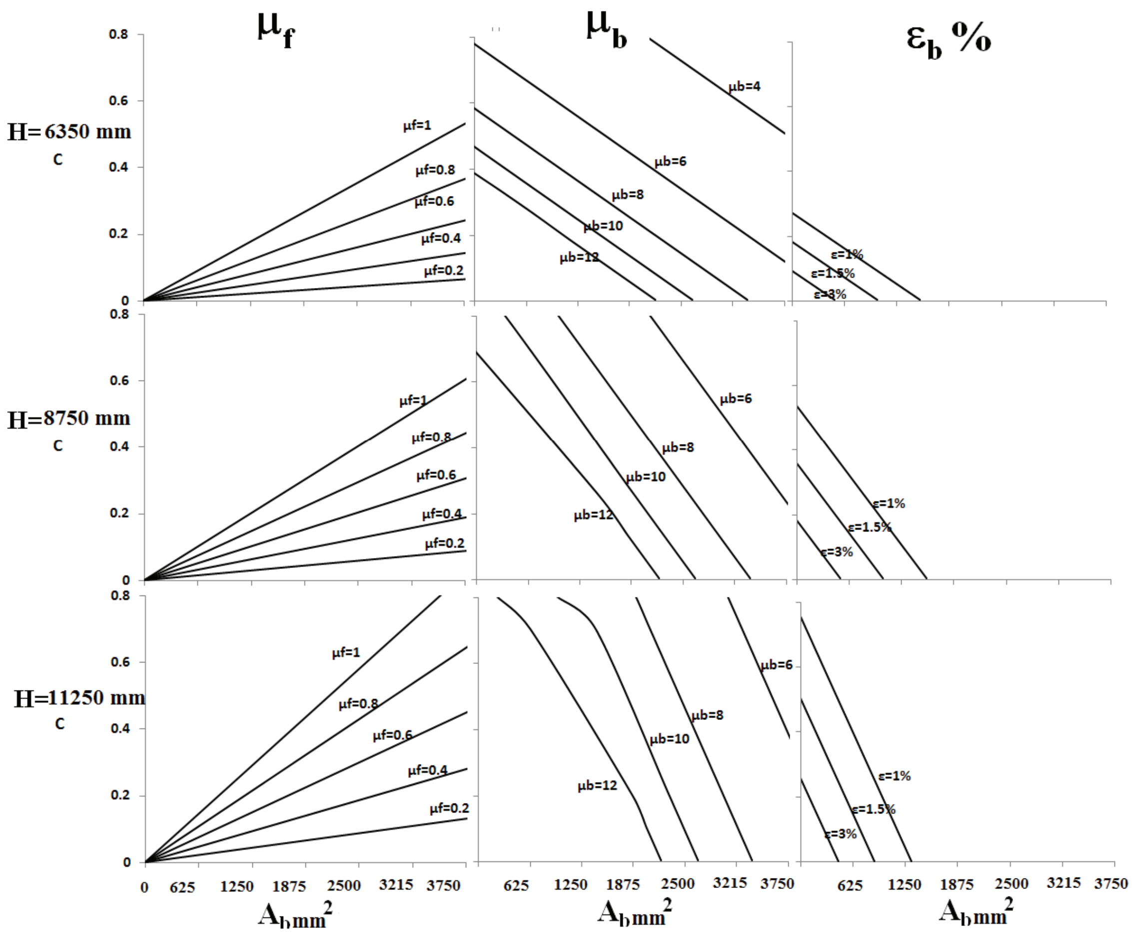

FIGURE 3-14 Effect of Changing the Height on Various Parameters (D=50in, ρ=2%)

3.3 General Parametric Study

3.3.1 Parameters Definitions

Results from the previous study were tied to specific structure geometry; a more general parametric study is presented here to account for several bent geometries and BRB configurations. New parameters are introduced and trends in behavior are observed, leading to strategies to obtain regions of admissible solutions for any bridge bent geometry and BRB configurations.

It is known that the target displacement in the constant velocity region of the spectrum can be calculated using the equal displacement theory which states that the maximum inelastic displacement for a given structure is equal to its maximum elastic displacement.

$$\delta_t = \frac{V_e}{K_{tot}} \tag{3-26}$$

While in the constant acceleration region the equal energy theory applies in which the maximum inelastic displacement is slightly greater that the maximum elastic displacement.

$$\delta_t = R_d \frac{V_e}{K_{tot}} \tag{3-27}$$

In the following parametric study, it was initially assumed that the periods of both the bare frame and the retrofitted structure lied in the constant velocity region of the spectra (i.e. R_d=1 (AASHTO), and C_I=1(NEHRP)). However, to ensure an adequate retrofit procedure, the resulting μ_f and μ_b were modified by multiplying by the actual values of C_I and R_d given in equations (3-8) and (3-10) respectively, and if the final period turned out to lie in the constant acceleration region of the spectra, as shown below.

The frame ductility can be calculated as follows:

$$\mu_f = \frac{\delta_t}{\Delta_{yf}} = \frac{V_e/K_{tot}}{V_{yf}/K_f} = \left(\frac{V_e}{V_{yf}}\right)\left(\frac{K_f}{K_{tot}}\right) = \left(\frac{V_e}{V_{yf}}\right)\left(\frac{K_f}{K_f + K_b}\right) = \left(\frac{V_e}{V_{yf}}\right)\left(\frac{1}{1 + K_b/K_f}\right) \tag{3-28}$$

and the BRB ductility can be calculated as:

$$\mu_b = \frac{\delta_t}{\Delta_{yb}} = \frac{V_e/K_{tot}}{V_{yb}/K_b} = \left(\frac{V_e}{V_{yb}}\right)\left(\frac{K_b}{K_{tot}}\right) = \left(\frac{V_e}{V_{yb}}\right)\left(\frac{K_b}{K_f + K_b}\right) = \left(\frac{V_e}{V_{yb}}\right)\left(\frac{1}{K_f/K_b + 1}\right) \tag{3-29}$$

Three parameters are introduced to simplify these equations, namely: the frame strength ratio, $\xi = \frac{V_e}{V_{yf}} = \frac{S_a mg}{V_{yf}}$, which relates the elastic base shear to the yield base shear of the bare frame; the stiffness ratio of the retrofitted frame, $\alpha = \frac{K_b}{K_f}$, which is the ratio between the lateral stiffness of the BRB and the lateral stiffness of the bare frame, and; the BRB strength ratio, $\eta = \frac{V_e}{V_{yb}}$,which is the ratio between the elastic base shear and the yield base shear of the BRB.

Using these three new parameters, if the period lies in the constant velocity region of the spectra, the frame ductility can be expressed as:

$$\mu_f = \xi\left(\frac{1}{1+\alpha}\right) \tag{3-30}$$

while if the period lies in the constant acceleration region of the spectra, the frame ductility is rather expressed as :

$$\mu_f = C_1\xi\left(\frac{1}{1+\alpha}\right) \text{ (NEHRP 2003)} \tag{3-31}$$

$$\mu_f = R_d\xi\left(\frac{1}{1+\alpha}\right) \text{ (AASHTO 2009)} \tag{3-32}$$

If the period lies in the constant velocity region of the spectra, the BRB ductility can be expressed as:

$$\mu_b = \eta\left(\frac{1}{1+1/\alpha}\right) = \eta\left(\frac{\alpha}{1+\alpha}\right) \tag{3-33}$$

while if the period lies in the constant acceleration region of the spectra, the BRB ductility can be expressed as:

$$\mu_b = C_1\eta\left(\frac{1}{1+1/\alpha}\right) = C_1\eta\left(\frac{\alpha}{1+\alpha}\right) \text{ (NEHRP 2003)} \tag{3-34}$$

$$\mu_b = R_d\eta\left(\frac{1}{1+1/\alpha}\right) = R_d\eta\left(\frac{\alpha}{1+\alpha}\right) \text{ (AASHTO 2009)} \tag{3-35}$$

The maximum ductility can now be expressed in terms of the new parameters as:

$$\mu_{\max} = \frac{\Delta_{yf}}{\Delta_{yb}} = \frac{V_{yf}/K_f}{V_{yb}/K_b} = \left(\frac{V_{yf}}{V_{yb}}\right)\left(\frac{K_b}{K_f}\right) = \left(\frac{\eta}{\xi}\right)\alpha \tag{3-36}$$

Graph plots have been constructed to study the relationship between the newly introduced parameters and the structural fuse system ductilities. Figure 3-15 shows the relationship between the Frame Strength Ratio, ξ, and the Stiffness Ratio, α, given by equation (3-30).

That equation for a given value of μ_f, gives straight line of slope $\frac{1}{\mu_f}$ and vertical ordinate equal to -1.

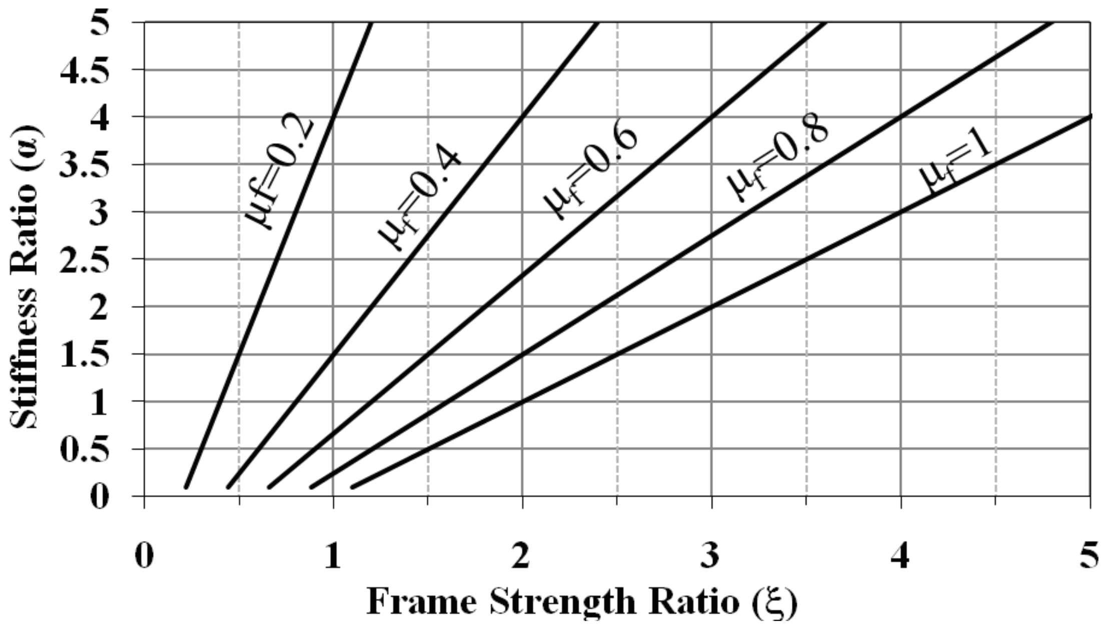

FIGURE 3-15 Relationship between the Frame Strength Ratio and the Stiffness Ratio in terms of Frame Ductility

The linear relationship in figure 3-15 indicates that whenever the frame strength increases (meaning that μ_f increases for a given frame stiffness), a proportional increase in the stiffness ratio, α, is required in order to achieve the same desired frame ductility. This observation is expected as increasing the frame strength ratio for a given frame stiffness would result in decreasing the frame yielding strength and yielding displacement, so for a given frame stiffness ratio, increasing the frame strength ratio would decrease the frame ductility.

Figure 3-16 shows the relationship between the BRB Strength Ratio, η, and the stiffness ratio, α, expressed by equation (3-33). Directly from that equation, for a given μ_b, η is equal to $\frac{\mu_b}{\alpha} + \mu_b$.

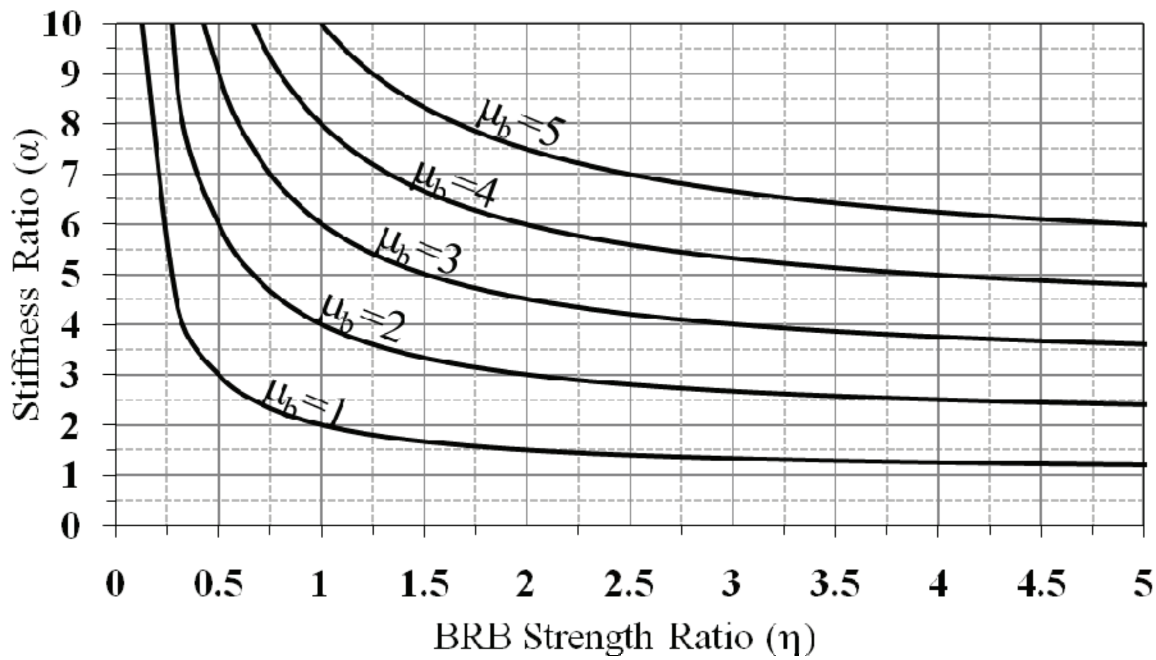

FIGURE 3-16 Relationship between the BRB Strength Ratio and the Stiffness Ratio in terms of BRB Ductility

As a result, mathematically, as observed in figure 3-16, if α is less than 2, a small change in the stiffness ratio significantly affects the BRB strength ratio needed to achieve a target BRB ductility, while if α is greater than 2, the stiffness ratio does not affect the BRB stiffness much (and is of little effect at α greater than 5). This physically means that if the stiffness of the BRB is large compared to that of the frame (i.e. large α), $\eta \approx \mu_b$ and $\frac{V_e}{V_{yb}} = \frac{\delta_t}{\Delta_{yb}}$, which means that the structural behavior approach that of a bilinear system with properties given by the BRB (i.e. impact of the frame itself becomes less significant). At the other extreme, if the stiffness of the BRB is too small compared to that of the frame (i.e. small α), it is impossible to make the structural fuse system works.

From equation (3-32), figure 3-17 shows the relationship between the Stiffness Ratio, α, and the BRB Strength Ratio, η, normalized by the Frame Strength Ratio, ξ, where each curve represents a constant value of the maximum ductility. This normalization is the ratio of the frame yield strength to the BRB yield strength.

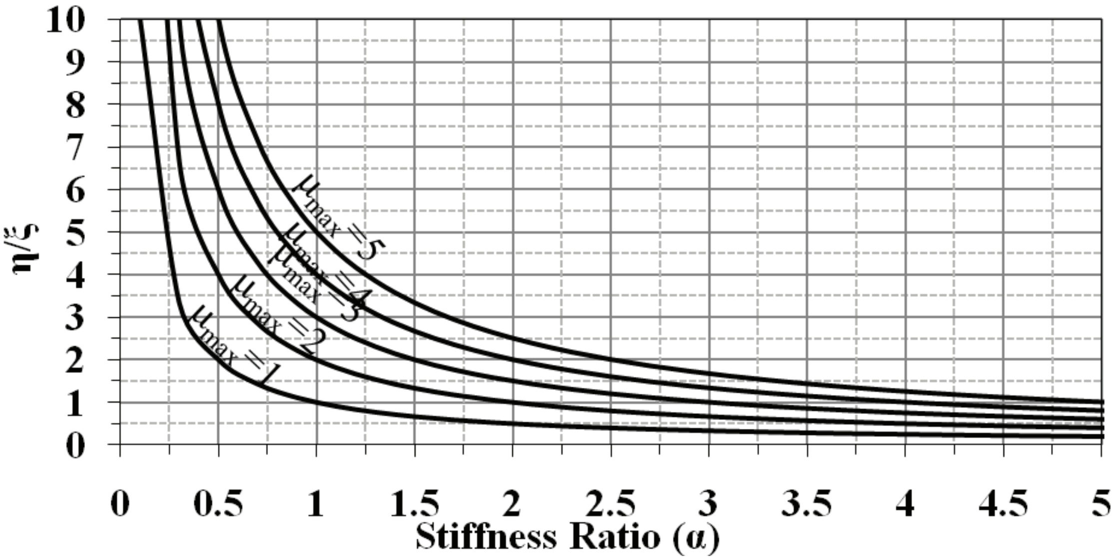

FIGURE 3-17 Relationship between the Stiffness Ratio and the BRB Strength Ratio normalized by the Frame Strength Ratio in terms of Maximum Ductility

It is observed that for α greater than 5, leads to almost the same values of $\frac{\eta}{\xi}$ are relatively small compared to cases when α is less than 1. For the latter case, a significant $\frac{\eta}{\xi}$ is required to achieve the desired maximum ductility. Again the same trend is seen as in the previous figure, and it physically means that if the stiffness of the BRB is too small compared to that of the frame, a very large value of BRB to frame strength ratio is required to achieve the structural fuse concept which is almost impossible.

The value of the BRB strain can be calculated as:

$$\varepsilon_b = \frac{\delta_t \cos\theta}{\left(\frac{L_{ysc}}{L_{BRB}}\right) H \Big/ \sin\theta} = \frac{\delta_t \sin\theta \cos\theta}{\left(\frac{L_{ysc}}{L_{BRB}}\right) H} = \frac{S_a g T_{eff}^2 \sin\theta \cos\theta}{4\pi^2 \left(\frac{L_{ysc}}{L_{BRB}}\right) H} \tag{3-37}$$

rearranging that equation one obtains:

$$\frac{\varepsilon_b H}{S_a} = \left(\frac{g}{4\pi^2}\right) \left(\frac{T_{eff}^2}{\left(\frac{L_{ysc}}{L_{BRB}}\right)}\right) (\sin\theta \cos\theta) \tag{3-38}$$

By substituting equation (3-6) and (3-11) into equation (3-16), the value of the BRB ductility can be rewritten as:

$$\mu_b = \frac{\delta_t}{\Delta_{yb}} = \frac{S_a g T_{eff}^2 E_s \sin\theta\cos\theta}{4\pi^2 f_{y_{BRB}} \left(\frac{L_{ysc}}{L_{BRB}}\right) H} \tag{3-39}$$

rearranging that equation:

$$\therefore \frac{\mu_b H}{S_a} = \left(\frac{g}{4\pi^2}\right)\left(\frac{E_s}{f_{y_{BRB}}}\right)\left(\frac{T_{eff}^2}{\left(\frac{L_{ysc}}{L_{BRB}}\right)}\right)(\sin\theta\cos\theta) \tag{3-40}$$

By dividing equation (3-38) by equation (3-40), it is shown that for the case of a chevron type BRB system:

$$\frac{\varepsilon_b}{\mu_b} = \frac{f_{y_{BRB}}}{E_s} \tag{3-41}$$

Using the previous relationships, for constant values of ξ, the values of μ_f and ε_b with respect to α can be calculated and plotted for BRB of different steel grades.

Figure 3-18 shows one such typical plot for a value of ξ=4 and f_{yBRB}= 350 MPa (50 ksi), where the horizontal axis is the stiffness ratio, α, while the vertical axis is the BRB ductility, μ_b. Each solid line curve in the figure represents a constant value of the BRB strength ratio, η. It can be seen that for a given value of stiffness ratio, increasing the BRB ductility would result in increasing the BRB strength ratio and accordingly decrease the BRB strength, which is expected as in order to increase the BRB ductility while preserving the stiffness, a reduction in the BRB strength is required in order to decrease the BRB yielding displacement and accordingly increase the BRB ductility. The horizontal dashed lines correspond to specific values of μ_b, which can be converted into equivalent BRB strains by equation (3-41). The upper dashed horizontal line represents the BRB strain that is selected as the design limit (1.5% in this particular example). It can be seen that increasing the stiffness ratio for a given BRB ductility does not affect the value of the BRB strain, which is expected as the relationship in equation (3-41), can be concluded directly from the geometry of the BRB, as the BRB ductility is the ratio between the BRB target strain and the BRB yield strain, which has nothing to do with the stiffness ratio and for a given value of BRB ductility a constant value of strain is obtained for a given steel grade. The vertical dashed lines correspond to various frame ductility, μ_f, obtained for specific values of the stiffness ratio, α, for a constant value of frame strength ratio, ξ. Various values of μ_f can be chosen by equation (3-31) to constrain the design, depending on the type of column failure mode, but μ_f can never be greater than 1 for the structural fuse concept to be effective. It can be seen that increasing the stiffness ratio corresponds to decreasing the frame stiffness, and for a given frame strength ration, decreasing the frame stiffness would result in increasing the frame yielding displacement and also the frame ductility.

The region of admissible solutions to achieve the structural fuse objectives is illustrated by the shaded area for a RC bridge bent having a typical flexural failure mode. The upper limit represents the maximum brace strain that can be achieved so that no fracture occurs in the brace, and the lower limit (μ_b=1) is the point below which the BRB will behave elastically and the benefits of having it dissipate energy will not exist. This region is vertically defined to the left by the value of μ_f corresponding to the applicable failure mode – here, $\mu_f = 1$ for flexural values, and lesser values if shear failures governed. The zone of admissible solution is unbounded to the right.

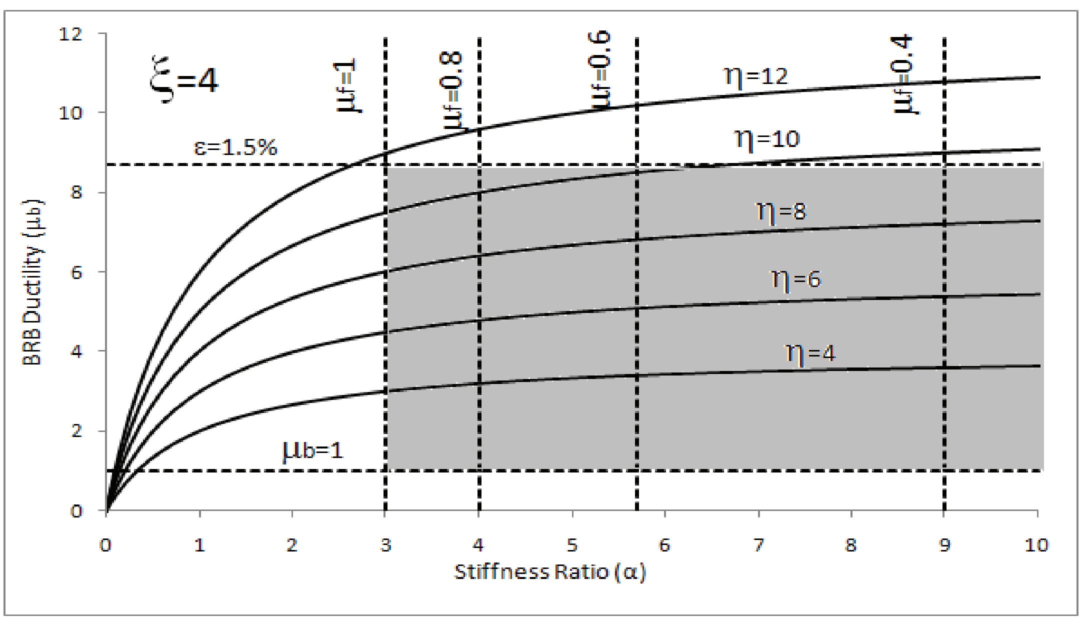

FIGURE 3-18 Regions of Admissible Solution for a Value of ξ=4, f_{yBRB} =350 MPa

Similar plots were constructed for different values of ξ considering steel grades A36 and A572 Gr.50 as shown in figure 3-19. Regions of admissible solutions are shown by the shaded areas in those plots. It can be seen that the region of admissible solutions decreases when increasing the values of ξ and f_{yBRB}. This can be explained by considering that whenever the frame strength ratio increases, the strength of the bare frame decreases and, for a given stiffness ratio, α, the value of the frame yield displacement will decrease followed by a decrease in the allowable ductility of the system, μ_{max}. Correspondingly a larger value of α is required to reach a value of μ_f equal to 1. Independently, increasing the value of BRB yield strength , f_{yBRB}, for a constant value of α, increases the value of the BRB yield displacement, resulting in a reduction of the allowable ductility of the system and proportional reduction in the value of μ_b when the strain limit of 1.5% is reached.

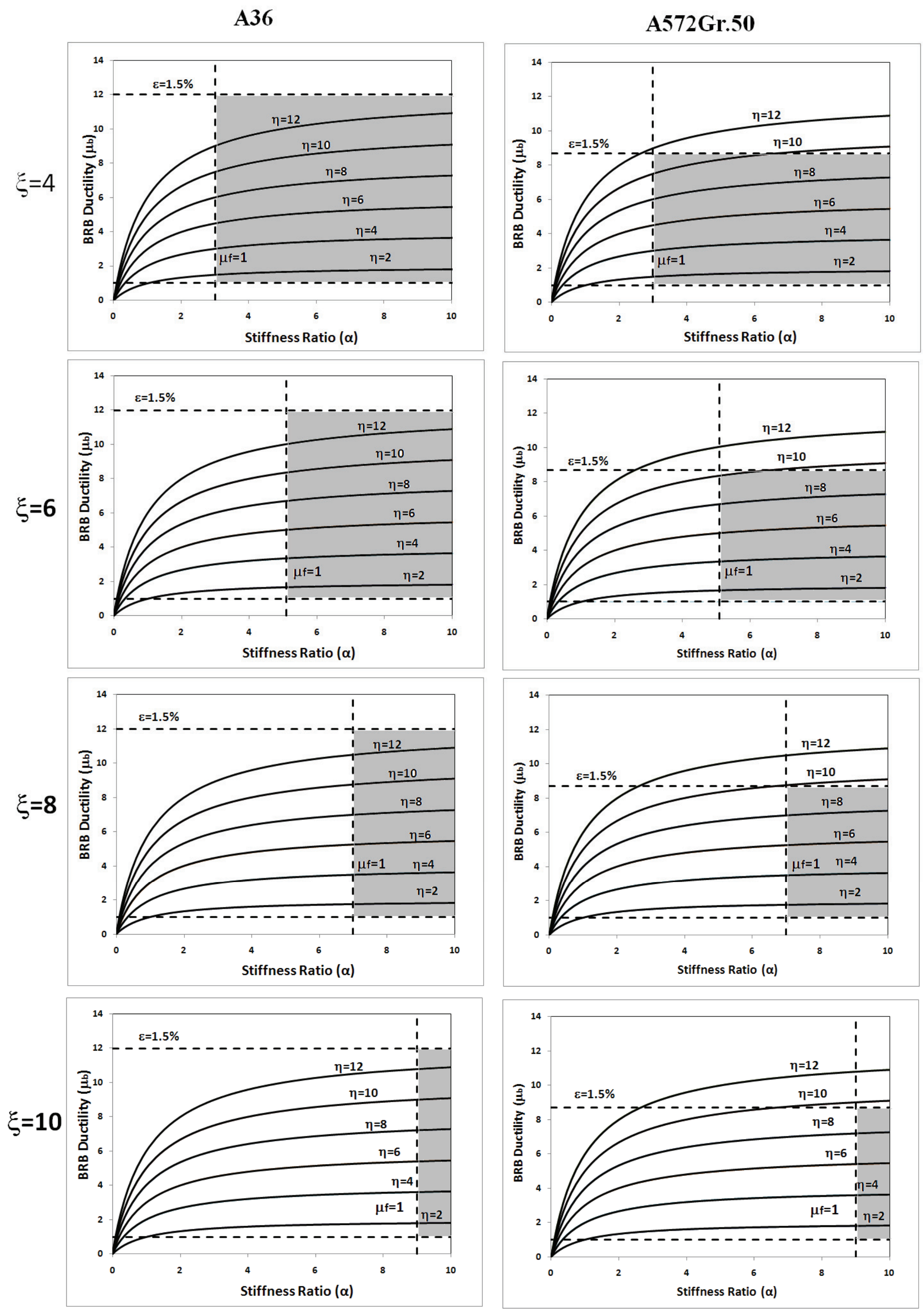

FIGURE 3-19 Regions of Admissible Solution for Different ξ and $f_{y_{BRB}}$

3.3.2 Modification Factors

The previous plots where presented for cases for which the period was always considered to be in the constant velocity zone (i.e. R_d=1(AASHTOO), and C_1=1(NEHRP)). As shown in equations (3-8) and (3-10) described earlier, the correction factors are a period dependant parameter (i.e. depends on the mass and stiffness for each individual case). As a result the transition point between the constant velocity and constant acceleration regions of the spectra is not tied to specific values of α, which is why it was not considered in the previous plots. For design purposes, the effect of the correction factor should be calculated separately (per equations (3-31) and (3-34)) and used to magnify the BRB ductility and frame ductility values found from the above plots.

For example, the effect of adding the correction factor is illustrated for a RC bent configuration of mass equal to 1.86 kips, η=6 and ξ=6, in figures 3-20 and 3-21which show the corrected BRB ductility and frame ductility values at different values of α respectively.

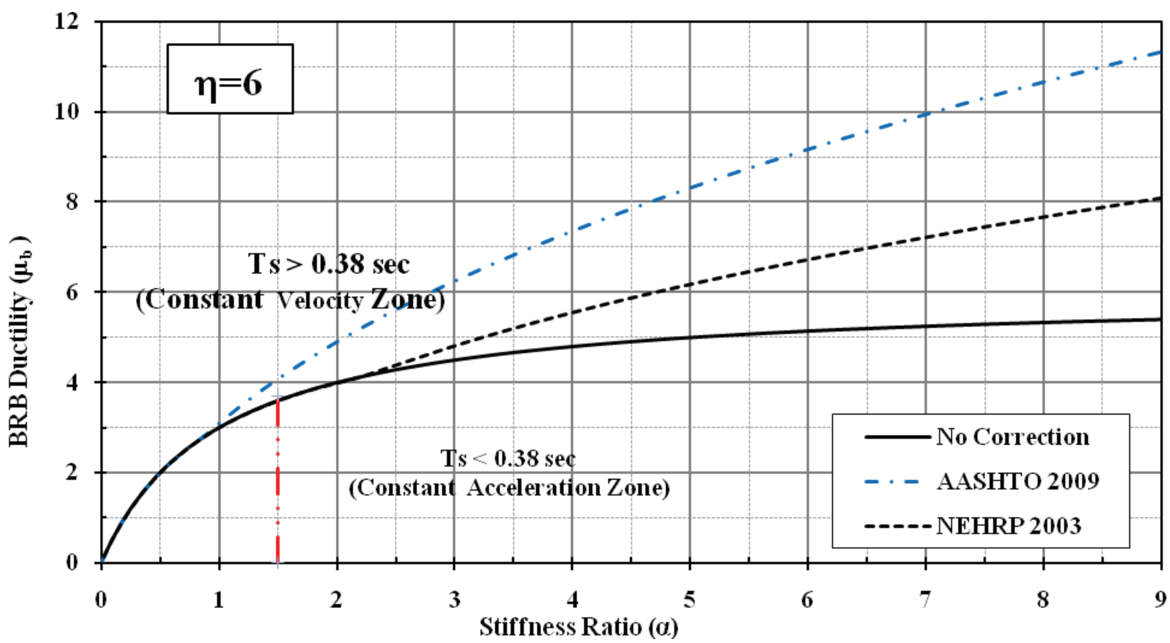

FIGURE 3-20 Effect of Adding the Correction Factors on the BRB Ductility for η=6 and ξ=6

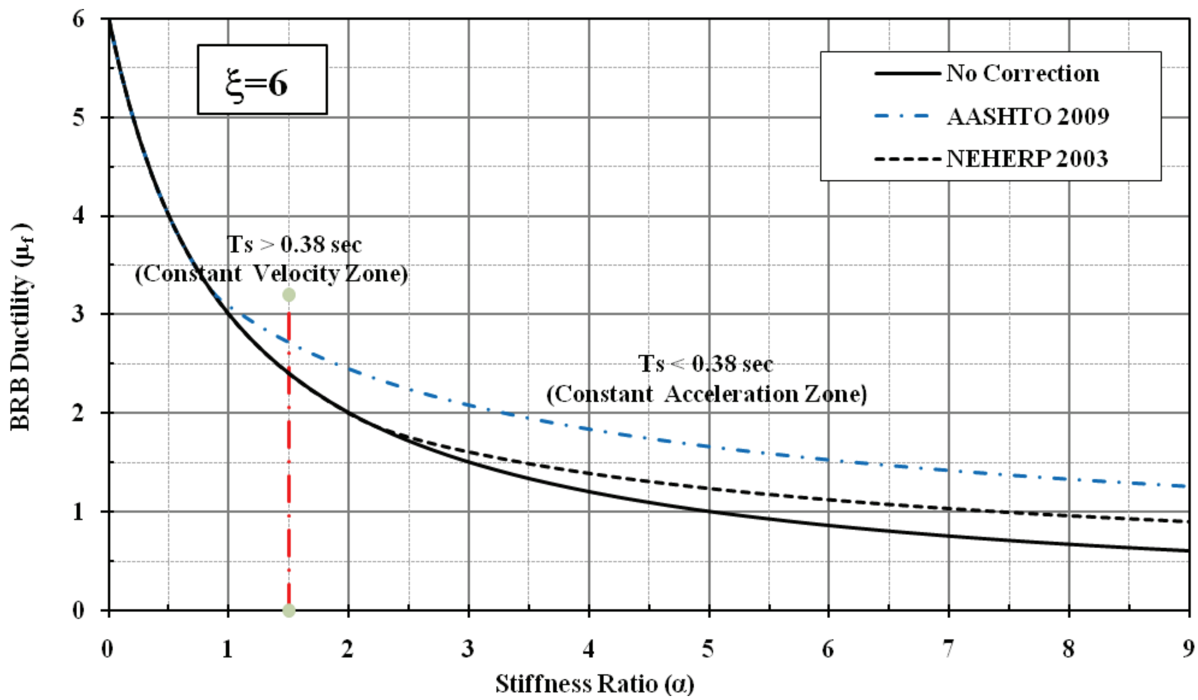

FIGURE 3-21 Effect of Adding the Correction Factors on the Frame Ductility for η=6 and ξ=6

3.4 Nonlinear Dynamic Response

3.4.1 Static Procedure Validation

To validate the above predicted system response based on pushover properties for retrofit using BRB structural fuses, a set of 9 artificial spectra-compatible accelerograms were generated using the TARSCTHS code (Papageorgiou et al. 2001). The time histories matched the target AASHTO (2009) acceleration response spectrum for the same site used in section 3.3. The spectral acceleration used for this purpose was taken from the USGS seismic hazard maps and found to be S_s=2.083g and S_1=0.803g. The resulting acceleration response spectra for the generated ground motions with 5% critical damping are shown in figure 3-22. An average response spectrum curve is generated and plotted against the compliant code spectrum for 5% critical damping as shown in figure 3-23. The same procedure could have been followed using the target spectra of various seismic specifications such as (NEHRP 2003) and remain the same otherwise.

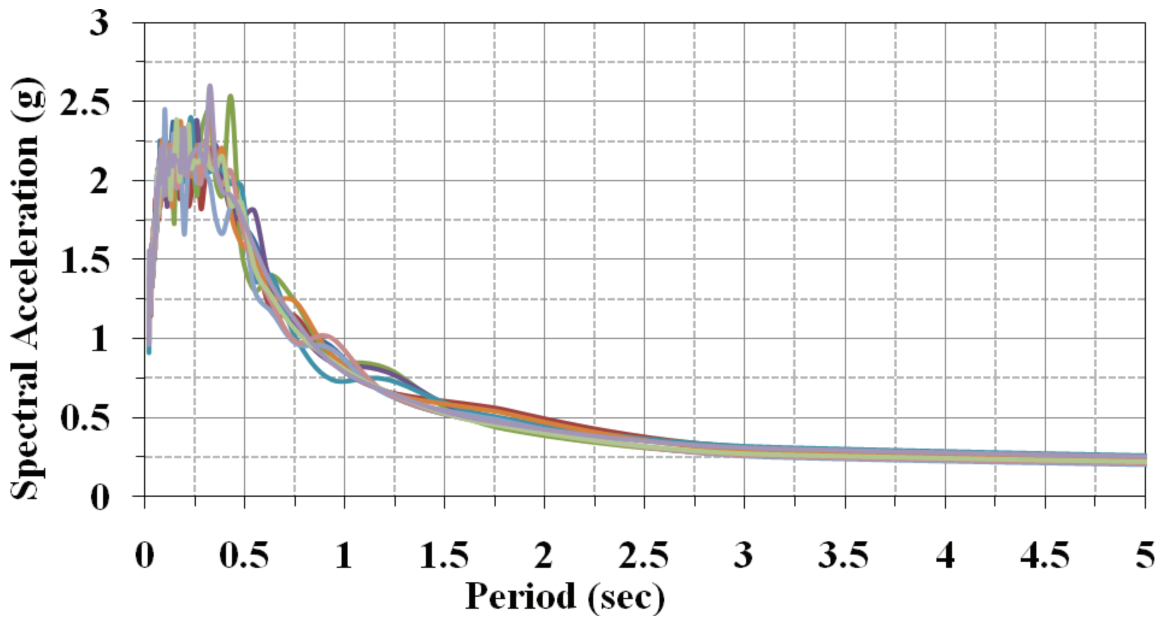

FIGURE 3-22 Acceleration Response Spectra for Synthetic Earthquakes (ξ=5%)

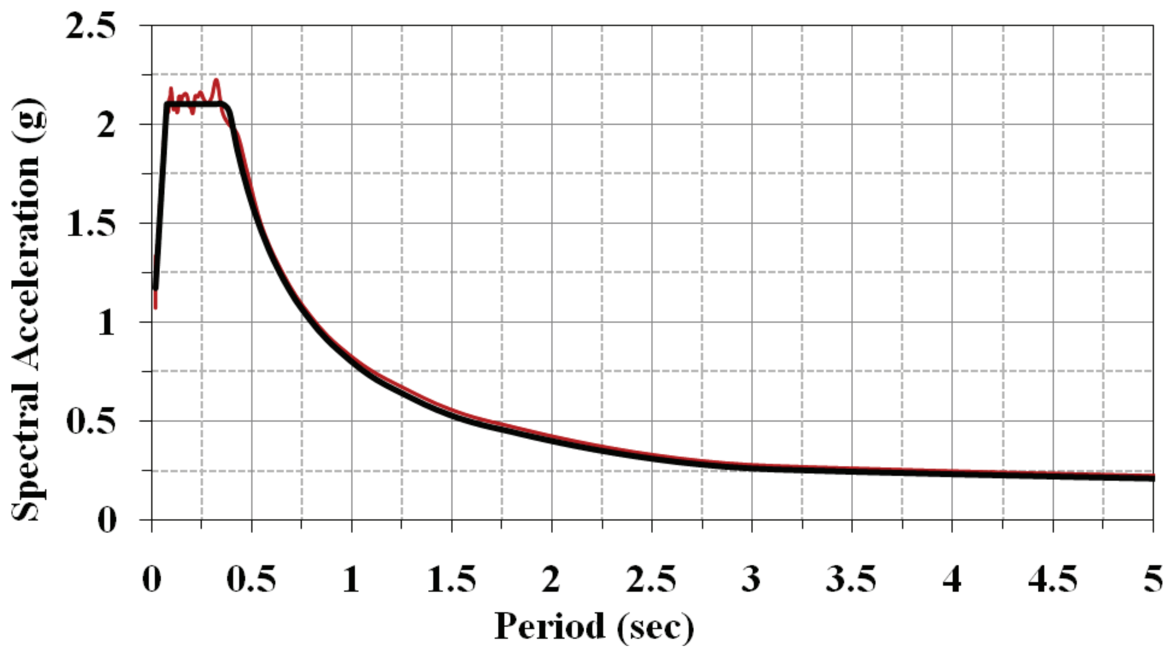

FIGURE 3-23 Elastic Response Spectra for Synthetic Earthquake (ξ=5%)

Time history analysis was performed using the SAP2000 software on a number of RC bents retrofitted by a chevron BRB bracing system configured as shown in figure 3-6. The total system mass was set to a constant value of 1.86 kips for all cases. Two sets of analyses were performed. For the first set of analyses, the value of the frame strength ratio ξ and the value of the BRB strength ratio η where chosen to be 2 for all cases. These values were chosen to ensure that all the system periods are located in the constant velocity zone of the spectra where R_d=1.

Different values of α ranging between 1 and 5 where used and the corresponding values of frame and BRB ductilities where calculated and compared to those from the proposed static procedure. Figures 3-24 and 3-25 show a comparison between the results obtained from all the synthetic records and the push-over analysis predictions for BRB and frame ductility respectively, while figures 3-26 and 3-27 show the same comparison with the mean response obtained from all 9 synthetic ground motions.

For the second set of analyses, the values of the frame strength ratio ξ and the BRB strength ratio η was set to be equal to 6 for all cases. These values were chosen to show the effect of adding the correction factor, R_d, for the cases in which the fundamental period of the total systems laid in the constant acceleration zone of the spectra. Different values of α ranging between 1 and 5 were also used and the corresponding values of frame and BRB ductilities where calculated and compared to those from the push-over analysis predictions taking into account the correction factor. Figures 3-28 and 3-29 show a comparison between the results obtained from all the synthetic records and the push-over analysis predictions for BRB and frame ductility respectively, while figures 3-30 and 3-31show the same comparison with the mean response obtained from all 9 synthetic ground motions. Note that in those figures, the dotted lines correspond to the corrected values.

For both sets of analyses considered, the agreement is good between the response predicted by the simple procedure and the results from the non-linear time history analyses. On average, the results obtained from the push-over analysis are about 13% higher than those obtained from the non-linear time history analyses.
Tables 3-1and 3-2 show frame and BRB ductilities results obtained from the non-linear time history analyses for the 9 earthquakes respectively at specified values of stiffness ratios, α, for a frame with ξ=6 and η=6. The average ductilities are then compared to those obtained from the push-over analysis.

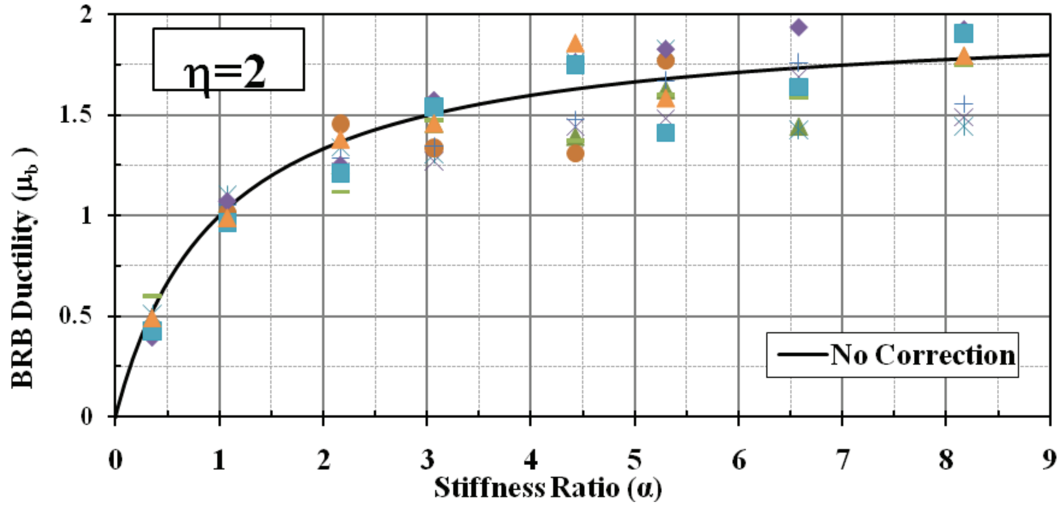

FIGURE 3-24 Comparison between Time History and Push-over Analysis Results for BRB Ductility at η=2 and ξ=2

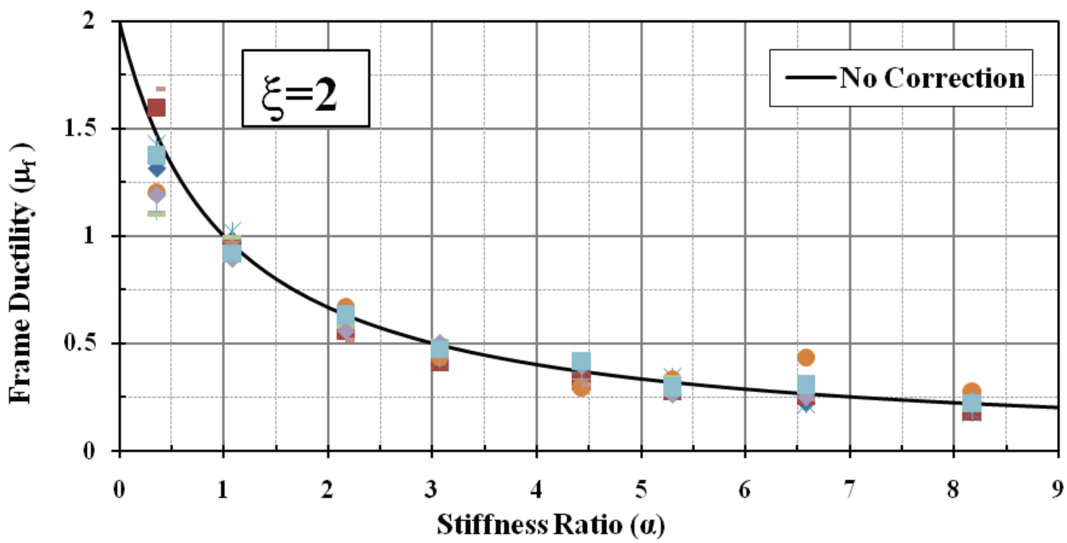

FIGURE 3-25 Comparison between Time History and Push-over Analysis Results for Frame Ductility at η=2 and ξ=2

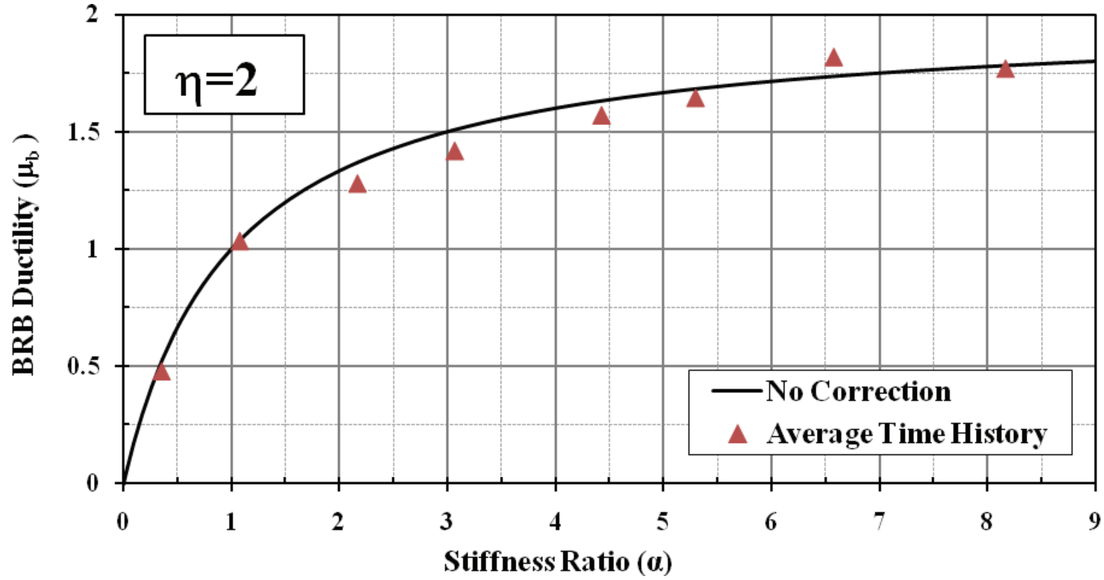

FIGURE 3-26 Comparison between Time History for Mean Record and Push-over Analysis Results for BRB Ductility at η=2 and ξ=2

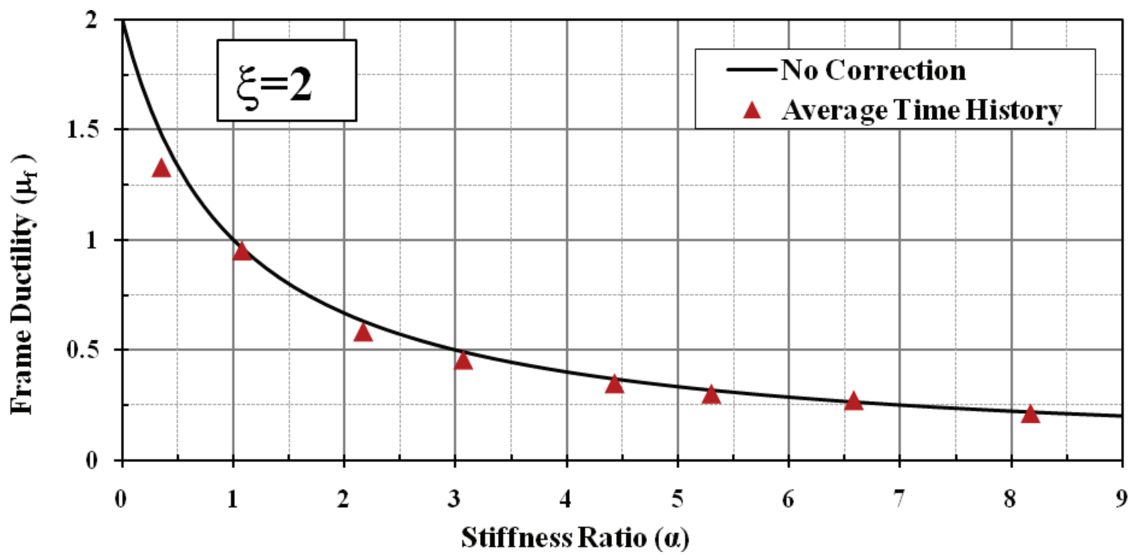

FIGURE 3-27 Comparison between Time History for Mean Record and Push-over Analysis Results for Frame Ductility at η=2 and ξ=2

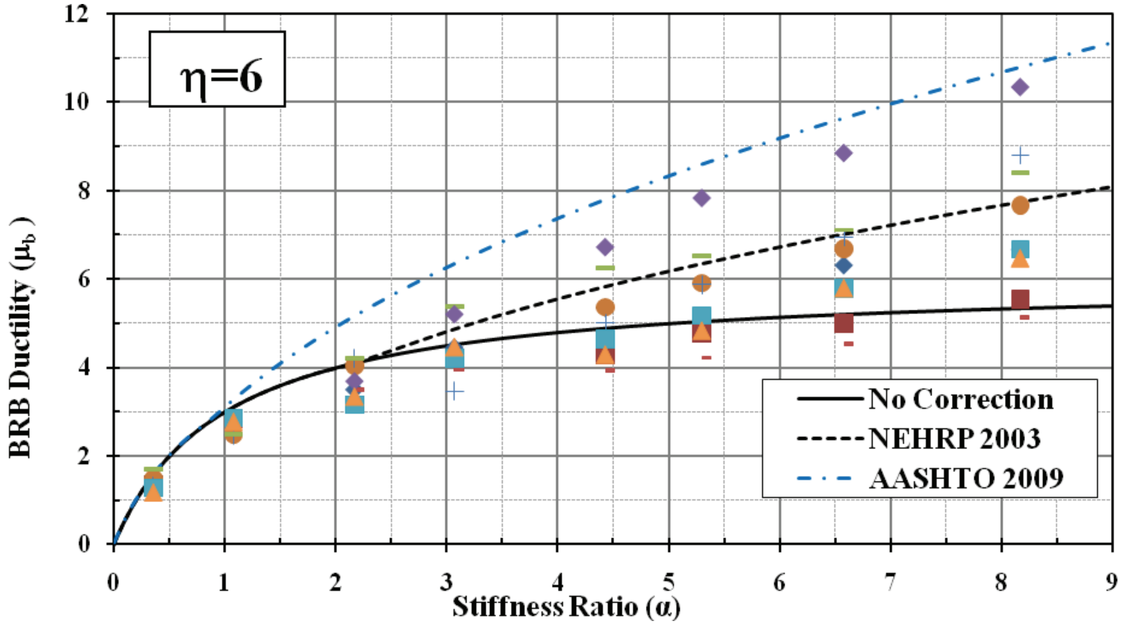

FIGURE 3-28 Comparison between Time History and Push-over Analysis Results for BRB Ductility at η=6 and ξ=6

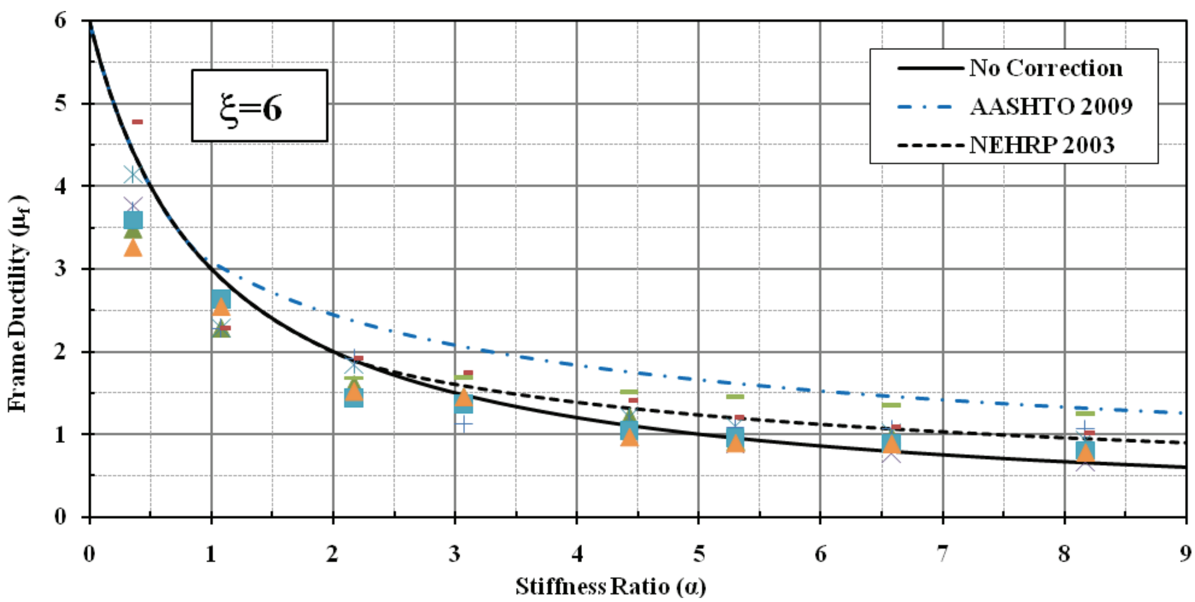

FIGURE 3-29 Comparison between Time History and Push-over Analysis Results for Frame Ductility at η=6 and ξ=6

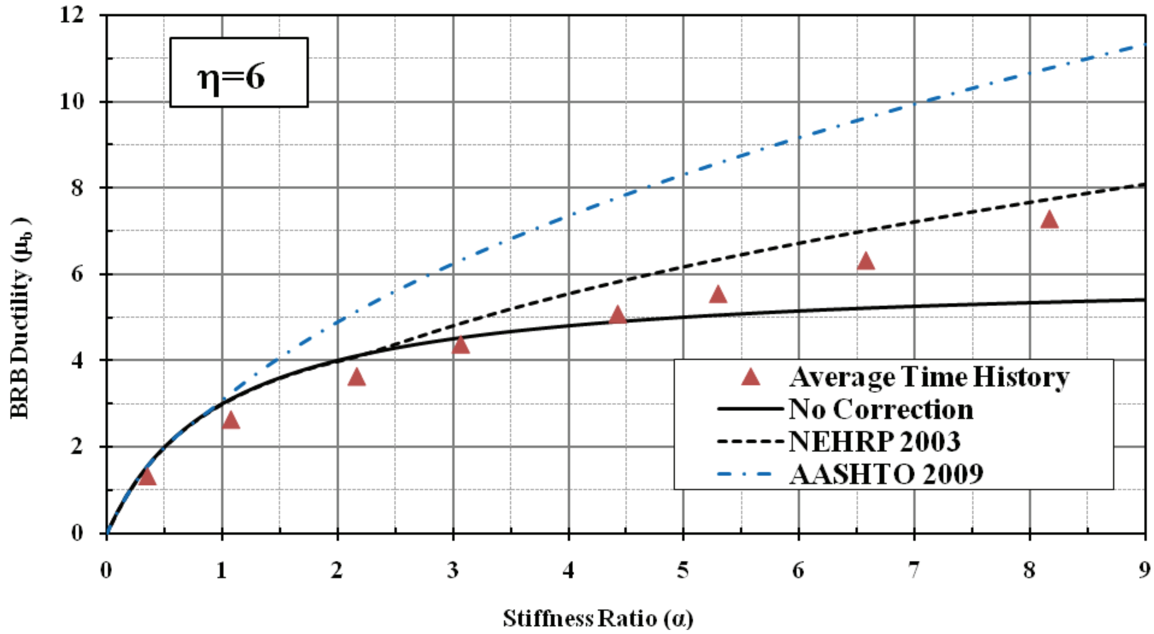

FIGURE 3-30 Comparison between Time History for Mean Record and Push-over Analysis Results for BRB Ductility at η=6 and ξ=6

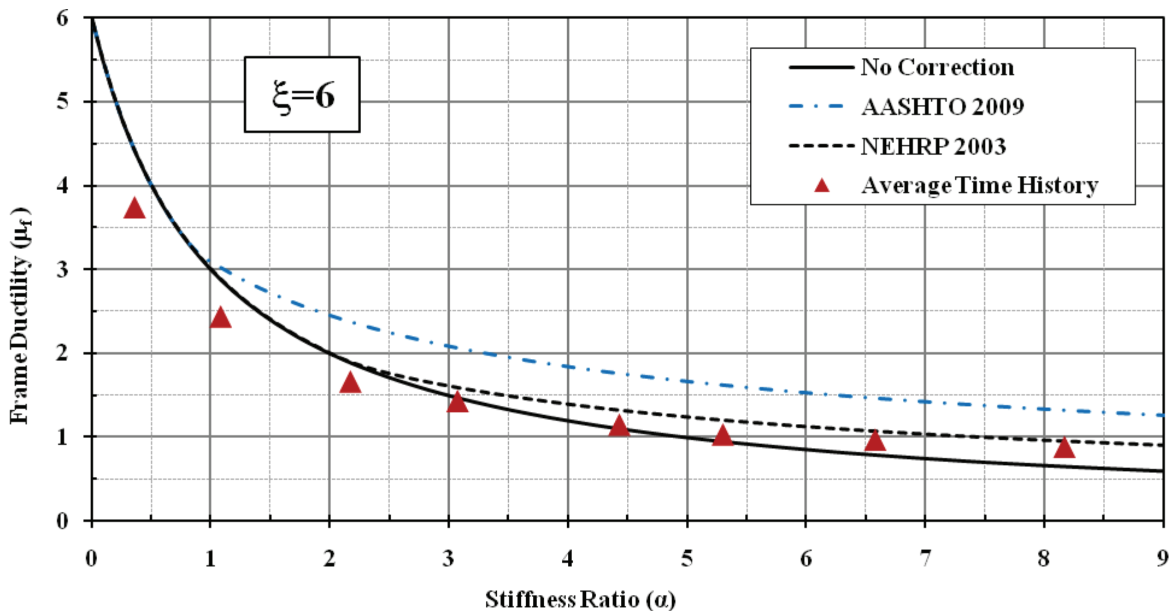

FIGURE 3-31 Comparison between Time History for Mean Record and Push-over Analysis Results for Frame Ductility at η=6 and ξ=6

TABLE 3-1 Frame Ductility Values from Dynamic and Push-over Analyses

α	EQ1	EQ2	EQ3	EQ4	EQ5	EQ6	EQ7	EQ8	EQ9	Av. μ_f	μ_f (Static)	%Error
0.36	1.2	1.3	1.5	1.3	1.2	1.7	1.3	1.3	1.2	3.7	4.4	18.2
1.1	2.5	2.9	2.5	2.5	2.7	2.5	2.8	2.9	2.8	2.4	2.9	18.2
2.2	3.5	3.2	4.0	4.2	3.5	4.2	3.7	3.2	3.3	1.7	1.9	13.7
3.1	4.5	4.2	4.2	3.5	4.0	5.4	5.2	4.2	4.5	1.4	1.6	11.1
4.4	5.4	4.3	5.4	5.0	3.9	6.3	6.7	4.6	4.3	1.1	1.3	14.8
5.5	4.9	4.8	5.9	5.9	4.2	6.5	7.8	5.2	4.8	1.0	1.2	15.4
6.6	6.3	5.0	6.7	6.9	4.5	7.1	8.8	5.8	5.8	1.0	1.1	10.3
8.2	6.7	5.5	7.7	8.8	5.1	8.4	10.3	6.7	6.5	0.9	1.0	7.6

TABLE 3-2 BRB Ductility Values from Dynamic and Push-over Analyses

α	EQ1	EQ2	EQ3	EQ4	EQ5	EQ6	EQ7	EQ8	EQ9	AV. μ_b	μ_b (Static)	%Error
0.36	3.5	3.8	4.1	3.7	3.7	4.8	3.6	3.6	3.3	1.3	1.6	18.5
1.1	2.3	2.6	2.3	2.3	2.3	2.3	2.5	2.6	2.5	3.6	4.1	12.8
2.2	1.6	1.4	1.8	1.9	1.9	1.9	1.7	1.4	1.5	4.4	4.9	11.1
3.1	1.5	1.4	1.4	1.1	1.1	1.8	1.7	1.4	1.5	5.1	5.8	14.5
4.4	1.2	1.0	1.2	1.1	1.1	1.4	1.5	1.0	1.0	5.6	6.4	15.1
5.5	0.9	0.9	1.1	1.1	1.1	1.2	1.5	1.0	0.9	6.3	7.0	10.5
6.6	1.0	0.8	1.0	1.1	1.1	1.1	1.4	0.9	0.9	7.3	7.8	6.2
8.2	0.8	0.7	0.9	1.1	1.1	1.0	1.3	0.8	0.8	2.6	3.1	17.6

3.4.2 Example

An arbitrary RC bridge bent was selected with dimensions L= 12.5 m (500") and H= 6.25 m (250"). Columns where chosen to be circular with diameter D= 1250 mm (50") having a longitudinal reinforcement ratio ρ=2%, and a transverse reinforcement similar to that of most bridges built prior 1970 (i.e. #4 bars spaced at 300 mm (12")). Concrete strength, f_c', was chosen to be 41 MPa (6ksi). The superstructure was assumed to be rigid so that the bent acted as a SDOF system with a lumped mass at the top of the columns, m, assumed to be 0.33 kN.sec^2/mm (1.86 kips.sec^2/in). The introduced BRB system was assumed to have a bilinear hysteretic behavior and a material strength, f_{yBRB}, of 275 MPa (40ksi). A response spectrum was constructed based on AASHTO 2009 Guide Specifications for LRFD Seismic

Bridge Design for a site with soil-type class B. The site was chosen to represents an area exposed to severe ground shaking. Resulting elastic spectral accelerations are shown in figure 3-32.

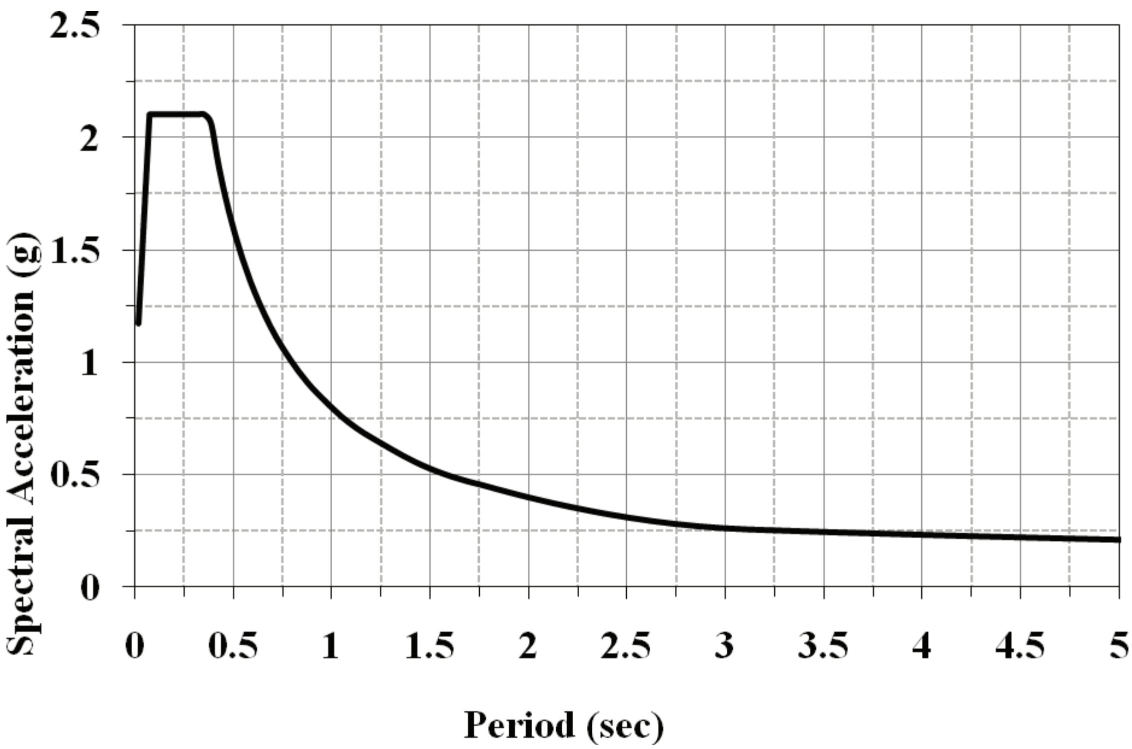

FIGURE 3-32 Elastic Response Spectra (5% critical damping)

A moment curvature analysis has been performed for the RC column using XTRACT software from which an idealized moment curvature curve has been generated; figure 3-33 shows a plot for both the moment curvature curve from the software and the idealized moment curvature curve.

General column properties were extracted from the software as:

ϕ_y=0.00008, ϕ_u=0.00068, M_y=3600 k.ft

Corresponding bare frame dynamic properties can be calculated as:

$$V_{yf} = \frac{4M_y}{H} = \frac{4*3600*12}{250} = 691.2 \text{ kips (3072 kN)}$$

$$\Delta_y = \frac{\phi_y H^2}{3} = \frac{0.000085*(250)^2}{3} = 1.77 \text{ in (44.25 mm)}$$

$$K_{eff} = \frac{V_{yf}}{\Delta_y} = \frac{691.2}{1.77} = 390 \text{ kip.in (43333 kN.mm)}$$

$$T_{eff} = 2\pi\sqrt{\frac{1.86}{390}} = 0.43\text{sec}$$

$$L_p = 0.08\frac{H}{2} + 0.15 f_y d_b = 0.08\frac{250}{2} + 0.15*60*1.1 = 19.9 \text{ in (498 mm)}$$

$$\theta_p = (\phi_u - \phi_y)L_p = (0.00068 - 0.000085)*19.9 = 0.0118 \text{ rad}$$

$$\Delta_u = \Delta_y + \theta_p\left(0.5H - 0.5L_p\right) = 1.77 + 0.0118(0.5*250 + 0.5*19.9) = 3.36 \text{ in (84 mm)}$$

Shear strength of each column in the frame was calculated in accordance to (Priestley et al. (1994):

$$V_c = k\sqrt{f_c^/} A_e = \left(3.5\sqrt{6000}*0.8*\frac{\pi}{4}(50)^2\right)\Big/1000 = 425.9kips(1893kN)$$

$$V_p = P\tan\alpha = \left(\frac{D-c}{2a}\right)P = \left(\frac{50-40}{250}\right)*1160 = 46.4kips(206kN)$$

$$V_s = \frac{\pi A_{sh} f_{yh} D^/}{2S}\cot 30^\circ = \frac{\pi*0.196*60*46}{2*12}\cot 30 = 122.6kips(545kN)$$

$$V_i / col = V_c + V_p + V_s = 425.9 + 46.4 + 122.6 = 594.9kips(2644kN)$$

where V_c is the concrete component for shear strength, V_p is the axial load component for shear strength enhancement, V_s is the truss mechanism component to take into account the contribution of transverse reinforcement.

For a two column bent the initial shear strength, V_i, can be calculated as:

$V_i = 2*594.9 = 1189.9kips(5289kN)$ (This indicates that no shear failure occurs prior to flexural yielding)

While the residual shear strength, V_r, which is a shear stress based on reduced concrete contribution can be calculated in accordance to Priestley et al. (1994) as:

$$V_c = k\sqrt{f_c^/} A_e = \left(1.2\sqrt{6000}*0.8*\frac{\pi}{4}(50)^2\right)\Big/1000 = 146kips(649kN)$$

$$V_r = 2\left(146 + 46.4 + 122.6\right) = 630kips(2800kN)$$

Figure 3-34 shows a comparison between the idealized force displacement curve for the bare frame, compared to its initial and residual shear strength. It is seen that V_{yf} is greater than $V_{i,}$ which indicates that the flexural yielding will occur before the shear failure at a displacement Δ_y equal to 44025 mm (1.77"), and flexural failure will occur at a displacement Δ_f equal to 83.75 mm (3.35"). Theoretical shear failure should start to occur at a displacement Δ_s equal to 132.5 mm (5.3") which means that the column will totally fail in flexure before any shear failure starts to occur.

From the response spectrum the spectral acceleration can be computed as S_a=1.9g,

$$\therefore \delta_t = \frac{1.9*(0.43)^2*386}{4\pi^2} = 3.4in(85mm)$$

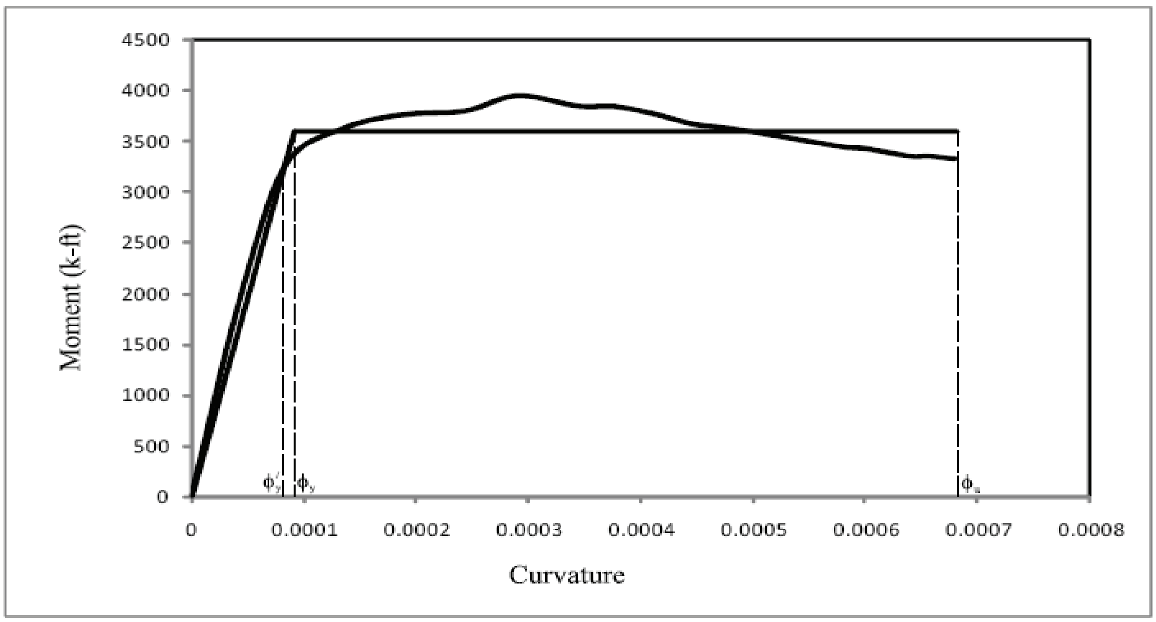

FIGURE 3-33 Original and Idealized Moment Curvature for bent column

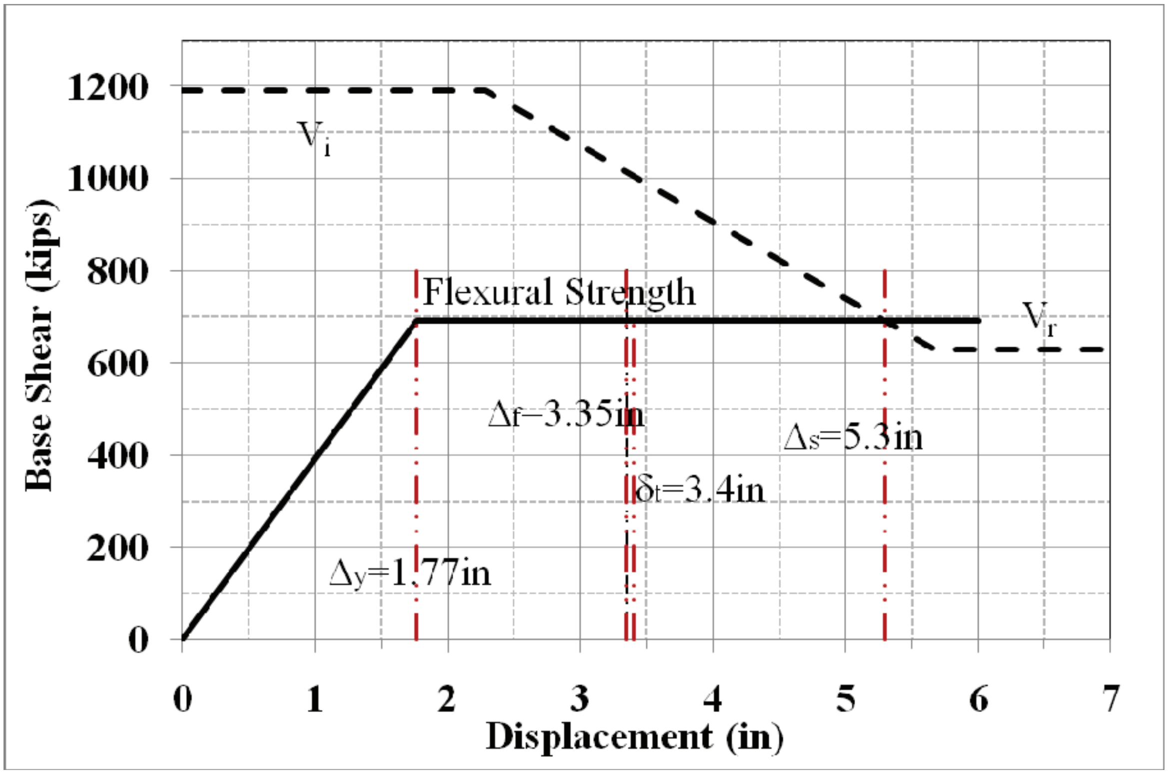

FIGURE 3-34 Idealized Pushover Curve for the Bare Frame

From the previous, the value of $\frac{V_i}{V_{yf}}$ is 1.74 (greater than 1), which leads to a desired frame ductility after the retrofit not to exceed 1 (i.e. μ_f<1). In this example, a value of μ_f equal to 0.6 is assumed as a target parameter to take into account the increase in ductility demand due to the equal energy theory. The BRB strength ratio, η, was taken equal to 6 in order to provide a reasonable BBR ductility ratio, μ_b of 4. The brace strain was assumed to be limited to 1.5% for reasons described earlier.

A value of the spectral acceleration of the retrofitted frame is assumed in the constant acceleration zone of the spectrum (S_a=2.1g)

The frame strength ratio can now be calculated as follows:

$$\xi = \frac{2.1*1.86*386}{691.2} \cong 2.18$$

From figure 3-19, a chart is chosen for a value of ξ equals to 2, and a steel grade of A572 Gr.50, the chosen figure is solely plotted in figure 3-35, values of $\alpha = 2.5$ and $\eta = 6$ can be chosen, from which values of the minimum required BRB strength and stiffness can be calculated as:

$$K_{b_{\min}} = \alpha_{\min} K_{eff} = 2.5*390 = 975 kip.in (108333 kN.mm)$$

$$V_{yb_{\min}} = \frac{S_a m}{\eta_{\max}} = \frac{2.1*1.86*386}{6} = 251 kips (1115.5 kN)$$

from which the minimum required BRB area can be calculated as:

$$A_{b_{\min}} = \frac{V_{yb_{\min}}}{2 f_{yb} \cos\theta} = \frac{251}{2*40*\cos 45} = 4.44 in^2 (2775 mm^2)$$

And the maximum yielding portion of the BRB can calculated as:

$$L_{b_{\max}} = \frac{2 E_s A_{b_{\min}} \cos\theta}{K_{b_{\min}}} = \frac{2*29000*4.44*\cos 45}{975} = 186.8 in (4670 mm)$$

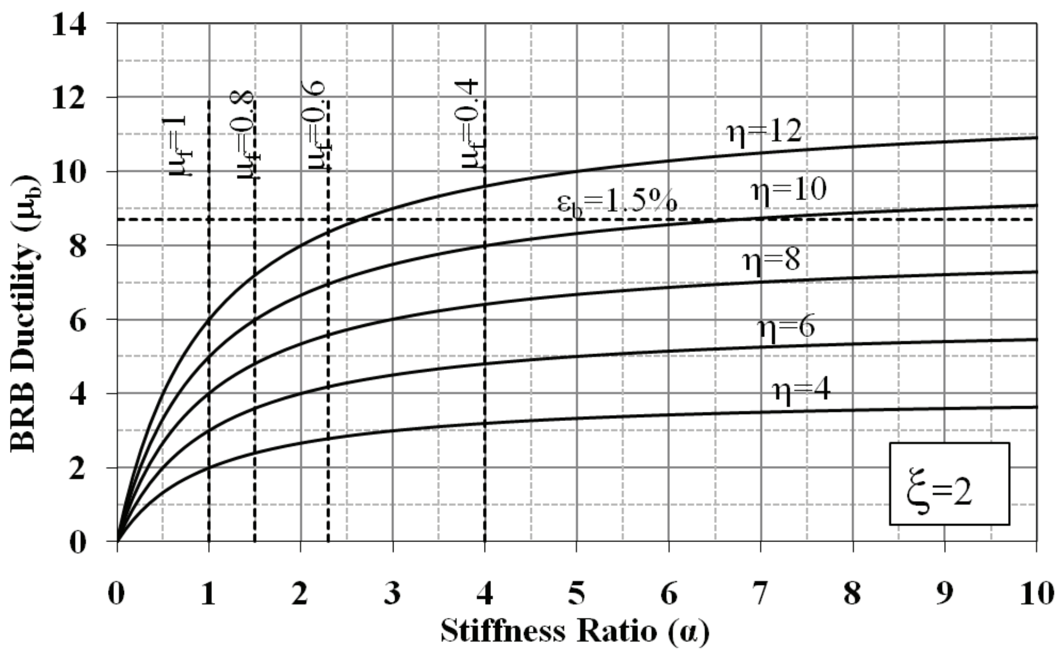

FIGURE 3-35 Regions of admissible solution for a value of ξ=2, $f_{y_{BRB}}$ =350 MPa (50 ksi)

where the total BRB length is 353in, and $\frac{L_{ysc}}{L_b} = \frac{186}{353} = 0.52$

Then, the yield displacement of the new BRB system can be calculated as:

$$\Delta_{yb} = \frac{V_{yb}}{K_{b_{\min}}} = \frac{251}{975} = 0.26in(6.5mm)$$

The total stiffness can now be calculated as:

$$K_{tot} = K_b + K_{eff} = 975 + 390 = 1365kip.in(151667kN.mm)$$

And the effective period of the retrofitted frame will be 0.23 sec < T_s, which means that the structure's spectral response comes from the constant acceleration region of the response spectra, and that the assumed S_a is the same as the actual one.

The modification factors can now be calculated, taking into account the equal energy theory:

$$R_d = \left(1 - \frac{1}{6}\right)\frac{1.25 * 0.39}{0.23} + \frac{1}{6} = 1.93 \text{ (AASHTO)}$$

$$\mathrm{C}_1 = \left(1 + \left(\frac{2.1}{942/718} * 1 - 1\right)\frac{0.4}{0.23}\right)\left(\frac{942/718}{2.1}\right) = 1.27 \text{ (NEHRP)}$$

Correcting previous values accordingly, the new target displacement is:

$$.\delta_t = \frac{R_d S_a T_{eff}^2}{4\pi^2} = \frac{1.93 * 2.1 * 0.23^2 * 386}{4\pi^2} = 2.09in \text{ (52.25 mm) (AASHTO)}$$

$$\delta_t = \frac{R_d S_a T_{eff}^2}{4\pi^2} = \frac{1.27 * 2.1 * 0.23^2 * 386}{4\pi^2} = 1.37in(34.25mm) \text{ (NEHRP)}$$

Since the AASHTO procedure gives more conservative values than the NEHRP one, it is found out here that the AASHTO procedure calculates a target displacement greater than the yield displacement of the bare frame, while the target displacement calculated using the NEHRP procedure satisfies the design requirement.

Continuing with the AASHTO procedure, a new α is chosen equal to 3.5, and repeating all the previous procedure we will get:

$K_b = 1365kip.in(151667kN.mm)$, $L_b = 133.4in(3335mm)$, $\Delta_{y_b} = 0.18in(4.5mm)$,

$K_{tot} = 1755kip.in(195000kN.mm)$, $T_{eff} = 0.2\sec$, $R_d = 2.1$, $\delta_t = 1.72in(43mm)$

the new frame parameters are:

$$\mu_f = R_d \xi \left(\frac{1}{1+\alpha} \right) = 2.1 * 2 \left(\frac{1}{1+3.5} \right) = 0.93$$

$$\mu_b = R_d \eta \left(\frac{1}{1+1/\alpha} \right) = 2.1 * 6 \left(\frac{1}{1+1/3.5} \right) = 9.8$$

and the value of $\mu_{\max}$ is equal to $\frac{\mu_b}{\mu_f} = \frac{9.8}{0.93} = 10.5$

Checking the BRB maximum strain according to the following equation:

$$\therefore \frac{\varepsilon_{BRB}}{\mu_b} = 100 \left(\frac{f_{y_{BRB}}}{E_s} \right)$$

$$\therefore \varepsilon_{BRB} = 9.8 * 100 \left(\frac{40}{29000} \right) = 1.35\% < 1.5\%$$

The resulting idealized pushover curve for the retrofitted frame is plotted against the ones for bare frame and the BRB in figure 3-36, together with some of the numerical values calculated above. It can be seen that the objective of satisfactory structural fuse performance is met according to figure 3-36.

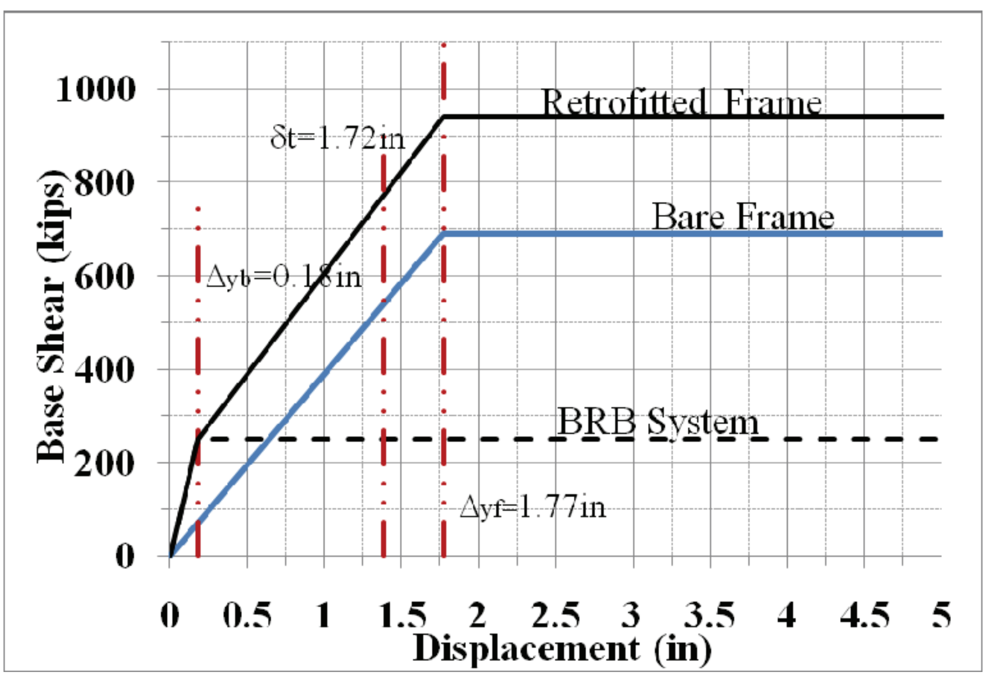

FIGURE 3-36 Idealized Pushover curve for the frame before and after retrofit

For comparison, one of the 9 compliant ground record generated using the TARSCTHS code was chosen to illustrate typical time history results. The selected accelerogram is shown in figure 3-37, time history analysis was performed using the SAP2000 software.

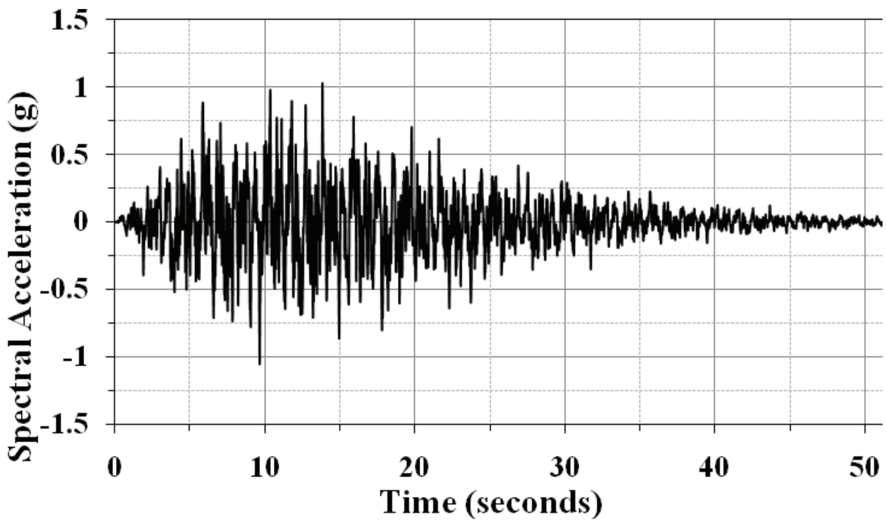

FIGURE 3-37 Generated Accelerogram by the TARSCTHS code

Displacement time histories for the bare frame and for the retrofitted frame are shown in figure 3-38. It is observed that the bare frame undergoes inelastic action as the maximum displacement obtained from the introduced accelerogram is 83.25 mm (3.33"), while the yield displacement of the bare frame is 44.25 mm (1.77") as shown in figure 3-36.

Figure 3-39 shows the displacement time history of the retrofitted frame. The maximum frame displacement is approximately 31.75 mm (1.27"), which means that the columns remain elastic. The yield displacement of the BRBs is 6.5 mm (0.26") as shown in figure 3-36, which indicated that the maximum BRB ductility reached 4.9, which corresponds to a brace strain of 0.75% which is within the limit of brace fracture strain and low cycle fatigue.

Hysteretic behavior of the retrofitted frame is shown in figure 3-40, confirming that the maximum displacement of 31.75 mm (1.27"), is less than the yield displacement of the frame. Hysteretic energy dissipation is achieved by yielding of the BRB, while no energy dissipation is done by the frame as it remains elastic.

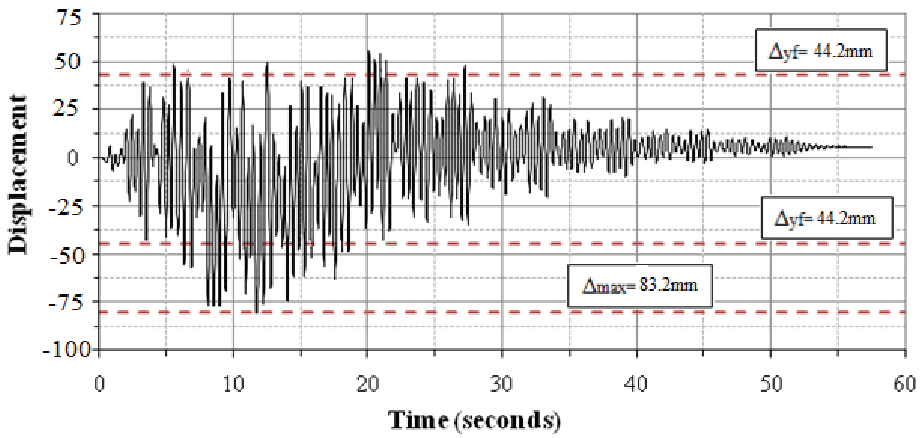

FIGURE 3-38 Displacement Time History Plot of the Bare Frame

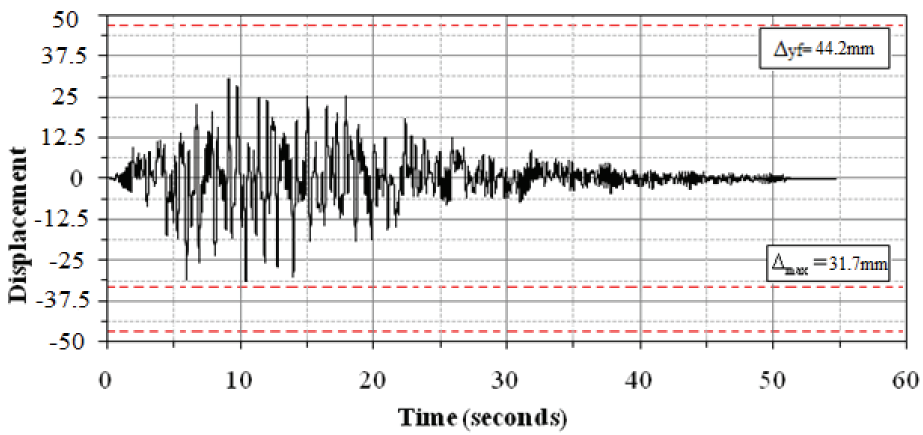

FIGURE 3-39 Displacement Time History Plot of the Retrofitted Frame

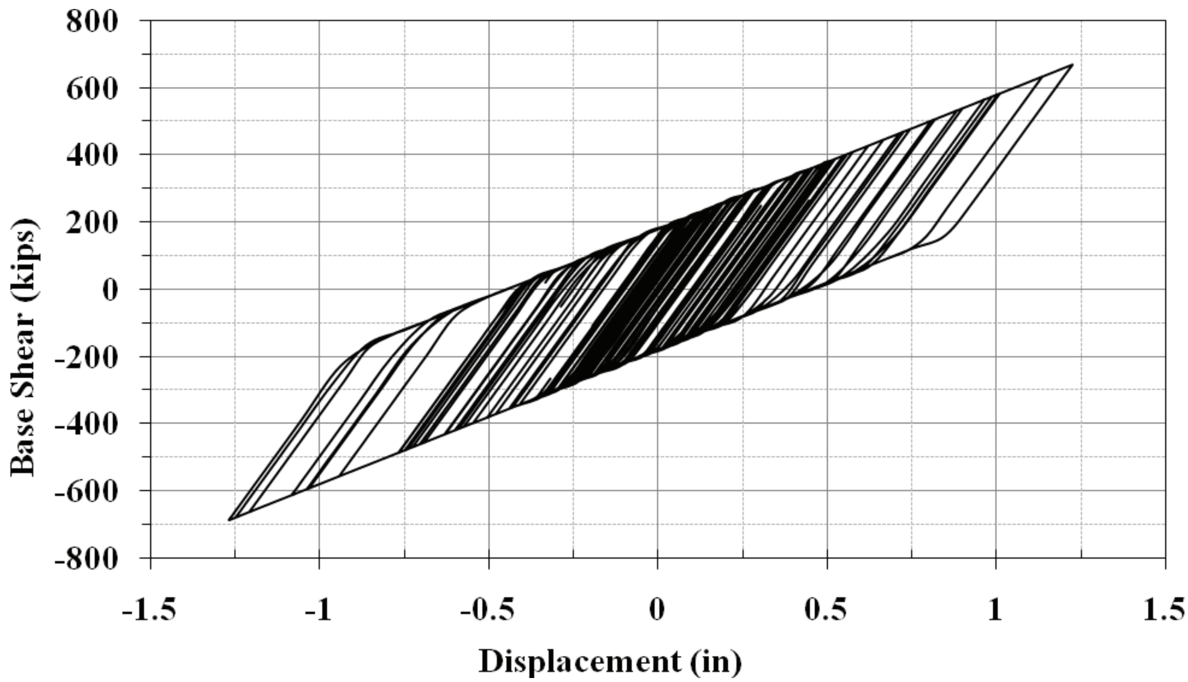

FIGURE 3-40 Retrofitted Frame Hysteretic Behavior

3.5 General Retrofit Procedure

3.5.1 Retrofit Design Steps and Flowchart

The previous study conceptually showed that the structural fuse concept can be achieved for an RC bridge bent using a combination of different parameters.

This knowledge must be augmented by guidelines on how to select suitable parameter values to achieve a satisfactory structural fuse system. A retrofit procedure is proposed and consists of the following steps illustrated in figure 3-41 by a flowchart.

1) Calculate the bare frame properties and perform a pushover analysis to define the idealized pushover curve from which Δ_{yf} and V_{yf} can be obtained.
2) Calculate initial shear strength of the bare frame V_i using procedures from ACI 318 or from the procedure proposed by (Priestley et al. 1994)
3) Calculate the ratio $\frac{V_i}{V_{yf}}$ to establish the failure mode of the frame.

4) If $\frac{V_i}{V_{yf}}$ is greater than 1, that means that the frame is will fail in flexure and that the desired μ_f is equal to 1. If the value of $\frac{V_i}{V_{yf}}$ is less than 1, that means that the frame will fail in shear and the desired μ_f is equal to the value of $\frac{V_i}{V_{yf}}$ (i.e. less than 1).
5) Select a maximum permissible brace strain ε to comply with the provisions of BRBs (a value of 1.5% is suggested).
6) Calculate the effective period of the bare frame, which is used to obtain the spectral acceleration from the chosen response spectrum.
7) Assume a spectral acceleration for the retrofitted frame. It should be greater than the one calculated for the bare frame preferably assumed to be in the constant acceleration region of the spectrum to decrease the initial number of iterations.
8) Estimate an initial value of ζ, where:

$$\xi = \frac{S_a m}{V_{yf}} \tag{3-42}$$

9) Calculate the BRB angle according to the bent geometry. Using a chevron layout,

$$\theta = \tan^{-1}\left(\frac{2H}{L}\right) \tag{3-43}$$

where L=bent span and H=bent height.

10) Enter the charts in figure 3-19 according to the calculated values of ξ and $f_{y_{BRB}}$. From those charts values of $\eta_{\max}$ and $\alpha_{\min}$ can be obtained. They are the theoretical values for the maximum BRB strength required and the minimum stiffness ratio required to achieve the identified target ductilities. These values can be modified later if the calculated BRB area and strength are found to be impractical.
11) Calculate the minimum required BRB stiffness and strength as:

$$K_{b_{\min}} = \alpha_{\min} K_f \tag{3-44}$$

$$V_{yb_{\min}} = \frac{S_a m}{\eta_{\max}} \tag{3-45}$$

from which the minimum required BRB area, $A_{b_{\min}}$, can be calculated as:

$$A_{b_{\min}} = \frac{V_{yb_{\min}}}{2 f_{y_{BRB}} \cos\theta} \tag{3-46}$$

and the maximum yielding length of the BRB, $L_{\max}$, can be calculated as:

$$L_{\max} = \frac{2E_s A_{b_{\min}} \cos\theta}{K_{b_{\min}}} \tag{3-47}$$

Note that the resulting BRBs must be physically realistic as not all sizes and strengths are available or doable. That means that the most economic theoretical solution on paper is not always the best one. As such, it would be important to keep practical limits in mind to deviate on purpose from the target parameters within the region of admissible solution or even to choose a different BRB layout than the chevron layout studied. If the theoretical solution is not doable, arrange the BRBs into a new layout, with smaller angle θ of different geometry altogether, to increase the number of BRBs, with smaller required areas for each one.

12) Assess whether the area calculated above can be provided and accommodated by the system. If it is found to be excessive, another layout is to be selected and θ is recalculated. For the purpose of this study, if such is the case, an alternative BRB layout is proposed as shown in figure 3-42, using multiple chevrons on top of each other, and the new BRB angle, θ^*, can be calculated as:

$$\theta^* = \tan^{-1}\left(\frac{2H}{nL}\right) \tag{3-48}$$

where n=number of chevron bracings

The new BRB lateral stiffness to maintain the desired μ_f is calculated as:

$$K_b^{/} = \frac{n^2 E_s A_b^{/} \sin 2\theta^*}{\left(\frac{L_{ysc}}{L_b}\right) H} \tag{3-49}$$

while in case of a single chevron bracing system the BRB lateral stiffness is calculated as:

$$K_b = \frac{E_s A_b \sin 2\theta}{\left(\frac{L_{ysc}}{L_b}\right) H} \tag{3-50}$$

It is required to maintain the same value of α, from which the new lateral stiffness, $K_b^{/}$, must be equal to K_b, which leads to:

$$A_b^{/} = A_b \left(\frac{1}{n^2}\right)\left(\frac{\sin 2\theta}{\sin 2\theta^*}\right) \tag{3-51}$$

From which the number of BRBs, n, can be increased until a reasonable BRB area is achieved.

After calculating $A_b^/$, the corresponding maximum yielding BRB length, $L_{\max}^/$, is calculated as:

$$L_{\max}^/ = \frac{2nE_s A_b^/ \cos\theta^*}{K_b^/} \tag{3-52}$$

13) If the calculated $L_{\max}^/$ is greater than the BRB length, this length can be reduced to the maximum feasible length (i.e. 0.8 L_b) where L_b is the BRB total length and the BRB area can be back calculated as follows:

$$A_b^/ = \frac{L_{\max}^/ K_b^/}{2nE_s \cos\theta^*} \tag{3-53}$$

Again if this area is impractical, step (11) is repeated until a reasonable value is obtained for $A_b^/$ and $L_{\max}^/$

The value of $\eta^/$ is then calculated as:

$$\because V_{yb} = 2A_b f_{y_{BRB}} \cos\theta \tag{3-54}$$

$$\because V_{yb}^/ = 2nA_b^/ f_{y_{BRB}} \cos\theta^* \tag{3-55}$$

$$\therefore \eta^/ = \eta\left(\frac{V_{yb}}{V_{yb}^/}\right) = \eta\left(\frac{1}{n}\right)\left(\frac{A_b}{A_b^/}\right)\left(\frac{\cos\theta}{\cos\theta^*}\right) = \lambda\eta \tag{3-56}$$

where $\lambda = \left(\frac{1}{n}\right)\left(\frac{A_b}{A_b^/}\right)\left(\frac{\cos\theta}{\cos\theta^*}\right)$

For the case of one chevron bracing λ=1

14) At this stage the total stiffness can be calculated to calculate the effective period of the retrofitted frame and the actual spectral acceleration can then be calculated.
15) If the calculated spectral acceleration is not the same as the assumed "constant acceleration region", assume a new spectral acceleration and go to step (8) and iterate until $S_{a_{assumed}} = S_{a_{actual}}$
16) Values of μ_b and μ_f can now be calculated, if the actual spectral acceleration lies in the constant acceleration zone, a modification must be applied to these values to take into

account the equal energy theory as it was mentioned before that the charts was formed assuming the equal displacement theory. New values of μ_b and μ_f can be calculated as:

$$R_d = \left(1 - \frac{1}{\mu_D}\right)\frac{1.25T_s}{T_{eff}} + \frac{1}{\mu_D} \tag{3-57}$$

$$\mu_f = R_d \xi \left(\frac{1}{1+\alpha}\right) \tag{3-58}$$

$$\mu_b = R_d \lambda \eta \left(\frac{1}{1+1/\alpha}\right) \tag{3-59}$$

17) The values of μ_f and μ_b can now be recalculated, and the value of $\mu_{\max}$ would be equal to $\frac{\mu_b}{\mu_f}$

18) Check for BRB strain according to the following equation:

$$\therefore \frac{\varepsilon_b}{\mu_b} = \frac{f_{y_{BRB}}}{E_s} \tag{3-60}$$

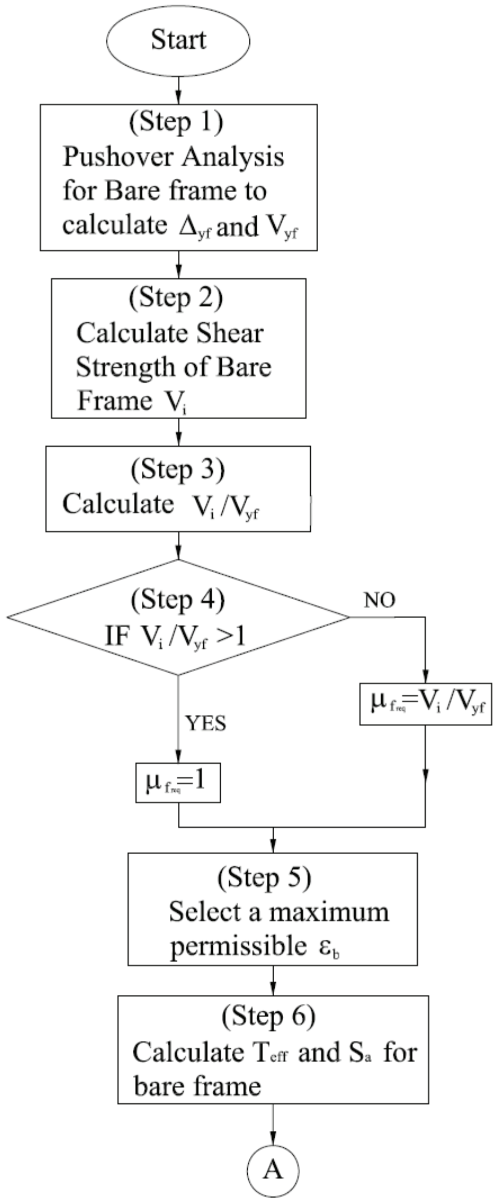

FIGURE 3-41 Procedure to Retrofit RC Bridge Bents Satisfying the Structural Fuse Concept

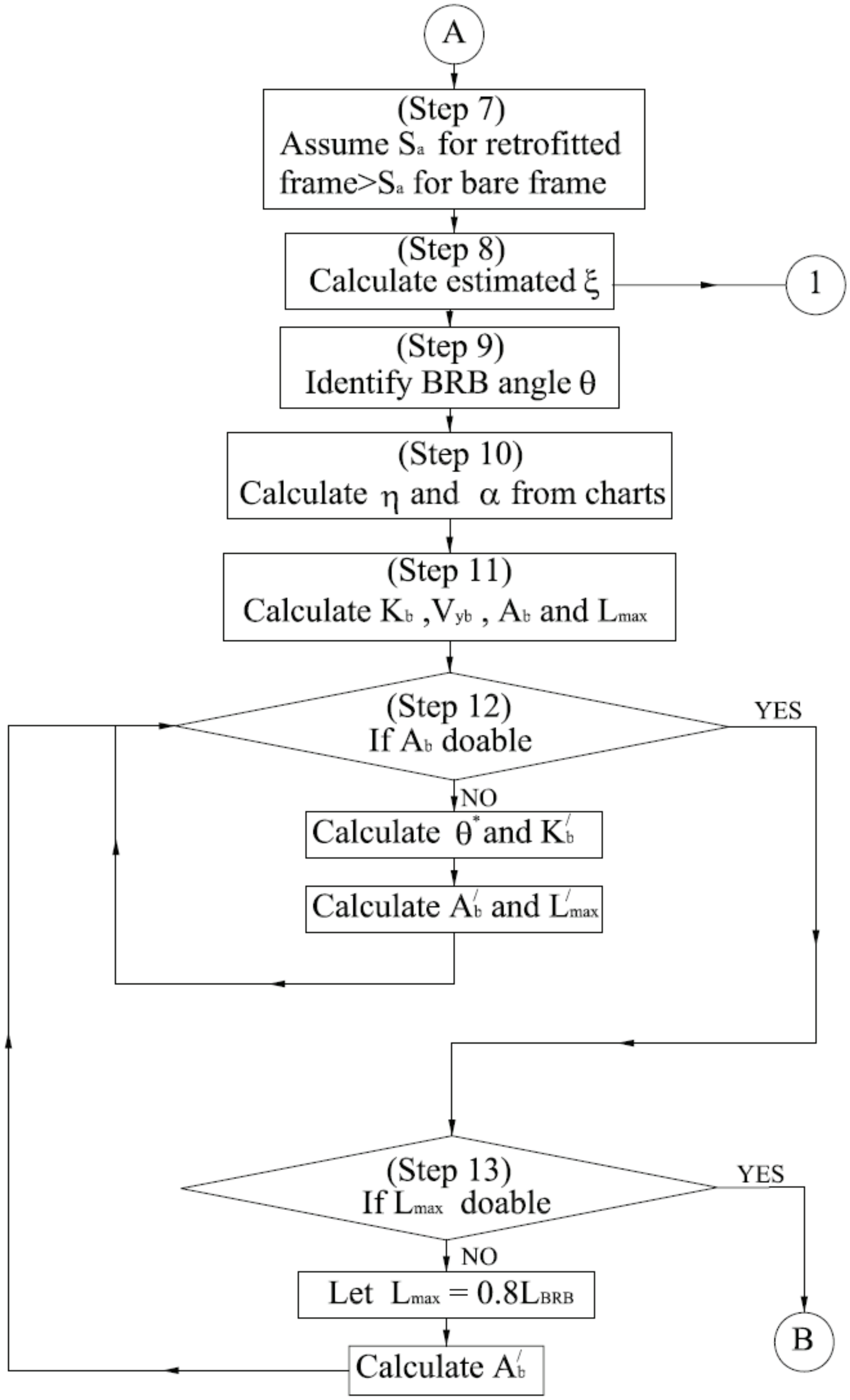

FIGURE 3-41 (CONT.) Procedure to Retrofit RC Bridge Bents Satisfying the Structural Fuse Concept

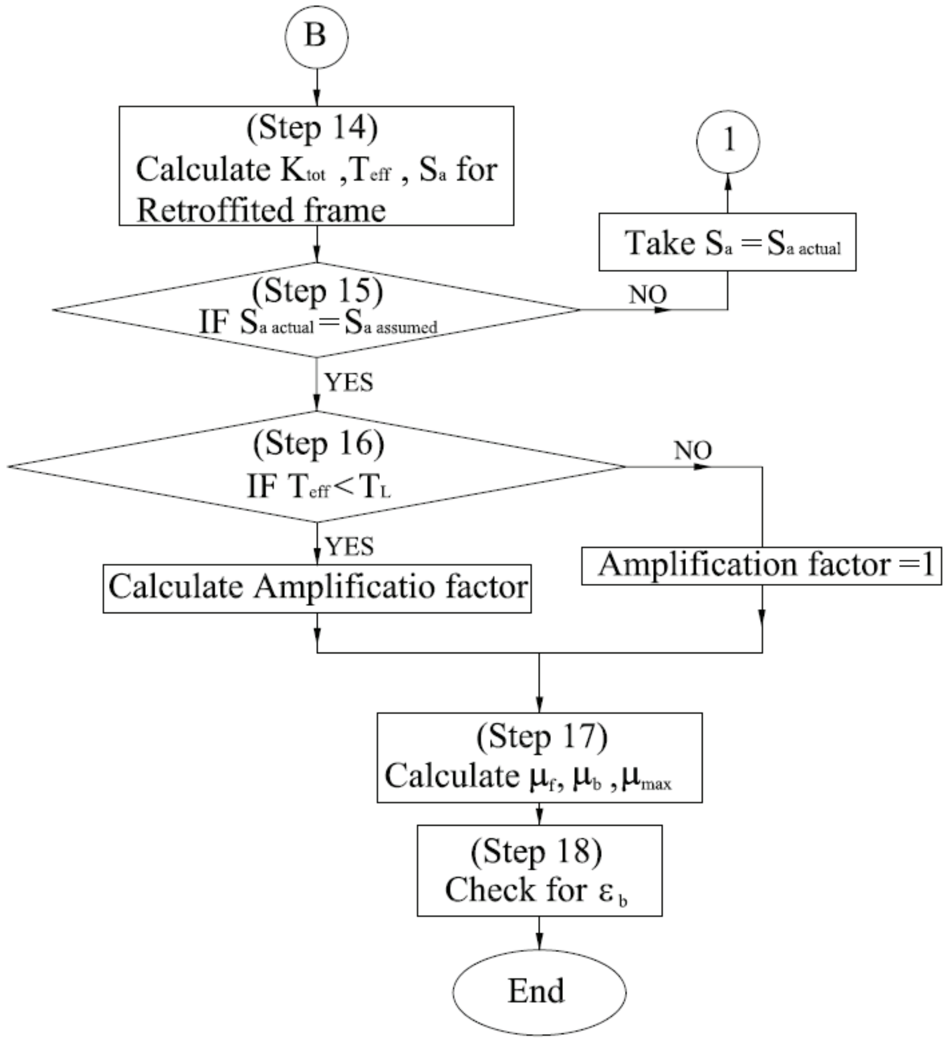

FIGURE 3-41 (CONT.) Procedure to Retrofit RC Bridge Bents Satisfying the Structural Fuse Concept

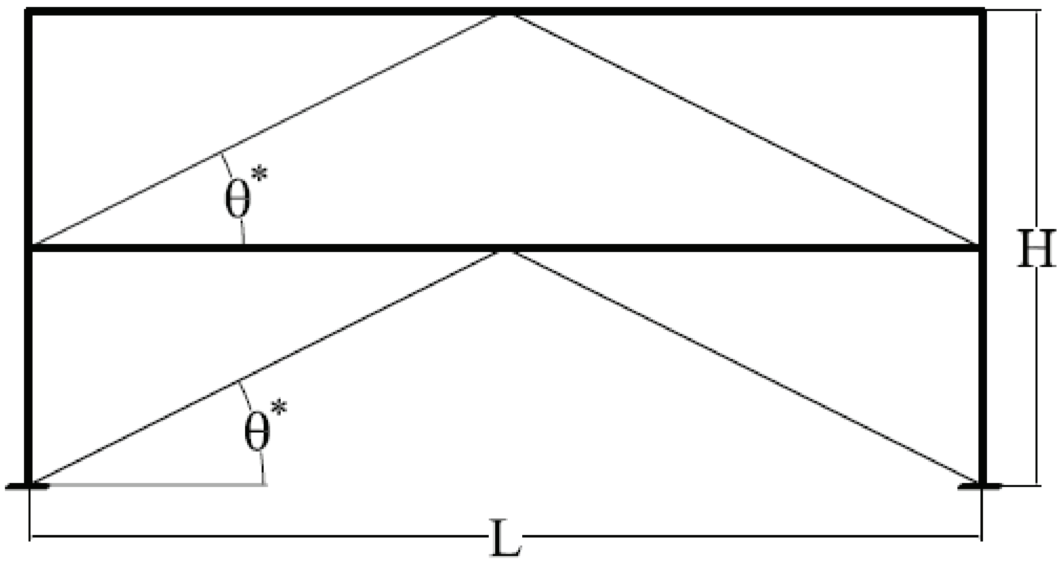

FIGURE 3-42 Alternate BRB Layout

3.5.2 Example

From the previous example in section 3.4, if the calculated BRB length or area is not feasible, a new layout of the BRBs would be proposed as shown in figure 3-42, continuing on from step 12 the new BRB angle is calculated as:

$$\theta^* = \tan^{-1}\left(\frac{2*250}{2*500}\right) = 26.6^\circ$$

$$A_b^/ = A_b\left(\frac{1}{n^2}\right)\left(\frac{\sin 2\theta}{\sin 2\theta^*}\right) = 4.44\left(\frac{1}{2^2}\right)\left(\frac{\sin 90}{\sin 53.13}\right) = 1.38 in^2 (862.5 mm^2)$$

$$L_{\max}^/ = \frac{2nE_s A_b^/ \cos\theta^*}{K_b} = \frac{2*2*29000*1.38*\cos 26.6}{975} = 147.6 in (3690 mm)$$

Where the total BRB length is 280 in, then $\frac{L_{ysc}}{L_b} = \frac{147.6}{280} = 0.53$ "yielding portion of the BRB"

The value of $\eta^/$ can now be calculated as:

$$\lambda = \left(\frac{1}{n}\right)\left(\frac{A_b}{A_b^/}\right)\left(\frac{\cos\theta}{\cos\theta^*}\right) = \left(\frac{1}{2}\right)\left(\frac{4.44}{1.38}\right)\left(\frac{\cos 45}{\cos 26}\right) = 1.27$$

$$\therefore \eta^/ = \lambda\eta = 1.27*6 = 7.62$$

And the yield strength of the new BRB system is now equal to:

$$V_{yb} = \frac{S_a m}{\eta^{/}} = \frac{2.1*1.86*386}{7.62} = 198 kips (880 kN)$$

The actual BRB stiffness can now be calculated as:

$$K_b^{/} = \frac{n^2 E_s A_b^{/} \sin 2\theta^*}{\left(\frac{L_{ysc}}{L_b}\right) H} = \frac{2^2 * 29000 * 1.38 * \sin 53}{0.53 * 250} = 965 kip.in (107222 kN.mm)$$

Then the yield displacement of the new BRB system can be calculated as:

$$\Delta_{yb} = \frac{V_{yb}}{K_b^{/}} = \frac{198}{965} = 0.2 in (5mm)$$

The total stiffness can now be calculated as:

$$K_{tot} = K_b + K_{eff} = 965 + 390 = 1355 kip.in (150556 kN.mm)$$

And the effective period of the retrofitted frame will be 0.2 sec < T_s" constant acceleration region", which means that the assumed S_a is the same as the actual.

The R_d factor can now be calculated to take into account the equal energy theory.

$$R_d = \left(1 - \frac{1}{6}\right)\frac{1.25*0.39}{0.23} + \frac{1}{6} = 1.93 \text{ (AASHTO)}$$

The new target displacement would be equal to:

$$.\delta_t = \frac{R_d S_a T_{eff}^2}{4\pi^2} = \frac{1.93*2.1*0.2^2*386}{4\pi^2} = 1.7 in (42.5mm)$$

The new frame parameters can be calculated as follows

$$\mu_f = R_d \xi \left(\frac{1}{1+\alpha}\right) = 1.93*2\left(\frac{1}{1+3.5}\right) = 0.86$$

$$\mu_b = R_d \lambda \eta^{/} \left(\frac{1}{1+1/\alpha}\right) = 1.93*1.27*6\left(\frac{1}{1+1/3.5}\right) = 11.4$$

Then the value of $\mu_{\max}$ would be equal to $\frac{\mu_b}{\mu_f} = \frac{11.4}{0.86} = 13.3$

Check for BRB strain according to the following equation:

$$\therefore \varepsilon = 11.4*100\left(\frac{40}{29000}\right)\left(\frac{1}{\cos 26.6}\right) = 1.75\% \text{ (which is slightly larger than 1.5\%)}$$

3.6 Summary and Observations

3.6.1 Summary

Buckling Restrained Braces where proposed as a structural fuse for retrofitting RC bridge bents to increase their strength and stiffness, and to dissipate seismic energy through hysteretic behavior while the bridge piers remain elastic. A parametric study for a typical prototype RC bridge bent retrofitted using BRBs was conducted in section 3.2 to investigate trends in behavior as a function of key parameters defining the proposed structural fuse system while using BRBs of different stiffnesses and strengths as the energy dissipating fuses. Regions of admissible solution where plotted for different BRB strength and stiffnesses. Changing the column dimension and height was investigated.

A more general parametric study, in terms of non-dimensionalized values was conducted in section 3.3 to consider general frame and BRB geometries. Key parameters that controls the behavior of the BRB as a structural fuse where identified, relationships between these parameters where investigated for the application at hand, and plots showing the regions of admissible solutions for several frame and BRB strengths and stiffnesses where constructed. The results were refined and validated using non-linear time history analyses in section 3.4 as a 9 compliant ground record was chosen to match the targeted response spectra, plots showing comparison of the time history results and the static procedure where introduced and validated with a numerical example.

A retrofit design procedure was then introduced in section 3.5 and was illustrated by a flow chart showing the necessary steps for the retrofit procedure.

3.6.2 Observations

It was observed that for a given value of stiffness ratio, increasing the BRB ductility would result in increasing the BRB strength ratio and accordingly decrease the BRB strength, as in order to increase the BRB ductility while preserving the stiffness, a reduction in the BRB strength is required in order to decrease the BRB yielding displacement and accordingly increase the BRB ductility. While increasing the frame strength ratio for a given frame stiffness would result in decreasing the frame yielding strength and yielding displacement, so for a given frame stiffness ratio, increasing the frame strength ratio would decrease the frame ductility.

It was also observed that increasing the stiffness ratio corresponds to decreasing the frame stiffness, and for a given frame strength ratio, decreasing the frame stiffness would result in increasing the frame yielding displacement and also the frame ductility.

It was also observed that for a given yielding length ratio and BRB area, increasing the column height would increase μ_b, and ε_b, while it would decrease μ_f, since increasing the column height would increase the target displacement, resulting in increasing the value of the BRB ductility as well as the BRB strain. Also increasing the column height would result in decreasing both of the stiffness and strength of the bare frame while at the same time increase its yielding displacement, this will result in decreasing the value of the frame ductility for a fixed period of the retrofitted frame.

It was also observed that for a given yielding length of BRB, increasing the BRB area reduces μ_f, μ_b, and ε_b, since the structure becomes stiffer and the spectral target drift reduces. Likewise, for a given BRB area, decreasing c has the same effect.
It was also observed that if the stiffness of the BRB is too small compared to that of the frame, a very large value of BRB to frame strength ratio is required to achieve the structural fuse concept which is almost impossible.

3.6.3 Needed Research

For the validation of the retrofit procedure, an experimental validation is then introduced in the next sections, where the structural fuse concept is implemented and tested on bridge piers to proof their efficiency.

SECTION 4
STEEL PLATE SHEAR LINK (SPSL)

4.1 Introduction

Earthquakes can cause significant damage to bridge substructures which may cause collapse and loss of life. The ability of a system to deform inelastically without significant loss of strength or stiffness can improve its seismic response, avoiding catastrophic collapses. One major benefit of ductile inelastic deformations is that they can limit the forces transmitted to adjacent members, allowing them to be of more reasonable dimensions; also it provides hysteretic energy dissipation to the system.

The concept of designing sacrificial members dissipating the seismic energy, while preserving the integrity of other main components, is known as the structural fuse concept. It was described in details in section 3. In this section, an innovative Steel Plate Shear Link (SPSL) is introduced. That new element is designed to act as a structural fuse dissipating all the seismic energy through inelastic shear deformation, while the rest of the bridge substructure remains elastic.

The newly proposed structural fuse element is first described, and its shear-moment interaction equation is derived. Equations are then developed to determine some critical design parameters of the link, namely the balanced link length and balanced link edge angle which will be discussed later in this section. Equations deriving the link ductility and lateral stiffness and strength are then described. A preliminary finite element model is then presented to validate the proposed concept.

4.2 Steel Plate Shear Link Description

The proposed SPSL shown in figure 4-1 consists of a steel plate restrained from out of plane buckling. Out of plane buckling can be resisted using any type of material that has the sufficient lateral stiffness to resist the out of plane motion of the plate. For example concrete encasement and an unbonding material to reduce friction between the steel and the concrete encasement can be used; thick steel plates could also be used to prevent the out of plane motion of the steel plate. The steel plate is designed to yield in shear, at a stress equal to $0.6F_y$ dissipating the seismic energy.

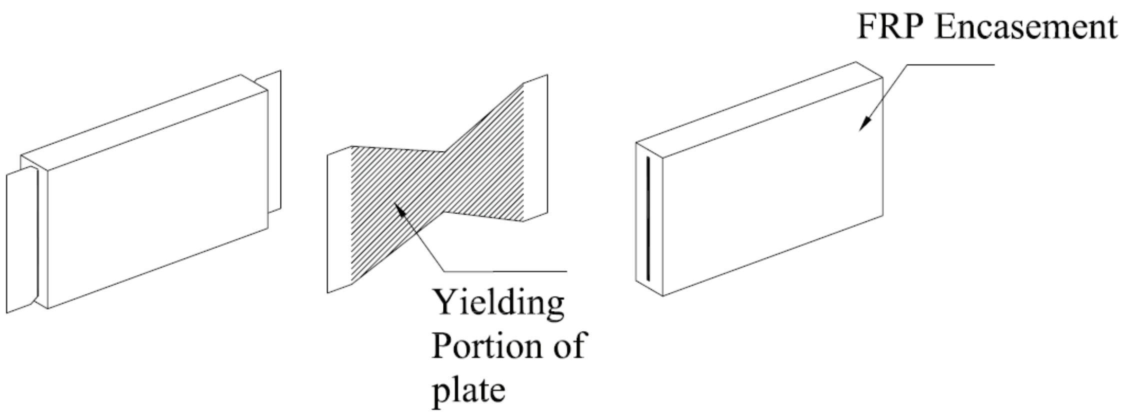

FIGURE 4-1 Proposed Link Sketch

4.3 Shear-Moment Interaction

Three types of plastic mechanisms can develop in laterally restrained links regardless of the shape of the cross section. The plastic mechanism that can develop depends mainly on the link length, and can be categorized as follows:

- Flexural links (pure flexural yielding) developing full plastic moment hinges, M_p, at the ends of the links and a corresponding shear force less than the full plastic shear force, V_p. These links dissipate energy by flexural plastic rotation.
- Shear links (pure shear yielding) developing full plastic shear force, V_p, over the entire length of the link, with corresponding moments at their ends less than the plastic moment reduced to account for the presence of shear, M_p^r. These links dissipate energy by shear plastic rotation.
- Intermediate links, which are links yielding in both flexure and shear where, one yielding mode develops after the other mode strain hardens.

Various experimental studies of link behavior by previous researchers reported that shear links exhibit the most stable and ductile cyclic behavior. For example, Kasai and Popov (1986a, b), and Whittaker et al. (1987) studied the behavior of shear links (short links) and concluded that their inelastic shear strains are fairly uniformly distributed over the entire length of the link, which permits the development of large inelastic deformations without the presence of high local strains. It was reported that a well detailed link can sustain a plastic rotation of 0.1 radian without failure. Engelhardt and Popov (1989) studied the behavior of flexural links (long links) and concluded that the high bending strains that develops at their ends can only sustain inelastic deformations that corresponds to a plastic rotation of 0.02 radian (about 5 times less than a shear link).

Given that the ultimate failure mode for shear links is inelastic web shear buckling, to delay that failure mode, Kasai and Popov (1986a) recommended adding vertical stiffeners, and provided simple rules to calculate the stiffeners spacing as a function of the maximum inelastic link rotation.

For the type of link proposed here, the web shear buckling is overcome by wrapping the steel plate with a material with sufficient lateral stiffness to overcome the out of plane buckling of the steel plate.

Given that this type of link varies from those used in conventional eccentrically braced frames (EBF), it is necessary for design purposes and behavior study to formulate shear-moment interaction equations for the proposed element. Shear-moment interaction equations have been previously studied for different hybrid steel sections; a lower bound interaction equation for hybrid built up I-sections was proposed in the ASCE special publication on plastic design in 1971 using the stress distribution shown in figure 4-2. Berman and Bruneau (2005) used a similar stress distribution to derive the interaction equation for shear links having hybrid tubular cross sections.

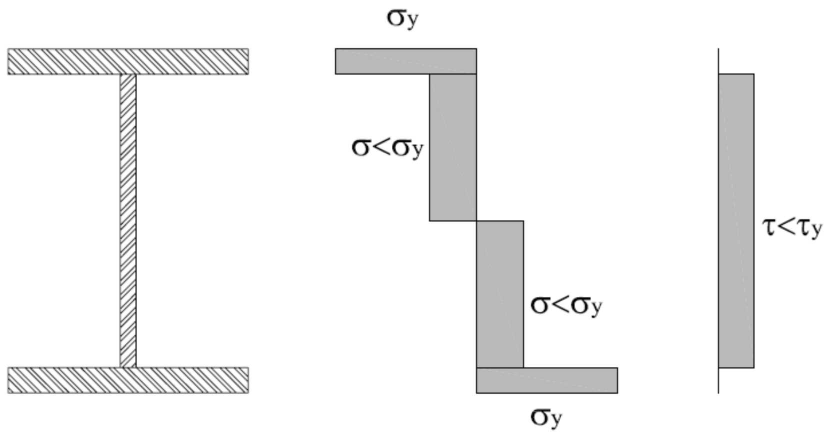

FIGURE 4-2 Assumed Normal and Shear Stress Distribution

For the new type of shear link proposed here, a similar assumed stress distribution is chosen, as shown in figure 4-3. In this approach, shear yielding is assumed to occur over a depth of y_o over the entire length of the link. Since the link is in double curvature, the mid-length point along the link is in pure shear, and moment increases from zero at this point to a value at the link ends equal to the plastic shear strength. The slope, θ, of the link edges must therefore vary linearly (like the moment diagram) to provide this needed moment strength. From that basis, the following equations can be derived:

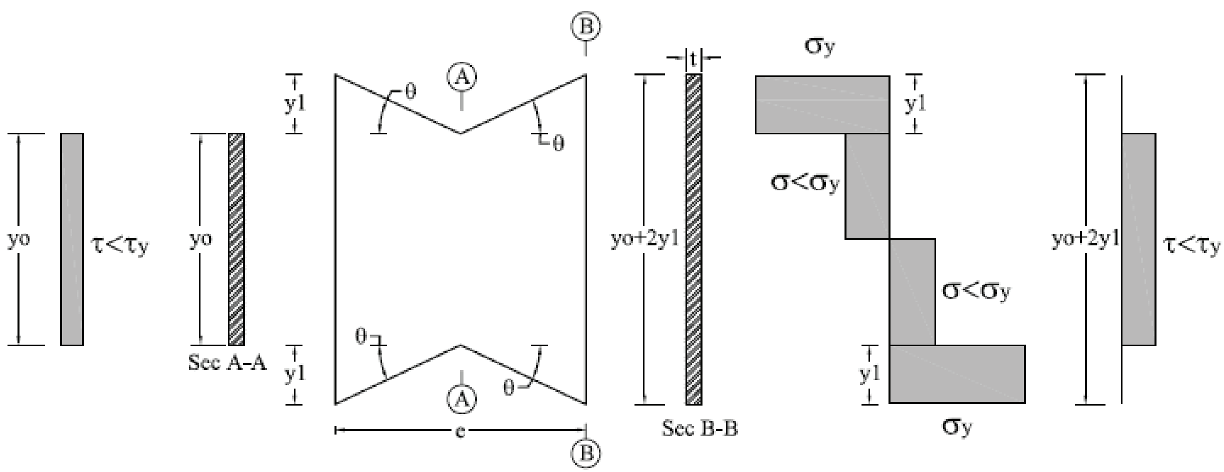

FIGURE 4-3 Assumed Stress Distribution in Mid and End plate

$$V = \tau t y_0 = \frac{\sigma}{\sqrt{3}} t y_0 \qquad (4\text{-}1)$$

$$M^{V} = \sigma_y y_1 t(y_0 + y_1) + \sigma \frac{t y_0^2}{4} \tag{4-2}$$

where V is the existing shear force along for section A-A, M^{V} is the corresponding moment in presence of shear force for section B-B, and σ_y is the yield stress of the plate.

For comparison, the full plastic moment and full plastic shear can be derived as:

$$M_p = \sigma_y \frac{t(y_0 + 2y_1)^2}{4} \tag{4-3}$$

$$M_{pr} = \sigma_y y_1 t(y_0 + y_1) \tag{4-4}$$

$$V_p = \frac{\sigma_y}{\sqrt{3}} t y_0 \tag{4-5}$$

where M_p is the full plastic moment of section B-B, M_{pr} is the reduced plastic moment of section B-B due to the presence of full plastic shear and V_p is the full plastic shear of section B-B.

Given that equations (4-1) and (4-2) are linked to each other by the following Von Misses yielding criteria for plane stress elements:

$$\sigma_y = \sqrt{\sigma^2 + 3\tau^2} \tag{4-6}$$

equations (4-1) and (4-5) can be rewritten as:

$$\tau = \frac{V}{t y_0} \tag{4-7}$$

$$t y_0 = \frac{\sqrt{3}}{\sigma_y} V_p \tag{4-8}$$

substituting equation (4-8) into (4-7), one obtains:

$$\tau = \frac{\sigma_y}{\sqrt{3}}\left(\frac{V}{V_p}\right) \tag{4-9}$$

substituting equations (4-9) in (4-6), the normal stress in the plate can be expressed as:

$$\sigma = \sigma_y \sqrt{1-\left(\frac{V}{V_p}\right)^2} \tag{4-10}$$

rewriting equation (4-3) as:

$$\sigma_y = M_p\left(\frac{4}{t(y_0+2y_1)^2}\right) \tag{4-11}$$

and substituting equation (4-10) into equation (4-2) to get:

$$M^V = \sigma_y y_1 t(y_0+y_1) + \sigma_y \sqrt{1-\left(\frac{V}{V_p}\right)^2} \tag{4-12}$$

equation (4-10) can be substituted into equation (4-12),

$$M^V = M_p\left(\frac{4}{t(y_o+2y_1)^2}\right)\left(y_1 t(y_o+y_1) + \sqrt{1-\left(\frac{V}{V_P}\right)^2}\right) \tag{4-13}$$

from which and interaction equation for the proposed element can be expressed as:

$$\frac{M^V}{M_p} = \frac{4y_1(y_o+y_1)}{(y_o+2y_1)^2} + \left(\frac{4}{t(y_o+2y_1)^2}\sqrt{1-\left(\frac{V}{V_P}\right)^2}\right) \tag{4-14}$$

Note that at $V=V_p$, M^V would be equal to M_{Pr}.

4.4 Shear Link Length

As mentioned before, links could be categorized as shear, flexural, or intermediate links, with shear links having the most stable and ductile cyclic behavior. These can be defined as a function of the link length, e, in terms of the balanced length, e^*, which is the point when the transition from flexural to shear yielding occurs. It can be calculated by considering the equilibrium of the free body diagram of the link shown in figure 4-4.

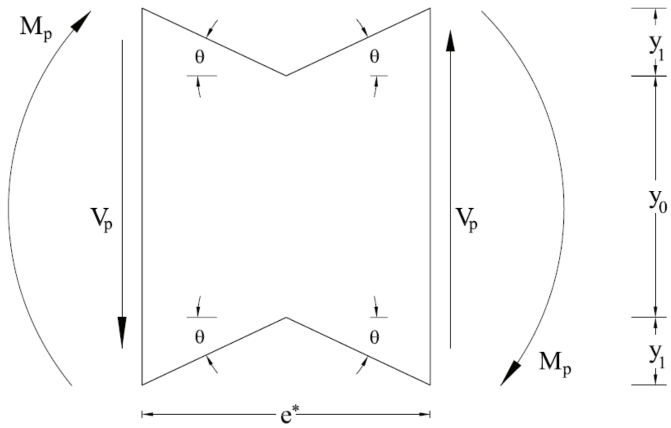

FIGURE 4-4 Free Body Diagram at the Balanced Link Length

Neglecting the effect of axial load and the reduced plastic moment due to shear, the balanced length is calculated as:

$$e^* = \frac{2M_p}{V_p} \tag{4-15}$$

For the case at hand, substituting equations (4-3) and (4-5) into (4-15), e^* is found out to be

$$e^* = \frac{\sqrt{3}}{2}\frac{(y_0 + 2y_1)^2}{y_0} \tag{4-16}$$

where:

$$y_1 = \frac{e^*}{2}\tan\theta \tag{4-17}$$

substituting equation (4-17) into (4-16) and rearranging, the value of the balanced link length is found out to be

$$e^* = \frac{\sqrt{3}(y_0 + e^* \tan\theta)^2}{y_0} \tag{4-18}$$

If the effect of the reduced plastic moment due to shear is taken into account, the balanced link length is calculated by substituting equation (4-4) and (4-5) into (4-15) and e^* would be equal to:

$$e^* = \frac{2\sqrt{3}y_1(y_0 + y_1)}{y_0} \tag{4-19}$$

then substituting (4-17) into (4-19):

$$e^{*} = \frac{2y_o}{\sqrt{3}\tan^2\theta}\left(1-\sqrt{3}\tan\theta\right) \tag{4-20}$$

The AISC has adopted this procedure for the design of wide flange links, with a margin of safety to account for strain hardening effects. As a result, per AISC, to insure shear yielding, the link length, *e*, must be less than or equal to $\frac{1.6M_p}{V_p}$, while to insure flexural yielding the value of the link length, *e*, must be greater than or equal to $\frac{2.6M_p}{V_p}$. For values in between, (i.e. intermediate links), yielding will start as either flexure or shear but strain hardening will eventually lead to the development of joint shear and flexural yielding. To comply with the AISC seismic provisions (2005), the chosen link length, *e*, is taken as:

$$e \le \frac{1.6y_o}{\sqrt{3}\tan^2\theta}\left(1-\sqrt{3}\tan\theta\right) \tag{4-21}$$

4.5 Balanced Link Edge Angle

Another important factor governing the behavior of the link is the link edge angle, θ. While changing the link length changes the behavior of the link from shear to flexure, changing the link edge angle, θ, changes the way yielding propagates in the plate.

On the basis of the assumed stress distribution presented in section 4.3, for yielding to develop in the plate following the pattern shown in figure 4-5, where flexural and shear yielding occurs simultaneously, geometry of the link is defined by the balanced link edge angle, θ_b, which can be obtained from the equilibrium of the balanced link length shown in figure 4-6.

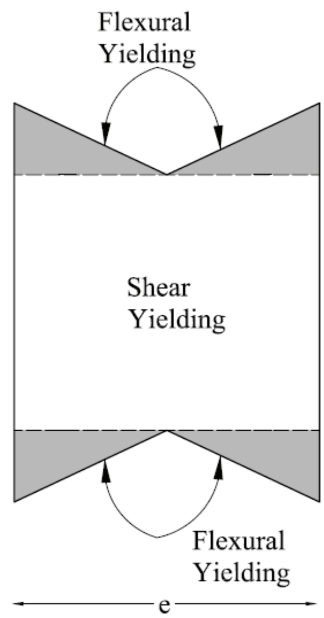

FIGURE 4-5 Proposed Yielding in Shear Link

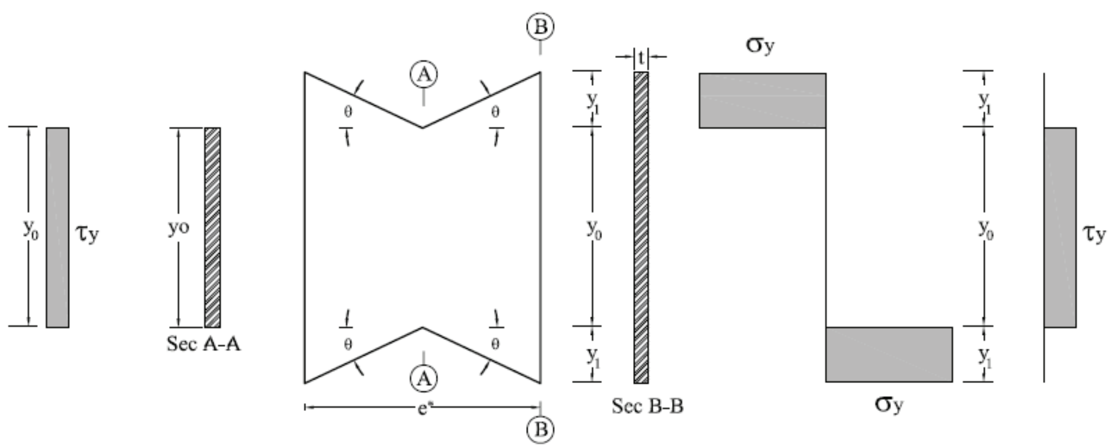

FIGURE 4-6 Assumed Stress Distribution at Balanced Link Edge Angle

Rearranging equation (4-20) can be rewritten as

$$y_1^2 + y_0 y_1 - \frac{y_0 e}{2\sqrt{3}} = 0 \tag{4-22}$$

then, substituting equation (4-17) into (4-22), an equation for the balanced link edge angle (θ_b) can be written as:

$$\tan^2 \theta_b + \frac{2y_0}{e}\tan\theta_b - \frac{2y_0}{e\sqrt{3}} = 0 \tag{4-23}$$

from which values of θ_b can be found with respect to $\frac{y_o}{e}$, itself an expression of the aspect ratio of the link with large values of $\frac{y_o}{e}$ corresponding to deeper links. This relationship is plotted in figure 4-7.

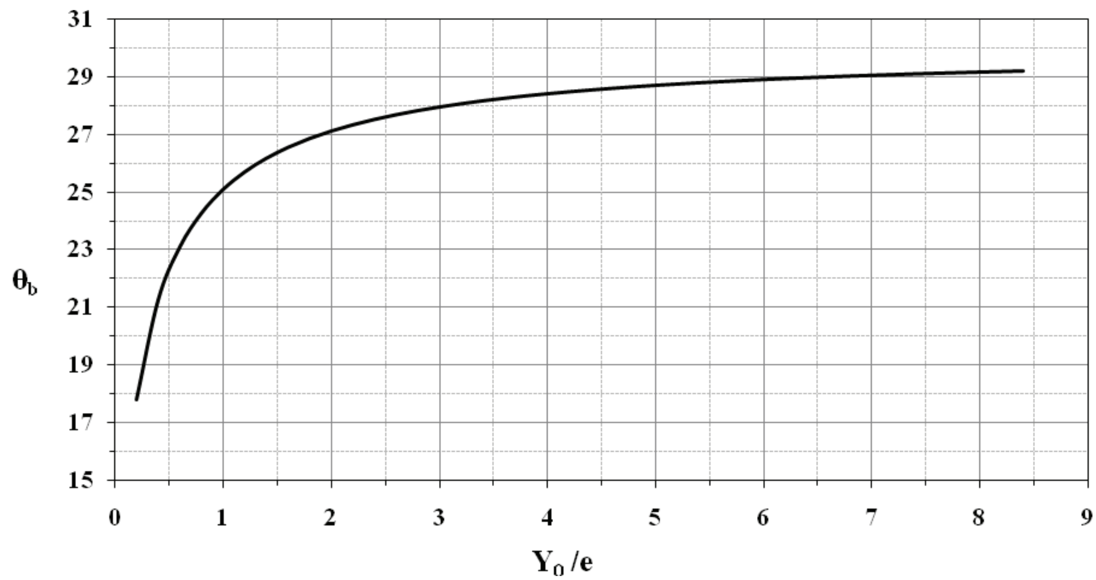

FIGURE 4-7 Balanced Link Edge Angle WRT Y_0 /e

It can be observed that the required balanced link edge angle increases rapidly for values of $\frac{y_0}{e}$ <3, while for values of $\frac{y_0}{e}$ >3 the increase is slow, with the balanced link edge angle for values of $\frac{y_0}{e}$ >3 approaching 30 degrees. The physical significance of having actual angle values either equal, below, or above the balanced link edge angle value is discussed in section 4.6.

4.6 Shear Link Types

Three types of shear links can be developed in relation to the link edge angle, θ. Note that the following is based on the assumption that all links will be designed to have a link length less than the balanced link length ($e \le e^*$) to ensure shear yielding (which is preferred over flexural yielding). In the following, the link is divided into two parts: the middle part, corresponding to the rectangular middle portion of the link shown in white in figure 4-5, and the wedge parts shown as the triangular shaded areas on that figure.

4.6.1 Links with Balanced Edge Angles ($\theta=\theta_b$)

For links having a link edge angle equal to the balanced link edge angle, shear yielding will occur across the middle part of the web accompanied by flexural yielding in the wedge parts for equilibrium. Flexural and shear yielding will occur simultaneously across the whole plate, as shown in figure 4-8.

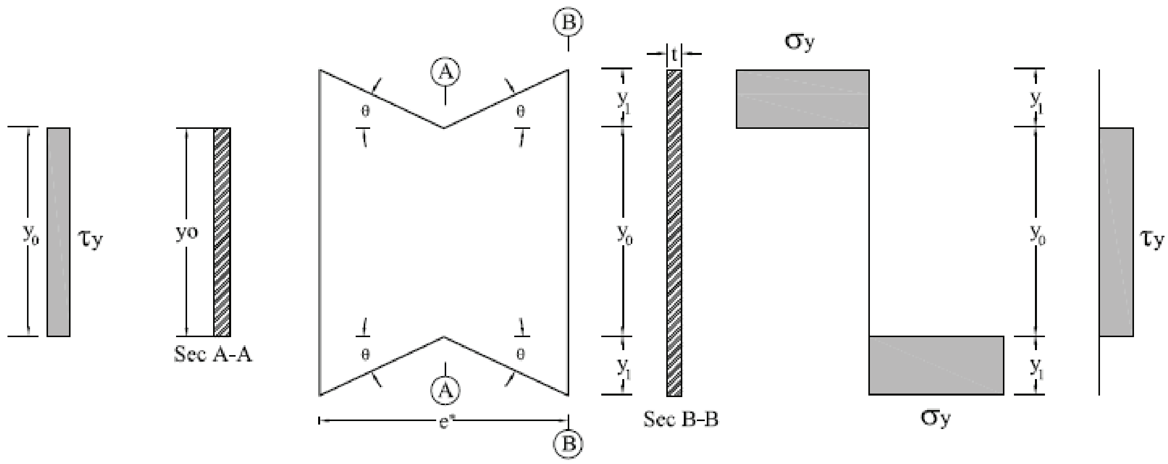

FIGURE 4-8 Proposed Stress Distribution for links with $\theta=\theta_b$

4.6.2 Links with Over Balanced Edge Angles ($\theta>\theta_b$)

For links having a link edge angle greater that the balanced link edge angle, per a lower bound approach, shear yielding is assumed to occur in the middle part of the plate, with a combination of normal and shear stresses developing in the wedge parts. In this particular case, yielding in the wedge part would occur if $\sqrt{\sigma^2+3\tau^2}=\sigma_y$ according to Von Misses yielding criteria depending on how much θ is greater than θ_b. While if $\sqrt{\sigma^2+3\tau^2}<\sigma_y$, no yielding will occur in the wedge parts and the plate will only experience shear yielding through the middle part. Figure 4-9 shows the proposed stress distribution for type (2) shear links.

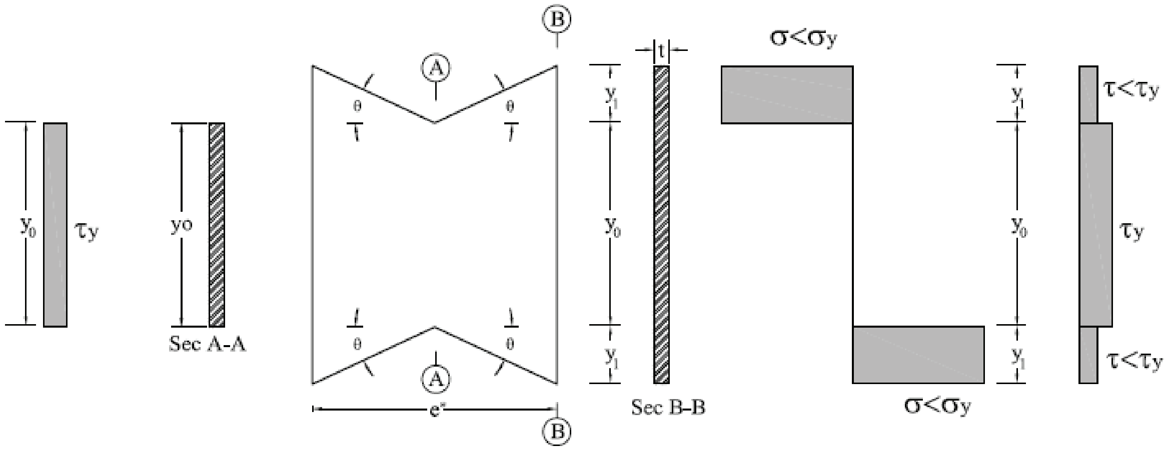

FIGURE 4-9 Proposed Stress Distribution for links with *θ>θ_b*

4.6.3 Links with Under Balanced Edge Angles ($\theta<\theta_b$)

For links having a link edge angle less that the balanced link edge angle, shear yielding is assumed to occur along a length, y, which is less than, y_0. While a combination of shear and flexural stresses is assumed to occur in the wedge parts and in the remaining middle part (y_0-y), decreasing the angle, θ, will result in decreasing the shear yielding part of the web which is undesirable. Figure 4-10 shows the assumed stress distribution at $\theta < \theta_b$

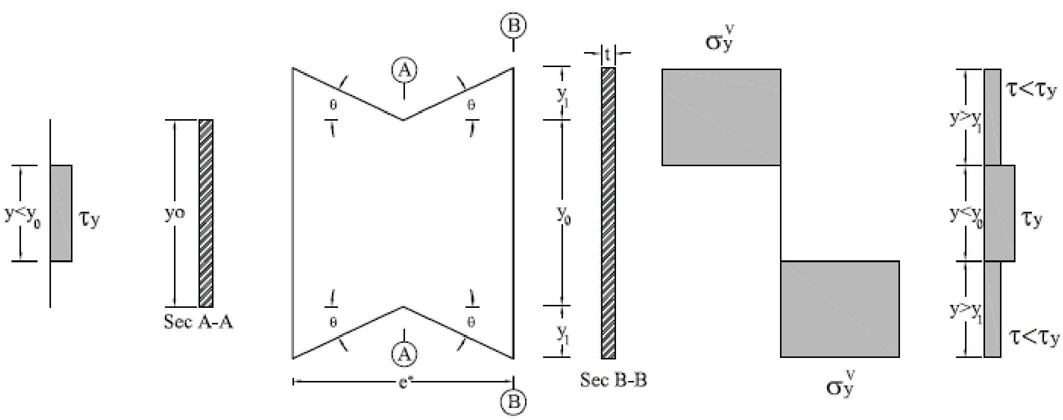

FIGURE 4-10 Proposed Stress Distribution for links with $\theta<\theta_b$

4.7 Link Rotation

One of the most important desired characteristics of this proposed Steel Plate Shear Link (SPSL) is the ability to dissipate by hysteretic behavior the seismic energy of the earthquake without introducing ductility in any other parts of the bridge piers. Expressions for the maximum ductility that a SPSL withstands were therefore developed in terms of the global dimensions of the bridge bent and the dimensions of the link itself. Figure 4-11 shows a typical SPSL introduced between two bridge pier segments per the strategy conceptually shown in Appendix A.

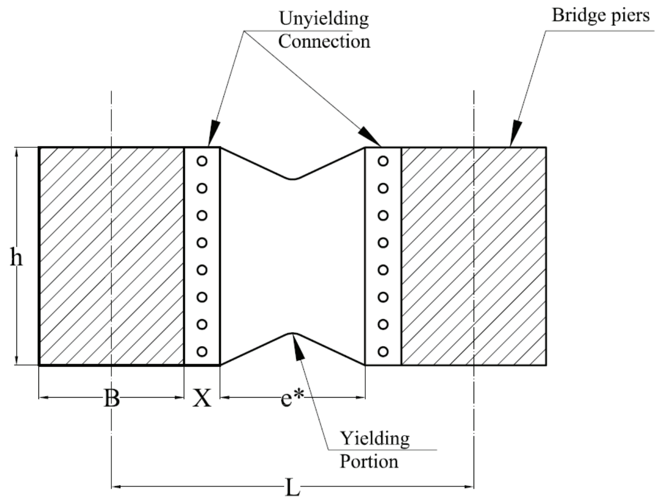

FIGURE 4-11 Typical SPSL introduced between two bridge column segments

The value of the link rotation, γ, in terms of the structure deformation can be derived from the geometry of the structure. No relative deformation is assumed to occur in the bridge pier segments adjacent to the links as they are considered rigid compared to the links. The link connection parts are also assumed to remain elastic; their relative deformations are ignored as they are relatively small compared to the plastic deformation in the links. The structure deformation can be considered by superposition of two effects, namely rotation of the bridge piers and relative vertical displacement between the bridge piers.

4.7.1 Rotation of Bridge Columns

First, rotation of the piers is considered as shown in figure 4-12, from which a value of the link rotation, γ, can be obtained as a function of the story drift, θ, as follows:

Three shaded triangles shown and labeled in figure 4-12, are used to develop some geometric relationships. From triangle (1), the value of the vertical displacement, Z_2, can be found to be equal to:

$$Z_2 = \theta_{rad}\left(B + X\right) \tag{4-24}$$

where B is the bridge column width and X is the width of the unyielding part of the SPSL.

From triangle (2), the value of the vertical displacement, Z_3, can be found to be equal to:

$$Z_3 = \theta_{rad} X \tag{4-25}$$

Finally, from triangle (3), the value of the vertical displacement, Z_1, can be found to be equal to:

$$Z_1 = \beta_{rad}\left(L - \left(B + 2X\right)\cos\theta\right) \tag{4-26}$$

also,

$$Z_1 = Z_2 + Z_3 = \theta_{rad}\left(B + 2X\right) \tag{4-27}$$

From equations (4-26) and (4-27), the value of the angle, β, can be found to be equal to:

$$\beta_{rad} = \frac{\theta_{rad}\left(B + 2X\right)}{L - \left(B + 2X\right)\cos\theta} \tag{4-28}$$

and since the value of the link total rotation, γ, is equal to:

$$\gamma_{rad} = \theta_{rad} + \beta_{rad} \tag{4-29}$$

substituting equation (4-28) into (4-29), the value of the link rotation is found to be equal to:

$$\gamma_{rad} = \frac{\theta_{rad}\left(B + 2X\right)}{L - \left(B + 2X\right)\cos\theta} + \theta_{rad} \tag{4-30}$$

let:

$$L - \left(B + 2X\right)\cos\theta = e^{'} \tag{4-31}$$

substituting (4-31) into (4-30), then the value of the link rotation can be rewritten as:

$$\gamma_{rad} = \frac{\theta_{rad}\left(B + 2X\right)}{e^{'}} + \theta_{rad} \tag{4-32}$$

rearranging the equation:

$$\gamma_{rad} = \theta_{rad}\left(1 + \frac{B + 2X}{e^{'}}\right) = \theta_{rad}\left(\frac{e^{'} + B + 2X}{e^{'}}\right) \tag{4-33}$$

which is the value of the story drift due to rotation of the columns. An approximate value could also be estimated by assuming that $e^{'}$ is equal to e^{*}, which is a reasonable estimate given that the angle θ is small (i.e. about 2 degrees, which corresponds to 0.035 radians or 3.5% story drift). Since θ is small, $\cos\theta$ tends to 1 and by substituting $\cos\theta=1$ into equation (4-31):

$$e^{'} = L - \left(B + 2X\right) = e \tag{4-34}$$

substituting equation (4-34) into (4-33):

$$\gamma_{rad} = \theta_{rad}\left(\frac{e+B+2X}{e}\right) = \theta_{rad}\left(\frac{L}{e}\right) \tag{4-35}$$

Since the story drift, θ, is related to the lateral displacement, Δ, by the height, h, at which the SPSL is installed,

$$\theta_{rad} = \frac{\Delta}{h} \tag{4-36}$$

the relationship between the horizontal displacement and the link total rotation can be found as:

$$\gamma_{rad} = \frac{\Delta L}{he} \tag{4-37}$$

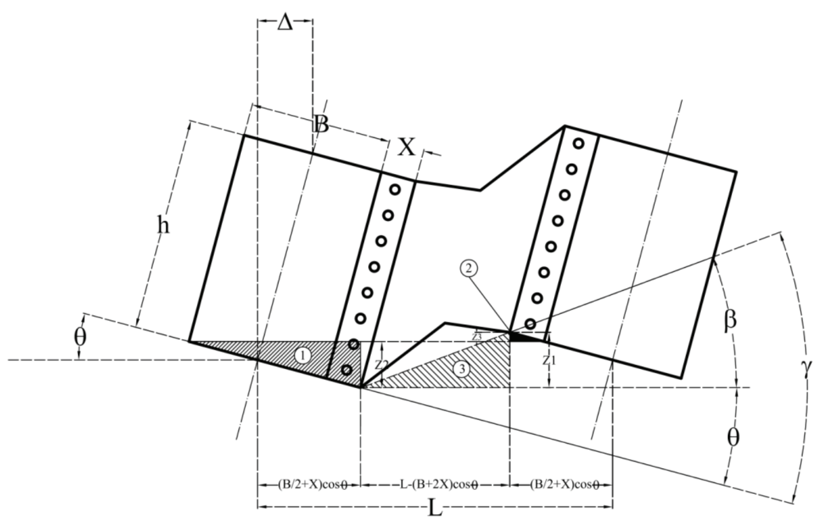

FIGURE 4-12 Link Deformation due to Rotation of Bridge Columns

4.7.2 Relative Vertical Displacement of Bridge Columns

Second, relative vertical displacement could occur between the bridge piers as shown in figure 4-13; this could result from elongation and contraction of the columns due to the axial forces induced by the overturning moment acting on the structure. This vertical displacement also contributes to the value of the link rotation, γ, as follows:

$$\gamma = \frac{\delta}{e} \tag{4-38}$$

where δ is the relative vertical displacement between the bridge piers.

This value of link rotation, γ, is added to the value of link rotation obtained from the previous section, and the total value of link rotation, γ_{tot}, can be found as:

$$\gamma_{tot} = \frac{\Delta L}{he} + \frac{\delta}{e} = \frac{1}{e}\left(\frac{\Delta L}{h} + \delta\right) \tag{4-39}$$

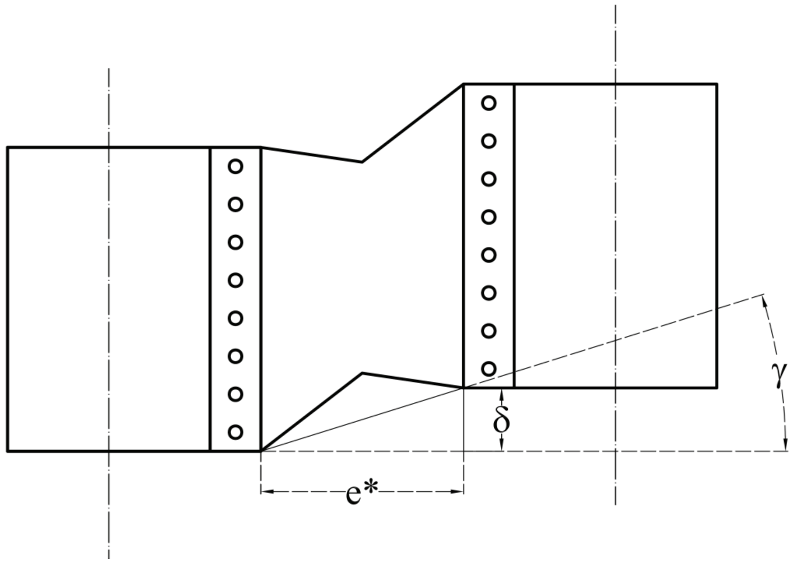

FIGURE 4-13 Link Deformation due to Relative Vertical Displacement of Bridge Columns

4.8 Link Ductility

Since the purpose of the SPSL is to introduce ductility to the system to dissipate the seismic energy without introducing any plastic deformation to the piers, and since the amount of plastic rotation of the SPSL is tied to the drift of the pier as mentioned, it is necessary to limit drift to not exceed the columns yield drift, Δ_{yf}, so that the columns remain elastic. Consequently, the maximum amount of plastic rotation produced by the SPSL is limited to:

$$\gamma_{\max} = \frac{1}{e}\left(\frac{\Delta_{yf} L}{h} + \delta\right) \tag{4-40}$$

To find the value of the link ductility, the maximum SPSL rotation is divided by the yield SPSL rotation, γ_y, which is found as:

$$\gamma_y = \frac{\tau_y}{G} \tag{4-41}$$

where τ_y is the yield shear stress of the SPSL, and G is the shear modulus calculated as:

$$G = \frac{E}{2(1+\nu)} \tag{4-42}$$

From equations (4-40) and (4-41) the value of the SPSL ductility, μ_{link}, can be found as:

$$\mu_{link} = \frac{\gamma_{\max}}{\gamma_y} = \frac{G}{e\tau_y}\left(\frac{\Delta_{yf} L}{h} + \delta\right) \tag{4-43}$$

and the plastic link rotation, γ_p, can be found as:

$$\gamma_p = \gamma_{\max} - \gamma_y \tag{4-44}$$

4.9 SPSL Lateral Strength and Stiffness

Adding SPSLs to the bridge column increases the elastic lateral stiffness of the total system. Unlike ductility demand, which varies in each SPSL depending on its location along the height of the pier, the elastic lateral stiffness of a SPSL is constant regardless of its location. Assuming that the total system behaves as a cantilever beam before yielding in the SPSLs takes place, with the columns being the flanges of the beam and the web being the SPSLs, a constant shear force exists along the height of the web, from which follows that the contribution of the SPSLs to the total elastic stiffness of the system is constant for each SPSL regardless its height along the columns.

4.9.1 SPSLs Restrained from Out of Plane Motion

The contribution of the restrained SPSLs to the elastic lateral stiffness of the total system can be calculated by finding the value of the seismic lateral load resisted by the link divided by the maximum lateral displacement of the bridge bent. To illustrate this, a Free Body Diagram (FBD) for a bridge bent before adding the SPSLs is shown in figure 4-14, where the columns maximum strength, $V_{Df,}$ can be calculated from the following equation:

$$V_{Df} = \frac{4M_P}{H_{tot}} \tag{4-45}$$

and where H_{tot} is the total height of the columns.

First, the columns effective lateral stiffness, K_{eff}, can be calculated from the following equation:

$$K_{eff} = \frac{24EI_{eff}}{H_{tot}^{\ 3}} \tag{4-46}$$

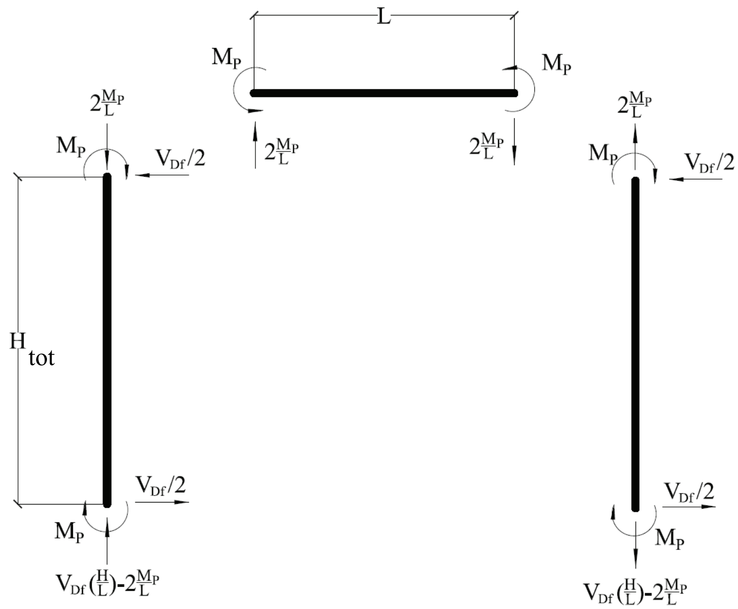

FIGURE 4-14 Free Body Diagram for the Bare Frame

Figure 4-15 shows a FBD of one of the columns after adding one restrained SPSL, from which the maximum system base shear, V_{Dt}, can be calculated by taking the moment around the base of the column as:

$$V_{Dt} = \frac{4M_P}{H_{tot}} + \frac{\sigma_y}{\sqrt{3}} ty_o \left(\frac{e+2X}{H_{tot}} \right) \tag{4-47}$$

It can be seen that the first term of the equation represents the maximum bare frame shear strength, from which it is concluded that the contribution of one laterally restrained SPSL to the maximum base shear strength, V_{DS}, is calculated as:

$$V_{DS} = \frac{\sigma_y}{\sqrt{3}} ty_o \left(\frac{e+2X}{H_{tot}} \right) \tag{4-48}$$

The total base shear due to adding multiple SPSLs could be calculated by multiplying the base shear contribution of the SPSL from equation (4-47) by the number of added links, *n*, as follows:

$$V_{Dt} = \frac{4M_P}{H_{tot}} + \frac{n\sigma_y}{\sqrt{3}} ty_o \left(\frac{e+2X}{H_{tot}} \right) \tag{4-49}$$

Knowing that the value of the lateral displacement, *Δ,* is given by:

$$\Delta = \theta_{rad} H_{tot} = \frac{Z_1}{(B+2X)} * H_{tot} \tag{4-50}$$

the contribution of a single SPSL to the total system's lateral stiffness can be determined as:

$$K_b = \frac{V_{Ds}}{\Delta} = \left(\frac{\frac{\sigma_y}{\sqrt{3}} ty_o}{Z_{1y}} \right) \frac{(B+2X)(e+2X)}{H_{tot}^2} \tag{4-51}$$

where K_b is the lateral stiffness of the SPSL, Z_{1y} is the yield vertical displacement of the link, and $\left(\frac{\frac{\sigma_y}{\sqrt{3}} \mathrm{ty_o}}{\mathrm{Z_{1y}}} \right)$ is the vertical stiffness of the SPSL, K_{ver}, which can be determined by dividing the yield shear force of the SPSL by the yield shear displacement as follows:

$$K_{ver} = \frac{\frac{\sigma_y}{\sqrt{3}} ty_o}{Z_{1y}} = \frac{\frac{\sigma_y}{\sqrt{3}} ty_o}{\gamma_y e} = \frac{\frac{\sigma_y}{\sqrt{3}} ty_o}{\left(\frac{\frac{\sigma_y}{\sqrt{3}}}{G} \right) e} = G \left(\frac{ty_0}{e} \right) \tag{4-52}$$

By substituting the value of K_{ver} into equation (4-46) and rewriting, the value of the elastic lateral stiffness contribution of a single SPSL to the total system can be written as:

$$K_b = \frac{Gty_0 (B+2X)(e+2X)}{eH_{tot}^2} \tag{4-53}$$

Again, the total elastic stiffness due to adding multiple SPSLs could be calculated by multiplying the elastic stiffness contribution of the SPSL from equation (4-53) by the number of added links, *n*, as follows:

$$K_{tot} = K_{eff} + \frac{nGty_0\left(B+2X\right)\left(e+2X\right)}{eH_{tot}^2} \tag{4-54}$$

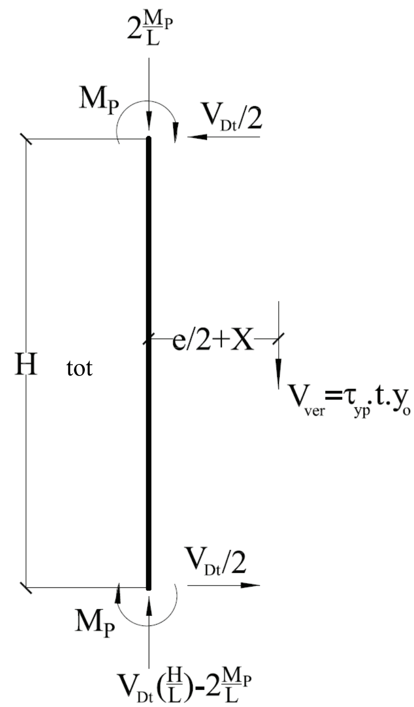

FIGURE 4-15 Free Body Diagram of Column with SPSL (With Restraints)

4.9.2 SPSLs Not Restrained from Out of Plane Motion

When the SPSLs are not restrained against out-of-plane motion, tension filed action instead develop in the links after buckling occurs due to inherent initial imperfections. This buckling results in a decreased contribution of the links to the lateral strength and stiffness of the total system. Figure 4-16 shows a schematic diagram of the forces acting in a SPSL due to the tension field action. The strip width, *S*, is assumed to be equal to 1/3 of the total width, *D*. This is an assumption based on the FEM results for the SPSLs described in section 4.11.4.3, as it was observed that the tension field in the plates is present in a strip with width of approximately 1/3 of the total width, at inclined by an angle, *α*, ranging from 40 to 60 degrees.

Figure 4-17 shows a FBD of one of the columns with laterally unrestrained SPSLs, from which the maximum system base shear, V_{Dt}, can be calculated by taking the summation of the vertical forces as:

$$V_{Dt} = \frac{4M_P}{H_{tot}} + n\sigma_y tS(\frac{L}{H_{tot}})\sin\alpha \tag{4-55}$$

Since the first term of the equation represents the maximum bare frame shear strength, the contribution of the laterally unrestrained SPSLs to the maximum shear strength, V_{DS}, is therefore given by:

$$V_{DS} = n\sigma_y tS\left(\frac{L}{H_{tot}}\right)\sin\alpha \tag{4-56}$$

Again knowing that the value of the lateral displacement, Δ, is given by:

$$\Delta = \theta_{rad} H_{tot} = \frac{Z_1 H_{tot}}{(B+2X)} \tag{4-57}$$

the value of the lateral stiffness of a single SPSL can be determined as:

$$K_b = \frac{V_{Ds}}{\Delta} = \frac{\sigma_y tS(B+2X)L\sin\alpha}{Z_{1y}H_{tot}^2} \tag{4-58}$$

where $\left(\frac{\sigma_y \text{tSsin}\alpha}{\text{Z}_{1\text{y}}}\right)$ is the vertical stiffness of the SPSL, K_{ver}, and equal to:

$$K_{ver} = \frac{\sigma_y \text{tSsin}\alpha}{Z_{1y}\gamma_y e} = \frac{\sigma_y \text{tSsin}\alpha}{\left(\frac{\sigma_y}{G\sqrt{3}}\right)e} = \sqrt{3}G\left(\frac{\text{tSsin}\alpha}{e}\right) \tag{4-59}$$

By substituting the value of K_{ver} into equation (4-58) and rewriting, the value of the elastic lateral stiffness contribution of a single unrestrained SPSL to the total system elastic lateral stiffness can be written as:

$$K_b = \sqrt{3}G\left(\frac{\text{tS}(B+2X)\text{Lsin}\alpha}{H_{tot}^2 e}\right) \tag{4-60}$$

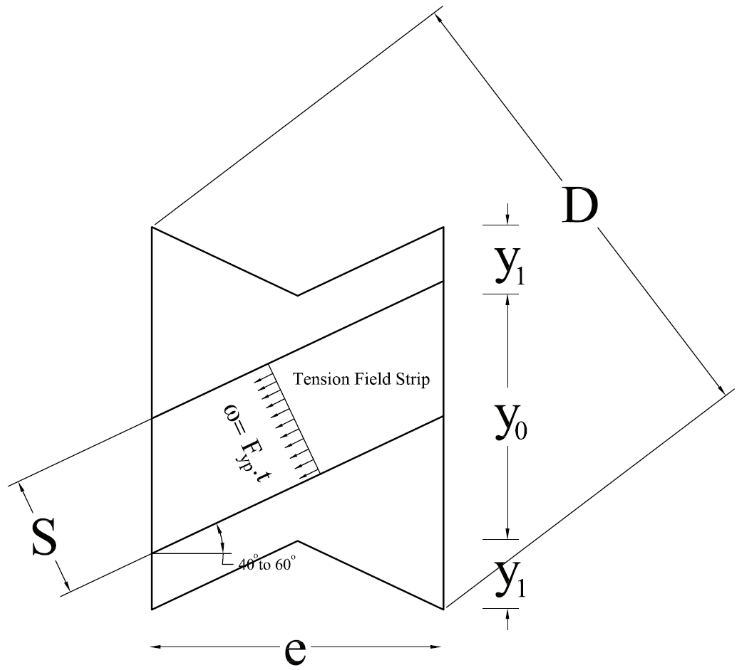

FIGURE 4-16 Forces Acting on SPSL after Initiation of Buckling

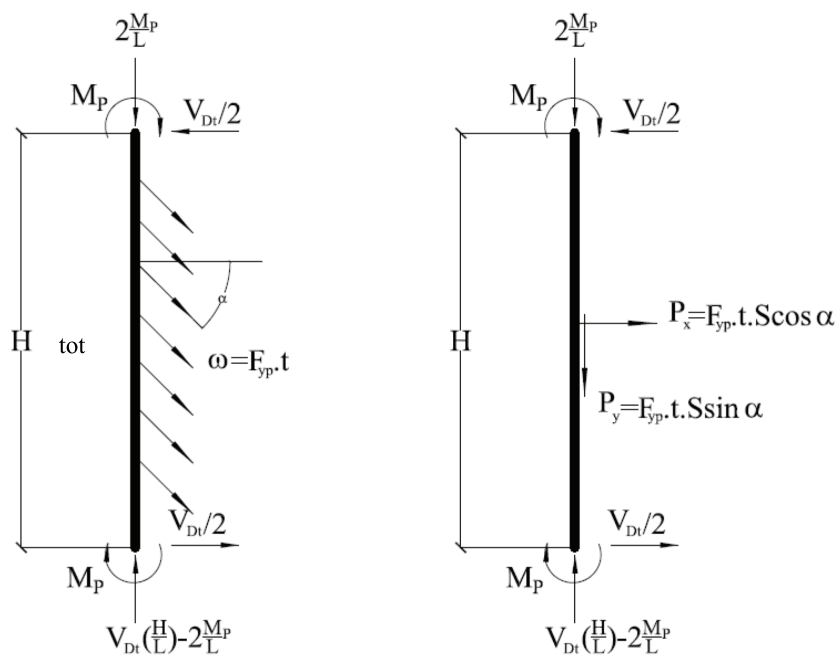

FIGURE 4-17 Free Body Diagram of Column with SPSL (No Restraints)

4.10 Over-strength

The calculated plastic shear capacity, V_p, can differ from the maximum shear strength developed by the link, V_{max} ; this is due to several factors including the strain hardening of the material at large plastic deformations, and the fact that steel typically has an actual yield strength that exceeds its specified value. The ratio of the maximum shear strength developed by the link to the plastic shear strength is denoted as the over-strength factor, Ω, where:

$$\Omega = \frac{V_{\max}}{V_p} \tag{4-61}$$

Underestimating the over-strength can lead to deficiencies in the design as failure modes could occur in undesired locations, such as the connection between the link and the columns. For the current design purpose (such as design of the connections and other capacity-protected elements of the structural system), an estimated over-strength factor of 1.5 was assumed for the SPSLs, which includes the strain hardening factor and the ratio of expected to specified strength, R_y, value according to the steel grade being used; for the A572Gr.50 steel used here, this value was assumed to be 1.1. From which the total shear strength of the SPSLs to be considered for capacity design principles, V_{DS}, can be rewritten as:

$$V_{DS} = n\Omega\sigma_y t y_o \left(\frac{e + 2X}{\sqrt{3}H_{tot}} \right) \quad \text{(Restrained SPSLs)} \tag{4-62}$$

$$V_{DS} = n\Omega\sigma_y t S \left(\frac{L}{H_{tot}} \right) \sin\alpha \quad \text{(Unrestrained SPSLs)} \tag{4-63}$$

4.11 Finite Element Model

A preliminary finite element analysis was conducted to validate the SPSL concept proposed above before moving on to the experimental phase of this research. This was deemed necessary to develop some confidence that the newly proposed system could works as expected and that yielding would occur in pure shear in the middle part of the SPSL (and that pure flexure yielding would develops simultaneously in the wedge parts in the case of a balanced link edge angle SPSL). This was also done to better quantify the width of the tension field strip that is expected to develop for the case of the unrestrained SPSL.

Two finite element models have been developed, both having the same exact dimensions and having a balanced link edge angle. The first was restrained against lateral buckling (i.e. no lateral displacement movement was allowed during the analysis), while the second was free to move in the lateral direction and consequently buckle.

4.11.1 Geometry Definition and Meshing

Geometry of the models was chosen to satisfy equations (4-18) and (4-23) which resulted in a SPSL of y_0 equal to 412mm (16.5"), and a link length, *e*, equal to 400mm (16"). The link edge angle, θ, was chosen to be equal to θ_b; which is approximately 25 degrees. An arbitrary thickness of 5mm (3/18") was also chosen for the analysis.

ABAQUS/CAE was used to represent the finite element models of the SPSLs. First the *Part Module* option of ABAQUS was used to define two parts in the SPSL model, one being the yielding portion of the link and the other being the thicker connection part of the link which contains the bolt holes and is required to remain elastic during the analysis.

Using the *Assembly Module* option of ABAQUS, the parts were then positioned relative to each other in a global coordinate system; the connection part was used twice in the assembly, once at each end of the link. After that, the *Interaction Module* was used to connect the parts using a *Tie Constrain* option that allows the merging of the interface nodes. Meshing was then generated using the *Mesh module* option, for which "seeding" of the edges was done by specifying the number of seeds desired along all the edges.

4.11.2 Material Definitions

An Elasto-perfectly Plastic material of yield strength equal to 350 MPa (50 ksi) was first chosen to validate the equations proposed in sections 4.4 and 4.5 for calculating the plastic moment and plastic shear of the SPSLs. The Von Misses yield criteria was chosen to define the plastic behavior of the link, as commonly done for steel. Poisson's ratio was assumed to be equal to 0.3, which is typical for structural grade steel.

4.11.3 Boundary Conditions and Loading

Using the *Load Module* option in ABAQUS, boundary conditions were specified by restraining all the nodes at one end of the link against displacement and rotation, and restraining all the nodes at the other end against rotation and translation in the X and Z directions while allowing translation in the vertical Y direction. The combination of these boundary conditions introduced constant shear on the link with equal end moments. Axial load was neglected in the analysis. For the case of the restrained SPSL, the *Load Module* was also used to constrain displacement in the Z direction along all the nodes of the SPSL, allowing the model to replicate the out-of-plane restraining condition. While for the case of the unrestrained SPSL, all the nodes where free to move in all direction, and an initial imperfection was introduced to the model to initial the out-of-plane buckling that was expected to occur.

“Loading” was applied for all models as a vertical monotonic displacement on a reference point RF1, defined as a master point, to which were slaved all the other nodes along the edge free from the vertical restrain. Loading was up to a total rotation of 0.13 rad, which was an arbitrary chosen value at which it was decided to stop the analysis.

4.11.4 Analysis

4.11.4.1 Element Definition and Meshing

Using the previously defined material, preliminary models where constructed using several mesh refinements to investigate the convergence of the models and select a final mesh refinement that could accurately represent the behavior of the SPSL with reasonable machine running time. For both the restrained and the unrestrained SPSLs, a mesh was chosen with element edge length of approximately 2”, denoted as Mesh 1as shown in figure 4-18(a). Another mesh was then developed by halving all the elements to obtain the mesh shown in figure 4-18(b) and denoted as Mesh 2, another mesh was then developed by halving the elements of Mesh 2 to obtain the mesh shown in figure 4-18(c) and denoted as Mesh 3. S4R shell elements were used for all the models.

The S4R element is a four node doubly curved general purpose shell element with reduced integration and hourglass control. It is similar to the S4 element but with one integration point instead of four. If the meshing is well distributed and the elements are not distorted, reduced integration with hourglass control can provide fairly accurate results with a significant reduction of running time.

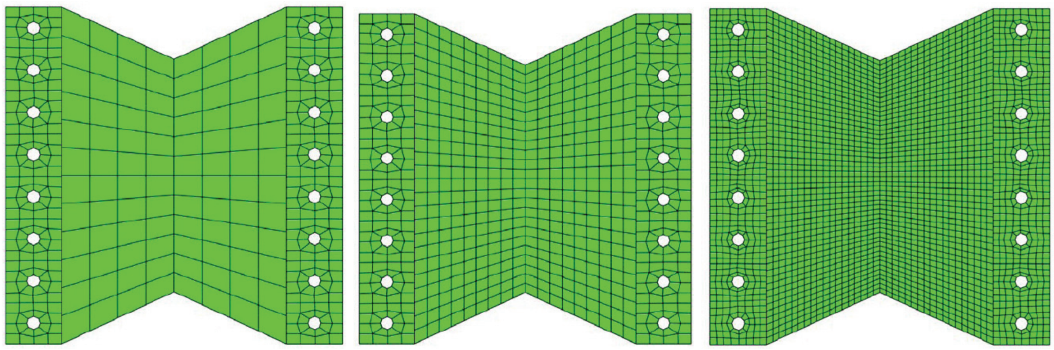

(a) (b) (c)

FIGURE 4-18 Mesh Refinements; (a) Mesh 1, (b) Mesh 2, (c) Mesh 3

Newton's method was used to solve the nonlinear equations using a series of time increments for the monotonic loading analysis. Results for the link shear versus average link rotation were then compared between Meshes 1, 2 and 3 for both restrained and unrestrained SPSLs, as shown in figures 4-19 and 4-20 respectively. Minor difference is observed in the global behavior of the restrained SPSL when changing the mesh size as seen in figure 4-19, while it can be seen from figure 4-20 that for the case of the unrestrained SPSL, Mesh 1 does not give an accurate estimate in capturing the local buckling of the SPSL, while difference between Mesh 2 and Mesh 3 was negligible which indicates that the mesh has converged. Due to the much greater running time of Mesh 3, Mesh 2 was preferred of the other two to represent the behavior of the unrestrained SPSL. In other words, Mesh 2, with its approximate element lengths of 1" for the largest element used, was retained to represent the SPSLs behaviors under investigation.

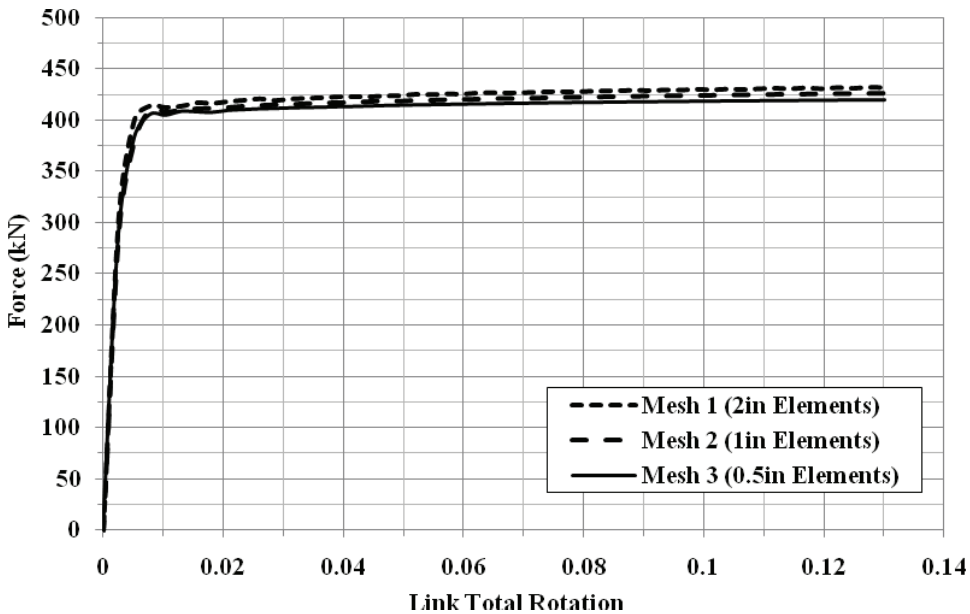

FIGURE 4-19 Link Shear vs. Total Link Rotation Comparison for Different Meshes of the Restrained SPSL

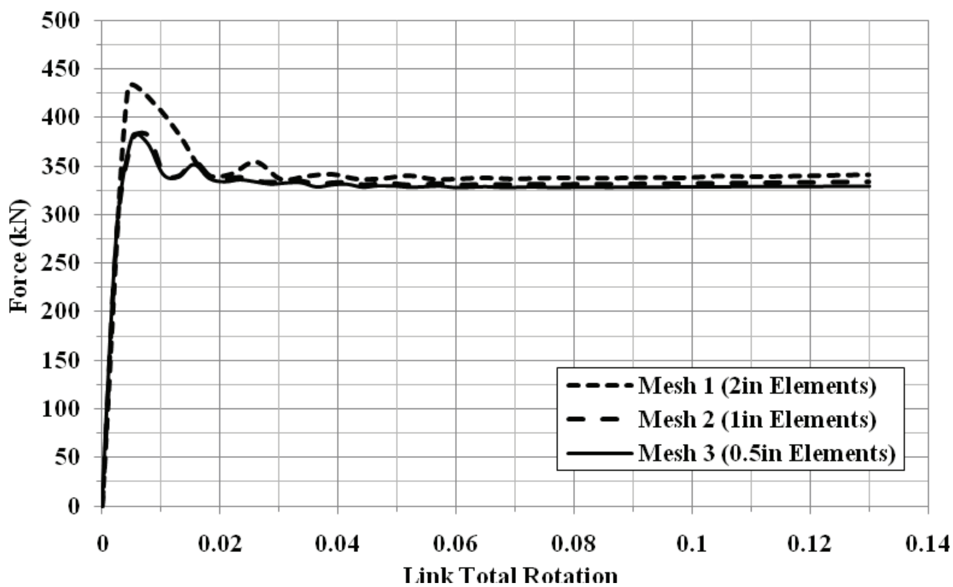

FIGURE 4-20 Link Shear vs. Total Link Rotation Comparison for Different Meshes of the Unrestrained SPSL

4.11.4.2 Restrained SPSL Behavior Analysis

Longitudinal and shear stress plots where developed at sections 1-1 and 2-2 shown in figure 4-21. Figure 4-22(a) shows the shear stress plot at mid-length of the link, identified as section

2-2 in that figure. The maximum shear strength observed can be calculated by integrating the shear stress plot at section 2-2 shown in the figure by:

$$V_{\max} = \int_0^H \sigma_{12} t\,dy \tag{4-64}$$

The value of the maximum shear force that was calculated from equation (4-64) is 405 kN (91 kips), and can also be seen in figure 4-19; the theoretical value of the plastic shear force calculated using equation (4-5) was found to be equal to 397 kN (90 kips).

The corresponding value of the plastic moment reduced by the presence of large shear stresses at the ends of the links (section 1-1) was calculated by integrating the longitudinal stress plot in figure 4-22(b) by:

$$M_{\max} = 2\int_0^{H/2} \sigma_{11} t y\,dy \tag{4-65}$$

The value of the plastic moment was calculated as 720 kip.in, compared to 712 kip.in calculated using equation (4-4).

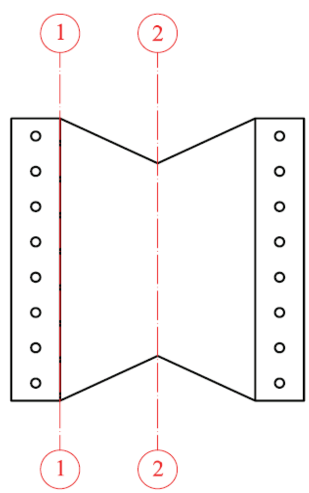

FIGURE 4-21 Sections for Longitudinal and Shear Stress Distribution

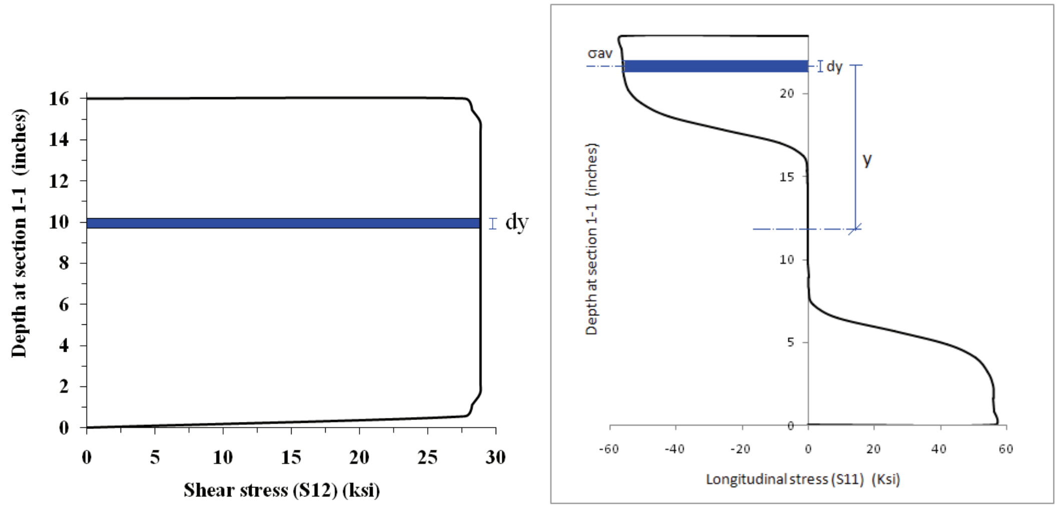

(a) (b)

FIGURE 4-22 Stress Distribution; (a) Shear Stress at Section 1-1, (b) Longitudinal Stress at Section 2-2

Contour plots for the longitudinal and shear stresses at a total link rotation of 0.13 rad are shown in figure 4-23. It can be seen from the plots that pure shear yielding is occurring in the middle part of the SPSL, while pure flexural yielding is occurring in the wedge parts.

The progressive increase of plastic link rotation as the loading is increased can be observed through figure 4-24, where yielding is observed to start at an average link rotation, γ_{av}, equal to 0.003, propagating along the mid section of the link upon increases in link rotation, progressively widening across the link until the link is fully plastified at a link rotation of approximately 0.035 rad. Yielding upon further plastic link rotation progresses across the entire link until the value of 0.13 rad is reached. Spreading of yielding across the whole link tends to increases the energy dissipation capability of the link and allows it to reach high values of plastic link rotation.

Obviously, these predicted responses rely on the adequacy of the restraint system to prevent out-of-plane buckling; the experimental studies will allow assessing some of the conditions for which such restraints are effective.

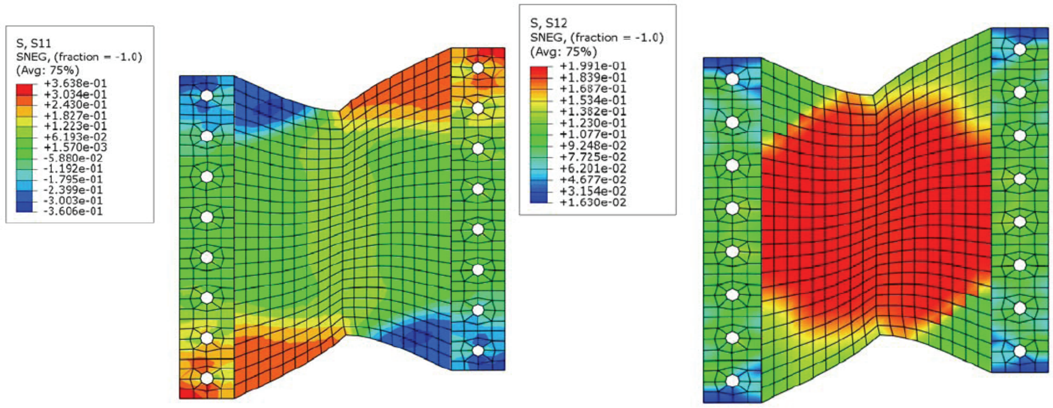

(a) (b)

FIGURE 4-23 Stresses for the Restrained SPSL at a Total Link Rotation of 0.13 rad; (a) Longitudinal Stresses, (b) Shear Stresses

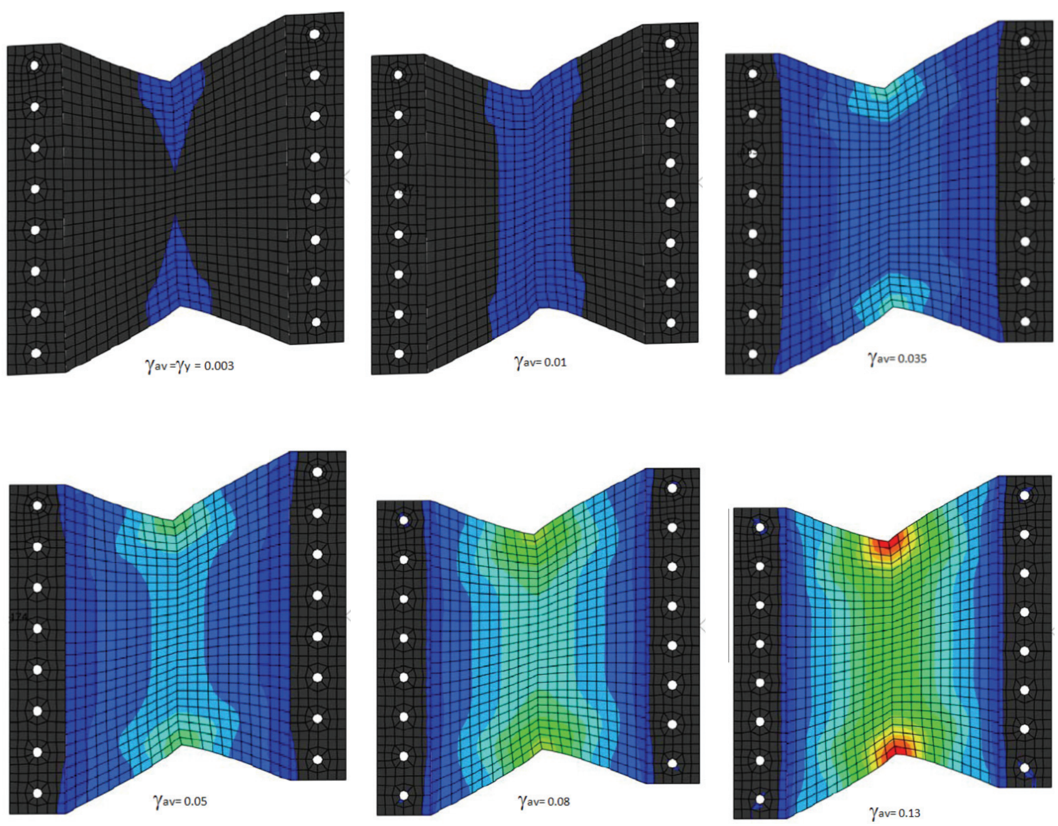

FIGURE 4-24 Propagation of Plastic Link Rotation

4.11.4.3 Unrestrained SPSL Behavior Analysis

As observed in figure 4-20 the load increases with respect to the total link rotation and the SPSLs behaves similarly to the restrained one up to a point where the geometric nonlinearities force the SPSL to buckle out-of-plate, at which point a drop of strength is observed (at 0.004 rad in that particular example) and the SPSL starts yielding by tension field action. Depending on the magnitude of initial imperfection introduced in the analysis, and for large plate slenderness, the peak value would typically not occur as the plate would transition "smoothly" into its buckled and diagonal tension mode (e.g. Vian and Bruneau 2005). Figure 4-25 shows the principal stress distribution for the unrestrained SPSL at a total link rotation of 0.13 rad. A tension field strip is observed in the figure with a strip width of approximately 1/3 the SPSL diagonal length, *D*.

Figure 4-26 shows the maximum in-plane principal stresses of the unrestrained SPSL at different total rotation levels. It can be seen that up to a total rotation of 0.004, the SPSL is behaving as a restrained SPSL, and that a tension field strip develops at larger rotations after buckling is initiated.

From figure 4-16, the unrestrained SPSL shear force value after buckling occurs can be calculated as:

$$V_{\max} = \sigma_y t S \sin\alpha \tag{4-66}$$

where S is calculated from the finite element model to be equal to 1/3D, and the strip is inclined with an angle α equal to approximately 55 degrees.

From equation (4-66), the value of the unrestrained SPSL force is found to be equal to 347kN (78 kips) compared to the 330 kN (74 kips) seen in figure 4-20 This value is about 80% of the total strength obtained if the link was restrained against out-of-plane buckling. A comparison between the strengths of both links is shown in figure 4-27.

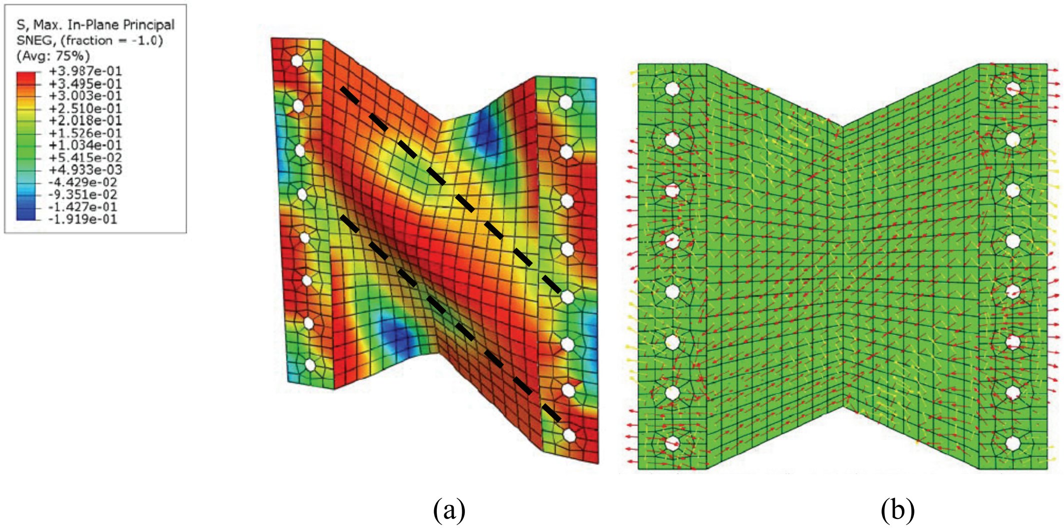

FIGURE 4-25 Unrestrained SPSL at a Total Link Rotation of 0.13 rad; (a) Max In-Plane Principal Stresses, (b) Principal Stresses Orientation

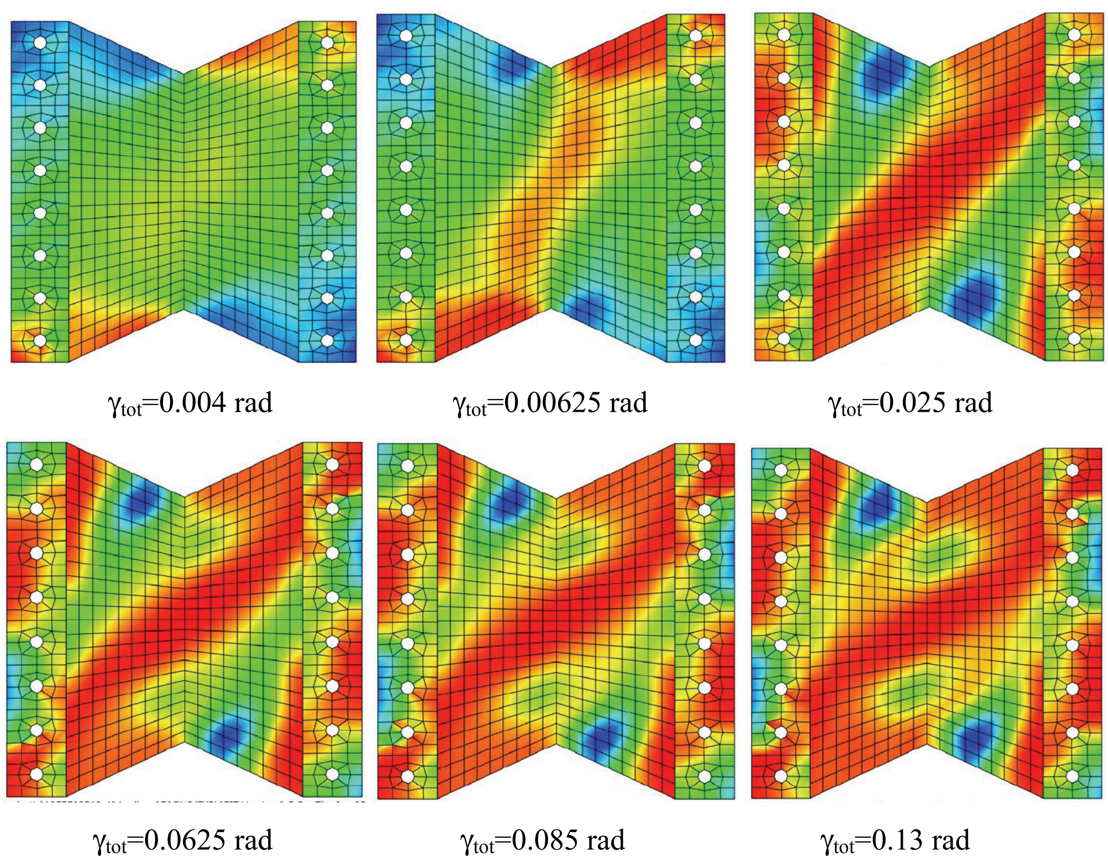

FIGURE 4-26 Max. In-Plane-Principal Stresses at various Total Link Rotation Levels

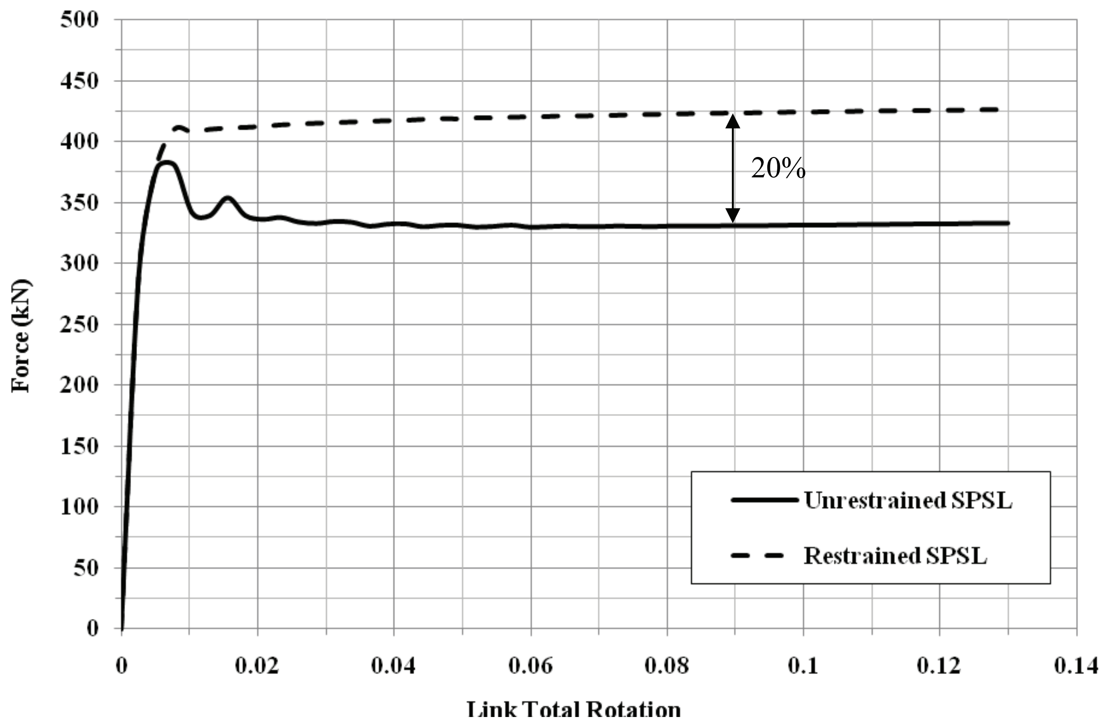

FIGURE 4-27 Comparison between Strengths of Restrained and Unrestrained SPSLs

4.12 Summary

In this section, an innovative Steel Plate Shear Link (SPSL) concept has been introduced, and its shear-moment interaction equation was derived. Equations were then developed to determine some critical design parameters of the link, namely the balanced link length and balanced link edge angle. Equations deriving the link ductility and lateral stiffness and strength were then described. A preliminary finite element model was used to investigate the adequacy of these equations and validate to a limited extent the proposed concept. Further experimental and analytical investigation validating the proposed SPSL concept is described in sections 5, 6 and 9.

SECTION 5
EXPERIMENTAL DESIGN AND SETUP

5.1 General

This section describes the design and detailing of two large-scale twin-column segmental bridge bent specimens per the strategy conceptually shown in Appendix A, having either Steel Plate Shear Links (SPSLs) or Buckling Restrained Braces (BRBs) as a series of structural fuses between the columns, and subjected to quasi-static cyclic tests. The columns used for the experiments were built with segments of Bi-Steel sections described in section 5.2; these sections were stacked on top of each other and connected by welding, then filled with concrete. The design of the specimens was partly controlled by limitations in the capacities of the strong wall, strong floor, and actuators available at the Structural and Earthquake Simulation Laboratory (SEESL) at the University at Buffalo, and partly by the theories developed earlier in section 3.

Here, three quasi-static tests were to be performed:

- For the 1st specimen (S1), it was planned to perform the test using SPSLs restrained from out of plane buckling and installed between the columns as a series of structural fuses until the onset of columns yielding. The test was then planned to continue until column failure investigating the behavior of Bi-Steel columns under cyclic loading. Due to unexpected weld failures described later in section 6, three tests were performed. For the first test, SPSLs were installed between the columns as a series of structural fuses until unexpected weld failure occurred at one the lower column splices in the elastic zone of both the links and the columns. The buckling restraints were then removed for reasons explained in section 6, and the second test was performed up to a drift corresponding to the onset of column yielding to investigate the effectiveness of adding the fuses in dissipating the seismic energy. The third test started from that point, with the SPSLs still in place until column failure.
    - The 2nd specimen (S2) was then installed and tested utilizing BRBs as a series of structural fuses (S2-1).

- The BRBs were then removed and bare frame cyclic test (S2-2) was performed until reaching failure of the columns.

The selected prototype bridge is described in section 5.3, followed by the tested specimen's dimensions in section 5.4. Design and detailing of the test specimens and fuses are presented in sections 5.5 to 5.7. Monotonic coupon test results for the material used in the fabrication of the Bi-Steel panels, SPSLs and BRBs are presented, together with cylinder tests for the concrete used in the Bi-Steel panels (section 5.8). Test setup construction (section 5.9), and instrumentation used to capture data (section 5.10) is described, including strain gauges, string displacement potentiometers, the Krypton dynamic measurement device, and video recording. The experimental data, as well as the analytical data that will be presented in later sections, will be used to assess the adequacy of the design recommendations as well as the effectiveness of adding structural fuses to bridge bents for seismic energy dissipation, providing an insight into the general behavior of the structural fuse system.

5.2 Bi-Steel Panels

Bi-Steel is a system of double skin steel–concrete–steel high performance rapid erect panels. These panels are composed of steel plates connected by an array of transverse friction welded shear connectors and filled with concrete. This system could be beneficial when strength or speed of construction is of vital importance. The panels can be quickly and easily fabricated on or off-site to create a wide range of structures. For most applications the Bi-Steel panels are filled with concrete after installation. It is this combination of a permanent steel formwork and concrete fill which makes Bi-Steel easy to erect and reduces the construction time that makes it a possible alternative to the pre-tensioned prefabricated segmental concrete columns which are often used for accelerated bridge construction. Figure 5-1 shows a typical panel of the Bi-Steel system. Such panels are available in a variety of dimensions, thicknesses and bar spacing, table 5-1 shows the ranges available for Bi-Steel Panels.

The Bi-Steel system is suited to extensive pre-fabrication (e.g. penetrations, attachments, connections and coatings) prior to site delivery. A major objective in using Bi- Steel is to minimize site work and hence site time, as accelerated construction is of major importance these days.

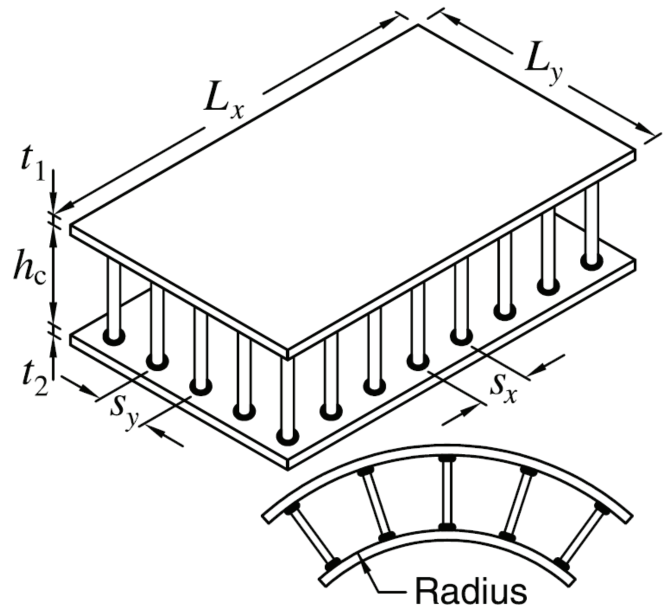

FIGURE 5-1 Typical Bi-Steel Panel (Bowerman et al. 1999)

TABLE 5-1 Range available for Dimensions, Thicknesses and bar Spacing (Bowerman et al. 1999)

Item	Minimum	Maximum
L_x	2 m	15 m
L_y	0.6 m	2 m
h_c	0.2 m	0.7 m
t_1	5 mm	20 mm
t_2	5 mm	20 mm
R	1500 mm	Flat
s_x	Greatest of 200 mm or 8 ($t_1 + t_2$)	Governed by design
s_y	Greatest of 150 mm or 8 ($t_1 + t_2$)	Governed by design

5.3 Prototype Bridge

The Prototype Bridge considered is a continuous bridge having three equal spans of 36m (120 ft), and two 9m (30 ft) high twin-column pier bents. The gravity load design (dead and live loads) has been done according to the AASHTO LRFD (2009) bridge design specifications and the columns were designed as composite rectangular columns using Bi-Steel panels. Figure 5-2 shows an elevation of the prototype bridge bent considered. Appendix B shows a detailed step by step design of the proposed Prototype Bridge. For a single twin-column, the bare frame base shear, V_{yf} was found to be equal to 1700 kN (382 kip) at a yield displacement of 88mm (3.5"). Recall that V_{yf} was defined in section 3.2.1.

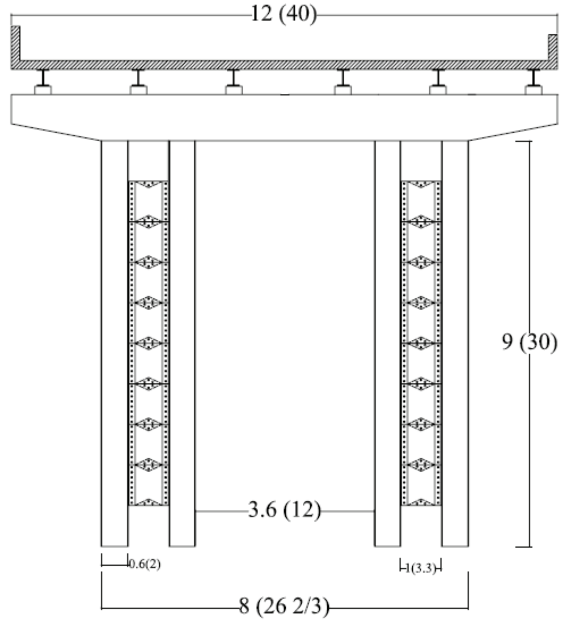

Dimensions in m (ft)

FIGURE 5-2 Prototype Bridge Bent

5.4 Specimen Dimensions and Scaling

While it is often desirable to build the largest possible specimen for an experimental investigation, in most cases, there are many limitations (such as dimensional restraints and loading equipment capabilities, not to forget cost of specimens) that constrain the size of a model. A 2/3 scale for the geometric properties of the specimen was chosen due to the limitations available at SEESL at the University at Buffalo. The height of the strong wall being 9.14m (30ft), the height of the specimen was set to be 7.62m (25ft) (leaving some distance under the overhead crane to facilitate construction). Also the specimen was designed for a maximum horizontal force of 1777 kN (400kips), leaving a generous margin against specimen over-strength when using 2 actuators available at SEESL each with a capacity of 1777 kN (400kips).

Note that it would have not been possible to build a much smaller specimen due to the limitations mentioned above in table 5-1 for the Bi-Steel panels' dimensions, thicknesses, and bar spacing. Specifically, L_y (Figure 5-1) has a minimum length of 600mm and was actually the controlling dimension for the sizing of the specimen.

Appendix B shows a detailed step by step design of the specimen. The bare frame yield base shear, V_{yf} was found to be equal to 730 kN (165 kip) at a yield displacement of 75mm (3"), while the maximum base shear, $V_{Df,}$ was calculated as 810 kN (182kips).

5.5 Design of Test Specimens

5.5.1 Column Segments

Segmental columns were used for the purpose of this experimental study; each column consisted of four Bi-Steel segments fabricated with different heights, and all having the same cross sectional dimension. While it would have been possible to have the columns constructed as continuous over their entire height, the segmental approach was deliberate to illustrate the construction procedure that could be followed on-site in the perspective of accelerated bridge construction for taller piers.

The cross section consists of a 600mm x 400mm (24"x16") Bi-Steel panel, with steel plate thickness equal to 8mm (5/16") with 25mm (1") diameter shear connector bars spaced at 200mm (8") c/c in both directions. The lower column segment height was 815mm (32.6") as shown in figure 5-3, allowing 600mm (24") to be embedded in the foundation base (FB), and 215mm (8.6") above the FB to be connected to the above segment. The following two middle segments were designed to be 2600mm (104") long, as shown in figure 5-4, while the upper column segment was set to be 1600mm (64") long, as shown in figure 5-5. For each column segment, the lower end was beveled to allow full penetration weld with the above segment, while a backup bar was connected to the upper end of each segment to facilitate the assembly and welding procedure for the column segments. The column splice detail is shown in figure 5-6. Note that the beveling detail was done according to the Bi-Steel design manual and procedures, which use a 2mm flat edge at the end of the bevel accompanied by a 2mm gap between the connected plates to achieve a full penetration weld. The Bi-Steel design manual also states that the beveled plate should be the upper one when connecting two vertical plates.

Although this was recognized to be different than U.S. practice for beveled edges, the certified welders of the SEESL facility at UB were confident that they could “burn through” to achieve the full penetration required. A slight perceived advantage of this splice detail is that it requires a lesser amount of deposited weld metal, but a disadvantage is that it requires tight tolerance control to fit the welded parts on top of each other and to achieve the required 2mm gap for the full penetration weld. Note that dimensions on all drawings for the rest of this section are in U.S. units, although both sets of units are provided in the text. Incidentally the Bi-Steel panels were detailed and manufactured in the UK using metric dimensions using soft conversions from the U.S. unit dimensions with some rounding-off to the nearest 5mm. The panels were shipped from the UK to the SEESL in Buffalo. Future panels for such applications could be provided from a Corus Bi-Steel manufacturing facility that is being contemplated for the U.S.A.

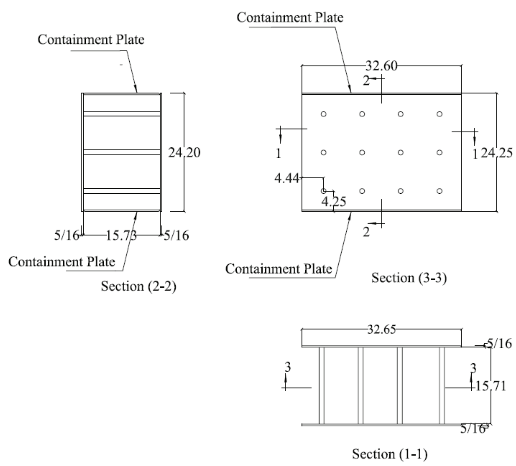

FIGURE 5-3 Lower Column Segment

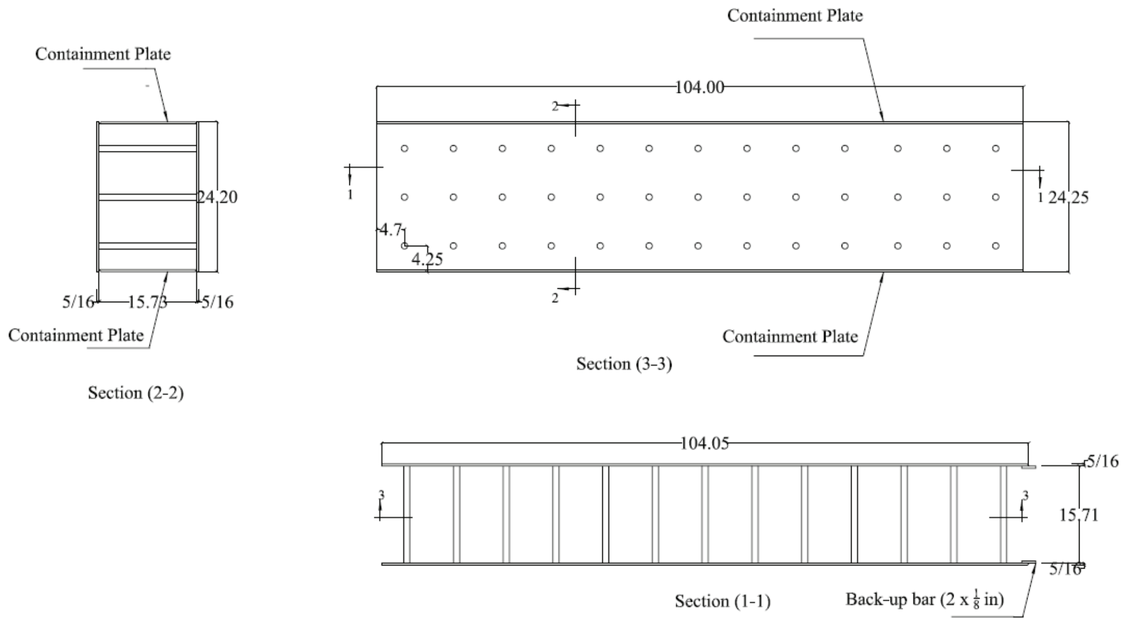

FIGURE 5-4 Middle Column Segment

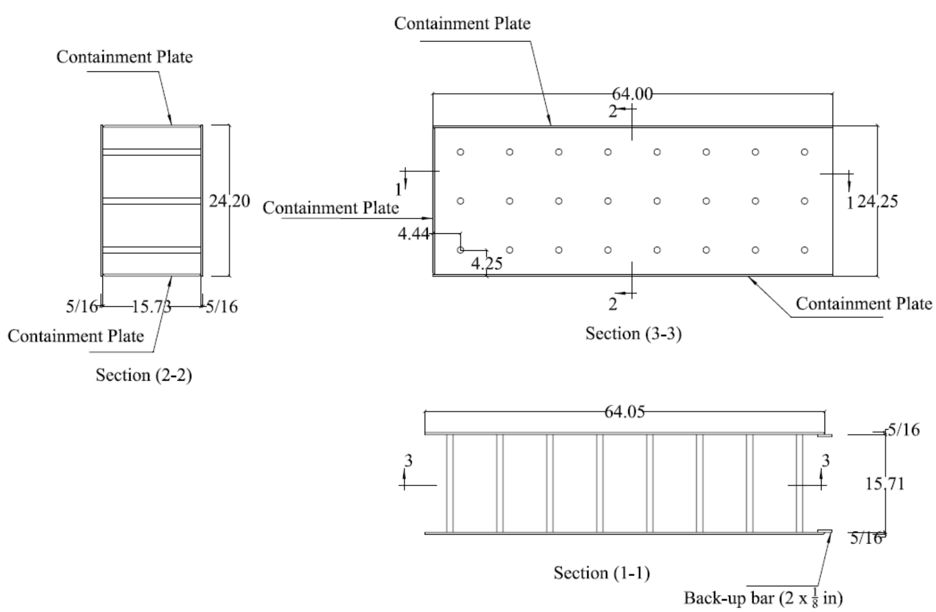

FIGURE 5-5 Upper Column Segment

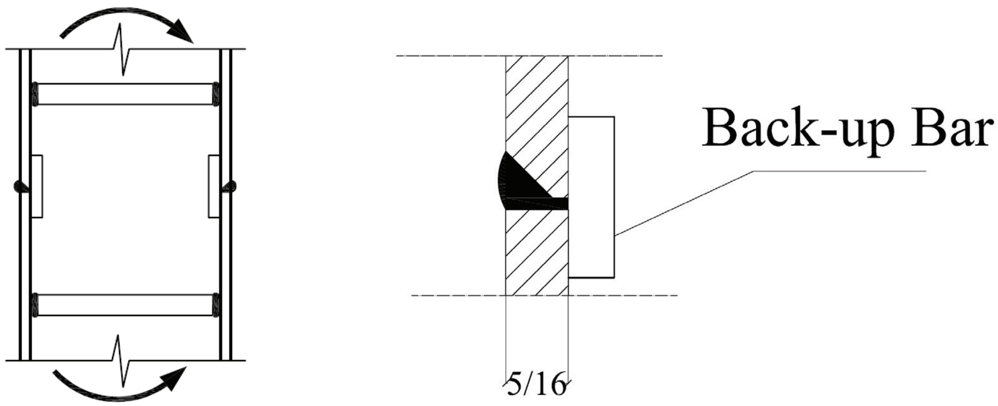

(a) (b)

FIGURE 5-6 Column Splice Detail; (a) Flat Back-up Bar, (c) Weld Close-up

5.5.2 Cap Beam (CB)

The cap beam consists of three parts, all of the same height of 1250mm (50"), with different widths. The middle and left part have a width of 600mm (24"), while the right part near the wall has a width of 750mm (30"), as shown in figure 5-7. The length of the cap beam was designed to be relatively rigid compared to the column segments and also to resist M_p and V_p of the columns, while remaining elastic.

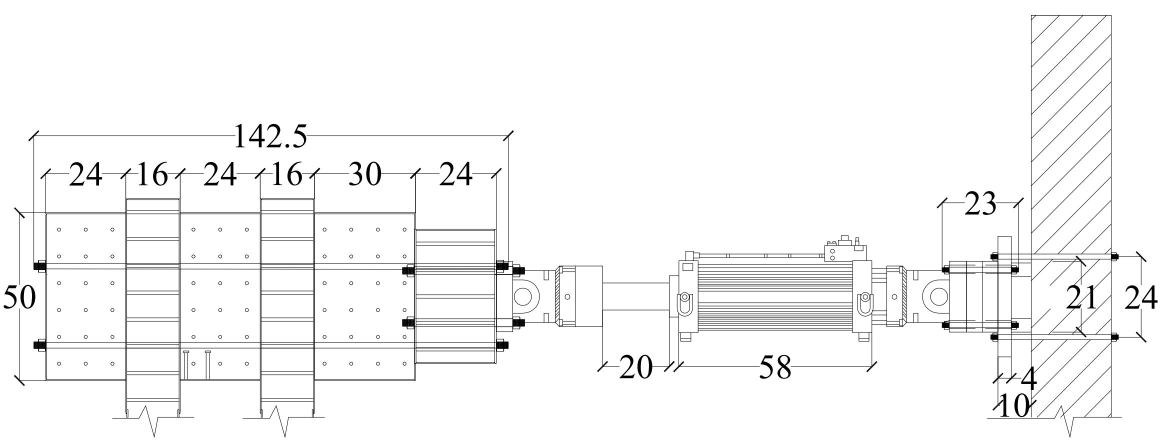

FIGURE 5-7 Connection between the Cap Beam and the Specimen (Elevation View)

5.5.3 Loading Beam (LB)

Two MTS servo-controlled static rated actuators each with a load capacity of 1777 kN (400 kips) and an available stroke of ±500mm (20") were used to apply lateral loads to the specimens. A Loading Beam (LB) was necessary to transfer the load from the two actuators to the specimen as shown in figure 5-8. The LB was designed to remain elastic and to experience negligible deformations during the testing procedure (i.e. rigid beam). The LB was connected to the CB using four 35mm (1 3/8") diameter threaded rods pretensioned to 0.6 of their yielding stress, to ensure that no separation would occur between the LB and the specimen while pulling the actuators. For added safety the LB was welded from both sides to the specimen using 275mm (15") long, 12.5mm (0.5") fillet welds. Also it was connected to each actuator using four threaded rods of 35mm (1 3/8") diameter. The resulting loading beam design was a Bi-Steel beam of dimensions 2500mm x 1000mm (100"x40") with a depth of 600mm (24") and plate thickness of 12.5mm (0.5").

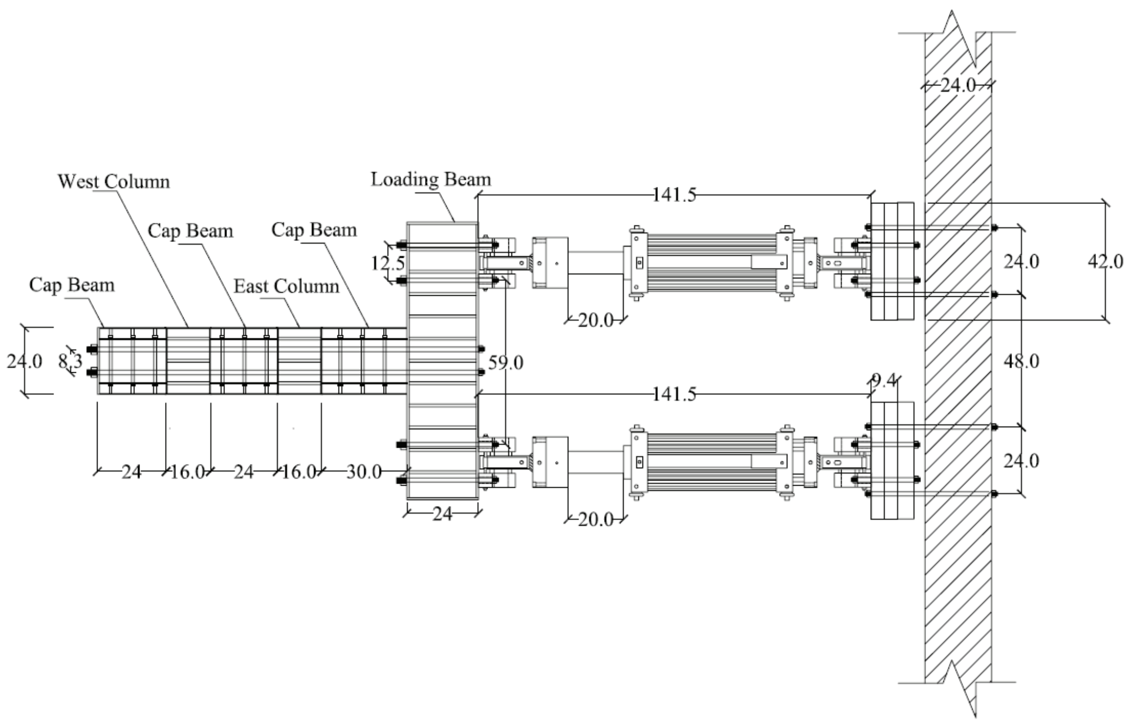

FIGURE 5-8 Connection between LB, Specimen and Actuators (Plan View)

5.5.4 Foundation Base (FB)

The Foundation Base (FB) was designed to remain elastic for the maximum actuator load that could be applied to the specimen with a factor of safety of 1.5. A total number of 16 Dywidag bars with a diameter of 35mm (1 3/8”) were used to tie the FB to the strong floor of the SEESL, and pre-tensioned to 60% of their yielding stress, which was sufficient to overcome the uplift and sliding forces produced by the actuator. The resulting design made use of a 4250mm (170”) long, 1850mm (74”) wide, and 600mm (24”) deep Bi-Steel panel with a plate thickness of 12.5mm (0.5”) as shown in figure 5-9. An 2162.5mm x 980mm (86.5”x39.2”) rectangular hole was cut in the plate of the FB, so that the lower segment of the columns could be welded to the lower plate as one step to achieve a fixed base for the specimen. A 600mm (24”) by 600mm (24”) pattern with 50mm (2”) diameter holes was then drilled in the two plates of the FB, to match the same whole pattern available in the strong floor of the SEESL. The upper and lower holes were then connected by 50mm (2”) steel tubes using fillet welds along the circumference of the tubes at the connection parts with the FB. Concrete was poured at a later stage as described in section 5.8.4.

A 2162.5mm x 980mm (86.5”x39.2”) rectangular plate of thickness 12.5mm (0.5”) was then fabricated and beveled along all its edges so that it could be butt welded to the FB after the lower segment of the column was welded to the base of the FB and concrete was poured. For the plate to fit, two holes were cut in that plate with dimensions similar to that of the columns with 1.5mm (1/16”) tolerance as shown in figure 5-10.

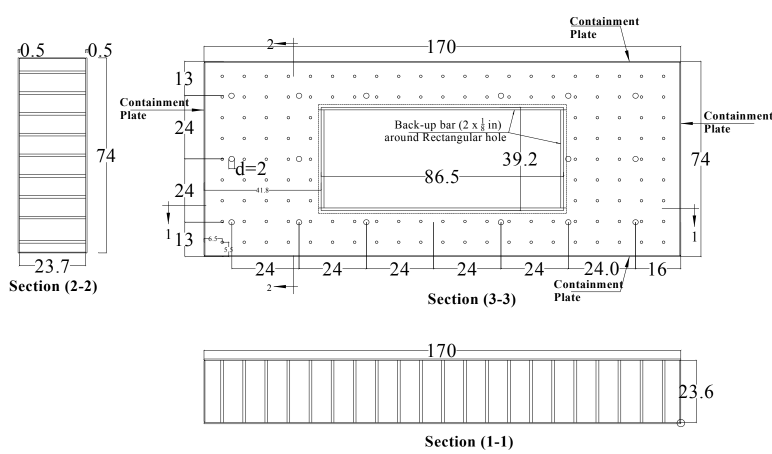

FIGURE 5-9 Foundation Base (FB)

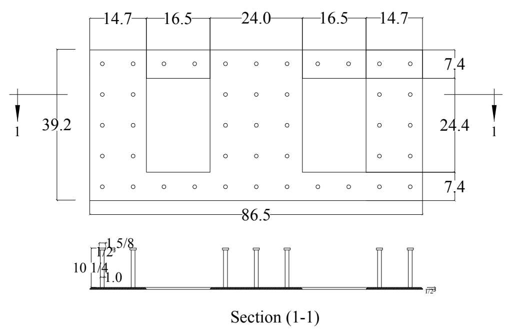

FIGURE 5-10 Foundation Base (FB) Cap

5.6 Design of Steel Plate Shear Link (SPSL)

The SPSLs were designed to meet several criteria; adequate shear and flexural strength was taken into account to increase the lateral stiffness and strength of the bare columns, and link length was chosen to provide the adequate link ductility required to dissipate the seismic energy as described in section 4. The design procedure developed in section 3 to achieve the structural fuse concept was also satisfied, ensuring that the columns remain elastic. The procedure for sizing the link for the experimental test is outlined below taking into consideration the above criteria and also the SEESL limitations mentioned earlier.

5.6.1 Link Design Procedure

To ensure that the designed link would provide an adequate ductility for energy dissipation, the link length, *e*, was chosen as per section 4.4

Choosing y_o to be equal to *e*, the link balanced angle, θ_b, and the link height, *h*, can be calculated from:

$$\tan^2\theta_b + \left(\frac{2y_0}{e}\right)\tan\theta_b - \frac{2y_0}{e\sqrt{3}} = 0 \tag{5-1}$$

$$h = y_o + e\tan\theta_b \tag{5-2}$$

The value of the link length, *e*, chosen is then checked to satisfy the following equation:

$$e \le \frac{2y_o}{\sqrt{3}\tan^2\theta}\left(1-\sqrt{3}\tan\theta\right) \tag{5-3}$$

Then, the number of added links, N_{links}, is calculated based on the available space to insert them, as:

$$N_{links} = \frac{H_{tot}}{h} - 2 \tag{5-4}$$

leaving an empty space at the top and bottom of the column, as inserting links at these locations would have interfered with the plastic hinging zones of the columns. Also, because no significant relative deformations between the columns occur at the top and bottom of the columns, links at those locations would likely not yield significantly.

Other parameters of the link design were chosen in compliance with the structural fuse design procedure presented in section 3. In that procedure, recall that to ensure that sufficient lateral stiffness is added by the link to reduce the target displacement to a level where the bent column remains elastic, a design spectrum must be chosen according to the location of the bridge (the spectral acceleration is first assumed to be in the acceleration zone of the spectrum, but that is to be checked and revised upon further design iterations), the weight of the columns plus the added links should be estimated. Here, for the purpose of developing a specimen for experimental verification of the concept, the values of S_S was taken as 2.1g and S_1 was taken as 0.8g. This is representative of a region exposed to severe ground shaking, for site soil-type class B and a 2% probability of exceedance in 50 years.

The bare bent yield shear force, V_{yf}, was calculated and the bare bent ductility, μ_f, was limited to 1, from which the bare frame strength ratio, ξ, and the minimum required stiffness ratio, α_{min} , where calculated as follows:

$$\xi = \frac{S_a mg}{V_{yf}} \tag{5-5}$$

$$\alpha_{\min} = \frac{\xi}{\mu_f} - 1 \tag{5-6}$$

where:

$$\alpha_{\min} = \frac{K_b}{K_f} \tag{5-7}$$

The relationship between the link's lateral and vertical stiffness was found in section 4.9.1, as:

$$K_b = K_{ver} \frac{(B+2X)(e+2X)}{H_{tot}^2} \quad (5\text{-}8)$$

where K_{ver} is the total vertical stiffness of the fuses. According to the chosen bent dimensions, and the calculated fuses' lateral stiffness, K_b, the minimum total vertical stiffness, K_{ver}, required for the fuses so that the columns of the bent remains elastic (i.e. μ_f=1) can be calculated from equation (5-8).

To ensure that a minimum required fuse ductility, μ_b, is provided, the required fuse thickness can be calculated by finding the total required strength for all fuses,η, to as follows:

$$\eta = \mu_b (1 + 1/\alpha) \quad (5\text{-}9)$$

here, a required value of μ_b = 4 is specified, from which the value of η can be found from equation (5-9). Then, the minimum required lateral fuses strength can be determined as follows:

$$V_{Ds\min} \leq \frac{S_a mg}{\eta_b} \leq V_{act} - V_f \quad (5\text{-}10)$$

Note that the value of the total lateral link strength should not exceed the value of the capacity of the actuators at SEESL, V_{act}, minus the value of the bare bent lateral strength, V_f. Also, forces from the link should not induce detrimental forces on the columns (e.g. axial forces, connection forces, etc.) and capacity design principles were applied to protect these structural elements.

The total minimum vertical strength required for the fuses to provide a specified link ductility of 4 could then be determined per section 4.9.1 as follows:

$$V_p = V_{Ds} \left(\frac{H_{tot}}{e+2X} \right) \quad (5\text{-}11)$$

Contrary to the design of BRBs as structural fuses (described in section 3), the strength and stiffness of the SPSL are coupled. Therefore, to calculate a required minimum SPSL thickness to satisfy the above requirements, two equations must be considered as follows: The minimum required link thickness to satisfy the strength requirement is calculated per section 4.3 as:

$$t_{\min 1} = \frac{\sqrt{3} * V_p}{n\sigma_y y_0} \tag{5-12}$$

where n is the number of fuses.

The minimum required link thickness to satisfy the stiffness requirement is calculated per section 4.9.1 as:

$$t_{\min 2} = \frac{K_{ver} e}{G y_o} \tag{5-13}$$

where G is the shear modulus.

A detailed design procedure for both the bare frame and the links is presented in Appendix B, also discussing the design of the foundation and the loading beam. The design made use of or a total of 8 links, each 5mm (3/16") thick, and the lateral force due to the contribution of the fuses, V_{yb} was found to be equal to 903 kN (203 kip) with a yield displacement of 9mm (0.33").

5.6.2 Link Specimen Description

The purpose of the links being that they would be used as replaceable fuses dissipating the seismic energy during a seismic event, their detailing therefore should allow them to be easily removed and replaced by new ones. Such a performance objective with a welded connection between the SPSLs and the frame columns is possible but would require, after an earthquake, that the old SPSLs be flame cut and the new SPSLs be welded on the other side of it's gusset. However, while workable, welding is sometimes less desirable in bridge applications, and a bolted connection was therefore selected as the preferred solution for that problem and for the sake of proving the bolted concept in this case. However, introducing bolt holes at the ends of the links would have weakened the end sections, makings them yield before the mid section, which was undesirable. To solve this problem, the thickness of the end sections were increased by welding 5mm (3/16") plates locally to the links to make the net area at the end sections greater than the gross area at the mid section and thus insure that mid section yielding governs. The resulting design made use of a link with thickness equal to 5mm (3/16") and dimensions as shown in figure 5-11. An 8mm (5/16") gusset plate was also welded to the columns of the 1st specimen over their entire height to which the SLSL's (S1) could be connected. The gusset plate and its welds were also designed to remain elastic during the testing procedure. A cross section drawing of S1 is shown in figure 5-12, and a detail for the link to column connection is shown in figure 5-13.

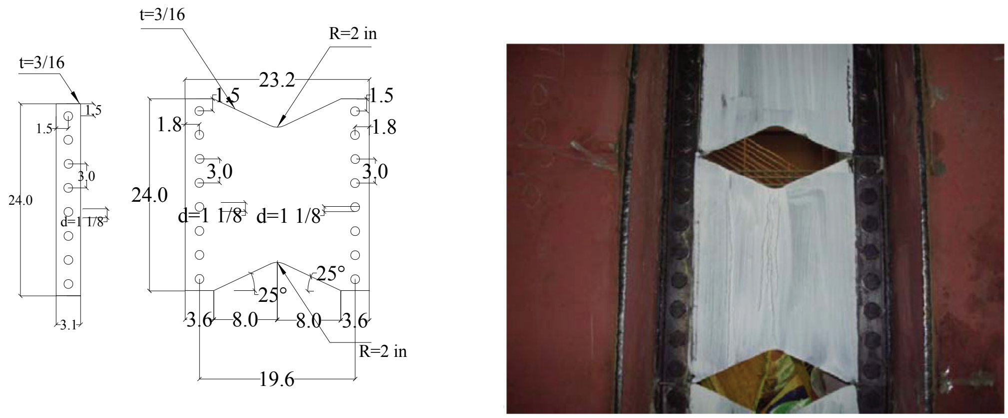

(a) (b)

FIGURE 5-11 SPSL Detail (Elevation): (a) Dimensions in inches (b) Photo

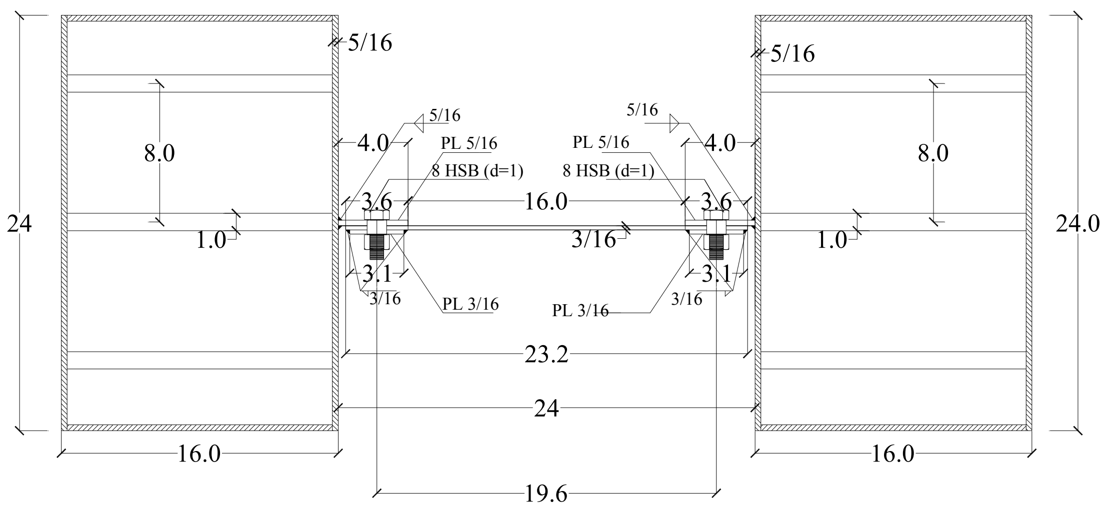

FIGURE 5-12 Columns Cross Section (Plan View Cross Section), Dims. in Inches

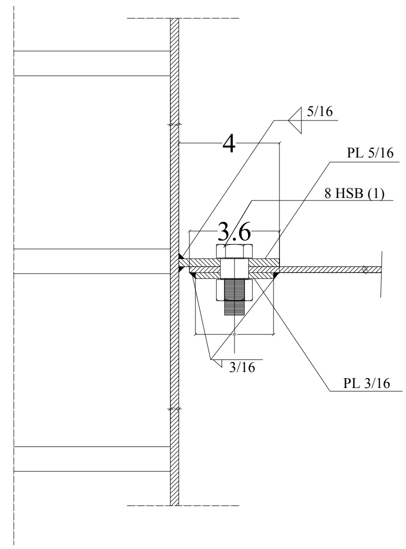

FIGURE 5-13 Link to Column Connection Detail (Plan View)

5.7 Design of Buckling Restrained Braces (BRBs)

For the first test on the second specimen (S2-1), BRBs manufactured by Star Seismic where used as a series of structural fuses inserted between the columns. A detailed design procedure for choosing the BRB strength is shown in Appendix B. The design made use of 6 BRBs having specified yield strength of 533 kN (120 kips) and F_y = 345 MPa (50 ksi), and a core length of 50%. Dimensions of a typical BRB are shown in figures 5-14 and 5-15 shows a photograph of the BRB used in specimen S2-1. Pin ended connections were used for the purpose of eliminating moment and shear at the connection points and to allow the rotation of the BRBs. Pins of 50mm (2") diameters were fabricated from high strength steel (A490) and were hammered into the 50mm (2") diameter holes at the BRBs gussets as shown in figure 5-16. To get rid of most of the sliding that could occur in the pin connection during cyclic loads reversal, zero tolerance between the pins and the pin holes was achieved by connecting an additional wedge part to one end of each pin, from which the pin could easily be hammered inside the hole. The wedge was an extension pin added to the cylindrical pin, 2" thick and tapered at an angle of approximately 5 degrees and temporarily held at one end of the pin by a bolt into a hole tapped into the pin.

In long BRBs, this sliding is of no significance, but in the current application, which requires short BRBs to tightly limit displacements, excessive slippage in the pin hole could have had a substantial negative impact on the structural fuse performance.

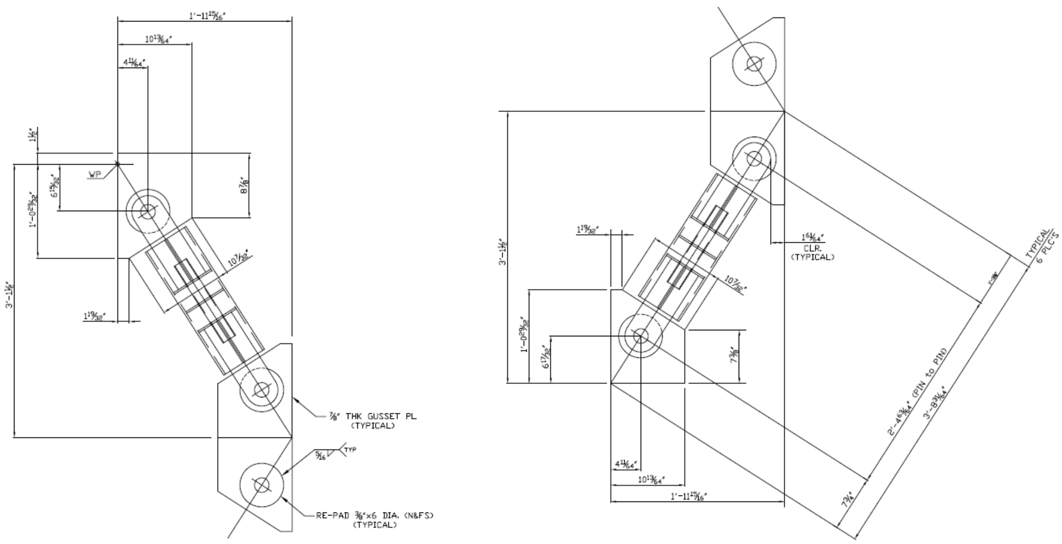

FIGURE 5-14 Buckling Restrained Brace Dimensions

FIGURE 5-15 Photograph of BRB used in Specimen S2-1

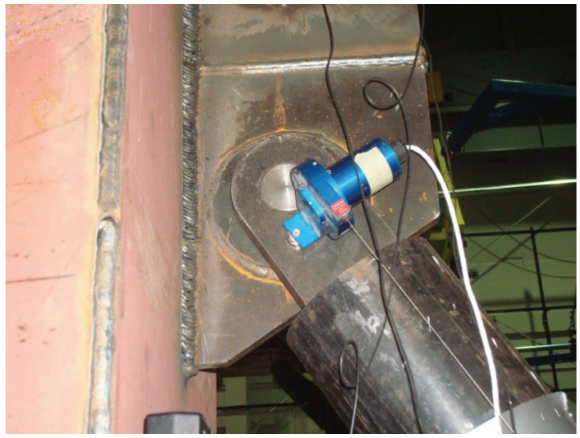

FIGURE 5-16 Photograph of Gusset Plate used in Specimen S2-1

5.8 Materials

5.8.1 BRB Material Testing

Steel used for the BRB's yielding core was specified to be ASTM A572 Gr. 50. Three tensile coupon tests were performed by star seismic on samples having a diameter of 12.5mm (0.5").Yielding was observed at 0.2% offset and the tests were performed to a maximum elongation of 50mm (2"). Yielding stress varied from 322 MPa (46.7 ksi) to 343 MPa (49.8 ksi). Results of the coupon tests are presented in table 5-2. A full stress strain curve is not available.

TABLE 5-2 BRB Coupon Test Results

Sample	Diameter (inches)	Area (in^2)	Tensile Load (LBS)	Tensile Strength (PSI)	Yield Load (LBS)	Yield Strength (PSI)
1	0.500	0.1963	14,280	73,000	9,352	47,600
2	0.500	0.1963	14,288	73,000	9,164	46,700
3	0.498	0.1948	14,201	73,000	9,704	49,800

5.8.2 Bi-Steel Material Testing

Design of the Bi-Steel panels was accomplished on the assumption of standard ASTM A572 Gr. 50 properties, in the perspective that the columns were to remain elastic for the range of the structural fuse application. On that basis, S355 J2G3 Bi-Steel (equivalent to ASTM A572 Gr. 50 steel) was chosen by Corus for this particular application. According to Corus, this steel is rated as high performance steel used in nuclear industry applications. Additional information on that steel became available after the test for reasons explained in section 6.

5.8.3 SPSLs Material Testing

ASTM A572 Gr. 50 steel was chosen for this particular application. These plates were provided and fabricated by a local steel manufacturer in Buffalo, NY. Monotonic tension tests were performed on two coupons from as shown in figure 5-17. Strains were monitored using a MTS extensometer with a 50mm (2") gage length, while the forces were monitored using an internally mounted load cell in a Tinius Olsen testing machine at the University at Buffalo. The coupons tested showed good ductility and reached a strain of 28% before fracture. The ratio of F_u/F_y was 1.11.

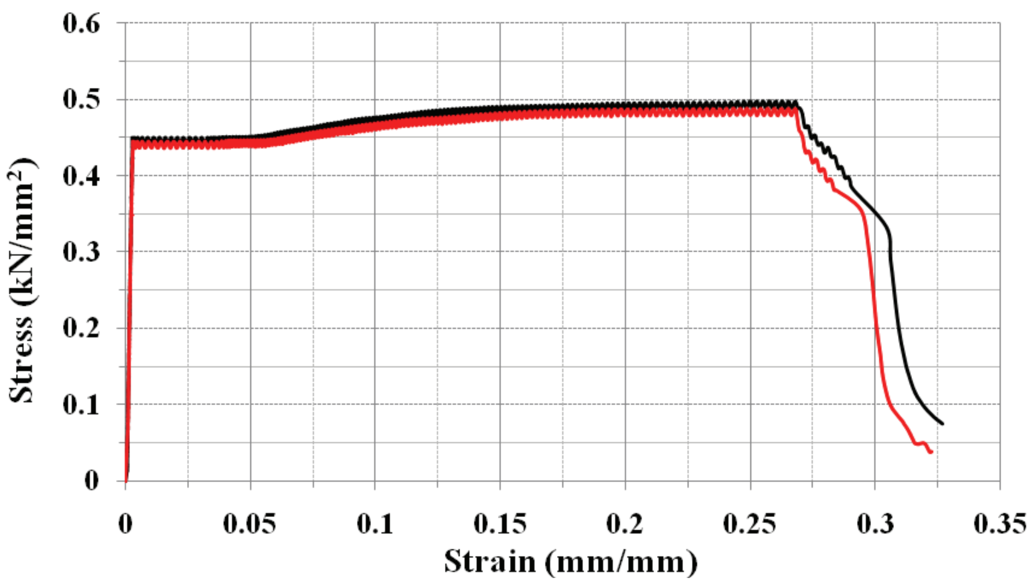

FIGURE 5-17 Tension Coupon Results for SPSLs Material

5.8.4 Concrete Cylinders

The concrete used in this experimental study was ordered from a ready-mix plant in Buffalo, NY. For each specimen, the grade of concrete ordered was 4 ksi. For specimen S1, concrete was poured over three different days to accommodate the construction sequence described in section 5.9.2. The foundation base and the lower column segments were poured from a first ready-mix truck (Pour A), and then the middle column segments were poured two weeks later using a pump truck (Pour B). Then the cap beam and the loading beam were poured one week later, also using a pump truck (Pour C).

Concrete taken from each ready-mix batch was poured into a total of seven plastic cylinders having a diameter of 6" and a height of 12". All concrete batches were treated on-site with super plasticizers to soften the mix before it hardens, increasing its workability without affecting the properties of the concrete in order to have a competent concrete at the base of the columns taking into account the height of the pour, and the shear studs present in the columns every 8".

The concrete cylinders were tested inside a compression test machine. For specimen S1, testing took place 30 days after pour C, and then all cylinders where tested at the same time, as it was not crucial to test each pour individually as they all exceeded the 28 days strength. Table 5-3 shows the strength of the concrete for all of the pours for specimen S1.

For specimen S2, concrete was poured over two different days to accommodate the construction sequence described in section 5.9.2. The foundation base and the lower column segments were poured from a first ready-mix truck (Pour A), and then the middle column segments, the cap beam, and the loading beam were poured three week later using a pump truck (Pour B).

Concrete taken from each ready-mix batch was poured into a total of seven plastic cylinders having a diameter of 6" and a height of 12". Again all concrete batches were treated on-site with super plasticizers.

Testing of specimen S2-1 took place 14 days after the second pour (Pour B) due to time constrains in SEESL, so it was crucial to test the cylinders of pour B immediately after the test, as the strength of concrete was expected to be approximately 70% of the specified 28-days strength at that time. Cylinders of pour A were also tested on the same day, and since they were cast three weeks before pour B, they were expected to have their full 28-days strength at the time of testing.

Table 5-4 shows the strength of the concrete for all of the pours for specimens S2-1, and S2-2.

Tables 5-5 to 5-8 represent the procedure for calculating the standard deviation for the group of tests on a mix with $f_c^{'}$ = 4,000 psi expected strength for both specimens. The data in the tables are organized to evaluate the data in accordance with ACI 318-08 Section 5.6.3.3, which requires that no 28-day average fall below the specified strength (4,000 psi) by more than 500 psi, and that the average of any three consecutive strength tests never fall below the specified strength. The data is further organized to easily compute the standard deviation. As per the ACI, this standard deviation points to excellent quality control procedures. The average values of $f_c^{'}$ obtained from the cylinder tests, and presented in tables 5-5 and 5-6 corresponding to the properties on the day of each respective specimen tests were then chosen for the analytical replication discussed in section 7. These values are 6.5 ksi, 3.5 ksi, and 3.5 ksi respectively for specimens S1, S2-1 and S2-2.

Note that these data were not available at the design stage but was used in the analytical stage in section 7. Figure 5-18 shows the gained strength for all pours with respect to time, plotted against the expected concrete age vs. time curves for 4000 psi and 6000 psi. It can be seen that the concrete strength matches more the 6000 psi curve in spite of the fact that 4000 psi concrete was ordered. The gained strengths for pours A and B for specimen S-1 were 8% and 3% respectively, as no significant gain in strength was expected after 28 days, while a gain in strength of 70% for pour B in specimen S2-2 is observed between day 14 and day 28.

TABLE 5-3 Concrete Strength for Specimen S1

Pour A (psi)	Pour B (psi)	Pour C (psi)
51-Days Strength	44-Days Strength	30-Days Strength
6900	6000	5900
6000	6000	5800
6400	6300	5600
6700	6300	5800
6500	5800	6100
6600	6200	5500
5600	5900	5900

TABLE 5-4 Concrete Strength for Specimens S2-1, and S2-2

Pour A (psi)	Pour B (psi)
35-Days Strength	14-Days Strength
5800	3200
5600	3900
6200	3700
6100	3400
5900	3300
5900	3700
6200	3500

TABLE 5-5 Average f_c' and s_s Calculation for Specimen S1 Cylinder Tests

	51-Day Strength (psi)			
Test	C1	C2	Average (Xi)	$(Xi\text{-}X)^2$
1	6900	6000	6450	4489
2	6400	6700	6550	1089
3	6500	6600	6500	1089
	Total Average (X)=6517			$\Sigma(Xi\text{-}X)^2$=6667

from table 5-5, the standard deviation, s_s, is calculated as:

$$s_s = \sqrt{\frac{\Sigma(X - Xi)^2}{n-1}} = \sqrt{\frac{6667}{2}} = 58\text{ psi} \tag{5-14}$$

TABLE 5-6 Average f_c' and s_s Calculation for Specimen S2-1 Cylinder Tests

	14-Day Strength (psi)			
Test	C1	C2	Average	Standard Deviation
1	3200	3900	3550	289
2	3700	3400	3550	289
3	3300	3700	3500	1089
	Total Average(X)=3533			$\Sigma(Xi\text{-}X)^2$=1667

from table 5-6, the standard deviation, s_s, is calculated as:

$$s_s = \sqrt{\frac{\Sigma(X - Xi)^2}{n-1}} = \sqrt{\frac{1669}{2}} = 29\,\text{psi} \tag{5-15}$$

TABLE 5-7 Average f_c' and s_s Calculation for Specimen S2-2 Cylinder Tests

	15-Day Strength (psi)			
Test	C1	C2	Average	Standard Deviation
1	5800	5600	5700	71289
2	6200	6100	6150	33489
3	5900	6200	6050	6889
	Total Average(X)=5967			$\Sigma(Xi\text{-}X)^2$=111667

from table 5-7, the standard deviation, s_s, is calculated as:

$$s_s = \sqrt{\frac{\Sigma(X - Xi)^2}{n-1}} = \sqrt{\frac{111667}{2}} = 236\,\text{psi} \tag{5-16}$$

TABLE 5-8 ACI Relation between Standard Deviation and Quality Control

3,000 to 4,000 psi concrete		> 10,000 psi concrete
Standard Deviation	**Quality Control**	**Standard Deviation**
300 to 400 psi	Excellent	300 to 500 psi
400 to 500 psi	Good	500 to 700 psi
500 to 600 psi	Fair	
> 600 psi	Poor	> 700 psi

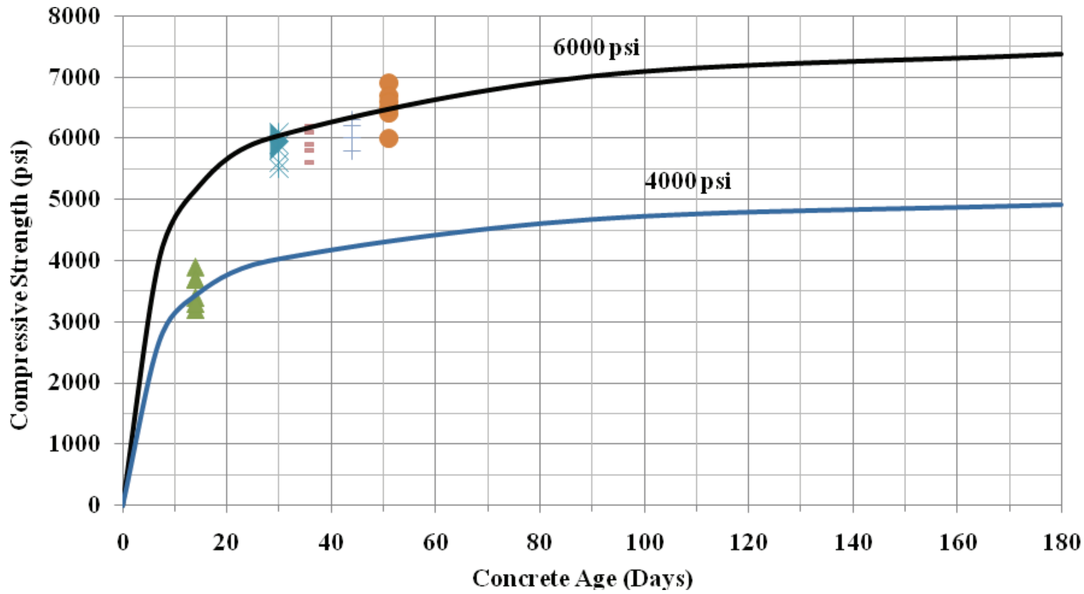

FIGURE 5-18 Expected Strength vs. Tested Cylinders Strength for all Batches in Specimens S1, S2-1, and S2-2

5.9 Test Setup

Figures 5-19 to 5-22 respectively show specimens S1, S2-1, and S2-2 prior to testing. Some details of the test setup described in the previous sections can be seen in the figures. Also, figures 5-23 to 5-25 respectively show drawings for the corresponding specimens showing all related dimensions.

FIGURE 5-19 Specimen S1 Prior to Testing (Test 1)

FIGURE 5-20 Specimen S1 Prior to Testing (Test 2) - the three lower links painted white

FIGURE 5-21 Specimen S2-1 Prior to Testing

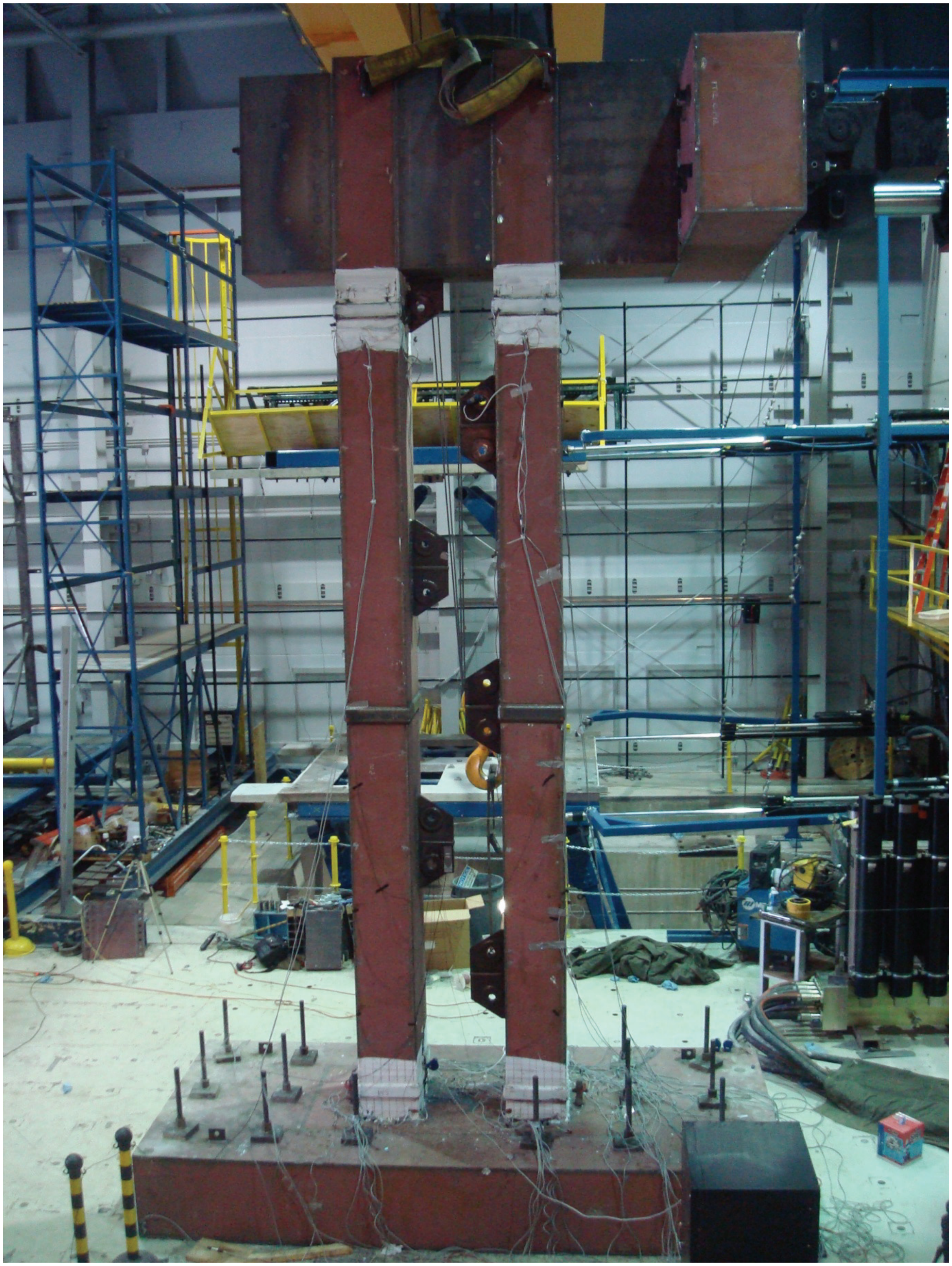

FIGURE 5-22 Specimen S2-2 Prior to Testing

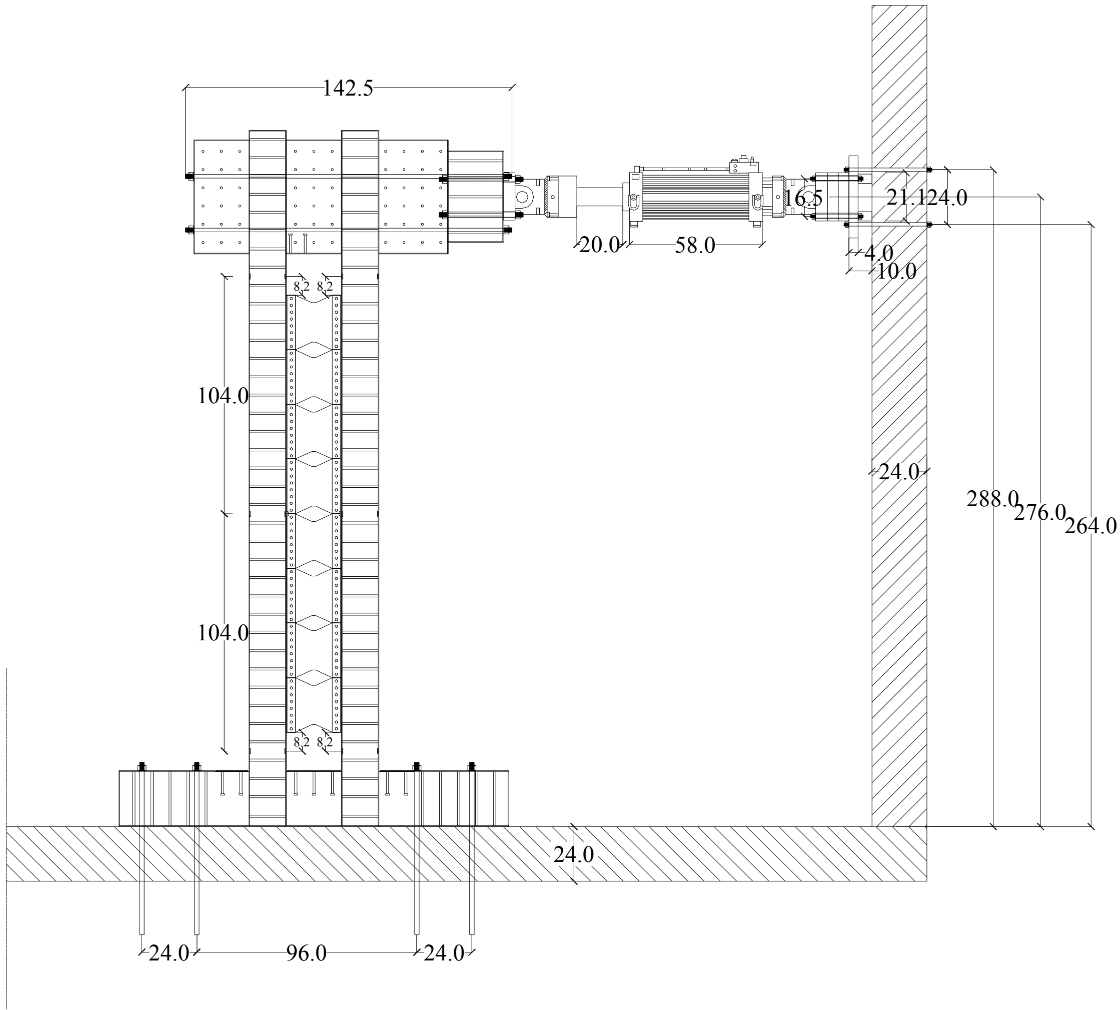

FIGURE 5-23 Specimen S1 (Elevation)

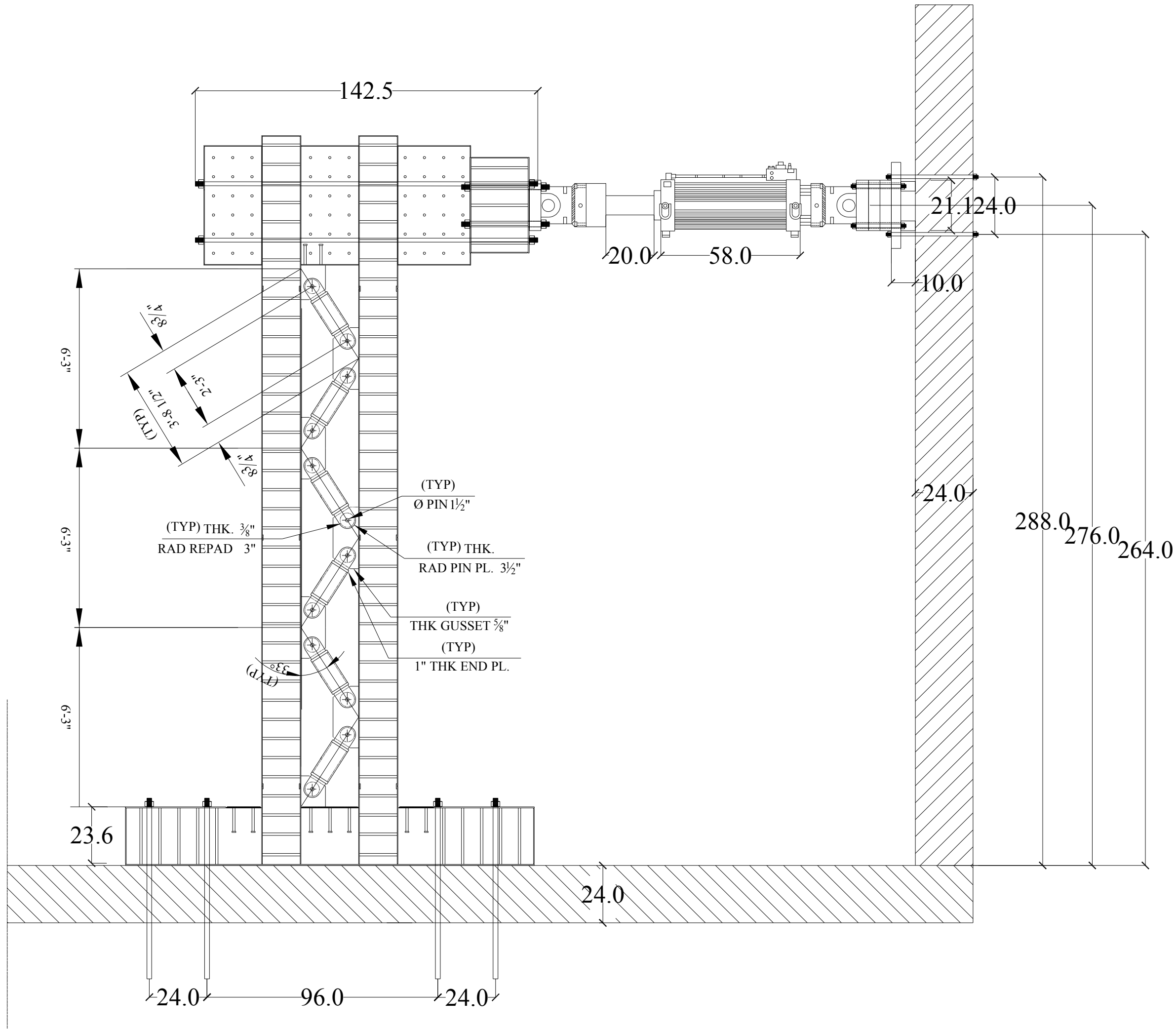

FIGURE 5-24 Specimen S2-1 (Elevation)

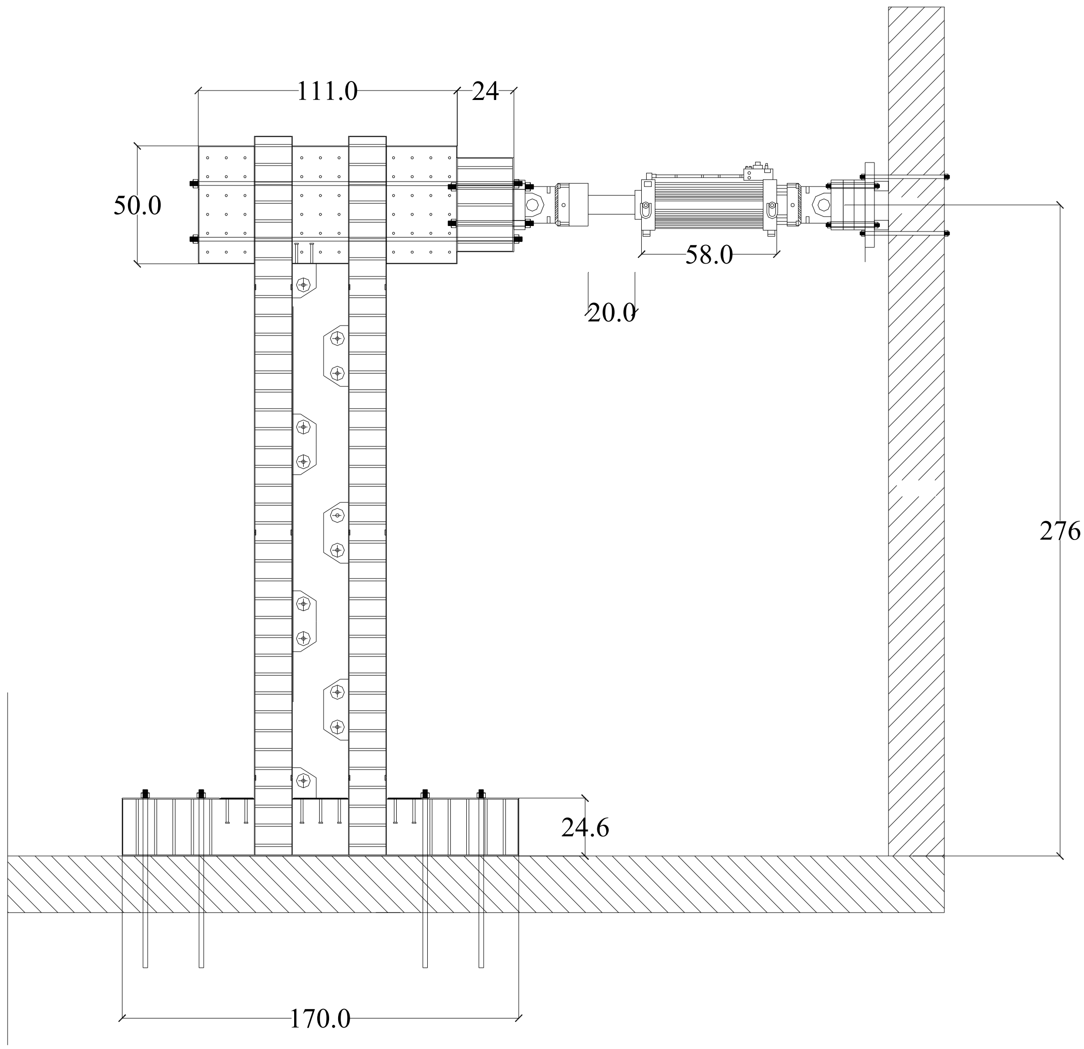

FIGURE 5-25 Specimen S2-1 (Elevation)

5.9.1 Actuator Mounting

Testing of all specimens was performed in the SEESL at the University at Buffalo. Two MTS servo-controlled static rated actuators with a load capacity of 1777 kN (400kips) each and an available stroke of ±500mm (20”) were first mounted to the strong wall of the SEESL at a height of 7500mm (300”)using four 35mm (1 3/8”) diameter pretensioned threaded rods for each actuator. Similar rods were used to connect the actuator to the loading beam.

5.9.2 Construction of Specimens

For specimen S1, the foundation base was first positioned on the strong floor of the lab. The lower column segments were then welded to the bottom plate of the foundation base, and concrete was poured into the base, as shown in figure 5-26. The foundation base cap plate was installed immediately after the concrete pour, as shown in figure 5-27 and welded immediately. The column segments were then erected and welded to each other. The second concrete pour took place 2 weeks after the first using a concrete pump. The cap beam was then welded to the columns, followed by attaching the loading beam to the specimen using four 35mm (1 3/8”) diameter pre-tensioned threaded rods and welded to the specimen for extra safety as mentioned in section 5.5.3. Concrete was then poured into the loading beam and cap beam using a concrete pump one week from the last pour as shown in figure 5-28. The actuators were then attached to the loading beam. The foundation was fixed to the strong floor after the concrete in the base had cured for 28 days; this was done using 16 pre-tensioned 35mm (1 3/8”) diameter Dywidags to ensure that no sliding or uplifting occurred as a result of the applied actuator load. The SPSLs were then bolted to the column using high strength (A490) 25mm (1”) diameter bolts designed to prevent slippage of the links. The torque of 1100 ft-lb required to reach the specified nut rotations was achieved using a HYTORC Blitz 4-A hydraulic torque wrench.

The same procedure for the installing the columns took place for specimen S2-1; the only difference being that BRBs were installed between the columns instead of the SPSLs. First, gusset plates were welded to the columns, and then the BRBs were installed in between the gussets using a 50mm (2”) diameter pin. Figure 5-29 shows the BRBs gusset plates. Finally, for specimen S2-2, the BRBs were removed as shown in figure 5-30, and the lower gusset plate was flame cut as shown in figure 5-31to insure that the gusset plate does not increase the moment capacity of the column section at the base.

FIGURE 5-26 Concrete Pouring in Foundation Base

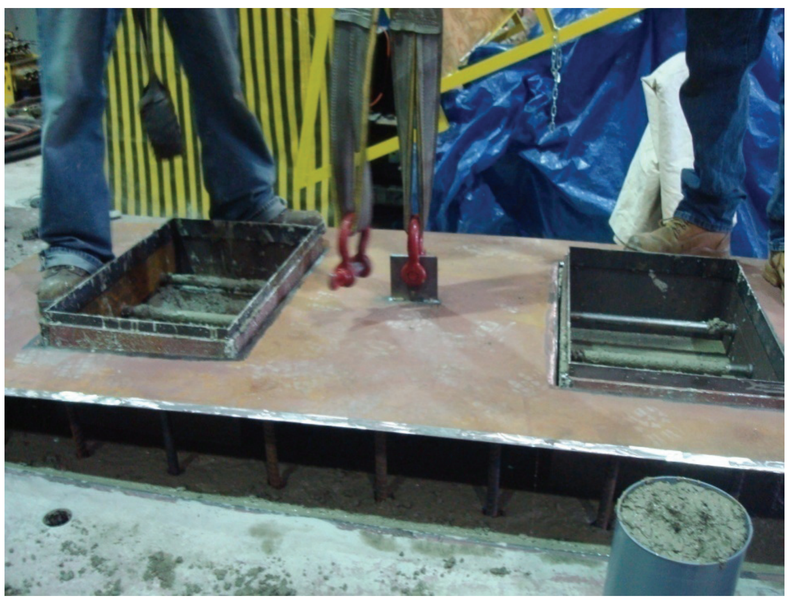

FIGURE 5-27 Foundation Base Cap Installment

FIGURE 5-28 Concrete Pouring in the loading Beam and Concrete Cap

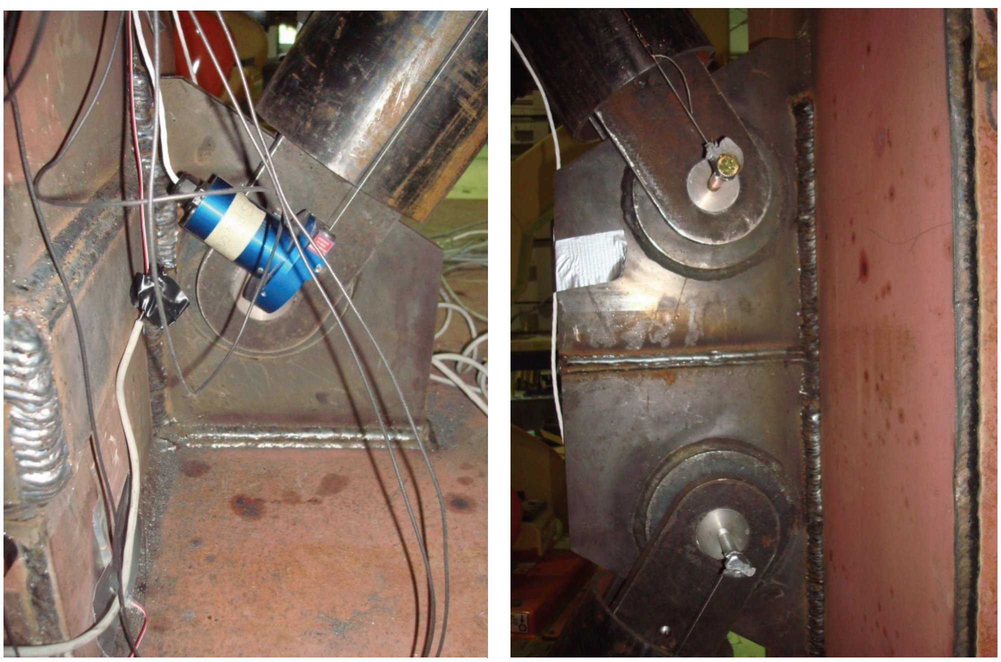

(a) (b)

FIGURE 5-29 Gusset Plates for BRBs; (a) End Gusset Plate, (b) Intermediate Gusset Plate

FIGURE 5-30 Specimen S2-2 after the removal of the BRBs

FIGURE 5-31 Lower Gusset Plate Removal

5.10 Instrumentation

A full list of all the instrumentation used in all the specimens is provided below in table 5-9 and the locations for each instrumentation is shown in figures 5-32 to 5-34. This instrumentation is briefly described below.

5.10.1 Strain Gauges

All specimens were instrumented with CAE-06-125-UW-120 strain gages manufactured by Vishay Measurements Group incorporated. Eight strain gages were installed at the top and bottom of each column (two per face) to monitor the moments and axial forces at these critical points for a total of 32 strain gages. A 30-60 rosette was also installed at the center of one of the middle links to monitor strains in the horizontal, vertical, and diagonal direction of the link and to give an estimate of the initiation and level of yielding in the links in the anticipated direction of maximum principal strain.

5.10.2 String Displacement Potentiometers

Five string displacement potentiometers (string-pots) were connected to the columns at different heights, and were then mounted to the strong wall of the SEESL. These string-pots were used to record the column's deflected shape and to give an average estimate of the top displacement to take into account any small deflections that could occur in the loading beam and affect the displacement reading of the actuators. Twelve other string-pots were installed diagonally across all the SPSLs to capture change in shear deformation occurring in the links for specimen S1. Six sting-pots were also used in specimen S2-1, installed along the BRBs (pin to pin) to capture the axial elongation of the BRBs.

5.10.3 Displacement Potentiometers

Four vertical displacement potentiometers were installed at the four corners of the foundation base to capture any sign of uplift that could occur due to the applied horizontal load. Also two horizontal displacement potentiometers were installed on the east side of the foundation base to capture any sliding that could occur to the foundation and could affect the results.

5.10.4 Krypton Dynamic Measurement Machine

The Krypton Dynamic Measurement Machine is composed of three sensitive infrared cameras mounted on a moveable frame, numerous light-emitting diodes (LEDs), and an independent data acquisition system. The LED's are 12.5mm (1/2") in diameter and can be attached to the specimen or test setup at any location visible to the cameras via hot glue, magnets, or other approaches. The three cameras then triangulate the location, velocity, and acceleration of the LEDs relative to a user defined coordinate system. Accuracy of the krypton measurements is of the order of 0.1mm (0.004") and can be as high as 0.05mm (0.002"), depending on the distance from the camera to the LEDs. Placement of the LEDs is limited by the viewable window for the cameras, which increases as the distance between the LEDs and the camera increases.

The window of the camera could not accommodate the entire specimen due to its substantial size and the limited distance available to position the cameras away from the specimen. As a result, the maximum area that was covered by the camera was half the height of the specimen. Consequently, the LEDs were at equal distances on both columns from the base up to the mid-height of the specimen. The LEDs were also used to monitor any twisting that could have happened to the specimens during testing, especially given that no lateral bracing system was used with the specimens. Also the LEDs were used as a redundant measurement for various other displacement quantities in case the string-pots failed to perform.

5.10.5 Video Recording

Digital video recording was done for all the tests. Each test was documented using four high definition cameras, recording the global view of the specimen, as well as local views including the column base and the links to capture any signs of local buckling that occur in the columns or links. Videos of the BRBs in specimen S2-2 were also recorded. Two standard definition cameras mounted into the ceiling of SEESL were also used, and where continuously recording during the whole construction time, taking 10 frames each minute to record the construction sequence of all specimens.

All videos were accelerated for the purpose having a better understanding of the behavior of each element being used. Videos are available at http://seesl.buffalo.edu.

TABLE 5-9 Instrumentation Key Table

Name	Type of Sensor	Note
SPFNW001	Potentiometer	Foundation North Side, Horizontal (E-W)
SPFSW001	Potentiometer	Foundation South Side, Horizontal (E-W)
SPFNW002	Potentiometer	Foundation North West Side, Vertical
SPFSW002	Potentiometer	Foundation South West Side, Vertical
SPFSE	Potentiometer	Foundation South East Side, Vertical
SPFNE	Potentiometer	Foundation North East Side, Vertical
SGCLWBNE	Strain Gauge	West Column Base, North East Side
SGCLWBNW	Strain Gauge	West Column Base, North West Side
SGCLWBSE	Strain Gauge	West Column Base, South East Side
SGCLWBSW	Strain Gauge	West Column Base, South West Side
SGCLWBEN	Strain Gauge	West Column Base, East North Side
SGCLWBES	Strain Gauge	West Column Base, East South Side
SGCLWBWN	Strain Gauge	West Column Base, West North Side
SGCLWBWS	Strain Gauge	West Column Base, West South Side
SGCLEBNE	Strain Gauge	East Column Base, North East Side
SGCLEBNW	Strain Gauge	East Column Base, North West Side
SGCLEBSE	Strain Gauge	East Column Base, South East Side
SGCLEBSW	Strain Gauge	East Column Base, South West Side
SGCLEBEN	Strain Gauge	East Column Base, East North Side
SGCLEBES	Strain Gauge	East Column Base, East South Side
SGCLEBWN	Strain Gauge	East Column Base, West North Side
SGCLEBWS	Strain Gauge	East Column Base, West South Side
SGCLWTNE	Strain Gauge	West Column Top, North East Side
SGCLWTNW	Strain Gauge	West Column Top, North West Side
SGCLWTSE	Strain Gauge	West Column Top, South East Side
SGCLWTSW	Strain Gauge	West Column Top, South West Side
SGCLWTEN	Strain Gauge	West Column Top, East North Side
SGCLWTES	Strain Gauge	West Column Top, East South Side
SGCLWTWN	Strain Gauge	West Column Top, West North Side
SGCLWTWS	Strain Gauge	West Column Top, West South Side
SGCLETNE	Strain Gauge	East Column Top, North East Side
SGCLETNW	Strain Gauge	East Column Top, North West Side
SGCLETSE	Strain Gauge	East Column Top, South East Side

SGCLETSW	Strain Gauge	East Column Top, South West Side
SGCLETEN	Strain Gauge	East Column Top, East North Side
SGCLETES	Strain Gauge	East Column Top, East South Side
SGCLETWN	Strain Gauge	East Column Top, West North Side
SGCLETWS	Strain Gauge	East Column Top, West South Side
SPPL001 to SPPL008	String Pot	Intermediate Plates
SP1 to SP5	String Pot	East Column, Top, 3/4 , Mid, 1/4, and Bottom
SPBRB1 to SPBRB6	String Pot	Buckling Restrained Brace top to bottom
KRCLW001 to KRCLW005	Krypton	West Column
KRCLE001 to KRCLE005	Krypton	East Column

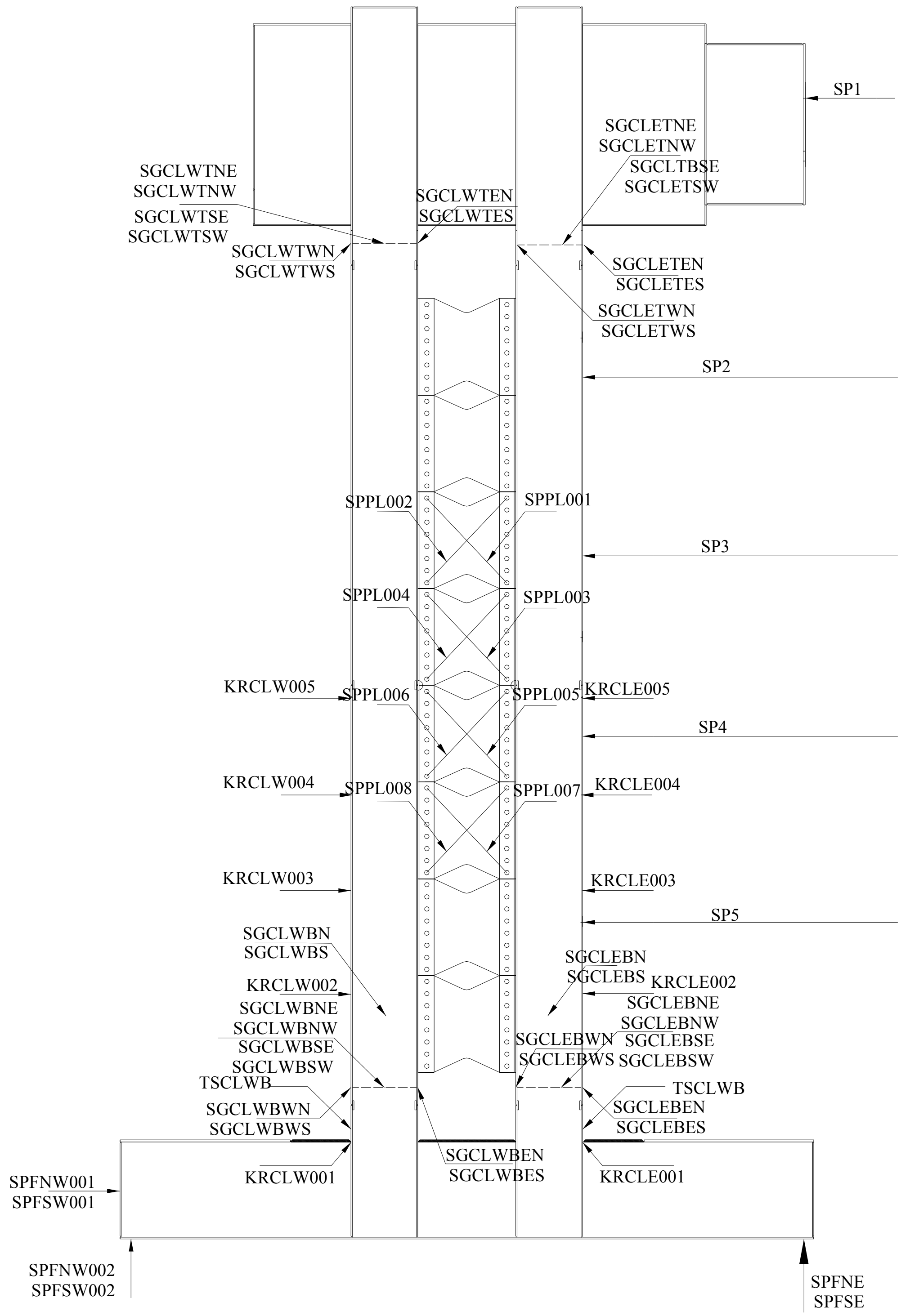

FIGURE 5-32 Instrumentation Setup for Specimen S1

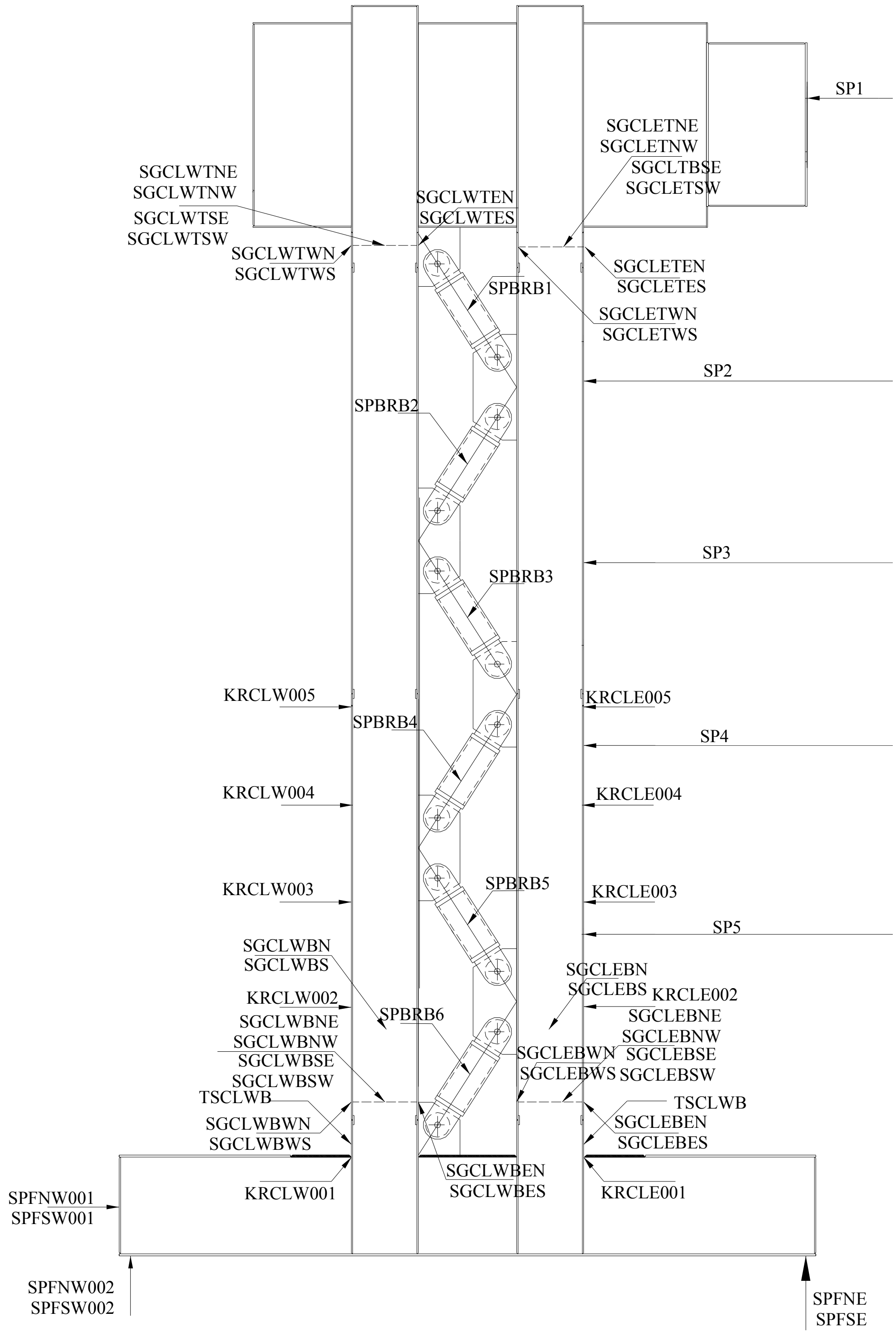

FIGURE 5-33 Instrumentation Setup for Specimen S2-1

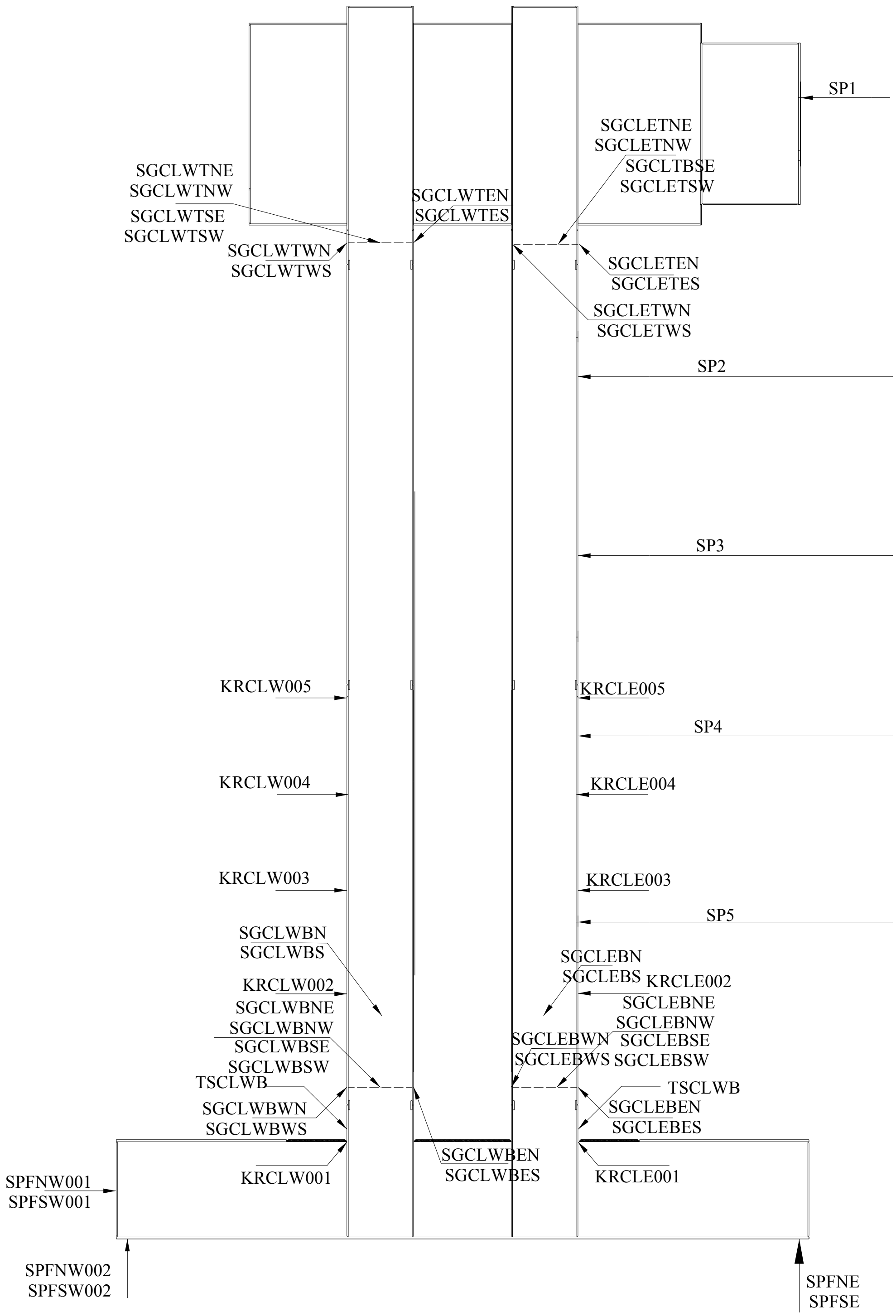

FIGURE 5-34 Instrumentation Setup for Specimen S2-2

SECTION 6
EXPERIMENTAL PROGRAM AND OBSERVATIONS

6.1 General

This section describes the loading protocols and experimental observations for the three specimens described earlier in section 5. Testing of each specimen is described in detail, and observations made regarding the behavior of each specimen are given through the steps of the applied displacement protocol.

6.2 Loading Protocol

Loading of all specimens was originally intended to proceed following quasi-static displacement control cycles carried out in accordance with the ATC 24 loading protocol. This document specifies that the specimen should be subjected to three cycles at each displacement step, up to a displacement equal to three times the yield displacement, after which only two cycles at each displacement magnitude are specified. ATC 24 specifies that reaching the yield displacement should be done in three steps as follows: three cycles at 1/3 of the yield displacement, and three cycles at 2/3 of the yield displacement, and then three cycles at the yield displacement, δ_y. Beyond that every step should be multiples of the yield displacement ($2\delta_y$, $3\delta_y$, etc.). This protocol was adjusted during the tests as necessary in response to specific observed behaviors, as described later.

6.3 Yield Displacement Estimation

For the purpose of this experimental program, it was necessary to estimate the value of the yield displacement at the top of the specimen for both the structural fuse elements and the bare frame itself. For the tests of specimens with structural fuses in place, (i.e. specimens S1 and S2-1), it was decided to stop testing before yielding occurred in the columns, to be able to test the undamaged columns on their own in following tests. Preliminary ABAQUS models were analyzed prior to testing to estimate the values of the yield displacements of both the fuses and the frame using pushover analysis. Since actual material properties were unavailable at that time, typical material properties of A572 Gr. 50 steel and specified concrete strength of 28Mpa (4ksi) were used in the analysis. Due to the flexibility of the strong wall (described later in section 7), the ABAQUS model predicted a much stiffer system, from which lesser values of yield displacements for both the fuses and the bare frame were predicted. Also, since the actual material yield strength of the frame turned out to be about 40% higher than expected, as described in section 5.8.2, using a typical A572 Gr. 50 steel material model in the preliminary finite element analysis resulted in predicting lesser values of the columns yield displacement. A decision was made during testing to experimentally define the yield values and proceed by recalibrating the displacement protocol from that value.

6.4 Actual Loading Protocol and Test Control

Due to the above reason, the ATC loading protocol described in section 6.2 was not exactly followed. In particular, an extensive number of elastic cycles were performed before reaching the experimentally defined yield values, from which all the other loading values were recalibrated. Furthermore, three tests were done on specimen S1 due to unexpected weld failures as will be described later. Therefore, after repair of the first failure, for the second test the entire loading protocol was repeated as the specimen was still in the elastic range during the first test when it experienced premature weld failure. The third test is considered a continuation of the second test and the loading protocol resumed from where it stopped when fracture occurred during the second test. The actual cyclic displacement histories used for all tests for specimen S1 are summarized in tables 6-1 and 6-2, where δ_{yb} is the yield displacement of the fuses, δ_{yf} is the yield displacement of the frame, and Δ is the top displacement applied to the frame.

For specimens S2-1 and S2-2, only one test was done for each specimen as shown in tables 6-3 and 6-4, at the magnitudes of displacements and number of cycles listed there.

In all cases, testing of all specimens was controlled by observing the real time plotting of the hysteretic curves of the applied load versus top lateral displacement for specimens S1, S2-1, S2-2 and adjusting the applied displacements to achieve the target load protocol; the resulting hysteretic curves obtained after all test cycles were completed are shown in figures 6-1, 6-2, and 6-3 respectively. Also the average strain at the bottom of the columns was monitored after each cycle to experimentally identify the yield displacement of the frame, Furthermore; cameras were installed at the bottom of the columns and close to the fuses to identify signs of local buckling.

6.5 Experimental Observations

This section describes observations on linear and nonlinear behavior made during execution of the tests for all three specimens.

6.5.1 Specimen S1

6.5.1.1 Test 1

Testing of specimen S1 proceeded in 3 steps due to unexpected failures in the full penetration welded splices connecting the columns segments, as described below. Figure 6-4 shows a photograph of specimen S1 at the start of Test 1 showing the SPSLs with their buckling restraints. In the first part of the test, the specimen remained elastic during the first 18 cycles listed in table 6-1 up to a displacement equal to 25mm (1", 0.36% drift). The number of elastic cycles was substantially greater than required by the ATC-24 test protocol, but this occurred because the specimen was not as stiff as expected. Therefore, since the actual yield displacement of both the SPSL and the columns were larger that the displacements calculated using the ABAQUS model, a slight increase in displacement was induced in every step, to search for the actual yield displacement of the structural fuse system (without exceeding it in a given cycle).

After the 1st half of the 24th cycle, at 50mm displacement (2", 0.72% drift), a loud bang was heard and the lateral load resisted by the specimen dropped by 80% from 613 kN (138kip) to 129 kN (29kip). This was due to an unexpected weld failure in the column segment connection in the lower end of the east column as shown in figures 6-5 and 6-6.

6.5.1.2 Failure Investigation and Repairs

An investigation was conducted to understand the cause of the failure, and the following observations were made. Figures 6-5 and 6-6 show that fracture developed along the bottom edge of the weld. The figures show evidence of undercut along the top edge of the weld and an amount of ‘roll over’ on the weld cap, which may not have contributed to the fracture but that casts doubts as to the quality of the weld execution.

Upon review of selected photos, Corus representatives suggested that the use of a single capping run may have contributed to the heavy undercut observed. They also noticed that the weld appeared to be uneven, which suggests inconsistencies in the travel speed. This may have had the effect of reducing the through thickness penetration (effectively creating a partial penetration butt weld) and generating a notch effect in the root area. The notch could also have lead to an increase in the localized stress levels in the root area, which may then have exceeded the yield point of the material, particularly when welding shrinkage stresses are included. This visual investigation indicated that full penetration has not been achieved for this splice connection.

A decision was made to repair/reinforce both lower splices of the specimen (the fractured and un-fractured ones) by adding a 5/8" thick 2" wide steel plate to create a new fillet welded splice all around the columns on top of the existing splice locations as shown in figures 6-7 and 6-8. These new splices were generously overdesigned to preclude any further failures at those locations.

Also a decision was made to take out the buckling restraints attached to the SPSLs, as at that time, as the cause of the “delayed” fuse yielding could not be explained; the intent was to make sure that the columns would not yield before the fuses, and since deformation of the fuses was not visible due to the presence of the restraints, it was judged prudent to remove them for the next phase of testing. Taking out the restraints decreases the contribution of the links to the total strength of the system as they will buckle and behave more like a Steel Plate Shear Wall with perforations.

6.5.1.3 Test 2

Since the specimen was almost completely elastic at the time of the weld failure, the testing protocol was restarted from the beginning. All the previously applied cycles were re-applied with similarly observed elastic behavior (but without weld fracture this time). Testing continued with applied lateral displacements beyond the one at which the connection splice failure had previously occurred. At the 1st half of the 19th step, at 37.5mm displacement (1.5", 0.54% drift), signs of yielding started to occur on the middle links as paint started to flake and fall off the links. Yielding had propagated to all links when 100mm displacement (4", 1.5% drift) was reached, as shown in figure 6-9.

At the 1st half of the 33rd cycle, at 100mm displacement (4", 1.5% drift), another loud bang was heard and the lateral load resisted by the specimen dropped by 41% from 887 kN (195kip) to 507 kN (114kip). This was due to another unexpected weld fracture in the column splice in the upper end of the west column as shown in figure 6-10.

6.5.1.4 Failure Investigation and Repairs

To better understand the cause of the recurring undesirable weld performance, a more intensive investigation was conducted on the type of welding material used, and the actual yield strength of the steel used for the Bi-Steel panels.

For this purpose, supplemental material information was obtained from Corus Bi-Steel. Those documents revealed that the steel used in the specimens came from 6 batches, each having different yield strength and tensile strength. Figure 6-11 shows an isometric view for the Bi-Steel panels used in the specimens, each panel is labeled and the batch ID is shown in table 6-5. Table 6-6 shows the mechanical properties for each batch.

Monotonic tension tests were performed on two coupons from the batch MP589-1. This particular batch was chosen for the coupon tests as the lower column segment consisted of steel from this batch, and since yielding was only expected at the bottom of the columns, it was suitable to consider that the properties of this particular batch has a dominant impact on behavior of the whole specimen. During coupon testing, strains were monitored using a MTS extensometer with a 2" gage length, while the forces were monitored using an internally mounted load cell in a Universal Testing machine at the University at Buffalo. The coupons tested showed good ductility and reached a strain of 25% before fracture. However, the yielding and fracture stress were about 40% higher than expected, with yield strengths of 470 Mpa (68ksi) and 520 Mpa (75ksi), and ultimate strengths of 530 Mpa (77ksi) and 580 Mpa (84 ksi) respectively. Also, the ratio of F_u/F_y was 1.1 and 1.09 for each of the coupons. Figure 6-12 shows the coupon test results.

The material inspection certificates were also reviewed for the S355 steel that was used in the Bi-Steel panels. The specified minimum yield strength of that material is 355MPa (50ksi). However, it was noted from the certificates that the yield strengths obtained by CORUS for these plates were 525Mpa, 474Mpa, 461MPa and 451 (i.e. 75ksi, 75ksi, 65ksi, 64ksi) and that the ultimate strengths were 579Mpa, 537Mpa, 538MPa and 523 (i.e. 84ksi, 78ksi, 78ksi, 754ksi). These higher than specified values are consistent with the coupon test results. The inspection certificates also reported Charpy-V values ranging from 81J to 88J, at temperatures ranging from 20 Celsius to -20 Celsius. A C.E. value of 0.32 was also reported, which indicate a substantial notch toughness and good weldability. However, the actual higher than specified yield strength raised questions as to the appropriateness of the welded electrodes used – originally selected to be matching for Grade 50 steel. Therefore, the welding procedure used was also investigated.

As shown by the specimen shop drawings and review of the welding procedures that were followed, each transverse butt weld in the 8mm thick plates of the Bi-Steel panels was accomplished using an AWS ER70-S6 (solid wire) consumable. The welding process used was MIG welding with a 0.035" ER70S-6 wire "Quantum Arc 6" which exceeds the AWS specifications. Typical tensile values for this welding wire are specified to be 551MPa (80 ksi); although the manufacturer's information suggests that values of up to 62Pa (90 ksi) can be obtained when welding with Argon shielding gas, as was the case here, this cannot be ensured. This welding wire also has a good Charpy-V rating of 50J. Each full penetration weld was done in two passes. One root pass to fuse the flat surface and penetrate into the backing bar, and a cap pass to fill the full penetration. The wire feed rate and voltage use were not recorded, and no pre-heat/post-heat was required for this plate thickness.
From the above limited investigation, it was concluded that the fractures were likely due to the compounding effect of the following contributing factors: (i) undercutting and possible other unknown defects that can't be identified due to absence of recorded voltage and wire deposition rate; (ii) the unusually high yield strength values (up to 525MPa) obtained by coupon tests and given on the mill-test certificates (even though mill tests are sometimes done at higher rates for an entire steel batch), which was above the minimum specified AWS tensile strength of E70 wires (70ksi) used.

The same repair/reinforcement detail as done before for the lower splices was implemented for both the upper splices of the specimen (the fractured and un-fractured ones) by adding a

5/8" thick 2" wide steel plate to create a new fillet welded splice all around the columns on top of the existing splice locations.

6.5.1.5 Test 3

Testing re-started from step 13 in table 6-2, by repeating the cycles at a displacement of 75mm (3", 1.1% drift). At the 2nd half of the 38th cycle, at 112.5mm displacement (4.5", 1.6% drift), signs of yielding of the lower west column west end were observed by whitewash flaking as shown in figure 6-13. Some pinging noises also started to be heard from now on at every cycle. The exact source of that noise could not be identified and was therefore attributed to possible minor slippage of the bolts connecting the SPSLs to the columns. At that level of drift, it was determined that the part of the experiment intended to illustrate the structural fuse concept had been completed, as further increase in lateral displacement would have resulted in the columns yielding and contributing (with the SPSLs) to in the hysteretic energy dissipation of the system.

Nevertheless, testing continued for the specific purpose of observing the ultimate behavior of the Bi-Steel columns in this particular application. Local buckling of the lower west column west face started to appear during the 1st half of the 43rd cycle, at 150mm displacement (6", 2.2% drift) as shown in figure 6-14, while fracture of that north-west corner started to occur at the 2nd half of the 43rd cycle, at 150mm displacement (6", 2.2% drift), as shown in figure 6-15. The fracture of that north-west corner propagated rapidly during the 2nd half of both the 44th and 45th cycles, at 187.5mm displacement (7.5", 2.7% drift) and the column was completely fractured along its west side as shown in figure 6-16. A huge load drop from 700 kN to 420 kN was observed on the hysteretic behavior at that point.

The lower east column east end started to locally buckle at the 2nd half of the 45th cycle, at 187.5mm displacement (7.5", 2.7% drift) as shown in figures 6-17 and 6-18 . At that point, the west column was severely damaged, and, as far as observing further damage to that column, imposing further cycles of inelastic displacement to that column from that point onward was judged to be of no benefit. However, it was decided to continue testing monotonically, imposing compression on the west column and tension on the east column until the east column was completely damaged. Testing continued until a displacement of

225mm (9”, 3.3% drift). At that point, crushed concrete started to come out of the fractured ends of the extensively damaged west column, as shown in figure 6-19. Excessive buckling was observed on the east column at that stage accompanied by a minor fracture that started to occur as shown in figures 6-20 and 6-21. It can be seen in the figures that the buckled shape is affected by the presence of the Bi-Steel shear connector which appeared to be effective as a buckling restraint point. Unfortunately the test ended when another unexpected sudden splice failure occurred, this time in the mid-height splice of the west column during the 2^{nd} half of the 46^{th} cycle, at 225mm displacement (9”, 3.3% drift) to end that test as shown in figure 6-22.

A visual weld inspection indicated that the fractured welds appeared to be clearly undercut and the full penetration weld was not always achieved as shown in figure 6-23. At that point it was impossible to re-align and repair the columns in place, and testing ended. Incidentally, subsequently to the continued undesirable splice performance observed with this specimen, it was decided to use the splice retrofit procedure described previously for all column splices in the next tests to avoid recurrence of the previously observed weld failures.

After completion of the test, the columns were then flamed cut at their base to investigate the state of the concrete inside the Bi-Steel shapes after the large cycles of inelastic deformations. Figures 6-24 and 6-25 show the concrete condition for both column bases after removal of the columns above; it can be seen that the concrete there appeared to be competent with no evidence of crushing. Incidentally, there was also no observed evidence of construction-related problems at that location, such as voids or segregation in the concrete. The condition of the shear connectors can also be seen in the figures, as there was no visible evidence of their buckling or yielding. Also no separation in the contact between the shear connectors and the steel plates was observed. For closer look at the concrete condition, the remaining steel plates where flamed-cut along their connecting edges to the foundation base and through the shear connectors, and “peeled-away” to reveal to condition of the concrete along its faces. Figure 6-26 shows the west column after removal of the west base, and figure 6-27 the concrete condition at the west base of the west column. It can be seen that some crushed concrete is observed near the edge. Figure 6-28 shows the condition of the concrete at the west column after removal of the south side, revealing some crushed concrete along the east and west sides of the column. Figure 6-29 shows the condition of the concrete of the east column after removal of all its sides, also revealing crushed concrete on the east and west sides of the column.

6.5.2 Specimen S2-1

To avoid a repeat of the problems due to weld failures, all splices of specimen S2-1 were reinforced prior to the test by adding steel plates at the locations of all the welded splices between the columns segments. Those plates had the same dimensions and fillet welds as used in the prior specimen.

Testing started following the protocol in table 6-3. Again, the number of elastic cycles was substantially greater than required by the ATC-24 test protocol as it was still unclear at that time why the specimens were less stiff than expected.

During the first 17 cycles of loading, specimen S2-1 reached a displacement of 37.5mm (1.5", 0.54% drift), and exhibited completely linear behavior. At the 1st half of the 18th cycle, at 50mm displacement (2", 0.72% drift), signs of yielding were observed by softening of the hysteretic loop; this was attributed to yielding of the BRBs, as no sign of yielding was observed in any of the columns. Note that no strain gages were installed on the BRBs, so this yielding could only be inferred from the shape of the hysteretic loops. From that point onwards, some pinging sounds were heard at the BRB-to-gusset connections. The source of the sound could not be identified, so it was attributed to possible friction between the BRB gussets and the pins as they rotate.

Until the 2nd half of the 25th cycle at 87.5mm displacement (3.5", 1.3% drift), no evidence of yielding was observed in the column bases neither through flaking of whitewash nor through strain gauges reading, also no signs of local buckling were observed in any part of the columns.

At the 2nd half of the 27th cycle, at 100mm displacement (4", 1.45% drift), first signs of local buckling were observed in the east face of the bottom east column as shown in figure 6-30. At this point, testing was terminated in order to preserve the integrity of the Bi-Steel columns for a final test in which only the bare frame was to be tested (without any fuses between the columns), and needed for comparison purposes.

6.5.3 Specimen S2-2

In order to quantify the contribution of the fuses to the strength and stiffness of the total system, bare frame testing was essential. After terminating testing on specimen S2-1, the BRBs where removed by removing their pins. Also the lower gusset was flamed-cut from the west column as shown in figure 6-31, to prevent increasing the cross section and stiffness of the column where yielding was expected to occur. The other gussets along the height of the columns where left in place as they had no major impact on the overall behavior of the frame.

A second objective of this test was to investigate the cyclic behavior of the Bi-Steel columns. Toward this end, the bare frame was subjected to cycles of progressively increasing lateral displacement magnitudes until failure of the columns. To properly quantify this behavior, it was critical to capture the onset of cracking that was expected to occur, as well as cracking propagation through the columns up to failure. Contrary to the previous tests, the unloading protocol was slightly different. For every cycle in the inelastic range, after reaching the peak displacement, unloading stopped at 80% of the maximum load reached, to allow a closer inspection of the condition of the columns and be able to capture the onset of any cracking that occurred in the columns (this intermediate step has been prevented in previous tests for safety reasons).

During the first 8 cycles, linear behavior was observed as expected, and this was confirmed by the hysteretic curve shown in figure 6-3 and also by the average strains read from the gages at the bottom of the columns. At the 2^{nd} half of the 9^{th} cycle, at 100mm displacement ($4^{"}$, 1.45% drift), signs of local buckling were observed at the east side of the bottom east column as shown in figure 6-32. At the 2^{nd} half of the 10^{th} cycle, at 100mm displacement ($4^{"}$, 1.45% drift), buckling propagated to the north side of the bottom east column as shown in figure 6-33.

At the 2^{st} half of the 12^{th} cycle, at 125mm displacement ($5^{"}$, 1.81% drift), a minor crack of approximately 12.5mm ($0.5^{"}$) was observed in the north east and south east corners weld of the bottom east column. Because of the concern that this might be an isolated weld defect that could lead to unrepresentative response, a decision was made to fix the welds before testing continued. Fixing of the weld was done by adding three weld passes of approximately

125mm (5") on top of the existing weld at the specific fracture location as shown in figure 6-34. Two strain gauges where lost due to the heat from the welding operation, but testing continued as planned.

At the 1st half of the 13th cycle, at 150mm displacement (6", 2.17% drift), local buckling started to develop on the west side of the bottom west column as shown in figure 6-35. A minor crack on the same face of the column was observed at the connection between the plate and the internal shear connectors as shown in figure 6-36. Another crack reappeared on top of the weld reinforcement at the 2nd half of the 13th cycle, at 150mm displacement (6", 2.17% drift), as shown in figure 6-37.

At the 2nd half of the 14th cycle, at 150mm displacement (6", 2.17% drift), a similar crack was observed on the east side of the bottom east column, as shown in figure 6-38. At the same time, a huge crack at the south east corner of the east column was observed and concrete started spalling out of the column as shown in figure 6-39.

Testing continued to 175mm displacement (7", 2.5% drift). At the 1st half of the 15th cycle at that displacement, the lateral load resisted by the specimen dropped 44% from 160 kip to 90 kip, as a loud bang was heard. Inspection of the specimen revealed that a crack had started from the south east corner of the bottom east column, and propagated along its east face as shown in figure 6-40.

As testing continued to better understand the progression of the failure mechanism (and because the specimen had a non-negligible residual strength), the crack propagated across the south side of the east column, during the 1st half of the 16th cycle as shown in figure 6-41 and the east column was totally damaged at this stage.

It was deemed not beneficial to cycle further beyond that point, but the west column was still intact having suffered only from local buckling. So it was decided to apply one more half cycle up to a displacement that would make the west column totally fails. The fractured column would be in compression during that half cycle, making that last stage of testing possible.

At 175mm displacement (7", 2.5% drift), a minor crack started to appear at the north west corner of the bottom west column as shown in figure 6-42. The crack started to grow and propagate as displacement was increased in the same direction. At the same time, the east column was suffering major damage as shown in figure 6-43 at 200mm displacement (8", 2.9% drift.

At 225mm displacement (9", 3.26% drift), the crack at the North West corner of the west column propagated as shown in figure 6-44. Concrete started spalling from the south east corner of the east column as shown in figure 6-45.

At 250mm displacement (10", 3.62% drift), the applied load started to drop gradually as shown on the hysteretic curve of figure 6-3, and the existing crack on the west face of the west column further propagated as shown in figure 6-46. At the same time, another large crack developed at the north east corner of the bottom east column and concrete rubble started to escape from the crack opening as shown in figure 6-47.

At 300mm displacement (12", 4.35% drift), the west column had reached the state of damage shown in figure 6-48, with 600mm long cracking along its base, and extensive local buckling, and concrete rubble started escaping from the north west corner crack as shown in figure 6-49. Testing was then terminated at that stage.

Again after completion of the test, the columns where flamed-cut to investigate the condition of the concrete. The concrete was again found to be competent with no observed segregation, with crushed concrete on the east and west sides of the column. Figures 6-50 and 6-51 show the concrete condition after test termination.

6.6 Summary

Three large scale specimens where tested under quasi-static loading. Specimen S1, having unconfined SPSLs as structural fuses between the Bi-Steel columns, specimen S2-1, having BRBs as structural fuses between the columns, and specimen S2-1 consisting only of the bare frame of Bi-Steel columns and tested for comparison purposes.

Specimen S1 performed successfully after unexpected failures and repairs of the welded splices between the segmental columns. After fixing the welds, the specimen behaved in a stable ductile manner until it reached 225mm displacement (9", 3.3% drift). The onset of column yielding was observed at 100mm displacement (4", 1.6% drift) accompanied with minor local buckling at the bottom of one column. A base shear of 875kN (197 kips) was observed at that level of drift. Failure of the specimen was due to fracture at the bottom of both columns due to low cycle fatigue which developed at the locations of repeated local buckling. A strength reduction of 33% from the peak value was observed at the maximum drift reached when testing had to stop due to failure of a mid-height column splice (this failure could not be repaired). Adding the SPSLs increased the elastic stiffness of the bare frame by 128%, while the strength increased by 31%. This strength increase was less than originally expected from the SPSLs due to the removal of the buckling restraints which decreased the SPSLs strength by 30%, as described in section 7.

Specimen S2-1 was also successfully tested up to a drift corresponding to the onset of column yielding at 100mm displacement (4",1.6%); a base shear of 881kN (198 kips) was observed at that level of drift. Because it was essential to keep the integrity of the column for testing the bare frame alone, testing stopped after minor signs of local buckling were observed on one of the columns. No failure was expected from this specimen but yielding of the BRBs dissipating the seismic energy was observed on the overall hysteretic behavior of the specimen. Additional testing and observations on the hysteretic behavior of individual BRBs will be presented in the next section. Adding the BRBs increased the elastic stiffness of the bare frame by 80%, while the strength increased by 20%.

Specimen S2-2 was tested successfully to 175mm displacement (7", 2.5% drift) until the east column failed. Non-cyclic testing continued in the other direction up to a displacement of 300mm (12", 4.45% drift) to fail the other column. Failure of the specimen was from fracture of the bottom of both columns due to low cycle fatigue which developed at the locations of repeated local buckling.

A comparison for the values of the elastic stiffness, base shear, ductility, drift, and strength reduction for each specimen is shown in table 6-7.

TABLE 6-1 Cyclic Displacement History- Specimen S1 (Test 1)

Displacement Step	Number of Cycles	Cumulative No. of Cycles	Disp. Δ/δ_{yb}	Disp. Δ/δ_{yf}	Disp. mm(inches)	Drift (%)
1	3	3	0.16	0.06	6.25(0.25)	0.09
2	3	6	0.24	0.09	9.5(0.38)	0.13
3	3	9	0.31	0.125	12.5(0.5)	0.18
4	3	12	0.39	0.16	15.5(0.62)	0.22
5	3	15	0.48	0.19	18.75(0.75)	0.27
6	3	18	0.62	0.25	25(1)	0.36
7	3	21	0.94	0.375	37.5(1.5)	0.54
8	3	24	1.25	0.5	50(2)	0.72

TABLE 6-2 Cyclic Displacement History- Specimen S1 (Tests 2&3)

Displacement Step	Number of Cycles	Cumulative No. of Cycles	Disp. Δ/δ_{yb}	Disp. Δ/δ_{yf}	Disp. mm (inches)	Drift (%)
1	3	3	0.16	0.06	6.25(0.25)	0.09
2	3	6	0.24	0.09	9.5(0.38)	0.13
3	3	9	0.31	0.125	12.5(0.5)	0.18
4	3	12	0.39	0.16	15.5(0.62)	0.22
5	3	15	0.48	0.19	18.75(0.75)	0.27
6	3	18	0.62	0.25	25(1)	0.36
7	3	21	0.94	0.375	37.5(1.5)	0.54
8	3	24	1.25	0.5	50(2)	0.72
9	3	27	1.4	0.56	56.25(2.25)	0.81
10	3	30	1.6	0.63	62.5(2.5)	0.91
11	2	32	1.9	0.75	75(3)	1.1
12	1	33	2.5	1	100(4)	1.5
13	2	35	1.9	0.75	75(3)	1.1
14	2	37	2.2	0.88	87.5(3.5)	1.3
15	2	39	2.8	1.12	112.5(4.5)	1.6
16	2	41	3.1	1.25	125(5)	1.8
17	2	43	3.8	1.5	150(6)	2.2
18	2	45	4.7	1.88	187.5(7.5)	2.7
19	1	46	5.6	2.25	225(9)	3.3

TABLE 6-3 Cyclic Displacement History- Specimen S2-1

Displacement Step	Number of Cycles	Cumulative No. of Cycles	Disp. Δ/δ_{yb}	Disp. Δ/δ_{yf}	Disp. mm(inches)	Drift (%)
1	3	3	0.156	0.06	6.25(0.25)	0.09
2	3	6	0.32	0.125	12.5(0.5)	0.18
3	3	9	0.47	0.187	18.75(0.75)	0.27
4	3	12	0.625	0.25	25(1)	0.36
5	3	15	0.78	0.312	31.25(1.25)	0.45
6	2	17	0.94	0.375	37.5(1.5)	0.54
7	2	19	1.25	0.5	50(2)	0.72
8	2	21	1.56	0.625	62.5(2.5)	0.91
9	2	23	1.875	0.75	75(3)	1.1
10	2	25	2.19	0.875	87.5(3.5)	1.3
11	2	27	2.5	1	100(4)	1.45

TABLE 6-4 Cyclic Displacement History- Specimen S2-2

Displacement Step	Number of Cycles	Cumulative No. of Cycles	Disp. Δ/δ_{yf}	Disp. mm(inches)	Drift (%)
1	2	2	0.25	25(1)	0.36
2	2	4	0.5	50(2)	0.72
3	2	6	0.75	75(3)	1.08
4	2	8	0.875	87.5(3.5)	1.27
5	2	10	1	100(4)	1.45
6	2	12	1.25	125(5)	1.81
7	2	14	1.5	150(6)	2.18
8	2	16	1.75	175(7)	2.5

TABLE 6-5 Batch ID Key Table for Bi-Steel Panels

Item Number	Batch Number	Panel Description	Plate (1) ID	Plate 2 ID
1	BIS1078-DPN-001	PANEL 001 (12mm)	7K05565HB	7K07815HC
2	BIS1078-DPN-002	PANEL 002 (8mm)	MP620-1	MP589-1
3	BIS1078-DPN-003	PANEL 003 (8mm)	MP616-1	MP589-1
4	BIS1078-DPN-004	PANEL 004 (8mm)	MP616-1	MP620-1
5	BIS1078-DPN-005	PANEL 005 (8mm)	MP586-1	MP586-1
6	BIS1078-DPN-006	PANEL 006 (8mm)	MP620-1	MP616-1
7	BIS1078-DPN-007	PANEL 007 (12mm)	7K07815HC	7K07815HC

TABLE 6-6 Mechanical Properties of Batches used in Specimens

Batch ID	Yield Strength (MPa)	Tensile Strength (MPa)	Elongation (%)
MP586-1	474	537	32
MP589-1	451	523	30
MP616-1	525	579	24
MP620-1	461	538	32
7K05565HB	430	560	31
7K07815HC	405	545	30

TABLE 6-7 Summary of Peak Results

Specimen	Elastic Stiffness (kN/mm)	Base Shear at Column Yielding (kN)	Maximum Base Shear (kN)	Fuse Ductility at Column Yielding	Fuse Ductility at Maximum Drift	Column Yielding Drift (%)	Maximum Drift (%)	Strength Reduction at Maximum Drift (%)
S1	19	875	982	4	8	1.6	3.3	33
S2-1	21.5	881	-	4	-	1.6	-	-
S2-2	8	666	806	-	-	1.6	4.3	29

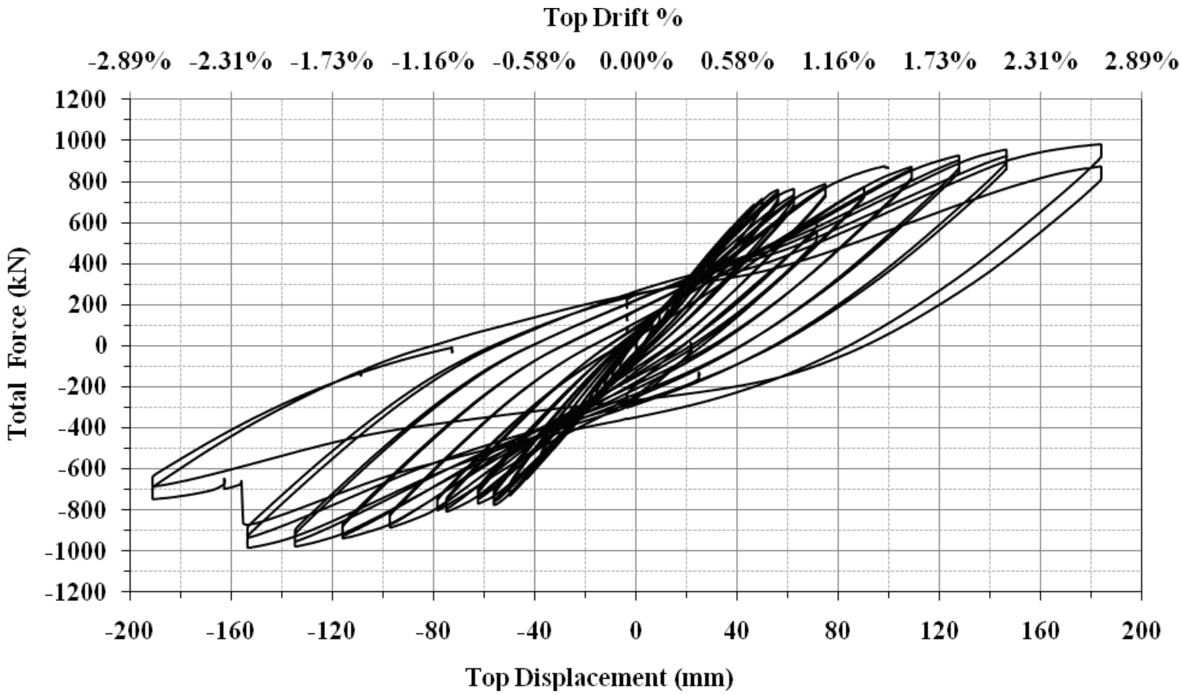

FIGURE 6-1 Hysteretic Curve of Specimen S1

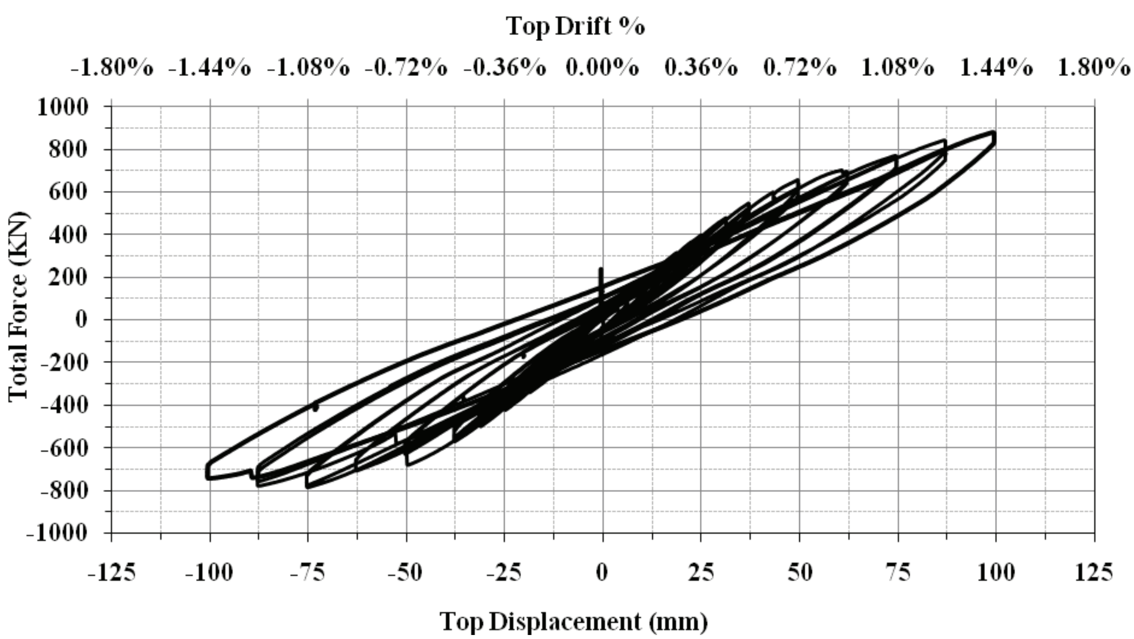

FIGURE 6-2 Hysteretic Curve of Specimen S2-1

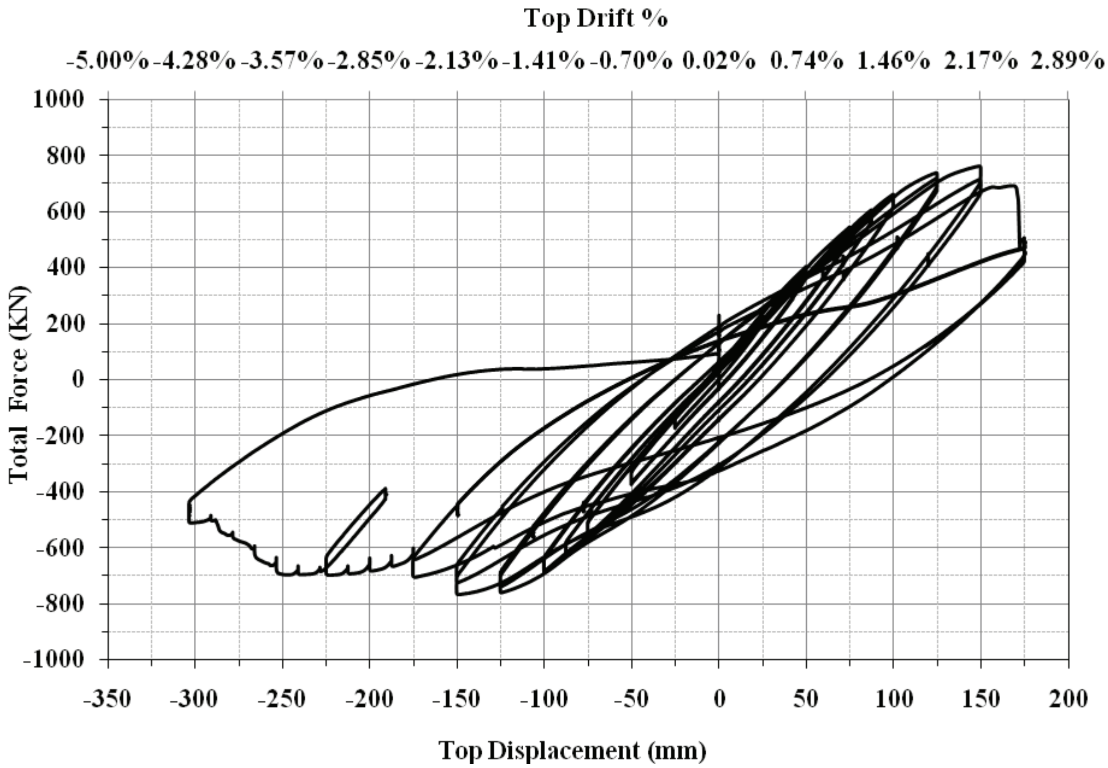

FIGURE 6-3 Hysteretic Curve of Specimen S2-2

FIGURE 6-4 Test 1 with SPSLs including Buckling Restraints

FIGURE 6-5 Premature Weld Failure at Lower End of East Column

FIGURE 6-6 Premature Weld Failure at Lower End of East Column

FIGURE 6-7 Reinforcing Strip at Lower East End

FIGURE 6-8 Reinforcing Strip at Lower West End

FIGURE 6-9 Whitewash Flaking of SPSLs at 1st half of the 33rd cycle (4", 1.5% drift)

FIGURE 6-10 Premature Weld Failure at Upper End of West Column

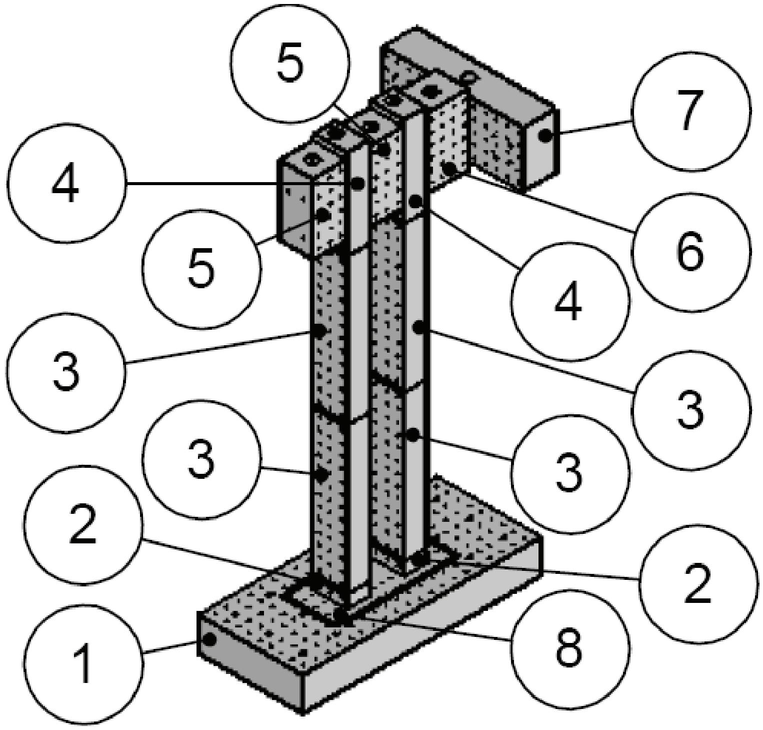

FIGURE 6-11 Isometric View of the Bi-Steel Panels

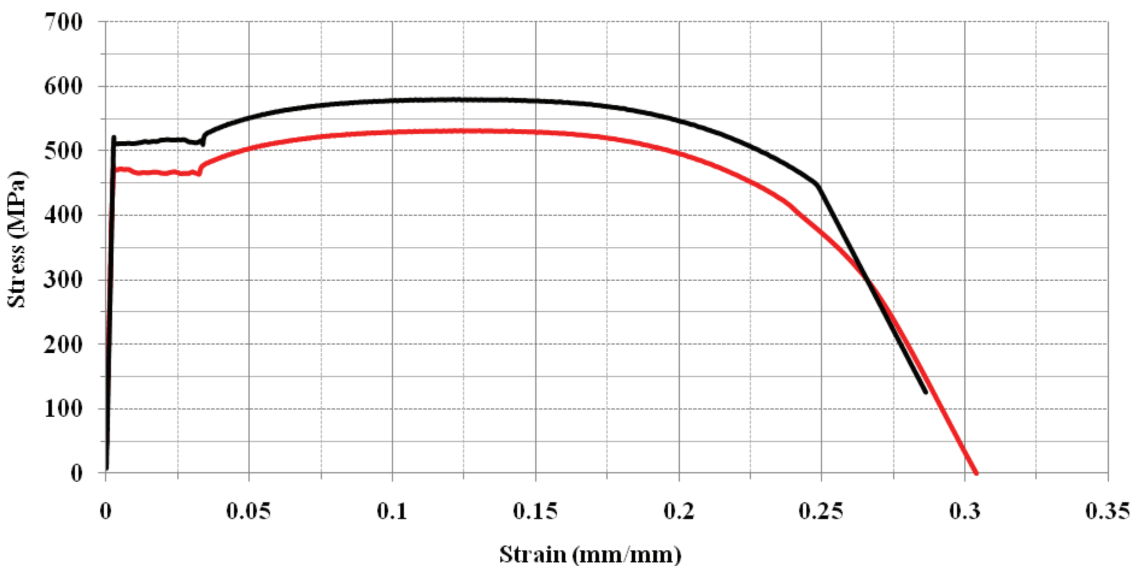

FIGURE 6-12 Tension Coupon Results for Bi-Steel Material

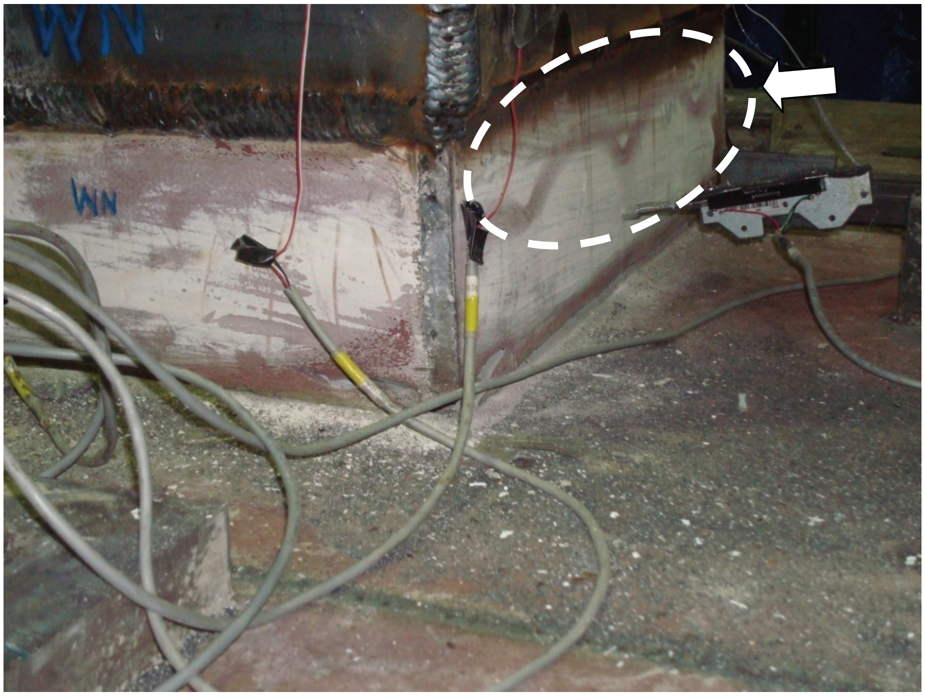

FIGURE 6-13 West Column West End Yielding

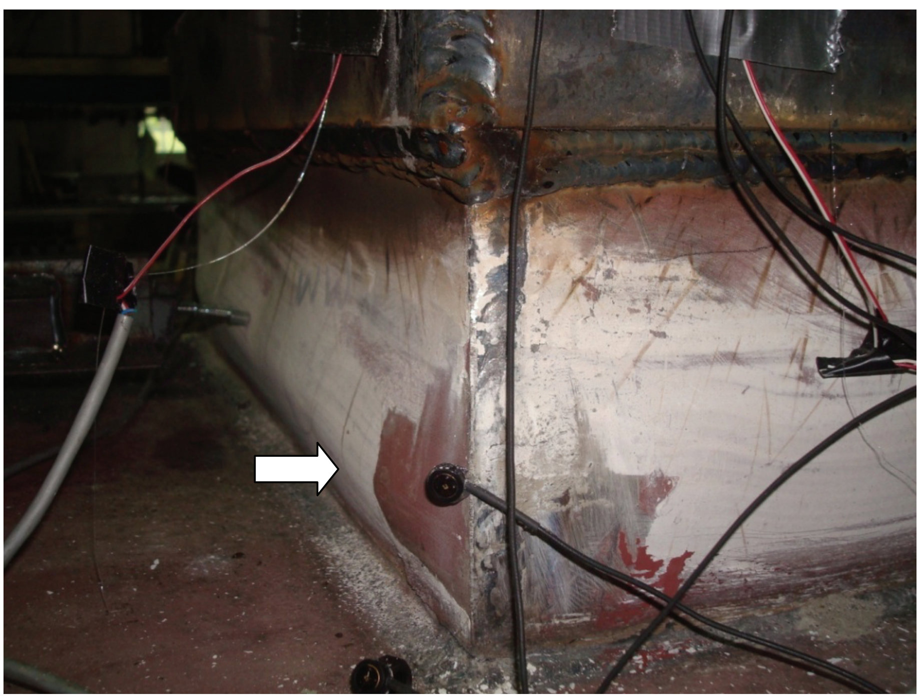

FIGURE 6-14 West Column West End Buckling

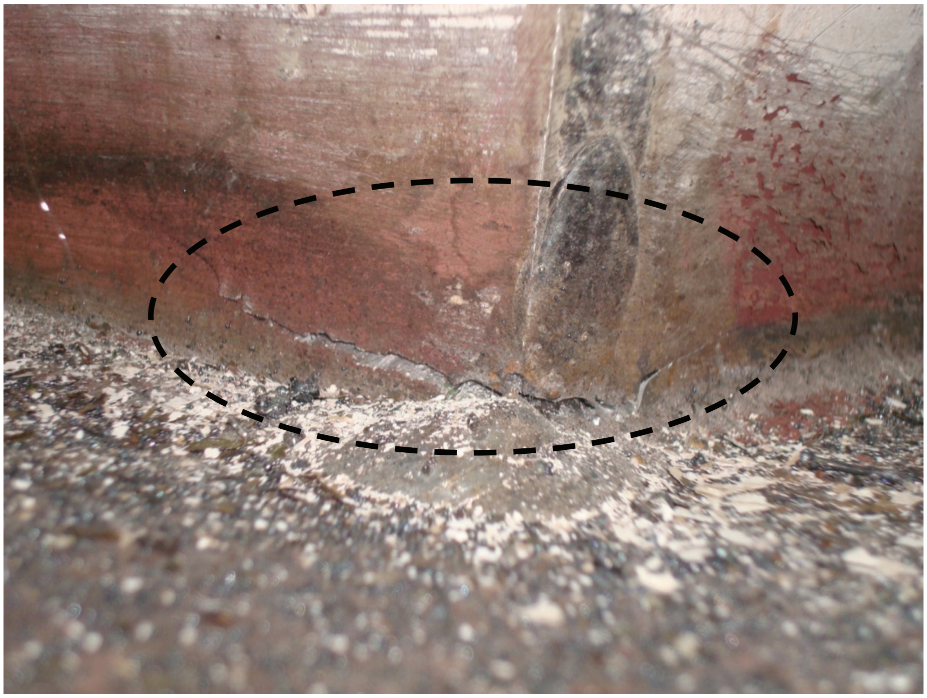

FIGURE 6-15 West Column North-West Corner Fracture

FIGURE 6-16 West Column Fracture Propagation at 187.5mm displacement (7.5", 2.7% drift)

FIGURE 6-17 East Column East End Buckling

FIGURE 6-18 East Column East End Buckling

FIGURE 6-19 West Column Damage at 2^{nd} half of 46^{th} Cycle (9", 3.3% Drift)

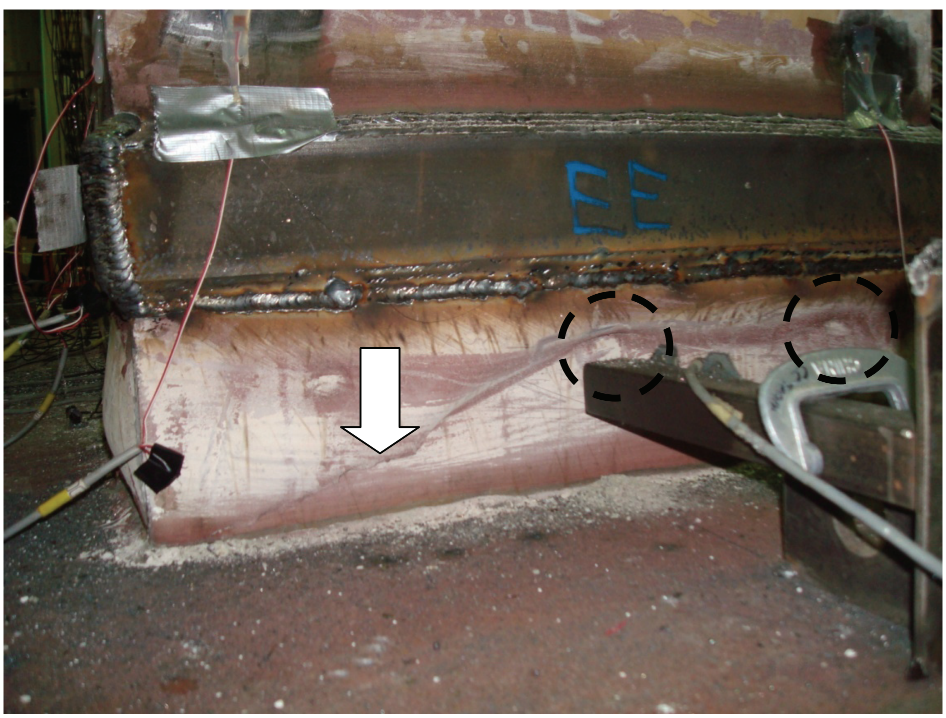

FIGURE 6-20 East Column Damage at 2^{nd} half of 46^{th} Cycle (9", 3.3% Drift)

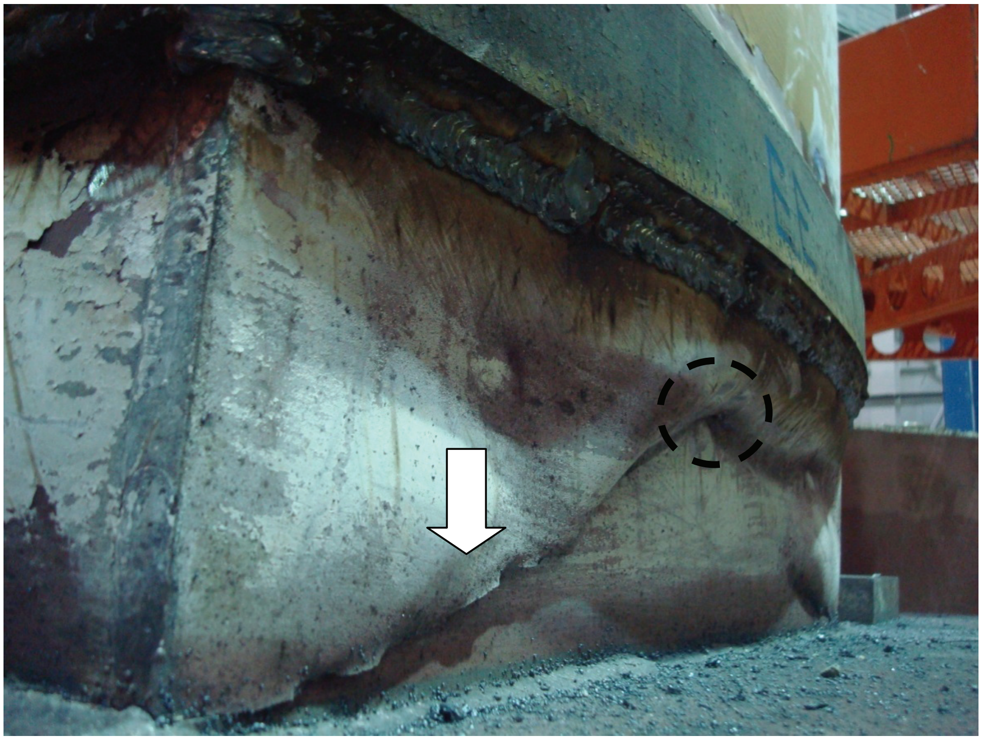

FIGURE 6-21 East Column Damage at 2nd half of 46th Cycle (9", 3.3% Drift)

FIGURE 6-22 Shear Failure at Middle Column Connection of West Column

FIGURE 6-23 Weld Undercut at Middle Column Connection of West Column

FIGURE 6-24 East Column Concrete Condition at the End of the Test

FIGURE 6-25 West Column Concrete Condition at the End of the Test

FIGURE 6-26 West Column Concrete Condition at Base

FIGURE 6-27 Crushed Concrete at the West Side of West Column

FIGURE 6-28 Concrete Condition at South Side of East Column

FIGURE 6-29 Concrete Condition after Removing all Sides of East Column

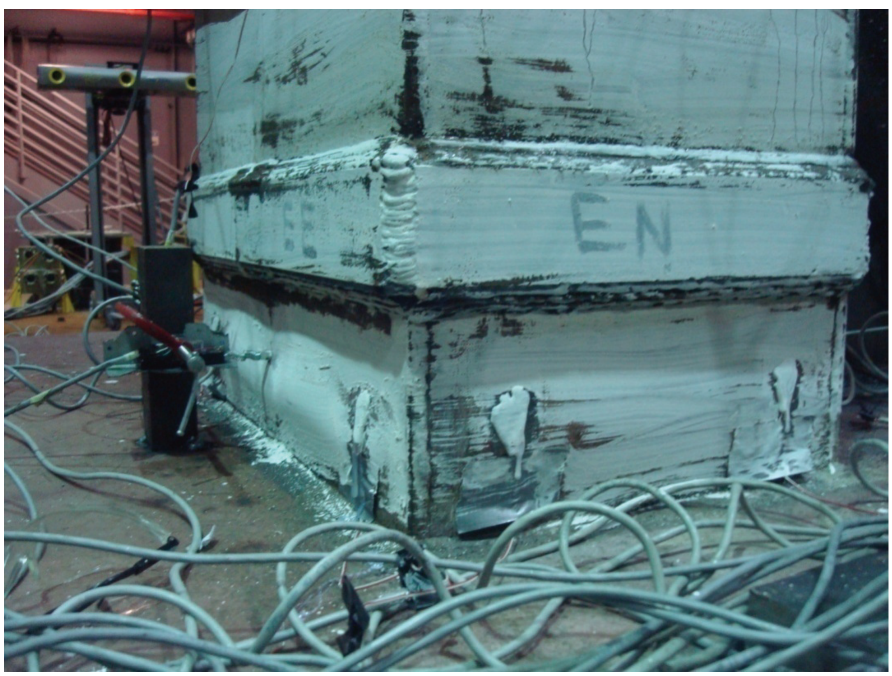

FIGURE 6-30 Minor Buckling Observation at the East Side of the East Column at 2nd Half of 27th Cycle (4", 1.45% Drift)

FIGURE 6-31 Removal of Gusset Plate at the lower End of the West Column

FIGURE 6-32 East Column Buckling at 2nd half of the 9th cycle (4", 1.45% drift)

FIGURE 6-33 East Column Buckling at the 2nd half of the 10th cycle (4", 1.45% drift)

FIGURE 6-34 East Column Weld Fixing at the 2nd half of the 12th cycle (5", 1.81% drift)

FIGURE 6-35 West Column Buckling at the 1st half of the 13th cycle (6", 2.17% drift)

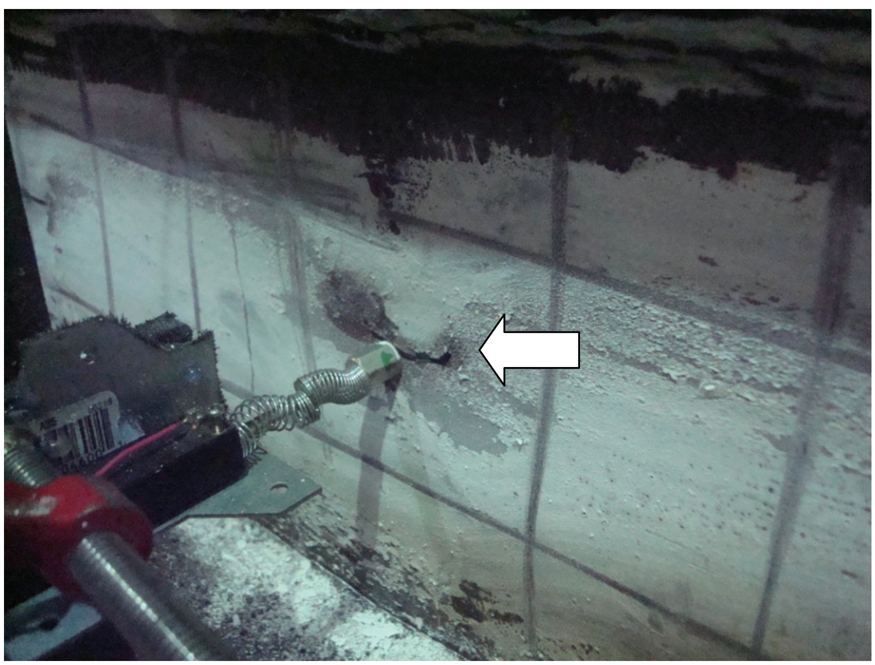

FIGURE 6-36 Crack at the Shear Connector Location at the West Column at the 1st half of the 13th cycle (6", 2.17% drift)

FIGURE 6-37 Crack at North East Corner of East Column at the 2nd half of the 13th cycle (6", 2.17% drift)

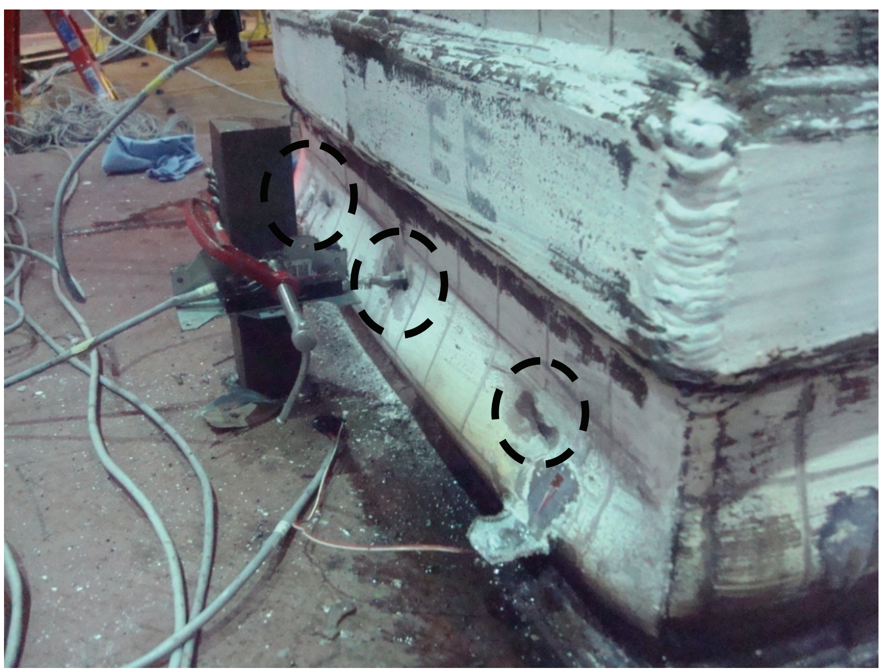

FIGURE 6-38 Crack at the Shear Connector Location at the East Column at the 2nd half of the 14th cycle (6", 2.17% drift)

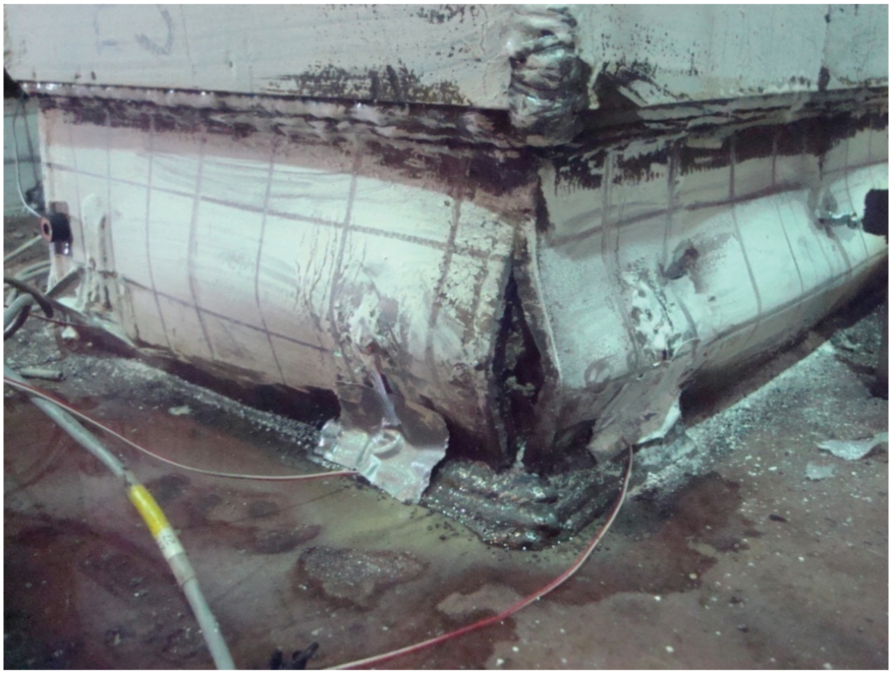

FIGURE 6-39 Crack in the South East Corner of the East Column at the 2nd half of the 14th cycle (6", 2.17% drift)

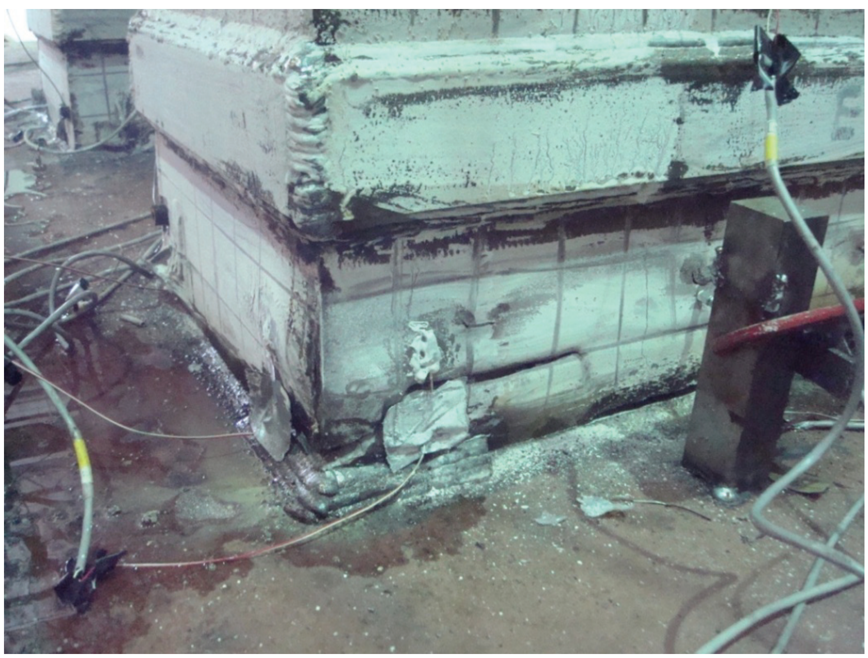

FIGURE 6-40 Crack Propagation at the East Side of the East Column at the 1st half of the 15th Cycle (7", 2.5% Drift)

FIGURE 6-41 Crack Propagation at the South Side of the East Column at the 1st half of the 16th Cycle (7", 2.5% Drift)

FIGURE 6-42 Crack at the North West Corner of the West Column (7", 2.5% Drift)

FIGURE 6-43 Damage at East Column at 8" Displacement (2.9% Drift)

FIGURE 6-44 Crack Propagation at the North West Corner of the West Column at 9" Displacement (3.26% Drift)

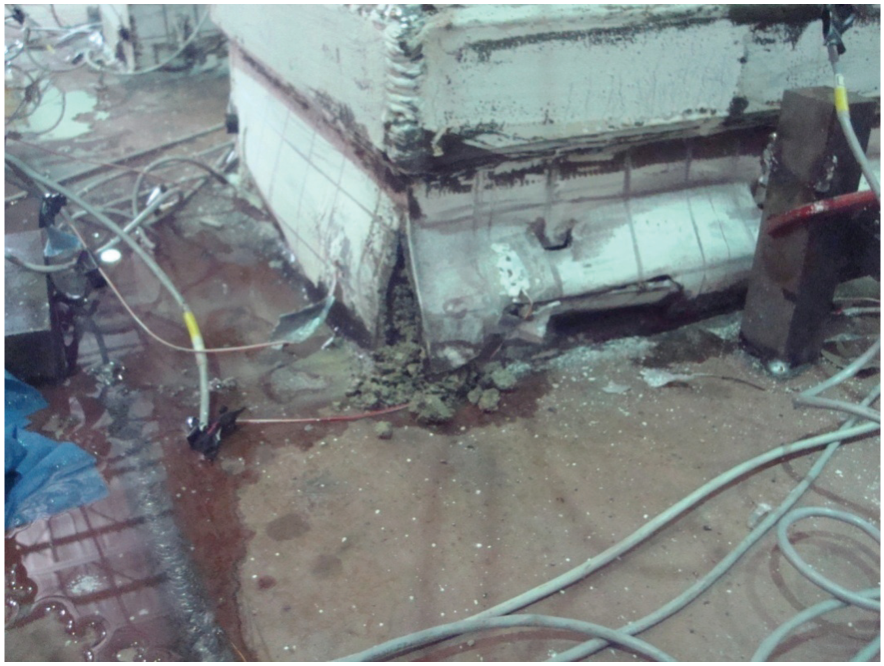

FIGURE 6-45 Concrete Spalling from the East Column at 9" Displacement (3.26% Drift)

FIGURE 6-46 Crack Propagation on the West Side of the West Column at 10" Displacement (3.62% Drift)

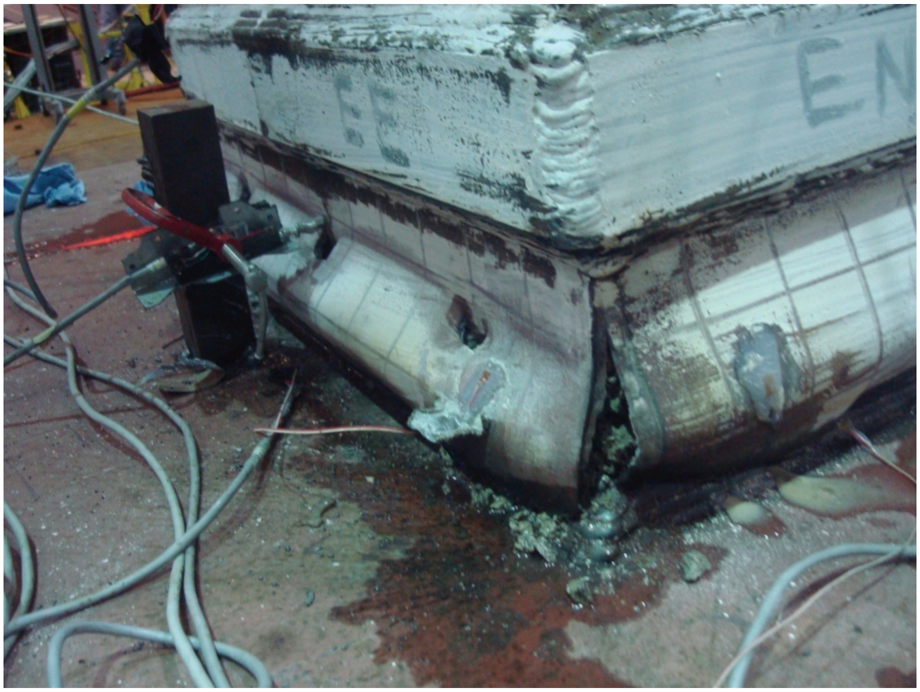

FIGURE 6-47 Damage at East Column at 10" Displacement (3.62% Drift)

FIGURE 6-48 Damage at West Column at 12" Displacement (4.35% Drift)

FIGURE 6-49 Concrete Spalling from the West Column at 12" Displacement (4.35% Drift)

FIGURE 6-50 Concrete Condition of West Column

FIGURE 6-51 Concrete Condition of East Column

SECTION 7

ANALYTICAL INVESTIGATION AND COMPARISON WITH EXPERIMENTAL RESULTS

7.1 General

This section describes the analytical investigation conducted to replicate the experimental results presented in section 6. First, an investigation was done to figure out why yielding occurred at greater displacements than originally expected (as stated in section 6). Other finite element analyses were then conducted to replicate the full range of results obtained from the experiments. Finally all results are compared to highlight the difference in behavior between all tested specimens.

7.2 Specimen Stiffness Investigation

It was stated in section 6 that all the specimens were more flexible than expected. Three hypotheses that might explain the observed greater yield displacements of the links and the columns where investigated; first, the magnitude of the measured sliding at the base of the specimen was checked to see if a significant additional rigid body displacement was added to the specimen due to sliding, even though those magnitudes were apparently insignificant when checked in real-time during the tests. Figure 7-1 shows a plot of the base sliding vs. time for the north and south side of the specimen. Only a minor amount of sliding of about 1mm was observed (i.e. average between -0.2mm and 1.2mm) recorded by the instruments positioned on the North and South sides of the foundation), which is insignificant; thus, additional rigid body displacement could not explain the discrepancy between the expected and observed yielding displacements of the links and columns.

Second, possible occurrence of base overturning was investigated; plots showing uplifting of the base corners are shown in figures 7-2 and 7-3. The maximum uplift displacement observed was 1.8mm which translates to a rotation angle of 8.5E-4 rad, and correspondingly, into about a 7mm top displacement due to rigid body rotation, which is a significant displacement with respect to the small displacements applied at the beginning of the test.

Third, since deformations at the top of the specimens were measured directly by the displacement transducers of the actuators (assuming a rigid reaction wall in the original instrumentation scheme), an investigation was conducted to assess the flexibility of the reaction wall under the applied loads to see if it experienced any significant elastic deformations, as a significant amount of force (about 1000kN) was applied to it at a height of 25ft from the base. Linear elastic finite element analysis was performed using ABAQUS by modeling the reaction wall, and applying a force equal to the maximum capacity of the actuators (1777kN) at a height of 25ft. An elastic analysis was conducted, and S4R solid elements were used for the analysis. Figure 7-4 shows the model used for the analysis. The deflected shape is shown in figure 7-5, and the displacement corresponding to the maximum force applied was calculated and shown in figure 7-6. It can be seen that at about 1000kN force, a horizontal displacement of 6mm is observed in the wall. This displacement, added to the 7mm contributed by the rigid body rotation described earlier, totals 13mm of additional displacement when a load of 1000kN was applied, which occurred during the final cycle of testing at a top displacement magnitude of 175mm, which is about 7.5% more than anticipated.

In addition to the above correction, note that some modeling issues that occurred in the preliminary finite element model used to predict specimen displacements during the test were discovered at a later stage after testing of the specimens. These are not reported here (as the solution was simply to fix the incorrect model), but this explains why yielding was observed to occur at a much larger displacement than originally anticipated for links. However, even with the modeling issues corrected, the above correction due to reaction wall flexibility was necessary to obtain correct analytical results.

Therefore, all results presented in this section take into account the above correction which is taken here as being linearly proportional to the load applied.

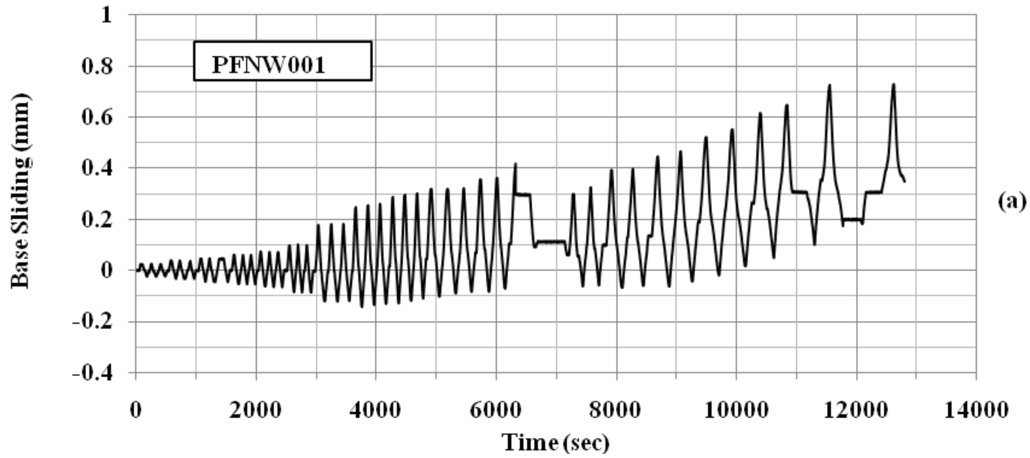

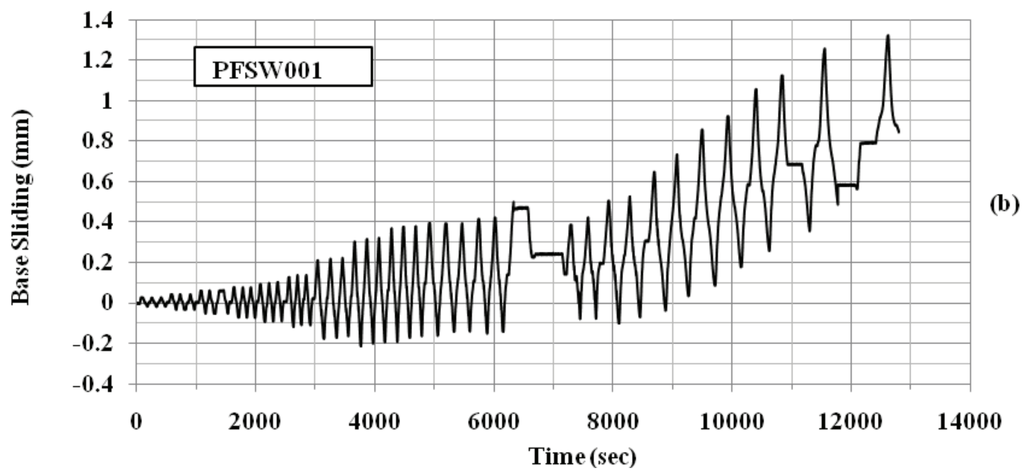

FIGURE 7-1 Base Sliding vs. Time; (a) North Side, (b) South Side

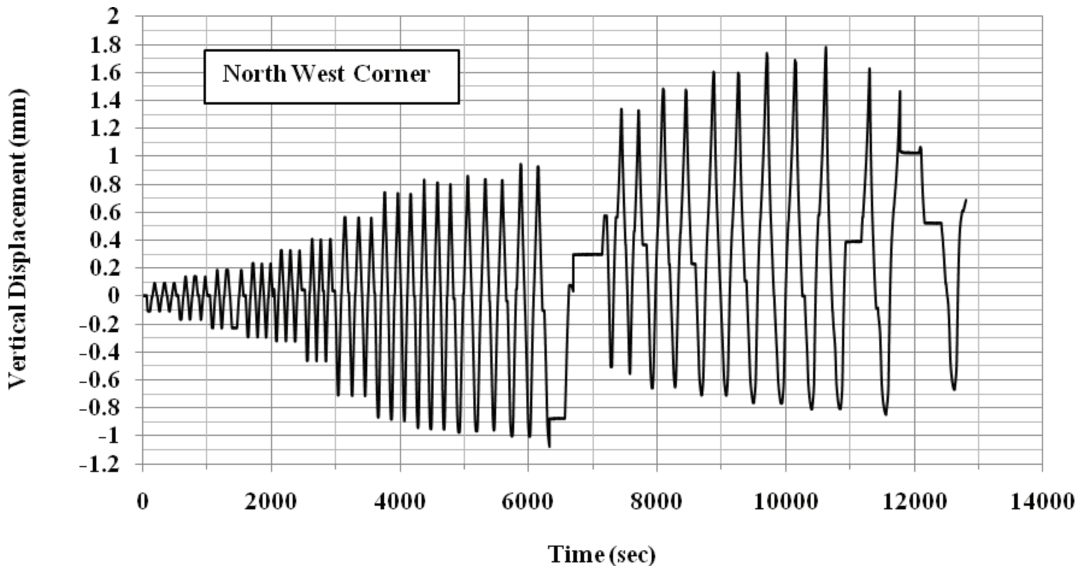

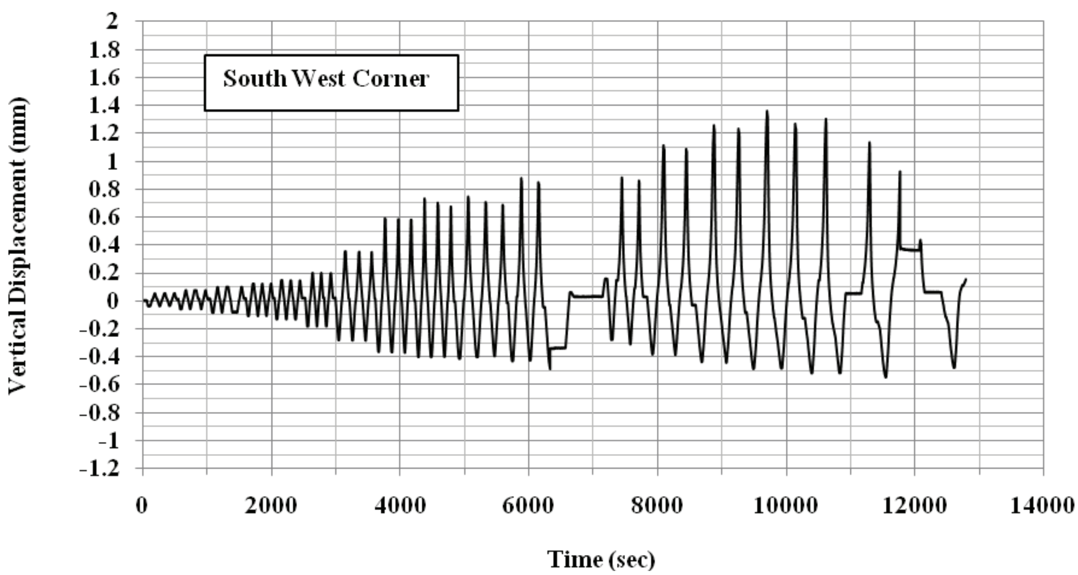

FIGURE 7-2 West Side Uplift

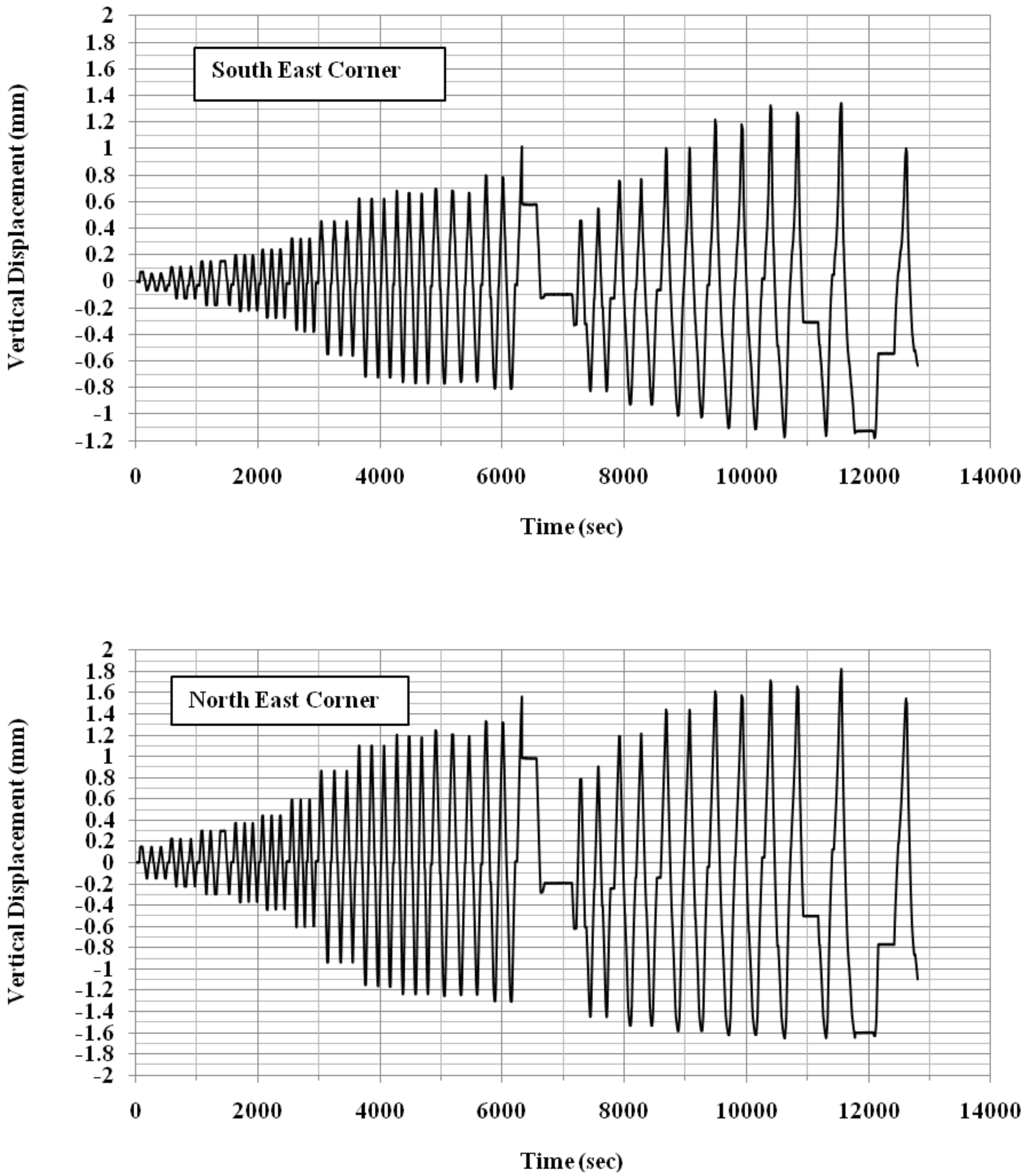

FIGURE 7-3 East Side Uplift

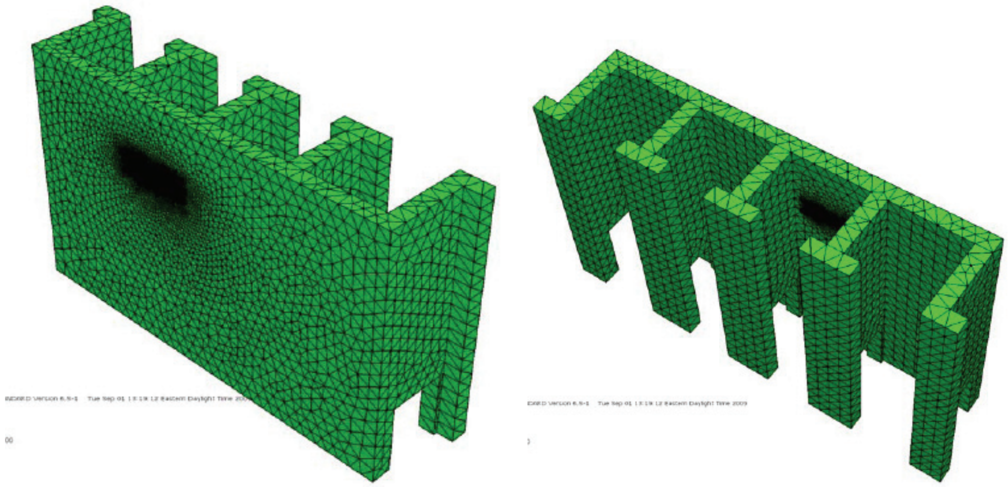

FIGURE 7-4 Reaction Wall Model

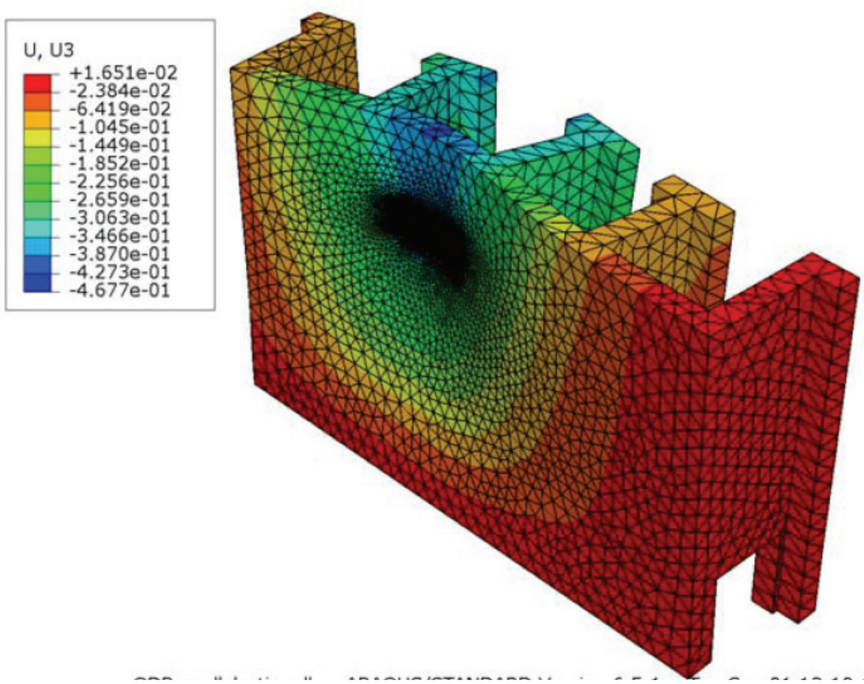

FIGURE 7-5 Horizontal Displacement at 25ft height

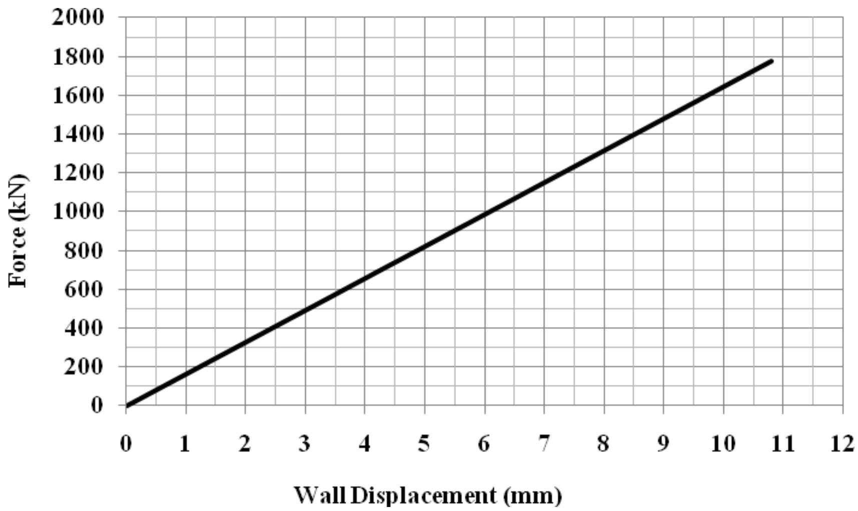

FIGURE 7-6 Wall Displacement vs. Applied Force

7.3 Specimen S2-2 Model

In this section, a finite element model was developed to replicate the observed experimental behavior of the specimen S2-2 using ABAQUS/Explicit. The structural fuses replicating elements were then added in sections 7.4 and 7.5 to replicate specimen S-1, and specimen S2-1. Dimensions of the specimens studied in this section match the dimensions of the specimens used in the experiments described in the previous sections. For each specimen, pushover and cyclic analyses were performed to replicate the experimental results discussed earlier.

7.3.1 Finite Element Description

7.3.1.1 Geometry Modeling and Meshing Algorithm

Geometry modeling of the bare frame started using the *Part Module* by defining the columns as a surface (to be filled later with 3D deformable shell elements) constructed by having a box shape of dimensions 600x400mm extruded to the total specimen height of 6900mm. The concrete inside the columns (to be filled later using 3D deformable solid elements) was also created from dimensions of 600x400mm, and extruded to a height of 6900mm. The cap beam was then generated into three parts using 3D rigid solid of dimensions 1250x600x600mm. Three dimension deformable wire elements were used to model the Bi-Steel shear studs embedded in the columns, and spaced at 200mm in both directions.

Using the *Assembly Module* tools, the parts were then positioned, relative to each other in a global coordinate system, to create the final assembly (note that some parts were used more than once). At this point, the parts are not yet connected to each other, even though one part may be located adjacent to other parts.

The *Interaction Module* tools were used to connect the parts in the model. The *Tie Constraints* option, which allows effectively merging the interface nodes, was used to tie the cap parts to the columns. *Tie Constrains* was also used to tie the shear studs to the columns. The *Tie Constraints* were assumed to replicate the welds present in the specimen instead of introducing weld constrain conditions in ABAQUS, as using the *Tie Constraints* option will decrease the time required to run the analyses taking into account that no weld failure was anticipated between the tied parts. However, the *Surface to Surface Contact* option was used between the columns and the infill concrete to replicate the contact condition between both surfaces and to allow normal separation from which buckling of the steel would be captured. A contact interaction property can define tangential behavior (friction and elastic slip) and normal behavior (hard, soft, or damped contact and separation). The tangential behavior was chosen using a friction model that defines the force resisting the relative tangential motion of the surfaces in a mechanical contact analysis. The *Penalty* option of ABAQUS was used; this option uses a stiffness (penalty) method that permits some relative motion of the surfaces (an "elastic slip") when they should be sticking. While the surfaces are sticking (i.e., $\tau < \tau_{critical}$), the magnitude of sliding is limited to this elastic slip. The coefficient of friction between steel and concrete was arbitrary taken as 0.35, as multiple analyses were conducted to investigate the sensitivity of changing this parameter; it was found out that no significant effect on the global behavior of the model was observed over a range of values that seemed reasonable, (ranging from 0.25 to 0.5) and the chosen value was selected for convenience. The behavior in the direction normal to the steel-concrete interface was defined using the *Hard Contact* pressure-overclosure relationship; the hard contact relationship minimizes the penetration of the slave surface into the master surface at the constraint locations and does not allow the transfer of tensile stress across the interface. When surfaces are in contact, any contact pressure can be transmitted between them. The surfaces separate if the contact pressure reduces to zero. Separated surfaces come into contact when the clearance between them reduces to zero.

7.3.1.2 Element Definitions

S4R shell elements were used for the steel columns; this is a four node doubly curved general-purpose conventional shell element with reduced integration and hourglass control. Reduced integration together with hourglass control can provide more accurate results, as long as the provided elements are not distorted (i.e., that they remain relatively close to being square in shape), and significantly reduce running time especially for three dimension analysis.

The S4R shell element basically has the same behavior as the S4 shell element; the difference between the two being the number of integration points. The S4R shell element has only one integration point (in the middle of the element) compared to four integration points for the S4 shell element. Later in this section, a comparison study is done to compare the results obtained by the two different element definitions.

C3D8R brick elements were used for the infill concrete and the cap; this is an eight node linear brick element with reduced integration (1 integration point) and hourglass control, having the same benefits mentioned above compared to the C3D8 brick element.

7.3.1.3 Material Definitions

The material nonlinearity was defined using the nonlinear combined kinematic/isotropic hardening plasticity model available in ABAQUS. The Von Misses yield criteria was chosen to define the plastic behavior of the link, which is suitable for ductile materials such as steel. Poisson's ratio was assumed to be equal to 0.3 which is typical for structural grade steel. For the analyses, the properties of the A572 Gr.50 steel that was used for the columns were taken from the coupon tests described earlier in section 5. From these properties, true stresses (Cauchy stresses) and logarithmic plastic strains where then calculated from the following equations.

$$\sigma_{true} = \sigma_{nom}(1+\varepsilon_{nom}) \tag{7-1}$$

$$\varepsilon_{\ln}^{pl} = Ln(1+\varepsilon_{nom}) - \frac{\sigma_{true}}{E} \tag{7-2}$$

A *Concrete Damaged Plasticity* model in ABAQUS was used to simulate the behavior of concrete infill. This model is based on the models proposed by Lubliner et al. (1989) and by Lee and Fenves (1998). The model defined in ABAQUS is a continuum plasticity-based damage concrete model that assumes two main failure mechanisms; namely tensile cracking and compressive crushing of the concrete material, and for which the uniaxial tensile and compressive response of concrete is characterized by damaged plasticity.

Figure 7-7 shows the stress-strain curve for the concrete damaged plasticity model used in the analyses, and a brief explanation of some of the key parameters that define this model follows.

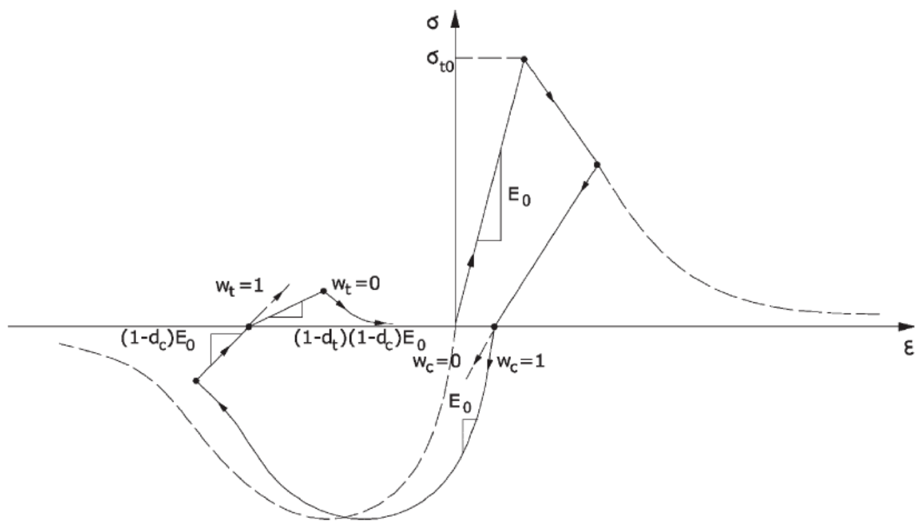

FIGURE 7-7 Stress-Strain Curve for Concrete Damaged Plasticity Model (ABAQUS Manual)

As defined in the ABAQUS manual, under uniaxial tension, the stress-strain response follows a linear elastic relationship up to a point where tensile failure occurs at a stress equal to σ_{to} at which micro-cracking starts to develop in concrete. Beyond this failure stress, the formation of micro-cracks is represented macroscopically with a softening stress-strain response.

On the other hand, under uniaxial compression the response is linear until the value of the initial yield stress, σ_{co}, and then the response is characterized by stress hardening in the plastic regime followed by strain softening beyond the ultimate stress, σ_{cu}. When the concrete is unloaded from any point on the strain softening branch of the stress-strain curves, the unloading response is weakened and the elastic stiffness of the material is degraded due to damage. The degradation of the elastic stiffness is characterized by two variables, namely d_t and d_c, these values are functions of the plastic strains and computed by the model and must be less than or equal to one and greater than or equal to zero, as they represent the percentage of damage in the cross section due to cracking in tension and crushing in compression respectively.

Under cyclic loading conditions the degradation mechanisms involves the opening and closing of previously formed micro-cracks and their interaction. The stiffness recovery effect, namely some recovery of the elastic stiffness as the load changes sign in cyclic test, is considered. The weight factors, w_t and w_c, (which are assumed to be material properties) control the recovery of the tensile and compressive stiffness upon load reversal. w_c, which results in the recovery of the compressive stiffness, is more important because when the load changes from tension to compression, tensile cracks will close. Default values of w_t and w_c proposed by the ABAQUS manual were chosen for the analysis, namely w_t=0, w_c=1. The effect of changing these values is illustrated in figure 7-7.

For the tension stiffening effect, *Concrete Tension Stiffening* (*Type=Strain*) option of ABAQUS was used. The tensile failure stress, σ_{to}, was assumed to be equal to 1/10 times of the compression yield stress, σ_{co}, and the reduction of concrete tensile strength to zero was assumed to occur at 10 times the compression strain at which failure occurs. Results from cylinder tests done for the concrete used in the experimental testing described earlier in section 5 were used to define the compression stress-strain curve of concrete that was used in the analyses. Note that this model does not account for possible increase in concrete compressive strength due to confinement, and allow for a limited range of plastic strains before progressive loss of compression strength. These were deemed to be reasonable assumptions given the scope of the current research.

7.3.1.4 Boundary Conditions and Loading

Using the *Load Module*, boundary conditions were specified by restraining all the nodes at the base of the columns, replicating a fixed end condition. Using the *Amplitude* option, two types of loading conditions were defined and applied to a reference point located on one edge of the rigid cap. The first was a monotonic pushover displacement, and the second was a cyclic displacement protocol replicating the one used for the bare frame in section 5.

7.3.1.5 Meshing Algorithm and Sensitivity

Meshes were generated on the merged model using the *Mesh Module* after "seeding" every edge by specifying the number of elements desired along that edge (*Edge by Number* rule). The models were meshed entirely using quadrilateral elements. The bare frame members were meshed using the *Structured Meshing Technique*. As stated in the ABAQUS manual "This technique is most appropriate for simple regions that have no holes, isolated edges, or isolated vertices like the columns."

Preliminary models where constructed using several mesh refinements to examine the convergence of the model to chose a final mesh refinement and element type that could fairly represent the behavior of the bare frame with reasonable machine running time. First a mesh was chosen with element edge length of approximately (150mm) for the steel columns and concrete infill, and denoted as Mesh (a). Another mesh was developed with element edge length of approximately (50mm) and denoted as Mesh (b). Both meshes are shown in figure 7-8.

Base shear versus top displacement results for the monotonic loading for both meshes are plotted in figure 7-9. It was observed that both meshes give exactly the same results.

In spite of the fact that local buckling was not observed in the pushover curve, Mesh (b) was chosen to represent the bare frame cyclic behavior, as it showed satisfactory performance in absence of buckling (i.e. adequate for the structural fuse concept investigated here). Also, although an accurate representation of the development of column local buckling was not the primary focus of this study, it was anticipated that the chosen mesh would allow capturing to some extent the columns local buckling that was expected to develop after yielding of the bare frame after 100mm top displacement. V_{yf} , Δ_{yf} , and K_f were calculated at the point where initiation of steel yielding started to occur in the finite element model, these values were found to be equal to 740kN, 100mm, and 7.4kN/mm respectively. Note that the initial softening in the push-over curve prior to those values is due to tension cracking of the concrete (modeled as a progressive tension strength loss by the concrete damaged plasticity material type described earlier).

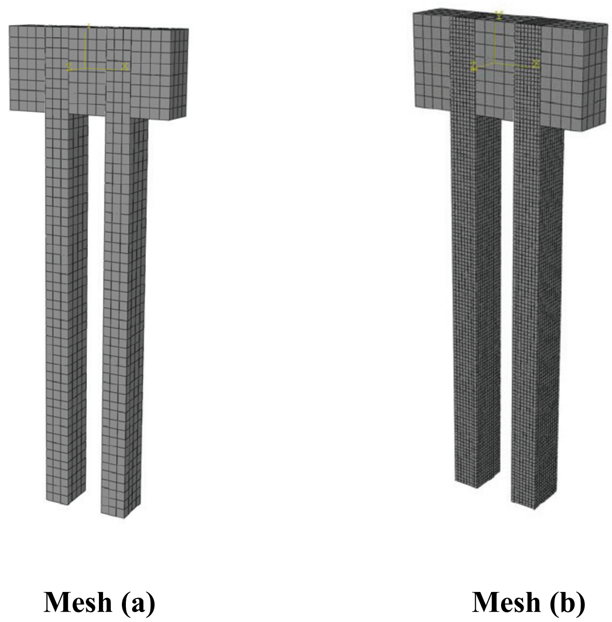

FIGURE 7-8 ABAQUS Models for Specimen S2-2

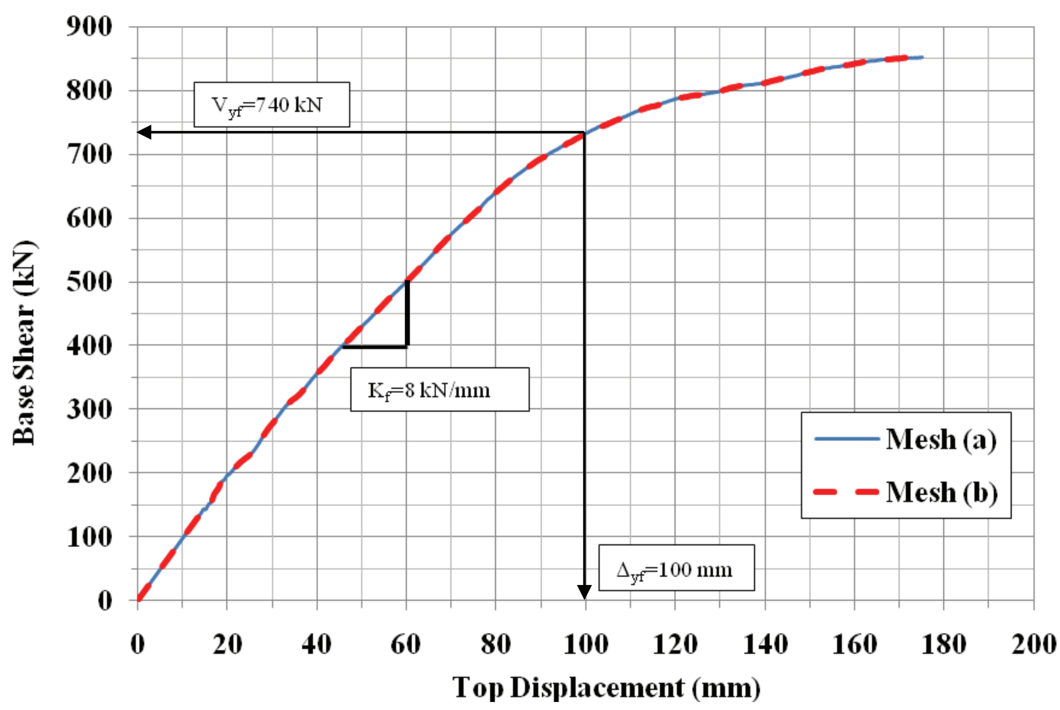

FIGURE 7-9 Pushover Comparison for Meshes (a) and (b)

7.3.2 Comparison with Experimental Results

Figure 7-10 shows a comparison between the experimental data, the ABAQUS cyclic analysis, and the ABAQUS pushover analysis. It can be seen that both the experimental and analytical cyclic data match well, as the entire peak base shear values were captured along with the strength and stiffness degradation of the specimen that occurred due to the local buckling of the columns. Only the last cycle did not match exactly the experimental data; this is due to the fracture that occurred in one of the columns as described in section 6, as the ABAQUS model considered here does not take into account fracture failure (no such damage modeling was attempted in the analysis).

It can also be seen that the pushover analysis gives slightly higher results than that of the cyclic analysis; this is attributed to the fact that the local buckling in the composite columns does not develop as easily during a pushover analysis because the faces of the composite box columns that are subjected to monotonic tension only stretch,(i.e. they are not subjected to the reversed loading under which these longer members would be easier to buckle), and the faces in compression can only develop local buckling if crushing starts to develop in the concrete infill. Under cyclic loading condition, local buckling can develop in both faces due to the fact that the stretched steel plates becomes longer and thus easier to buckle when compressed after being stretched (even if concrete was infinitely rigid and strong in compression). Figure 7-11 shows Von Misses contour results for the pushover analysis of specimen S2-2 up to a top displacement of 175mm (2.5% drift), it can be seen that only minor local buckling is observed at the compression sides, which again explains the reason for having higher base shear values that anticipated for the pushover analysis.

Figure 7-12 shows a comparison between the ABAQUS Cyclic Analysis and Experimental Cyclic Data for the East Column at 150mm Top Displacement (2.17% Drift). It can be seen that the ABAQUS model captured the local buckling in the columns that was observed during testing.

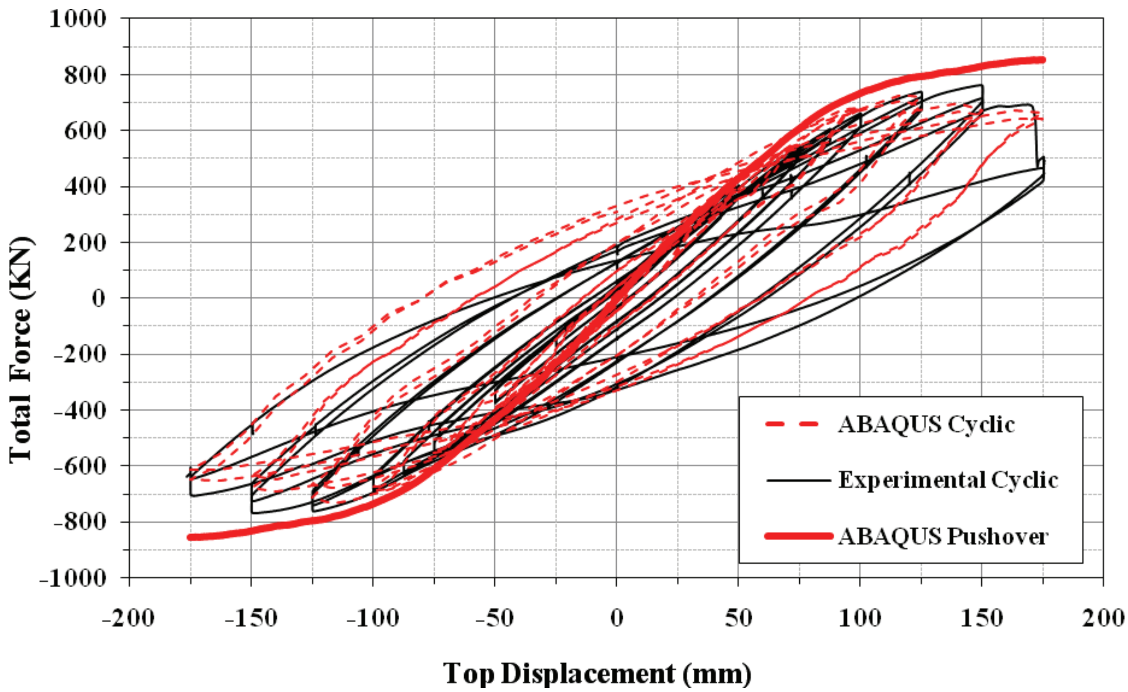

FIGURE 7-10 Comparison between Experimental and Analytical Results for Specimen S2-2

Figure 7-13 shows a comparison between the locations of local buckling observed at the west column after the test was terminated and the columns has been flamed cut, and the local buckling captured by finite element analysis. Concrete has been removed from the results shown in figure 7-13(a), as well as all the steel above the location where local buckling was observed to better show the other faces, and the bars inside. The similarity between both results can be seen: buckling at the east side of the column is located between two rows of shear studs in both cases, and buckling developing on both the south face of the column as well as at its north-east corner can be seen.

Figure 7-14 shows a comparison between the Experimental data obtained for the deflected shape of the columns versus the ABAQUS analytical results. The experimental data was obtained using the 5 string potentiometers located at 1000mm, 2700mm, 3900mm, 5300mm, and 6700mm respectively from the top of the foundation. It can be seen that the analytical and experimental results match well. A double curvature behavior with an inflection point at about 1/3 height from the base is observed; indicating that the two twin columns behaves as a frame with bending moments developing more at the bottom than the top of the columns.

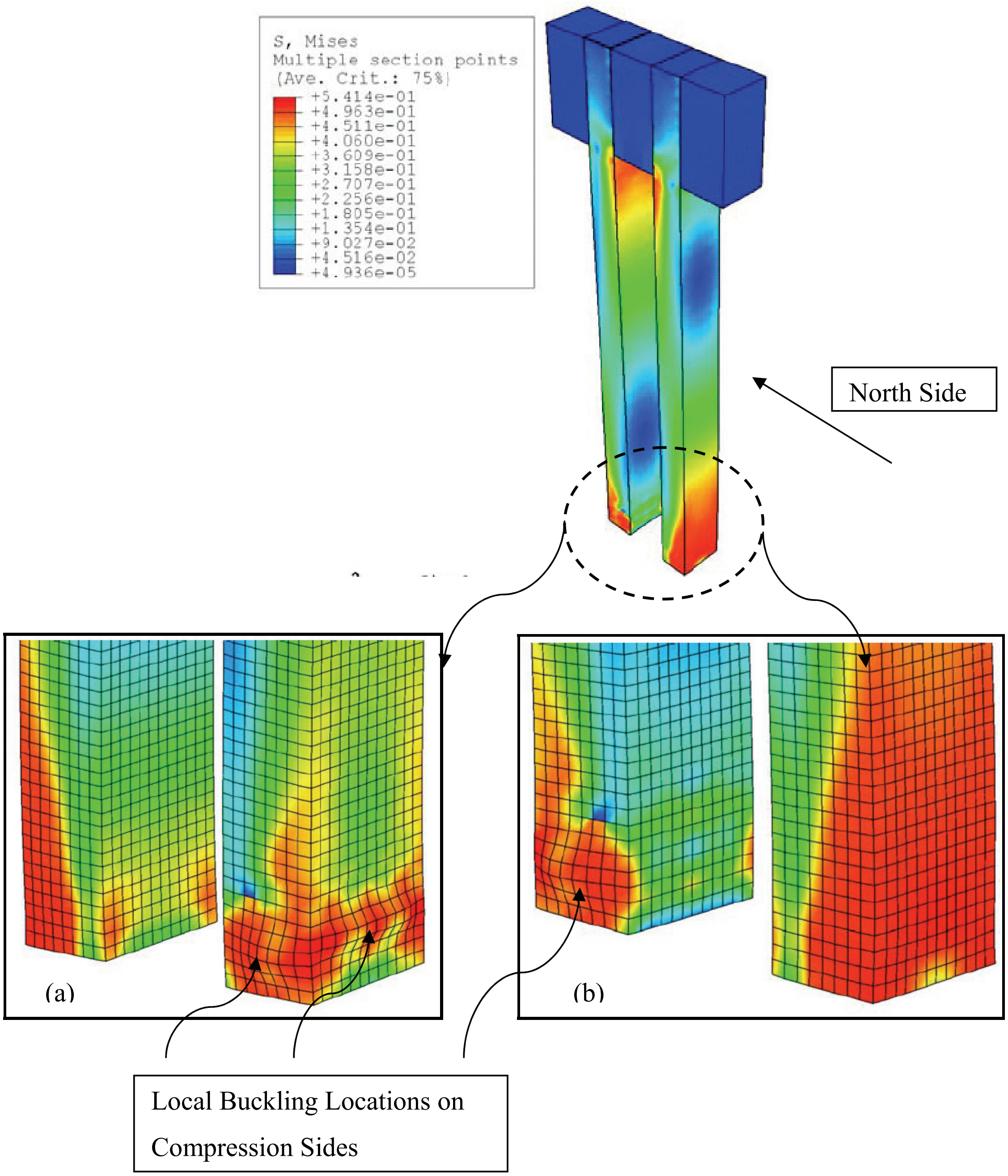

FIGURE 7-11 Von Misses Contours Results for Pushover Analysis of Specimen S2-2 at 175mm Top Displacement (2.5% Drift); (a) South Side, (b) North Side

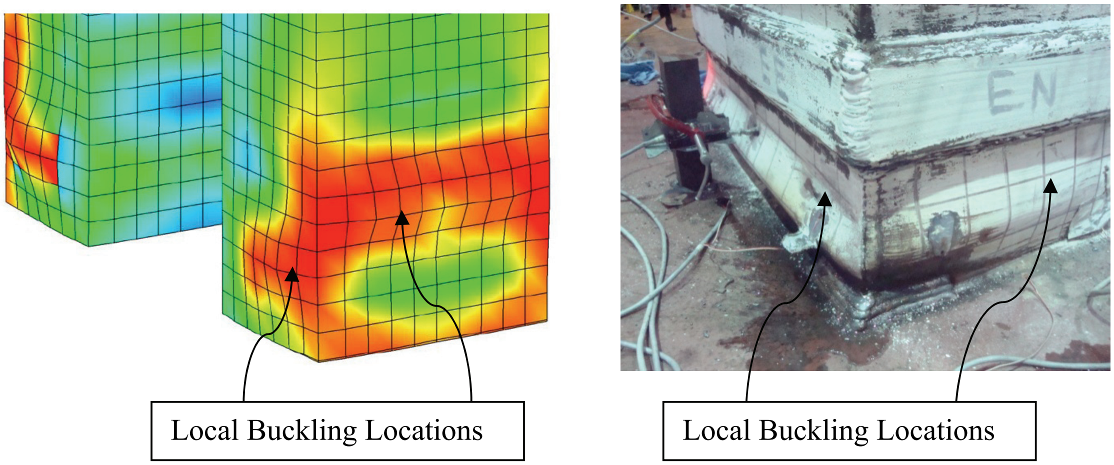

FIGURE 7-12 Comparison between the ABAQUS Cyclic Analysis and Experimental Cyclic Data for the East Column at 150mm Top Displacement (2.17% Drift)

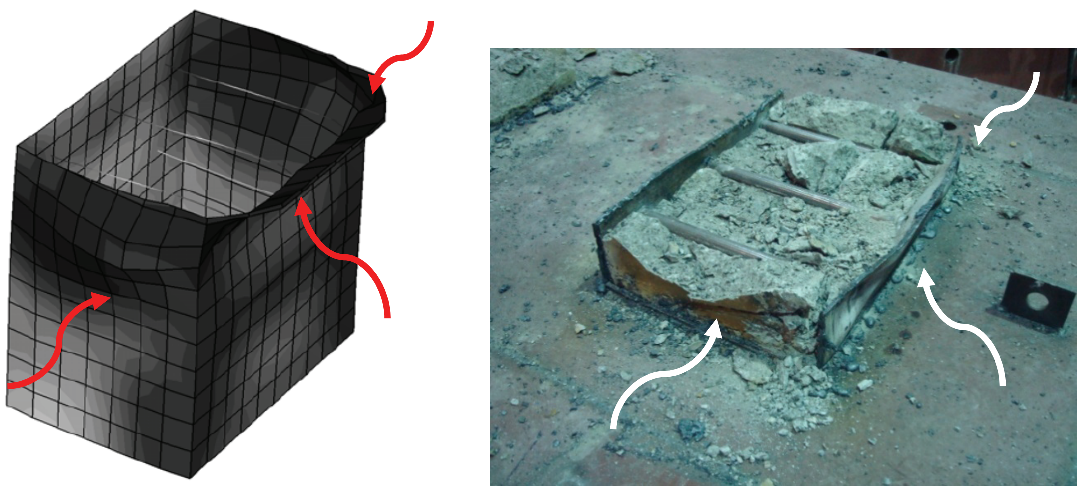

(a) (b)

FIGURE 7-13 Local Buckling of West Column at End of Test

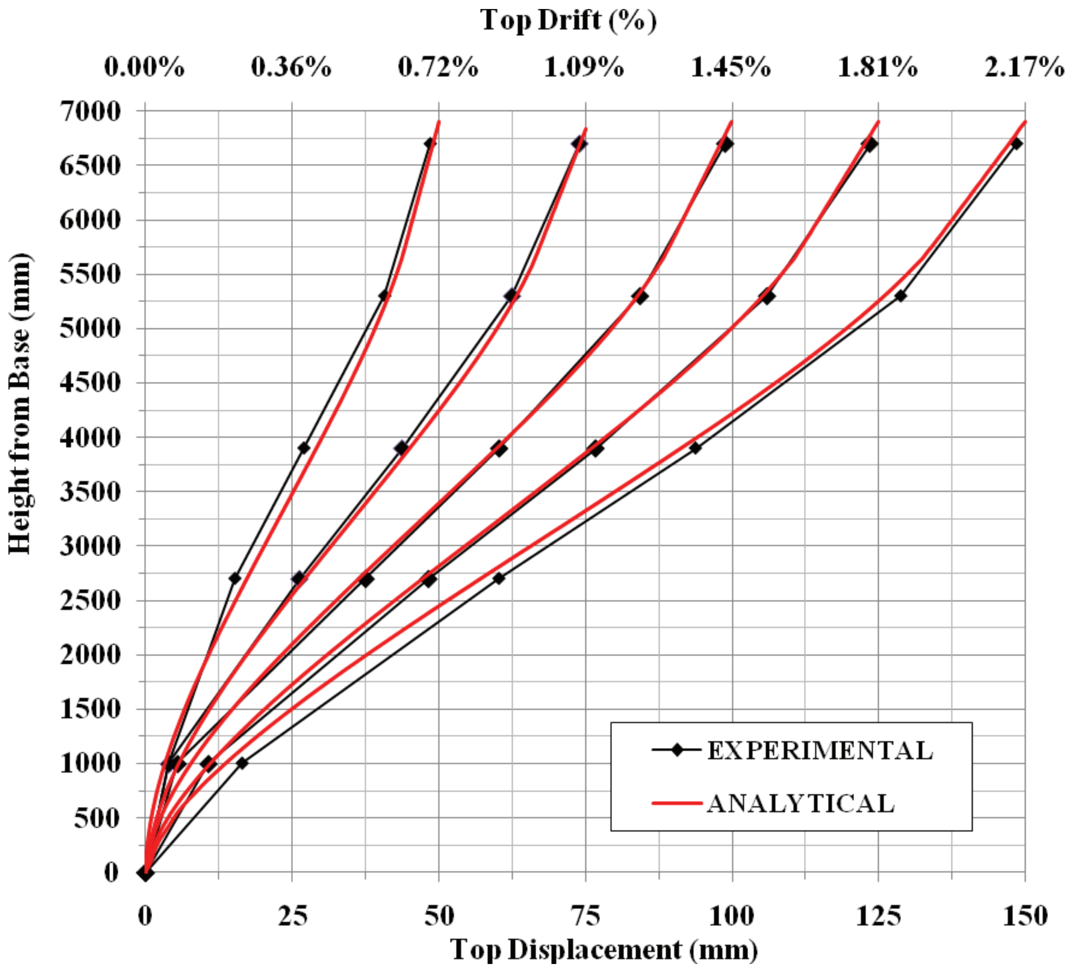

FIGURE 7-14 Comparison between the Deflected Shape of Columns at Various Drift Levels for Specimen S2-2

As stated in section 5.10.1, eight strain gages were installed at the top and bottom of each column (two per face) to monitor the moments and axial forces at these critical points for a total of 32 strain gages. Average strain values for the two strain gages installed on each face were calculated, and the corresponding results are presented through the rest of this section. Average strain values obtained from strain gages for both columns at top and bottom are shown in figures 7-15 and 7-16. It is observed that the bottom of the columns started to yield before the top. Also local buckling can be inferred by the sudden increase of strain readings in the bottom of both columns. All of the readings from the strain gages at the top of the columns were elastic except the west side of the top east column, which experienced sudden increase in strain readings. As no signs of local buckling was observed at the top of the columns during testing, this sudden increase could be attributed to a malfunction in one of the strain gauges that were installed at the west side of the top east column.

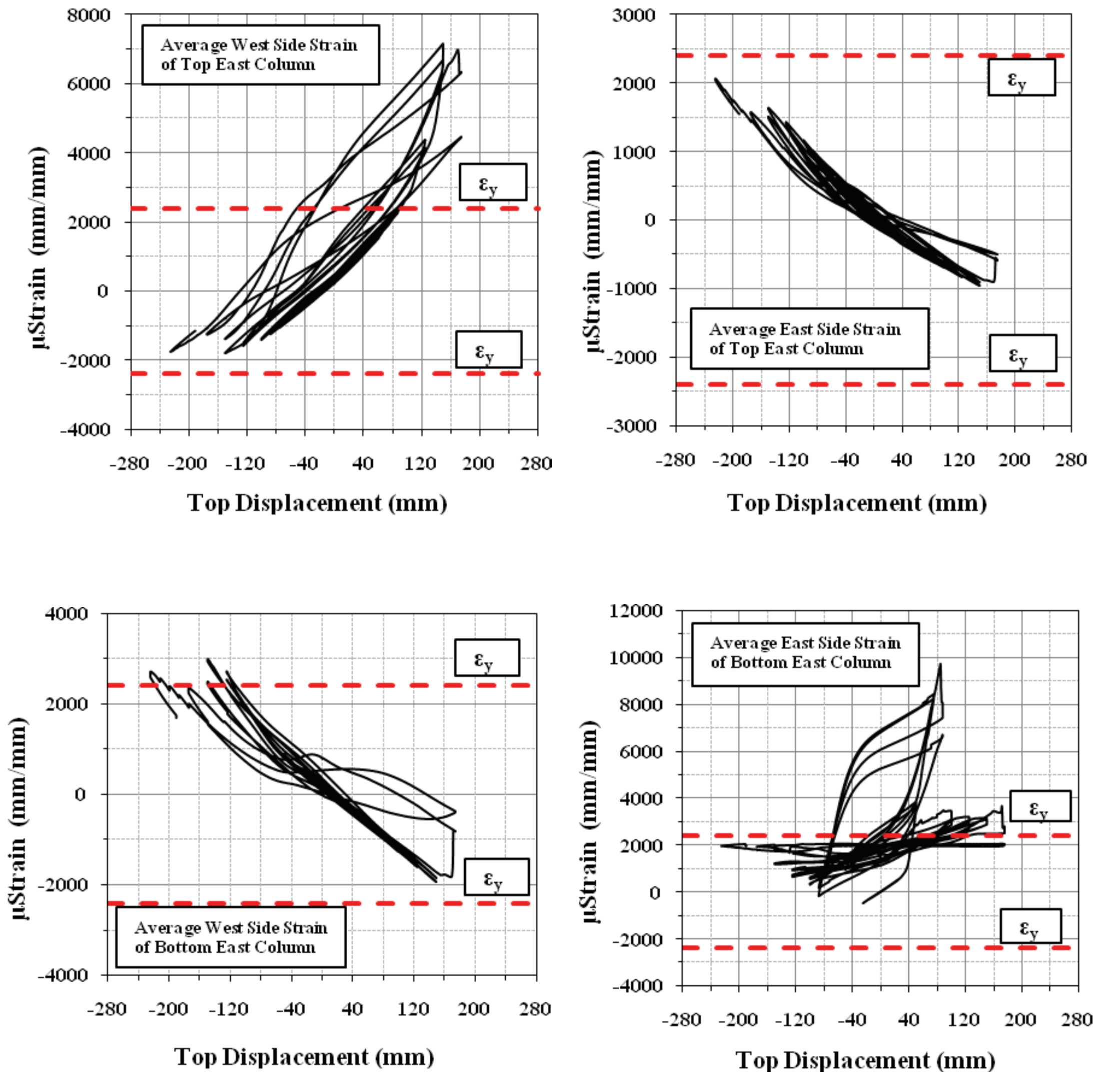

FIGURE 7-15 Average Strain Values for Top and Bottom of the East Column from Strain Gages (different vertical axis scales used)

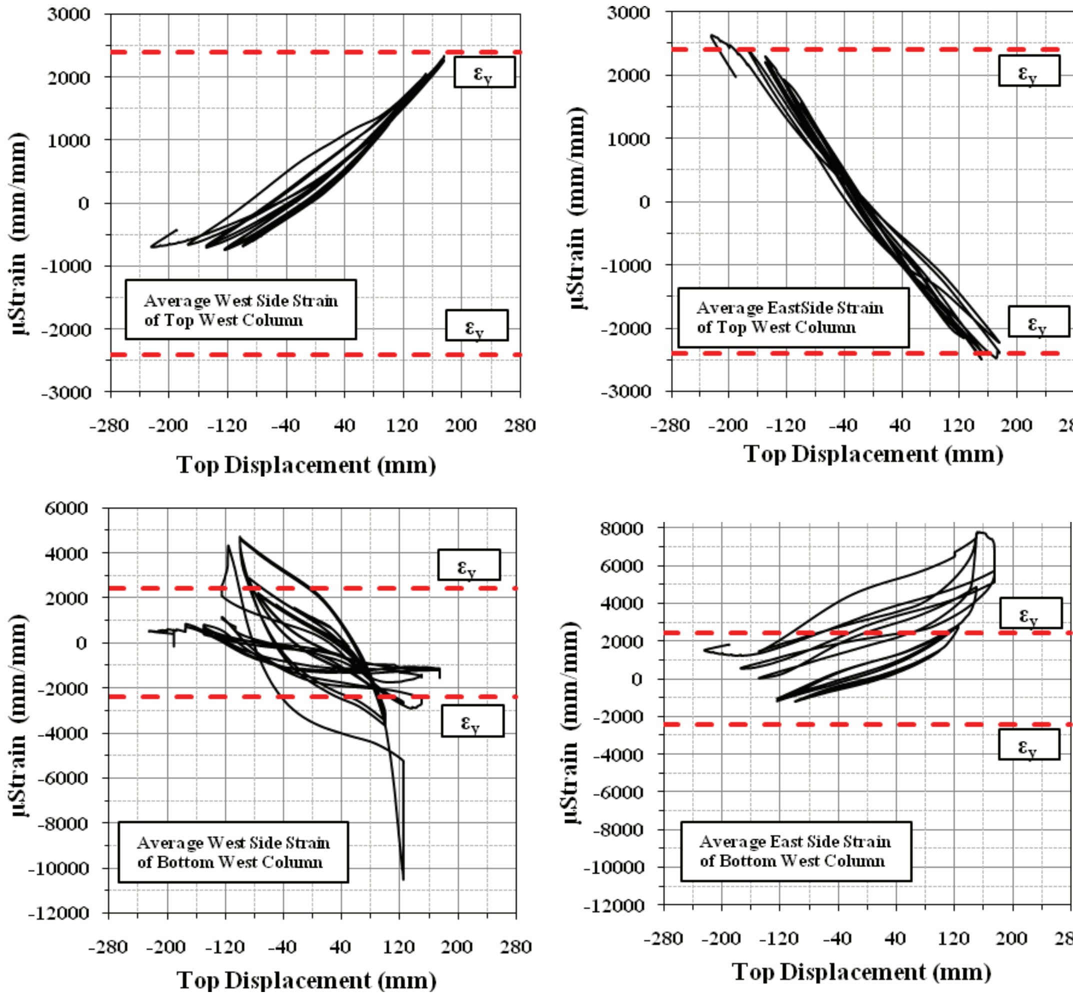

FIGURE 7-16 Average Strain Values for Top and Bottom of the West Column from Strain Gages (different vertical axis scales used)

The first yielding points were located at the East side of the bottom East column, and at the West side of the bottom West column, at 75mm top displacement. Average strain gage readings were transformed into stresses by multiplying them by the steel elastic modulus (as all the strains where elastic up to this point), then compared to average stress readings (S_{11}) from the ABAQUS model (at the same location of the strain gages) as shown in table 7-1.

TABLE 7-1 Stresses Comparison between FEM and Experimental at 75mm Top Displacement

	Bottom				Top			
	East Column		West Column		East Column		West Column	
	East Side	West Side	East Side	West Side	East Side	West Side	East Side	West Side
Exp.	+0.48	-0.2	+0.2	-0.48	-0.1	+0.38	-0.35	+0.13
FEM	+0.49	-0.25	+0.25	-0.50	-0.1	+0.42	-0.41	+0.12

7.4 Specimen S1 Model

7.4.1 Finite Element Description

7.4.1.1 Geometry Modeling

The same bare frame model used for specimen S2-2 was used here for specimen S1, and augmented by the addition of the SPSLs as structural fuses. For specimen S1, two ABAQUS models where conducted: A first one to represent the experiments performed for the SPSLs without lateral restraints (Test 2 and Test 3 as described in section 6), and a second model to represent the incomplete testing performed on the SPSLs with the presence of the lateral restraints (Test 1 as described in section 6).

For both models, the *Part Module* was used to define two 3D deformable planar shell parts; one is the yielding portion of the SPSL with thickness equal to 5mm (3/16"), and the other is the connection part of the SPSL which contains the bolt holes with thickness equal to 8mm (5/16") and required to remain elastic during the analysis.

Using the *Assembly Module* the SPSL parts were then positioned relative to each other in a global coordinate system. After that the *Interaction Module* was used to connect the parts using the *Tie Constrain* option that allows the merging of the interface nodes. Again the *Tie Constrain* was used to merge the edges of the yielding portion of the SPSLs to the connection parts, then merging the connection parts to the steel columns. The only difference between the two models constructed for this specimen is that, in one case (i.e. for Test 1), the SPSLs are restrained from out- of- plane motion using the *Load Module* to impose a boundary condition of zero displacement in the out-of-plane direction. Figure 7-17 shows the ABAQUS model of specimen S1.

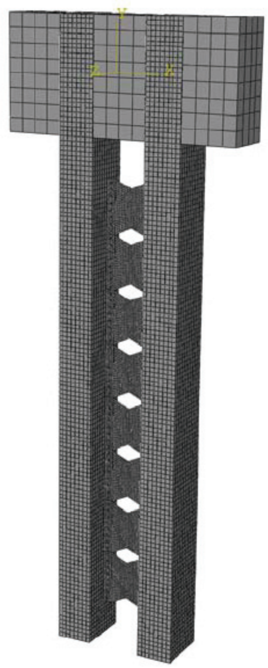

FIGURE 7-17 ABAQUS Model for Specimen S1

7.4.1.2 Material Definitions

Properties of the A572 Gr.50 steel used for the SPSLs were obtained from coupon tests described earlier in section 5, and true stresses (Cauchy stresses) and logarithmic plastic strains where then calculated using equations (7-1), and (7-2).

7.4.1.3 Meshing Algorithm and Sensitivity

Meshing was then generated using the *Mesh module*; seeding of the edges was done by specifying the number of seeds required for all the edges, and a structured mesh was then chosen.

Meshing sensitivity for the SPSLs was studied earlier in section 4.11.4.1 to examine the convergence of the results and to choose a final mesh refinement that could fairly represent the behavior of the SPSL with reasonable computational time. A SPSL mesh with approximate element lengths of 1" for the largest element used was retained to represent the SPSLs behaviors under investigation.

Note that meshing of the bare frame was chosen as mesh (b) for that particular analysis. Base shear versus top displacement results for the monotonic loading for the bare frame with SPSLs is plotted in figure 7-18.

It can be seen from figure 7-18 that the yield displacement of the SPSLs, Δ_{yb}, is equal to 32mm, and the yield strength at that displacement level, $V_{yb,}$ is equal to 510 kN. While the total yield strength of the system, Δ_{ytot} , is equal to 900 kN and calculated at 100mm displacement (i.e the yield displacement of the bare frame). A maximum ductility, μ_{max}, of 3.125 is achieved before yielding of the columns.

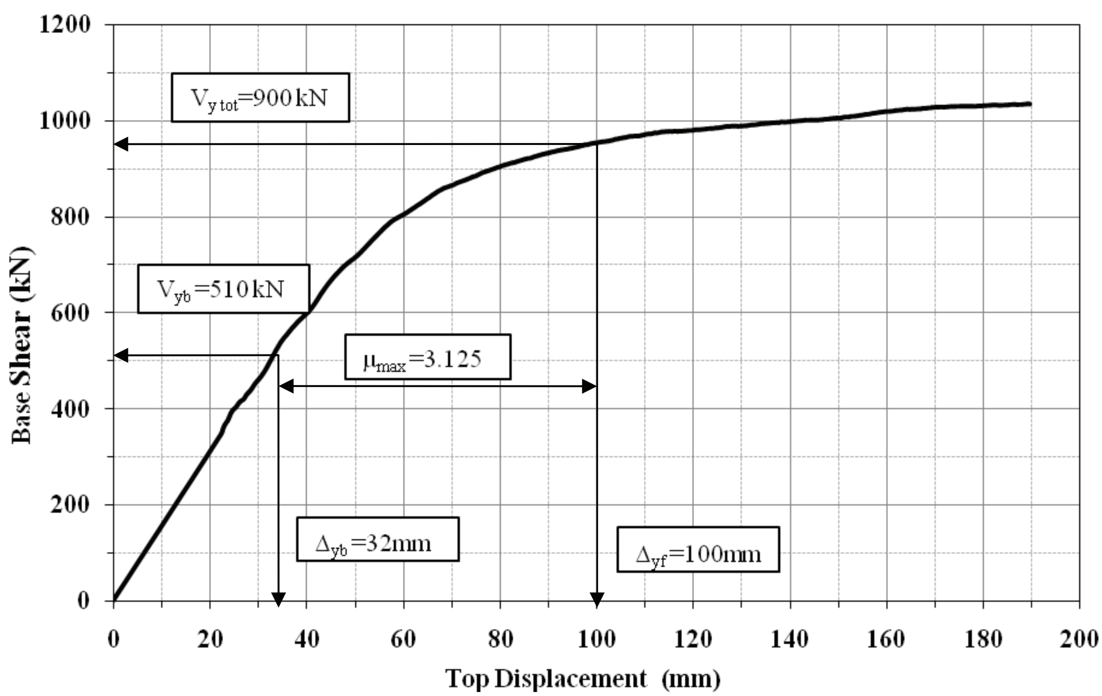

FIGURE 7-18 Pushover Curve for the Bare Frame with SPSLs Added

7.4.2 Comparison with Experimental Results (Test 2 & Test 3)

Figure 7-19 shows a comparison between the experimental data, the ABAQUS cyclic analysis, and the ABAQUS pushover analysis for the cases with laterally unrestrained SPSLs. It can be seen that both the experimental and analytical cyclic data match well, as the entire peak base shear values were captured along with the strength and stiffness degradation of the specimen that occurred due to the local buckling of the columns. Only the last cycle did not match exactly the experimental data due to the fracture that occurred in one of the columns as described in section 6.

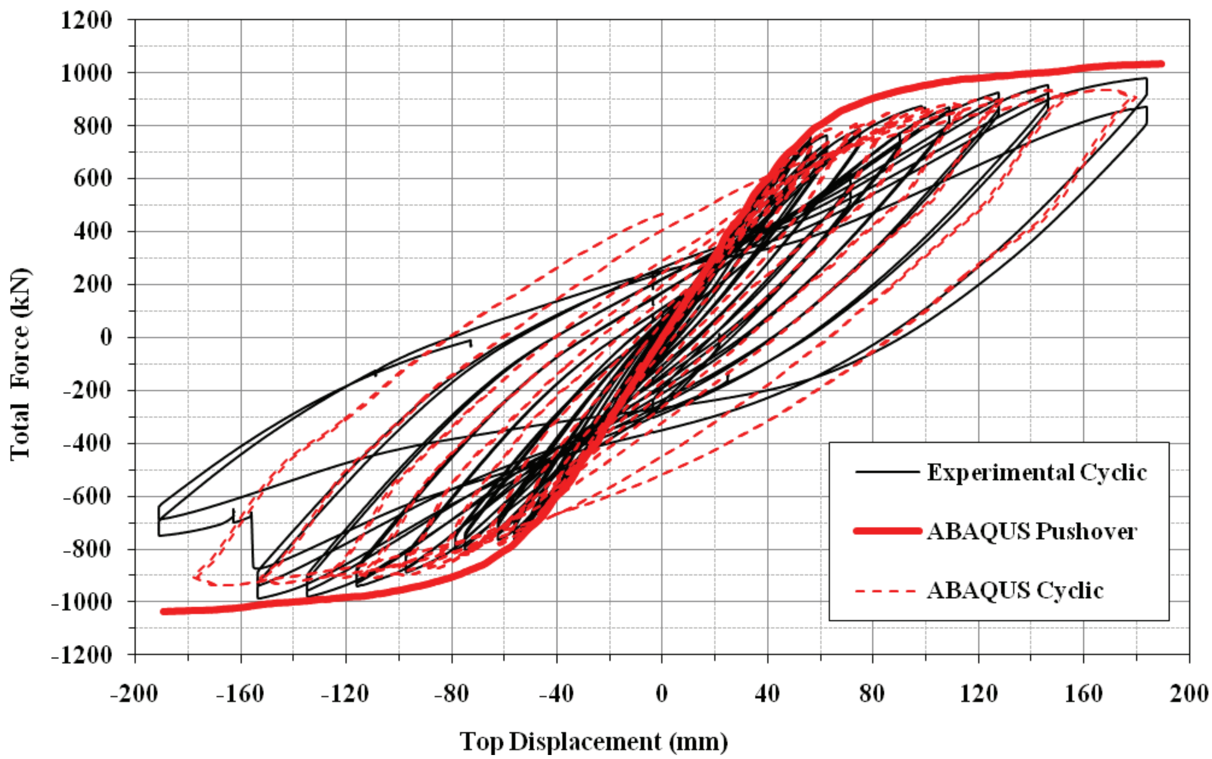

FIGURE 7-19 Comparison between Experimental and Analytical Results for Specimen S1 (Test 2 & Test 3)

Figure 7-20 shows a comparison between the experimental data obtained for the deflected shape of the columns versus the ABAQUS analytical results. As explained before, the experimental data was obtained using the 5 string potentiometers located at 1600mm, 3000mm, 4400mm, 5700mm, and 6800mm respectively from the top of the foundation. It can be seen that the analytical and experimental results match well. The columns behave differently before and after yielding of the SPSLs. Before the SPSLs yield, the entire pier consisting of the two columns and the links behave as one vertical cantilever member, with the columns being the flanges of that member, and the links being its web. Therefore a single curvature behavior is observed for the system up to the point where the SPSLs start to yield at 32mm (0.46% drift); thereafter the columns behave individually as two columns in a frame and a double curvature develops.

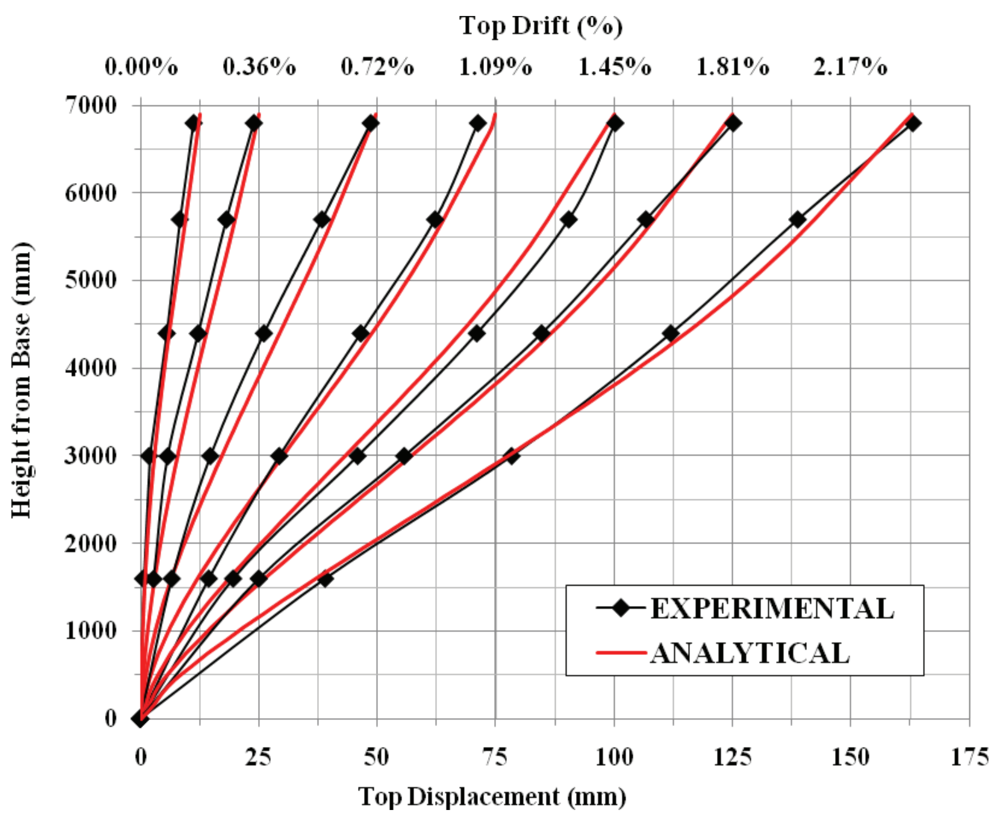

FIGURE 7-20 Comparison between the Deflected Shape of Columns at Various Drift Levels for Specimen S1

Figure 7-21 shows the average strain values for the bottom of both columns of specimen S1 up to 75mm top displacement (1% drift). In spite of the fact that testing continued until the columns failed, the average strains are reported here only up to the point where yielding started to occur in the columns (i.e. end of the structural fuse strategy). This is to illustrate that all the hysteretic behavior seen is only due to the contribution of the fuses while the columns are still elastic up to that point. It can be seen that the columns are still elastic at that level of drift and the observed hysteretic behavior of the total system is a result of the SPSLs yielding. Signs of yielding started to appear in the columns at the 100mm top displacement cycle (1.5% drift), i.e. beyond the range of displacements shown in figure.

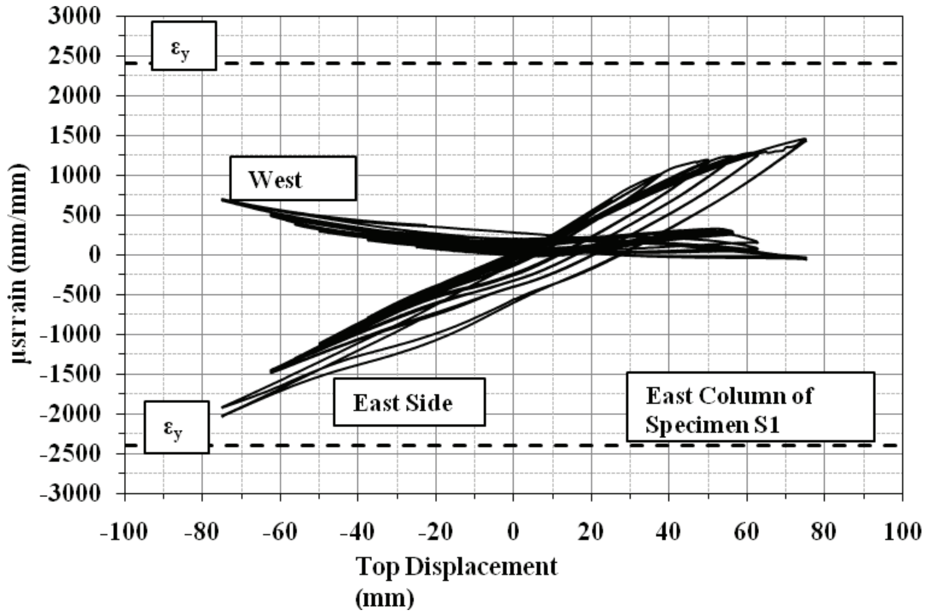

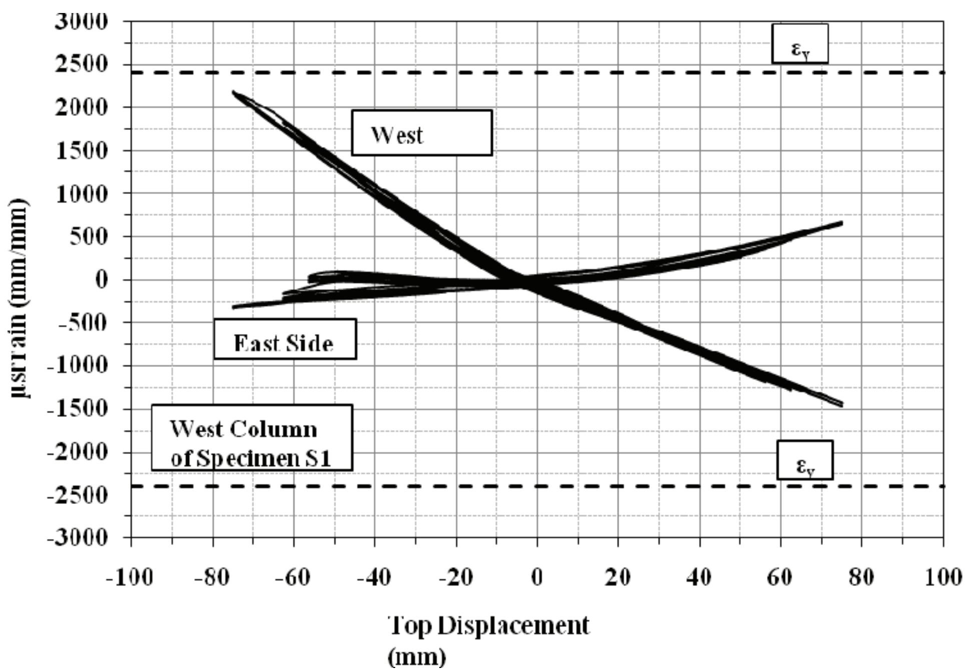

FIGURE 7-21 Average Strain Values for Bottom of the Columns from Strain Gages up to 75mm Top Displacement (1% Drift) for Specimen S2-1

Figure 7-22 shows the applied top displacement vs. time until the onset of column yielding at 6500 sec which was observed to develop at a 100mm top displacement based on strain gages readings. Figure 7-23 shows the link displacement vs. time for SPSL 5, 6, and 7 for the two diagonal string pots installed at the corners of each SPSL as described earlier in section 5.10.2. The time window selected for the plot is the same as for figure 7-22, i.e. from the beginning of the test until signs of yielding started to occur at the column base. It is seen from the figure that the SPSLs are oscillating around the zero elongation value and positive and negative elongation values are observed in the figure, due to the fact that the columns shear the SPSLs in both directions during the cyclic loading. After the point where the SPSLs yielding started to occur at 3000 sec (corresponding to a 32mm top displacement), residual elongations started to build up, shifting the plot form the zero elongation point. This behavior was further investigated using the finite element model. It was found out that before yielding of the SPSLs, the forces developed in the SPSLs are shear forces that translates into axial forces in the columns. While after the SPSLs yield, tension field action starts to develop in the links introducing both axial and transverse forces on the columns. These transverse forces tend to pull the columns closer to each other. The distance moved by the columns observed by the finite element simulation at the onset of column buckling was found out to be 5mm, which is almost the same residual negative elongation measured by the instruments at the end of the test as shown in figure 7-23.

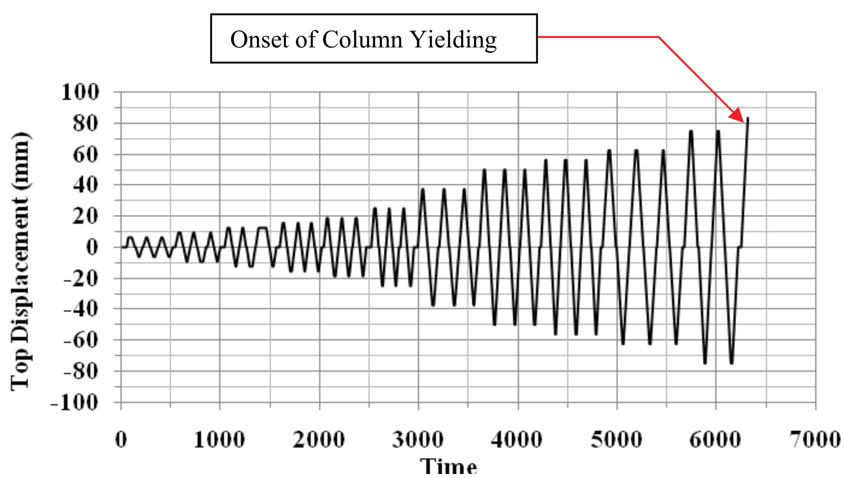

FIGURE 7-22 Applied Top Displacement vs. Time until the Onset of Column Yielding

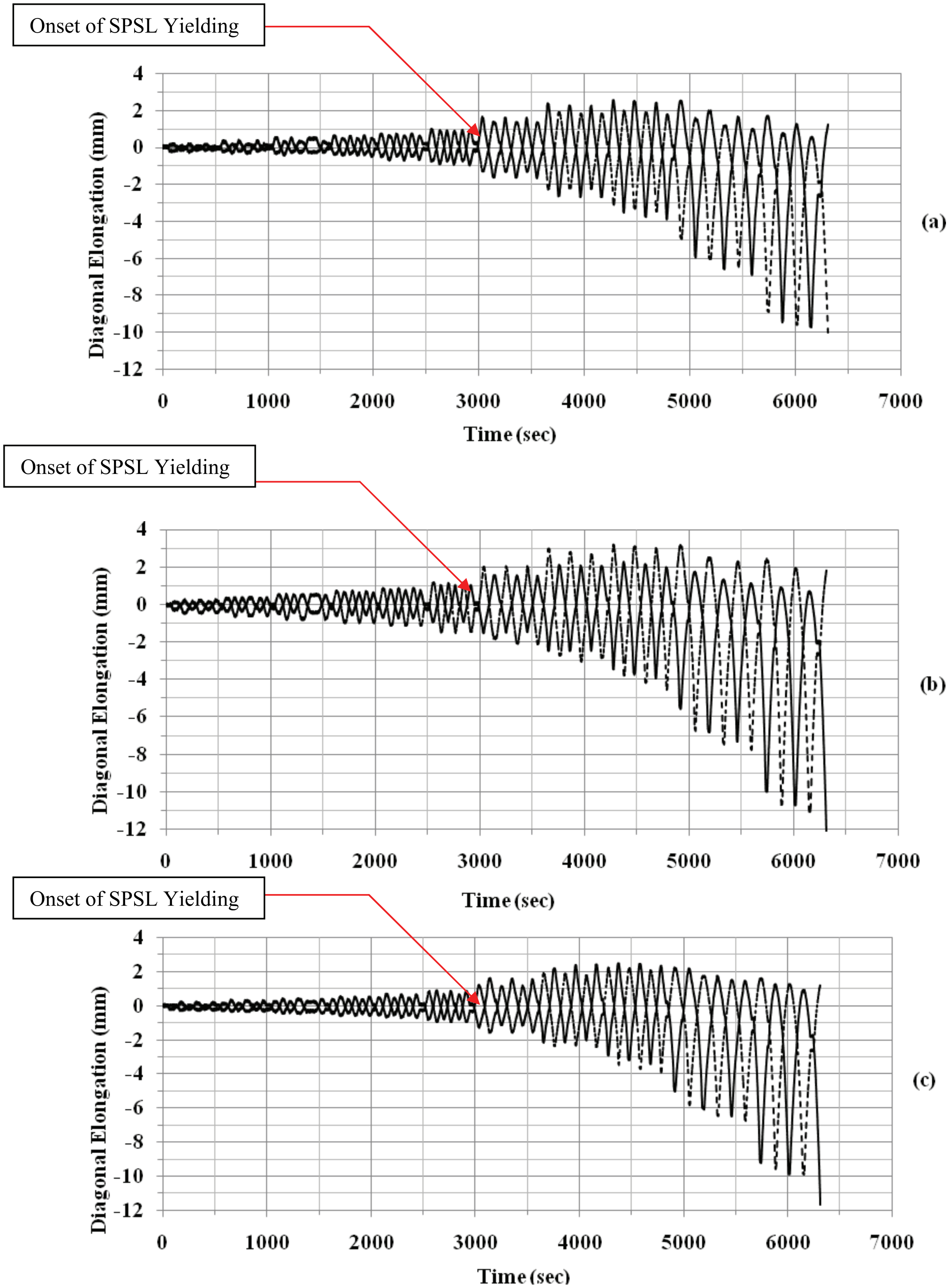

FIGURE 7-23 Links Diagonal Elongation vs. Time; (a) SPSL 5, (b) SPSL 6, (c) SPSL 7

Figure 7-24 shows the deformed shape of the SPSLs at the end of testing; similar behavior is observed in the FEM model. Figure 7-25 shows the analytically obtained out of plane deformation of the SPSLs due to the local buckling of the links at 175 mm top displacement

(2.5% drift); the maximum out of plane displacement is about 75mm. The links are numbered 1 to 8 from top to bottom.

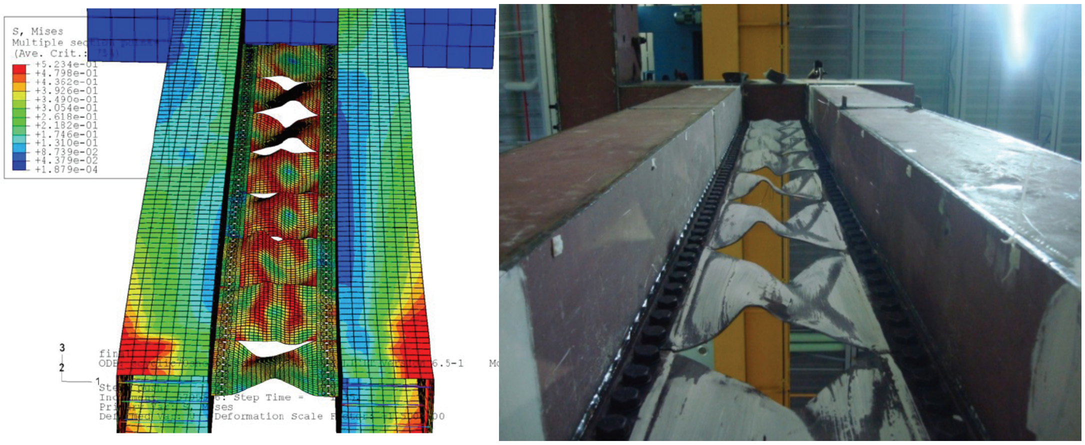

FIGURE 7-24 SPSLs Deformation at Test Termination

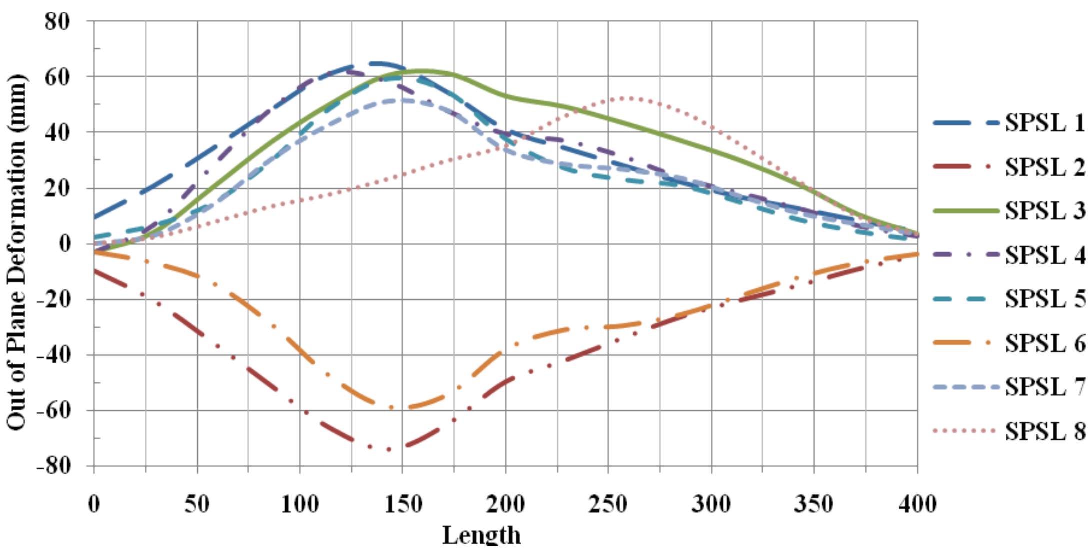

FIGURE 7-25 Out of Plane Deformation of SPSLs at 175mm Top Displacement (2.5% Drift)

Figure 7-26 shows the in-plane principal stresses vectors and contours for SPSL 4 at 175mm top displacement (2.5% drift). A Tension field strip can be seen to develop along the diagonal of the SPSL with a width of about 228mm (9"), and an angle of 55 degrees to the horizontal. Further investigation, looking at the stress vectors also shown in that figure, actually reveals a diagonal tension field acting at 45 degrees in the middle of the plate (showing the dominance of pure shear yielding there), and stresses re-orienting to remain parallel to the plate edges near those edges, where shear and flexure combine.

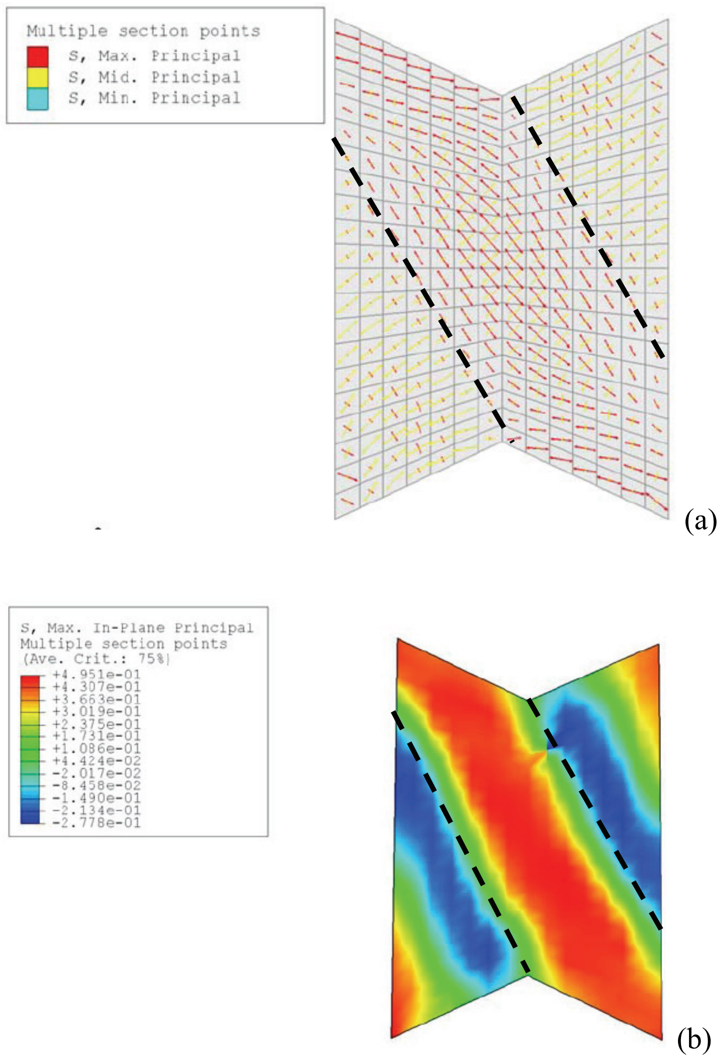

FIGURE 7-26 In-Plane Principal Stresses at 175mm Top Displacement (2.5% Drift); (a) Vectors, (b) Contours

7.4.3 Analytical Results for Test 1 Model

Figure 7-27 shows a comparison between the experimental and analytical results for Specimen S1 (Test 1) having laterally restrained SPSLs. It was unfortunate that the experimental testing of test 1 was terminated at a top displacement of 50mm (0.72% drift) due to a sudden weld failure at one of the bottom splices as described earlier in section 6.

Nevertheless, the comparison between the analytical models and experimental results for the previous tests gave confidence about the accuracy of the analytical model, and the analytically predicted behavior of the frame with the laterally restrained SPSLs calculated using the ABAQUS model is presented in figure 7-27 as if the entire cyclic history had been applied to that case, for information purposes. Obviously, that extrapolation is speculative and not verified by experimental results at this stage; however, further studies on laterally restrained SPSL presented in Section 9 will further investigate the conditions under which this behavior could have been obtained.

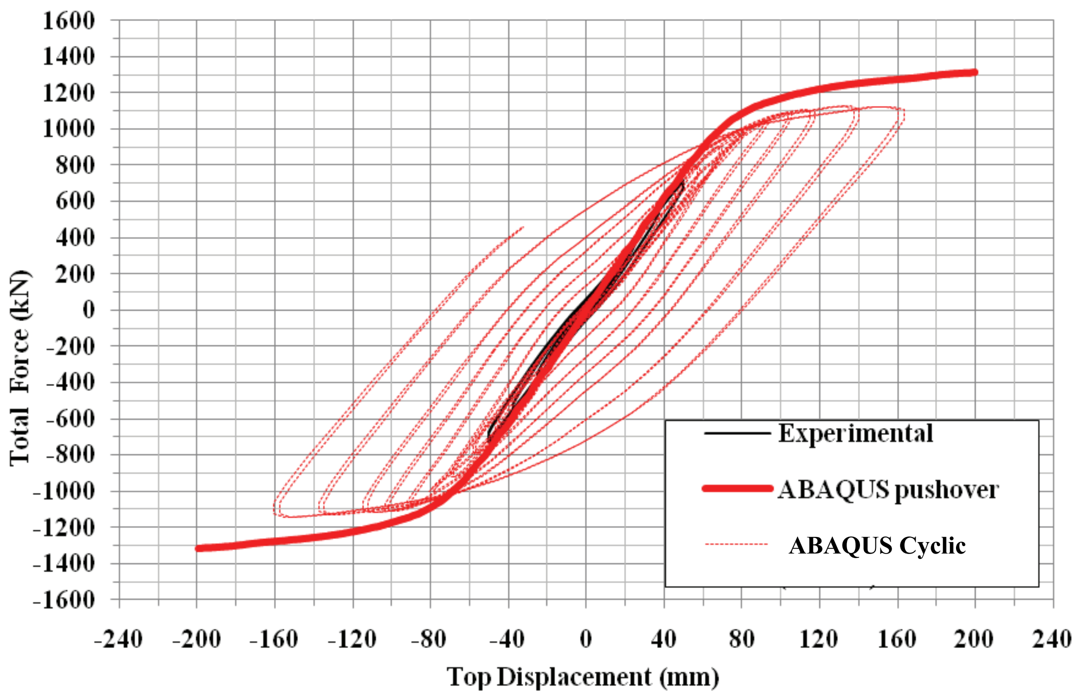

FIGURE 7-27 Comparison between Experimental and Analytical Results for Specimen S1 (Test 1)

Figure 7-28 shows the maximum in-plane principal stresses contour plot for SPSL 4 at 175mm top displacement (2.5% drift). Pure shear yielding can be seen in the middle part of the link, while pure flexural yielding is observed in the top and bottom of the links as seen in the figure. Again, this will be further investigated in Section 9.

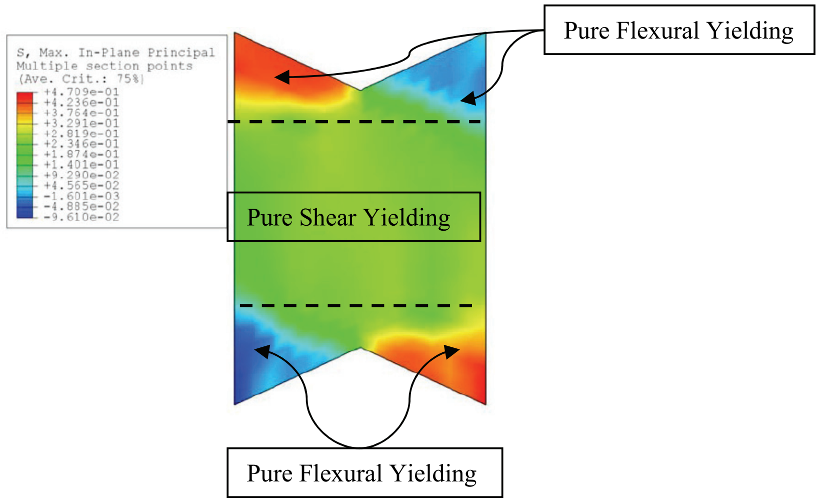

FIGURE 7-28 Maximum In-Plane Principal Stresses at 175mm Top Displacement (2.5% Drift)

7.5 Specimen S2-1 Model

7.5.1 Finite Element Description

7.5.1.1 Geometry Modeling and Meshing Algorithm

The same bare frame model used for specimen S2-2 was used here for specimen S2-1 model, in addition of the BRBs as the structural fuses. First the *Part Module* was used to define two 3D deformable wire parts, one is the yielding portion of the BRB and the other is the connection part of the BRB which was required to remain elastic during the analysis by modifying its thickness.

Using the *Assembly Module* the parts was then positioned relative to each other in a global coordinate system; the connection part was used twice in the assembly. After that the *Interaction Module* was used to connect the parts using the *Tie Constrain* option that allows the merging of the interface nodes. Again the *Tie Constrain* was used to merge the edges of the BRBs to the steel columns. Note that the gusset plates to which the BRB connected were not modeled; therefore, some stress concentration due to the “point load” effect of connecting the BRBs to single nodes in the steel was expected. Nevertheless, these few points of fictitiously high stress concentration were not expected to affect the global system behavior being investigated.

Meshing was then generated using the *Mesh module*, first seeding of the edges was done by specifying the number of seeds required for all the edges, a structured mesh was then chosen. Figure 7-29 shows the ABAQUS model of specimen S2-1.

7.5.1.2 Material Definitions

Steel used for the BRB's yielding core was specified to be ASTM A572 Gr. 50 and obtained from coupon tests described earlier in section 5.8.1. True stresses (Cauchy stresses) and logarithmic plastic strains where then calculated using equations (7-1), and (7-2).

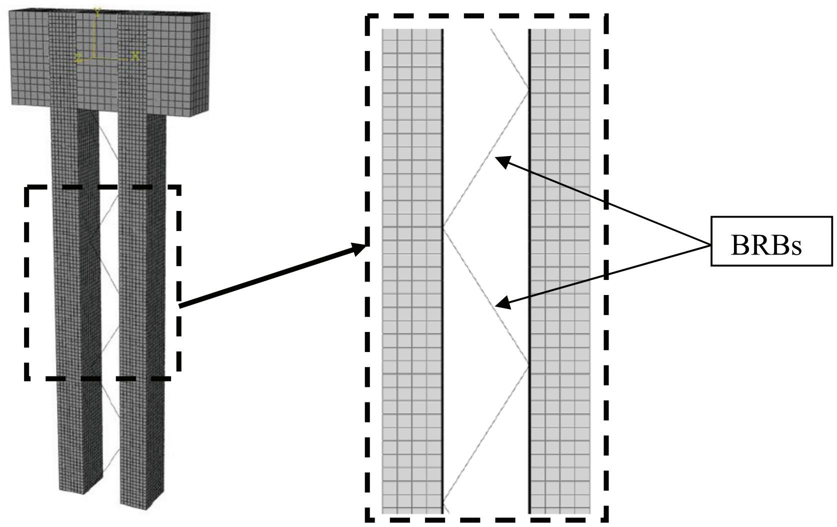

FIGURE 7-29 ABAQUS Model for Specimen S2-1

7.5.2 Comparison with Experimental Results

Figure 7-30 shows a comparison between the experimental data, the ABAQUS cyclic analysis results, and the ABAQUS pushover analysis results. It can be seen that both the experimental and analytical cyclic data match well, as the entire peak base shear values were captured along with the strength and stiffness degradation of the specimen that occurred due to the local buckling of the columns.

Figure 7-31 shows a comparison between the Experimental data obtained for the deflected shape of the columns versus the ABAQUS analytical results. The experimental data was obtained using 5 string potentiometers located at 2000mm, 3400mm, 4500mm, 5600mm, and 6500mm respectively from the top of the foundation. It can be seen that the analytical and experimental results match well. The columns behave differently before and after yielding of the BRBs, similarly to what was observed for the SPSLs case. Before the BRBs yield, the entire pier consisting of the two columns and the BRBs behave as one vertical cantilever member, with the columns being the flanges of that member, and the links being its web. Therefore a single curvature behavior is observed for the system up to the point where the SPSLs start to yield at 32mm (0.46% drift); thereafter the columns behave individually as two columns in a frame and a double curvature develops.

Figure 7-32 shows average strain gage readings for the bottom of both columns of specimen S2-1. Similarly to what was observed for the SPSLs case, it can be seen that both sides of both columns remained elastic during testing, except at the 100mm (1.5% drift) cycle the east face of the west column started to yield accompanied by minor local buckling as described in section 6.

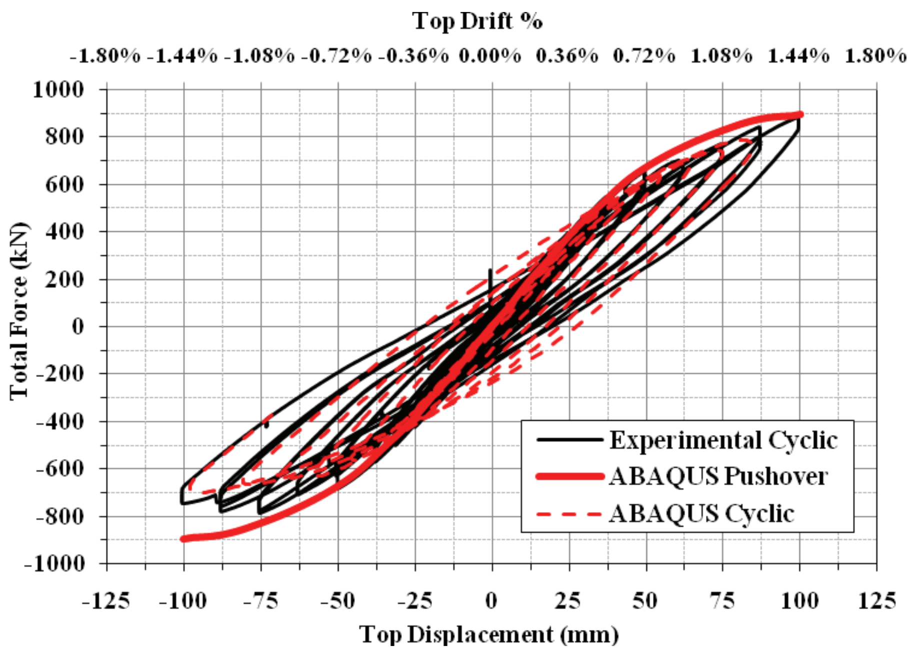

FIGURE 7-30 Comparison between Experimental and Analytical Results for Specimen S2-1

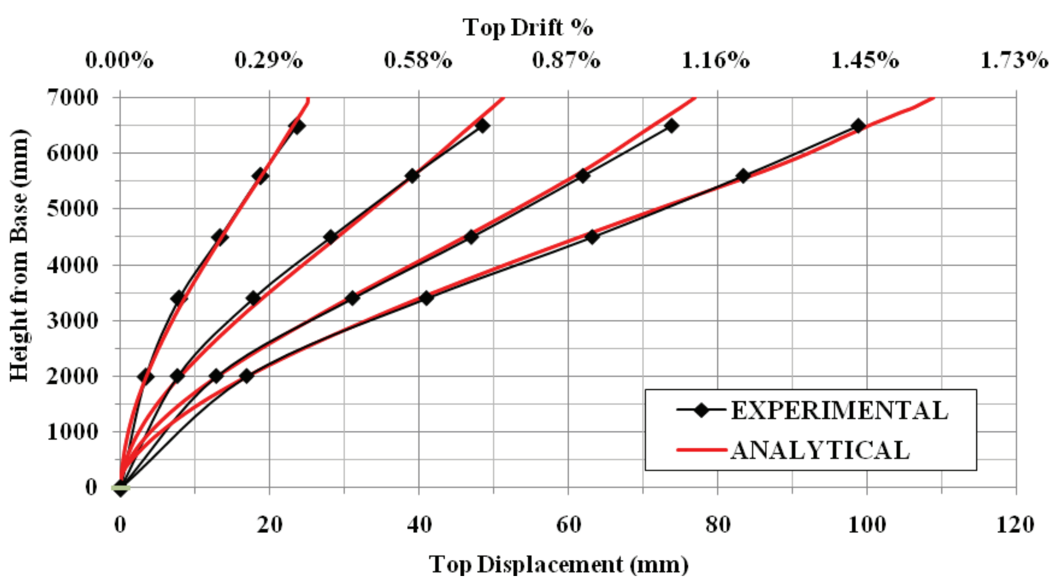

FIGURE 7-31 Comparison between the Deflected Shape of Columns at Various Drift Levels for Specimen S2-1

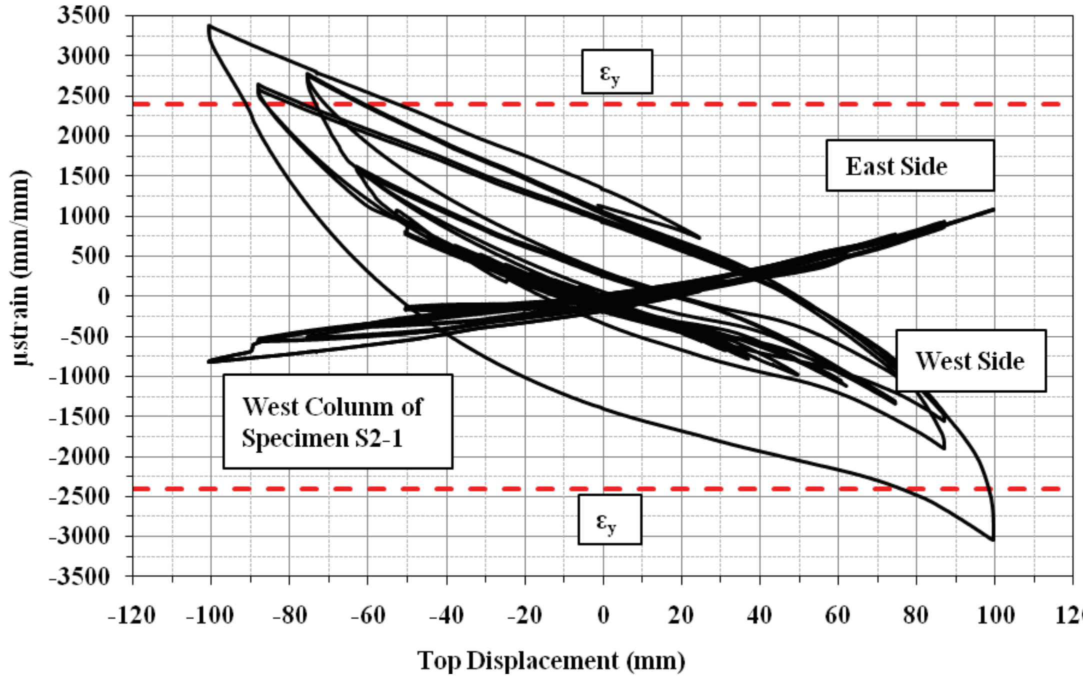

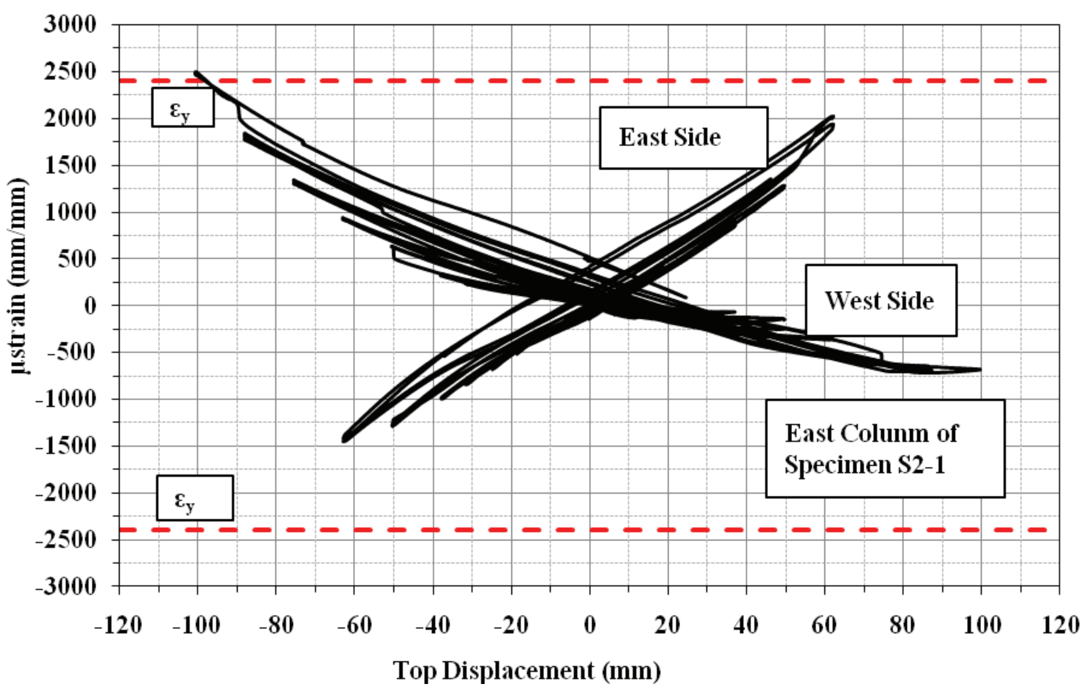

FIGURE 7-32 Average Strain Values for Bottom of the Columns from Strain Gages for Specimen S2-1

7.5.3 Buckling Restrained Braces Results

For illustration purposes, figure 7-33 shows a plot for the total lateral force vs. the axial BRB displacement hysteretic curve for BRB3 (numbered from top to bottom), as the high inelastic deformation was expected to occur in the middle BRBs, while the top and bottom BRBs were expected to have relatively low inelastic deformations due to the fixed end conditions of the top and bottom. It was difficult to obtain a representation of the hysteretic behavior of a typical BRB due to the absence of direct measurement of the axial forces in the BRBs used in this specimen. Total lateral force is therefore used as a proxy for the possible axial force acting in a typical BRB for the current purpose. To complete the information presented here, the experimental behavior of the BRB used in this specimen is further investigated in Section 8.

Nevertheless, it can be observed from the figure that the typical BRB shown experienced inelastic deformation and that a maximum deformation of $12\Delta_y$ was reached (equivalent is to 2% strain in the BRB yielding core) at the onset of the column yielding. The hysteretic curves for all other BRBs are presented in figure 7-34. Table 7-2 summarizes some key BRB results. It can be seen that BRB 4 is the one experiencing the maximum axial displacement ($24\Delta_y$, 4% strain), while the maximal axial deformation of the BRBs decreases for those BRBs located closer to the top and bottom of the columns, which is expected as explained earlier. Note that BRB4 is experiencing more axial displacement than BRB3, because the inflection point of the columns was not observed at their centerline but rather below the centerline.

It can also be seen from the figures that the plots are not exactly typical of what is expected from a BRB hysteretic curve. As will be described in more details in Section 8, this is due to the facts that only one string potentiometer was installed for each BRB to measure their axial displacements, and that the BRBs experienced some differential rotation between their pins, which could not be predicted before testing, and which affected the results obtained by the instrumentation.

As mentioned above, it was decided after termination of the test to retest some of the BRBs that experienced only small inelastic deformations and that were therefore still in their close to “virgin” state, such as BRBs 1 and 6 (i.e. the top and bottom BRBs). In these further BRB components testing, four string potentiometers will be used to measure the average axial displacement of the BRBs, allowing to better understand and to eliminate the effect of the rotation that was experienced during testing, to obtain correct hysteretic curves for the types of BRBs used here. These further tests will also allow obtaining actual hysteretic curves for the BRBs expressed in terms of the measured actual axial forces applied to the BRBs. These experiments and results for BRB component testing will be discussed in section 8.

TABLE 7-2 Summary of BRB Results

BRB	Δ_{max} (mm)	Δ/Δ_y	Strain
1	2	3	0.67%
2	4	6	1.33%
3	6	8	2%
4	12	17	4%
5	6	8	2%
6	5	7	1.67%

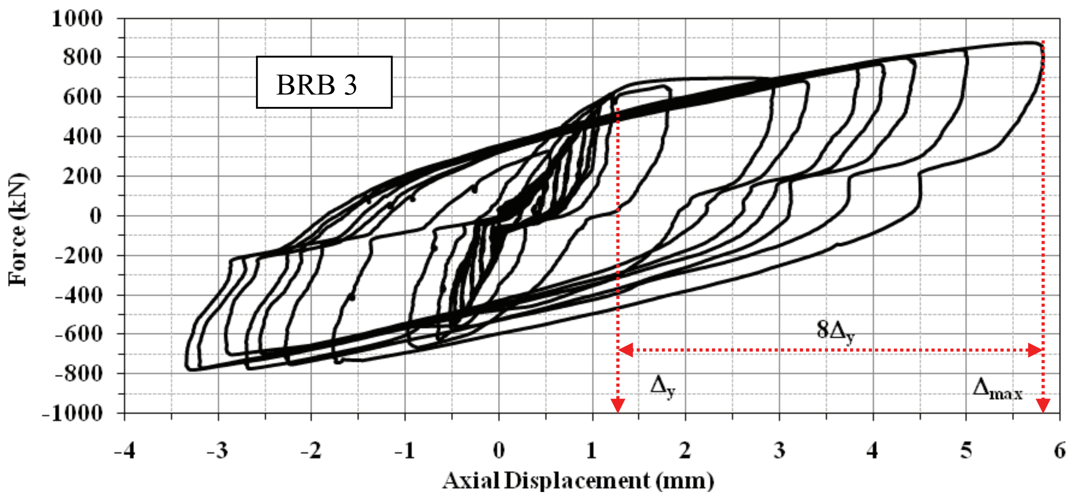

FIGURE 7-33 Total Lateral Force vs. Axial BRB Displacement Hysteretic Curve for BRB3

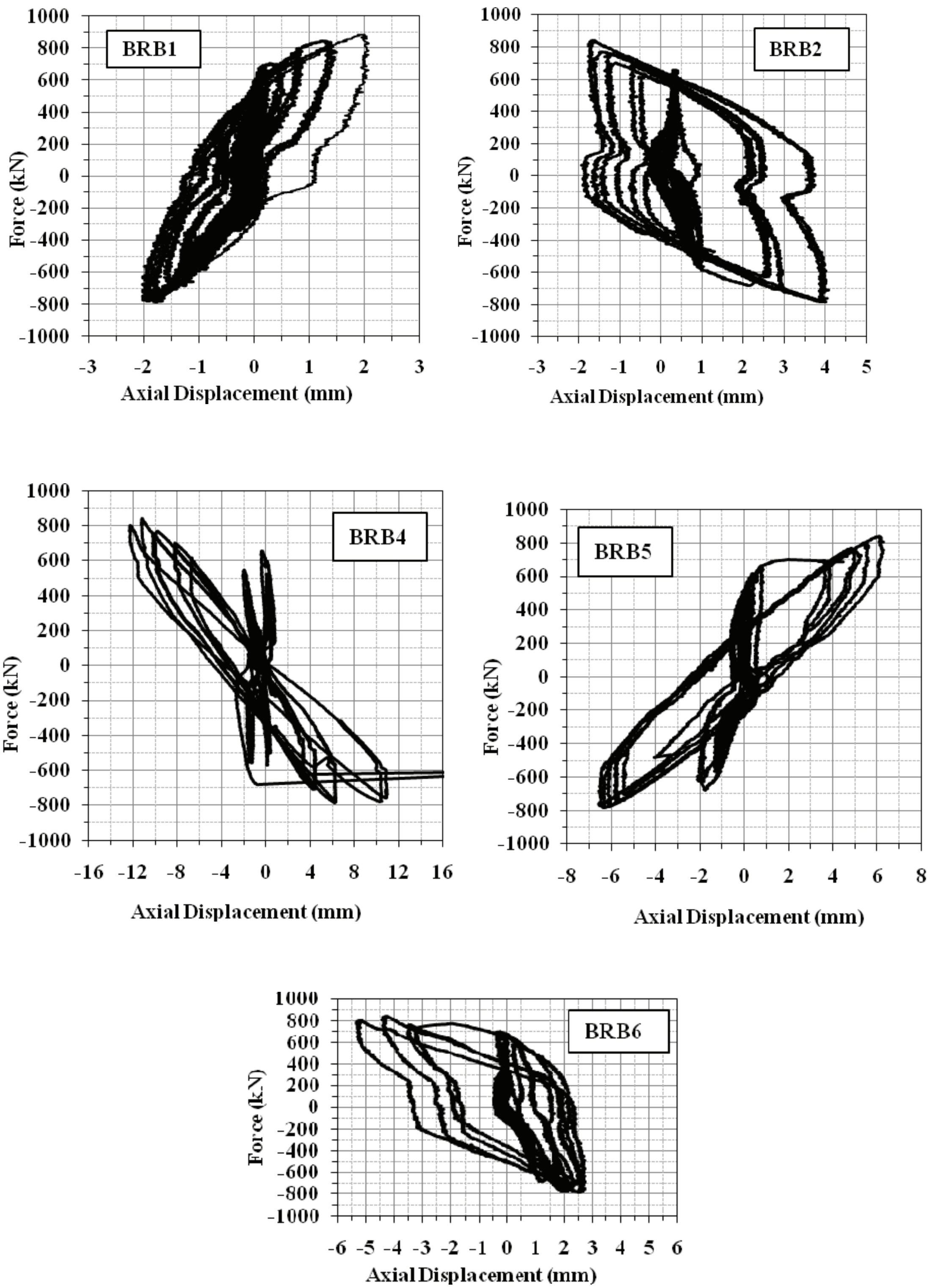

FIGURE 7-34 Total Lateral Force vs. Axial BRB Displacement Hysteretic BRBs Curves

7.5.4 Plastic Analysis

Figure 7-35 shows the free body diagram for a single column utilizing the BRBs, from which the maximum system base shear, V_{Dt}, can be calculated by taking sum of the forces along the vertical axis:

$$V_{Dt} = \frac{4M_P}{H_{tot}} + n\sigma_y A_b \sin\theta\left(\frac{L}{H_{tot}}\right) \tag{7-3}$$

where n is the number of BRBs, A_b is the cross section area of the yielding portion of the BRB, and σ_y is the yield strength of the BRB.

Similarly to the case of SPSLs described before in section 4.9, it can be seen that the first term of the equation represents the maximum bare frame shear strength, from which it is concluded that the contribution of the BRBs to the maximum shear strength, V_{DS}, is calculated as:

$$V_{Ds} = n\sigma_y A_b \sin\theta\left(\frac{L}{H_{tot}}\right) \tag{7-4}$$

The contribution of the BRBs to the total elastic lateral stiffness of the system can be calculated by dividing the contribution of the BRBs to the maximum shear strength, V_{DS}, by the top horizontal displacement that corresponds to the onset of BRB yielding. Figure 7-36 show the geometric relationship between the top displacement and the BRB displacement. The following relationships can be concluded from the figure as follows:

$$\cos\theta = \frac{\Delta_x}{\Delta} \tag{7-5}$$

$$\frac{\Delta}{\Delta_{max}} = \frac{H}{H_{tot}} \tag{7-6}$$

$$\Delta_x = \varepsilon_{BRB} L_{ysc} \tag{7-7}$$

where L_{ysc} is the yielding portion of the BRB.

Substituting equation (7-7) into equations (7-5) and (7-6) then rearranging:

$$\Delta_{max} = \frac{\varepsilon_{BRB} L_{ysc} H_{tot}}{H \cos\theta} \tag{7-8}$$

The BRB lateral stiffness contribution, K_b, can now be calculated as:

$$K_b = \frac{V_{Ds}}{\Delta_{y\,max}} \tag{7-9}$$

where Δ_{ymax}, is the top displacement that corresponds to the onset of BRB yielding. Substituting equations (7-4) and (7-8) into equation (7-9), the value of K_{lat} can be calculated as:

$$K_{lat} = \frac{n\sigma_y A_b LH \sin\theta \cos\theta}{\varepsilon_{yBRB} L_{ysc} H_{tot}^2} \tag{7-10}$$

where ε_{yBRB} is the yield strain of the BRB.

Taking into account that:

$$E = \frac{\sigma_y}{\varepsilon_{yBRB}} \tag{7-11}$$

substituting equations (7-11) into equation (7-10):

$$K_b = \frac{nEA_b LH \sin\theta \cos\theta}{L_{ysc} H_{tot}^2} \tag{7-12}$$

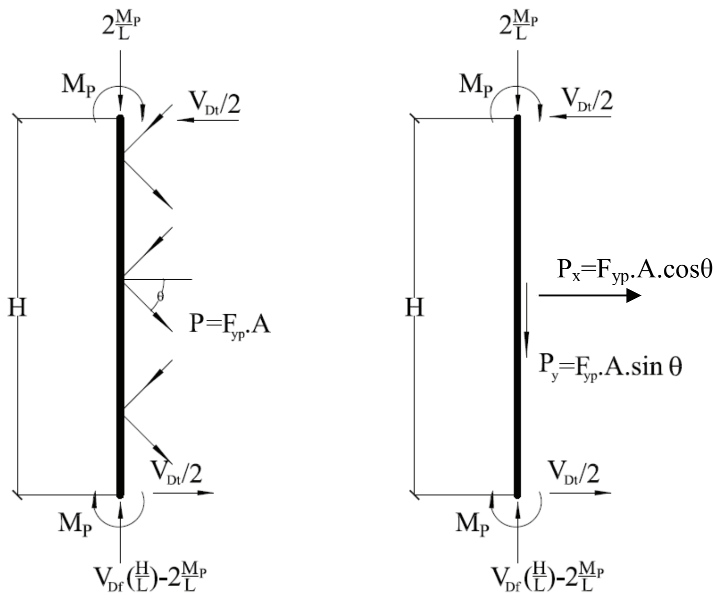

FIGURE 7-35 Free Body Diagram of a Single Column with BRBs

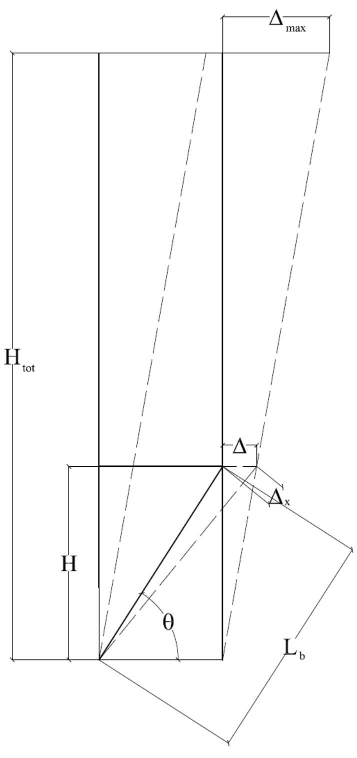

FIGURE 7-36 Geometric Relationship between BRBs and the Columns

7.6 Comparison of Pushover Results

Figure 7-37 shows the pushover results comparison for all specimens. A stiffness increase of 80% is observed between the bare frame (specimen S2-2) and the frame with the structural fuses inserted between the columns. A 30% strength increase is also observed between Specimen S2-2 and Specimen S1, while a 20% increase is observed between Specimen S2-2 and Specimen S2-1. A 60% strength increase would have been expected if the lateral restraints had been left in place for the test, from which it is concluded that, the lateral restraints has a huge effect of strength increase. Recall that the desired increase in strength and maximum ductility are parameters selected by the designer; for the case at hand, this was dictated in many aspects by experimental constraints as described in Section 5.

Equations developed earlier in sections 4.9 and 7.5.4 to estimate the elastic stiffness and the base shear of the specimen utilizing both the SPSLs and the BRBs were compared against the FEM and the experimental data. Table 7-3 summarizes these results, it can be seen that the equations gives good estimates of both the stiffness and the base shear compared to the FEM and the experimental data. Detailed calculations of the base shear and elastic stiffness for all specimens are presented in Appendix B.

TABLE 7-3 Comparison Summary of Peak Results

Specimen	Elastic Stiffness (kN/mm) (Exp.)	Elastic Stiffness (kN/mm) (equations)	Base Shear at Column Yielding (kN) (Exp.)	Base Shear at Column Yielding (kN) (FEM-Pushover)	Base Shear at Column Yielding (kN) (FEM-Cyclic)	Max. Base Shear (kN) (Exp.)	Max. Base Shear (kN) (FEM-Cyclic)	Maximum Base Shear (kN) (equations)	Fuse Ductility at Column Yielding (Exp.)	Column Yielding Drift (%) (Exp.)	Max. Drift (%) (Exp.)	Strength Reduction at Maximum Drift (%) (Exp.)
S1 (Unrest.)	22	24	875	950	880	982	980	1133	4	1.6	3.3	33
S1 (Rest.)	22	22	-	1150	1100	-	1150	1243	-	-	-	-
S2-1	21.5	32	881	900	885	-	-	1149	4	1.6	-	-
S2-2	8	9.7	666	740	670	770	760	788	-	1.6	4.3	29

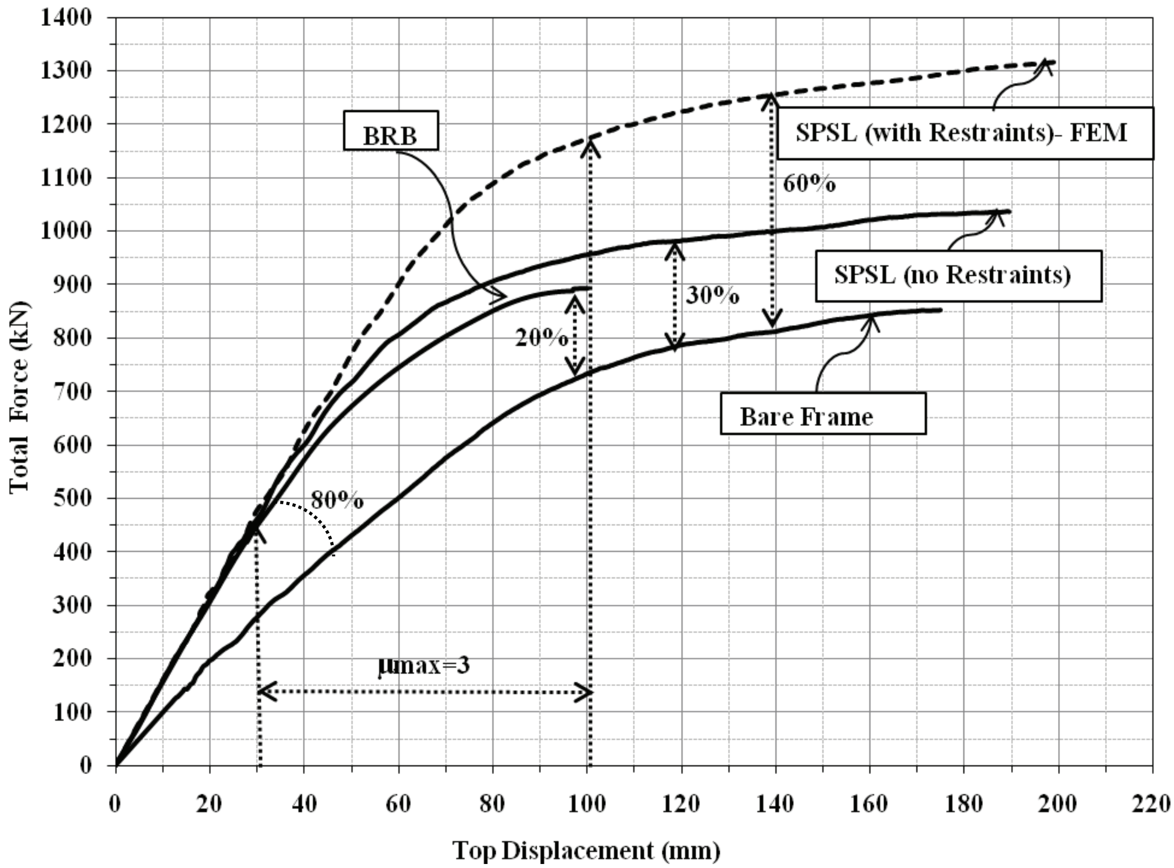

FIGURE 7-37 Pushover Results Comparison for All Specimens

SECTION 8
EXPERIMENTAL TESTING OF BUCKLING RESTRAINED BRACES HAVING SHORT YIELDING CORE LENGTH

8.1 General

After completion of specimen S2-1 test, it was decided to perform uniaxial cyclic tests on the BRBs that had been used in that test. These component tests were to serve many purposes. First, the hysteretic curves obtained for the BRBs during testing of the full specimen S2-1 did not truly represent their individual behavior, as the axial force resisted by each individual BRB was not measured and all the BRB plots obtained were in terms of the total horizontal force applied to the system, as shown in the previous section. Second, another reason for performing the uniaxial tests is that some welding deficiencies were observed in the BRB cores after testing specimen S2-1 which was of concern for the overall performance of the system as discussed later in this section. Furthermore, since the BRBs used in this testing program were of a new prototype created for applications having short yielding lengths, tests conducted prior to specimen S2-1 on prototypes of the BRBs with smaller cross section were performed and also reported in this section. Together, these two BRB test series also allow to investigate the effect of changing the cross section on the overall behavior, considering that the yielding core of the BRB used here is short compared to the BRBs that are been used in building projects to date.

Therefore, two sets of BRBs where used for the tests reported in this section. The first set consisted of prototypes of the BRBs used in specimen S2-1; the prototype had the same exact external dimensions (length and width) but with a yield-core cross section diameter of 22mm (0.88in), which was equivalent to a 30 kips yield force for the BRB when using A572 Gr. 50 steel. The second set consisted of the actual BRBs that has been already used in specimen S2-1 testing; these BRBs have a cross section diameter of 44mm (1.75in), which was equivalent to a 120 kips yield force when using A572 Gr. 50 steel. For both sets, the BRBs used had a pin-to-pin dimension of 610mm (24in), and a yielding core length of 305mm (12in).

8.2 BRB Description

The new BRB design concept proposed by Star Seismic eliminates the need for a transition length between the yielding core and the non yielding part of the BRB, which allows for shorter BRBs. Another advantage of the newly proposed BRB assembly is that it is entirely made of steel (i.e. without a concrete fill) which reduced its weight substantially.

The BRB assembly is shown in figure 8-1 and composed of a yielding circular steel core, welded to four oversized gusset-plates (two at each end). The steel core is inserted in an outer hollow steel tube, which is used to prevent the expected local buckling of the yielding core due to compression. The outer hollow steel tube is stiffened by circular steel plates at equal distances along its length, these stiffeners provide the hollow steel tube with the necessary lateral stiffness required to prevent the yielding core from buckling in any direction and forcing it to yield in compression as well as in tension. The described assembly is inserted in a bigger hollow steel circular tube; this outer tube is kept in place by tack welding the inner stiffeners to it (through pre-drilled holes in the tube). In this concept, the load transfer between the BRB and the surrounding structural components rely on the weld between the yielding core and the gussets; as in all BRB designs, the BRB inwards are not visible once assembled and delivered to the site and quality control mechanism are primordial.

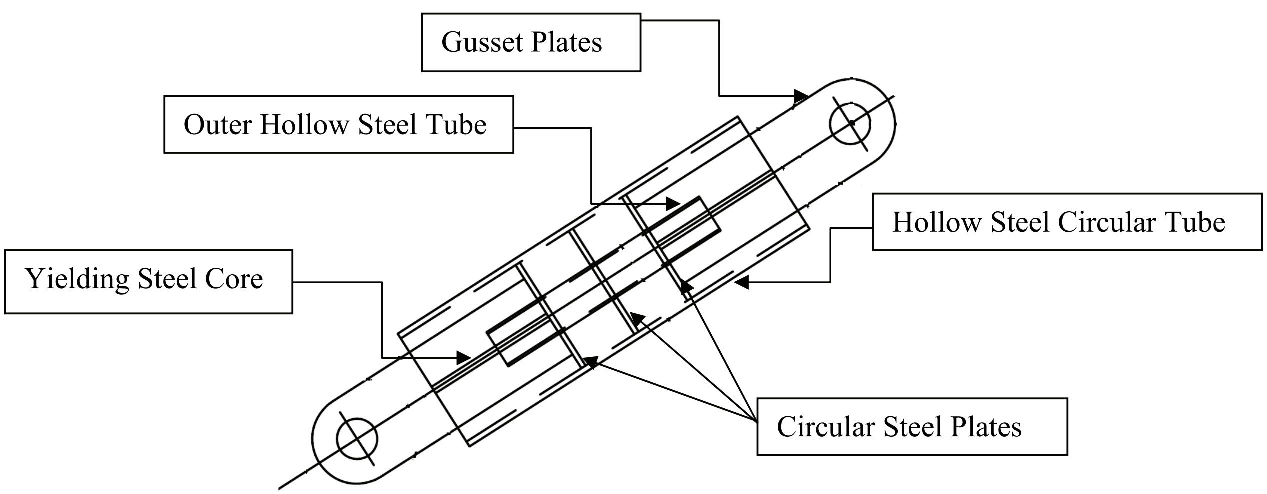

FIGURE 8-1 BRB Assembly Sketch

8.3 Test Setup

8.3.1 BRB Set I

To test the first set of BRBs, a Universal Machine available in the Structural Engineering Department at the State University of New York at Buffalo was used. It has been selected for the ease of the testing setup required to perform the test. Unfortunately, that Universal Machine could not be used for the second set of BRBs as their strength exceeded the machine's maximum capacity of 100 kips; these other tests were therefore conducted on another axial loading facility at the University at Buffalo SEESL, described below.

8.3.2 BRB Set II

The axial loading facility used to test the second set of BRBs consisted of a foundation beam, reaction blocks, and a hydraulic actuator with a capacity of 1111 kN (250 kips). The gusset-plates used where designed to represent the same type of connection that has been used in specimen S2-1 testing. Two gusset-plates where used, one attached to the reaction block and the other one attached to the actuator head, while the BRBs were connected to both ends. Figure 8-2 shows a schematic elevation view and a photograph of the axial loading facility used for the axial testing of the second set of BRBs.

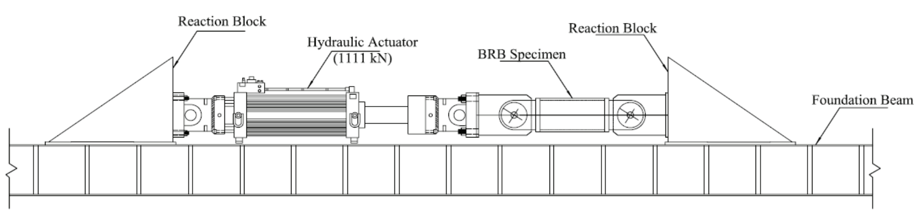

(a)

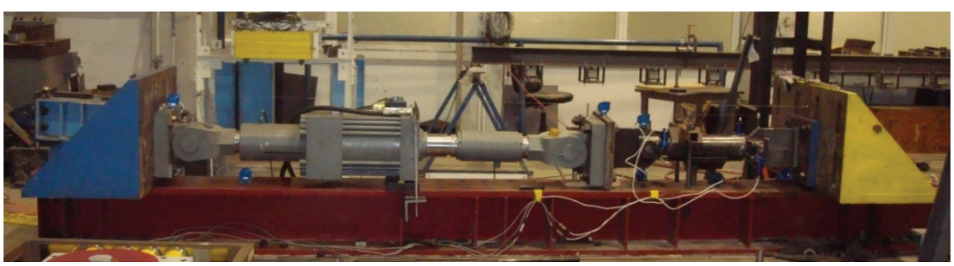

(b)

FIGURE 8-2 (a) Schematic Elevation View of The Axial Loading Facility used for The Axial Testing of The Second Set of BRBs; (b) Photo

A particular challenge for this test setup is created by the presence of four hinges, two along each side of both the BRBs and the actuator. The presence of the hinges, in absence of other restraints, create an unstable system during the axial compression phase of each cycle which would, due to geometric nonlinearity, impose a vertical force on the BRB. For that particular reason, a vertical restraint applied at the middle of the BRB was designed to overcome this vertical force, allowing the BRB to stay in place during compression. The actuator was also restrained from the vertical motion by tying it to the foundation beam. Figure 8-3 shows the vertical restraint used to prevent the vertical motion of the BRB specimen.

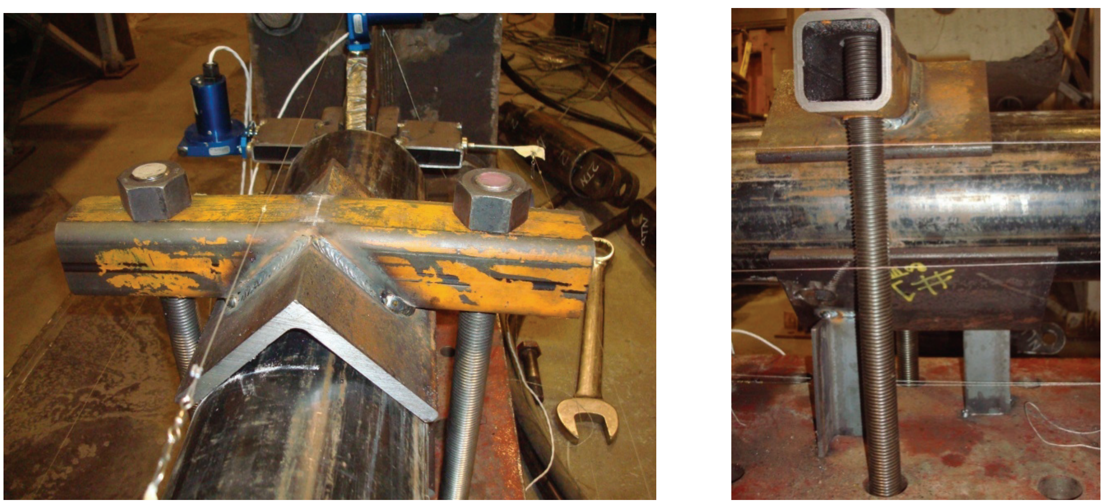

FIGURE 8-3 Vertical Restraint used to Prevent Vertical Motion of BRB Specimen

A gusset-plate having the same thickness as that used in specimen S2-1 testing was fabricated replicating the pin-ended condition for the BRBs used in that test. The same exact 50mm (2in) pins used before for the specimen S2-1 test was reused for the axial testing here; the pins were also pounded in the gusset-plates to reduce the effect of slippage to the minimum reduction possible. Figure 8-4 shows the gusset-plate connection to the BRB.

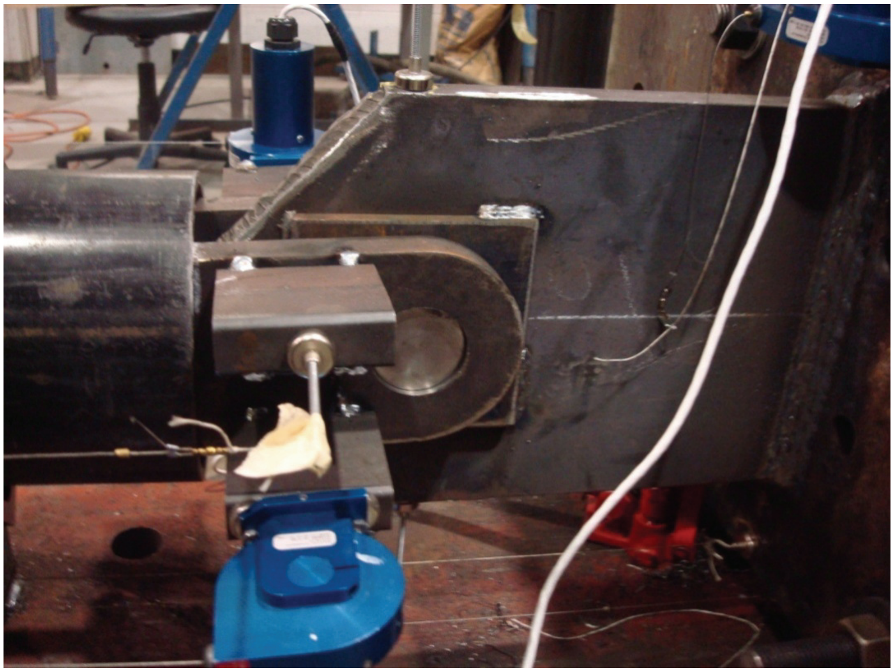

FIGURE 8-4 Gusset-Plate to BRB connection

8.4 Test Set-up Design and Instrumentation

The applied load was measured by a load cell installed in the actuators used for both test setups. According to the Seismic Provisions for Structural Steel Buildings (AISC, 2005), the axial strength of a BRB is calculated as per the following equation:

$$P_{ysc} = \beta\omega R_y F_{ysc} A_{sc} \tag{8-1}$$

where β and ω are the compression and strain hardening adjustment factors respectively, and R_y is the ratio of the expected yield stress to the specified minimum yield stress, F_{ysc}, and A_{sc}, is the area of the steel core. Since all these values but A_{sc} are calculated from the experimental hysteretic curve of the BRB, approximate values of β, ω, and R_y were taken from previous studies as 1.2, 1.5, and 1.1 respectively to calculate the maximum expected strength of the BRBs to ensure that they would not exceed the actuator capacities. Instrumentation specific to each test set-up is described below.

8.4.1 BRB Set I

For the BRBs tested in the Universal testing machine, the longitudinal movement of the actuator was measured using a linear variable displacement transducer (LVDT), located inside the actuator itself. To measure the actual displacement of the BRBs without taking into account any slippage that occurs between the bolts and the gusset plates, two LVDTs were installed left and right of each BRB tested as shown in figure 8-5. The load applied on the BRBs was measured by a load cell installed inside of the actuator.

8.4.2 BRB Set II

For the BRBs tested in the axial testing facility, the longitudinal movement of the actuator was measured using LVDTs, located inside the actuator itself. In addition, a string potentiometer was installed across the actuator from the end plate attached to the reaction block to the end plate attached to the BRB specimen. Two string potentiometers were used to monitor if any sliding in the reaction blocks would occur, as this would have to be taken into account to accurately monitor the BRB displacement if slippage was to occur. For the BRB specimen, six string potentiometers were used to monitor the actual axial displacement that occurred in the BRB. Two of the six string potentiometers where installed on top and bottom of the BRB from pin to pin; the average displacement of these two potentiometers would represent the axial displacement of the BRB including any slippage that would occur between the pins and the gusset plates. The other four were installed east and west of the BRB specimen (two at the top and two at the bottom) and were located such as not to include the slippage of the pins and only measure the BRB actual displacement. Note that all these potentiometers were installed across the BRB specimen in order to capture the effect of the pin-end rotations that occurred during the testing of specimen S2-1, and that had a negative effect on the accuracy of the data obtained for the BRBs. Figures 8-5 and 8-6 show photographs of the instrumentation used for a both BRB sets. The load applied on the BRBs was measured by a load cell installed inside of the actuator.

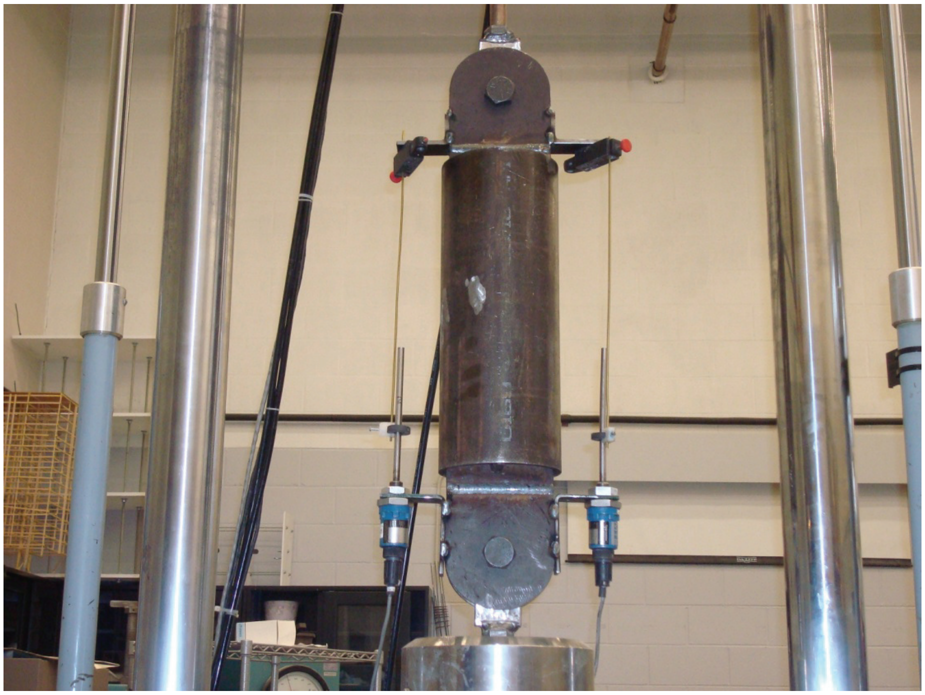

FIGURE 8-5 Instrumentation Used for BRB Set I

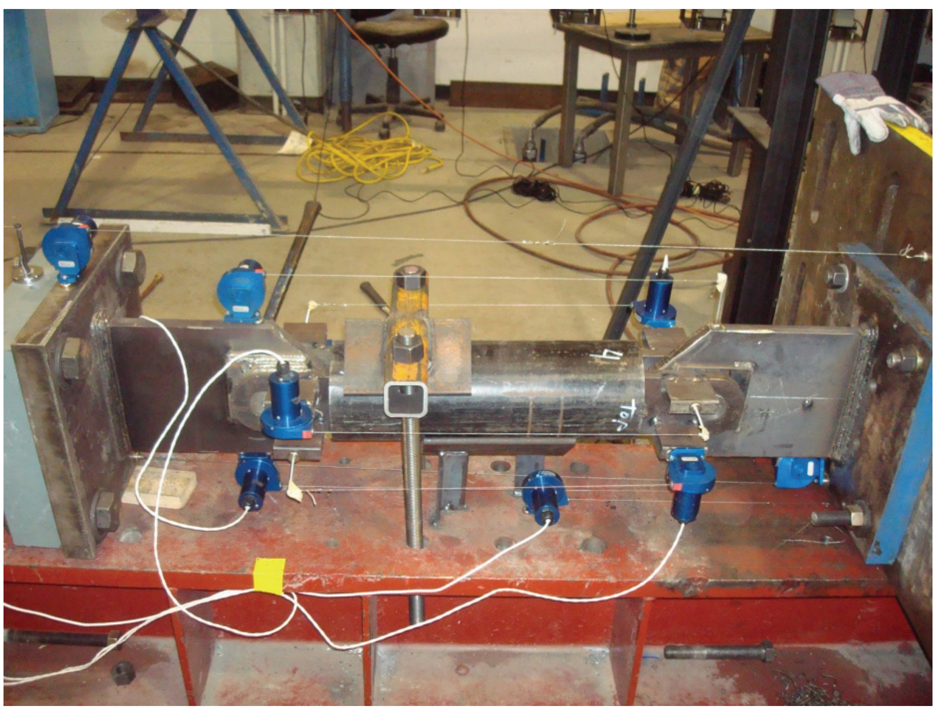

FIGURE 8-6 Instrumentation Used for BRB Set II

8.5 Loading Protocol

Both BRB sets were tested according to the protocol proposed by the Seismic Provisions for Structural Steel Buildings (AISC 2005), followed by additional cycles to satisfy the OSHPD requirements for cumulative inelastic deformation. For brief, when OSHPD loading protocol is stated in this section it means additional cycles needed to satisfy the OSHPD recommendations.

Loading protocol for all tests is presented in table 8-1. The brace deformation at the design story drift, Δ_{bm}, was taken as 5 times the yield displacement of the brace, Δ_{by}, as proposed by the Seismic Provisions (AISC 2005). Note that the yielding core length is equal to 305mm (12in) for all specimens, and A572 Gr. 50 steel is used, from which the BRB yield displacement is calculated to be equal to 0.72mm.

After completion of the standard loading protocol, low-cycle fatigue tests were conducted with amplitude of $15\Delta_{by}$ and equivalent to $3\Delta_{bm}$ until fracture occurs. AISC requires BRBs to achieve a cumulative inelastic deformation of $200\Delta_{by}$ before failure. This amount of inelastic deformation is achieved and exceeded by the end of the standard loading protocol. Additional cumulative inelastic deformations are added for each BRB specimen during the low cycle fatigue tests. Individual total cumulative inelastic deformations for each BRB specimen tested is reported later on this section.

TABLE 8-1 Loading Protocol for BRB Uniaxial Tests

Cycles	Axial Deformation		Inelastic Deformation	Cumulative Inelastic Deformation	Axial Deformation (mm)
4	$0.2\Delta_{bm}$	$1.0\Delta_{by}$	$0\Delta_{by}$	$0\Delta_{by}$	0.5
4	$0.3\Delta_{bm}$	$1.5\Delta_{by}$	$4\Delta_{by}$	$4\Delta_{by}$	0.75
4	$0.5\Delta_{bm}$	$2.5\Delta_{by}$	$12\Delta_{by}$	$16\Delta_{by}$	1.25
4	$1.0\Delta_{bm}$	$5.0\Delta_{by}$	$32\Delta_{by}$	$48\Delta_{by}$	2.5
4	$1.5\Delta_{bm}$	$7.5\Delta_{by}$	$52\Delta_{by}$	$100\Delta_{by}$	3.75
4	$2.0\Delta_{bm}$	$10\Delta_{by}$	$72\Delta_{by}$	$172\Delta_{by}$	5
2	$2.5\Delta_{bm}$	$12.5\Delta_{by}$	$46\Delta_{by}$	$218\Delta_{by}$	6.25
2	$3.0\Delta_{bm}$	$15\Delta_{by}$	$56\Delta_{by}$	$274\Delta_{by}$	7.5

8.6 Experimental Testing and Observations

8.6.1 BRB Set I

Three BRBs were tested in the Universal Testing Machine each for a particular purpose. The BRBs were denoted as BRB W-I, BRB B-I, and BRB BW-I and tested successively. The first BRB was directly welded to the gusset plate connected to the grip of the machine denoted as (central grip gusset plate), and the second BRB was bolted to the central grip gusset plate, while the third BRB had a combination of both welds and bolts as discussed later. Note that with respect to labeling of the BRB's specimens, (W) refers to the welded detail, (B) to the bolted one, while (I) is the BRB set considered (I being the smaller BRBs as described earlier).

8.6.1.1 BRB W-I

The first BRB tested was BRBW-I. This BRB was directly welded to the central grip gusset plate to eliminate slippage that might otherwise have occurred at the BRB's end. This type of fixture, though not realistic, was necessary to understand the behavior of the BRB without consideration of these other effects, as this type of BRB assembly was new and never been tested before. Figure 8-7 shows the end fixture of BRB W-I.

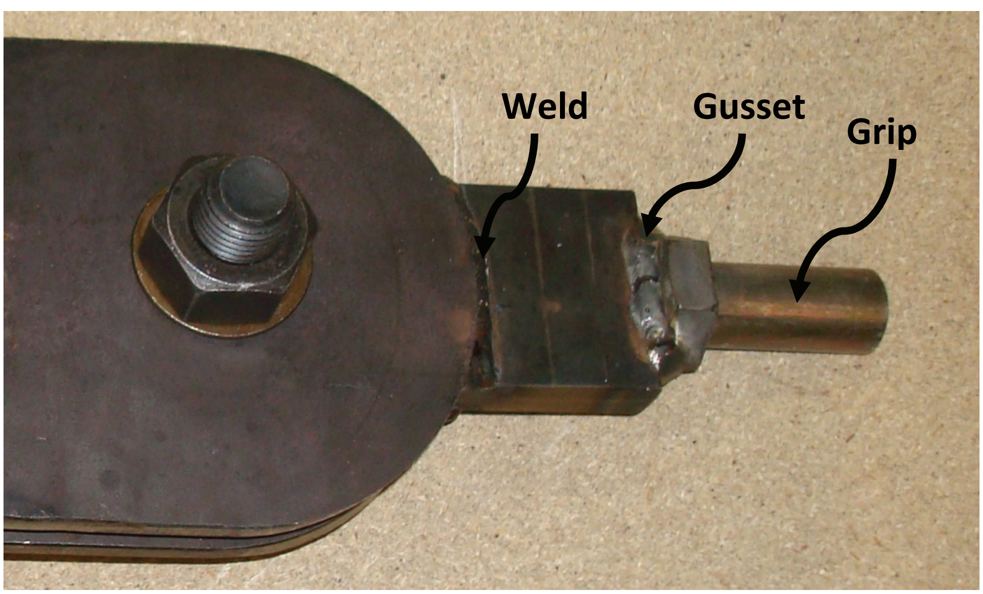

FIGURE 8-7 BRB W-I End Fixture to Machine

Testing started by applying the AISC loading protocol; yielding was observed at about 0.5mm axial BRB displacement. The AISC loading protocol finished successfully, and the BRB exhibited stable and symmetric hysteretic curve. The OSHPD loading protocol was then applied by performing two cycles at $12.5\Delta_y$, then two cycles at $15\Delta_y$. At the compression part of the $15\Delta_y$ displacement at 5mm (0.2in) axial displacement, a minor jump in the strength was observed and was attributed to the friction between the steel core and the steel tube.

BRB displacements were computed using three different approaches; the first was by directly plotting the displacements obtained from the machine actuator assuming that the machine had an infinite elastic stiffness compared to the BRB. Unfortunately this was not the case, as the machine turned out to be substantially more flexible than anticipated and introduced an important error in the measured displacements, which resulted in the illusion of a more flexible BRB than anticipated.

The second approach for calculating the BRB displacements was by averaging the displacements obtained by two Temposonic displacement transducers installed on both sides of the BRB. This approach gave results matching the anticipated BRB elastic stiffness within 5%, the difference being attributed to a minor rotation in the BRB gussets that was observed during testing at the elastic cycles which may have affected the Temposonics readings.

This approach highlighted the contribution of the machine to the previously measured displacements. Nevertheless, at larger inelastic cycles, it was felt that somewhat inaccurate results were obtained from the Temposonics transducers as significant rotations were observed in the BRB ends, not always consistently about the same axis. To compensate for that effect, it was decided to use four displacement transducers for the second set of BRBs (but was not done for the current test setup, as discovery of that phenomenon occurred during the analyses and study of accelerated videos conducted following the tests). Figure 8-8 shows the elastic stiffness comparison calculated by the first two approaches vs. the expected elastic stiffness.

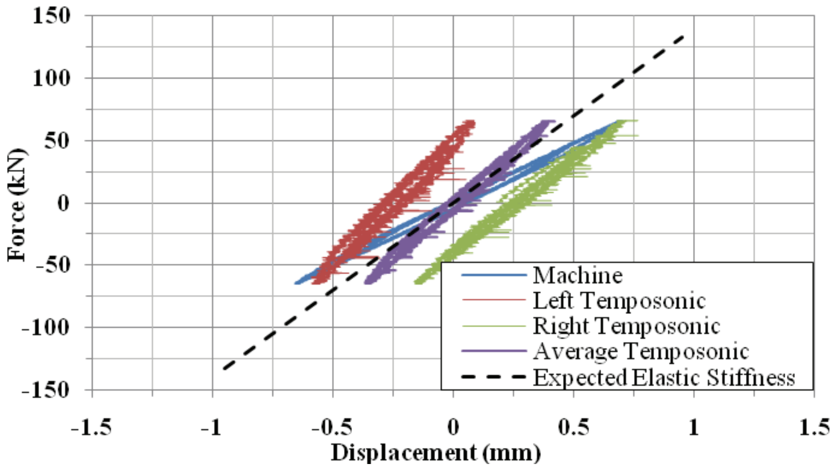

FIGURE 8-8 Comparison of Elastic Stiffness Computed by Different Approaches

A third approach for calculating the BRB displacements was by subtracting the elastic displacements due to the testing machine flexibility from the total displacements measured directly from the machine's actuator; this assumes that the machine remained elastic during the tests, which is a reasonable assumption. To calculate the machine contribution to the displacements calculated, the BRB stiffness, K_{BRB}, was calculated as:

$$K_{BRB} = \frac{EA}{L_{ysc}} \tag{8-2}$$

from which K_{BRB} was calculated as140 kN/mm from the given BRB dimensions, where L_{ysc} is the yielding portion length and taken as 305mm (12") here. The total stiffness, K_{tot}, was calculated from figure 8-8 as 91kN/mm, from which the elastic machine stiffness, K_m, can be calculated as 260kN/mm using the following equation assuming that the machine and the specimen are connected in series in the test setup:

$$\frac{1}{K_{tot}} = \frac{1}{K_m} + \frac{1}{K_{BRB}} \tag{8-3}$$

After calculating the testing machine elastic stiffness, its contribution to the total displacement can be calculated using the following equation:

$$\Delta_m = \frac{F}{K_m} \tag{8-4}$$

from which ,F, is the total force calculated by the machine actuator.

The BRB displacement, Δ_{BRB}, can then be calculated as follows:

$$\Delta_{BRB} = \Delta_{tot} - \Delta_m \tag{8-5}$$

Figure 8-9 shows a comparison between the elastic stiffness calculated using the 3rd approach and the expected BRB elastic stiffness. All hysteretic behavior plots for the first BRB set were plotted using the displacements computed from the 3rd approach; as a result, the displacements actually applied to the BRBs do not exactly match the loading protocol as all displacements are lesser by the component Δ_m. This difference is mostly notable in the elastic range and less significant in the plastic range.

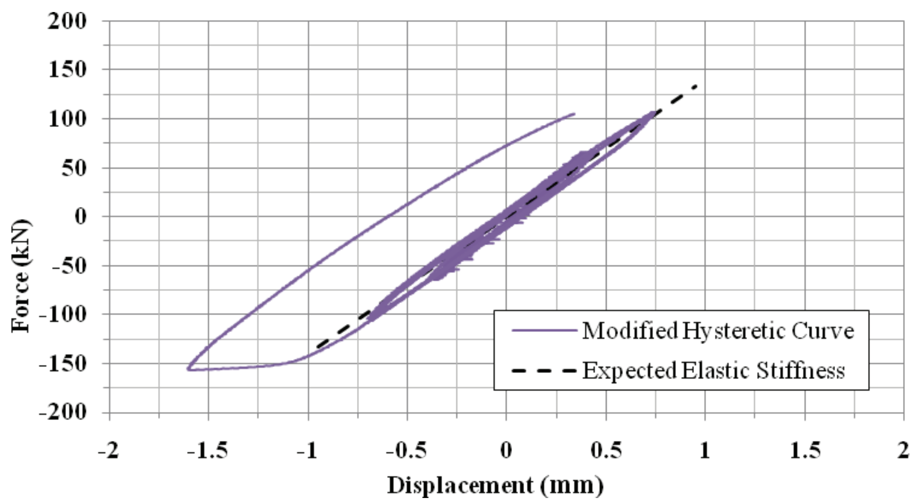

FIGURE 8-9 Expected Elastic BRB Stiffness vs. Elastic BRB Stiffness Calculated Using the 3rd Approach (For Part of the Hysteretic Curve Only)

Figure 8-10 shows the hysteretic behavior of the BRB W-I for the combined AISC/OSHPD loading protocol described earlier. Testing then continued with the low cycle fatigue loading protocol performing 4 cycles until failure as shown in figure 8-11. Average values of R_y, β, and ω where computed from the hysteretic curve at $2.0\Delta_{bm}$ as 1.1, 1.02, and 1.38 respectively for the range of deformations corresponding to 2.0 times the design story drift, Δ_{bm}, as per the AISC seismic provisions, which corresponds here to 10 times the BRB yield displacement, Δ_{by}. Note that the BRBs were ordered to accommodate a design displacement, Δ_{bm}, of 2.5 mm, and were tested up to a maximum displacement of 7.5mm, corresponding to a displacement ductility of $3.0\Delta_{bm}$ ($56\Delta_{by}$). The maximum cumulative inelastic deformation was $386\Delta_{by}$, which satisfied the AISC requirement of $200\Delta_{by}$ and translates into a large energy dissipation capacity.

After completion of the test, BRB W-I was taken apart to investigate the failure that occurred in the BRB. No signs of local buckling were observed in the yielding core; this might be due to the core's relatively small length compared to its diameter and free distance within its surrounding tube (however, only a percentage of the full length was visible and this observation was not verified with a straight edge over the core's length). Figure 8-12 shows the fracture of the yielding core of BRB W-I.

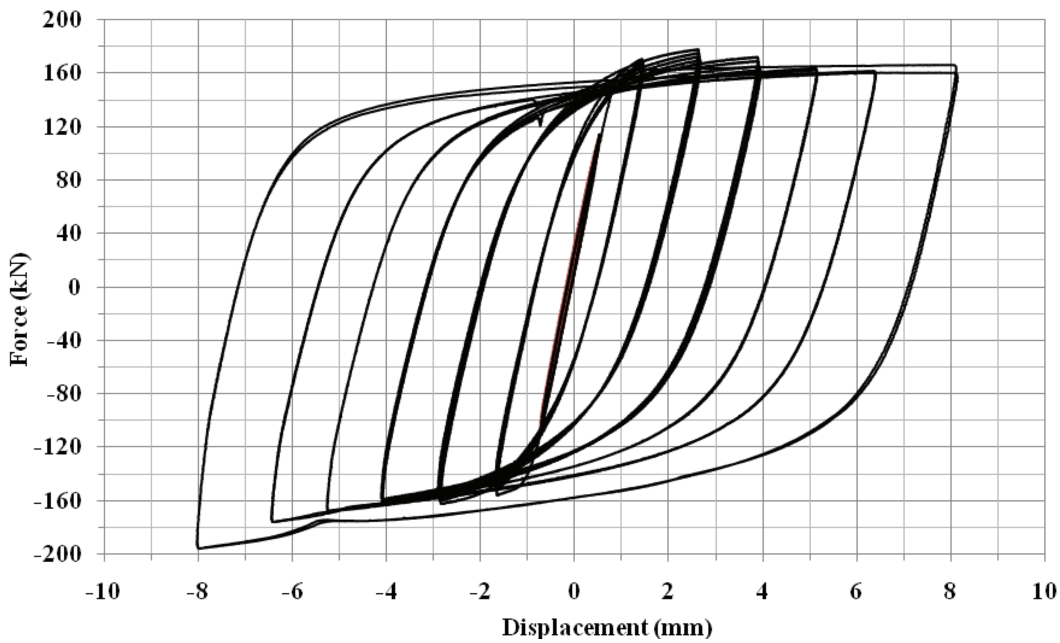

FIGURE 8-10 Hysteretic Curve for AISC and OSHPD Loading Protocols for BRB W-I

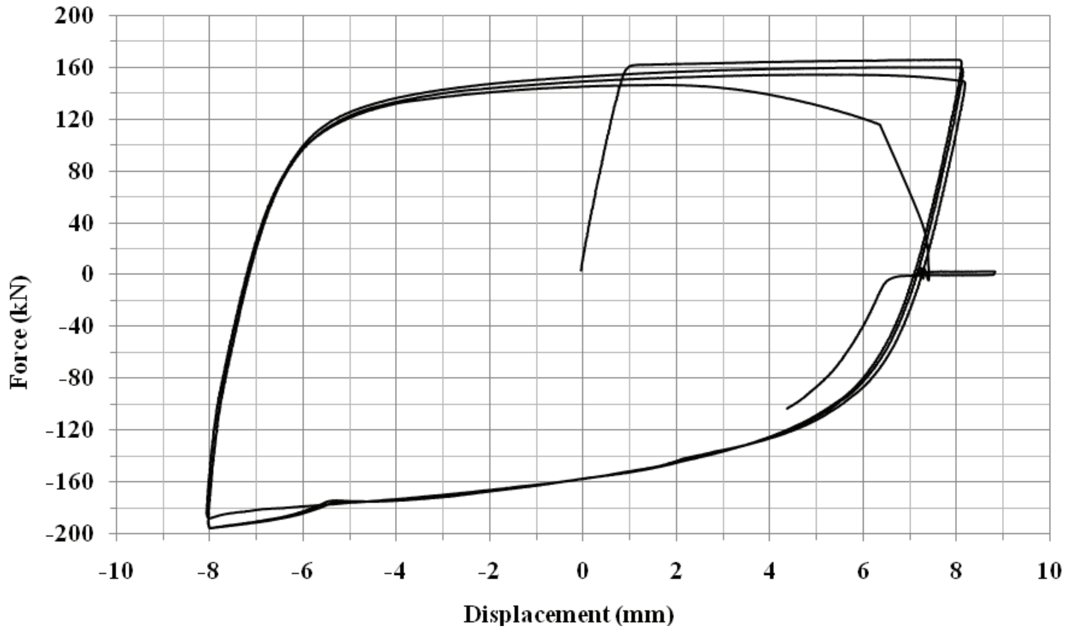

FIGURE 8-11 Hysteretic Curves for Low Cycle Fatigue Loading Protocol for BRB W-I

FIGURE 8-12 Fracture of BRB W-I at Test Completion

8.6.1.2 BRB B-I

A second BRB was then tested, denoted as BRB B-I. This BRB was bolted to the central grip gusset plate using A490 bolts of diameter 25mm (1in). The bolts where torqued to the maximum value required to achieve slip resistance (1200N.m, 910 ft.lbs). Nevertheless, full slip resistance was not expected to be achieved as the BRB gussets' relatively large flexural stiffness resisted the lateral forced applied by the bolts when torqued; this stiffness prevented the gussets' deflection necessary to clamp them to the central grip gusset plate. Figure 8-13 shows the end fixture of BRB B-I to the machine.

Testing started by applying the AISC loading protocol, yielding was again observed at about 0.5mm axial BRB displacement. The AISC loading protocol finished successfully, and the BRB exhibited stable and symmetric hysteretic curve. Then the OSHPD loading protocol was applied. Figure 8-14 shows the hysteretic behavior of the BRB B-I for the AISC and OSHPD loading protocols. The BRB displacements were measured including and excluding pin slippage as shown in the figure. For figure 8-14 (a), some jaggedness appears in the hysteretic curve at the point where slippage started to occur. Nevertheless, slippage is not observed in the hysteretic curve, as the measured displacement was from pin-to-pin excluding the pin slippage. This jaggedness is likely due to the sensitivity of the sting potentiometer, as sliding of the BRB may have introduced minor irregularities in the potentiometer reading. For figure 8-14 (b), BRB displacements were measured from gusset plate to gusset plate, which therefore includes slippage the hysteretic curve. Slippage is observed at an average of 60kN (13.5 kips), which was the load required to overcome the friction resistance between the gusset plates and the central grip gusset plate. Note that the design force required to overcome the pretension force for that particular bolt diameter and double shear condition is 225kN (50.0 kips), but this force was not achieved due to the relatively large flexural stiffness of the gusset plates as mentioned earlier. A slippage of about 2mm (0.08") is observed in the hysteretic curve, which is about the same tolerance between the bolt diameter and the bolt hole in the gusset plates. Testing then continued with the low cycle fatigue loading protocol performing 7 cycles until failure as shown in figure 8-15 which also shows hysteretic curves including and excluding slippage at the pins.

Average values of R_y, β, and ω where computed from the hysteretic curve at $2.0\Delta_{bm}$ as 1.1, 1.05, and 1.39 respectively, while the maximum cumulative inelastic deformation was $330\Delta_{by}$, which satisfied the AISC requirement of $200\Delta_{by}$ and translates into a large energy dissipation capacity.

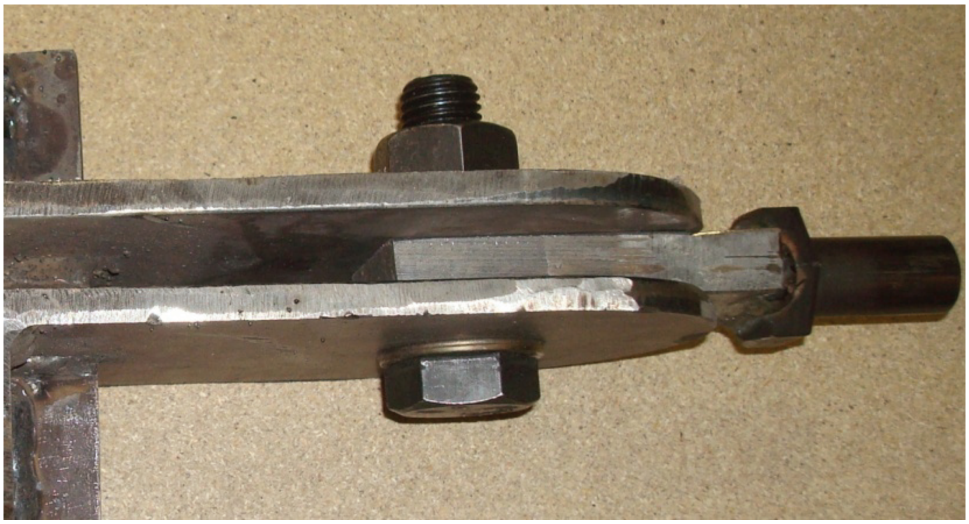

FIGURE 8-13 BRB B-I End Fixture to Machine

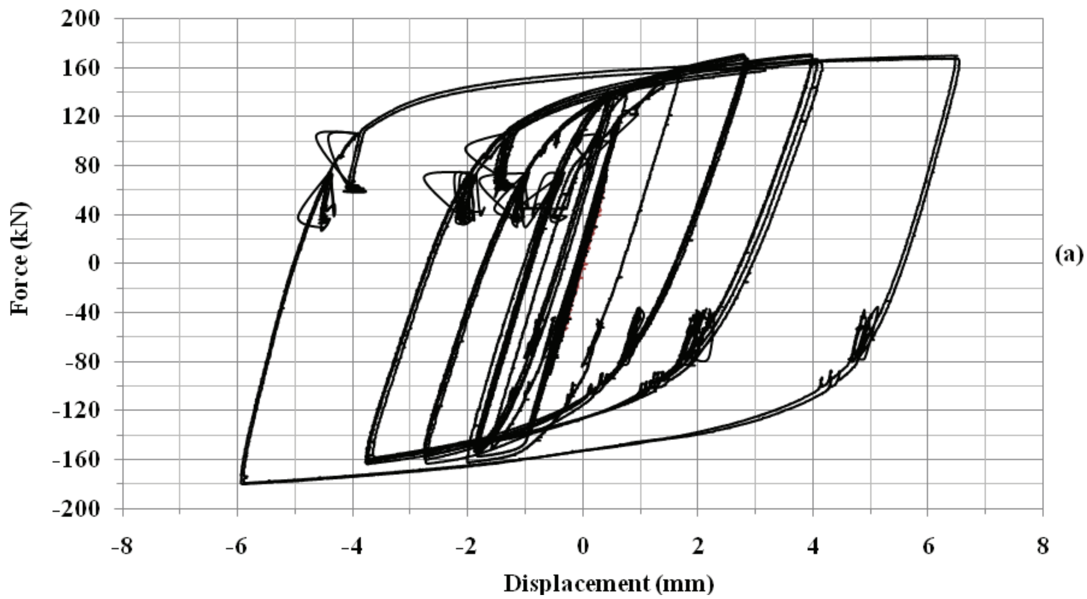

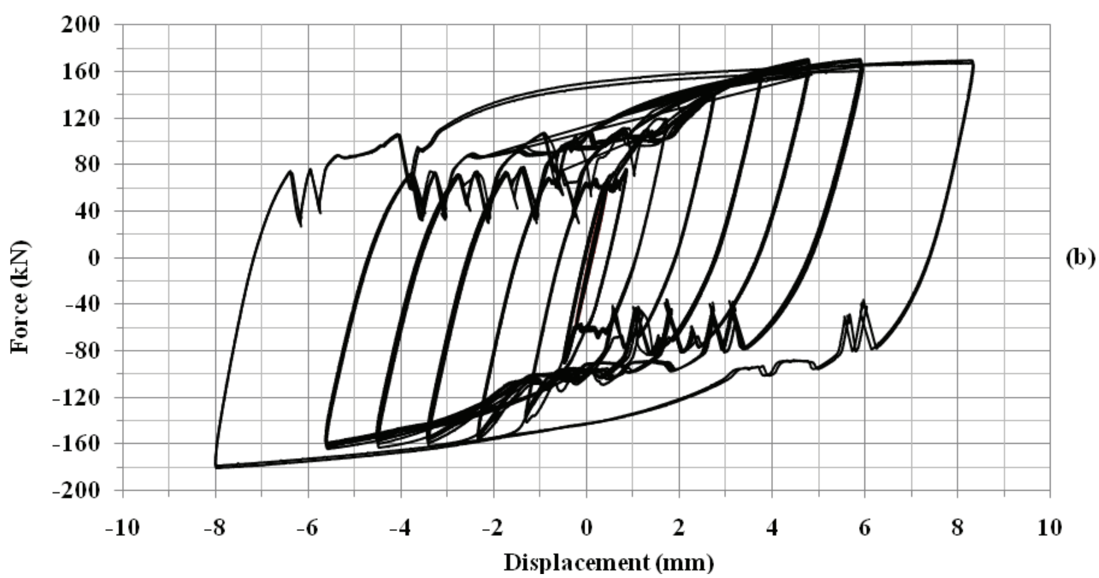

FIGURE 8-14 Hysteretic Curve for AISC and OSHPD Loading Protocols for BRB B-I; (a) Excluding Pin Slippage, (b) Including Pin Slippage

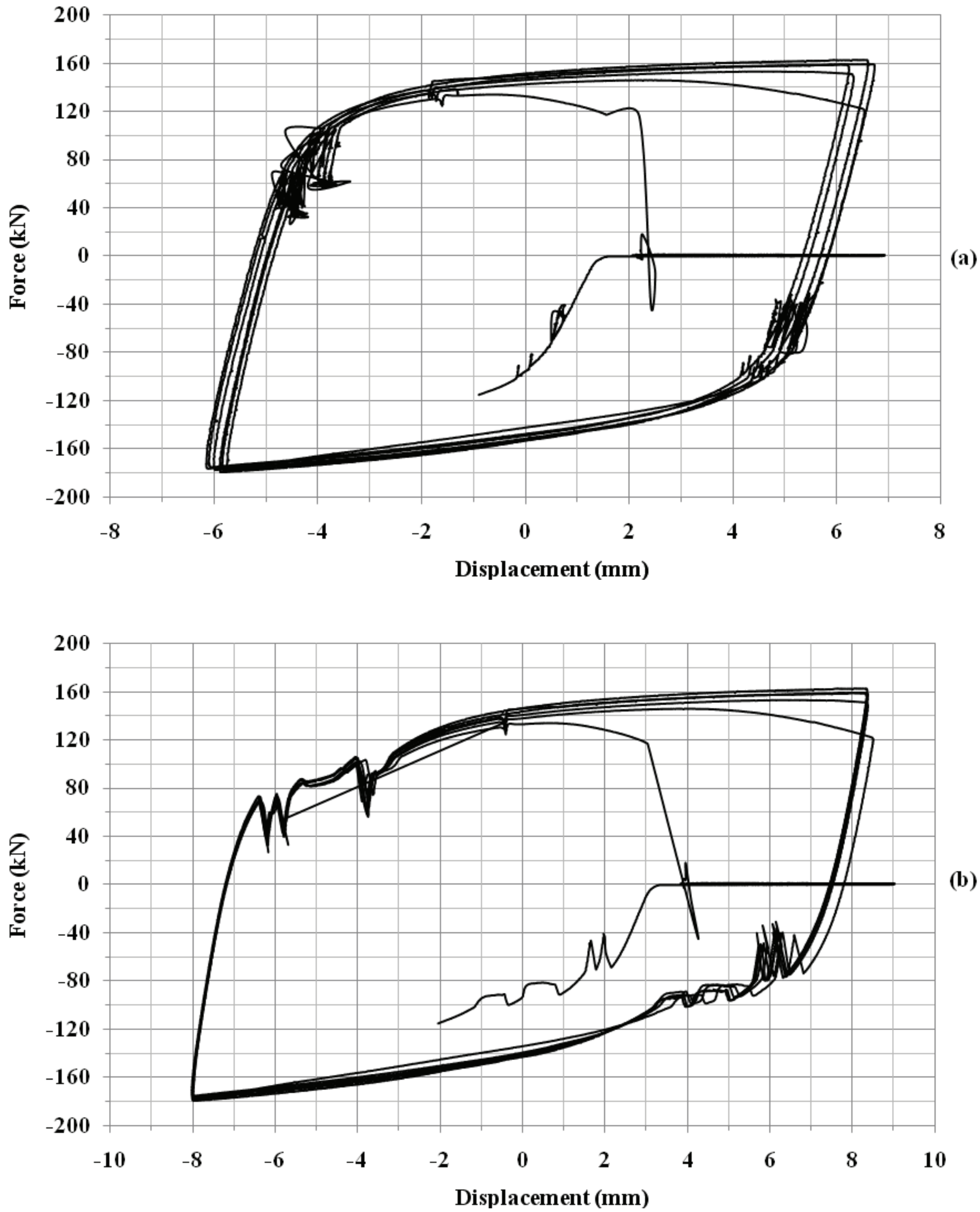

FIGURE 8-15 Hysteretic Curve for Low Cycle Fatigue for BRB B-I; (a) Excluding Pin Slippage, (b) Including Pin Slippage

8.6.1.3 BRB BW-I

A third and final BRB was then tested, denoted as BRB BW-I. For the purpose of this final test, the objective was to modify the BRB details such as to achieve a bolted connection developing full friction resistance between the BRB and the central grip gusset plate without having to weld parts of the assembly together as was done for BRB-W-I. To achieve this, one of the two BRB gussets was cut and beveled to be re-welded after the assembly was bolted together. As such, the bolt was inserted and the maximum torque required to achieve slip resistance (1200N.m, 910 ft.lbs) could be applied, allowing the free plate to displace and achieve full contact without restraints due to flexural stiffness. The whole unit was then welded back to the BRB as shown in figure 8-16.

As done before, testing first followed the AISC loading protocol; yielding was observed at about 0.5mm axial BRB displacement. The AISC loading protocol finished successfully, and the BRB exhibited stable and symmetric hysteretic curve with no signs of bolt slippage. The OSHPD loading protocol was then applied by performing two cycles at $12.5\Delta_{by}$, then two cycles at $15\Delta_{by}$. The same jump in strength during the compression cycle was observed as for BRB W-I and again was attributed to possible friction between the steel core and the steel tube. Figure 8-17 shows the hysteretic behavior of the BRB BW-I specimen for the AISC and OSHPD loading protocols. Testing then continued with the low cycle fatigue loading protocol performing 4 cycles until failure as shown in figure 8-18.

Average values of R_y, β, and ω where computed from the hysteretic curve at $2.0\Delta_{bm}$ as 1.13, 1.25, and 1.39 respectively, while the maximum cumulative inelastic deformation was $386\Delta_{by}$, which satisfied the AISC requirement of $200\Delta_{by}$. Note that a relatively higher value of β is calculated compared to the BRB W-I and BRB B-I; this is attributed to a friction force that started to develop between the yielding core and the steel sleeve for that specimen, which resulted in an increase the compression force resisted by the BRB (as read by the actuator load cell). If an extrapolation of the curve before its sudden change in slope was made to remove the effect of this friction, a β value of about 1.05 would have been calculated.
After completion of the test, BRB BW-I was taken apart to investigate the failure that occurred in the BRB. No signs of local buckling were observed in the yielding core, with the same caveats described earlier. Figure 8-19 shows the fracture of the yielding core of BRB BW-I.

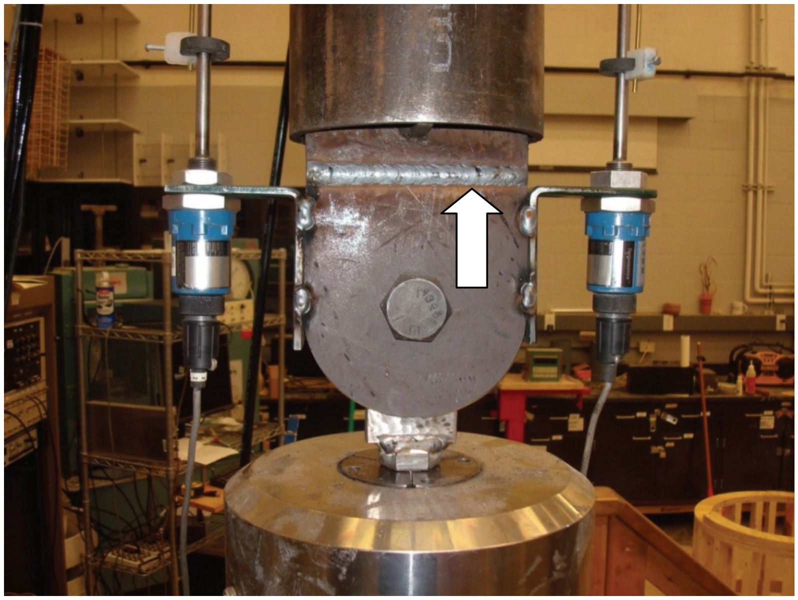

FIGURE 8-16 BRB BW-I End Fixture

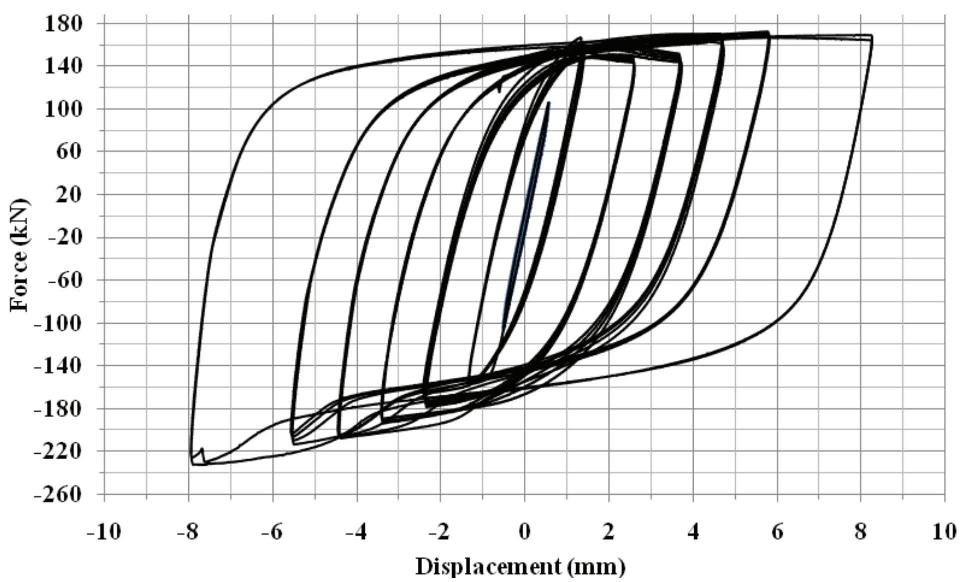

FIGURE 8-17 Hysteretic Curve for AISC and OSHPD Loading Protocols for BRB BW-I

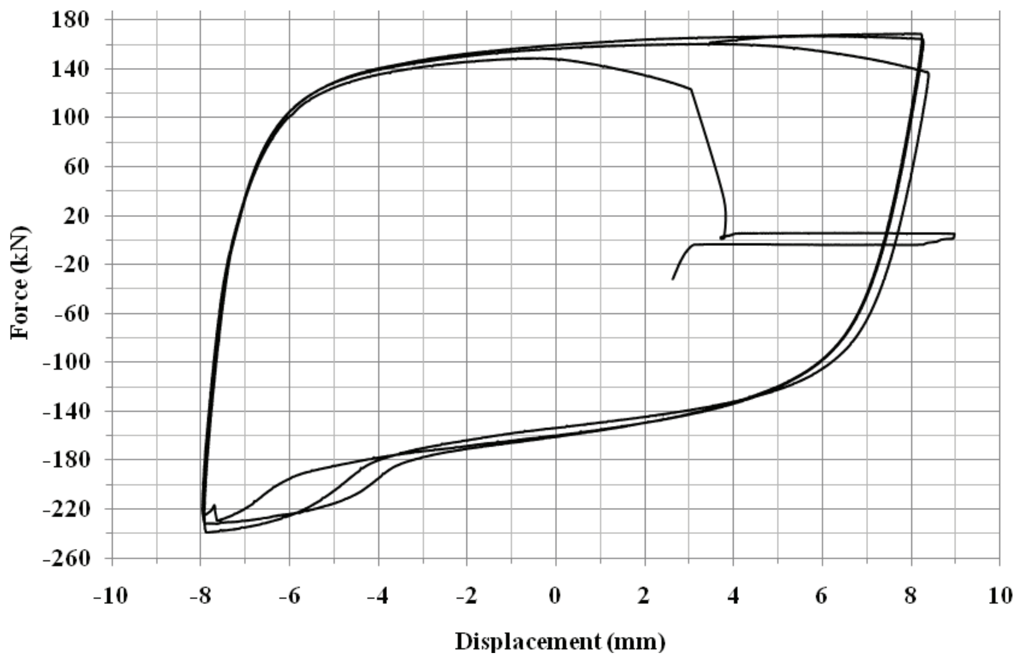

FIGURE 8-18 Hysteretic Curves for Low Cycle Fatigue Loading Protocol for BRB BW-I

FIGURE 8-19 Fracture of BRB BW-I at Test Completion

8.6.2 BRB Set II

Three of the BRBs used in specimen S2-1 were retested using the axial testing facility developed for this purpose (described in Section 8.3.2). The BRBs chosen for the uniaxial test's were the ones that underwent the least amount of inelastic deformations during the testing of specimen S2-1, based on predictions from finite element models and measured extensions during the test, namely BRB 1-II, BRB 6-II, and BRB5-II. This is because these were located near the ends of the columns where relative displacements of the columns in double curvature were of lesser magnitude. Note that the numbering of the specimens indicates the position where the BRB was located in specimen S2-1, with BRB 1 being at the top and BRB 6 at the bottom, while the roman numbering indicates which set the BRBs belongs to.

After termination of specimen S2-1 testing, the BRBs where visually inspected. Unfortunately, major cracks occurred in some of the welds connecting the yielding core to the BRB gussets as shown in figure 8-20. This was observed in BRB 2-II, BRB3-II, and BRB 4-II, where they experienced inelastic deformations of $6\Delta_{by}$, $8\Delta_{by}$, and $17\Delta_{by}$ respectively. This indicated that the weld size used between the yielding core and the BRB gussets was not sufficient to resist the axial forces that developed in the BRBs after their yielding, and those observed fractures developed before reaching the 50% strain hardening observed in the uniaxial tests of retrofitted BRBs described later. A more serious matter observed in BRB 1-II and BRB 6-is that that some of the welds connecting the yielding core to the rest of the BRB were missing as shown in figure 8-21. These fabrication errors were reported to the BRB manufacturer (Star Seismic), who took the necessary rigorous steps to prevent re-occurrence of this quality control failure.

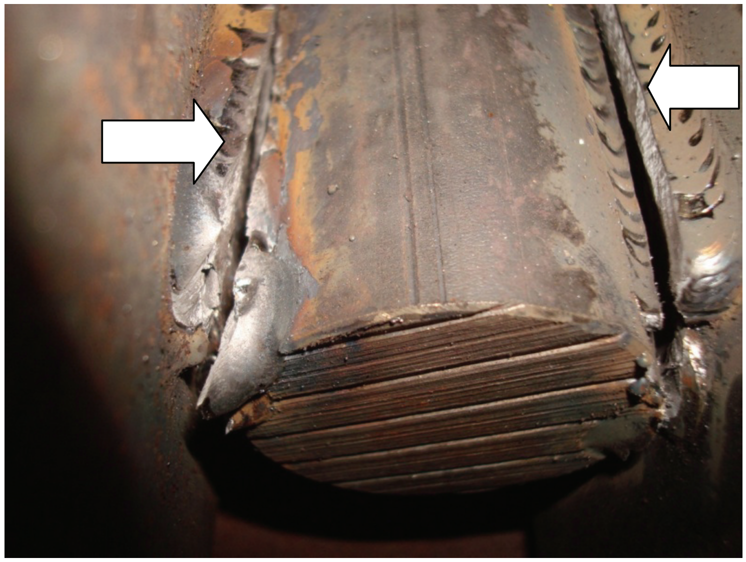

FIGURE 8-20 Weld Failure in BRB4-II after Termination of Specimen S2-1 Testing

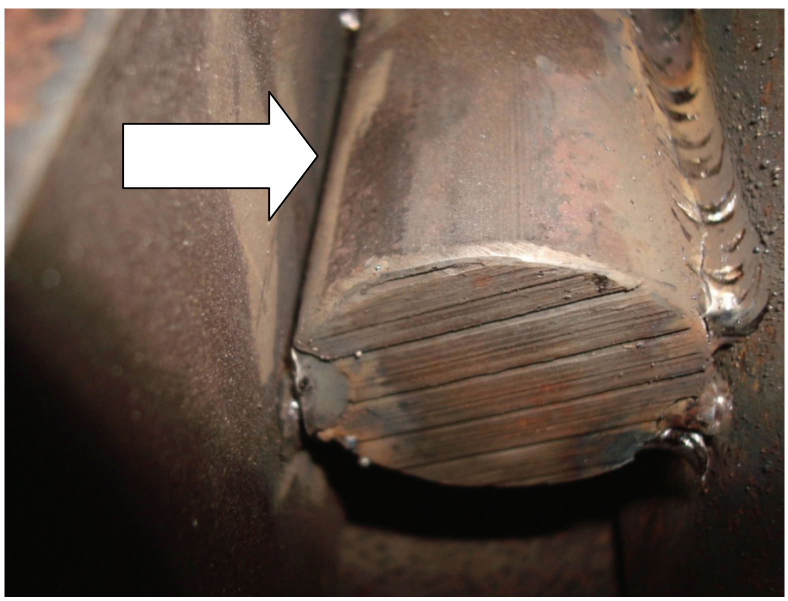

FIGURE 8-21 Missing Weld in BRB1-II

8.6.2.1 BRB 5-II

BRB 5-II was located second from the bottom in specimen S2-1. The maximum BRB inelastic deformation observed during specimen S2-1 testing for BRB 5-II was $8\Delta_{by}$, as described in section 7.5.3. BRB 5-II was tested as is, as after visual inspection no cracks in the welds connecting the yielding core with the gusset plate were observed, as shown in figure 8-22. It was expected that failure could occur in the weld before termination of the test as several BRBs suffered weld fracture during the tests of the structural fuse specimen S2-1, as stated earlier, but it was decided to test it as is, in order to establish (at least approximately, as the welds would vary from BRB to BRB) how much inelastic rotation it could likely withstand before the welds fail. It was not known at what elongation level the BRB's welds fractured during specimen S2-1 testing, as there was a concern that they could have fractured early in the test and therefore only experienced minor (or no) inelastic deformation from which minor (or no) hysteretic energy would have been dissipated by the BRBs. In this case, controlling the test displacement protocol was done by monitoring the average of the four string potentiometers installed pin-to-pin along the BRB, which does not include the pin slippage. In addition, the BRBs displacements including pin slippage was captured using two string potentiometers installed top and bottom along the gusset plates.

Figure 8-23 shows the resulting hysteretic curve for BRB 5-II, including pin slippage and measured by string potentiometers installed pin-to-pin, as well as excluding pin slippage and measured by string potentiometers installed gusset plate to gusset plate. It can be seen from the figure that the BRB exhibited a stable and symmetric hysteretic curve, and yielding was observed at about 0.6mm axial BRB displacement. A 1mm (0.04") pin slippage can also be observed in the figure. Unlike the first BRB set, slippage here is observed at the zero force level when the BRB starts to reverse the direction of its motion, due to the fact that no pretention was induced between the gusset plates as a true pin condition was used (with pins rather than pre-tensioned bolts); as a result, slip occurred between the pin and the gusset at zero load until the pins hit the edge of their respective hole, repeating the process upon load reversal, also at zero load. Fracture of the BRB weld occurred at the 4th cycle of the $7.5\Delta_{by}$ displacement magnitude, after the BRB experienced a cumulative inelastic deformation of $100\Delta_{by}$. Fracture developed in the welds as shown in figure 8-24. The BRB did not pass the $200\Delta_{by}$ AISC recommendation, from which it was decided to redesign the welds and reinforce one of the BRB with missing welds and tests again.

Average values of R_y, β, and ω where computed from the hysteretic curve at $1.5\Delta_{bm}$ ($7.5\Delta_{bm}$) as the specimen did not reach the $2\Delta_{bm}$ ($10\Delta_{by}$) specified by the AISC seismic provisions for calculating these values. These values were found to be equal to 1.01, 1.06, and 1.2 respectively, while the maximum cumulative inelastic deformation was $100\Delta_{by}$, which did not satisfy the AISC requirement of $200\Delta_{by}$.

FIGURE 8-22 Weld Condition in BRB 5-II after Termination of Specimen S2-1 Testing

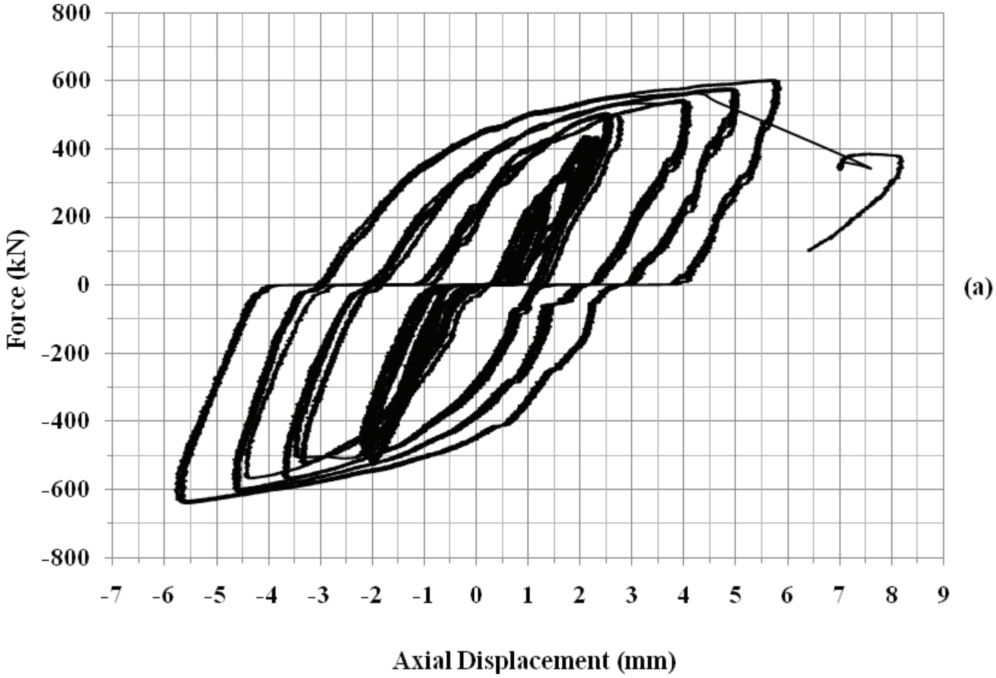

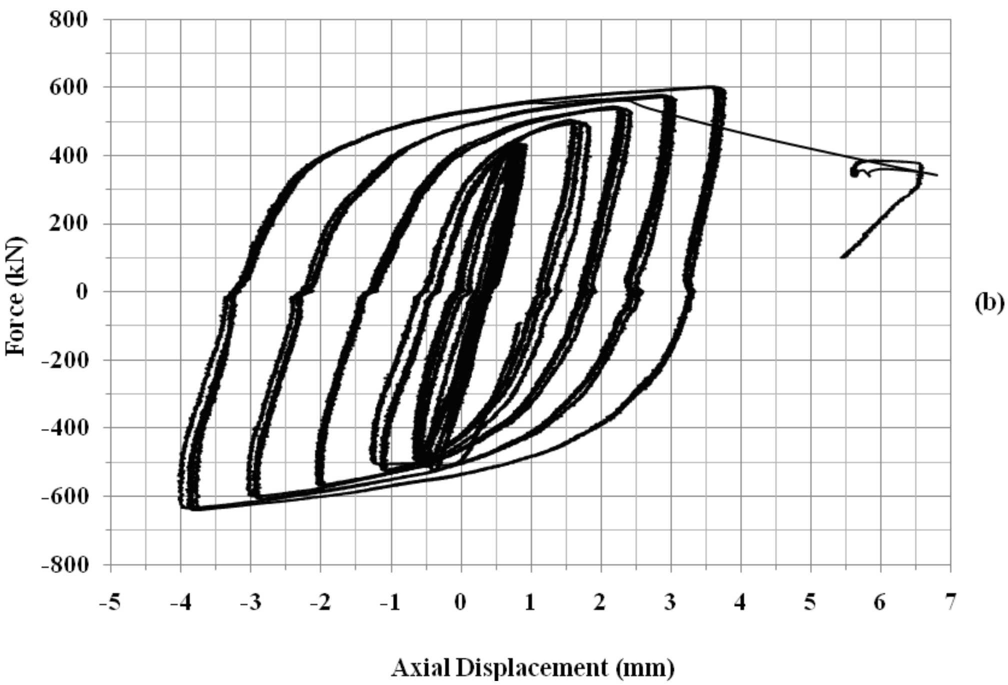

FIGURE 8-23 Hysteretic Curves for BRB 5-II for the AISC Protocol; (a) Including Pin Slippage, (b) Excluding Pin Slippage

FIGURE 8-24 Weld Failure of BRB 5-II at 7.5Δ_{by}

8.6.2.2 BRB 1-II

BRB1-II was chosen for the next test. Welding reinforcement for the existing welds was performed prior to testing. BRB 1-II was located at the top of specimen S2-1 and experienced an inelastic deformation of 3Δ_{by}. Figure 8-25 shows the BRB 1-II after redesigning the welds. Testing started using the AISC/OSHPD loading protocol and yielding was observed at about 0.55mm axial BRB displacement, and the BRB exhibited stable and symmetric hysteretic curve until reaching 7.5Δ_{by} where a sudden oil leak in the hydraulic system of the actuator being used took place. Figure 8-26 shows the hysteretic curve for BRB 1-II until 7.5Δ_{by}, excluding the pin slippage. The actuator was then removed and replaced by another one having the same dimensions and capacity. It was decided to continue testing the same BRB even though obtaining a total hysteretic curve was challenging as all the setup including instrumentations had to be removed and redone to replace the actuator, but a sense of the number of inelastic cycles that the BRB could withstand after redoing the welds could be obtained and the question that the welds could sustain the repetitive inelastic cycles could be answered. Testing restarted from 7.5Δ_{by} axial displacement, and continued till the end of the loading protocol. After reaching an axial displacement of 10Δ_{by}, rotation of the gusset plate connecting the BRB to the actuator was observed in the compression part of the cycle. This was due to the geometric nonlinearity of the system, from which under an axial compression load of 800 kN (180kips) and the presence of two pins side by side as described earlier, rotation of the gusset plate was observed. This rotation influenced the hysteretic curve, as an increase in the axial load was observed in the compression side to overcome the rotation of the BRB. It was decided to terminate testing at that point and do not continue with the fatigue cycles, as excessive rotation in the BRB would be observed and inaccurate results would be obtained for the hysteretic curve of the BRB. Figure 8-27 shows the hysteretic curve for BRB 1-II starting from $7.5\Delta_{by,}$ excluding the pin slippage.

Average values of R_y, β, and ω where computed from the hysteretic curve at $2.0\Delta_{bm}$ as 1.03, 1.27, and 1.16, respectively. Again the relatively high β value is attributed to the friction force that develops between the yielding core and the steel sleeve. The maximum cumulative inelastic deformation was $274\Delta_{by}$, which satisfied the AISC requirement of $200\Delta_{by}$ and translates into a large energy dissipation capacity.

FIGURE 8-25 Redesigned Welds for BRB 1-II

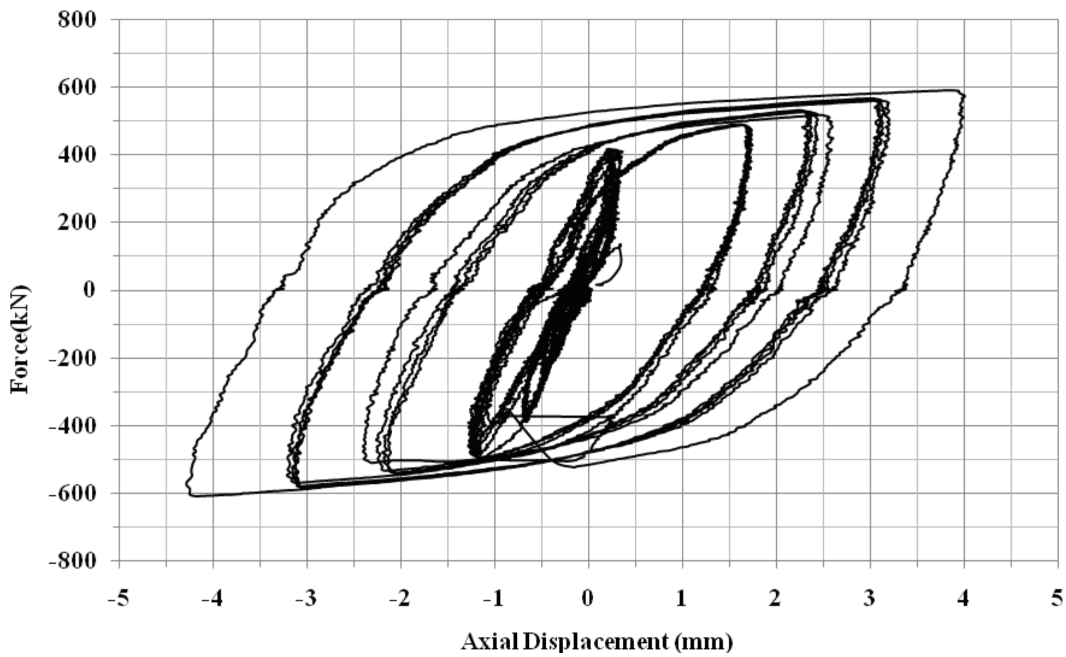

FIGURE 8-26 Hysteretic Curve for BRB 1-II until 7.5Δ_y,

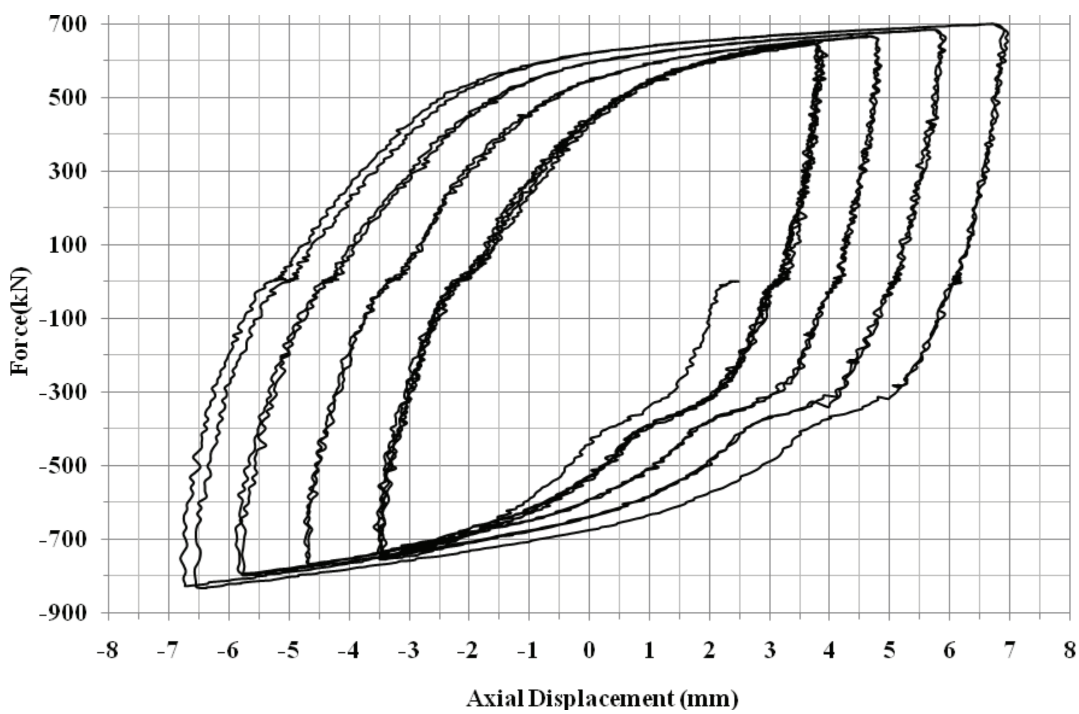

FIGURE 8-27 Hysteretic Curve for BRB 1-II starting from 7.5Δ_y

8.6.2.3 BRB 6-II

A final BRB was chosen to be tested to obtain a more reasonable and complete hysteretic curve, taking into account all the challenges that occurred in the two previous tests. BRB 6-II was chosen for that final test; this BRB was located at the bottom of specimen S2-1 and exhibited an inelastic deformation of $7\Delta_{by}$. The same welding reinforcement as in BRB 1-II was done, to overcome the deficiencies in the welds provided by the manufacturer as described earlier. Also to overcome the gusset plate rotation that was observed in the previous test, it was decided to illuminate one of the rotating pins by welding the BRB directly to the gusset plate connected to the actuator. The back draw of this procedure is that the gusset plate could not be used again for another test, but since this was the last test the matter was not of a concern. The other end connected to the reaction block was left as is, as slippage effect could also be captured. Figure 8-28 shows a photograph of the BRB connected to the gusset plate by welding.

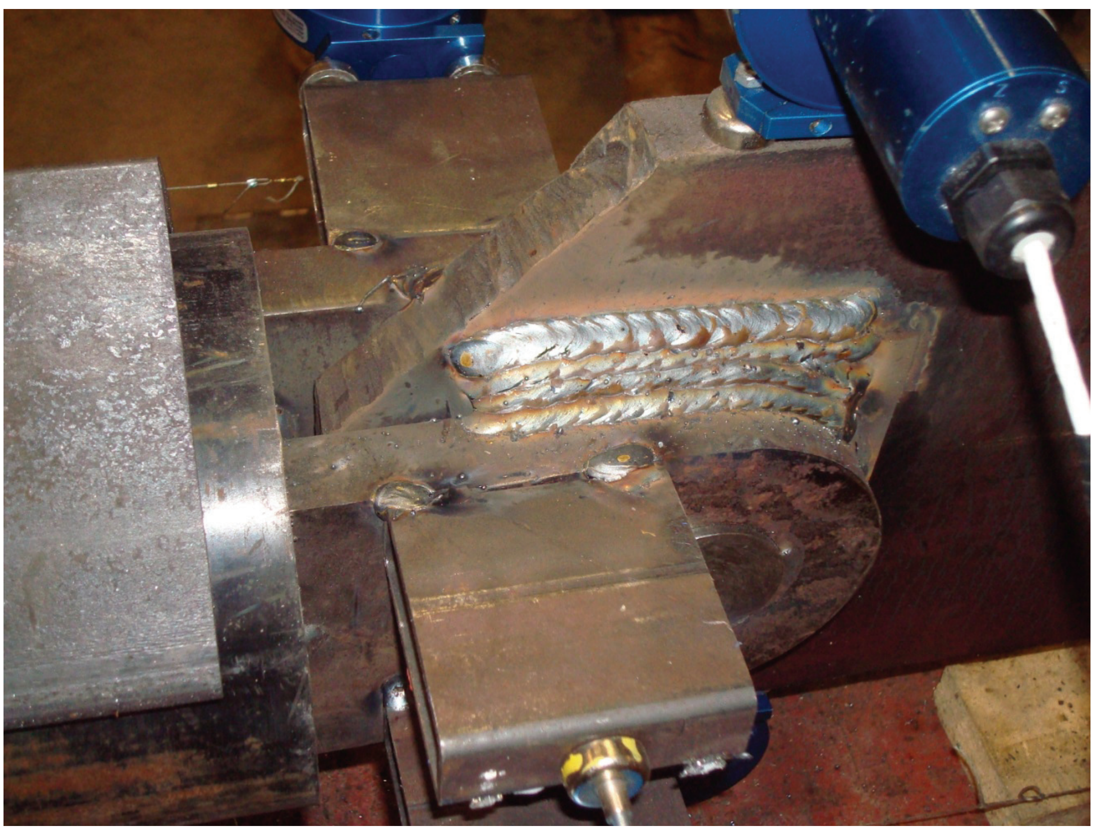

FIGURE 8-28 BRB6-II to Gusset Plate Connection at the Actuator Side

Testing started by applying the AISC loading protocol, yielding was observed at about 0.5mm axial BRB displacement. The AISC loading protocol finished successfully, and the BRB exhibited stable and symmetric hysteretic curve. The OSHPD loading protocol was then applied by performing two cycles at $12.5\Delta_{by}$, then two cycles at $15\Delta_{by}$. At the compression part of the first cycle of displacement $15\Delta_{by}$, twisting of the BRB gusset plate connected to the actuator was observed and the BRB was out of alignment with the actuator as shown in figure 8-29. It was decided to continue with the final cycle of the OSHPD protocol, and install two angles along the gusset plate to act as guides preventing the BRB from being out of alignment with the actuator and preventing the gusset plate from further twisting.

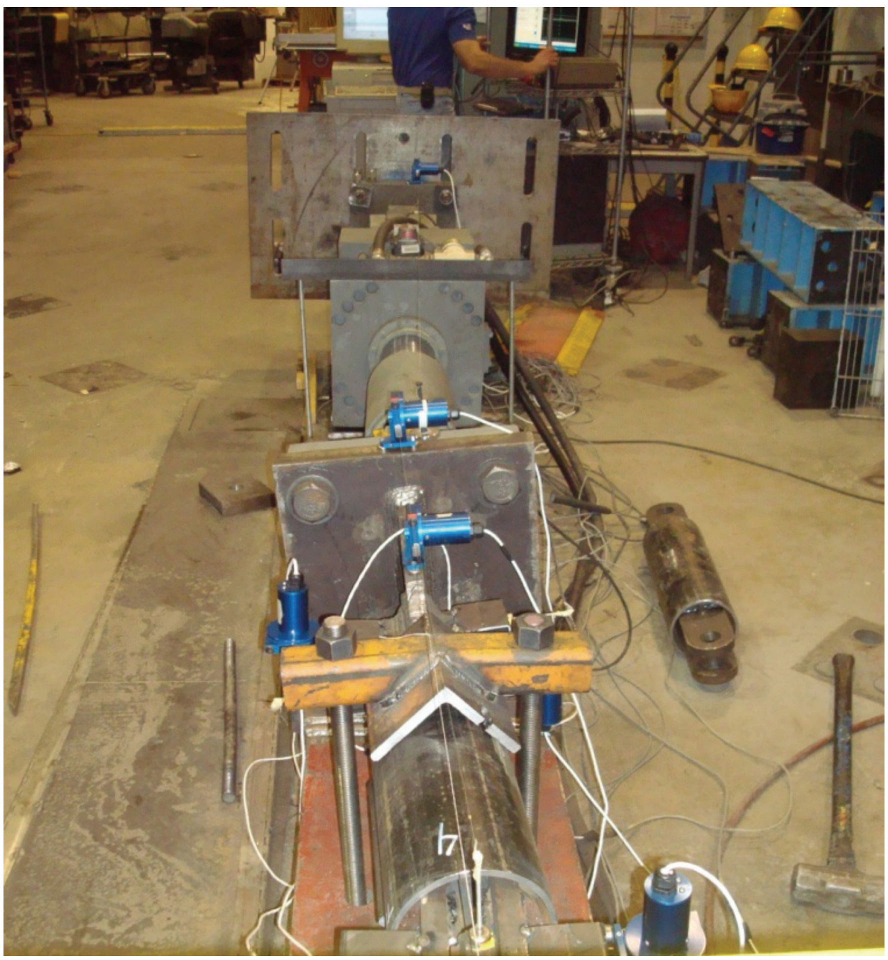

FIGURE 8-29 Gusset Plate twisting at $15\Delta_y$

Testing then continued with the low cycle. Minor twisting of the gusset plate was expected and occurred at the compression part of each cycle as shown in figure 8-30. Nevertheless the BRB stayed in place due to the presence of the guide angles shown in the figure.

Figure 8-31 shows the hysteretic behavior of the BRB 6-II for the AISC and OSHPD loading protocols. Figure 8-32 shows the hysteretic behavior of the BRB for the low cycle fatigue. At the compression part of each cycle, a squeaky noise was heard beyond a displacement of 2mm (0.08"), this was attributed to the friction that occurred between the gusset plate as is twists and the guide angles. The effect of friction can easily be seen in the hysteretic curve as a sudden jump in strength occurs at 2mm (0.08") displacement in the compression side. A total of 13 cycles were performed and the BRB behaved in a stable manner, at the compression part of the 14th cycle, a moderate bang was heard and the load dropped by 20%, the tension part of the cycle was then performed and the load drop was constant until reaching a displacement of 5mm (0.2"), there a huge bang was heard and the load dropped to zero and the test was called to an end.

Figure 8-33 shows a comparison between the final cycle of the OSHPD loading protocol (before installing the guide angles), and the low cycle fatigue cycles (after installing the guide angles). It can be seen that at 2mm (0.08") displacement a jump in the strength occurs at the compression side of the loop due to the friction that occurs between the twisting gusset plate and the guide angles. The effect of that friction can be illuminated by comparison as shown in the figure.

Average values of R_y, β, and ω where computed from the hysteretic curve at $2.0\Delta_{bm}$ as 1.0, 1.14, and 1.19 respectively, while the maximum cumulative inelastic deformation was $666\Delta_{by}$, which satisfied the AISC requirement of $200\Delta_{by}$ and translates into a large energy dissipation capacity.

After completion of the test, BRB 6-II was taken apart to investigate the failure that occurred in the BRB. It was observed that the BRB was not fractured, and failure occurred in the welds connecting the rod to the BRB gussets due to fatigue of the welds as shown in figure 8-34. From which it was concluded that the BRB could sustain even more inelastic cycles beyond the experiment if weld fatigue was taken into account when designing the welds and the failure was controlled to occur in the rod.

Finally, to investigate the observed BRB gusset plate rotation, plots for the horizontal and vertical BRB gusset plate rotation were constructed using the four string potentiometer installed across the BRB. The horizontal BRB gusset plate rotation was calculated by averaging the top and bottom string potentiometer readings installed at the east side of the BRB, then the resulting readings were subtracted from the average string potentiometer readings installed top and bottom of the west side of the BRB. The results were then divided by the average horizontal distance between the string pots. Figure 8-35 shows a plot between the horizontal BRB gusset plate rotation being in the vertical axis of the plot, and the BRB force being on the horizontal axis of the plot. It can be seen from the figure that the amount of horizontal rotation increased at each cycle and that a maximum horizontal rotation of about 0.05 rad developed in the BRB.

Using the same approach, the vertical rotation of the BRB gusset plate was calculated by averaging both top string potentiometer readings installed at the east and west sides of the BRB, and the resulting readings was subtracted from the average string potentiometer readings installed bottom of the west and east sides of the BRB. The results were then divided by the average vertical distance between the string pots. Figure 8-36 shows a plot between the vertical BRB gusset plate rotation and the BRB force. It can also be seen that the vertical rotation increased at each cycle up to a maximum observed vertical rotation of about 0.013 rad. Vertical movement of the gusset inside the tube was also observed, but not measured.

These rotations could have contributed to the weld failure observed at the end of the test due to unanticipated bending stresses. On that basis, it may be desirable for BRBs of this type to be designed in ways to decrease this rotation phenomenon. Slight alterations would be possible to eliminate gaps that exist between the gusset plate and the outer steel sleeve (by increasing the dimensions of the gusset plate), or it might be possible to add an extra cap at both ends of the BRB welded to the outer sleeve and having a hole with minimum tolerance through which the gusset could move freely while guided to remain centered.

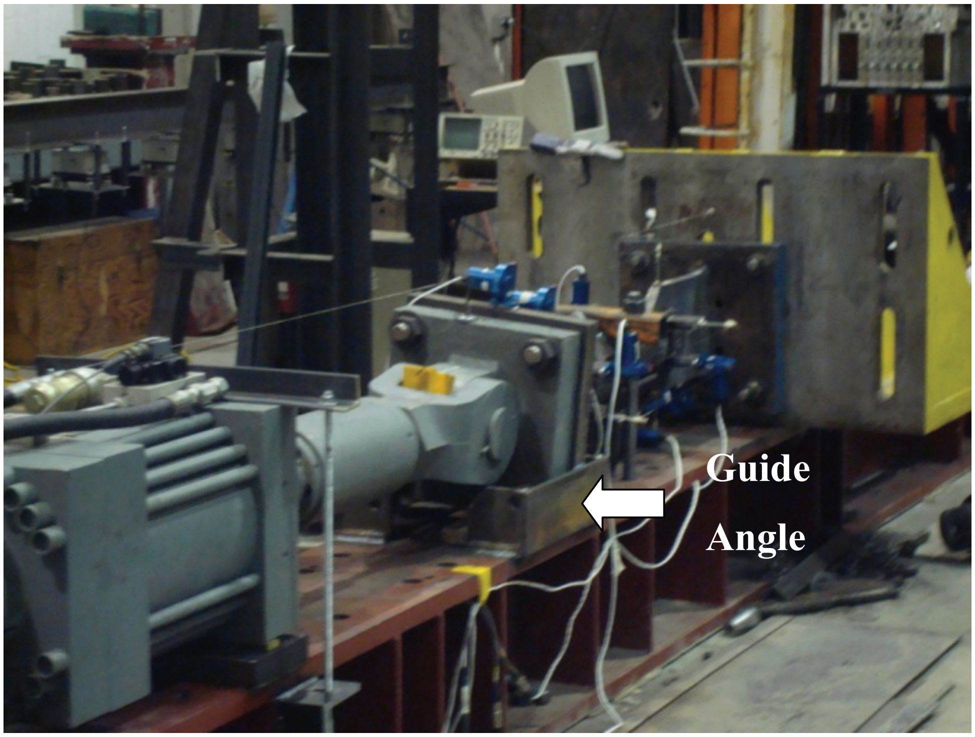

FIGURE 8-30 Twisting of Gusset Plate at Low Cycle Fatigue Cycles

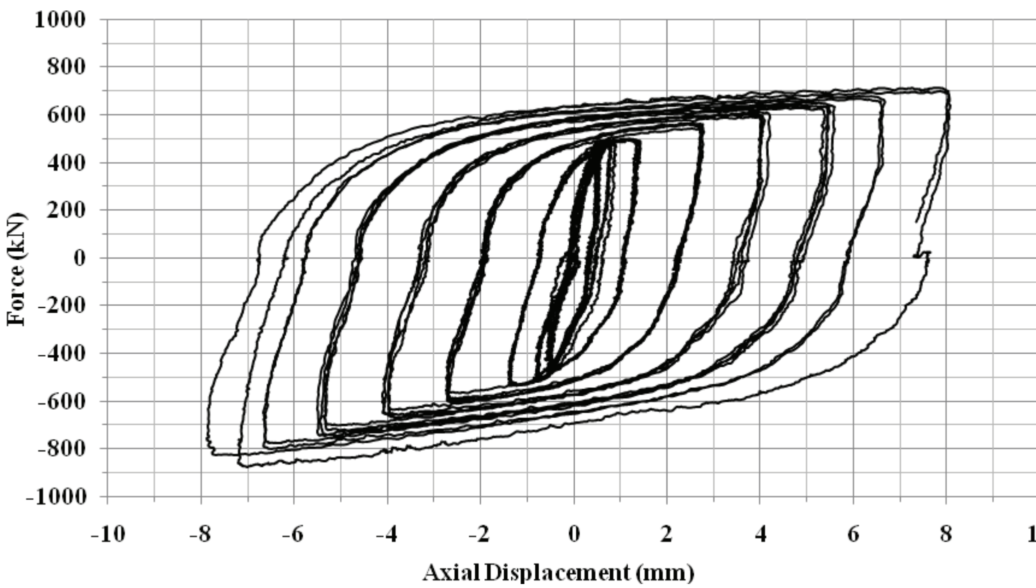

(a)

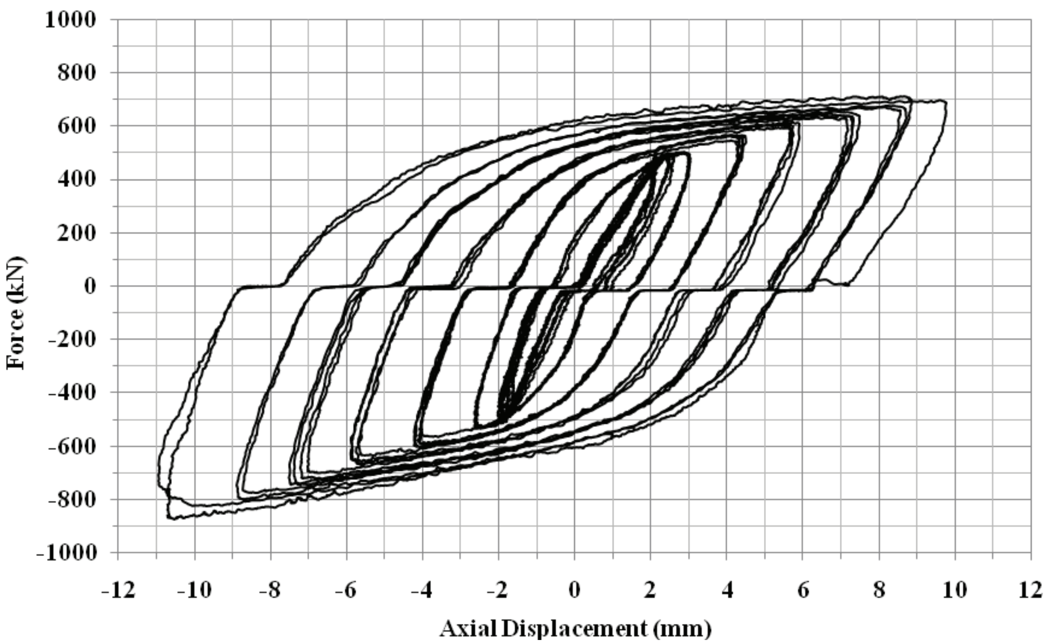

(b)

FIGURE 8-31 Hysteretic Curve for AISC and OSHPD Loading Protocols for BRB 6-II; (a) Excluding Pin Slippage, (b) Including Pin Slippage

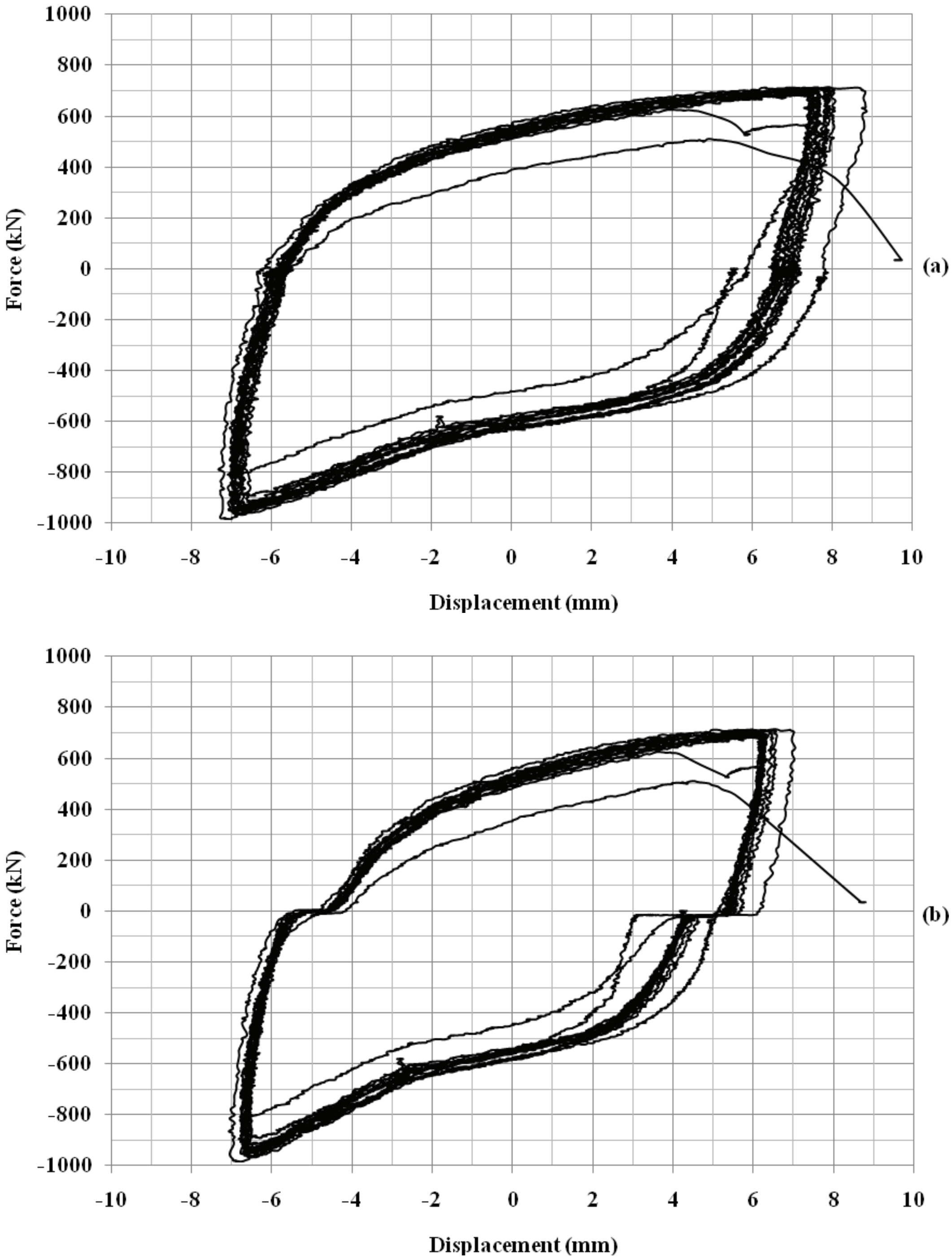

FIGURE 8-32 Hysteretic Curves for Low Cycle Fatigue Loading Protocol for BRB6-II; (a) Excluding Pin Slippage, (b) Including Pin Slippage

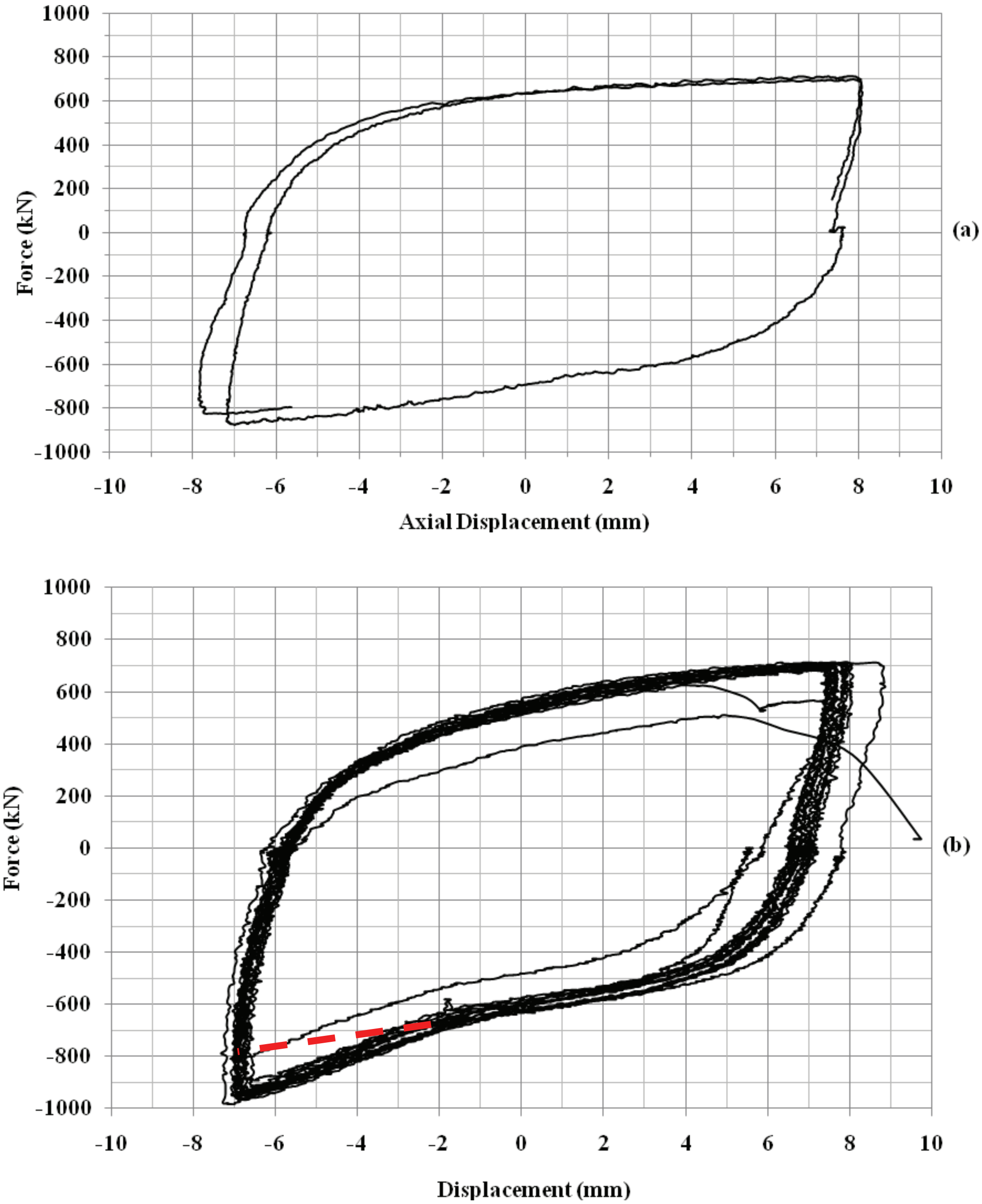

FIGURE 8-33 Comparison between; (a) Last Cycle of the OSHPD Loading Protocol at 15Δ_{by}, (b) Hysteretic Curve of Low Cycle Fatigue Loading Protocol

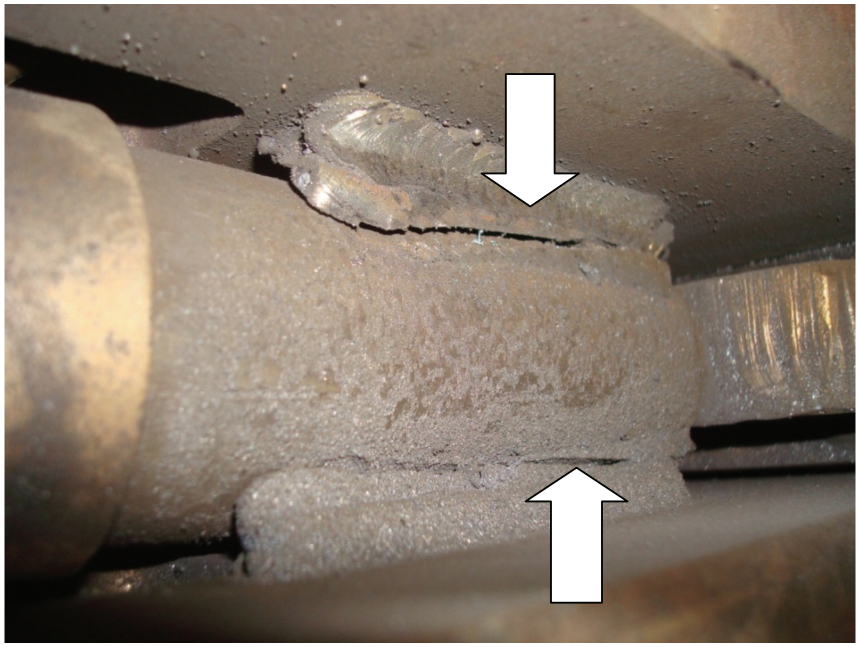

FIGURE 8-34 Weld Fatigue of BRB 6-II

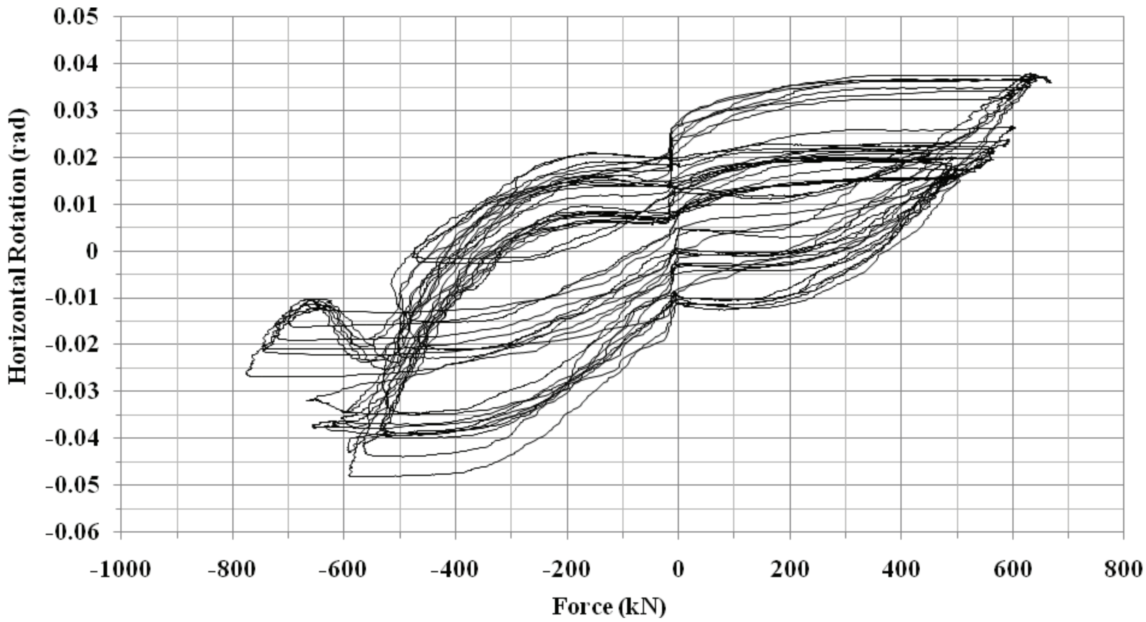

FIGURE 8-35 Horizontal BRB Gusset Plate Rotation vs. BRB Force

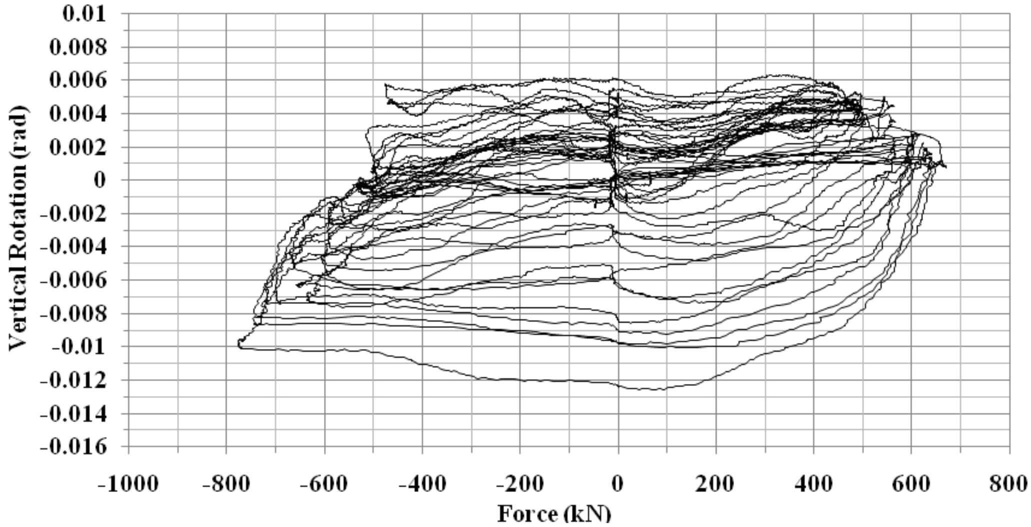

FIGURE 8-36 Vertical BRB Gusset Plate Rotation vs. BRB Force

8.7 Summary

Experimental axial testing has been performed on two sets of BRBs having the same yielding core length but different in axial strength and end fixture conditions. All results exhibited stable hysteretic behavior and dissipated energy more that the required by the AISC seismic provisions. Tabulated results summarizing the measured properties for all tests along with the maximum results are presented in table 8-2.

TABLE 8-2 Static Test Results

Test	P_{ysc} (kN)	Δ_{by} (mm)	K_b (kN/ mm)	T_{max} (kN)	C_{max} (kN)	R_y	β	ω	Cycles to fracture	Fracture Disp.	Cum. Inel. Def./
BRB W-I	153	0.5	280	165	168	1.15	1.02	1.38	32	$15\Delta_{by}$	386
BRB B-I	149	0.5	298	167	176	1.12	1.05	1.39	35	$15\Delta_{by}$	330
BRB BW-I	150	0.5	300	167	210	1.13	1.25	1.39	32	$15\Delta_{by}$	386
BRB 5-II	538	0.6	846.6	600	633	1.01	1.06	1.2	20	$7.5\Delta_{by}$	100
BRB 1-II	549	0.55	912.7	677	779	1.03	1.27	1.16	28	$15\Delta_{by}$	274
BRB 6-II	533	0.5	1000	663	758	1.0	1.14	1.19	42	$15\Delta_{by}$	666

SECTION 9
EXPERIMENTAL AND ANALYTICAL INVESTIGATION OF STEEL PLATE SHEAR LINKS AS STRUCTURAL FUSES

9.1 General

This section describes the design and detailing of SPSLs for quasi-static cyclic testing, the design of a setup to carry out the testing, and the instrumentation used to capture results. The dimensions of the SPSLs to be tested were selected using design equations described in section 4. The loading protocol used and observations made during the quasi-static testing are then described. Specimen link shear versus total rotation hysteresis curves are then plotted. Photographs and a description of observations made during the cyclic history are also provided for each SPSL. Throughout this section, all rotations referred to are total rotations, i.e., combined elastic and plastic rotations. Finite element models are then generated to replicate the observed hysteretic behavior of the SPSLs being tested, and provide insight into the general behavior of the SPSLs.

9.2 SPSLs Selection

Seven SPSLs were selected for quasi-static testing and shown in figure 9-1. Three of those were restrained against out of plane motion, and were shaped to have one of two different link edge angles representing the balanced and the over balanced cases described earlier in section 4.6. Four of the seven SPSLs specimens were unrestrained against out-of-plane buckling: two had a balanced link angle and was tested to compare their behavior with the restrained ones, and two were unrestrained square specimens.

The three SPSLs restrained against out of plane motion were denoted as SP-R1, SP-R2, and SP-R3. All links had the same outer dimensions of 600mm x 400mm (24" x 16"). The differences between the specimens are the angle θ and type of lateral restraint; where θ is the link edge angles and defined in section 4.5. This angle θ was equal to θ_b for SP-R1 and SP-R2, and θ was greater than θ_b for SP-R3, where θ_b is the balanced link edge angle and also defined in section 4.5. As shown in figure 9-1, θ was 25 degrees and 40 degree for figure

9-1(a) and figure 9-1(b) respectively. The angle selected for SP-R1 and SP-R2 was intended to insure that shear yielding in the middle part of the specimen occurs simultaneously with flexural yielding at the wedges parts for both specimens as described earlier in section 4.6.

Restraining out-of-plane buckling for specimens SP-R1, SP-R2, and SP-R3 was done by using a fiberglass building panel material known as Composolite, which is a patented advanced composite building panel system suitable for major load bearing structural applications. It has a major advantages of having relatively high ultimate tensile strength (214MPa, 31.1ksi), being light weight and corrosion resistant. These FRP panels were received as larger components originally 2'x24', and cut to the small panels of 2'x1.3' needed to fit around the specimens. Wood pieces of dimensions 50mm x 100mm (2"x4") were inserted in the hollow parts of the panels. These wood pieces were installed to enhance the flexural strength of the panels; this was also done to prevent the connecting bolts from punching through the panels during testing, as a tensile force of about 10kN (2.5kips) was expected to develop per bolt to prevent the specimen from buckling. Dimensions and weight of a typical Composolite panel unit is shown in figure 9-2. Mechanical properties are also shown in table 9-1.

During testing of specimen SP-R1, while the fiberglass was found to have an adequate strength to resist the out of plane forces resulting from buckling of the specimen's steel plate, it was also found to be more flexible than anticipated and not effective to prevent the development of buckling in the SPSL, as described in section 9.7.2. To increase the stiffness of the panels, two W4x13 cross beams were installed on each panel for the testing of specimens SP-R2 and SP-R3, understanding that this was done for expediency and that a more aesthetic solution would have to be implemented in the field (which was not possible in this case due to the tight testing schedule). Figures 9-3 and 9-4 show the lateral restraining system details used for all specimens; a photo is also shown in figure 9-5.

A link length, e, of 400mm (16") was selected according to the design requirements presented in section 4.4, from which the balanced link angle, θ_b, was then calculated from equation (4-23) to be as 25 degrees. The link length was then checked to not exceed the limit specified by equation (4-20) as exceeding this limit would have resulted in the link yielding in flexure rather than shear. A constant link thickness of 5mm (3/16") was then chosen for all specimens, which resulted in an approximate calculated maximum shear force of 667kN

(150kips) for the strongest link specimen tested. These dimensions were the same as the links tested for specimen S-1 in sections 5 and 6, which was desirable to easily investigate the behavior of the link being tested in the bridge pier.

The unrestrained SPSLs were denoted as SP-U1, and SP-U2. These SPSLs had the exact same dimensions and link edge angle as SP-R1and SP-R2, but no lateral restraining system was provided and the links were free to buckle out of plane. Figure 9-6 shows a photo of the unrestrained specimens.

The square unrestrained links were denoted as SQ-U1, and SQ-U2, and also had the same outer dimensions as SP-R1. Figure 9-7 shows a photo of these specimens.

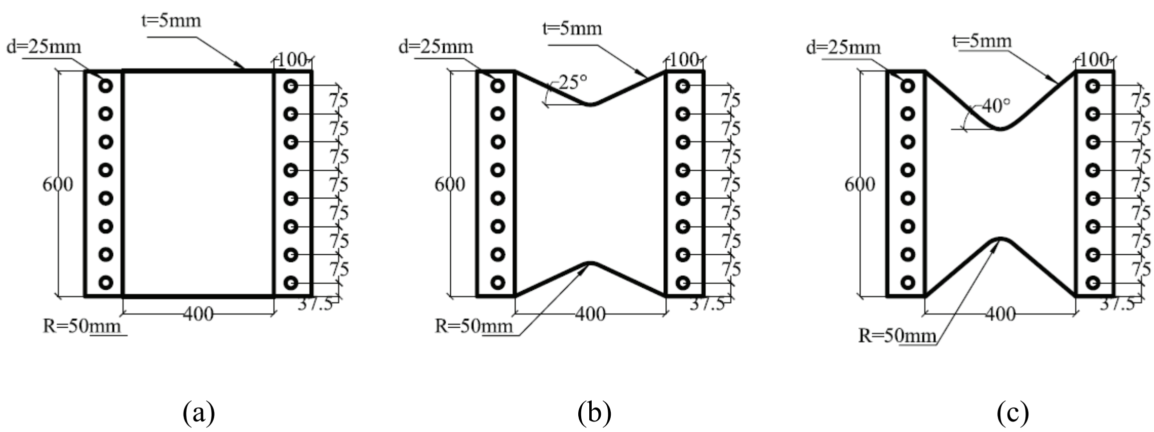

FIGURE 9-1 Specimens Dimensions; (a) SQ-U1, and SQ-U2, (b) SP-R1, SP-R2, SP-U1, and SP-U2, (c) SP-R3

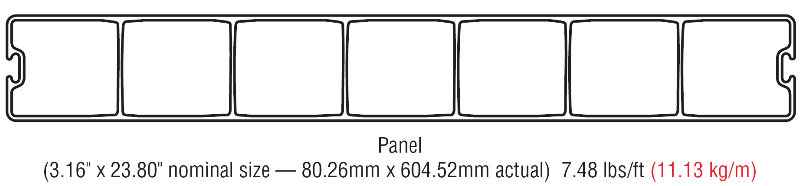

FIGURE 9-2 Composolite Panel Cross Section

TABLE 9-1 Composolite Mechanical Properties

Properties	ASTM Test Method	Value MPa (ksi)
Flexural Strength (Strong Direction)	D790	169 (24.5)
Flexural Strength (weak Direction)	D790	57 (8.2)
Tensile Strength (Strong Direction)	D638	214 (31.1)
Short Beam Shear (Strong Direction)	D2344	22 (3.19)

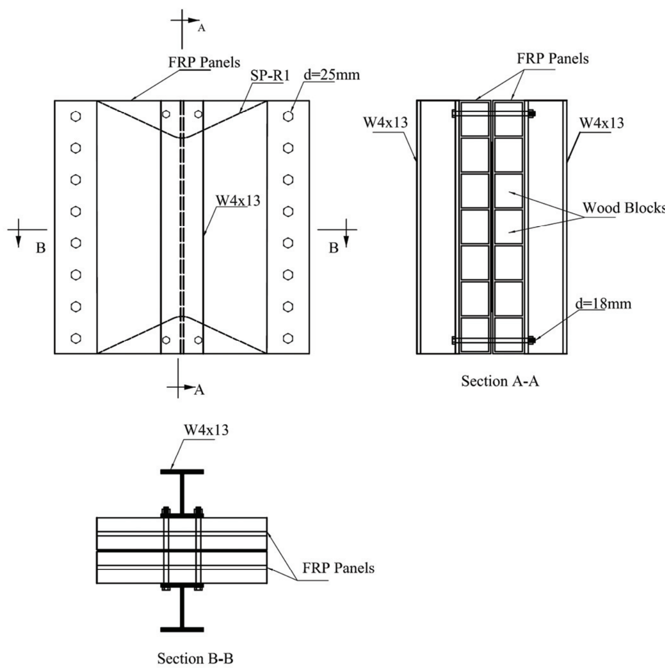

FIGURE 9-3 Specimen SP-R2 Lateral Restraining System Details

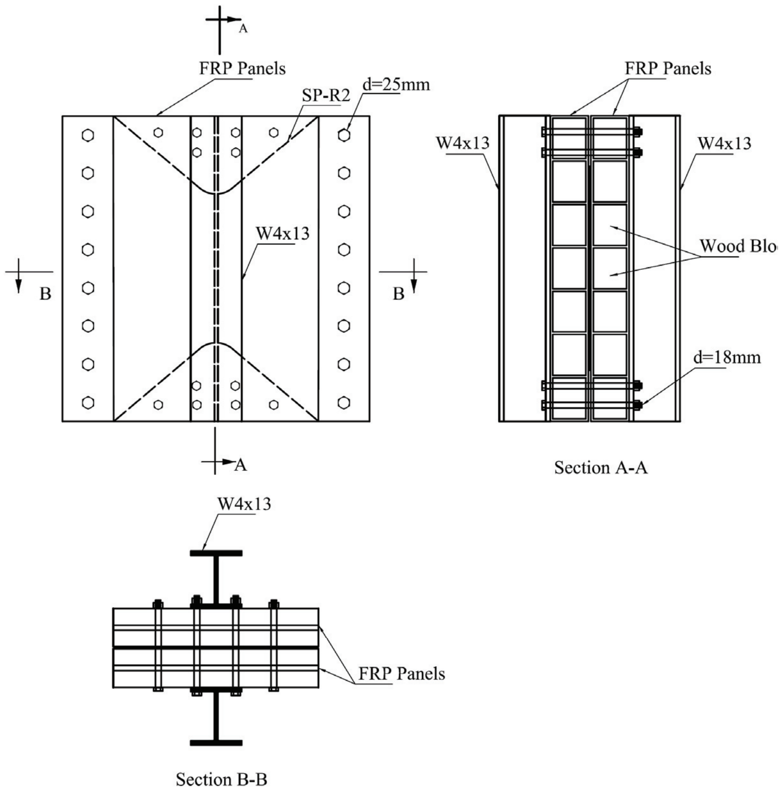

FIGURE 9-4 Specimen SP-R3 Lateral Restraining System Details

(a) (b) (c)

FIGURE 9-5 Specimens Lateral Restraining System Photos; (a) SP-R1, (b) SP-R2, (c) SP-R3

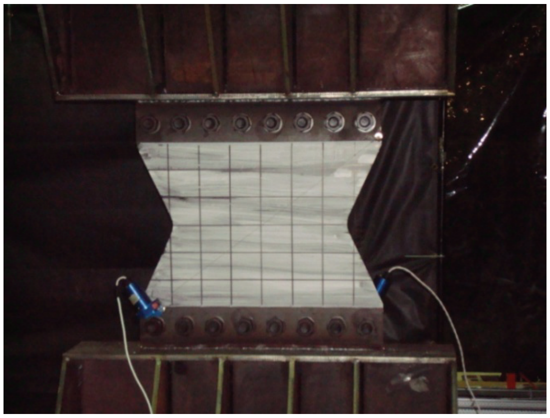

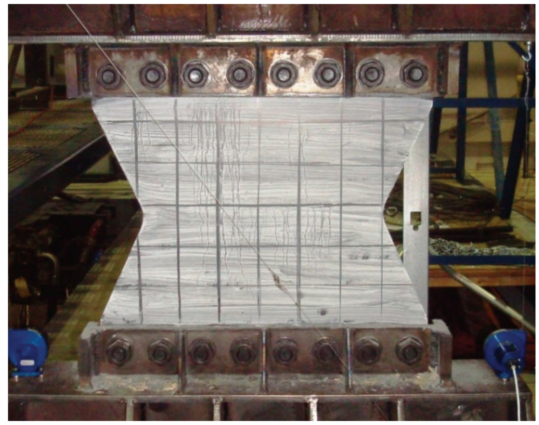

(a) (b)

FIGURE 9-6 Unrestrained Specimens Photos; (a) SP-U1, (b) SP-U2

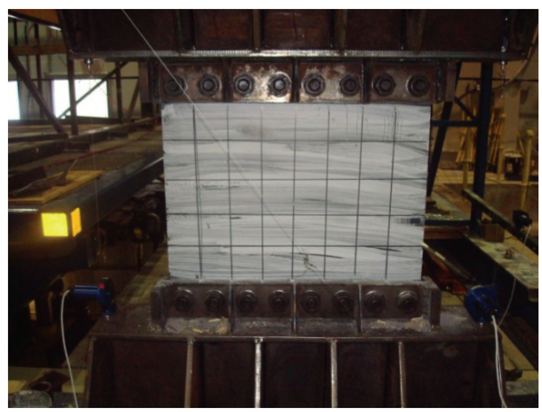

(a) (b)

FIGURE 9-7 Square Specimens Photos; (a) SQ-U1, (b) SQ-U2

9.3 SPSLs Material Testing

ASTM A572 Gr. 50 steel was chosen for this particular application. Monotonic tension tests were performed on two coupons from as shown in figure 9-8. Strains were monitored using a MTS extensometer with a 50mm (2") gage length, while the forces were monitored using an internally mounted load cell in a Tinius Olsen testing machine at the University at Buffalo. The coupons tested showed good ductility and reached a strain of 28% before fracture. The ratio of F_u/F_y was 1.11 which is 18% less than the specified ASTM value of 1.3, and compares with the expected ratio of R_tF_u/R_yF_y of 1.42 that can be calculated using the values in AISC 2005. Such a low ration can be problematic to design bolted connections.

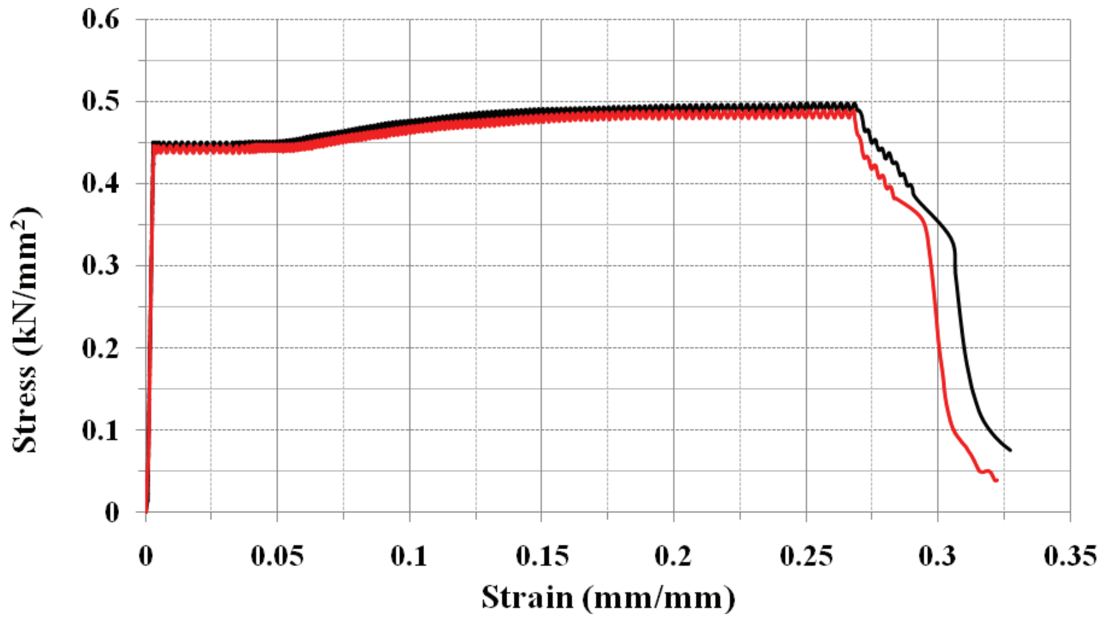

FIGURE 9-8 Tension Coupon Results for SPSLs Material

9.4 Test Setup Design

The test setup shown in figure 9-9 was originally designed by Berman and Bruneau (2006). The setup is a pantograph that was designed to apply a shear force on short-length specimens. This is accomplished by a double-acting servo-hydraulic actuator acting on a loading beam (LB) through the LB-actuator beam and LB- actuator brace as shown in figure 9-9. This results in axial loads and moments in the loading beam, those are transferred as shear and end moment to the link and then to the foundation beam (FB). Note that the line of action of the actuator force coincides with the link midpoint, resulting in equal and opposite link end moments and zero moment at the link midpoint, assuming rigid loading and foundation beams. Therefore, the actuator load is equal to the link shear force (the axial forces in the pin-ended members of the pantograph members at the west end of the test setup are equal and opposite and do not create a horizontal shear resultant).

The pantograph functions to prevent rotation of the loading beam while allowing the link to deform unrestrained in the axial and horizontal directions, preventing the introduction of axial load in the link when deformed in shear and flexure.

At the east end of the actuator, the load is transferred to the FB through the FB actuator beam and FB brace. The result is that the setup is a self-restrained reaction frame, meaning that the actuator force is resisted by axial load in the foundation beam, not by friction between the strong floor and foundation beam. Attachment to the strong floor was therefore designed only to resist uplift forces.

9.4.1 Foundation Beam (FB)

The W610x217 (W24x146) that was selected by Berman and Bruneau (2006) for the FB is shown in figure 9-10. The FB was fastened to the floor in five locations along its length, with one 35 mm (1.375") diameter Gr. 150 dywidag bar on each side of the web at each location. FB stiffeners details are shown in figure 9-11. The W450x97 (W18x65) and W410x85 (W16x57) used as FB actuator beam and FB brace respectively are shown in figure 9-12.

The 31.75 mm (1.25") mounting plate fillet welded all around to the FB flange with holes to accept the bolts from the links mounting Beam is shown in figure 9-13. The mounting plate and connection to the FB flange are also reinforced by the presence of Type C and Type D FB stiffeners.

9.4.2 Loading Beam (LB)

The loading beam (LB) was also designed by Berman and Bruneau (2006) making use of a W610x217 (W24x146) as shown in figure 9-14. The LB-actuator beam is a W460x97 (W18x65) and the LB-brace is a W310x74 (W12x50). The same detail and stiffeners of the FB actuator beam are found where the flange width of the LB actuator beam extends for connection with the actuator. The link mounting beam-to-LB connection also has similar mounting plate and stiffener reinforcement configurations, as shown in figure 9-15.

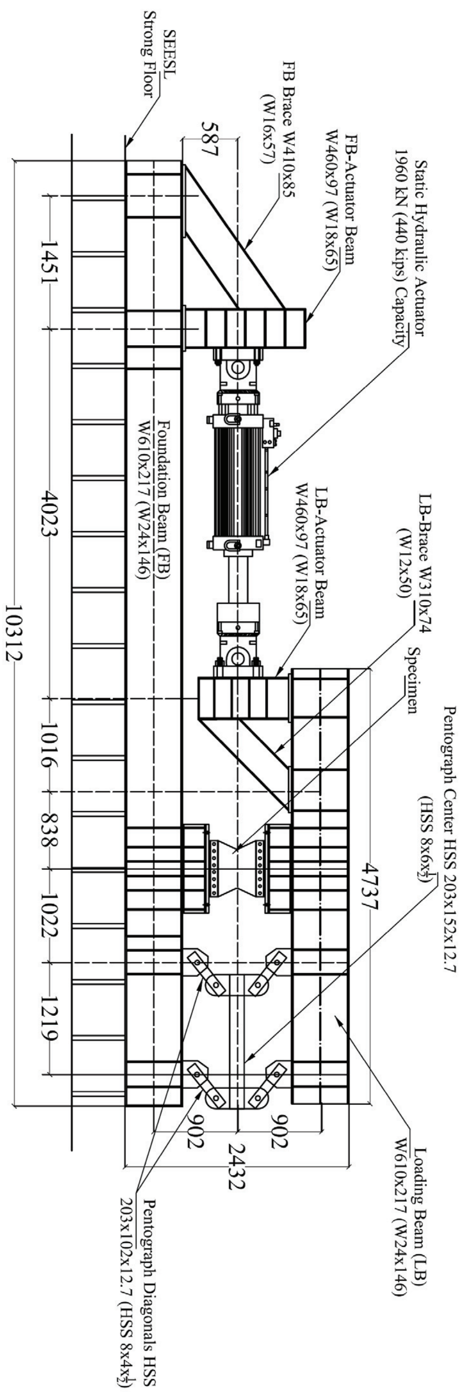

(a)


(b)

FIGURE 9-9 Test Setup for all Specimens; (a) Details, (b) Photo

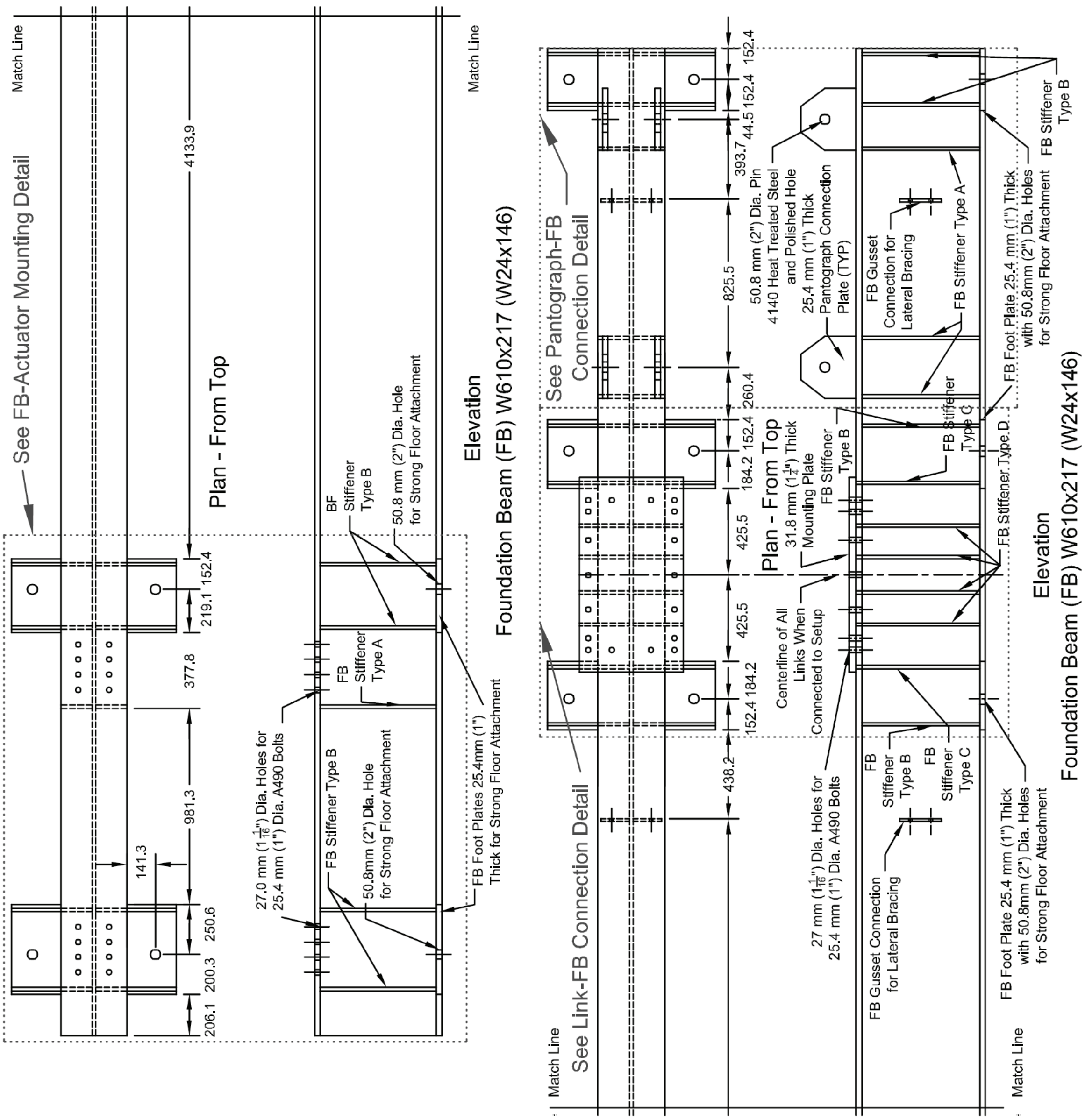

FIGURE 9-10 Foundation Beam Details (Berman and Bruneau 2006)

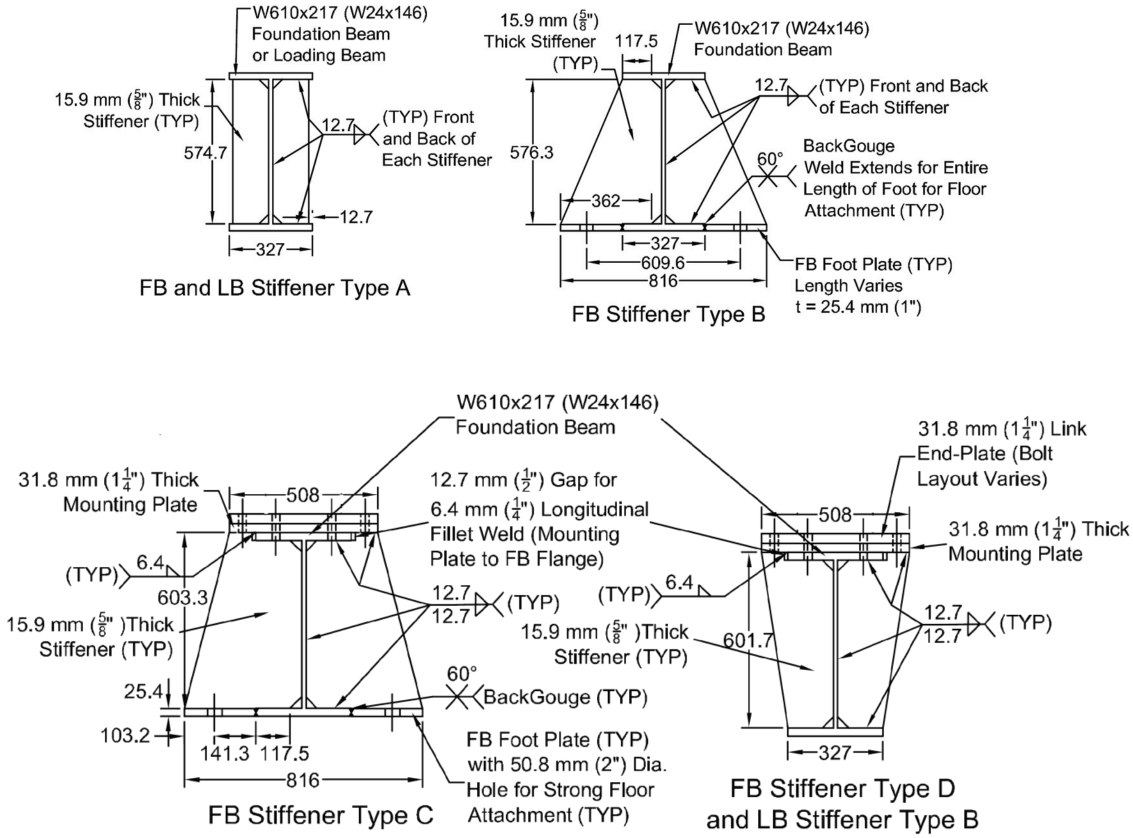

FIGURE 9-11 Foundation Beam Stiffeners Details (Berman and Bruneau 2006)

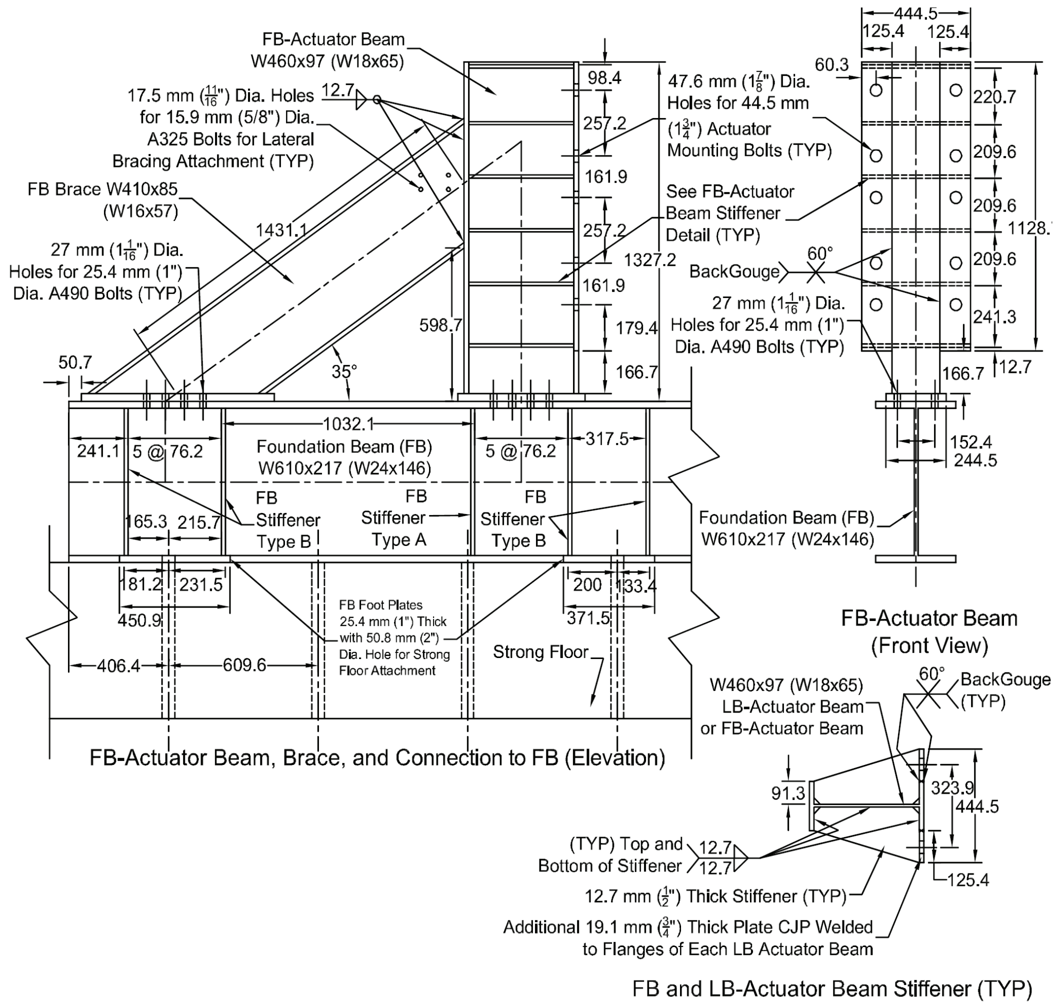

FIGURE 9-12 Actuator Beam, Brace, and Connection to FB (Berman and Bruneau 2006)

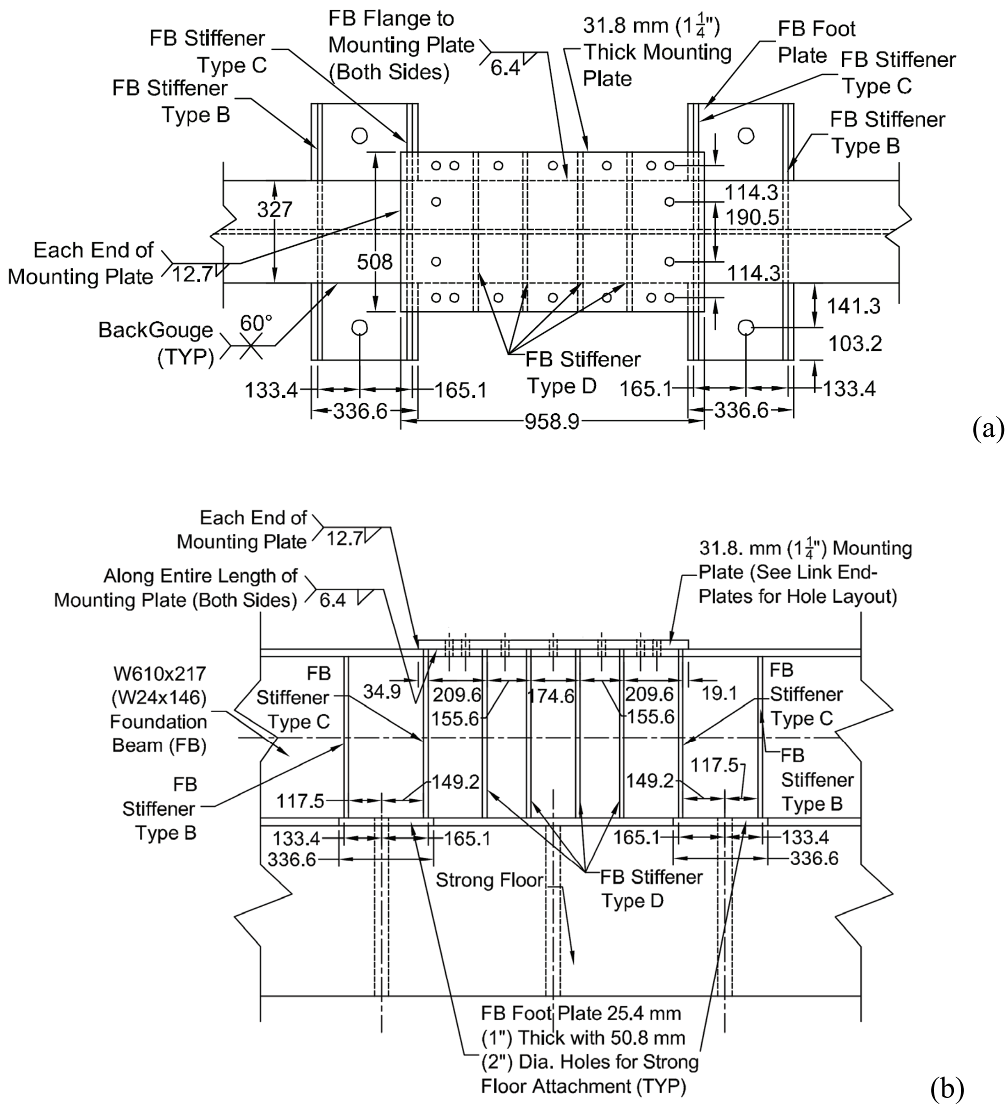

FIGURE 9-13 Foundation Beam to Link Mounting Beams Connection; (a) Plan, (b) Elevation (Berman and Bruneau 2006)

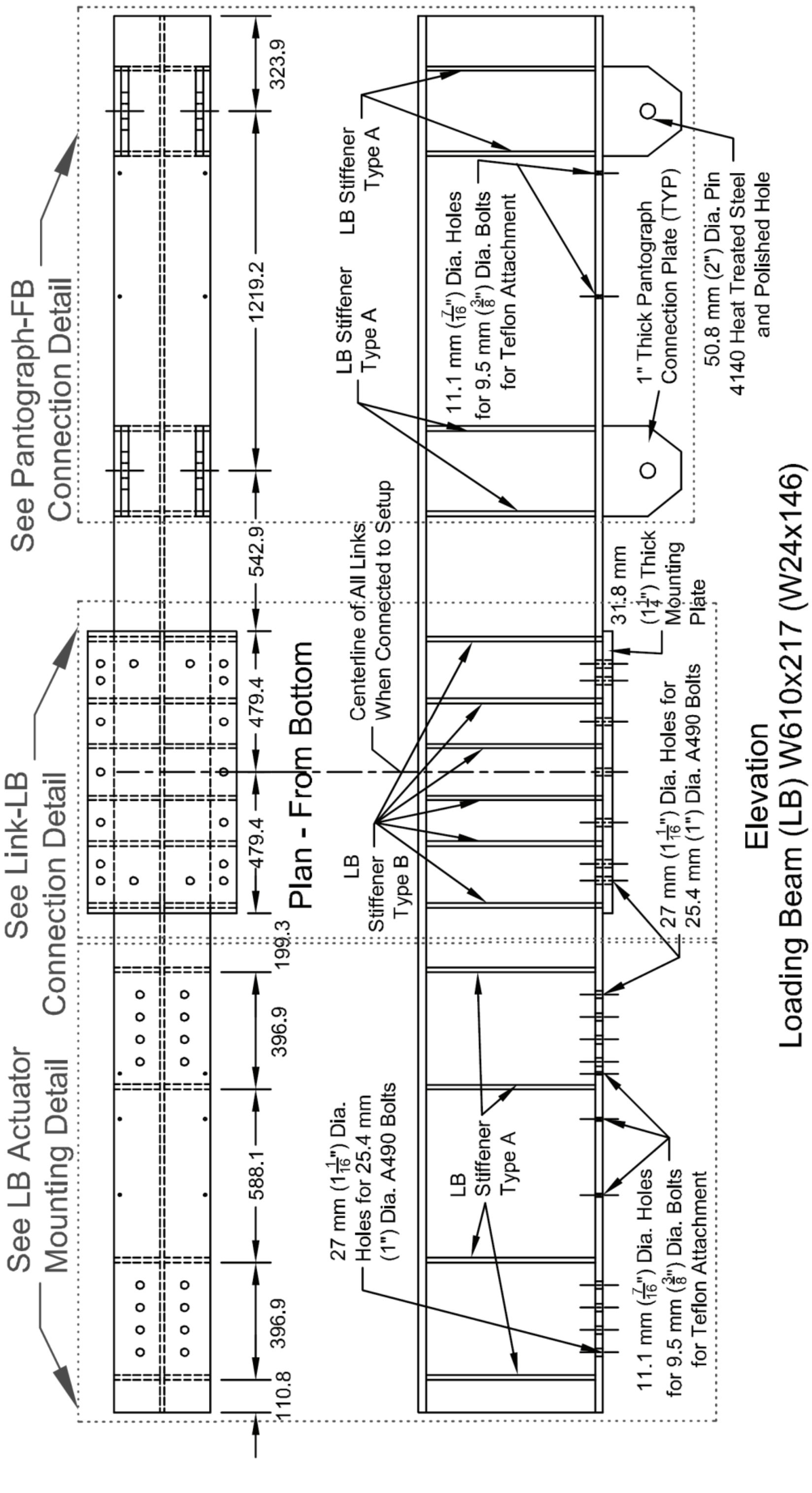

FIGURE 9-14 Loading Beam Detail (Berman and Bruneau 2006)

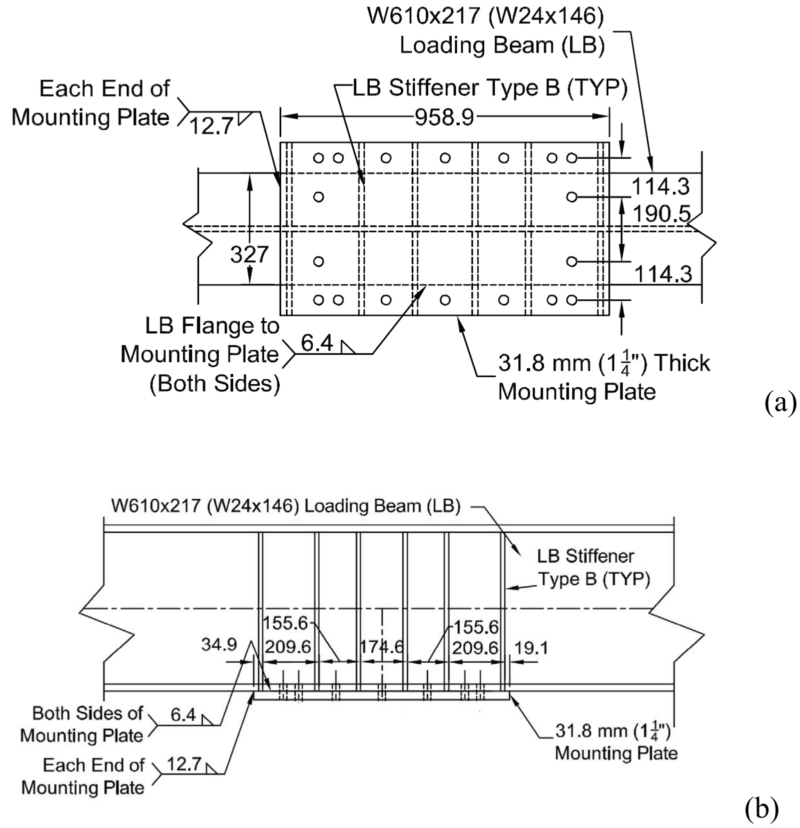

FIGURE 9-15 Loading Beam to Link Mounting Beams Connection; (a) Plan, (b) Elevation (Berman and Bruneau 2006)

9.4.3 Links Mounting Beams

Due to the fact that the pantograph was not originally configured to accommodate the SPSLs, it was necessary to design and fabricate two short mounting beams to connect the SPSLs to the LB and FB and to ensure that the centerline of the specimens align with the centerline of the actuator as mentioned before. The mounting beams were selected to be built-up W shape beams with dimensions shown in figure 9-16. The bottom of the mounting beam was detailed to be connected to the FB; while the gusset plate on top of the mounting beam was detailed to be connected to the specimens using 8 A490 bolts 25mm (1") in diameter. These bolts were designed for slip resistance to resist a shear force of 1111kN (250 kips), with a factor of safety of 2.0 as the anticipated strength of the strongest specimen was not to exceed 556kN (125kips). The gusset plate connecting the SPSLs to the mounting beam was initially designed to have the same dimensions as the gusset plates used to connect the SPSLs to the columns for specimen S1 in sections 5 and 6. Nevertheless, during testing of the first specimen (SP-U1), buckling was observed at the gusset plate at high rotation levels as described later in section 9.7.1. Given the fact that this gusset plate was intended to be reused for all remaining specimens, it was flamed-cut after the termination of specimen SP-U1, and a new gusset plate was overdesigned to be elastic and reinforced by stiffeners every 150mm (6"). The new gusset plate was designed to resist an out of plane force of 10% the anticipated maximum shear force (556kN) that would applied to the strongest SPSL, which is an over estimation of the out-of-plane load that was anticipated to occur due to the plate buckling . Different in-plane failure modes like tension yielding of gross section, shear fracture at net section, and shear yielding at gross section were also taken into account for the gusset design.

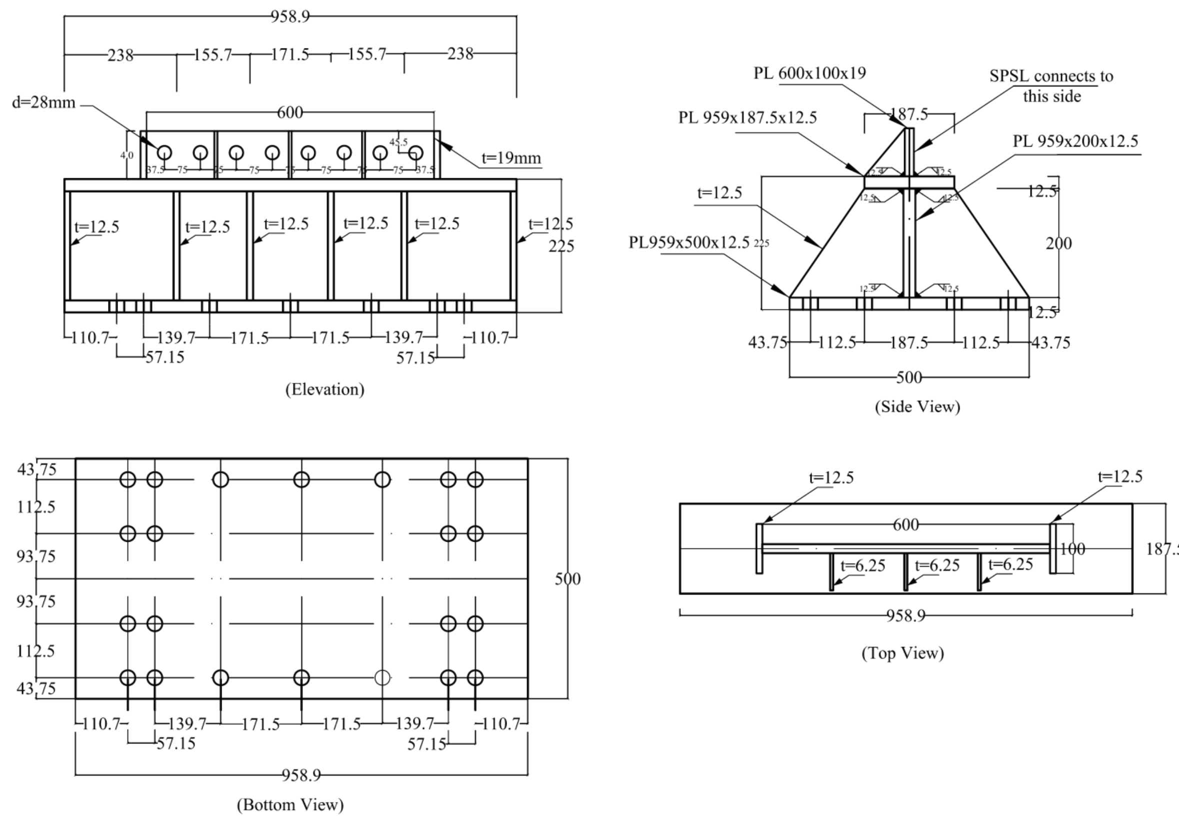

FIGURE 9-16 Mounting Beam Detail

9.4.4 Pantograph Articulated Members

The pantograph articulated members consists of diagonal truss members oriented at a certain angle with the horizontal, and connected to a center member and the LB and FB using high strength pin connections. The function of these members is to allow the LB to translate vertically and horizontally with no resistance but does not allow it to rotate, thereby preventing axial force in the SPSLs while also providing for approximately equal link end moments. More details on the pantograph articulated members design are presented in Berman and Bruneau (2006).

No changes were required to the existing pantograph articulated members for the purpose of the tests conducted as part of the current research project. Pantograph diagonals and center member are HSS 203x102x12.7 (8x4x1/2) and HSS 203x152x12.7 (8x6x1/2) respectively, connected at their ends using 50.8 mm (2") diameter steel pins as show in figures 9-17 and 9-18. The pantograph diagonals are reinforced with a 12.7 mm (½") thick plate around the holes at every pin connection. In addition, 25.4 mm (1") plates and 22.2 mm (7/8") fillet welds connect the pantograph member to the LB and FB.

9.4.5 Lateral Bracing

Lateral bracing was provided to the test setup at three locations to prevent out-of-plane displacement of the actuator and LB, and lateral torsional buckling of the LB. Lateral bracing attached to the FB brace, is shown in figure 9-19; the lateral bracing at that location consists of two HSS 50.8x50.8x6.4 (2x2x1/4) sections connected to the FB brace by bolts and welded to channels that are fastened to the strong floor using a single 35 mm (1.375") dywidag bar at each location.

Lateral bracing for the loading beam utilized vertical W250x32.7 (W10x22) shapes to “sandwich” the beam at two locations as shown in figure 9-20. The vertical members were bolted to the FB using gusset plates, bearing against the LB as originally designed. Vertical members were then connected to each other using threaded rods which were tightened to insure proper contact between the vertical members and the LB. At each of the two loading beam lateral bracing connections, one of the vertical members that were braced to the floor using a HSS 76.2x76.2x6.4 (3x3x1/4) connected to a channel was fastened to the strong floor. Photos of Lateral Bracing of the LB and FB brace are shown in figures 9-21and 9-22 respectively.

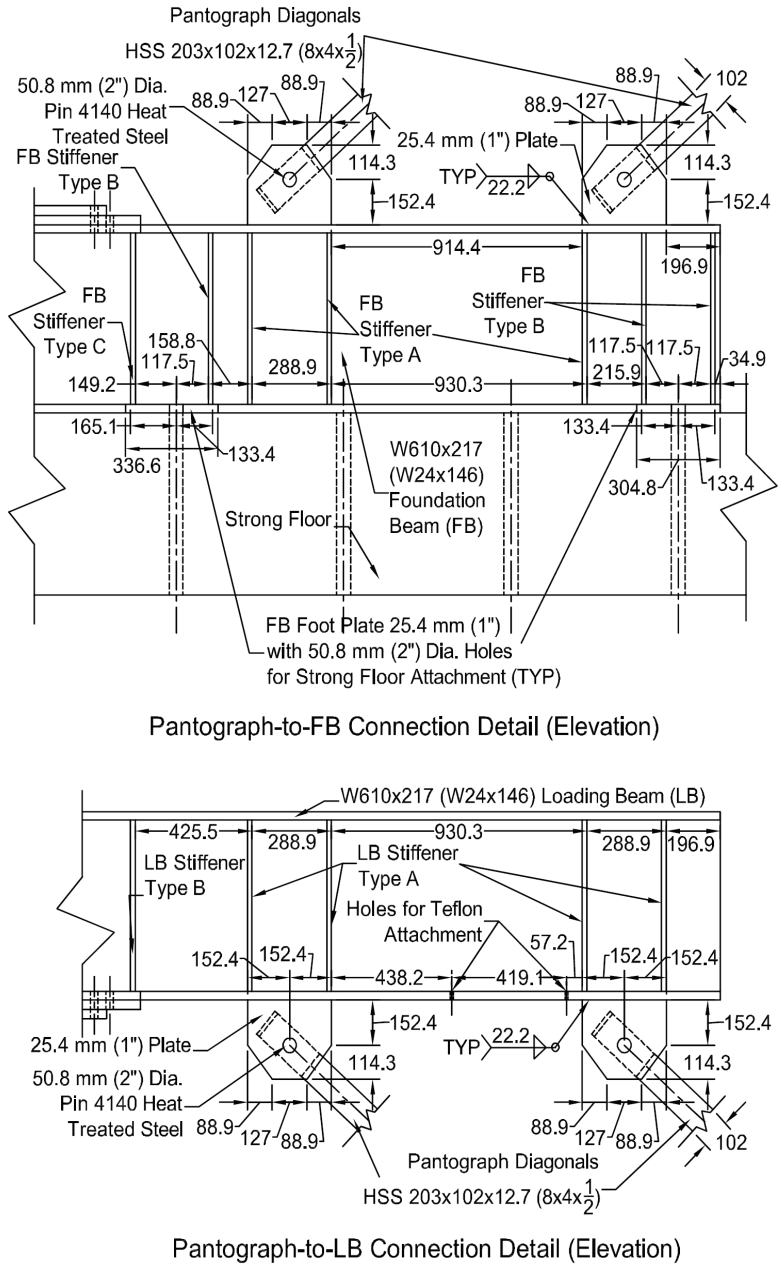

FIGURE 9-17 Pantograph Connection to FB and LB Details (Berman and Bruneau 2006)

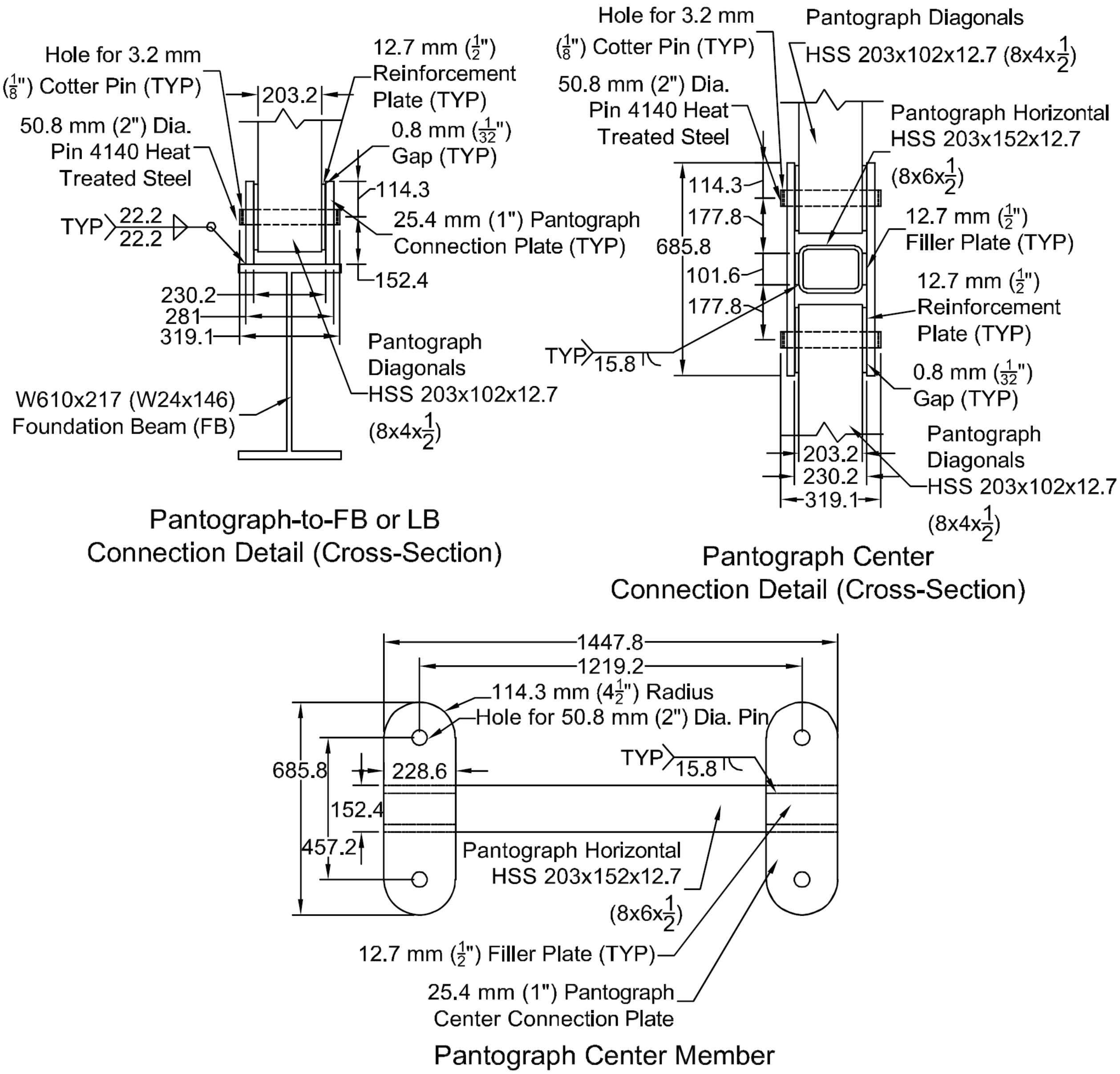

FIGURE 9-18 Pantograph Connection Details and Center Member (Berman and Bruneau 2006)

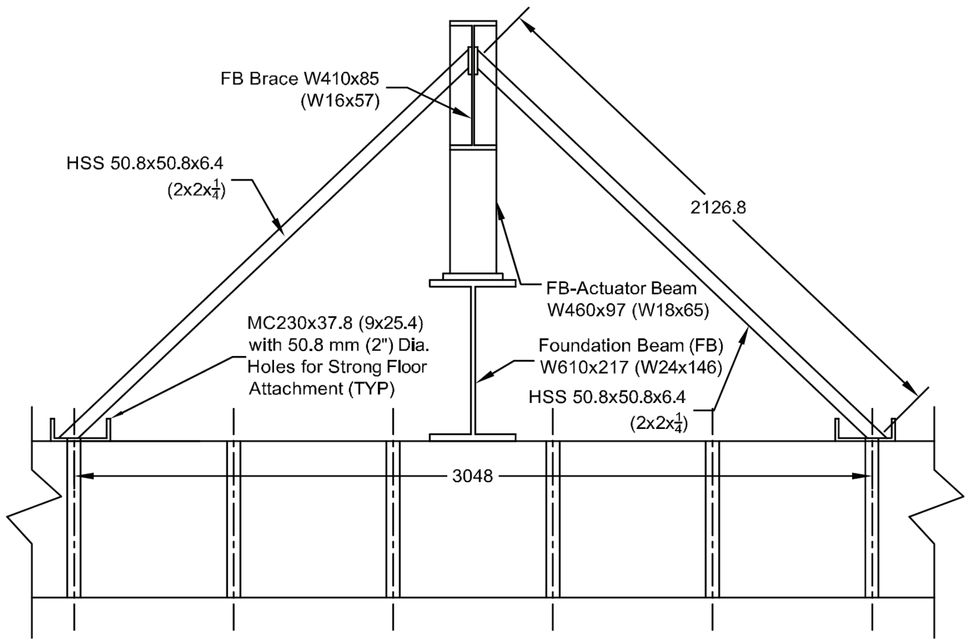

Lateral Bracing of FB Actuator Brace (Cross-Section)

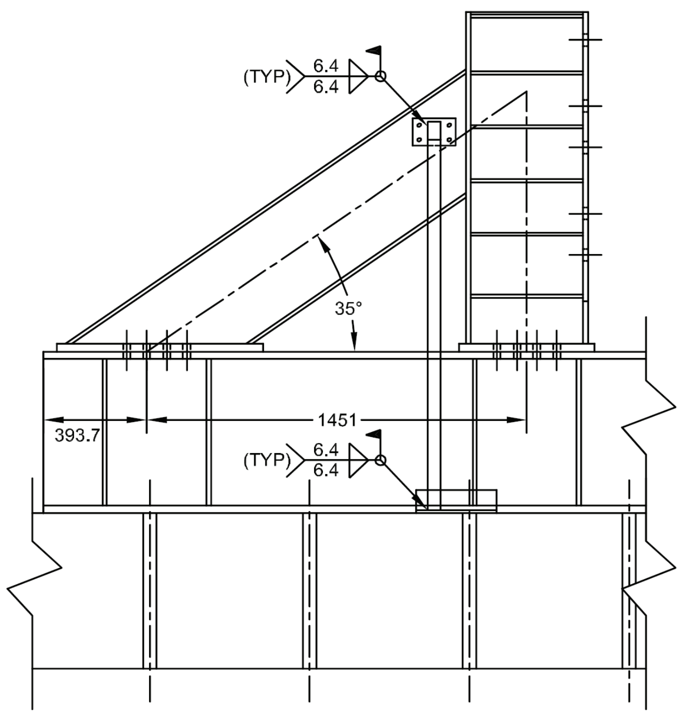

Lateral Bracing of FB Actuator Brace (Elevation)

FIGURE 9-19 Lateral Bracing to FB Brace Details (Berman and Bruneau 2006)

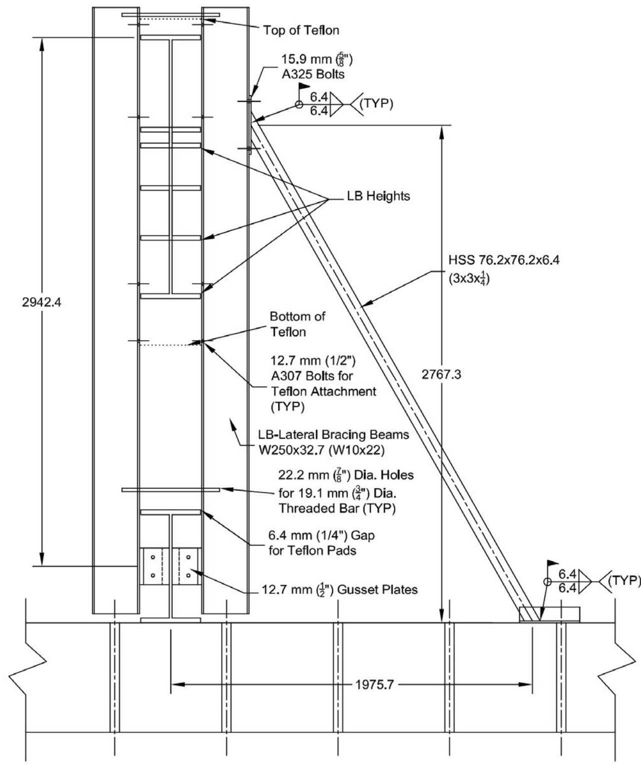

FIGURE 9-20 Cross Section of Setup at LB Lateral Bracing (Berman and Bruneau 2006)

FIGURE 9-21 Lateral Bracing of LB Photo

FIGURE 9-22 Lateral Bracing to FB Brace Photo

9.4.6 Vertical Load Carrying System

As indicated above, the pantograph restrains the LB from rotation and only allows it to translate vertically and horizontally; however, allowing vertical translations would have been problematic because, as a result, the SPSL would have had to carry the gravity load of the LB, which would not have been desirable. To carry the weight of the LB and the vertical tension force developing due to yielding of the specimens, the steel block shown in figure 9-23 was used to fill the 225mm (9") gap between the FB and the LB-Actuator beam. Restraining the vertical motion by adding the steel block was intended to provide a direct load-path for the vertical loads, restricting the LB to be only able to translate horizontally. The block surface was greased to minimize the additional force produced due to friction of the LB-actuator beam with the steel block.

FIGURE 9-23 Gravity Load Carrying System

9.5 Instrumentation

9.5.1 String Displacement Potentiometers

Four string displacement potentiometers (string-pots) were used for each specimen, as shown in figure 9-24, namely two vertical ones located east and west of the specimen and denoted as SP-VE and SP-VW, and two diagonal ones denoted as SP-D1 and SP-D2 installed to connect opposing corners of the specimen. The vertical string-pots were used to monitor any vertical translation and rotation in the LB. The specimen shear rotation was calculated using two different methods; the first was by dividing the actuator displacement by the height of the specimen (400mm, 16"), while the second method was by using the two diagonal sting-pots as follows:

$$\gamma = \frac{\sqrt{\left(h\sqrt{2}+\delta_{SP}\right)^{2}-\left(h\right)^{2}}-h}{e^{*}} \tag{9-1}$$

where δ_{SP} is the diagonal string-pot elongation shown in figure 9-25.

The second method gave more accurate results, as minor additional displacement was captured by the first method due to some flexibility of the setup. From which, the second method was used throughout this section to represent the specimen rotation.

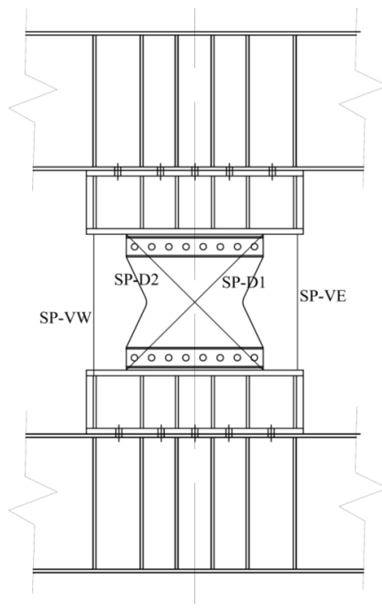

FIGURE 9-24 String Displacement Potentiometers Layout

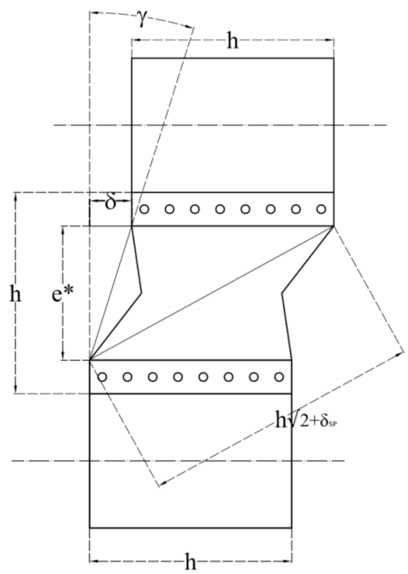

FIGURE 9-25 SPSL Diagonal String Potentiometer Elongation

9.5.2 Video Recording

Digital videos of each test were recorded. Every test had one high definition digital video camera setup to view the specimen from the front. Additionally, a standard digital video camera was setup to view the specimen from an angle of approximately 45 degrees south of west. For some of the tests, another standard definition camera was setup at a distance to capture overall specimen deformation and LB vertical translation and rotation (if any). Videos are available at http://seesl.buffalo.edu.

9.6 Loading Protocol

The loading protocol used for testing the SPSLs was the one specified by the 2005 AISC Seismic Provisions for Eccentrically Braced Frames (EBFs), modified as described below. The AISC loading protocol is based on the total rotation of the specimen and specifies six cycles at each of the total link rotation levels of 0.00375, 0.005, 0.0075, and 0.01 radians, followed by four cycles at 0.015 and 0.02 radians. Two cycles are then specified at 0.03 radians, then one cycle at each of the total link rotation levels of 0.04, 0.05, 0.07, and 0.09 radians. One cycle of rotation at progressive increment of 0.02 radians beyond 0.09 radians is then specified until failure occurs in the specimen. However, here, for testing of the SPSLs, the loading followed the 2005 AISC Seismic Provisions protocol until a rotation level of 0.02 radians, beyond which three cycles were applied at each of the radians values above instead of the one cycle specified. Although more severe than the specified loading protocol, the actual loading protocol was done to investigate behavior of SPSLs under repeated cycles, which was deemed to be important given that SPSLs without lateral support were anticipated to exhibit less energy dissipation upon repeated cycles. Displacement of the actuator was used as the control parameter during testing, which required that the specified rotation levels be converted into displacements using the SPSLs and setup geometries. For this purpose the mounting beams and the gusset plate connecting the SPSLs to the mounting beams were considered to be rigid and the actuator displacement was taken as the rotation times the SPSLs length of 400mm (16"). Table 9-2 shows the applied loading protocol for all specimens.

TABLE 9-2 Loading Protocol for SPSLs

Cycles	Total Rotation (γ_{tot})	Actuator Displacement (mm)
6	0.00375	1.5
6	0.005	2
6	0.0075	3
6	0.01	4
4	0.015	6
4	0.02	8
3	0.03	12
3	0.04	16
3	0.05	20
3	0.07	28
3	0.09	36
Increment of 0.02 radians (8mm) with three cycles		

9.7 Links Testing Observations

Links testing observations are described below for the seven links tested using the pantograph setup. Links shear forces versus the total rotation hysteretic curves measured from the string potentiometer and the actuator displacement are presented, along with photographs of each specimen at various levels of total rotations. For all specimens, loading started with positive forces and rotation values as the actuator pushed the specimens; negative values of both forces and rotations were then recorded when the actuator retracted.

9.7.1 Specimen SP-U1

SP-U1 was the first specimen being tested; figure 9-26 shows the hysteretic behavior observed during testing. At γ_{tot}=0.002 rad, loss of stiffness was observed in the hysteretic curves at a shear force of 80kN (18 kips). At γ_{tot}=0.02 rad, the specimen started to pick up load significantly up to γ_{tot}=0.03 rad. Due to the unavoidable geometric imperfections buckling started to initiate in the plate at γ_{tot}=0.04 rad, from which a drop in strength from 280kN (63kips) to 250kN (56kips) was observed as shown in figure 9-27. The specimen started to pick up strength gradually after that at each incremental cycle. Significant pinching in the hysteretic curves was then observed and expected as the plate stretches and relax. A strength reduction was also observed at each rotation level for the repetitive cycles. At γ_{tot}=0.09 rad, out-of-plane buckling of the gusset plate was observed as shown in figure 9-28, from which it was concluded that the gusset plate was yielding and contributing to the hysteretic curve of the specimen, which would result in an unreliable in an actual structure given that replacement of the links was an intended objective. Testing was continued until net section fracture occurred in the upper gusset plate as shown in figure 9-29. Testing was then terminated, and the gusset plate was flamed-cut and replaced by an overdesigned gusset plate described earlier in section 9.4.3. While the results of this test with gusset buckling are interesting, it was surprising that buckling initiated given that no such buckling was observed in the bridge pier specimen which had gussets of identical thickness – the only difference being that the gussets in the full bridge pier were continuous along the column height, which may have had a beneficial effect not quantified here.

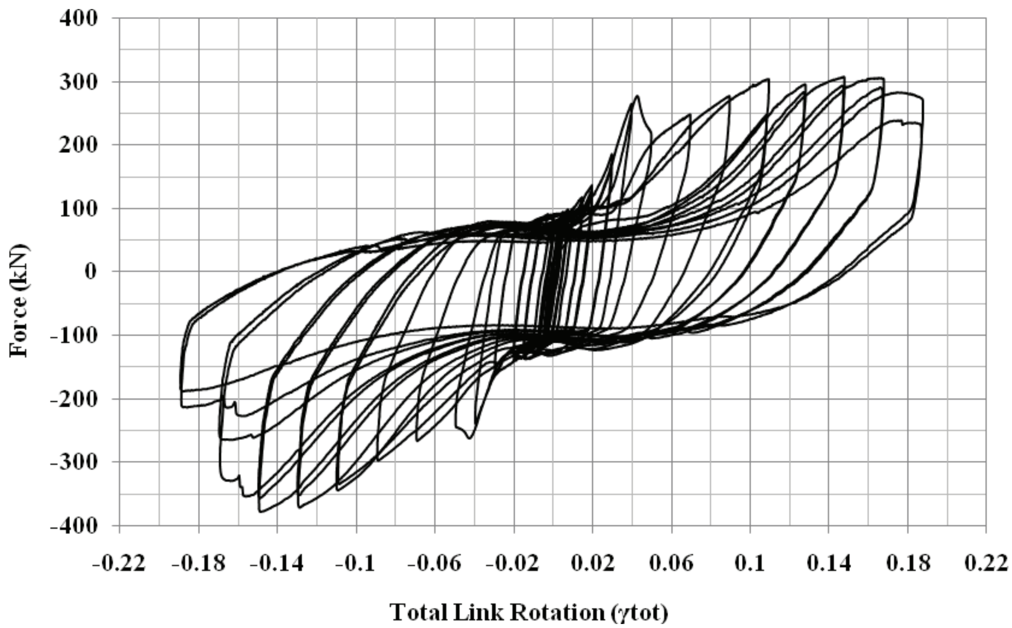

FIGURE 9-26 Link Shear vs. Total Rotation Hysteretic Curve for Specimen SP-U1

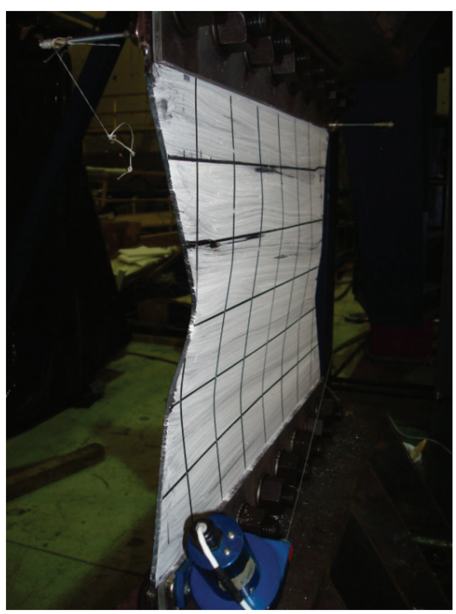

FIGURE 9-27 Initiation of Buckling at γ_{tot}=0.04 rad

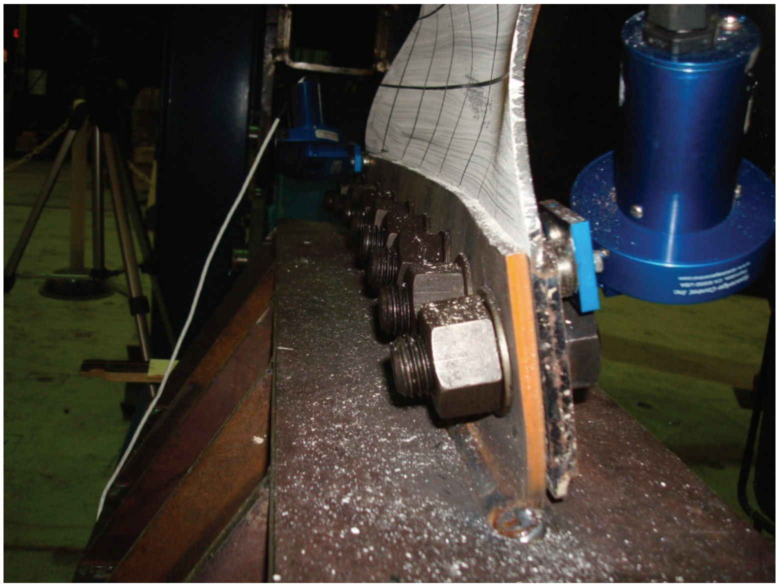

FIGURE 9-28 Out-of-Plane Buckling of Gusset Plate

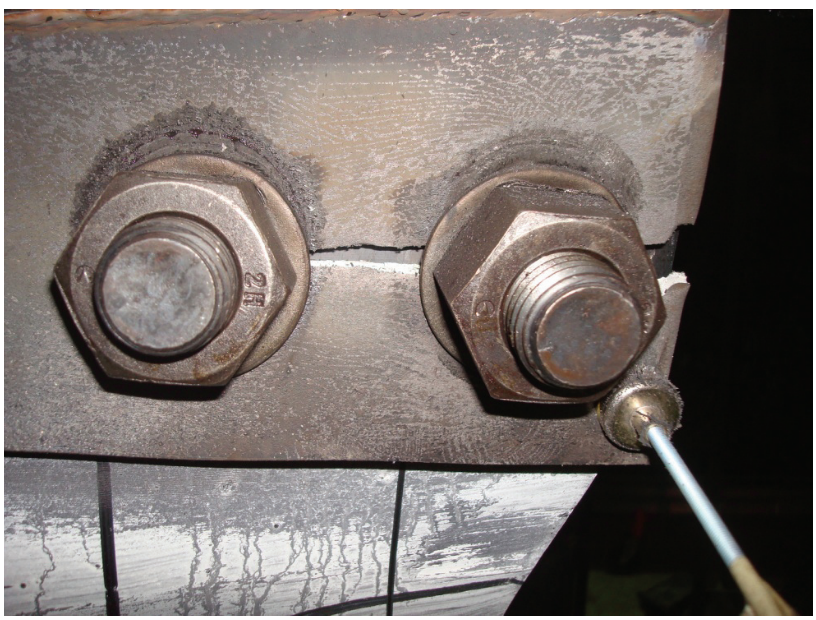

FIGURE 9-29 Net Section Fracture of Gusset Plate at γ_{tot}=0.19 rad

9.7.2 Specimen SP-R1

After replacing the gusset plate, specimen SP-R1 was tested. This specimen was identical to the links used for specimen S1: the link had a link edge angle equal to the balanced link edge angle and was restrained from out of plane buckling using the FRP panels described in section 9.2. Figure 9-30 shows the hysteretic behavior observed during testing. Up to a rotation of 0.02 rad, the shear strength developed by the specimen was only 100 kN (23kips), which was less than the anticipated yield shear strength of 385 kN (86 kips) . Starting at a rotation of 0.02 rad, a more significant shear force was resisted by the specimen. At a rotation of 0.04 rad in the negative direction of the curve, the specimen reached the anticipated yield force and out-of-plane buckling developed in the middle part of the link and was observed as a noticeable deflection in the FRP panels. This was due to the fact that the lateral stiffness of the FRP restraints was not sufficient to prevent such buckling (shown in figure 9-31) to occur. This buckling resulted in a significant drop in the strength of the specimen, accompanied by pinching of the hysteretic curves during incremental cycles. At the same time, a drop of load from 470 kN (106 kips) to 350 kN (79kips) was observed on the hysteretic curve as the specimen buckled. The same behavior was also observed in the positive direction of the curve but at a rotation of 0.07 rad and a force of 360 kN (81 kips), which is a force less than the anticipated yield force.

This "lag" in developing the strength of the specimen could not be explained at the time of the test, but after investigating the accelerated videos of the specimen during testing, two observations where clear. First, it was observed that the loading beam was not moving in a perfect horizontal manner and a vertical downward motion was seen to have developed during each loading and unloading cycle. This downward motion affected the behavior of the SPSLs at low rotation levels by underestimating the shear forces resisted by the specimen, while had at higher rotation levels, additional pinching was observed in the unloading cycles. The effect of this downward motion on the global behavior of the SPSLs was further investigated in sections 9.8 and 9.9. Second, slippage in the end bolts were also observed, which resulted in delaying the yielding of the specimen.

At a total rotation of 0.09 radians, the FRP panels started to crack at their line of bolts as shown in figure 9-32, and completely failed at 0.11 radians as shown in figure 9-33. At this level of damage, the FRPs were removed and the condition of the SPSL is shown in figure 9-34.

Testing continued per the loading protocol. A crack that initiated at the center of the SPSL at 0.13 radians is shown in figure 9-35. Propagation of the crack during successive cycles is shown in figure 9-36. As the crack propagated at every incremental rotation, a gradual loss of strength was observed in the hysteretic behavior. At a total rotation of 0.2 rad, the specimen was considered to be totally fractured. While the specimen was tested until complete fracture, for sake of learning about failure mode, failure of the specimen is defined as the point where 80% of the maximum strength is reached after the first peak where buckling starts to occur. On the basis of that definition, the specimen was deemed failed at a rotation of 0.17 radians.

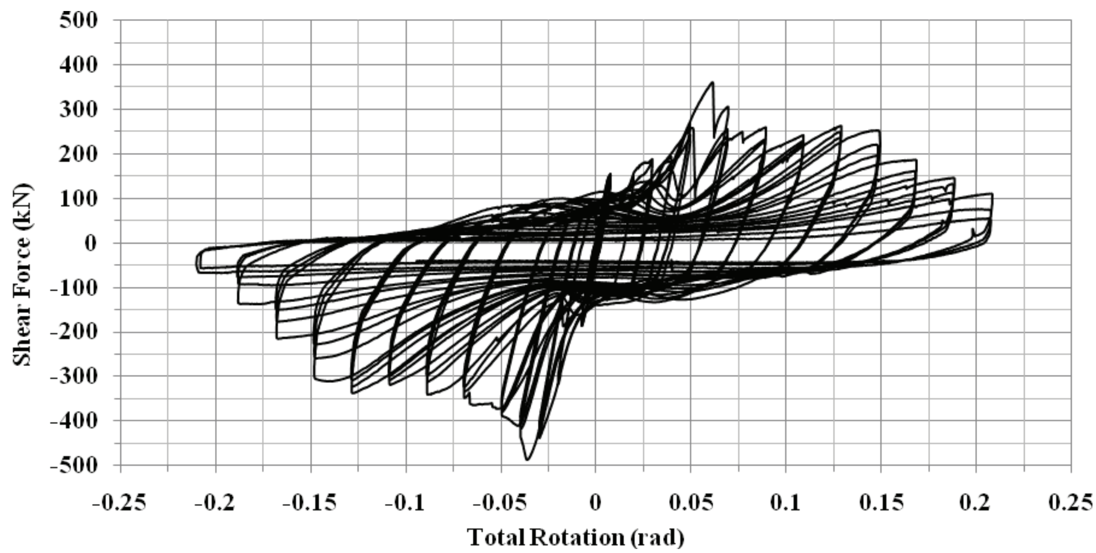

FIGURE 9-30 Link Shear vs. Total Rotation Hysteretic Curve for Specimen SP-R1

FIGURE 9-31 Deflection of Lateral Restraints

FIGURE 9-32 FRP Panel Cracking at 0.09 radians

FIGURE 9-33 Failure of FRP Panel at 0.11 radians

FIGURE 9-34 SPSL Condition at 0.11 radians After Removal of the FRP

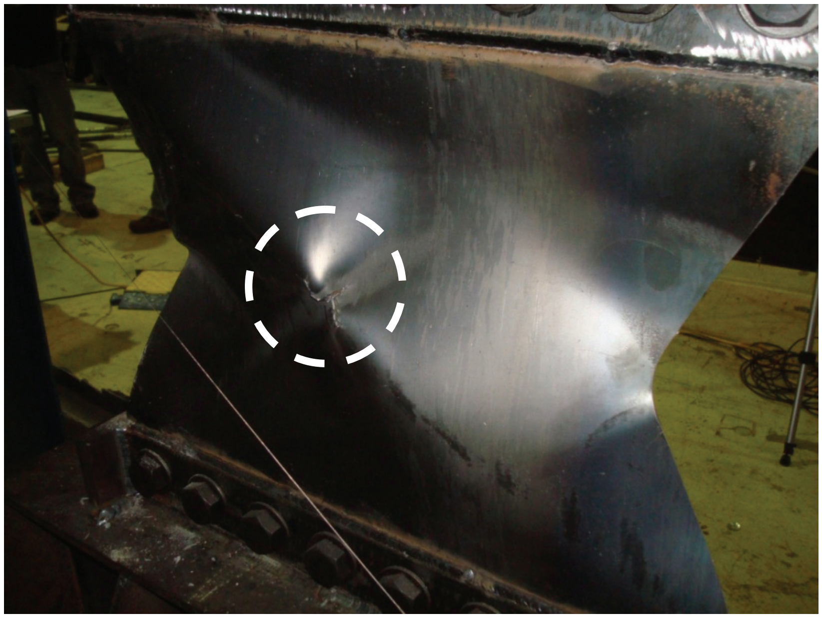

FIGURE 9-35 Initiation of Cracking at 0.13 radians

γ_{tot} =0.15 rad

γ_{tot} =0.17 rad

γ_{tot} =0.19 rad

γ_{tot} =0.21 rad

γ_{tot} =0.23 rad

γ_{tot} =0.25 rad

FIGURE 9-36 Damage Progression of SP-R1 at Various Total Rotation Levels

9.7.3 Specimen SP-R2

As described in section 9.2, specimen SP-R2 was the link with $\theta=\theta_b$ and restrained against out of plane buckling. For this specimen, two horizontal beams were added alongside the

FRP panels (as shown in figure 9-5) to enhance the flexural stiffness of the FRP restraints as discussed in section 9.2. Figure 9-37 shows the hysteretic behavior observed during testing. At γ_{tot}=0.002 rad, loss of stiffness was observed in the hysteretic curves at a shear force of 100kN (23 kips). Up to a rotation of 0.02 rad, the shear strength of the specimen was only 200 kN (45kips), which was less than the anticipated yield shear strength of 385 kN (86 kips). Starting at a rotation of 0.02 rad, a significant amount of shear force was gained by the specimen, and the specimen was yielding as anticipated. This behavior could not be explained at the time of the test, but after investigating the accelerated videos of the specimen testing, the same two observations regarding the movement of the loading beam and the slippage of the bolts where possible, similarly to specimen SP-R1. At a total rotation of 0.05 rad, buckling was observed. This was anticipated to eventually happen due to flexural yielding of the wedge parts of the specimen, as they stretch during the one half of a cycle then buckle at the second half of the cycle; again, the lateral stiffness of the FRP restraints was not sufficient to prevent such buckling to occur, as shown in figure 9-38. A combination of shear yielding (middle part) and flexural yielding and buckling (wedge part) was experienced by the specimen, accompanied by significant pinching action in the hysteretic curves due to the buckling of the wedge parts. As the magnitude of buckling increased in the wedge parts at every incremental rotation, the loss of strength for successive cycles at the same rotation level increases as observed in the hysteretic curve. Propagation of wedge buckling for incremental cycles is shown in figure 9-39. At a total rotation of 0.12 rad, the specimen was considered to be totally failed, as a drop in strength from 520kN (117kips) at 0.1 rad to 400kN (90kips) at 0.09 rad was observed in the positive side of the hysteretic curve, which is about a 20% loss in strength. Testing continued until the specimen totally fractured during the 3rd cycle of the 0.12 rad rotation. The FRP was then removed, and photos of the specimen at the end of the test were taken and shown in figures 9-40 to 9-42. It can be seen from the photos that no significant buckling occurred at the mid part of the specimen, which suggests that yielding of the middle part was due to shear yielding rather than by development of diagonal tension field action. Buckling of the wedge parts was also observed, the length of the buckles providing evidence of successive cycles of stretching and compression, which indicates that the yielding mode of the wedge parts was flexural and not due to shear. Initiation of cracks was assumed to have occurred first in the wedge parts and propagated from there horizontally towards the center. This fracture mode of the middle part of the link might not have occurred if the wedge parts had not buckled; in such a case, fracture would presumably have initiated at the center of the specimen (but this could obviously not be verified by this test).

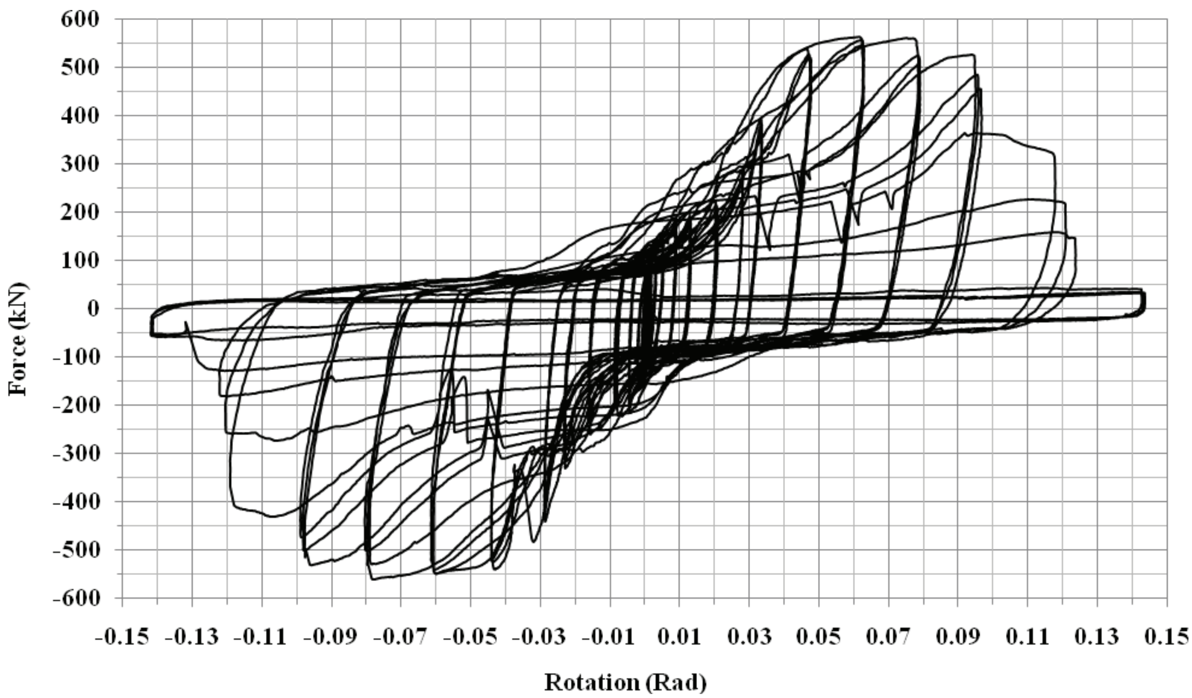

FIGURE 9-37 Link Shear vs. Total Rotation Hysteretic Curve for Specimen SP-R2

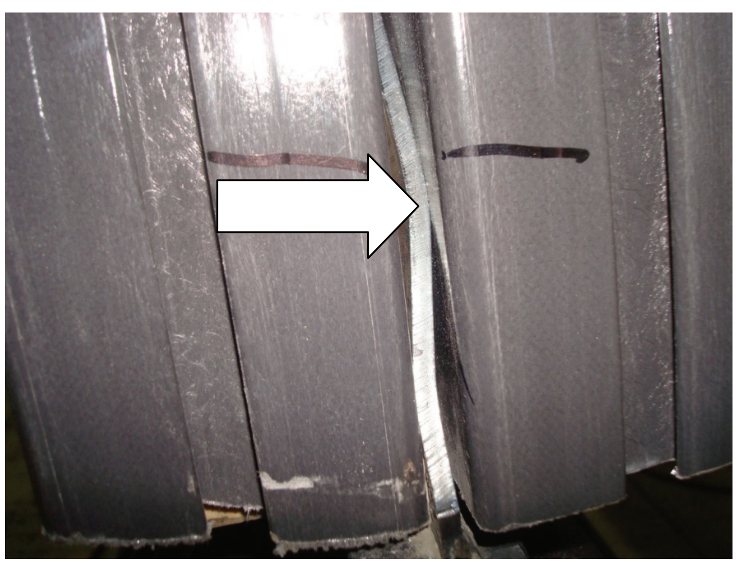

FIGURE 9-38 Local Buckling of Wedge Parts of Specimen SP-R2 at γ_{tot}=0.05 rad

(a) (b) (c)

FIGURE 9-39 Wedge Buckling of Specimen SP-R2 at Different Rotation Levels; (a) γ_{tot}=0.07, (b) γ_{tot}=0.09, γ_{tot}=0.11

FIGURE 9-40 Lower Side Fracture of Specimen SP-R2 at End of Test

FIGURE 9-41 Fracture of Upper Part Corners of Specimen SP-R2; (a) Upper East Corner, (b) Upper West Corner

(a) (b)

FIGURE 9-42 Middle Part Condition of SP-R2; (a) Elevation, (b) Side View

9.7.4 Specimen SP-R3

Specimen SP-R3 was the link with $\theta > \theta_b$ and restrained against out-of-plane buckling using the FRP panes and the two steel beams as described in section 9.2. Figure 9-43 shows the hysteretic behavior observed during testing. The same trend of behavior was observed at γ_{tot}=0.002 rad, as loss of stiffness was observed in the hysteretic curves at a shear force of 150kN (34 kips) for the same reasons mentioned before for specimen SP-R2. Yielding started to occur at a total rotation of 0.015 rad and a shear force of 250 kN (56 kips), the anticipated shear yield force was 240 kN (54 kips). No buckling was observed in the wedge parts as they were designed to remain elastic ($\theta > \theta_b$), and consequently no significant loss in strength at repetitive cycles for the same rotation level was observed at that level of rotations. This was attributed to the fact that the middle part was the only part yielding in the specimen, and was designed to yield in pure shear. At a rotation level of 0.08 rad, a drop in strength from 400kN (90kips) to 380kN (86kips) was observed in the hysteretic behavior in the positive direction of the curve (pushing the specimen); this was attributed to a fracture that might have started to propagate somehow in the middle part of the link, but this could not be confirmed or seen at that time due to the presence of the restraints. At the same rotation level in the negative direction of the curve, a significant loss in strength from 450kN (101kips) to 350kN was observed, this was about a 20% loss in strength from the maximum strength reached, and by definition, the specimen was deemed to have failed in terms of performance. However, testing continued until the specimen totally fractured. Loss of strength continued at the same rotation level for each of the three cycles performed due to the propagation of the anticipated crack. A significant loss in strength was then observed at a rotation level of 0.1 rad, and the strength dropped to almost zero at the 3rd cycle at that rotation level. At that point, testing was terminated and the restraints were removed to investigate the link condition at the end of the test. Figure 9-44 shows the specimen condition at the final rotation level achieved before removing the restraints, no buckling was observed from the sides of the restraints as shown in the figure. Figure 9-45 shows the specimen condition after removal of the restraints. It can be seen that the wedge parts appear to be elastic as no signs of buckling can be seen in them. Also it appears that all the yielding was localized in the middle part of the specimen.

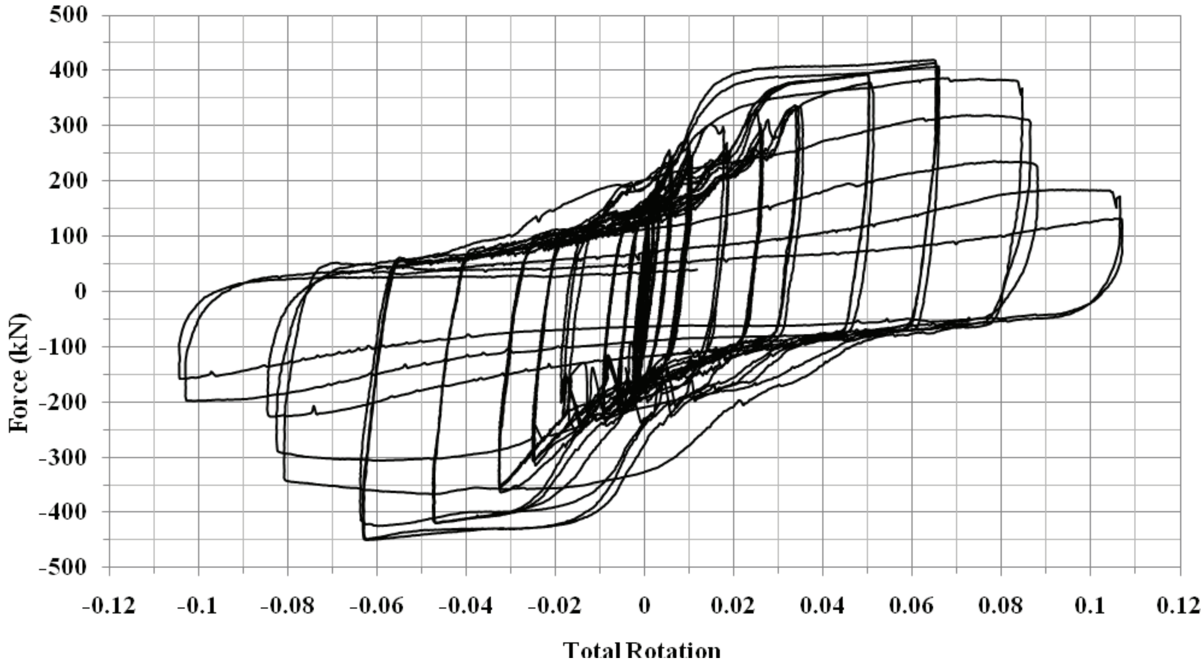

FIGURE 9-43 Link Shear vs. Total Rotation Hysteretic Curve for Specimen SP-R3

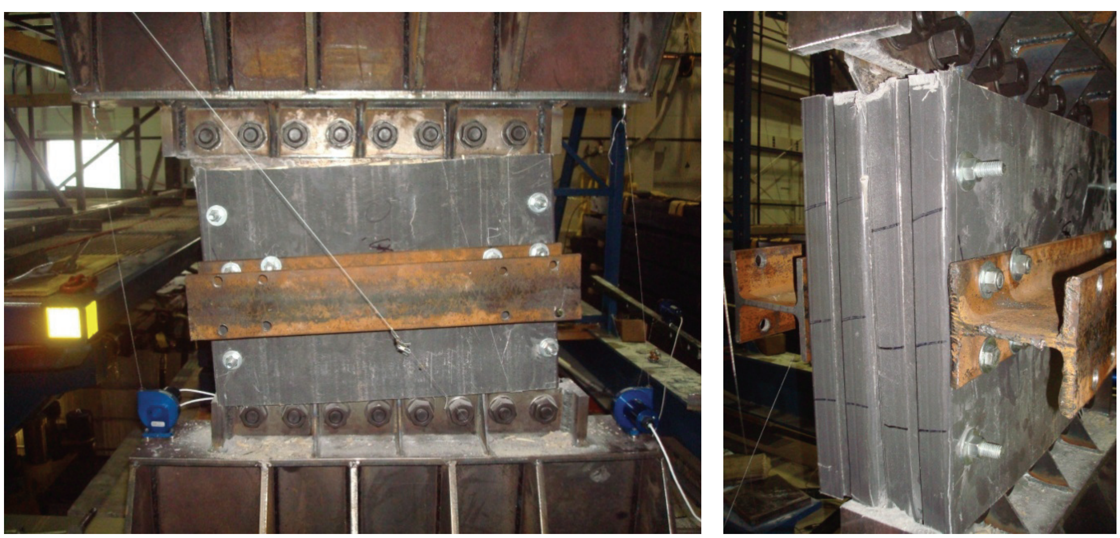

(a) (b)

FIGURE 9-44 Specimen Sp-R3 Condition at γ_{tot} of 0.1 rad; (a) Elevation, (b) Side View

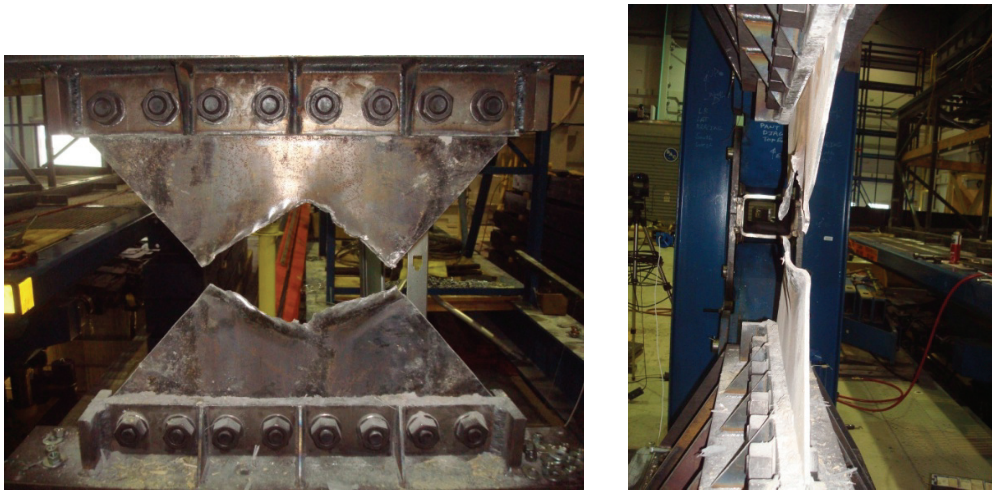

(a) (b)

FIGURE 9-45 Specimen SP-R3 Condition after Removing the Restraints; (a) Elevation, (b) Side View

9.7.5 Specimen SP-U2

Specimen SP-U2 was the link with $\theta=\theta_b$ and unrestrained against out of plane buckling. Figure 9-46 shows the hysteretic behavior observed during testing. Again the same trend of behavior was observed at γ_{tot}=0.002 rad, as loss of stiffness was observed in the hysteretic curves at a shear force of 150kN (34 kips). At a rotation level of 0.02 rad, a sudden drop in strength was observed and was attributed to the initiation of buckling that occurred in the middle part of the specimen and shown in figure 9-47. Up to that point, the specimen was assumed to be yielding in shear (similar to the restrained specimens), this is due to the fact that no signs of buckling was observed in the specimen from which no tension field action is assumed to develop. Due to the unavoidable geometric imperfections buckling started to initiate in the plate, and significant strength loss was observed. The specimen then started to pick up strength gradually at each incremental cycle. Significant pinching in the hysteretic curves is also observed and expected as the plate stretches and relax. A strength reduction is also observed at each rotation level for the repetitive cycles. Progression of buckling for successive rotation levels is shown in figure 9-48. At a rotation level of 0.13 rad, a crack at the upper east corner of the wedge part initiated and propagated at incremental rotation levels as shown in figure 9-49, no significant strength loss was observed in the hysteretic curve. As the crack propagated, gradual softening in the hysteretic curve was observed in both directions. Another crack initiated in the Upper West corner at a rotation level of 0.15 rad and shown in figure 9-50. At that point the cracks propagated rapidly, at a significant loss in strength from 350kN (79kips) to 250kN (56kips) was observed in the negative side of the curve at a rotation level of 0.16 rad, that is about a 30% loss in strength. At the same rotation level at repetitive cycles, the specimen totally fractured and the strength dropped to zero as shown in figure 9-51.

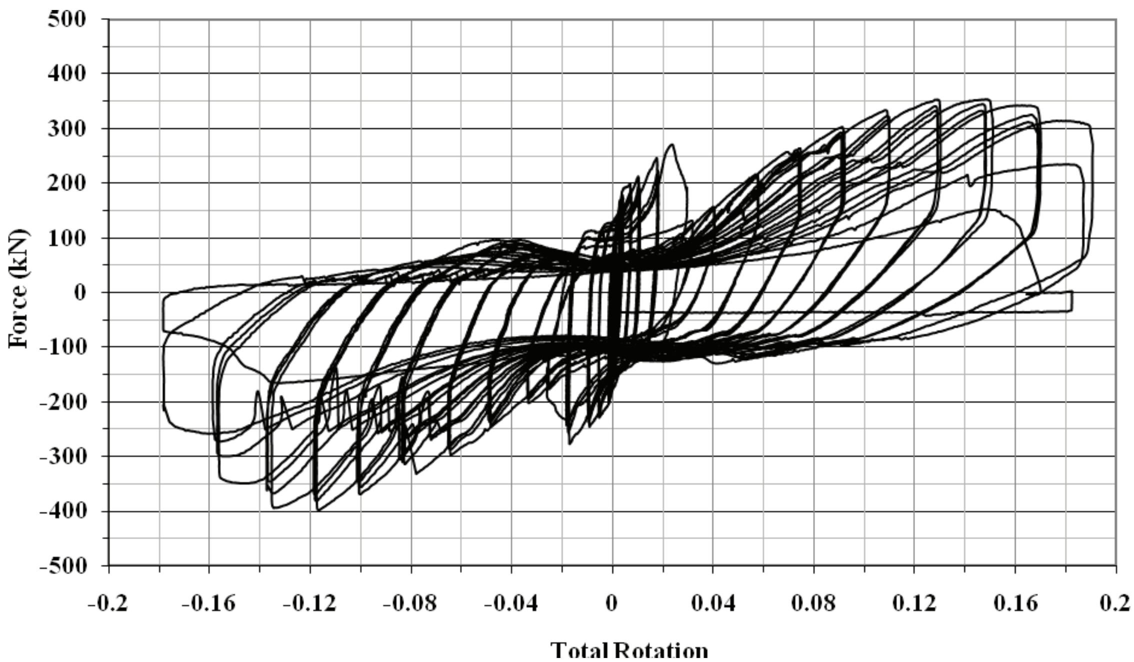

FIGURE 9-46 Shear vs. Total Rotation Hysteretic Curve for Specimen SP-U2

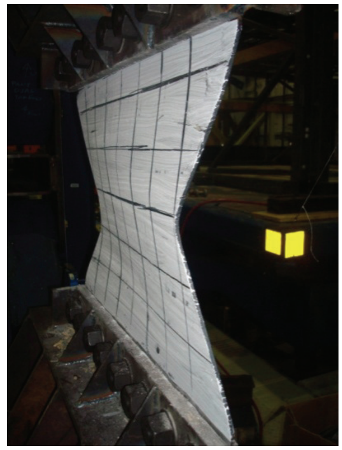

FIGURE 9-47 Buckling Initiation at γ_{tot}=0.02 rad

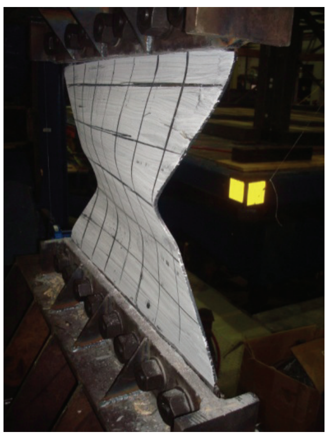 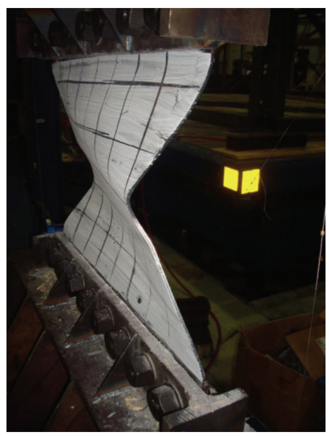 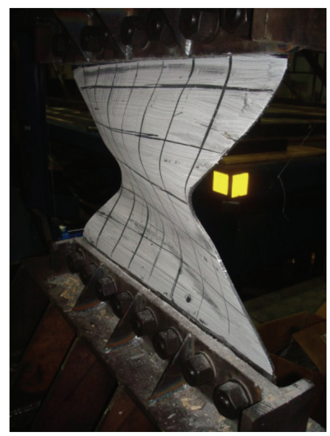

γ_{tot}=0.03 rad γ_{tot}=0.04 rad γ_{tot}=0.05 rad

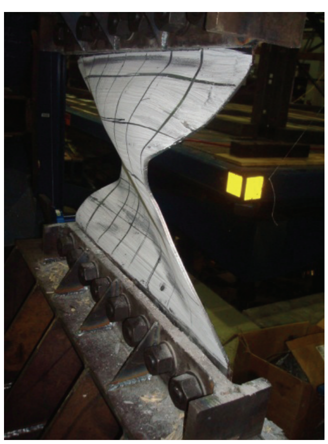  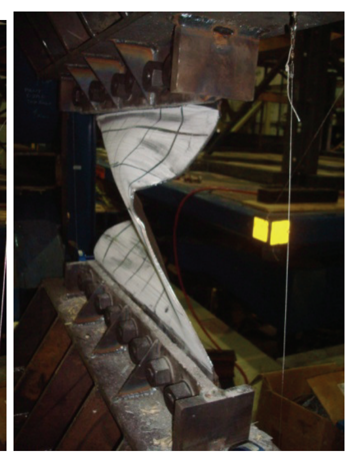

γ_{tot}=0.09 rad γ_{tot}=0.11 rad γ_{tot}=0. 13 rad

FIGURE 9-48 Progression of Buckling at Different Rotation Levels

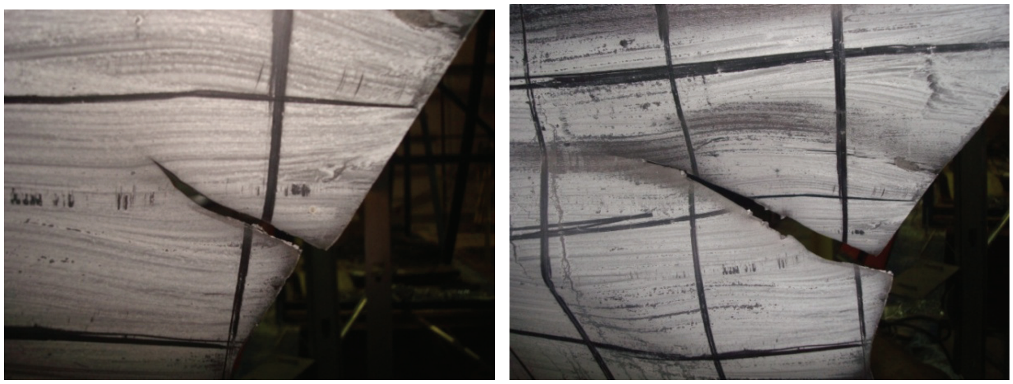

γ_{tot}=0.13 rad γ_{tot}=0.15 rad

FIGURE 9-49 Upper East Crack Initiation and Propagation

FIGURE 9-50 Upper West Crack Initiation

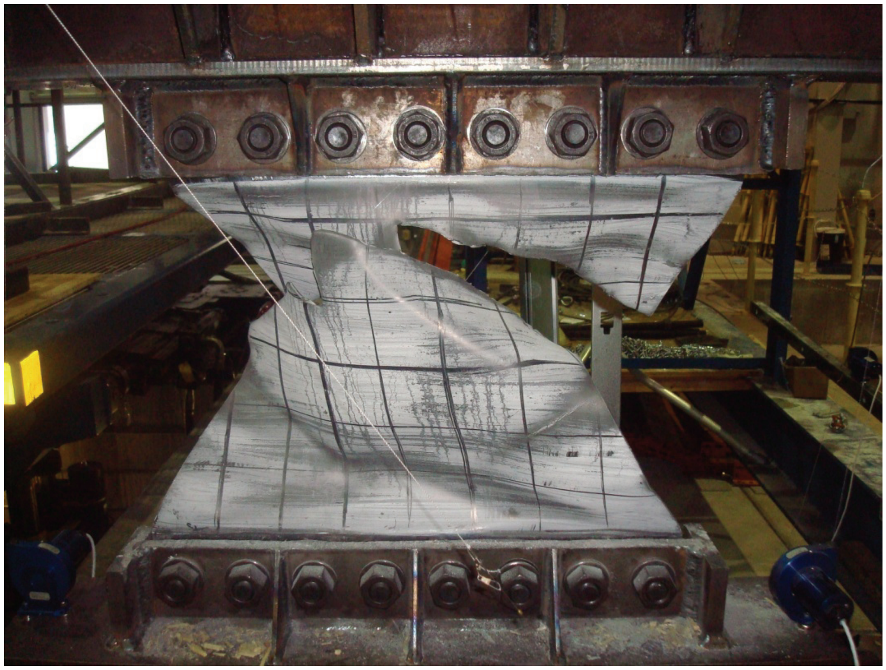

FIGURE 9-51 Specimen SP-U2 at Eng of Test

9.7.6 Specimen SQ-U1

Specimen SQ-U1 was the square link unrestrained against out of plane buckling. Figure 9-52 shows the hysteretic behavior observed during testing. This specimen experienced a linear elastic behavior up to a rotation level of 0.01 rad, a shear force of 350kN (79 kips) was observed. A sudden drop in strength from 350kN (79kips) to 200kN (45kips) was observed after 0.01 rad, and was attributed to the initiation of buckling that occurred in the middle part of the specimen and shown in figure 9-53. Significant pinching in the hysteretic curves was then observed after the buckling initiated. A strength reduction was also observed at each rotation level for the repetitive cycles. Progression of buckling for successive rotation levels is shown in figure 9-54. At a rotation level of 0.13 rad, a crack at the upper east and west corners initiated as shown in figure 9-55, no significant strength loss was immediately observed in the hysteretic curve. However, as the cracks propagated, gradual softening in the hysteretic curve was observed in both directions until the specimen totally fractured. At a rotation level of 0.15 rad, a significant loss in strength from 400kN (90kips) to 200kN (45kips) in the positive direction of the curve was observed, followed by a loss of strength from 350kN (79kips) to 150kN (34kips) at the same rotation level in the negative direction of the curve. This is a 50% drop of strength from the maximum value reached, and the specimen was deemed failed in terms of performance. Testing continued at the same rotation level, the strength dropped to zero and the specimen totally fractured after 3 additional cycles, as shown in figure 9-56.

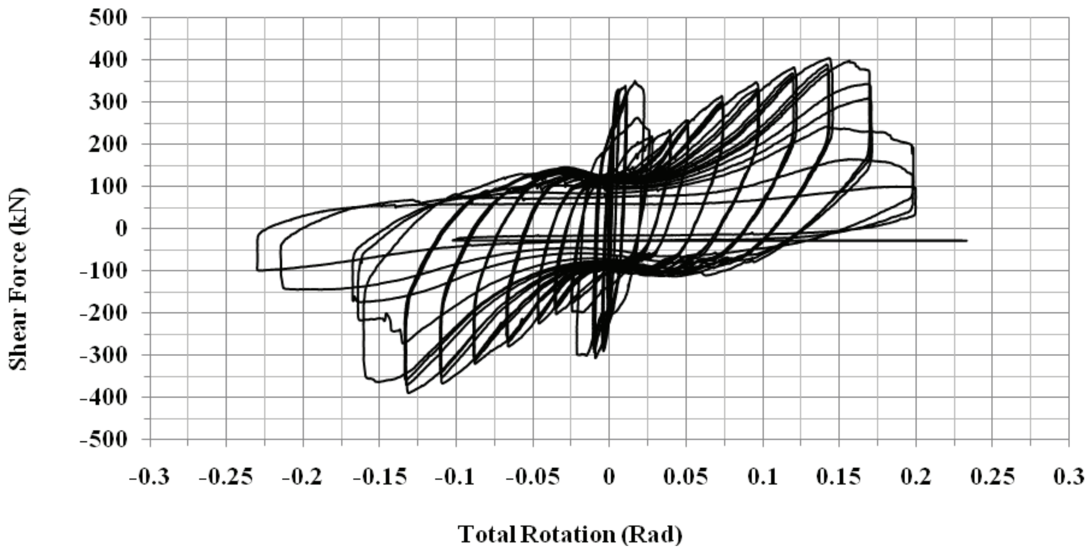

FIGURE 9-52 Shear vs. Total Rotation Hysteretic Curve for Specimen SQ-U1

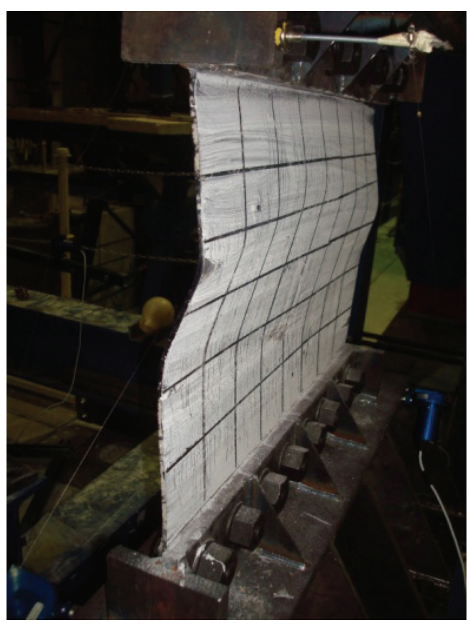

FIGURE 9-53 Buckling Initiation at γ_{tot}=0.01 rad

γ_{tot}=0.02 rad γ_{tot}=0.03 rad γ_{tot}=0.04 rad

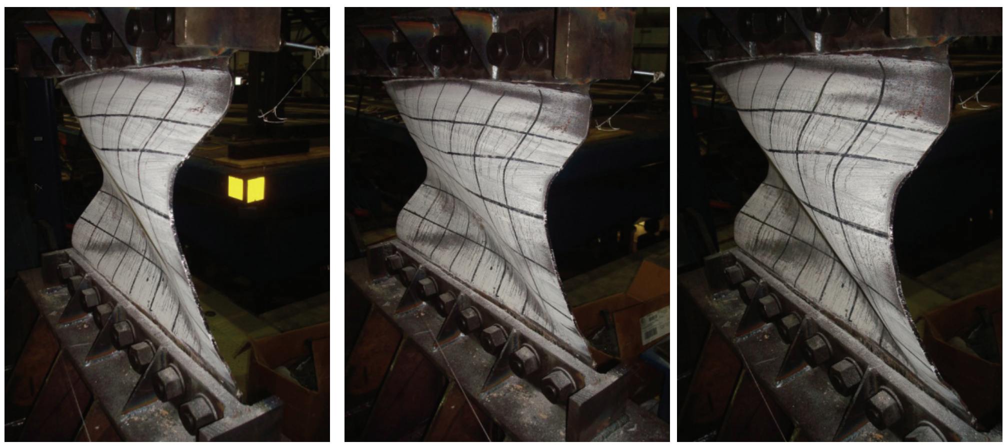

γ_{tot}=0.05 rad γ_{tot}=0.07 rad γ_{tot}=0.09 rad

FIGURE 9-54 Buckling Progression at Different Rotation Levels for Specimen SQ-U1

(a) (b)

FIGURE 9-55 Crack Initiation at γ_{tot}=0.13 rad; (a) Upper West Corner, (b) Upper East Corner

FIGURE 9-56 Specimen SQ-U1 Condition at the End of the Test

9.7.7 Specimen SQ-U2

The final tested specimen was SQ-U2. Figure 9-57 shows the hysteretic behavior observed during testing. A linear elastic behavior up to a rotation level of 0.005 rad and a shear force of 200kN (45 kips) was observed. A drop in stiffness was observed up to a rotation level of 0.03 rad. Then a sudden drop in strength from 350kN (79kips) to 200kN (45kips) was observed where buckling started to initiate as shown in figure 9-58. Similarly to specimen SQ-U1, significant pinching in the hysteretic curves was then observed after buckling initiated. A strength reduction was also observed at each rotation level for the repetitive cycles. At a rotation level of 0.09 rad, a crack at the upper west corner initiated as shown in figure 9-59. Minor strength loss was observed in the hysteretic curve at the rotation level of 0.11 rad. As the cracks propagated, a sudden drop in strength from 300kN (68kips) to 200kN (45kips) was observed in the positive side of the curve, which is about a 33% strength reduction from the maximum strength value reached during the test, from which the specimen was deemed to have failed in terms of performance. Testing continued and the strength dropped to zero and the specimen totally fractured at a rotation level of 0.13 rad as shown in figure 9-60.

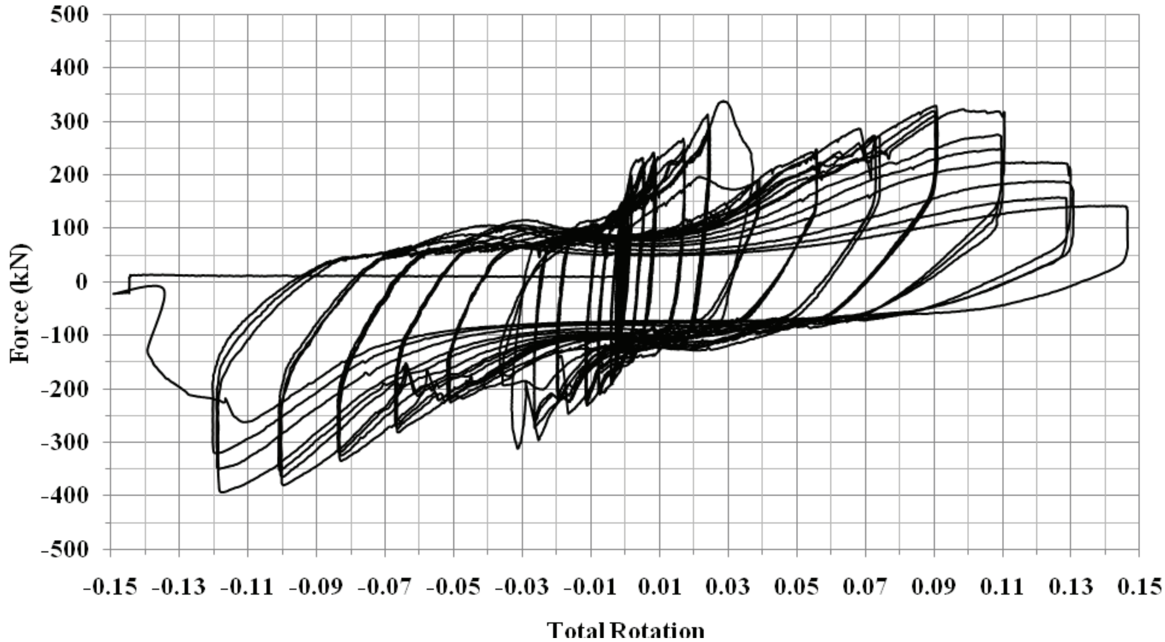

FIGURE 9-57 Shear vs. Total Rotation Hysteretic Curve for Specimen SQ-U2

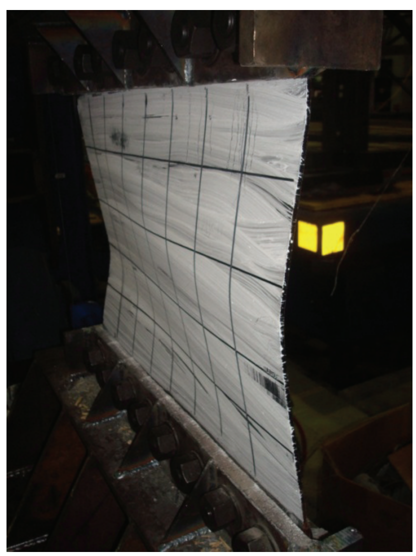

FIGURE 9-58 Buckling Initiation at γ_{tot}=0.03 rad

FIGURE 9-59 Crack Initiation at the Upper West Corner of Specimen SQ-U2

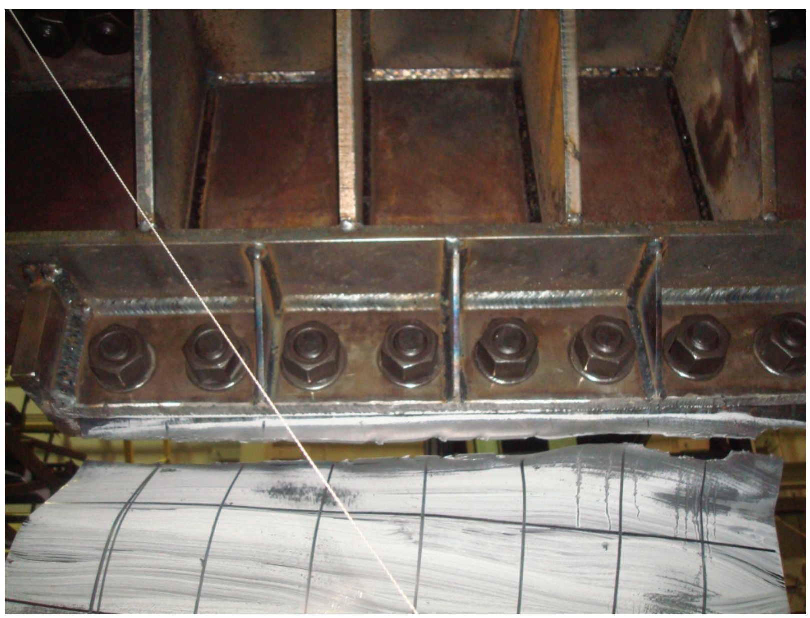

FIGURE 9-60 Specimen Condition at γ_{tot}=0.13 rad

9.8 Investigation on the Vertical Movement of the Setup

Although it was impossible to quantify the amount of force loss that developed along the SPSLs at low rotation levels due to the observed vertical movement of the loading beam, it was attempted to quantifying the amount of vertical movement that have occurred. This vertical displacement could be calculated using the various vertical and diagonal displacement transducers installed along the SPSL specimens as shown in figure 9-61.

Assuming that point *A* and *B* represents the initial positions of the upper west and east points of the SPSL respectively, and points $A^{'}$ and $B^{'}$ represents the final position of these points at an arbitrary horizontal displacement, Δ_h, and a corresponding undesired vertical displacement, Δ_v. Given that the elongation in the displacement transducers are known and denoted as $\delta_{(SP\text{-}D1)}$, and $\delta_{(SP\text{-}D2)}$ for the diagonal displacement transducers and $\delta_{(SP\text{-}VE)}$, and $\delta_{(SP\text{-}VE)}$ for the vertical displacement transducers, the total length of these transducers are then calculated by adding their initial length, h, to their corresponding elongation.

The values of the horizontal displacement, Δ_h, and a corresponding vertical displacement, Δ_v, for point *B* could then be calculated as follows:

For the shaded triangle, given that the lengths of all the sides are known; the value of the angle θ can be calculated as:

$$\cos\theta = \frac{\left(\left(h+\delta_{(SP-VE)}\right)^2 + h^2 - \left(h+\delta_{(SP-D2)}\right)^2\right)}{2h^2\left(h+\delta_{(SP-VE)}\right)} \tag{9-2}$$

from which the value of the angle γ can be calculated as:

$$\gamma = 180 - \theta \tag{9-3}$$

From the dotted triangle, the values of the horizontal displacement, Δ_h, and a corresponding vertical displacement, Δ_v, could then be calculated as:

$$\Delta_h = \left(h+\delta_{(SP-VE)}\right)\cos\gamma \tag{9-4}$$

$$\Delta_v = \left(h + \delta_{(SP-VE)}\right)\sin\gamma - h \tag{9-5}$$

The same approach could be implemented to calculate the values of the horizontal displacement, Δ_h, and a corresponding vertical displacement, Δ_v, for point *A*. Taking the average values of Δ_h and Δ_v for both points, a plot showing the vertical displacement of the upper beam corresponding to the applied horizontal displacement for specimen SP-U2 (arbitrary chosen for illustration) is shown in figure 9-62.

It can be seen from the figure that a vertical displacement of about 35mm (1.4") occurs when a horizontal drift level of about 0.2 rad was reached. This vertical displacement affected the behavior of the SPSLs; at low rotation levels (up to 0.03 rad) by preventing them to reach the anticipated shear forces, and at high rotation levels by introducing some pinching to the system in the unloading cycles. This was proven by the finite element analyses of all specimens, presented in section 9.9.

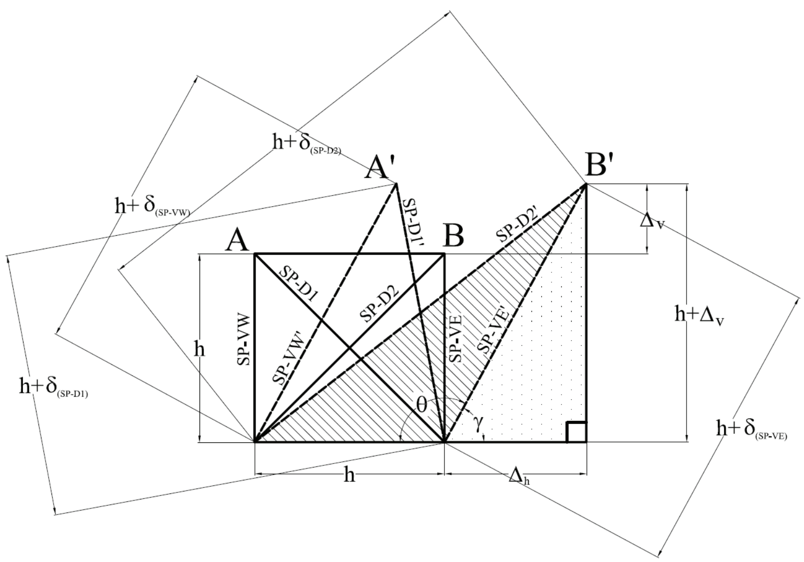

FIGURE 9-61 Geometry of String Pots used to Calculate the Amount of Vertical Movement

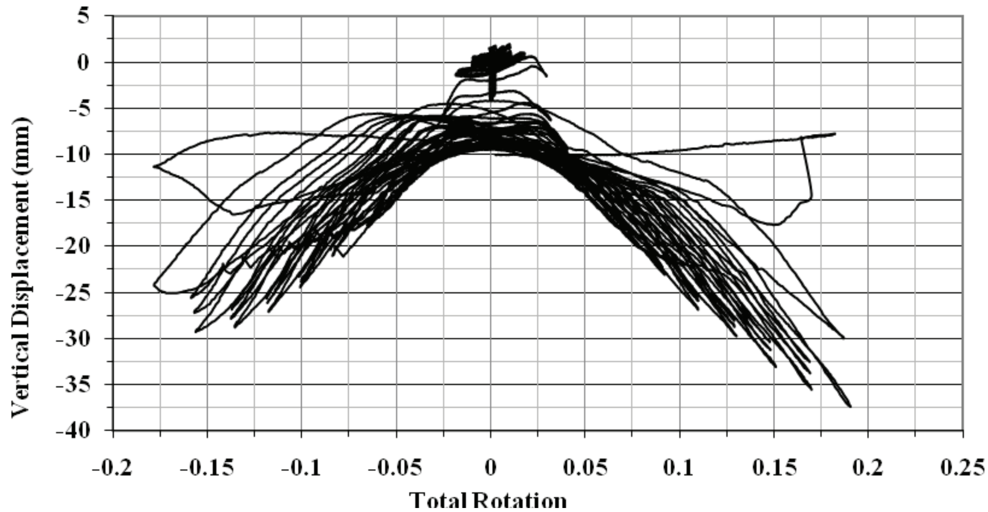

FIGURE 9-62 Vertical Displacement vs. Total Horizontal Drift for the Upper Beam

9.9 Finite Element Analysis

Finite element analysis using the same modeling procedure presented in section 4.12 was conducted to better understand the results of the SPSLs pantograph testing of the individual links, and also to quantify the effect of the downward movement of the loading beam on the global behavior of the specimen ABAQUS models were generated in attempt to replicate the obtained hysteretic curves for specimens SP-R2, SP-R3, SP-SQ1, and SP-U2 obtained by testing using the loading protocol presented in table 9-2 and material models presented in section 9.3. It was challenging to replicate the behavior of specimens SP-R1 and SP-U1, given the fact that the FRP restraint failed at the middle of the test SP-R1 (and that testing continued without it afterwards), and the fact that the gusset plate yielded and distorted for specimen SP-U1. Nonetheless, finite element validation was also found to be crucial to investigate the behavior of the specimens.

9.9.1 Specimen SP-R3

A comparison between the hysteretic curve obtained by testing and the ABAQUS hysteretic curve for specimen SP-R3 is shown in figure 9-63. It can be observed from the figure that the model represented well the elastic stiffness of the specimen as well as its ultimate shear strength. The difference between the experimental and the analytical hysteretic curves is the presence of substantial pinching in the experimental curve and the inability of the model to capture strength degradation due to crack propagation up to fracture. This pinching was attributed to the vertical movement of the loading beam that was observed during testing due to some flexibility of the set-up that could not be prevented in spite of the fact that a steel block was inserted under the loading beam as shown in figure 9-23 to prevent this vertical motion.

Figure 9-64 shows a plot of the Von Misses stresses obtained from the FEM analysis, with the red zone indicating yielding, and for comparison the final state of the specimen after testing is also shown in figure 9-64(b). It can be observed that tearing of the specimen took place around the zone of yielding of the specimen, while the rest of the specimen remained elastic. The actual tearing zone appears to be a bit larger than the yielded part in the model, but this is reasonable as one must recognize that the finite element analysis did not model fracture and its propagation. Figure 9-65 shows similar plots for S11 (being the stress in the horizontal direction), S22 (being the stress in the vertical direction), and S12 (being the shear stress) respectively, where the red zones indicate yielding. This confirms that yielding of the link is due to pure shear yielding in the narrowest part of the link, and that no flexural stresses have contributed to the yielding of the plate.

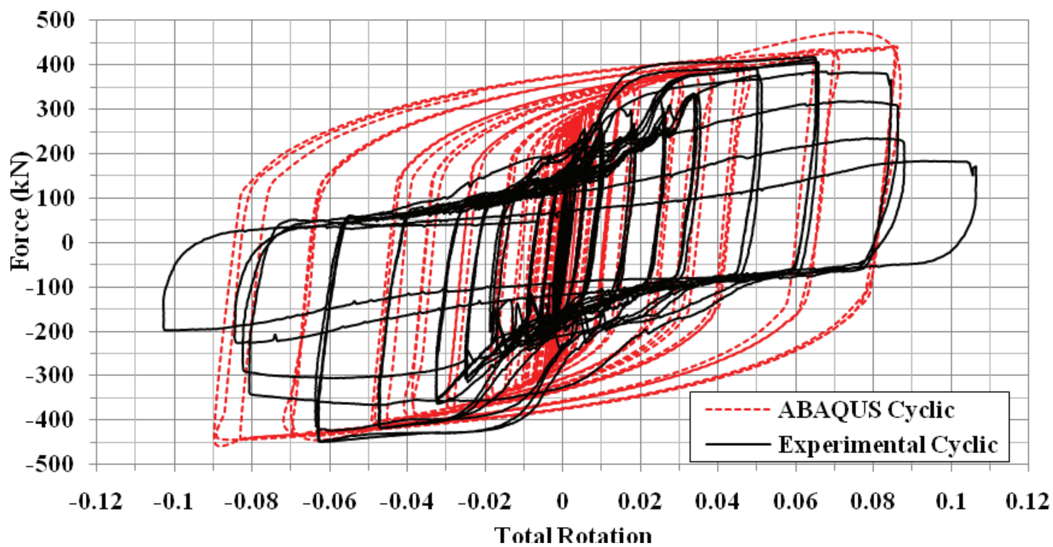

FIGURE 9-63 Hysteretic Behavior of Specimen SP-R3

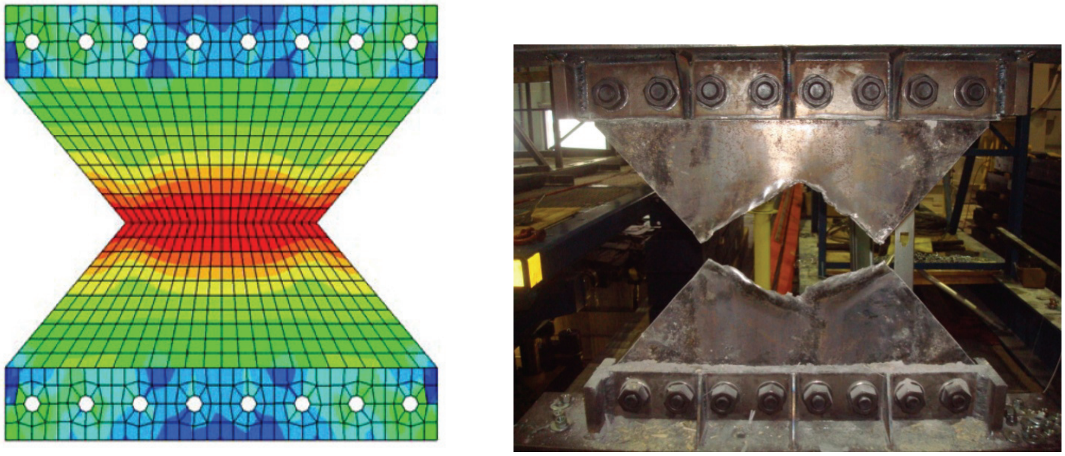

(a) (b)

FIGURE 9-64 Yielding of Specimen SP-R3; (a) FEM, (b) Experimental

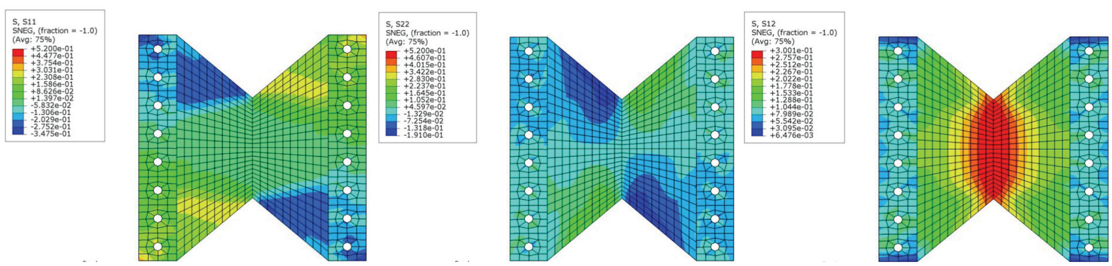

(a) (b) (c)

FIGURE 9-65 FEM results; (a) S11, (b) S22, (c) S12

9.9.2 Specimen SP-R2

A comparison between the hysteretic curve obtained by testing and the ABAQUS hysteretic curve for specimen SP-R3 is shown in figure 9-66. Again, it is observed from the figure that the model represents well the elastic stiffness of the specimen as well as the shear forces at high rotation levels (beyond 0.03 rad). A major difference between the experimental and the analytical hysteretic curves is that the shear forces measured at low rotation levels were smaller than anticipated, and the presence of substantial pinching in the experimental curve in the unloading cycles at high rotation levels. In this case, the pinching is substantially more than what was observed for specimen SP-R3.This is attributed to two factors; first, the vertical movement of the loading beam that was observed during testing due to some flexibility of the set-up; second, the buckling that was observed in the top and bottom of the specimen and that was described earlier in section 9.7.2.

Figure 9-67 shows results plots for S11, S22, and S12 respectively at 0.1 rad, where blue and red indicates yielding in both tension and compression respectively for S11 and S22, while red indicates shear yielding for S12. It can be observed that the yielding of the link is due to a combination of pure shear yielding at the middle part, and flexural yielding in the wedge parts that occurs simultaneously.

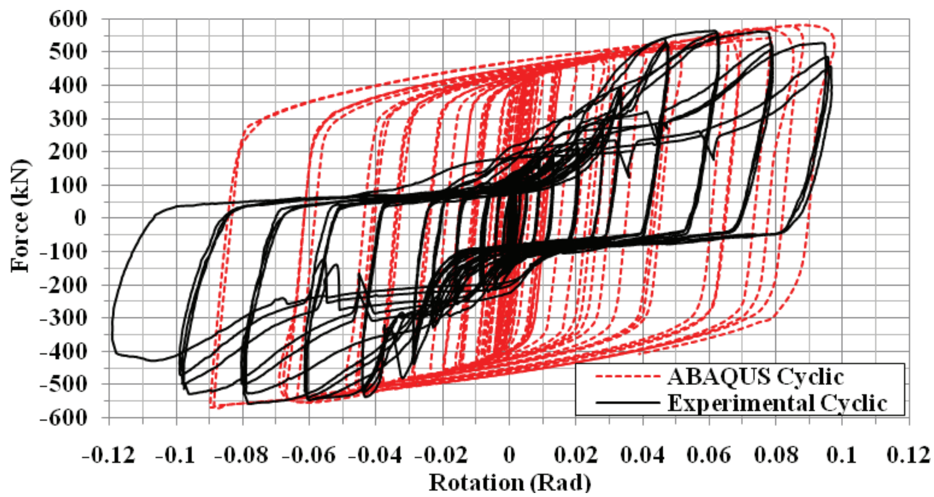

FIGURE 9-66 Hysteretic Behavior of Specimen SP-R2

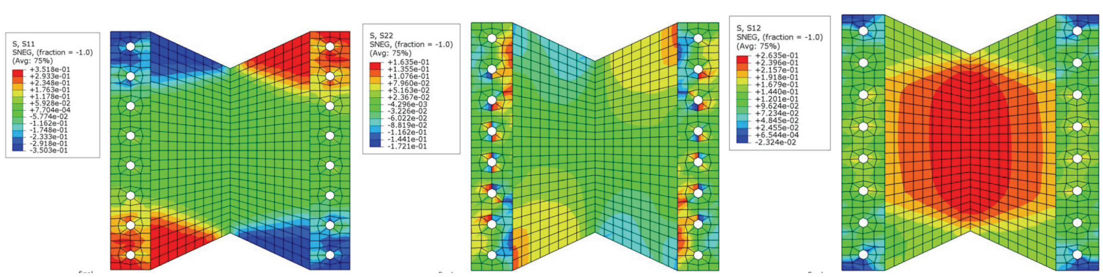

(a) (b) (c)

FIGURE 9-67 FEM results at 0.1 rad; (a) S11, (b) S22, (c) S12

9.9.3 Specimen SP-U1

A comparison between the hysteretic curve obtained by testing and the ABAQUS hysteretic curve for specimen SP-U1 is shown in figure 9-68. It can be seen from the figure that the experimental results gave substantially lower than expected shear forces until reaching a total rotation of about 0.08 in both cycling directions, beyond which the model represents well the behavior of the specimen albeit with the presence of some additional pinching due to the downward motion of the loading beam. Also from a stiffness perspective; the initial stiffness of the model matches well with the experiment. It was also observed that the unloading stiffness of the model matches well with that of the experimental curve. At about 100kN (23kips) in both directions, the unloading stiffness drops dramatically as seen in the experimental hysteretic curve. This vertical motion of the top beam created premature buckling of the plate; which is why the elastic base shear was lower than what was predicted by the model. Also as the loading beam moves downwards, lesser forces are resisted by the specimen up to a point where the beam settles (which was around 0.08 rad). Also during the unloading cycle, the sudden drop of the shear force resisted by the plate is also attributed to the vertical motion of the beam.

A comparison between the deflected shape of the specimen and the finite element model at the end of the 0.13 rad cycle is shown in figure 9-69. A plot showing the maximum in plane principal stress at a peak rotation level of 0.13 rad is shown in figure 9-70, the tension field developed can be seen in the figure.

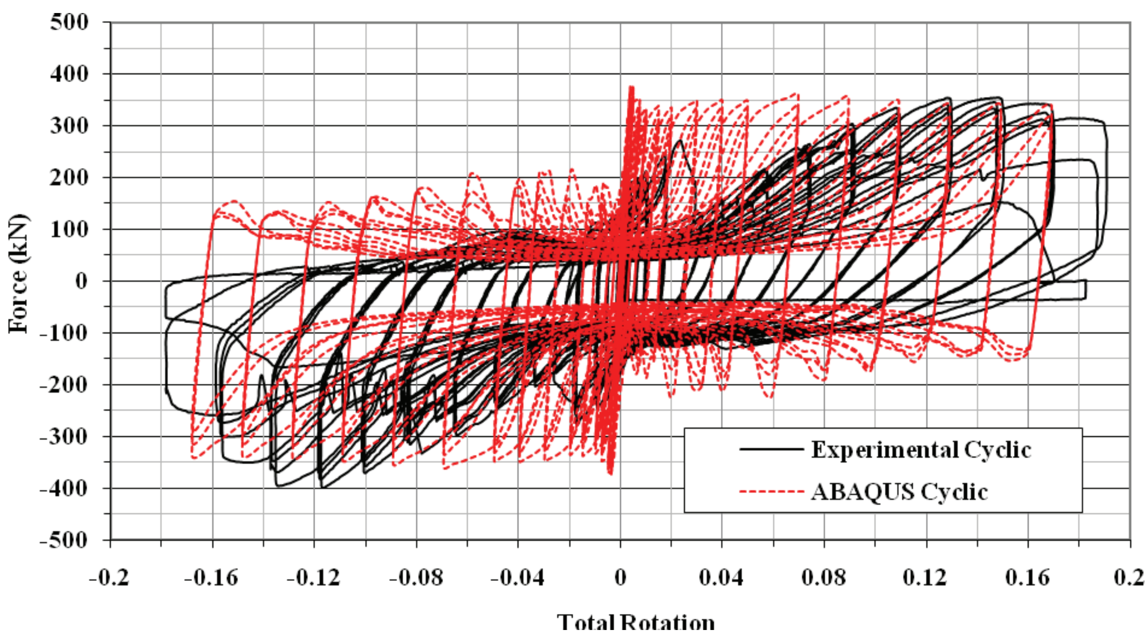

FIGURE 9-68 Hysteretic Behavior of Specimen SP-U1

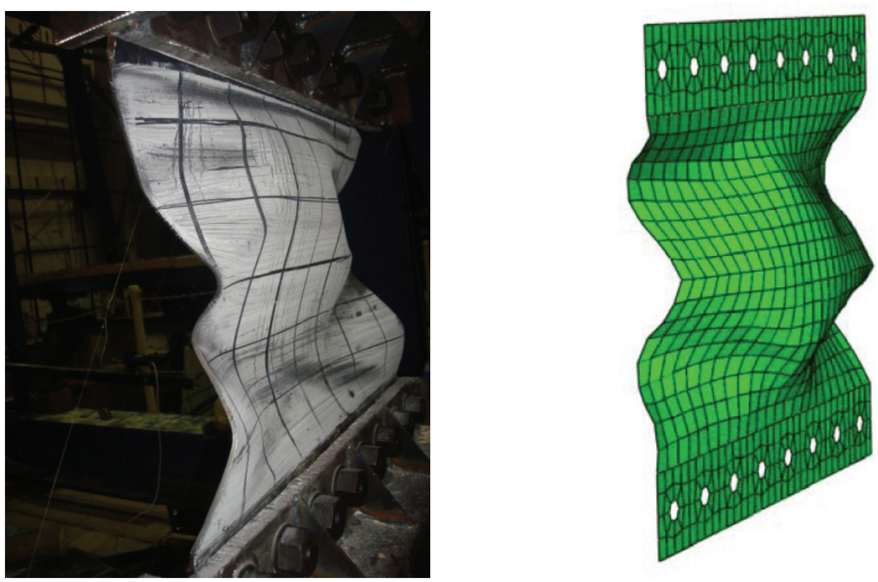

(a) (b)

FIGURE 9-69 Deflected shape at the end of the 0.13 rad Cycle; (a) Experimental, (b) FEM

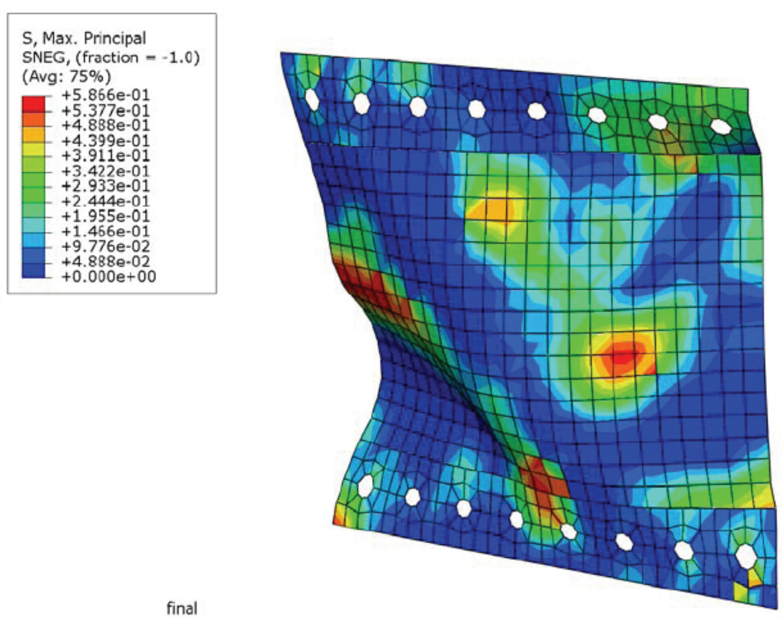

FIGURE 9-70 Maximum In-Plane Principal Stress at 0.13 rad

9.9.4 Specimen SQ-U1

A comparison between the hysteretic curve obtained by testing and the ABAQUS hysteretic curve for specimen SQ-U1 is shown in figure 9-71. It can also be seen from the figure that the experiment again gave lower than anticipated shear forces until reaching a total rotation of about 0.08 in both cycling directions, and then the model matches well with the experimental hysteretic curve. Also the unloading stiffness of the model matches well with that of the experimental curve up to a constant point in each cycle where the load drops in both directions in the experimental hysteretic curve. Again these differences were attributed to the same reason mentioned in section 9.8.3., which is the vertical motion of the loading that was observed in the experiment.

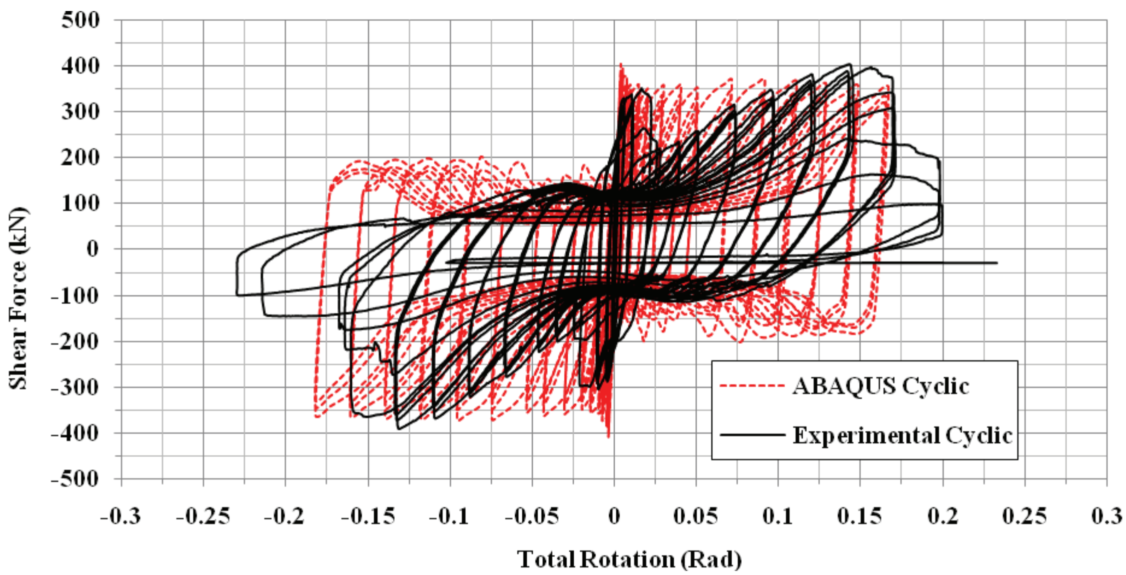

FIGURE 9-71 Hysteretic Behavior of Specimen SQ-U1

9.10 Summary

This section describes the experimental testing performed of SPSLs with various link edge angles and lateral restraint conditions. Table 9-3 summarizes the maximum base shear and total rotations for all specimens except SP-R1 and SP-U1 up to the point where failure is considered. It was observed that adding the restraints increased the base shear capacity for the specimens having the same dimensions. Also adding the restraints improved the hysteretic performance of the specimens as they reduced the pinching observed in the behavior of the unrestrained specimens, and also improved behavior under repetitive cycles. As in the case of the unrestrained specimens, repeating the cycles at the same rotation level resulted in reducing the shear capacity of the specimen as the steel could only stretch once, while in the case of the restrained specimen, the same shear capacity could be obtained at upon repetitive cycles at the same rotation level. Nevertheless, adding the restraints decreased the rotation capacities in comparison with the unrestrained specimens; this is attributed to the localization of plastic strains in the middle part of the specimens when yielding in shear in the case of the restrained specimens, compared to distributed plastic strains along diagonal strips in the case of unrestrained specimens.

The effect of the observed downward motion of the loading beam on the global behavior of the SPSLs was also investigated. It was found out that due to this downward motion, the experiments results showed that the anticipated shear strength of the specimens was only reached at high rotation levels, and substantial pinching was introduced in the hysteresis curves.

TABLE 9-3 Summary of Peak Results

Specimen	Max. Shear Force (kN)	Total Rotation at Failure
SP-R2	550	0.09
SP-R3	450	0.08
SP-U2	400	0.16
SQ-U1	400	0.16
SQ-U2	400	0.11

SECTION 10
SUMMARY, CONCLUSIONS, AND RECOMMENDATIONS FOR FUTURE WORK

10.1 Summary

Research was conducted to investigate strategies to implement a structural fuse concept for the seismic design and retrofit of bridges. The concept was first developed for the retrofit of multiple column R/C bents, but was then extended to consider application to a proposed multi-column accelerated bridge construction (ABC) pier design made of concrete-filled steel box columns. Analytical studies have been conducted to evaluate the efficiency of two different types of structural fuses, namely Steel Plate Shear Links (SPSLs) and Buckling Restrained Braces (BRBs), for bents with RC columns as well ABC columns. The proposed ABC column system was then retrained for the subsequent experimental phase of the project. Using finite element models, static pushover and pseudo-static cyclic hysteretic curves have been obtained for the proposed bridge pier systems.

Previous studies have used different definition of structural fuses, in different contexts. Here, the focus has been on structural fuses defined as sacrificial and easy-to-replace elements designed to protect the substructure and the gravity-resisting elements of a bridge, allowing seismic energy dissipation by the fuses while the bridge substructure remain elastic. Governing parameters defining the behavior and design of the fuse system were identified. Seismic response was validated through parametric analyses of the studied systems, and design guidance was provided for the sizing of the fuse system as a function of the total system strength.

BRBs were first proposed as a structural fuse for retrofitting RC bridge bents to increase their strength and stiffness, and to dissipate seismic energy through hysteretic behavior while the existing RC bridge piers remain elastic. A parametric study, in terms of non-dimensionalized values was conducted to consider general frame and BRBs geometries. Key parameters that control the behavior of the BRBs as a structural fuse were identified, relationships between these parameters were investigated for the application at hand, and plots showing the regions of admissible solutions for several frame and BRBs strengths and stiffnesses were constructed. The results were then refined and validated using non-linear time history analyses. Nine spectra-compatible ground records were generated to match the targeted response spectra. Plots showing comparison of the time history results and the proposed static procedure where presented. A retrofit design procedure was then formulated, showing the necessary steps to achieve the design objectives.

For the experimental phase of this research, a prototype three span continuous bridge having two twin-columns pier bents with fixed base spaced at 36m (120 ft) and 9m (30 ft) tall, was designed according to the AASHTO LRFD bridge design specifications. Its piers were designed using double composite rectangular columns of Bi-Steel panels, and structural fuses. A corresponding 2/3 scale model was then developed and tested at the SEESL at the University at Buffalo. Specimens were subjected to quasi-static testing, starting with the Steel Plate Shear Link (SPSL) as a series of structural fuses inserted between the columns. Analytical and experimental results were then presented to verify the proposed concept.

After completion of the two twin-columns pier bents tests, it was decided to perform uniaxial cyclic tests on the BRBs and SPSLs used as structural fuses as the hysteretic curves obtained for the fuses during testing of the full specimens did not truly represent their individual behavior, and because the forces resisted by each individual fuse could not be measured individually during the pier tests. For the BRBs individual tests, two sets of BRBs having different cross sections were used. Together, in addition to getting important fundamental data on the behavior of this type of BRB, these two BRB test series allowed to investigate the effect of changing the cross section on the overall behavior. Note that the BRBs used are a new prototype created for short length BRB applications; they use a different design to prevent buckling in compression to accommodate the short yielding core length needed for the current application (i.e. much shorter compared to the BRBs that are been used in building projects to date).

Experimental testing was also performed on individual SPSLs with various geometry and lateral restraint conditions. Photographs and a description of observations made during the cyclic history were provided for the individual SPSLs. Finite element models were then generated to replicate the observed hysteretic behavior of the SPSLs being tested, and provide insight into the general behavior of the SPSLs.

10.2 Conclusions

This research demonstrated that the proposed design procedure leads to robust and reliable structural fuse systems that can exhibit satisfactory seismic performance. The range of admissible solutions that satisfy the structural fuse concept were also parametrically defined.

Experimental and analytical investigations of the twin-columns bridge pier with structural fuses showed that the specimens tested exhibited stable hysteretic behavior as the seismic energy was dissipated through the structural fuses. Adding the fuses increased both the stiffness and strength of the bare frame. While the proposed design procedure allows to select many desired performance strength and stiffness for the structural fuse system that meet the design objectives in various way, for the specimen designed and experimentally tested, adding the fuses increased stiffness and strength by about 40% and substantially increased the amount of hysteretic energy dissipated by the frame, while keeping the columns elastic up to the target design displacement.

Experimental axial testing performed on the new BRBs having short lengths showed that the newly proposed BRB assembly exhibited stable hysteretic behavior and dissipated energy substantially, exceeding the values required by the AISC seismic provisions for qualification of BRBs.

Experimental and analytical investigations of the individual SPSLs showed that adding lateral restraints increased their base shear capacity (by 40% for the specific dimensions considered here) over unrestrained specimens having the same dimensions. Also adding the restraints improved the hysteretic performance of the specimens as they reduced the pinching observed in the behavior of the unrestrained specimens, and improve behavior under repetitive cycles.

10.3 Recommendations for Future Work

Given that this research has predominantly looked into the implementation of structural fuses in accelerated bridge construction applications, the columns used for the experimental phase of this research were of a composite-type, namely steel boxes filled with concrete columns. Most of the accelerated bridge construction applications for bridge columns to date have used prestressed concrete segments; therefore, there are opportunities for future research to investigate how to implement the structural fuse concept for these types of columns, both in the perspective of global behavior and in terms of the types of connections that would need to be developed to implemented steel fuses between the concrete prestressed columns.

As the experiments conducted on the bridge piers in this research applied pseudo-static cyclic loading using static actuators at the top of the pier, future experiment could experimentally investigate the proposed concept dynamically, by testing bridge piers using structural fuses on shake tables using a wide range of possible earthquake acceleration time histories, also including near-fault ground motions (which has not been considered in this study).

Further investigations could also investigate alternative strategies to provide lateral restraints for the SPSLs, to achieve an improved performance. An improved testing setup for the shear testing of the SPSLs is also recommended to illuminate some problematic issues with the test setup that have been faced in this research.

Further investigation should also be considered to investigate the effect of increasing the accelerations of the total system on the design of the foundations, due to the addition of the structural fuses. Also the effect of the increased acceleration on the bridge deck and acceleration sensitive items at that level could be investigated.

Investigation on combining different types of fuses in one system could also be investigated as a future research to reach an optimum fuse solution. Furthermore, the effect of three dimensional earthquake excitation and response of the structural system is worthy of additional exploration, to determine if torsional response of the columns or the links could noticeably modify behavior on the structural system.

Beyond the structural fuse concept, it is also recommended to further investigate the cyclic behavior of the double skin concrete filled columns used in this research and known as Bi-Steel columns. Much needs to be done in this regard to develop a better understanding of their effectiveness in seismic regions. In particular, it would be of interest to investigate the effect of changing the tie bars spacing on the global ductile behavior of the system, as it would be expected that smaller spacing would result in a decreased propensity for local buckling, which should be beneficial. Yet, at the same time, by analogy with the global buckling behavior of concentrically braced frames, a less slender element develops plastic local buckling and questions arise to whether this would detrimentally magnify the plastic strains in the buckled portions of the columns. It is unclear whether increasing or decreasing the spacing of the ties (or finding an optimum) would be best in this particular case to ensure the greater fatigue life of the columns and to delay their fracture up to relatively larger drift levels. Data on the cyclic inelastic behavior of Bi-Steel columns built with steels having actual yield strength closer to the values commonly encountered in practice would also be of great interest.

SECTION 11
REFERENCES

AASHTO, L. (2009). "Bridge Design Specifications, Customary US Units, with 2009 Interim Revisions." *American Association of State Highway and Transportation Officials, Washington, DC*.

ABAQUS, I. (2005). "ABAQUS/CAE User's Manual." *Electronic Version*, 6, 4-5.

ACI. (2008). "Building Code Requirements for Structural Concrete (ACI 318-08) and Commentary (318R-08)." American Concrete Institute, Farmington Hills, MI.

Aiken, I., Clark, P., Tajirian, F., Kasai, K., Kimura, I., and Ko, E. (2000) "Unbonded Braces in the United States-Design Studies, Large-Scale Testing and the First Building Application." *Proceedings of the International Post-SMiRT Conference Seminal*, Korea Earthquake Research Center, Volume I, pp. 317-337.

Aiken, I., and Kimura, I. (2001) "The use of buckling-restrained braces in the United States." *Porceedings, Japan Passive Control Symposium*, Tokyo Institute of Technology, Yokohama, Japan.

AISC. (2005). "Seismic Provisions for Structural Steel Buildings." American Institute of Steel Construction, Chicago, Illinois.

Ang, B. G., Priestley, M., and Paulay, T. (1989). "Seismic shear strength of circular reinforced concrete columns." *ACI Structural Journal*, 86(1).

ASTM, A. "6/A 6M(2007) Standard Specification for General Requirements for Rolled Structural Steel Bars." *Plates, Shapes, and Sheet Piling*.

ASTM, A. (1996). "370-96 Standard Test Methods and Definitions for Mechanical Testing of Steel Products." *American Society for Testing and Materials (ASTM), West Conshohocken, FA*.

ATC. (1992). "Guidelines for Seismic Testing of Components of Steel Structures Report-24." Applied Technology Council, Redwood City, CA.

Berman, J., and Bruneau, M. (2005). "Approaches for the seismic retrofit of braced steel bridge piers and proof-of-concept testing of an eccentrically braced frame with tubular link." *Technical Rep. MCEER-05*, 4.

Berman, J., and Bruneau, M. (2006). "Further development of tubular eccentrically braced frame links for the seismic retrofit of braced steel truss bridge piers." *Technical Rep. No. MCEER-06*, 6.

Black, C., Markis, N., and Aiken, I. D. (2004). "Component testing, seismic evaluation and characterization of buckling-restrained braces." *Journal of Structural Engineering*, 130(6).

Bowerman, H., Gough, M., and King, C. (1999). "Bi-Steel design and construction guide." *British Steel Ltd, Scunthorpe (London)*.

Buckle, I., Friedland, I., and Cooper, J. (1994). "A Seismic Retrofitting Manual for Highway Bridges." *NIST SPECIAL PUBLICATION SP*, 47-47.

Caltrans, S. (2004). "Caltrans Seismic Design Criteria version 1.3." *California Department of Transportation, Sacramento, California*.

Carden, L., Itani, A., PE, F., and Buckle, I. (2006). "Seismic performance of steel girder bridges with ductile cross frames using buckling-restrained braces." *Journal of Structural Engineering*, 132, 338.

Chaallal, 0., Guizani, L., and Malenfant, P (1996). “Classification Methodology for Coupled Shear Walls.” *J. Struct. Engrg. Volume 122, Issue 12, pp. 1453-1458*

Clark, P., Aiken, I., Kasai, K., and Kimura, I. (2000) "Large-scale testing of steel unbonded braces for energy dissipation." *Proceedings of the Structural Congress*, Philadelphia, Pennsylvania.

Conner, J., Iwata, M., and Huang, Y. (1997). "Damage-controlled structures. I: Preliminary design methodology for seismically active regions." *Journal of Structural Engineering*, Volumne 123, No. 4, ASCE, pp. 423-431.

Council, B. (2003). "NEHRP recommended provisions for seismic regulations for new buildings and other structures." *Rep. No. FEMA*, 450.

Di Sarno, L., Manfredi, G., and Acanfora, M. (2007) "Design Approach For The Seismic Strengthening Of An Existing Rc Building With Buckling Restrained Braces." *10th World Conference on Seismic Isolation, Energy Dissipation and Active Vibrations Control of Structures*, Istanbul, Turkey.

Engelhardt, M., and Popov, E. (1989). "Behavior of long links in eccentrically braced frames." *Report No. UCB/EERC-89*, 1.

FEMA (2004), "FEMA 450: NEHRP Recommended Provisions For Seismic Regulations for New New Buildings And Other Structures." Building Seismic Safety Council for the Federal Emergency Management Agency, Washington, D.C.

Fintel, M., and Ghosh, S. (1981). "Structural Fuse: An Inelastic Approach to Seismic Design of Buildings." *Civil Engineering ASCE*, 51(1), 48-51.

Goodyear, D., and Sun, J. (2003). "New developments in cable-stayed bridge design, San Francisco." *Structural Engineering International*, 13(1), 59-63.

Hasegawa, H., Takeuchi, T., Iwata, M., Yamada, S., and Akiyama, H. (1999). "Experimental study on dynamic behavior of unbonded-braces." *Journal of Architecture*, 114(1448), 103-106.

Hibbitt, K. (2000). *ABAQUS/Explicit: user's manual*, Hibbitt, Karlsson and Sorenson Inc.

Huang, Y., Wada, A., Iwata, M., and Mahin, S. (2002). "Design of damage-controlled structures." *Innovative Approaches to Earthquake Engineering. Billerica, MA: WIT Press, 2002.*, 85-118.

Islam, S., Skokan, M., and Huang, S. (2006) "Innovative Hi Tech Solution for a Concrete Residential High Rise Tower."

Iwata, M., Kato, T., and Wada, A. (2000) "Buckling-Restrained Braces as Hysteretic Dampers." *Behavior of Steel Structures in Seismic Areas*, STESSA, 33-38.

Kabeyasawa, T., Shiorara, H., Otani, S., and Aoyama, H. (1982). "Analysis of the full-scale seven-story reinforced concrete test structure: test PSD3." *Proc. 3rd Joint Tech. Coordinating Com., U.S.-Japan Cooperative Earthquake Res. Program,* Building Research Institute, Tsukuba, Japan.

Kabeyasawa, T., Shiorara, H., and Otani, S. (1984). "U.S.-Japan cooperative research on RC full-scale building test-Part 5: discussion on dynamic response system." *Proc. 8th World Con/. on Earthquake Engrg.,6.* Prentice-Hall, Inc., Englewood Cliffs, N.J.

Kasai, K., and Popov, E. (1986a). "Cyclic web buckling control for shear link beams." *Journal of Structural Engineering*, 112(3), 505-523.

Kasai, K., and Popov, E. (1986b). "General behavior of WF steel shear link beams." *Journal of Structural Engineering*, 112(2), 362-382.

Kelly, J., Skinner, R., and Heine, A. (1972). "Mechanisms of Energy Absorption In Speical Devises For Use In Earthquake Resistant Structures." *Bull. N.Z. Nat. Soc. for Earthquake Eng.*, Vol. 5,(No. 3).

Lee, J., and Fenves, G. L. (1998). "Plastic-damage model for cyclic loading of concrete structures." *Journal of Engineering Mechanics*, 124, 892.

Lopez, W., Gwie, D., Saunders, M., and Lauck, T. (2002) "Lessons learned from large-scale tests of unbonded braced frame subassemblage." *Proceedings 71st Annual Convention, Structural Engineers Association of California*, Sacramento, California, 171-183.

López, W., and Sabelli, R. (2004). "Seismic design of buckling-restrained braced frames." *Steel Tips, Structural Steel Education Council (www. steeltips. org)*.

Lubliner, J., Oliver, J., Oller, S., and Onate, E. (1989). "A plastic-damage model for concrete." *International Journal of Solids and Structures*, 25(3), 299-326.

Morgan, T., and Walters, M. (2004). "Innovative Approaches to Performance-based Seismic Rehabilitation of Concrete Buildings." *Pacific Earthquake Engineering Research Center, College of Engineering, University of California, Berkeley*, 89.

Papageorgiou, A., Halldorson, B., and Dong, G. (2001). "TARSCTHS, a computer program for Target Acceleration Spectra Compatible Time Histories." *Department of Civil, Structural and Environmental Engineering, University at Buffalo, New York.*

Park, R., and Paulay, T. (1975). *Reinforced concrete structures*, John Wiley & Sons Inc.

Paulay, T. (1971). "Coupling beams of RC shear walls." *J. Struct.Engrg.,* ASCE, 97(3), 843-862.

Priestley, M., and Park, R. (1987). "Strength and ductility of concrete bridge columns under seismic loading." *ACI Structural Journal*, 84(1).

Priestley, M., Seible, F., and Calvi, G. (1996). *Seismic design and retrofit of bridges*, Wiley-Interscience.

Priestley, M., Verma, R., and Xiao, Y. (1994). "Seismic shear strength of reinforced concrete columns." *Journal of Structural Engineering*, 120(8), 2310-2329.

Ranf, R., EERI, M., Eberhard, M., Malone, S., and EERI, A. (2007). "Post-earthquake prioritization of bridge inspections." *Earthquake Spectra*, 23, 131.

Reina, P., and Normile, D. (1997). "Fully braced for seismic survival." *Engineering News-Record*, 34–36.

Roeder, C., and Popov, E. (1977). "Inelastic Behavior of Eccentric Braced Steel Frames under Cyclic Loadings." *Earthquake Engineering Research Center, University of California, Berkeley, Report No. 77*, 18.

Schiff, A. (1998). *Hyogoken-Nanbu (Kobe) earthquake of January 17, 1995: lifeline performance*, Amer Society of Civil Engineers.

Shaw, A., and Bouma, K. (2000) "Seismic Retrofit of the Marin County Hall of Justice Using Steel Buckling-Restrained Braced Frames." *Proceedings, 69th Annual Convention, Structural Engineers Association of California*, Sacramento, California.

Shimizu, K., Hashimoto, J., Kawai, H., and Wada, A. (1998). "Application of Damage Control Structure using Energy Absorption Panel." *Structural Engineerign World Wide, Elsevier Science, Ltd.*(T105-2).

Schnobrich, W. C. (1977). "Behaviour of RC structures predicted by finite element method." *Comp. and Struct.,* 7(3), 365-376.

Stiemer, S., Godden, W., and Kelly, J. (1981). "Experimental behavior of a spatial piping system with steel energy absorbers subjected to a simulated differential seismic input. Prepared for the Department of Energy, and the Nuclear Regulatory Commission." College of Engineering.

Usami, T., Lu, Z., and Ge, H. (2005). "A seismic upgrading method for steel arch bridges using buckling-restrained braces." *Earthquake engineering & structural dynamics*, 34(4-5), 471-496.

Vargas, R., and Bruneau, M. (2009a). "Analytical Response and Design of Buildings with Metallic Structural Fuses. I." *Journal of Structural Engineering*, 135, 386.

Vargas, R., and Bruneau, M. (2009b). "Experimental Response of Buildings Designed with Metallic Structural Fuses. II." *Journal of Structural Engineering*, 135, 394.

Vian, D., Bruneau, M. (2005). "Steel Plate Walls for Seismic Design and Retrofit of Building Structures." Multidisciplinary Center for Earthquake Engineering Research, State University of New York at Buffalo, NY,.

Wada, A., Connor, J., Kawai, H., Iwata, M., and Watanabe, A. (1994) "Damage Tolerant Structures." *Proceedings of: Fifth U.S.-Japan Workshop on the Improvement of Structural Design and Construction Practices*, Applied Council Technology, 27–39.

Wada, A., and Huang, Y. (1995) "Preliminary seismic design of damage tolerant tall building structures." *Proceedings of Symposium on a New Direction in Seismic Design*, Architectural Institute of Japan, Tokyo, Japan, 77-93.

Wada, A., and Huang, Y. (1999) "Damage-controlled Structures in Japan." *U.S-Japan Workshop on Performance-Based Earthquake Engineering Methodology for Reinforced Concrete Building Structures*, 279-289.

Wada, A., Huang, Y., and Iwata, M. (2000). "Passive damping technology for buildings in Japan." *Progress in Structural Engineering and Materials*, 2(3).

Wada, A., Saeki, E., Takeuchi, T., and Watanabe, A. (1989). "Development of unbonded brace." *Nippon Steel's Unbonded Braces (promotional document)*, 1–16.

Watanabe, A., Hitomi, Y., Saeki, E., Wada, A., and Fujimoto, M. (1988) "Properties of brace encased in buckling-restraining concrete and steel tube." *Proceedings of Ninth World Conference on Earthquake Engineering,*, Tokyo- Kyoto, Japan,, 719–724.

Watanabe, F., and Ichinose, T. (1992). "Strength and ductility design of RC members subjected to combined bending and shear." *Concrete Shear in Earthquake, Eds. Hsu and ST Mau, Elsevier Applied Science, New York, New York*, 429-438.

Wen, Y. (1976). "Method for random vibration of hysteretic systems." *Journal of the Engineering Mechanics Division*, 102(2), 249-263.

Whittaker, A. S., Uang, C.M. and Bertero, V.V. (1987). "Earthquake Simulation Tests and Associated Studies of a 0.3-Scale Model of a Six-Story Eccentrically Braced Steel Frame." University of California, Berkeley, California.

Wight, J. K. (1988). "Earthquake design compared to measured response." *J. Struct. Engrg.,* ASCE, 112(1), 149-164.

Wong, Y., Paulay, T., and Priestley, M. (1993). "Response of circular reinforced concrete columns to multi-directional seismic attack." *ACI Structural Journal*, 90(2).

Xiao, Y., Tomii, M., and Sakino, K. (1986). "Experimental study on design method to prevent shear failure of reinforced concrete short circular columns by confining in steel tube." *Transactions of Japan Concrete Institute*, 8, 535-542.

APPENDIX A

TOTAL SYSTEM BEHAVIOR WITH STRUCTURAL FUSES

The total system behavior is presented in figure A-1. Where before yielding of the fuses, the total system would act as a single cantilever beam, with the column being its flanges and the fuses being its web. The expected base reaction for that system would be a large moment acting at the base with corresponding shear forces as shown in the figure, with a point of zero shear that lies in the middle of the fuses. The resulting forces will lead to one of the column being in compression, while the other one will be in tension (depending on the direction of loading).

After yielding of the fuses (while the columns are still elastic), the total system behavior is anticipated to change from a single cantilever system to a regular moment frame behavior, from which each column would behave independently in a moment frame, and would be subjected to moment and shear.

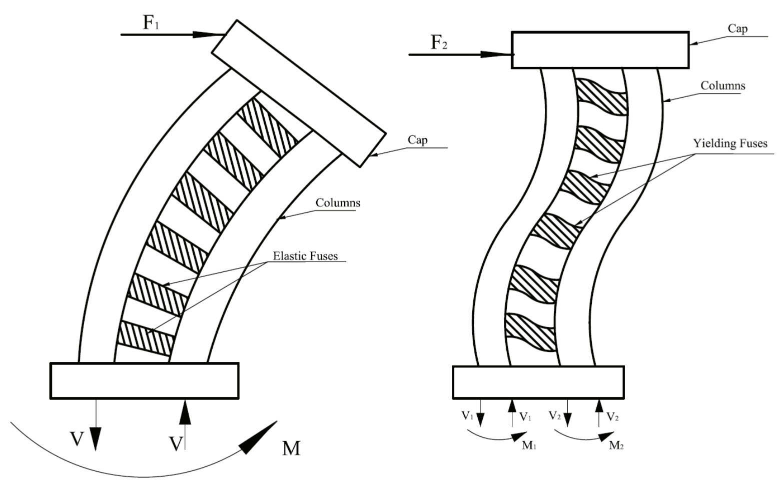

(a) (b)

FIGURE A-1 Total System Behavior; (a) Before yielding of Fuses, (b) After Yielding of Fuses

APPENDIX B

PROTOTYPE BRIDGE DESIGN

B.1 Prototype Bridge

The Prototype bridge considered is a three span continuous bridge with two twin column pier bents with fixed base spaced at 36m (120 ft) and 9m (30 ft) high. The deck width is 12m (40 ft) as shown in figure B-1. The effective deck weight (Girders + Concrete Slab + guard rails) was taken as 1 psi for simplicity. The columns were designed as composite rectangular columns using Bi-Steel panels. A response spectrum was constructed based on the National Earthquake Hazard Reduction Program Recommended Provisions (NEHRP 2003) for a site of site soil-type class B, This site was chosen as it is represents a hazardous area which is vulnerable to severe ground shaking. Mapped spectral accelerations are shown in figure B-2.

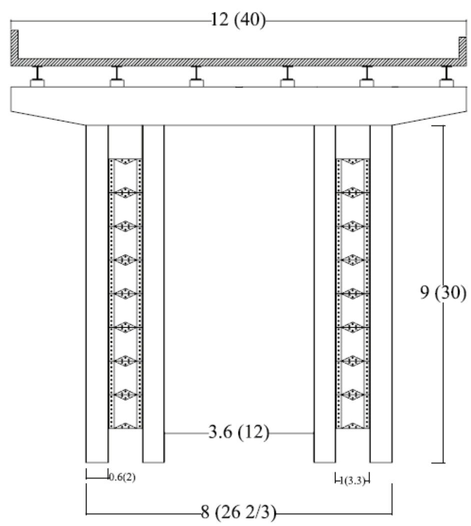

Dimensions in m (ft)

FIGURE B- 1 Prototype Bridge Dimensions

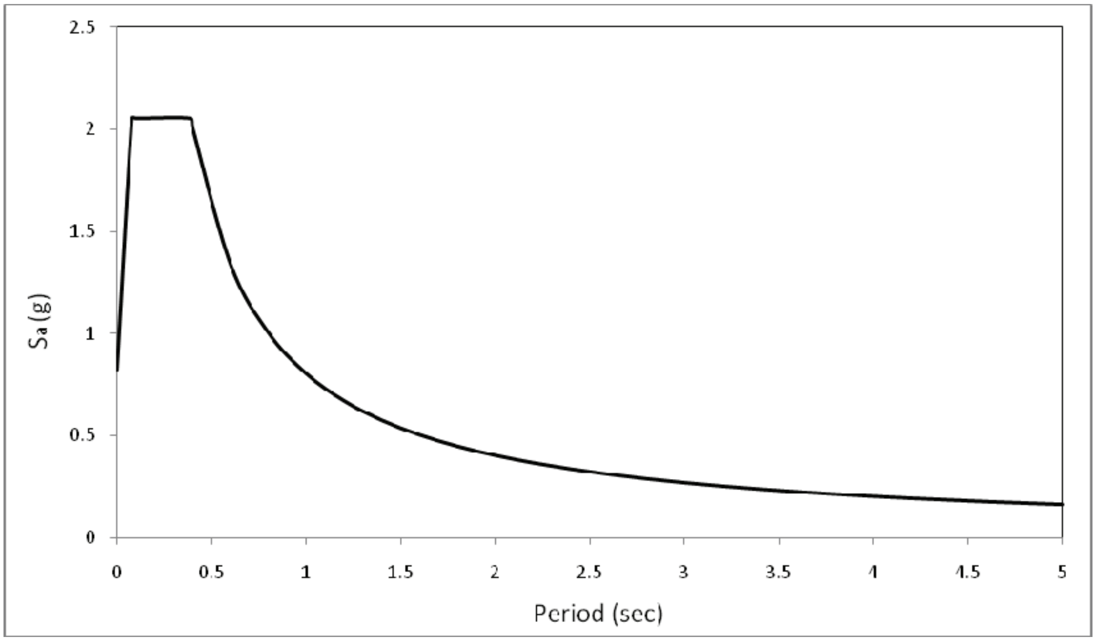

FIGURE B- 2 Elastic Response Spectra (5% critical damping)

B.2 Bridge Columns Design

Tributary gravity weight (W) = (480*1440*1)/1000=691.2 kips

Four columns are assumed to carry the gravity load from which the average axial load per each column is 172.8 kips.

Assuming that each column carries about 10% from its squash load, the axial capacity of each column should be 1728 kips.

Assuming a Bi-Steel Composite column of dimensions shown in figure B-3, and assuming that all the axial force will be carried by the concrete, the cross sectional area of each column is 36*24=864in^2, from which the axial load ratio is

Axial load ratio= $\dfrac{P}{f_c^{/} A_g} = \dfrac{172.8}{4*864} = 0.05$ <0.1 ok

Note that the assumed section is stronger than what is required due to the limitations on the Bi-Steel panel as a minimum of 3 bars is required for one panel with a minimum spacing of 8 in.

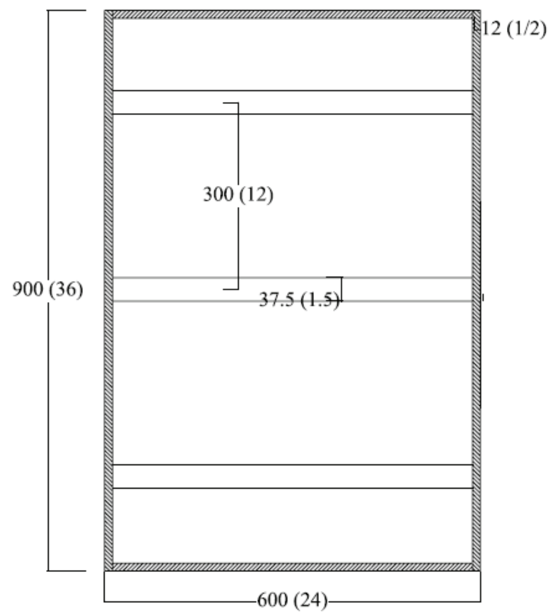

Dimensions in mm (in)

FIGURE B- 3 Prototype Column Dimensions

A moment curvature analysis is then run on the proposed column using XTRACT software; a confined concrete model and A572Gr.50 steel where used in the analysis; figure B-4 shows the moment-curvature plot of the section. Effective yield curvatures were determined as 0.1619E-3 1/in and the effective yield moment was determined as 34350 kip.in, while the EI_{eff} was found to be 2.12E8 kip.in^2.

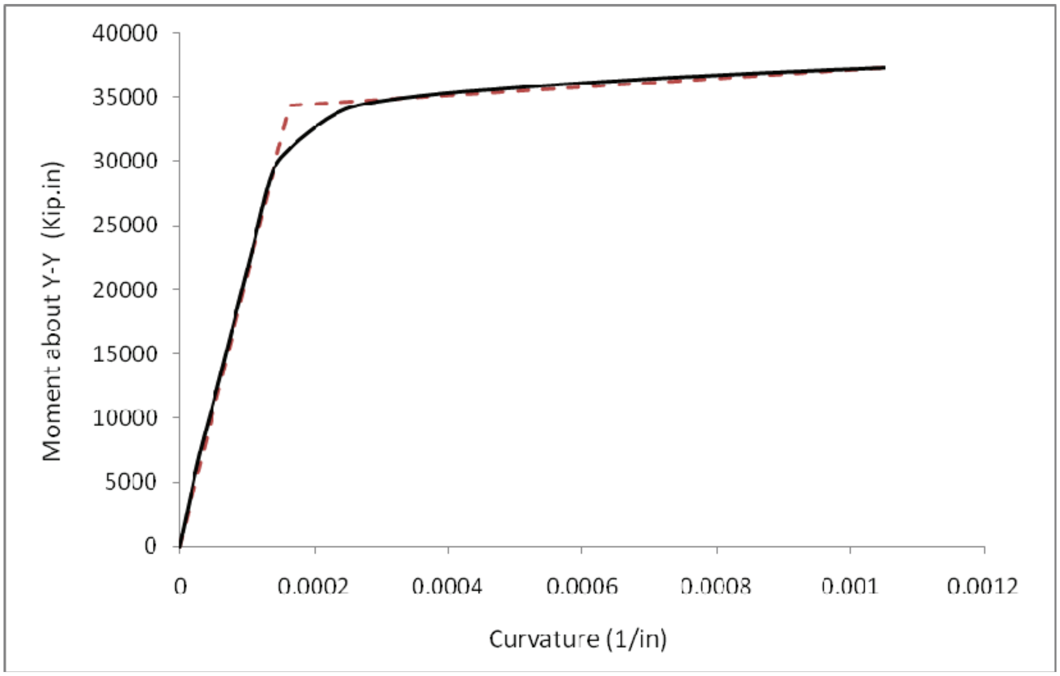

FIGURE B- 4 Moment-Curvature of Prototype Bridge Column

The total lateral stiffness of the bare bridge bent can now be calculated as follows:

$$K_{eff} = \frac{48EI_{eff}}{H_{tot}^3} = \frac{48*2.12*10^8}{(30*12)^3} = 218\,\text{kip/in}$$

The yield displacement of the bent can also be calculated as follows:

$$\Delta_y = \frac{2\phi_y (H_{tot}/2)^2}{3} = \frac{2*0.1619*10^{-3}*(30*12/2)^2}{3} = 3.5\,\text{in}$$

The yield lateral force of the bent can now be calculated as:

$$V_{y_{bent}} = K_{bent}\Delta_y = 218*3.5 = 763\ \text{kips}$$

From which the yield lateral force of a single column is 763/4=191 kips

And the natural period of the bare bent can be calculated as:

$$T = 2\pi\sqrt{\frac{W}{K_{eff}g}} = 2\pi\sqrt{\frac{691.2}{218*386}} = 0.57\text{ sec}$$

B.3 Specimen Design

For the specimen a 1.5 scale for the geometric properties of the specimen ($S_L = 2/3$) was chosen due to the limitations available at SEESL at the University at Buffalo, the maximum height of the strong wall is 30ft. so the maximum height of the specimen was set to be 20ft. Also the specimen was designed for a maximum horizontal force of 400kips, using 2 actuators available at SEESL each with a capacity of 220kips.

Using XTRACT software, properties of the column specimen are extracted as:

M_p=10200 kip.in, φ_y=0.2725E-3 1/in, EI_{eff}=4.8E7 ksi, and assuming 20% overstrength (Ω)

For the twin column specimen:

$$K_{eff} = \frac{24EI_{eff}}{H_{tot}^3} = \frac{24*4.8*10^7}{(276)^3} = 55\text{ kip/in (9.6 kN/mm)}$$

$$V_{Df} = \frac{\Omega 4M_P}{H_{tot}} = \frac{1.2*4*10200}{276} = 177\text{ kips (788 kN)}$$

$$\Delta_y = \frac{2\phi_y\left(H_{tot}/2\right)^2}{3} = \frac{2*0.2725*10^{-3}*\left(276/2\right)^2}{3} = 3.5\text{ in}$$

B.3.1 Restrained SPSL Design

A desired link ductility of 4 is assumed; a link length, *e*, of 16" and a distance y_o of 16" were chosen. The link edge angle, θ_b and the link height, *h*, can then be calculated as follows:

$$\tan^2\theta_b + \left(\frac{2y_0}{e}\right)\tan\theta_b - \frac{2y_0}{e\sqrt{3}} = 0$$

$$\tan^2\theta_b + \left(\frac{2*16}{16}\right)\tan\theta_b - \frac{2*16}{16\sqrt{3}} = 0$$

$$\theta_b = 25^0$$

$$h = y_o + e\tan\theta_b$$

$$h = 16 + 16\tan(25) = 23.46in$$

The value of the link length, *e*, chosen is then checked to satisfy the following equation:

$$e \le \frac{2y_o}{\sqrt{3}\tan^2\theta}\left(1-\sqrt{3}\tan\theta\right) \le \frac{2*16}{\sqrt{3}\tan^2 25}\left(1-\sqrt{3}\tan 25\right) \le 16.3$$

The maximum number of links that can be added can now be calculates as:

Maximum number of links= $\left(\frac{H}{h}-2\right) = \left(\frac{251}{24}-2\right) = 8.45$ links (8 links between the twin columns where chosen)

Assuming that the spectral acceleration of the final bent lies in the constant acceleration zone $S_a = 2.1g$, the bare bent strength ratio, ξ, can be calculated as:

$$\xi = \frac{S_a m}{V_{Df}} = \frac{2.1*691.2/3.375}{177} = 2.43$$

Setting the required bare bent ductility, μ_f, to be less that 1, the minimum stiffness ratio, α_{min}, can be calculated as:

$$\alpha_{\min} \ge \frac{\xi}{\mu_f} - 1 \ge 1.43$$

The total lateral stiffness required by the fuses can be now calculated as:

$$K_b = \alpha_{\min} K_f = 1.43*55 = 78.65 \text{ kip/in}$$

From which the total vertical stiffness required by the fuses is calculated as:

$$K_{ver} = \frac{K_b H_{tot}^2}{L\left(B+2X\right)\left(e+2X\right)} = \frac{78.65*(276)^2}{(16+2*4)^2} = 10401 \text{ kips/in}$$

And the vertical stiffness required per fuse will be equal to 10401/8=1300 kips/in

Assuming that the minimum required link ductility is 4, the link's strength ratio can be calculated as:

$$\eta = \mu_b\left(1+1/\alpha\right) = 4*(1+1/1.43) = 8.5$$

$$V_{DS\min} = \frac{S_a m}{\eta_{req}} = \frac{2.1*691.2/3.375}{8.5} = 50.6 \text{ kips}$$

From which the total vertical strength of the fuses is :

$$V_p = V_{Ds}\left(\frac{H_{tot}}{e+2X}\right) = 50.6*\left(\frac{276}{16+2*4}\right) = 582 \text{ kips}$$

And the vertical strength per fuse will be equal to 581/8=73 kips.

And the required link thickness is:

$$t_{\min 1} = \frac{\sqrt{3}*V_p}{n\sigma_y y_0} = \frac{\sqrt{3}*73}{50*16} = 0.157 \text{ in}$$

$$t_{\min 2} = \frac{K_{ver}e}{Gy_o} = \frac{1300*16}{11154*16} = 0.117 \text{ in}$$

Using plates of thickness 3/16 in, the vertical strength per fuse can be back calculated as 98 kips, and the total vertical fuses strength will be 98*8=785 kips, while the vertical fuse stiffness will be 2091 kip/in and the total vertical fuse stiffness will be 2091*8=16731 kip/in.

Assuming 50% overstrength in the plates, the total lateral fuses stiffness and strength can be calculated as:

$$K_b = K_{ver}\frac{(B+2X)(e+2X)}{H_{tot}^2} = \frac{16731(24)^2}{(276)^2} = 126.5 \text{ kip/in (22 kN/mm)}$$

$$V_{Ds} = \Omega V_p\left(\frac{e+2X}{H_{tot}}\right) = 1.5*785\left(\frac{24}{276}\right) = 102 \text{ kips (455 kN)}$$

The actual lateral stiffness per fuse will be 126.5/8= 15.8 kip/in, and the actual lateral strength per fuse will be 102/8=12.75 kips

The total system elastic lateral stiffness and strength can be calculated as:

$$K_{eff} = K_f + K_b = 55 + 126.5 = 181.5 \text{ kips/in (31.7 kN/mm)}$$

$$V_{Dt} = V_{Df} + V_{Ds} = 177 + 102 = 279 \text{ kips (1240 kN)}$$

Checking for the assumed spectral acceleration by calculating the natural period of the system:

$$T = 2\pi\sqrt{\frac{W}{K_{eff}\,g}} = 2\pi\sqrt{\frac{691.2/3.375}{181.5*386}} = 0.34 \text{ sec } <0.5 \text{ sec ok}$$

The yield lateral displacement of the fuses can be determined as:

$$\Delta_{y_{fuses}} = \frac{V_b}{K_b} = \frac{102}{126.5} = 0.81in$$

From which a maximum link ductility of 3.5/0.81=4.3 can be obtained before yielding of the columns.

B.3.1.1 Connection Design

- **Bolts**

For the connection region, the LRFD design considerations for bolted connections (Slip-Critical) where used for the design, 8 bolts of diameter d_b = 1" where assumed with edge distance equal to 1.5" and spacing equal to 3". The minimum edge distance for bolts at sheared edges according to the (LRFD manual Table J3.4) for 1" bolt diameter is 1.25", also the minimum spacing requirement was satisfied as it is 3d which is equal to 3" and the maximum spacing requirement is 6" which is also satisfied.

The available shear strength of a single shear single bolt of A490 steel is 44.2 kips threaded bolt (Table 7-1 LRFD manual)

$$C_{\min} = \frac{P_u}{\phi r_n} = \frac{98*1.4}{44.2} = 3.1$$

From (table 7-7 LRFD manual) the coefficient C for the eccentrically loaded bolt group with angle=0 can be found for an eccentricity of 10" and 8 bolts per row. The value of C is found to be equal to 4.0 which is greater than the minimum C required.

To ensure that section 1-1 will not yield, the net area should be greater than the gross area of the link.

The bolt hole size is $d = d_b + 1/16 = 1 + 0.0625 = 1.0625$ in

$$A_{net} = \left(h - 8d\right) * t^{/} \geq ht$$

Assume $t^{/} = 3t$ from which:

$$A_{net} = \left(24 - 8*1.0625\right)*0.32 = 4.9in^2$$

$$A_{gross} = 24*0.1875 = 4.5in^2 \text{ ok}$$

To ensure that the connection doesn't fail by plate bearing, (Section J-LRFD manual) is used to calculate the available bearing strength at a single standard bolt hole, the available bearing strength is:

$$\phi R_n = \phi 1.2 L_c t F_u \leq \phi 2.4 d t F_u$$

Where $L_c = L_e - d/2 = 1.5 - 1.0625/2 = 0.97$ in (For Edge Bolts)

$$\phi R_n = 0.75 * 1.2 * 0.97 * 0.3125 * 65 \le 0.75 * 2.4 * 1.0625 * 0.3125 * 65$$

$$\phi R_n = 18.15 \text{ Kips/bolt}$$

For other bolts:

$$L_c = S - d/2 = 3 - 1.0625/2 = 2.47$$

$$\phi R_n = 0.75 * 1.2 * 2.47 * 0.3125 * 65 \le 0.75 * 2.4 * 1.1875 * 0.3125 * 65$$

$$\phi R_n = 51 \text{ Kips/bolt}$$

From which the total bearing force of the plate is 2(18.15)+5(51)= 293 kips

Because no slippage is permitted, the connections is classified as Slip Critical, For A490 bolts of diameter (1"), the minimum bolt pretension T_b can be found from (Table J3-1AISC manual) and was equal to 64 Kips/bolt, from which:

$$\phi R_n = \phi \mu D_u h_{sc} T_b N_s$$

$$\phi R_n = 1 * 0.35 * 1.13 * 1 * 64 * 1 = 25.3 \text{ Kips/bolt}$$

For 8 bolts:

$$\phi R_n = 8 * 25.3 = 202.5 \text{ kips}$$

Elastic Analysis has been performed to determine the actual shear force on each bolt as follows:

$$P_{act} = \frac{V_{\max}}{n} + \frac{M_x}{\Sigma y^2}$$

Where $\Sigma y^2 = 2\left((1.5)^2 + (4.5)^2 + (7.5)^2 + (10.5)^2\right) = 378\,\text{in2}$

$$P_{act} = \frac{140}{8} + \frac{140(10)}{378} = 21.2\ \text{Kips/bolt}$$

From which the total shear force acting on the connection is 8(21.2) =170kips <202.5 kips OK

- **Welds**

For the design of weld between the connecting plates and the column, using two fillet weld lines with thickness equal 5mm, using E70XX electrodes the nominal weld strength can be calculated as:

$$\phi R_n = \phi\left[0.707 t_w L_w F_w\right] = 0.75 * 0.707 * 0.1875 * 2 * 24 * (0.6 * 70) = 187\,\text{kips}$$

Elastic analysis is used to determine the actual shear strength on the weld line in the horizontal and vertical directions as follows:

$$f_v = \frac{p}{A_w} = \frac{140}{24 * 2 * 0.1875} = 15.56\,\text{ksi}$$

$$I_{x_{weld}} = \frac{t_w h_w^3}{12} = \frac{2 * 0.1875 * 24^3}{12} = 432\,\text{in}^4$$

$$f_H = \frac{M_x}{I_x} y = \frac{140 * 10 * 24/2}{432} = 38.8\,\text{ksi}$$

$$f_r = \sqrt{f_v^2 + f_H^2} = \sqrt{(15.56)^2 + (38.8)^2} = 41.8\,\text{ksi} \quad < 60\ \text{ksi}\ \ \text{OK}$$

B.3.2 BRB Design

$$V_{Ds} = \Omega n \sigma_y A_b \sin\theta \left(\frac{L}{H_{tot}} \right) = 81.6\,\text{kips}$$

choosing 6 BRB, the area of the BRB required is calculated as:

$$A_b = \frac{81.6 * 276}{1.5 * 6 * 50 * \sin 57 * 24} = 2.4\,\text{in}^2$$

To calculate the maximum required yielding length of the BRB:

$$K_b = \frac{nEA_b LH \sin\theta \cos\theta}{L_{ysc} H_{tot}^2} = 95.7\,\text{kip/in}$$

$$L_{ysc} = \frac{6 * 29000 * 2.4 * 24 * 37 * \sin 57 * \cos 57}{95.7(276)^2} = 23\text{in}$$

A yielding length of 12in was chosen, which is equivalent to 0.5 of the total BRB length. The K_b was then back calculated to be equal to 185 kip/in (32kN/mm)

The total system elastic lateral stiffness and strength can be calculated as:

$$K_{eff} = K_f + K_b = 55 + 185 = 240\,\text{kip/in (42 kN/mm)}$$

$$V_{Dt} = V_{Df} + V_{Ds} = 177 + 81.6 = 258.6\,\text{kips (1149 kN)}$$

B.3.3 Unrestrained SPSL Design

$$V_{DS} = \Omega n \sigma_y t S \left(\frac{L}{H_{tot}} \right) \sin\alpha$$

$$V_{DS} = 1.5*8*50*0.1875*\frac{34}{3}*\frac{24}{276}*\sin 45 = 78\,\text{kips (346.6 kN)}$$

$$K_b = \sqrt{3}G\left(\frac{\text{tS}\left(B+2X\right)\text{Lsin}\alpha}{H_{tot}^2 e}\right)$$

$$K_b = \sqrt{3}*11154\left(\frac{0.1875*\frac{34}{3}*24*24*\sin 45}{16*\left(276\right)^2}\right) = 137\,\text{kip/in (24kN/mm)}$$

The total system elastic lateral stiffness and strength can be calculated as:

$$K_{eff} = K_f + K_b = 55 + 137 = 192\,\text{kip/in (33.5 kN/mm)}$$

$$V_{Dt} = V_{Df} + V_{Ds} = 177 + 78 = 255\,\text{kips (1133 kN)}$$

B.4 Connectors Design

Connectors should be designed according their longitudinal shear capacity (V_L) as failure could occur due to the failure of the bar connector to transfer the longitudinal forces from the steel plates into the concrete. The second failure mode is the failure of the bar in tension from which the transverse shear capacity (V_T) should be checked. The (Bi-Steel Design Manual Guidelines) was used for the design of the connectors.

B.4.1 Longitudinal Shear

The actual longitudinal shear force can split into two components:

$$V_{L_1} = \frac{V_{y_c} A \bar{y}}{I} L_{vi}$$

Where:

V_{L_1} : The longitudinal shear component for a single bare column

V_{y_c} : Yield base shear for a single bare column

A : Area of steel Plate

$\bar{y}$: Distance between the centroid of the area and the section neutral axis

L_{vi} : Length of shear zone

I : Moment of Inertia using the flexural neutral axis

To determine the moment of inertia the flexural neutral axis (y_m) must first be determined as:

$$y_m = -B + \left(B^2 - 2C\right)^{0.5}$$

Where:

$$B = mt_c + mt_t - t_t$$

$$C = -hmt_t + \frac{mt_t^2}{2} - \frac{mt_c^2}{2} + \frac{t_c^2}{2}$$

Where (m) is the modular ratio and is taken as 13.3, shown in figure B-5 all the parameters in the equations.

$$B = 13.3*0.5 + 13.3*0.5 - 0.5 = 12.8$$

$$C = -24*13.3*0.5 + \frac{13.3*0.5^2}{2} + \frac{0.5^2}{2} = -161.4$$

$$y_m = -12.8 + \left(12.8^2 + 2*161.4\right)^{0.5} = 9.26\ \text{in}$$

From which (I) can be calculated as follows:

$$I = bt_c(y_m - t_c/2)^2 + \frac{b(y_m - t_c)^3}{3m} + bt_t(h - y_m - t_t/2)^2$$

$$I = 36*0.5(9.26 - 0.5/2)^2 + \frac{24(9.26-0.5)^3}{3*13.3} + 36*0.5(24 - 9.26 - 0.5/2)^2 = 5645\ in^4$$

From which (V_{L_1}) can be calculated as:

$$V_{L_1} = \frac{191(36*0.5)*(14.49)*(15*12)}{5645} = 1588.5\ \text{Kips}\ \ (7066\ \text{KN})$$

The actual shear force per rod from the first component can be calculated as follows:

$$P_{act_1} = \frac{V_L S_x S_y}{bL_{vi}}$$

Setting the bar spacing as $S_x = 300$ mm and $S_y = 225$ mm, the actual shear force per bar is:

$$P_{act_1} = \frac{1588.5*12*9}{36*15*12} = 26.47 \text{ Kips (118 KN)}$$

The second component of the shear force arises from the links and this is a local additional shear force on the middle row of rods, each link is connected to approximately 4 rods according to the spacing of the rods, so an additional shear force of 200/4=50 Kips is added to the actual shear force locally at these rods, so the total shear force is 76.47 Kips (340 KN)

The shear capacity of a single bar connector is the lesser of the following:

$$P_{bar_1} = 0.8 k_L f_u A_{bar} / \gamma_V$$

$$P_{bar_2} = 0.29 \alpha d^2 (f_{cu} E_c)^{0.5} / \gamma_V$$

$$k_L = (0.024t + 0.76) \leq 1 \quad \text{(equation in mm)}$$

Where:

P_{bar} : Shear design capacity of a single bar

f_u : Ultimate tensile strength of a bar (73 ksi, 500N/mm2)

d: Diameter of the bar

α: Connector height/ diameter factor (α=1)

γ_V : Material Factor for bar connectors equals to 1.25

From which:

$$k_L = 0.024*0.5*25 + 0.76 = 1.06 \quad \text{, Take } k_L = 1$$

$$P_{bar_1} = 0.8*1*73*\frac{\pi(1.5)^2}{4} / 1.25 = 82.6 \text{ kips (controls)}$$

$$P_{bar_2} = 0.29*1*(1.5)^2*\left(6*4415\right)^{0.5} / 1.25 = 85 \text{ Kips}$$

The shear capacity of a single rod is higher than the actual shear force   ok

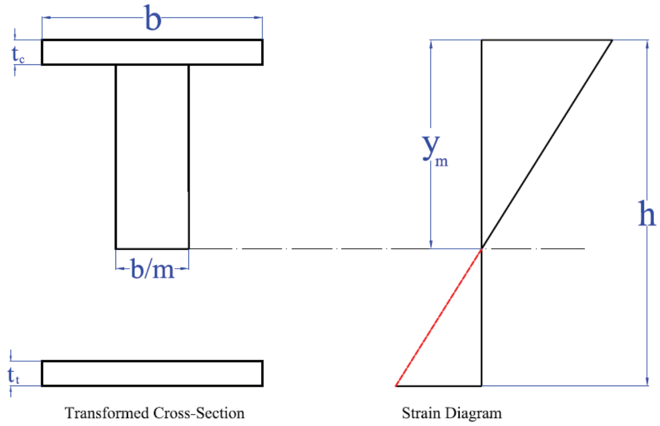

FIGURE B- 5 Transformed section and strain diagram for pure bending case

B.4.2 Transverse Shear

The transverse shear capacity of the bar connectors should also be checked, according to the Bi-Steel design manual, the transverse shear capacity of the section is the least of:

$(V_{wd}+V_{Rd1})$, V_{Rd2} and $V_{Rd2_{red}}$

$$V_{wd}=0.9k_T\left(\frac{A_{bar}}{s_x}\right)\left(\frac{h_c f_{yb}}{\gamma_{Ma}}\right)$$

$$V_{Rd1}=\left[\frac{0.0525}{\gamma_{Mc}}f_{cu}^{2/3}k\left(1.2+40\rho_1\right)+0.15\sigma_{cp}\right]bh_c$$

$$V_{Rd2}=0.45\nu f_{cu}bh_c/\gamma_{Mc}$$

$$V_{Rd2_{red}}=1.67V_{Rd2}\left(1-\frac{\sigma_{cp}\gamma_{Mc}}{f_{cu}}\right)$$

Where:

$k_T=2.5\left(\frac{f_y}{f_{y_b}}\right)\left(\frac{t}{d}\right)^{1.25}$

$k=1.6-h_c\geq 1.0$ (h_c in meters)

$\rho_1=t/h_c\leq 0.02$

$\nu=0.7-\left(\frac{f_{cu}}{200}\right)\geq 0.5$

σ_{cp}: Average compressive strength in concrete due to axial load

f_{yb} : Yield Strength of the bar connector (355 N/mm2)

γ_{Ma} : Material factor for Steel equal to 1.1

γ_{Mc} : Material factor for concrete equal to 1.5

From which:

$$k_T = 2.5\left(\frac{355}{355}\right)\left(\frac{12}{25}\right)^{1.25} = 1$$

$$k = 1.6 - 0.576 = 1.024$$

$$\rho_1 = 12/576 = 0.02$$

$$\nu = 0.7 - \left(\frac{40}{200}\right) = 0.5$$

$$\sigma_{cp} = \frac{P}{A} = \frac{770*1000}{600*900} = 1.42 \text{ N/mm2}$$

$$V_{wd} = 0.9*1\left(\frac{1104.5}{300}\right)\left(\frac{576*355}{1.1}\right)\Big/1000 = 616\,\text{KN}$$

$$V_{Rd1} = \left(\left[\frac{0.0525}{1.5}40^{0.67}*1.024\left(1.2+40*0.02\right)+0.15*1.42\right]900*576\right)/1000 = 550\,\text{KN}$$

$$V_{Rd2} = \left(0.45*0.5*40*900*576/1.5\right)\Big/1000 = 3110\,\text{KN}$$

$$V_{Rd2_{red}} = 1.67*3110\left(1-\frac{1.42*1.5}{40}\right) = 4917\,\text{KN}$$

From which the transverse shear capacity of the section is 616+550=1166 KN

And the actual transverse shear is equal to 191 kips (850 KN) from which the transverse shear is concluded as safe.

B.5 Foundation Design

A Bi-Steel panel is used to represent the foundation, 12 dywidags are used spaced as shown in figure B-6, the maximum actual tensile force acting on each dywidag is calculated as follows:

$2\left[3r_u\left(48\right)+3r_u\left(72\right)\right]=121440$

$r_u = 169\,\text{kips}$

Choosing 12 dywidags of diameter 1 3/8 in, the maximum pretensioning force of $0.8A_{dw}F_{y_{dw}}$ is equal to 189.6 kips > ru OK

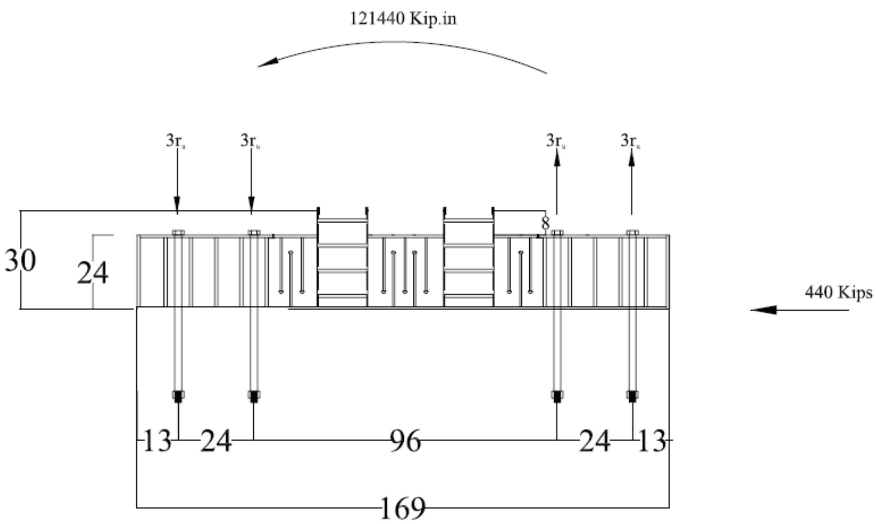

FIGURE B- 6 Specimen Foundation Detail

For shear along the foundation base, slip critical connection is assumed from which:

$$\phi R_n = \phi \mu D_u h_{sc} T_b N_s$$

$$\phi R_n = 1*0.35*1.13*1*189.6*1 = 75\,\text{kips/bolt}$$

While the actual shear/bolt is equal to 440/12=37 kips < 75 OK

B.5 Cap Beam Design

A Bi-Steel panel is also used to represent the cap beam of the prototype bridge, figure B-7 shows the detail of the cap beam used in the model. The maximum shear force acting on the cap beam can be calculated from the plastic moment expected to occur on the specimen, which can be calculated as:

$$V_u = \frac{M_p * 1.4}{h_c} = \frac{10177 * 1.4}{16} = 891 \text{kips} \ \ (446 \text{ kips/ plate})$$

Using a plate thickness of 8mm (5/16 in), the yield shear force per inch length of the plates can be calculated as:

$$V_y / in = \tau_y t = \frac{50}{\sqrt{3}} * 0.3125 = 9.02 \text{kips/in}$$

From which a plate length of 446/9.02=49.4 in is required

Take L=50 in

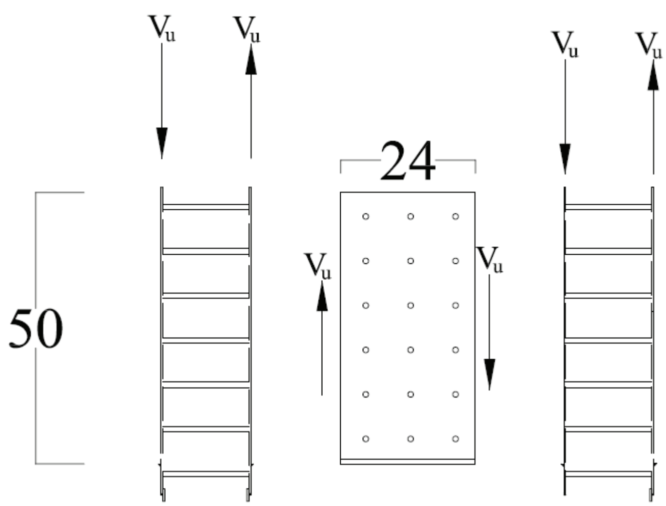

FIGURE B- 7 Cap Beam Detail

B.7 Threaded bars design

For the threaded bars connecting the transfer beam to the specimen, 4 ASTM A193 bars of diameter 1 1/8 in where chosen with ultimate tensile stress of 138 ksi . The maximum pretension force of $0.8 f_u A_b = 0.8 * 138 * \frac{\pi}{4} * (1.125)^2 = 110$ kips.

The maximum actual tensile force acting on each bar is 440/4=110 kips OK

B.8 Transfer Beam Design

The transfer beam was considered as a simply supported beam of span equal to 100 in, from which the bending moment was calculated as 440(100)/4=11000 kip.in and the shear force as 440/2=220 kips, figure B-8 shows the detail of the transfer beam.

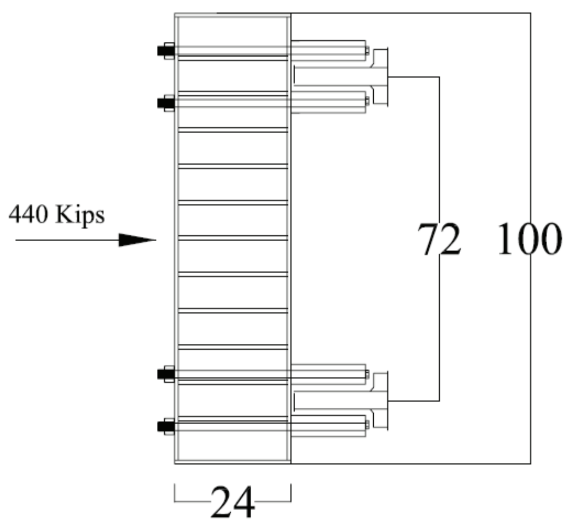

FIGURE B- 8 Transfer Beam Detail

The bi-steel design software was used for the analysis of the transfer beam and the results are shown below.

The plate thickness was chosen to be 12mm (0.47 in) and the concrete depth hc=24in and bar spacing 8 in.

B.9 Bi-Steel Panel Design

Member properties

Lx = 8.3 ft	Ly = n/a ft	Rx = n/a ft
Ry = n/a ft	Lvix = 4.15 ft	αax = 1
αbx = n/a		

Section geometry

hc = 24 in	t1 = 0.472440 in	d = 0.984251 in
t2 = 0.472440 in	bx = 24 in	

Optimised bar spacing, rounded down to the nearest 10mm sx = sy = 9.06 in

Material partial factors

γMa = 1.1	γMc = 1.5	γ*v* = 1.25

Forces

M1y = 920 kip-ft	Nsdx = 0 kips	V1x = 220 kips

q_{cp} = 0.003480 ksi q_{ip} = n/a ksi Tx = n/a kip-ft

Locked-in stress (□□pbar,ave) = 0 ksi

B.9.1 Effective modular ratio

For conservative calculation of the effective modular ratio,

the face plate with the greater yield strength is used.

Therefore fy = 51.49 ksi

m = 11.65

$$m_{\lim} = 1.2\frac{f_y}{f_{ck}}$$

Therefore m = 13.31

B.9.2 Preliminary section properties

$$B = m(t_c + t_t)$$

= 12.58 in

$$C = -m\left(h_c t_t + \frac{t_t^2}{2} - \frac{t_c^2}{2}\right)$$

= -150.944 in ^{2}

$$x = -B + \sqrt{(B^2 - 2C)}$$

$$= 8.87 \quad \text{in}$$

$$A_b = b\left(t_t + t_c + \frac{x}{m}\right)$$

$$= 38.67 \quad \text{in}^2$$

$$y_c = \frac{b}{A_b}\left(-\frac{t_c^2}{2} + \frac{x^2}{2m} + \frac{t_t^2}{2} + h_c t_t\right)$$

$$= 8.87 \quad \text{in}$$

$$I = b\left[t_c\left(y_c + \frac{t_c}{2}\right)^2 + t_t\left(h_c - y_c + \frac{t_t}{2}\right)^2\right.$$

$$\left. + \frac{x^3}{12m} + \frac{x}{m}\left(y_c - \frac{x}{2}\right)^2\right]$$

$$= 4036.88 \quad \text{in}^4$$

$$I_{zz} = \left(t_t + t_c + \frac{x}{m}\right)\frac{b^3}{12}$$

$$= 1856.2 \quad \text{in}^4$$

$$A_s = \frac{bh_c}{m}$$

$$= 43.27 \quad \text{in}^2$$

B.9.3 Effective forces

$\alpha = 1$

$$N_{cr,eff} = N_{cr} \big/ \left[1 + N_{cr} F_v\right]$$

$= 108039.5$ kips

$$\Delta M = \frac{N_{Sd}(e_1 + e_2 + e_R)}{(1 - N_{Sd} / N_{cr,eff})}$$

$= 0$ kip-ft

$$\Delta V = \left(\frac{e_1 + e_2}{e_0} \frac{\pi}{L} + \frac{e_R}{e_0} \frac{4}{L} \right) \Delta M$$

$= 0$ kips

$$M_{Sd} = M_1 + \Delta M$$

$= 920$ kip-ft

$$V_{Sd} = V_1 + \Delta V$$

$= 220$ kips

Distance from underside of compression flange to neutral axis, x

$x = 8.87$ in

B.9.4 Cross section properties

$$A_b = b\left(t_t + t_c + \frac{x}{m}\right)$$

$= 38.67 \quad \text{in}^2$

$$y_c = \frac{b}{A_b}\left(-\frac{t_c^2}{2} + \frac{x^2}{2m} + \frac{t_t^2}{2} + h_c t_t\right)$$

$= 8.87 \quad \text{in}$

$$I = b\left[t_c\left(y_c + \frac{t_c}{2}\right)^2 + t_t\left(h_c - y_c + \frac{t_t}{2}\right)^2\right.$$

$$\left. + \frac{x^3}{12m} + \frac{x}{m}\left(y_c - \frac{x}{2}\right)^2\right]$$

$= 4036.88 \quad \text{in}^4$

$$W_c = I \Big/ \left(y_c + \frac{t_c}{2}\right)$$

$= 443.24 \quad \text{in}^3$

$$W_t = I / \left(h_c - y_c + \frac{t_t}{2} \right)$$

$= 262.74$ in ^{3}

B.9.5 Shear capacity of bar connector

$$\sigma_{aca} = \sigma_{ata} = \frac{N_{Sd}}{A_b}$$

$= 0$ ksi

$$\sigma_{acb} = \frac{M_{Sd}}{W_c}$$

$= 24.91$ ksi

$$\sigma_{atb} = \frac{M_{Sd}}{W_t}$$

$= 42.02$ ksi

$\sigma ac = \sigma aca \pm \sigma acb = 24.91$ ksi

$\sigma at = \sigma atb \pm \square\, \sigma ata = -42.0191$ ksi

$\sigma tbc = 0$ ksi

$$K_L = (0.024t + 0.76)\frac{f_y}{355} - \frac{\gamma_{Ma}}{f_{yb}}(\sigma_{tbc})$$

$= 1$

$$P_{Rd1} = 0.8K_L f_{ub}\frac{\pi d^2}{4} / \gamma_v$$

$= 35.31$ kips

$$P_{Rd2} = 0.29\alpha d^2 (f_{ck}E_{cm)})^{1/2} / \gamma_v$$

$= 33.28$ kips

*P*Rd = lesser of *P*Rd1 *and* *P*Rd2 = 33.28 kips

B.9.6 Longitudinal shear

$$\bar{y}_1 = y_c + \frac{t_c}{2}$$

$= 9.11$ in

$$V_{L1} = \frac{V_{Sd}A_c\bar{y}_1}{I} \cdot L_{vi}$$

$= 280.27$ kips

$$\bar{y}_2 = h_c - y_c + \frac{t_t}{2}$$

$= 15.36$ in

$$V_{L2} = \frac{V_{Sd} A_t \bar{y}_2}{I} \cdot L_{vi}$$

$= 472.81$ kips

VL = greater of VL1 and VL2 = 472.81 kips

Bar spacing

$$s_{\text{Prelim}} = \left(\frac{b_x L_{vix} P_{Rd}}{V_L} \right)^{1/2}$$

$= 9.17$ in

Therefore sx = sy = 9.06 in

B.9.7 Axial stresses in plate

Kf = 566.28

σp = $q$ip$K$f = 0 ksi

σbc.cf = $q$cp$K$f = 1.97 ksi

$$\tau = \frac{T}{2 t_t b h_c}$$

$= 0$ ksi

B.9.8 Face plate buckling parameter

Kd = 2.69

ep = $q$ip$K$d = 0 in

$$e_1 = \frac{s_y^2}{5.7 \times 10^5}$$

$= 0.007874$ in

$$e_r = R\left(1 - \cos\left(\frac{s_y}{2R}\right)\right)$$

$= 0$ in

e0 = e1 + er + ep = 0.007874 in

$$\eta = 3(1 - v^2)\left(\frac{e_0}{t}\right)$$

$= 0.0455$

$$\sigma_{cr} = \frac{4\pi^2 E_a}{12(1 - v^2)}\left(\frac{t}{s_y}\right)^2$$

$= 292.6$ ksi

$$\chi = \frac{1+(\eta+1)\left(\frac{\sigma_{cr}}{f_y}\right)}{2} - \sqrt{\left(\frac{1+(\eta+1)\left(\frac{\sigma_{cr}}{f_y}\right)}{2}\right)^2 - \left(\frac{\sigma_{cr}}{f_y}\right)}$$

= 0.948215

B.9.9 Stress checks

Compression plate buckling

$\chi f y$ / γMa = 44.38 ksi

$$\sigma_{ac} \le \chi f_y / \gamma_{Ma}$$

σac = 24.91 ksi OK

Compression plate yielding

$f y$ / γMa = 46.81 ksi

$$\sigma_{ac} + \sigma_p + \sigma_{pbar,ave} + \sigma_{bc,cf}\frac{50}{s_y} \le \frac{f_y}{\gamma_{Ma}}$$

σbc.cf ≤ fy/γMa

σbc.cf = 1.97 ksi

σac +σp +σp.bar,ave +σbc.cf 50/sy = 25.34 ksi OK

Tension plate yielding

$\sigma_{at} \leq f_y / \gamma_{Ma}$

σat = 42.02 ksi OK

Transverse shear check

VSd = 220 kips

$V_{Sd} \leq (V_{wd} + V_{Rd1}), \; V_{Rd2} \quad and \quad V_{Rd2,red}$

(Vwd + VRd1) = 283.47 kips

VRd2 = 433.08 kips

VRd2,red = 723.24 kips OK

Longitudinal shear check

$\frac{1}{s_x s_y} \geq \left(\frac{V_L}{(b\, \mathrm{L_{vi}}\, \mathrm{P_{rd}})} \right)$

1/(sxsy) = 1.89E-05

(VL)/(bLvi$P$Rd) = 1.84E-05

AND 0.64 < sx/sy <1.56

sx/sy = 1 OK

MCEER Technical Reports

MCEER publishes technical reports on a variety of subjects written by authors funded through MCEER. These reports are available from both MCEER Publications and the National Technical Information Service (NTIS). Requests for reports should be directed to MCEER Publications, MCEER, University at Buffalo, State University of New York, 133A Ketter Hall, Buffalo, New York 14260. Reports can also be requested through NTIS, P.O. Box 1425, Springfield, Virginia 22151. NTIS accession numbers are shown in parenthesis, if available.

NCEER-87-0001 "First-Year Program in Research, Education and Technology Transfer," 3/5/87, (PB88-134275, A04, MF-A01).

NCEER-87-0002 "Experimental Evaluation of Instantaneous Optimal Algorithms for Structural Control," by R.C. Lin, T.T. Soong and A.M. Reinhorn, 4/20/87, (PB88-134341, A04, MF-A01).

NCEER-87-0003 "Experimentation Using the Earthquake Simulation Facilities at University at Buffalo," by A.M. Reinhorn and R.L. Ketter, to be published.

NCEER-87-0004 "The System Characteristics and Performance of a Shaking Table," by J.S. Hwang, K.C. Chang and G.C. Lee, 6/1/87, (PB88-134259, A03, MF-A01). This report is available only through NTIS (see address given above).

NCEER-87-0005 "A Finite Element Formulation for Nonlinear Viscoplastic Material Using a Q Model," by O. Gyebi and G. Dasgupta, 11/2/87, (PB88-213764, A08, MF-A01).

NCEER-87-0006 "Symbolic Manipulation Program (SMP) - Algebraic Codes for Two and Three Dimensional Finite Element Formulations," by X. Lee and G. Dasgupta, 11/9/87, (PB88-218522, A05, MF-A01).

NCEER-87-0007 "Instantaneous Optimal Control Laws for Tall Buildings Under Seismic Excitations," by J.N. Yang, A. Akbarpour and P. Ghaemmaghami, 6/10/87, (PB88-134333, A06, MF-A01). This report is only available through NTIS (see address given above).

NCEER-87-0008 "IDARC: Inelastic Damage Analysis of Reinforced Concrete Frame - Shear-Wall Structures," by Y.J. Park, A.M. Reinhorn and S.K. Kunnath, 7/20/87, (PB88-134325, A09, MF-A01). This report is only available through NTIS (see address given above).

NCEER-87-0009 "Liquefaction Potential for New York State: A Preliminary Report on Sites in Manhattan and Buffalo," by M. Budhu, V. Vijayakumar, R.F. Giese and L. Baumgras, 8/31/87, (PB88-163704, A03, MF-A01). This report is available only through NTIS (see address given above).

NCEER-87-0010 "Vertical and Torsional Vibration of Foundations in Inhomogeneous Media," by A.S. Veletsos and K.W. Dotson, 6/1/87, (PB88-134291, A03, MF-A01). This report is only available through NTIS (see address given above).

NCEER-87-0011 "Seismic Probabilistic Risk Assessment and Seismic Margins Studies for Nuclear Power Plants," by Howard H.M. Hwang, 6/15/87, (PB88-134267, A03, MF-A01). This report is only available through NTIS (see address given above).

NCEER-87-0012 "Parametric Studies of Frequency Response of Secondary Systems Under Ground-Acceleration Excitations," by Y. Yong and Y.K. Lin, 6/10/87, (PB88-134309, A03, MF-A01). This report is only available through NTIS (see address given above).

NCEER-87-0013 "Frequency Response of Secondary Systems Under Seismic Excitation," by J.A. HoLung, J. Cai and Y.K. Lin, 7/31/87, (PB88-134317, A05, MF-A01). This report is only available through NTIS (see address given above).

NCEER-87-0014 "Modelling Earthquake Ground Motions in Seismically Active Regions Using Parametric Time Series Methods," by G.W. Ellis and A.S. Cakmak, 8/25/87, (PB88-134283, A08, MF-A01). This report is only available through NTIS (see address given above).

NCEER-87-0015 "Detection and Assessment of Seismic Structural Damage," by E. DiPasquale and A.S. Cakmak, 8/25/87, (PB88-163712, A05, MF-A01). This report is only available through NTIS (see address given above).

NCEER-87-0016 "Pipeline Experiment at Parkfield, California," by J. Isenberg and E. Richardson, 9/15/87, (PB88-163720, A03, MF-A01). This report is available only through NTIS (see address given above).

NCEER-87-0017 "Digital Simulation of Seismic Ground Motion," by M. Shinozuka, G. Deodatis and T. Harada, 8/31/87, (PB88-155197, A04, MF-A01). This report is available only through NTIS (see address given above).

NCEER-87-0018 "Practical Considerations for Structural Control: System Uncertainty, System Time Delay and Truncation of Small Control Forces," J.N. Yang and A. Akbarpour, 8/10/87, (PB88-163738, A08, MF-A01). This report is only available through NTIS (see address given above).

NCEER-87-0019 "Modal Analysis of Nonclassically Damped Structural Systems Using Canonical Transformation," by J.N. Yang, S. Sarkani and F.X. Long, 9/27/87, (PB88-187851, A04, MF-A01).

NCEER-87-0020 "A Nonstationary Solution in Random Vibration Theory," by J.R. Red-Horse and P.D. Spanos, 11/3/87, (PB88-163746, A03, MF-A01).

NCEER-87-0021 "Horizontal Impedances for Radially Inhomogeneous Viscoelastic Soil Layers," by A.S. Veletsos and K.W. Dotson, 10/15/87, (PB88-150859, A04, MF-A01).

NCEER-87-0022 "Seismic Damage Assessment of Reinforced Concrete Members," by Y.S. Chung, C. Meyer and M. Shinozuka, 10/9/87, (PB88-150867, A05, MF-A01). This report is available only through NTIS (see address given above).

NCEER-87-0023 "Active Structural Control in Civil Engineering," by T.T. Soong, 11/11/87, (PB88-187778, A03, MF-A01).

NCEER-87-0024 "Vertical and Torsional Impedances for Radially Inhomogeneous Viscoelastic Soil Layers," by K.W. Dotson and A.S. Veletsos, 12/87, (PB88-187786, A03, MF-A01).

NCEER-87-0025 "Proceedings from the Symposium on Seismic Hazards, Ground Motions, Soil-Liquefaction and Engineering Practice in Eastern North America," October 20-22, 1987, edited by K.H. Jacob, 12/87, (PB88-188115, A23, MF-A01). This report is available only through NTIS (see address given above).

NCEER-87-0026 "Report on the Whittier-Narrows, California, Earthquake of October 1, 1987," by J. Pantelic and A. Reinhorn, 11/87, (PB88-187752, A03, MF-A01). This report is available only through NTIS (see address given above).

NCEER-87-0027 "Design of a Modular Program for Transient Nonlinear Analysis of Large 3-D Building Structures," by S. Srivastav and J.F. Abel, 12/30/87, (PB88-187950, A05, MF-A01). This report is only available through NTIS (see address given above).

NCEER-87-0028 "Second-Year Program in Research, Education and Technology Transfer," 3/8/88, (PB88-219480, A04, MF-A01).

NCEER-88-0001 "Workshop on Seismic Computer Analysis and Design of Buildings With Interactive Graphics," by W. McGuire, J.F. Abel and C.H. Conley, 1/18/88, (PB88-187760, A03, MF-A01). This report is only available through NTIS (see address given above).

NCEER-88-0002 "Optimal Control of Nonlinear Flexible Structures," by J.N. Yang, F.X. Long and D. Wong, 1/22/88, (PB88-213772, A06, MF-A01).

NCEER-88-0003 "Substructuring Techniques in the Time Domain for Primary-Secondary Structural Systems," by G.D. Manolis and G. Juhn, 2/10/88, (PB88-213780, A04, MF-A01).

NCEER-88-0004 "Iterative Seismic Analysis of Primary-Secondary Systems," by A. Singhal, L.D. Lutes and P.D. Spanos, 2/23/88, (PB88-213798, A04, MF-A01).

NCEER-88-0005 "Stochastic Finite Element Expansion for Random Media," by P.D. Spanos and R. Ghanem, 3/14/88, (PB88-213806, A03, MF-A01).

NCEER-88-0006 "Combining Structural Optimization and Structural Control," by F.Y. Cheng and C.P. Pantelides, 1/10/88, (PB88-213814, A05, MF-A01).

NCEER-88-0007 "Seismic Performance Assessment of Code-Designed Structures," by H.H-M. Hwang, J-W. Jaw and H-J. Shau, 3/20/88, (PB88-219423, A04, MF-A01). This report is only available through NTIS (see address given above).

NCEER-88-0008 "Reliability Analysis of Code-Designed Structures Under Natural Hazards," by H.H-M. Hwang, H. Ushiba and M. Shinozuka, 2/29/88, (PB88-229471, A07, MF-A01). This report is only available through NTIS (see address given above).

NCEER-88-0009 "Seismic Fragility Analysis of Shear Wall Structures," by J-W Jaw and H.H-M. Hwang, 4/30/88, (PB89-102867, A04, MF-A01).

NCEER-88-0010 "Base Isolation of a Multi-Story Building Under a Harmonic Ground Motion - A Comparison of Performances of Various Systems," by F-G Fan, G. Ahmadi and I.G. Tadjbakhsh, 5/18/88, (PB89-122238, A06, MF-A01). This report is only available through NTIS (see address given above).

NCEER-88-0011 "Seismic Floor Response Spectra for a Combined System by Green's Functions," by F.M. Lavelle, L.A. Bergman and P.D. Spanos, 5/1/88, (PB89-102875, A03, MF-A01).

NCEER-88-0012 "A New Solution Technique for Randomly Excited Hysteretic Structures," by G.Q. Cai and Y.K. Lin, 5/16/88, (PB89-102883, A03, MF-A01).

NCEER-88-0013 "A Study of Radiation Damping and Soil-Structure Interaction Effects in the Centrifuge," by K. Weissman, supervised by J.H. Prevost, 5/24/88, (PB89-144703, A06, MF-A01).

NCEER-88-0014 "Parameter Identification and Implementation of a Kinematic Plasticity Model for Frictional Soils," by J.H. Prevost and D.V. Griffiths, to be published.

NCEER-88-0015 "Two- and Three- Dimensional Dynamic Finite Element Analyses of the Long Valley Dam," by D.V. Griffiths and J.H. Prevost, 6/17/88, (PB89-144711, A04, MF-A01).

NCEER-88-0016 "Damage Assessment of Reinforced Concrete Structures in Eastern United States," by A.M. Reinhorn, M.J. Seidel, S.K. Kunnath and Y.J. Park, 6/15/88, (PB89-122220, A04, MF-A01). This report is only available through NTIS (see address given above).

NCEER-88-0017 "Dynamic Compliance of Vertically Loaded Strip Foundations in Multilayered Viscoelastic Soils," by S. Ahmad and A.S.M. Israil, 6/17/88, (PB89-102891, A04, MF-A01).

NCEER-88-0018 "An Experimental Study of Seismic Structural Response With Added Viscoelastic Dampers," by R.C. Lin, Z. Liang, T.T. Soong and R.H. Zhang, 6/30/88, (PB89-122212, A05, MF-A01). This report is available only through NTIS (see address given above).

NCEER-88-0019 "Experimental Investigation of Primary - Secondary System Interaction," by G.D. Manolis, G. Juhn and A.M. Reinhorn, 5/27/88, (PB89-122204, A04, MF-A01).

NCEER-88-0020 "A Response Spectrum Approach For Analysis of Nonclassically Damped Structures," by J.N. Yang, S. Sarkani and F.X. Long, 4/22/88, (PB89-102909, A04, MF-A01).

NCEER-88-0021 "Seismic Interaction of Structures and Soils: Stochastic Approach," by A.S. Veletsos and A.M. Prasad, 7/21/88, (PB89-122196, A04, MF-A01). This report is only available through NTIS (see address given above).

NCEER-88-0022 "Identification of the Serviceability Limit State and Detection of Seismic Structural Damage," by E. DiPasquale and A.S. Cakmak, 6/15/88, (PB89-122188, A05, MF-A01). This report is available only through NTIS (see address given above).

NCEER-88-0023 "Multi-Hazard Risk Analysis: Case of a Simple Offshore Structure," by B.K. Bhartia and E.H. Vanmarcke, 7/21/88, (PB89-145213, A05, MF-A01).

NCEER-88-0024 "Automated Seismic Design of Reinforced Concrete Buildings," by Y.S. Chung, C. Meyer and M. Shinozuka, 7/5/88, (PB89-122170, A06, MF-A01). This report is available only through NTIS (see address given above).

NCEER-88-0025 "Experimental Study of Active Control of MDOF Structures Under Seismic Excitations," by L.L. Chung, R.C. Lin, T.T. Soong and A.M. Reinhorn, 7/10/88, (PB89-122600, A04, MF-A01).

NCEER-88-0026 "Earthquake Simulation Tests of a Low-Rise Metal Structure," by J.S. Hwang, K.C. Chang, G.C. Lee and R.L. Ketter, 8/1/88, (PB89-102917, A04, MF-A01).

NCEER-88-0027 "Systems Study of Urban Response and Reconstruction Due to Catastrophic Earthquakes," by F. Kozin and H.K. Zhou, 9/22/88, (PB90-162348, A04, MF-A01).

NCEER-88-0028 "Seismic Fragility Analysis of Plane Frame Structures," by H.H-M. Hwang and Y.K. Low, 7/31/88, (PB89-131445, A06, MF-A01).

NCEER-88-0029 "Response Analysis of Stochastic Structures," by A. Kardara, C. Bucher and M. Shinozuka, 9/22/88, (PB89-174429, A04, MF-A01).

NCEER-88-0030 "Nonnormal Accelerations Due to Yielding in a Primary Structure," by D.C.K. Chen and L.D. Lutes, 9/19/88, (PB89-131437, A04, MF-A01).

NCEER-88-0031 "Design Approaches for Soil-Structure Interaction," by A.S. Veletsos, A.M. Prasad and Y. Tang, 12/30/88, (PB89-174437, A03, MF-A01). This report is available only through NTIS (see address given above).

NCEER-88-0032 "A Re-evaluation of Design Spectra for Seismic Damage Control," by C.J. Turkstra and A.G. Tallin, 11/7/88, (PB89-145221, A05, MF-A01).

NCEER-88-0033 "The Behavior and Design of Noncontact Lap Splices Subjected to Repeated Inelastic Tensile Loading," by V.E. Sagan, P. Gergely and R.N. White, 12/8/88, (PB89-163737, A08, MF-A01).

NCEER-88-0034 "Seismic Response of Pile Foundations," by S.M. Mamoon, P.K. Banerjee and S. Ahmad, 11/1/88, (PB89-145239, A04, MF-A01).

NCEER-88-0035 "Modeling of R/C Building Structures With Flexible Floor Diaphragms (IDARC2)," by A.M. Reinhorn, S.K. Kunnath and N. Panahshahi, 9/7/88, (PB89-207153, A07, MF-A01).

NCEER-88-0036 "Solution of the Dam-Reservoir Interaction Problem Using a Combination of FEM, BEM with Particular Integrals, Modal Analysis, and Substructuring," by C-S. Tsai, G.C. Lee and R.L. Ketter, 12/31/88, (PB89-207146, A04, MF-A01).

NCEER-88-0037 "Optimal Placement of Actuators for Structural Control," by F.Y. Cheng and C.P. Pantelides, 8/15/88, (PB89-162846, A05, MF-A01).

NCEER-88-0038 "Teflon Bearings in Aseismic Base Isolation: Experimental Studies and Mathematical Modeling," by A. Mokha, M.C. Constantinou and A.M. Reinhorn, 12/5/88, (PB89-218457, A10, MF-A01). This report is available only through NTIS (see address given above).

NCEER-88-0039 "Seismic Behavior of Flat Slab High-Rise Buildings in the New York City Area," by P. Weidlinger and M. Ettouney, 10/15/88, (PB90-145681, A04, MF-A01).

NCEER-88-0040 "Evaluation of the Earthquake Resistance of Existing Buildings in New York City," by P. Weidlinger and M. Ettouney, 10/15/88, to be published.

NCEER-88-0041 "Small-Scale Modeling Techniques for Reinforced Concrete Structures Subjected to Seismic Loads," by W. Kim, A. El-Attar and R.N. White, 11/22/88, (PB89-189625, A05, MF-A01).

NCEER-88-0042 "Modeling Strong Ground Motion from Multiple Event Earthquakes," by G.W. Ellis and A.S. Cakmak, 10/15/88, (PB89-174445, A03, MF-A01).

NCEER-88-0043 "Nonstationary Models of Seismic Ground Acceleration," by M. Grigoriu, S.E. Ruiz and E. Rosenblueth, 7/15/88, (PB89-189617, A04, MF-A01).

NCEER-88-0044 "SARCF User's Guide: Seismic Analysis of Reinforced Concrete Frames," by Y.S. Chung, C. Meyer and M. Shinozuka, 11/9/88, (PB89-174452, A08, MF-A01).

NCEER-88-0045 "First Expert Panel Meeting on Disaster Research and Planning," edited by J. Pantelic and J. Stoyle, 9/15/88, (PB89-174460, A05, MF-A01).

NCEER-88-0046 "Preliminary Studies of the Effect of Degrading Infill Walls on the Nonlinear Seismic Response of Steel Frames," by C.Z. Chrysostomou, P. Gergely and J.F. Abel, 12/19/88, (PB89-208383, A05, MF-A01).

NCEER-88-0047 "Reinforced Concrete Frame Component Testing Facility - Design, Construction, Instrumentation and Operation," by S.P. Pessiki, C. Conley, T. Bond, P. Gergely and R.N. White, 12/16/88, (PB89-174478, A04, MF-A01).

NCEER-89-0001 "Effects of Protective Cushion and Soil Compliancy on the Response of Equipment Within a Seismically Excited Building," by J.A. HoLung, 2/16/89, (PB89-207179, A04, MF-A01).

NCEER-89-0002 "Statistical Evaluation of Response Modification Factors for Reinforced Concrete Structures," by H.H-M. Hwang and J-W. Jaw, 2/17/89, (PB89-207187, A05, MF-A01).

NCEER-89-0003 "Hysteretic Columns Under Random Excitation," by G-Q. Cai and Y.K. Lin, 1/9/89, (PB89-196513, A03, MF-A01).

NCEER-89-0004 "Experimental Study of `Elephant Foot Bulge' Instability of Thin-Walled Metal Tanks," by Z-H. Jia and R.L. Ketter, 2/22/89, (PB89-207195, A03, MF-A01).

NCEER-89-0005 "Experiment on Performance of Buried Pipelines Across San Andreas Fault," by J. Isenberg, E. Richardson and T.D. O'Rourke, 3/10/89, (PB89-218440, A04, MF-A01). This report is available only through NTIS (see address given above).

NCEER-89-0006 "A Knowledge-Based Approach to Structural Design of Earthquake-Resistant Buildings," by M. Subramani, P. Gergely, C.H. Conley, J.F. Abel and A.H. Zaghw, 1/15/89, (PB89-218465, A06, MF-A01).

NCEER-89-0007 "Liquefaction Hazards and Their Effects on Buried Pipelines," by T.D. O'Rourke and P.A. Lane, 2/1/89, (PB89-218481, A09, MF-A01).

NCEER-89-0008 "Fundamentals of System Identification in Structural Dynamics," by H. Imai, C-B. Yun, O. Maruyama and M. Shinozuka, 1/26/89, (PB89-207211, A04, MF-A01).

NCEER-89-0009 "Effects of the 1985 Michoacan Earthquake on Water Systems and Other Buried Lifelines in Mexico," by A.G. Ayala and M.J. O'Rourke, 3/8/89, (PB89-207229, A06, MF-A01).

NCEER-89-R010 "NCEER Bibliography of Earthquake Education Materials," by K.E.K. Ross, Second Revision, 9/1/89, (PB90-125352, A05, MF-A01). This report is replaced by NCEER-92-0018.

NCEER-89-0011 "Inelastic Three-Dimensional Response Analysis of Reinforced Concrete Building Structures (IDARC-3D), Part I - Modeling," by S.K. Kunnath and A.M. Reinhorn, 4/17/89, (PB90-114612, A07, MF-A01). This report is available only through NTIS (see address given above).

NCEER-89-0012 "Recommended Modifications to ATC-14," by C.D. Poland and J.O. Malley, 4/12/89, (PB90-108648, A15, MF-A01).

NCEER-89-0013 "Repair and Strengthening of Beam-to-Column Connections Subjected to Earthquake Loading," by M. Corazao and A.J. Durrani, 2/28/89, (PB90-109885, A06, MF-A01).

NCEER-89-0014 "Program EXKAL2 for Identification of Structural Dynamic Systems," by O. Maruyama, C-B. Yun, M. Hoshiya and M. Shinozuka, 5/19/89, (PB90-109877, A09, MF-A01).

NCEER-89-0015 "Response of Frames With Bolted Semi-Rigid Connections, Part I - Experimental Study and Analytical Predictions," by P.J. DiCorso, A.M. Reinhorn, J.R. Dickerson, J.B. Radziminski and W.L. Harper, 6/1/89, to be published.

NCEER-89-0016 "ARMA Monte Carlo Simulation in Probabilistic Structural Analysis," by P.D. Spanos and M.P. Mignolet, 7/10/89, (PB90-109893, A03, MF-A01).

NCEER-89-P017 "Preliminary Proceedings from the Conference on Disaster Preparedness - The Place of Earthquake Education in Our Schools," Edited by K.E.K. Ross, 6/23/89, (PB90-108606, A03, MF-A01).

NCEER-89-0017 "Proceedings from the Conference on Disaster Preparedness - The Place of Earthquake Education in Our Schools," Edited by K.E.K. Ross, 12/31/89, (PB90-207895, A012, MF-A02). This report is available only through NTIS (see address given above).

NCEER-89-0018 "Multidimensional Models of Hysteretic Material Behavior for Vibration Analysis of Shape Memory Energy Absorbing Devices, by E.J. Graesser and F.A. Cozzarelli, 6/7/89, (PB90-164146, A04, MF-A01).

NCEER-89-0019 "Nonlinear Dynamic Analysis of Three-Dimensional Base Isolated Structures (3D-BASIS)," by S. Nagarajaiah, A.M. Reinhorn and M.C. Constantinou, 8/3/89, (PB90-161936, A06, MF-A01). This report has been replaced by NCEER-93-0011.

NCEER-89-0020 "Structural Control Considering Time-Rate of Control Forces and Control Rate Constraints," by F.Y. Cheng and C.P. Pantelides, 8/3/89, (PB90-120445, A04, MF-A01).

NCEER-89-0021 "Subsurface Conditions of Memphis and Shelby County," by K.W. Ng, T-S. Chang and H-H.M. Hwang, 7/26/89, (PB90-120437, A03, MF-A01).

NCEER-89-0022 "Seismic Wave Propagation Effects on Straight Jointed Buried Pipelines," by K. Elhmadi and M.J. O'Rourke, 8/24/89, (PB90-162322, A10, MF-A02).

NCEER-89-0023 "Workshop on Serviceability Analysis of Water Delivery Systems," edited by M. Grigoriu, 3/6/89, (PB90-127424, A03, MF-A01).

NCEER-89-0024 "Shaking Table Study of a 1/5 Scale Steel Frame Composed of Tapered Members," by K.C. Chang, J.S. Hwang and G.C. Lee, 9/18/89, (PB90-160169, A04, MF-A01).

NCEER-89-0025 "DYNA1D: A Computer Program for Nonlinear Seismic Site Response Analysis - Technical Documentation," by Jean H. Prevost, 9/14/89, (PB90-161944, A07, MF-A01). This report is available only through NTIS (see address given above).

NCEER-89-0026 "1:4 Scale Model Studies of Active Tendon Systems and Active Mass Dampers for Aseismic Protection," by A.M. Reinhorn, T.T. Soong, R.C. Lin, Y.P. Yang, Y. Fukao, H. Abe and M. Nakai, 9/15/89, (PB90-173246, A10, MF-A02). This report is available only through NTIS (see address given above).

NCEER-89-0027 "Scattering of Waves by Inclusions in a Nonhomogeneous Elastic Half Space Solved by Boundary Element Methods," by P.K. Hadley, A. Askar and A.S. Cakmak, 6/15/89, (PB90-145699, A07, MF-A01).

NCEER-89-0028 "Statistical Evaluation of Deflection Amplification Factors for Reinforced Concrete Structures," by H.H.M. Hwang, J-W. Jaw and A.L. Ch'ng, 8/31/89, (PB90-164633, A05, MF-A01).

NCEER-89-0029 "Bedrock Accelerations in Memphis Area Due to Large New Madrid Earthquakes," by H.H.M. Hwang, C.H.S. Chen and G. Yu, 11/7/89, (PB90-162330, A04, MF-A01).

NCEER-89-0030 "Seismic Behavior and Response Sensitivity of Secondary Structural Systems," by Y.Q. Chen and T.T. Soong, 10/23/89, (PB90-164658, A08, MF-A01).

NCEER-89-0031 "Random Vibration and Reliability Analysis of Primary-Secondary Structural Systems," by Y. Ibrahim, M. Grigoriu and T.T. Soong, 11/10/89, (PB90-161951, A04, MF-A01).

NCEER-89-0032 "Proceedings from the Second U.S. - Japan Workshop on Liquefaction, Large Ground Deformation and Their Effects on Lifelines, September 26-29, 1989," Edited by T.D. O'Rourke and M. Hamada, 12/1/89, (PB90-209388, A22, MF-A03).

NCEER-89-0033 "Deterministic Model for Seismic Damage Evaluation of Reinforced Concrete Structures," by J.M. Bracci, A.M. Reinhorn, J.B. Mander and S.K. Kunnath, 9/27/89, (PB91-108803, A06, MF-A01).

NCEER-89-0034 "On the Relation Between Local and Global Damage Indices," by E. DiPasquale and A.S. Cakmak, 8/15/89, (PB90-173865, A05, MF-A01).

NCEER-89-0035 "Cyclic Undrained Behavior of Nonplastic and Low Plasticity Silts," by A.J. Walker and H.E. Stewart, 7/26/89, (PB90-183518, A10, MF-A01).

NCEER-89-0036 "Liquefaction Potential of Surficial Deposits in the City of Buffalo, New York," by M. Budhu, R. Giese and L. Baumgrass, 1/17/89, (PB90-208455, A04, MF-A01).

NCEER-89-0037 "A Deterministic Assessment of Effects of Ground Motion Incoherence," by A.S. Veletsos and Y. Tang, 7/15/89, (PB90-164294, A03, MF-A01).

NCEER-89-0038 "Workshop on Ground Motion Parameters for Seismic Hazard Mapping," July 17-18, 1989, edited by R.V. Whitman, 12/1/89, (PB90-173923, A04, MF-A01).

NCEER-89-0039 "Seismic Effects on Elevated Transit Lines of the New York City Transit Authority," by C.J. Costantino, C.A. Miller and E. Heymsfield, 12/26/89, (PB90-207887, A06, MF-A01).

NCEER-89-0040 "Centrifugal Modeling of Dynamic Soil-Structure Interaction," by K. Weissman, Supervised by J.H. Prevost, 5/10/89, (PB90-207879, A07, MF-A01).

NCEER-89-0041 "Linearized Identification of Buildings With Cores for Seismic Vulnerability Assessment," by I-K. Ho and A.E. Aktan, 11/1/89, (PB90-251943, A07, MF-A01).

NCEER-90-0001 "Geotechnical and Lifeline Aspects of the October 17, 1989 Loma Prieta Earthquake in San Francisco," by T.D. O'Rourke, H.E. Stewart, F.T. Blackburn and T.S. Dickerman, 1/90, (PB90-208596, A05, MF-A01).

NCEER-90-0002 "Nonnormal Secondary Response Due to Yielding in a Primary Structure," by D.C.K. Chen and L.D. Lutes, 2/28/90, (PB90-251976, A07, MF-A01).

NCEER-90-0003 "Earthquake Education Materials for Grades K-12," by K.E.K. Ross, 4/16/90, (PB91-251984, A05, MF-A05). This report has been replaced by NCEER-92-0018.

NCEER-90-0004 "Catalog of Strong Motion Stations in Eastern North America," by R.W. Busby, 4/3/90, (PB90-251984, A05, MF-A01).

NCEER-90-0005 "NCEER Strong-Motion Data Base: A User Manual for the GeoBase Release (Version 1.0 for the Sun3)," by P. Friberg and K. Jacob, 3/31/90 (PB90-258062, A04, MF-A01).

NCEER-90-0006 "Seismic Hazard Along a Crude Oil Pipeline in the Event of an 1811-1812 Type New Madrid Earthquake," by H.H.M. Hwang and C-H.S. Chen, 4/16/90, (PB90-258054, A04, MF-A01).

NCEER-90-0007 "Site-Specific Response Spectra for Memphis Sheahan Pumping Station," by H.H.M. Hwang and C.S. Lee, 5/15/90, (PB91-108811, A05, MF-A01).

NCEER-90-0008 "Pilot Study on Seismic Vulnerability of Crude Oil Transmission Systems," by T. Ariman, R. Dobry, M. Grigoriu, F. Kozin, M. O'Rourke, T. O'Rourke and M. Shinozuka, 5/25/90, (PB91-108837, A06, MF-A01).

NCEER-90-0009 "A Program to Generate Site Dependent Time Histories: EQGEN," by G.W. Ellis, M. Srinivasan and A.S. Cakmak, 1/30/90, (PB91-108829, A04, MF-A01).

NCEER-90-0010 "Active Isolation for Seismic Protection of Operating Rooms," by M.E. Talbott, Supervised by M. Shinozuka, 6/8/9, (PB91-110205, A05, MF-A01).

NCEER-90-0011 "Program LINEARID for Identification of Linear Structural Dynamic Systems," by C-B. Yun and M. Shinozuka, 6/25/90, (PB91-110312, A08, MF-A01).

NCEER-90-0012 "Two-Dimensional Two-Phase Elasto-Plastic Seismic Response of Earth Dams," by A.N. Yiagos, Supervised by J.H. Prevost, 6/20/90, (PB91-110197, A13, MF-A02).

NCEER-90-0013 "Secondary Systems in Base-Isolated Structures: Experimental Investigation, Stochastic Response and Stochastic Sensitivity," by G.D. Manolis, G. Juhn, M.C. Constantinou and A.M. Reinhorn, 7/1/90, (PB91-110320, A08, MF-A01).

NCEER-90-0014 "Seismic Behavior of Lightly-Reinforced Concrete Column and Beam-Column Joint Details," by S.P. Pessiki, C.H. Conley, P. Gergely and R.N. White, 8/22/90, (PB91-108795, A11, MF-A02).

NCEER-90-0015 "Two Hybrid Control Systems for Building Structures Under Strong Earthquakes," by J.N. Yang and A. Danielians, 6/29/90, (PB91-125393, A04, MF-A01).

NCEER-90-0016 "Instantaneous Optimal Control with Acceleration and Velocity Feedback," by J.N. Yang and Z. Li, 6/29/90, (PB91-125401, A03, MF-A01).

NCEER-90-0017 "Reconnaissance Report on the Northern Iran Earthquake of June 21, 1990," by M. Mehrain, 10/4/90, (PB91-125377, A03, MF-A01).

NCEER-90-0018 "Evaluation of Liquefaction Potential in Memphis and Shelby County," by T.S. Chang, P.S. Tang, C.S. Lee and H. Hwang, 8/10/90, (PB91-125427, A09, MF-A01).

NCEER-90-0019 "Experimental and Analytical Study of a Combined Sliding Disc Bearing and Helical Steel Spring Isolation System," by M.C. Constantinou, A.S. Mokha and A.M. Reinhorn, 10/4/90, (PB91-125385, A06, MF-A01). This report is available only through NTIS (see address given above).

NCEER-90-0020 "Experimental Study and Analytical Prediction of Earthquake Response of a Sliding Isolation System with a Spherical Surface," by A.S. Mokha, M.C. Constantinou and A.M. Reinhorn, 10/11/90, (PB91-125419, A05, MF-A01).

NCEER-90-0021 "Dynamic Interaction Factors for Floating Pile Groups," by G. Gazetas, K. Fan, A. Kaynia and E. Kausel, 9/10/90, (PB91-170381, A05, MF-A01).

NCEER-90-0022 "Evaluation of Seismic Damage Indices for Reinforced Concrete Structures," by S. Rodriguez-Gomez and A.S. Cakmak, 9/30/90, PB91-171322, A06, MF-A01).

NCEER-90-0023 "Study of Site Response at a Selected Memphis Site," by H. Desai, S. Ahmad, E.S. Gazetas and M.R. Oh, 10/11/90, (PB91-196857, A03, MF-A01).

NCEER-90-0024 "A User's Guide to Strongmo: Version 1.0 of NCEER's Strong-Motion Data Access Tool for PCs and Terminals," by P.A. Friberg and C.A.T. Susch, 11/15/90, (PB91-171272, A03, MF-A01).

NCEER-90-0025 "A Three-Dimensional Analytical Study of Spatial Variability of Seismic Ground Motions," by L-L. Hong and A.H.-S. Ang, 10/30/90, (PB91-170399, A09, MF-A01).

NCEER-90-0026 "MUMOID User's Guide - A Program for the Identification of Modal Parameters," by S. Rodriguez-Gomez and E. DiPasquale, 9/30/90, (PB91-171298, A04, MF-A01).

NCEER-90-0027 "SARCF-II User's Guide - Seismic Analysis of Reinforced Concrete Frames," by S. Rodriguez-Gomez, Y.S. Chung and C. Meyer, 9/30/90, (PB91-171280, A05, MF-A01).

NCEER-90-0028 "Viscous Dampers: Testing, Modeling and Application in Vibration and Seismic Isolation," by N. Makris and M.C. Constantinou, 12/20/90 (PB91-190561, A06, MF-A01).

NCEER-90-0029 "Soil Effects on Earthquake Ground Motions in the Memphis Area," by H. Hwang, C.S. Lee, K.W. Ng and T.S. Chang, 8/2/90, (PB91-190751, A05, MF-A01).

NCEER-91-0001 "Proceedings from the Third Japan-U.S. Workshop on Earthquake Resistant Design of Lifeline Facilities and Countermeasures for Soil Liquefaction, December 17-19, 1990," edited by T.D. O'Rourke and M. Hamada, 2/1/91, (PB91-179259, A99, MF-A04).

NCEER-91-0002 "Physical Space Solutions of Non-Proportionally Damped Systems," by M. Tong, Z. Liang and G.C. Lee, 1/15/91, (PB91-179242, A04, MF-A01).

NCEER-91-0003 "Seismic Response of Single Piles and Pile Groups," by K. Fan and G. Gazetas, 1/10/91, (PB92-174994, A04, MF-A01).

NCEER-91-0004 "Damping of Structures: Part 1 - Theory of Complex Damping," by Z. Liang and G. Lee, 10/10/91, (PB92-197235, A12, MF-A03).

NCEER-91-0005 "3D-BASIS - Nonlinear Dynamic Analysis of Three Dimensional Base Isolated Structures: Part II," by S. Nagarajaiah, A.M. Reinhorn and M.C. Constantinou, 2/28/91, (PB91-190553, A07, MF-A01). This report has been replaced by NCEER-93-0011.

NCEER-91-0006 "A Multidimensional Hysteretic Model for Plasticity Deforming Metals in Energy Absorbing Devices," by E.J. Graesser and F.A. Cozzarelli, 4/9/91, (PB92-108364, A04, MF-A01).

NCEER-91-0007 "A Framework for Customizable Knowledge-Based Expert Systems with an Application to a KBES for Evaluating the Seismic Resistance of Existing Buildings," by E.G. Ibarra-Anaya and S.J. Fenves, 4/9/91, (PB91-210930, A08, MF-A01).

NCEER-91-0008 "Nonlinear Analysis of Steel Frames with Semi-Rigid Connections Using the Capacity Spectrum Method," by G.G. Deierlein, S-H. Hsieh, Y-J. Shen and J.F. Abel, 7/2/91, (PB92-113828, A05, MF-A01).

NCEER-91-0009 "Earthquake Education Materials for Grades K-12," by K.E.K. Ross, 4/30/91, (PB91-212142, A06, MF-A01). This report has been replaced by NCEER-92-0018.

NCEER-91-0010 "Phase Wave Velocities and Displacement Phase Differences in a Harmonically Oscillating Pile," by N. Makris and G. Gazetas, 7/8/91, (PB92-108356, A04, MF-A01).

NCEER-91-0011 "Dynamic Characteristics of a Full-Size Five-Story Steel Structure and a 2/5 Scale Model," by K.C. Chang, G.C. Yao, G.C. Lee, D.S. Hao and Y.C. Yeh," 7/2/91, (PB93-116648, A06, MF-A02).

NCEER-91-0012 "Seismic Response of a 2/5 Scale Steel Structure with Added Viscoelastic Dampers," by K.C. Chang, T.T. Soong, S-T. Oh and M.L. Lai, 5/17/91, (PB92-110816, A05, MF-A01).

NCEER-91-0013 "Earthquake Response of Retaining Walls; Full-Scale Testing and Computational Modeling," by S. Alampalli and A-W.M. Elgamal, 6/20/91, to be published.

NCEER-91-0014 "3D-BASIS-M: Nonlinear Dynamic Analysis of Multiple Building Base Isolated Structures," by P.C. Tsopelas, S. Nagarajaiah, M.C. Constantinou and A.M. Reinhorn, 5/28/91, (PB92-113885, A09, MF-A02).

NCEER-91-0015 "Evaluation of SEAOC Design Requirements for Sliding Isolated Structures," by D. Theodossiou and M.C. Constantinou, 6/10/91, (PB92-114602, A11, MF-A03).

NCEER-91-0016 "Closed-Loop Modal Testing of a 27-Story Reinforced Concrete Flat Plate-Core Building," by H.R. Somaprasad, T. Toksoy, H. Yoshiyuki and A.E. Aktan, 7/15/91, (PB92-129980, A07, MF-A02).

NCEER-91-0017 "Shake Table Test of a 1/6 Scale Two-Story Lightly Reinforced Concrete Building," by A.G. El-Attar, R.N. White and P. Gergely, 2/28/91, (PB92-222447, A06, MF-A02).

NCEER-91-0018 "Shake Table Test of a 1/8 Scale Three-Story Lightly Reinforced Concrete Building," by A.G. El-Attar, R.N. White and P. Gergely, 2/28/91, (PB93-116630, A08, MF-A02).

NCEER-91-0019 "Transfer Functions for Rigid Rectangular Foundations," by A.S. Veletsos, A.M. Prasad and W.H. Wu, 7/31/91, to be published.

NCEER-91-0020 "Hybrid Control of Seismic-Excited Nonlinear and Inelastic Structural Systems," by J.N. Yang, Z. Li and A. Danielians, 8/1/91, (PB92-143171, A06, MF-A02).

NCEER-91-0021 "The NCEER-91 Earthquake Catalog: Improved Intensity-Based Magnitudes and Recurrence Relations for U.S. Earthquakes East of New Madrid," by L. Seeber and J.G. Armbruster, 8/28/91, (PB92-176742, A06, MF-A02).

NCEER-91-0022 "Proceedings from the Implementation of Earthquake Planning and Education in Schools: The Need for Change - The Roles of the Changemakers," by K.E.K. Ross and F. Winslow, 7/23/91, (PB92-129998, A12, MF-A03).

NCEER-91-0023 "A Study of Reliability-Based Criteria for Seismic Design of Reinforced Concrete Frame Buildings," by H.H.M. Hwang and H-M. Hsu, 8/10/91, (PB92-140235, A09, MF-A02).

NCEER-91-0024 "Experimental Verification of a Number of Structural System Identification Algorithms," by R.G. Ghanem, H. Gavin and M. Shinozuka, 9/18/91, (PB92-176577, A18, MF-A04).

NCEER-91-0025 "Probabilistic Evaluation of Liquefaction Potential," by H.H.M. Hwang and C.S. Lee," 11/25/91, (PB92-143429, A05, MF-A01).

NCEER-91-0026 "Instantaneous Optimal Control for Linear, Nonlinear and Hysteretic Structures - Stable Controllers," by J.N. Yang and Z. Li, 11/15/91, (PB92-163807, A04, MF-A01).

NCEER-91-0027 "Experimental and Theoretical Study of a Sliding Isolation System for Bridges," by M.C. Constantinou, A. Kartoum, A.M. Reinhorn and P. Bradford, 11/15/91, (PB92-176973, A10, MF-A03).

NCEER-92-0001 "Case Studies of Liquefaction and Lifeline Performance During Past Earthquakes, Volume 1: Japanese Case Studies," Edited by M. Hamada and T. O'Rourke, 2/17/92, (PB92-197243, A18, MF-A04).

NCEER-92-0002 "Case Studies of Liquefaction and Lifeline Performance During Past Earthquakes, Volume 2: United States Case Studies," Edited by T. O'Rourke and M. Hamada, 2/17/92, (PB92-197250, A20, MF-A04).

NCEER-92-0003 "Issues in Earthquake Education," Edited by K. Ross, 2/3/92, (PB92-222389, A07, MF-A02).

NCEER-92-0004 "Proceedings from the First U.S. - Japan Workshop on Earthquake Protective Systems for Bridges," Edited by I.G. Buckle, 2/4/92, (PB94-142239, A99, MF-A06).

NCEER-92-0005 "Seismic Ground Motion from a Haskell-Type Source in a Multiple-Layered Half-Space," A.P. Theoharis, G. Deodatis and M. Shinozuka, 1/2/92, to be published.

NCEER-92-0006 "Proceedings from the Site Effects Workshop," Edited by R. Whitman, 2/29/92, (PB92-197201, A04, MF-A01).

NCEER-92-0007 "Engineering Evaluation of Permanent Ground Deformations Due to Seismically-Induced Liquefaction," by M.H. Baziar, R. Dobry and A-W.M. Elgamal, 3/24/92, (PB92-222421, A13, MF-A03).

NCEER-92-0008 "A Procedure for the Seismic Evaluation of Buildings in the Central and Eastern United States," by C.D. Poland and J.O. Malley, 4/2/92, (PB92-222439, A20, MF-A04).

NCEER-92-0009 "Experimental and Analytical Study of a Hybrid Isolation System Using Friction Controllable Sliding Bearings," by M.Q. Feng, S. Fujii and M. Shinozuka, 5/15/92, (PB93-150282, A06, MF-A02).

NCEER-92-0010 "Seismic Resistance of Slab-Column Connections in Existing Non-Ductile Flat-Plate Buildings," by A.J. Durrani and Y. Du, 5/18/92, (PB93-116812, A06, MF-A02).

NCEER-92-0011 "The Hysteretic and Dynamic Behavior of Brick Masonry Walls Upgraded by Ferrocement Coatings Under Cyclic Loading and Strong Simulated Ground Motion," by H. Lee and S.P. Prawel, 5/11/92, to be published.

NCEER-92-0012 "Study of Wire Rope Systems for Seismic Protection of Equipment in Buildings," by G.F. Demetriades, M.C. Constantinou and A.M. Reinhorn, 5/20/92, (PB93-116655, A08, MF-A02).

NCEER-92-0013 "Shape Memory Structural Dampers: Material Properties, Design and Seismic Testing," by P.R. Witting and F.A. Cozzarelli, 5/26/92, (PB93-116663, A05, MF-A01).

NCEER-92-0014 "Longitudinal Permanent Ground Deformation Effects on Buried Continuous Pipelines," by M.J. O'Rourke, and C. Nordberg, 6/15/92, (PB93-116671, A08, MF-A02).

NCEER-92-0015 "A Simulation Method for Stationary Gaussian Random Functions Based on the Sampling Theorem," by M. Grigoriu and S. Balopoulou, 6/11/92, (PB93-127496, A05, MF-A01).

NCEER-92-0016 "Gravity-Load-Designed Reinforced Concrete Buildings: Seismic Evaluation of Existing Construction and Detailing Strategies for Improved Seismic Resistance," by G.W. Hoffmann, S.K. Kunnath, A.M. Reinhorn and J.B. Mander, 7/15/92, (PB94-142007, A08, MF-A02).

NCEER-92-0017 "Observations on Water System and Pipeline Performance in the Limón Area of Costa Rica Due to the April 22, 1991 Earthquake," by M. O'Rourke and D. Ballantyne, 6/30/92, (PB93-126811, A06, MF-A02).

NCEER-92-0018 "Fourth Edition of Earthquake Education Materials for Grades K-12," Edited by K.E.K. Ross, 8/10/92, (PB93-114023, A07, MF-A02).

NCEER-92-0019 "Proceedings from the Fourth Japan-U.S. Workshop on Earthquake Resistant Design of Lifeline Facilities and Countermeasures for Soil Liquefaction," Edited by M. Hamada and T.D. O'Rourke, 8/12/92, (PB93-163939, A99, MF-E11).

NCEER-92-0020 "Active Bracing System: A Full Scale Implementation of Active Control," by A.M. Reinhorn, T.T. Soong, R.C. Lin, M.A. Riley, Y.P. Wang, S. Aizawa and M. Higashino, 8/14/92, (PB93-127512, A06, MF-A02).

NCEER-92-0021 "Empirical Analysis of Horizontal Ground Displacement Generated by Liquefaction-Induced Lateral Spreads," by S.F. Bartlett and T.L. Youd, 8/17/92, (PB93-188241, A06, MF-A02).

NCEER-92-0022 "IDARC Version 3.0: Inelastic Damage Analysis of Reinforced Concrete Structures," by S.K. Kunnath, A.M. Reinhorn and R.F. Lobo, 8/31/92, (PB93-227502, A07, MF-A02).

NCEER-92-0023 "A Semi-Empirical Analysis of Strong-Motion Peaks in Terms of Seismic Source, Propagation Path and Local Site Conditions, by M. Kamiyama, M.J. O'Rourke and R. Flores-Berrones, 9/9/92, (PB93-150266, A08, MF-A02).

NCEER-92-0024 "Seismic Behavior of Reinforced Concrete Frame Structures with Nonductile Details, Part I: Summary of Experimental Findings of Full Scale Beam-Column Joint Tests," by A. Beres, R.N. White and P. Gergely, 9/30/92, (PB93-227783, A05, MF-A01).

NCEER-92-0025 "Experimental Results of Repaired and Retrofitted Beam-Column Joint Tests in Lightly Reinforced Concrete Frame Buildings," by A. Beres, S. El-Borgi, R.N. White and P. Gergely, 10/29/92, (PB93-227791, A05, MF-A01).

NCEER-92-0026 "A Generalization of Optimal Control Theory: Linear and Nonlinear Structures," by J.N. Yang, Z. Li and S. Vongchavalitkul, 11/2/92, (PB93-188621, A05, MF-A01).

NCEER-92-0027 "Seismic Resistance of Reinforced Concrete Frame Structures Designed Only for Gravity Loads: Part I - Design and Properties of a One-Third Scale Model Structure," by J.M. Bracci, A.M. Reinhorn and J.B. Mander, 12/1/92, (PB94-104502, A08, MF-A02).

NCEER-92-0028 "Seismic Resistance of Reinforced Concrete Frame Structures Designed Only for Gravity Loads: Part II - Experimental Performance of Subassemblages," by L.E. Aycardi, J.B. Mander and A.M. Reinhorn, 12/1/92, (PB94-104510, A08, MF-A02).

NCEER-92-0029 "Seismic Resistance of Reinforced Concrete Frame Structures Designed Only for Gravity Loads: Part III - Experimental Performance and Analytical Study of a Structural Model," by J.M. Bracci, A.M. Reinhorn and J.B. Mander, 12/1/92, (PB93-227528, A09, MF-A01).

NCEER-92-0030 "Evaluation of Seismic Retrofit of Reinforced Concrete Frame Structures: Part I - Experimental Performance of Retrofitted Subassemblages," by D. Choudhuri, J.B. Mander and A.M. Reinhorn, 12/8/92, (PB93-198307, A07, MF-A02).

NCEER-92-0031 "Evaluation of Seismic Retrofit of Reinforced Concrete Frame Structures: Part II - Experimental Performance and Analytical Study of a Retrofitted Structural Model," by J.M. Bracci, A.M. Reinhorn and J.B. Mander, 12/8/92, (PB93-198315, A09, MF-A03).

NCEER-92-0032 "Experimental and Analytical Investigation of Seismic Response of Structures with Supplemental Fluid Viscous Dampers," by M.C. Constantinou and M.D. Symans, 12/21/92, (PB93-191435, A10, MF-A03). This report is available only through NTIS (see address given above).

NCEER-92-0033 "Reconnaissance Report on the Cairo, Egypt Earthquake of October 12, 1992," by M. Khater, 12/23/92, (PB93-188621, A03, MF-A01).

NCEER-92-0034 "Low-Level Dynamic Characteristics of Four Tall Flat-Plate Buildings in New York City," by H. Gavin, S. Yuan, J. Grossman, E. Pekelis and K. Jacob, 12/28/92, (PB93-188217, A07, MF-A02).

NCEER-93-0001 "An Experimental Study on the Seismic Performance of Brick-Infilled Steel Frames With and Without Retrofit," by J.B. Mander, B. Nair, K. Wojtkowski and J. Ma, 1/29/93, (PB93-227510, A07, MF-A02).

NCEER-93-0002 "Social Accounting for Disaster Preparedness and Recovery Planning," by S. Cole, E. Pantoja and V. Razak, 2/22/93, (PB94-142114, A12, MF-A03).

NCEER-93-0003 "Assessment of 1991 NEHRP Provisions for Nonstructural Components and Recommended Revisions," by T.T. Soong, G. Chen, Z. Wu, R-H. Zhang and M. Grigoriu, 3/1/93, (PB93-188639, A06, MF-A02).

NCEER-93-0004 "Evaluation of Static and Response Spectrum Analysis Procedures of SEAOC/UBC for Seismic Isolated Structures," by C.W. Winters and M.C. Constantinou, 3/23/93, (PB93-198299, A10, MF-A03).

NCEER-93-0005 "Earthquakes in the Northeast - Are We Ignoring the Hazard? A Workshop on Earthquake Science and Safety for Educators," edited by K.E.K. Ross, 4/2/93, (PB94-103066, A09, MF-A02).

NCEER-93-0006 "Inelastic Response of Reinforced Concrete Structures with Viscoelastic Braces," by R.F. Lobo, J.M. Bracci, K.L. Shen, A.M. Reinhorn and T.T. Soong, 4/5/93, (PB93-227486, A05, MF-A02).

NCEER-93-0007 "Seismic Testing of Installation Methods for Computers and Data Processing Equipment," by K. Kosar, T.T. Soong, K.L. Shen, J.A. HoLung and Y.K. Lin, 4/12/93, (PB93-198299, A07, MF-A02).

NCEER-93-0008 "Retrofit of Reinforced Concrete Frames Using Added Dampers," by A. Reinhorn, M. Constantinou and C. Li, to be published.

NCEER-93-0009 "Seismic Behavior and Design Guidelines for Steel Frame Structures with Added Viscoelastic Dampers," by K.C. Chang, M.L. Lai, T.T. Soong, D.S. Hao and Y.C. Yeh, 5/1/93, (PB94-141959, A07, MF-A02).

NCEER-93-0010 "Seismic Performance of Shear-Critical Reinforced Concrete Bridge Piers," by J.B. Mander, S.M. Waheed, M.T.A. Chaudhary and S.S. Chen, 5/12/93, (PB93-227494, A08, MF-A02).

NCEER-93-0011 "3D-BASIS-TABS: Computer Program for Nonlinear Dynamic Analysis of Three Dimensional Base Isolated Structures," by S. Nagarajaiah, C. Li, A.M. Reinhorn and M.C. Constantinou, 8/2/93, (PB94-141819, A09, MF-A02).

NCEER-93-0012 "Effects of Hydrocarbon Spills from an Oil Pipeline Break on Ground Water," by O.J. Helweg and H.H.M. Hwang, 8/3/93, (PB94-141942, A06, MF-A02).

NCEER-93-0013 "Simplified Procedures for Seismic Design of Nonstructural Components and Assessment of Current Code Provisions," by M.P. Singh, L.E. Suarez, E.E. Matheu and G.O. Maldonado, 8/4/93, (PB94-141827, A09, MF-A02).

NCEER-93-0014 "An Energy Approach to Seismic Analysis and Design of Secondary Systems," by G. Chen and T.T. Soong, 8/6/93, (PB94-142767, A11, MF-A03).

NCEER-93-0015 "Proceedings from School Sites: Becoming Prepared for Earthquakes - Commemorating the Third Anniversary of the Loma Prieta Earthquake," Edited by F.E. Winslow and K.E.K. Ross, 8/16/93, (PB94-154275, A16, MF-A02).

NCEER-93-0016 "Reconnaissance Report of Damage to Historic Monuments in Cairo, Egypt Following the October 12, 1992 Dahshur Earthquake," by D. Sykora, D. Look, G. Croci, E. Karaesmen and E. Karaesmen, 8/19/93, (PB94-142221, A08, MF-A02).

NCEER-93-0017 "The Island of Guam Earthquake of August 8, 1993," by S.W. Swan and S.K. Harris, 9/30/93, (PB94-141843, A04, MF-A01).

NCEER-93-0018 "Engineering Aspects of the October 12, 1992 Egyptian Earthquake," by A.W. Elgamal, M. Amer, K. Adalier and A. Abul-Fadl, 10/7/93, (PB94-141983, A05, MF-A01).

NCEER-93-0019 "Development of an Earthquake Motion Simulator and its Application in Dynamic Centrifuge Testing," by I. Krstelj, Supervised by J.H. Prevost, 10/23/93, (PB94-181773, A-10, MF-A03).

NCEER-93-0020 "NCEER-Taisei Corporation Research Program on Sliding Seismic Isolation Systems for Bridges: Experimental and Analytical Study of a Friction Pendulum System (FPS)," by M.C. Constantinou, P. Tsopelas, Y-S. Kim and S. Okamoto, 11/1/93, (PB94-142775, A08, MF-A02).

NCEER-93-0021 "Finite Element Modeling of Elastomeric Seismic Isolation Bearings," by L.J. Billings, Supervised by R. Shepherd, 11/8/93, to be published.

NCEER-93-0022 "Seismic Vulnerability of Equipment in Critical Facilities: Life-Safety and Operational Consequences," by K. Porter, G.S. Johnson, M.M. Zadeh, C. Scawthorn and S. Eder, 11/24/93, (PB94-181765, A16, MF-A03).

NCEER-93-0023 "Hokkaido Nansei-oki, Japan Earthquake of July 12, 1993, by P.I. Yanev and C.R. Scawthorn, 12/23/93, (PB94-181500, A07, MF-A01).

NCEER-94-0001 "An Evaluation of Seismic Serviceability of Water Supply Networks with Application to the San Francisco Auxiliary Water Supply System," by I. Markov, Supervised by M. Grigoriu and T. O'Rourke, 1/21/94, (PB94-204013, A07, MF-A02).

NCEER-94-0002 "NCEER-Taisei Corporation Research Program on Sliding Seismic Isolation Systems for Bridges: Experimental and Analytical Study of Systems Consisting of Sliding Bearings, Rubber Restoring Force Devices and Fluid Dampers," Volumes I and II, by P. Tsopelas, S. Okamoto, M.C. Constantinou, D. Ozaki and S. Fujii, 2/4/94, (PB94-181740, A09, MF-A02 and PB94-181757, A12, MF-A03).

NCEER-94-0003 "A Markov Model for Local and Global Damage Indices in Seismic Analysis," by S. Rahman and M. Grigoriu, 2/18/94, (PB94-206000, A12, MF-A03).

NCEER-94-0004 "Proceedings from the NCEER Workshop on Seismic Response of Masonry Infills," edited by D.P. Abrams, 3/1/94, (PB94-180783, A07, MF-A02).

NCEER-94-0005 "The Northridge, California Earthquake of January 17, 1994: General Reconnaissance Report," edited by J.D. Goltz, 3/11/94, (PB94-193943, A10, MF-A03).

NCEER-94-0006 "Seismic Energy Based Fatigue Damage Analysis of Bridge Columns: Part I - Evaluation of Seismic Capacity," by G.A. Chang and J.B. Mander, 3/14/94, (PB94-219185, A11, MF-A03).

NCEER-94-0007 "Seismic Isolation of Multi-Story Frame Structures Using Spherical Sliding Isolation Systems," by T.M. Al-Hussaini, V.A. Zayas and M.C. Constantinou, 3/17/94, (PB94-193745, A09, MF-A02).

NCEER-94-0008 "The Northridge, California Earthquake of January 17, 1994: Performance of Highway Bridges," edited by I.G. Buckle, 3/24/94, (PB94-193851, A06, MF-A02).

NCEER-94-0009 "Proceedings of the Third U.S.-Japan Workshop on Earthquake Protective Systems for Bridges," edited by I.G. Buckle and I. Friedland, 3/31/94, (PB94-195815, A99, MF-A06).

NCEER-94-0010 "3D-BASIS-ME: Computer Program for Nonlinear Dynamic Analysis of Seismically Isolated Single and Multiple Structures and Liquid Storage Tanks," by P.C. Tsopelas, M.C. Constantinou and A.M. Reinhorn, 4/12/94, (PB94-204922, A09, MF-A02).

NCEER-94-0011 "The Northridge, California Earthquake of January 17, 1994: Performance of Gas Transmission Pipelines," by T.D. O'Rourke and M.C. Palmer, 5/16/94, (PB94-204989, A05, MF-A01).

NCEER-94-0012 "Feasibility Study of Replacement Procedures and Earthquake Performance Related to Gas Transmission Pipelines," by T.D. O'Rourke and M.C. Palmer, 5/25/94, (PB94-206638, A09, MF-A02).

NCEER-94-0013 "Seismic Energy Based Fatigue Damage Analysis of Bridge Columns: Part II - Evaluation of Seismic Demand," by G.A. Chang and J.B. Mander, 6/1/94, (PB95-18106, A08, MF-A02).

NCEER-94-0014 "NCEER-Taisei Corporation Research Program on Sliding Seismic Isolation Systems for Bridges: Experimental and Analytical Study of a System Consisting of Sliding Bearings and Fluid Restoring Force/Damping Devices," by P. Tsopelas and M.C. Constantinou, 6/13/94, (PB94-219144, A10, MF-A03).

NCEER-94-0015 "Generation of Hazard-Consistent Fragility Curves for Seismic Loss Estimation Studies," by H. Hwang and J-R. Huo, 6/14/94, (PB95-181996, A09, MF-A02).

NCEER-94-0016 "Seismic Study of Building Frames with Added Energy-Absorbing Devices," by W.S. Pong, C.S. Tsai and G.C. Lee, 6/20/94, (PB94-219136, A10, A03).

NCEER-94-0017 "Sliding Mode Control for Seismic-Excited Linear and Nonlinear Civil Engineering Structures," by J. Yang, J. Wu, A. Agrawal and Z. Li, 6/21/94, (PB95-138483, A06, MF-A02).

NCEER-94-0018 "3D-BASIS-TABS Version 2.0: Computer Program for Nonlinear Dynamic Analysis of Three Dimensional Base Isolated Structures," by A.M. Reinhorn, S. Nagarajaiah, M.C. Constantinou, P. Tsopelas and R. Li, 6/22/94, (PB95-182176, A08, MF-A02).

NCEER-94-0019 "Proceedings of the International Workshop on Civil Infrastructure Systems: Application of Intelligent Systems and Advanced Materials on Bridge Systems," Edited by G.C. Lee and K.C. Chang, 7/18/94, (PB95-252474, A20, MF-A04).

NCEER-94-0020 "Study of Seismic Isolation Systems for Computer Floors," by V. Lambrou and M.C. Constantinou, 7/19/94, (PB95-138533, A10, MF-A03).

NCEER-94-0021 "Proceedings of the U.S.-Italian Workshop on Guidelines for Seismic Evaluation and Rehabilitation of Unreinforced Masonry Buildings," Edited by D.P. Abrams and G.M. Calvi, 7/20/94, (PB95-138749, A13, MF-A03).

NCEER-94-0022 "NCEER-Taisei Corporation Research Program on Sliding Seismic Isolation Systems for Bridges: Experimental and Analytical Study of a System Consisting of Lubricated PTFE Sliding Bearings and Mild Steel Dampers," by P. Tsopelas and M.C. Constantinou, 7/22/94, (PB95-182184, A08, MF-A02).

NCEER-94-0023 "Development of Reliability-Based Design Criteria for Buildings Under Seismic Load," by Y.K. Wen, H. Hwang and M. Shinozuka, 8/1/94, (PB95-211934, A08, MF-A02).

NCEER-94-0024 "Experimental Verification of Acceleration Feedback Control Strategies for an Active Tendon System," by S.J. Dyke, B.F. Spencer, Jr., P. Quast, M.K. Sain, D.C. Kaspari, Jr. and T.T. Soong, 8/29/94, (PB95-212320, A05, MF-A01).

NCEER-94-0025 "Seismic Retrofitting Manual for Highway Bridges," Edited by I.G. Buckle and I.F. Friedland, published by the Federal Highway Administration (PB95-212676, A15, MF-A03).

NCEER-94-0026 "Proceedings from the Fifth U.S.-Japan Workshop on Earthquake Resistant Design of Lifeline Facilities and Countermeasures Against Soil Liquefaction," Edited by T.D. O'Rourke and M. Hamada, 11/7/94, (PB95-220802, A99, MF-E08).

NCEER-95-0001 "Experimental and Analytical Investigation of Seismic Retrofit of Structures with Supplemental Damping: Part 1 - Fluid Viscous Damping Devices," by A.M. Reinhorn, C. Li and M.C. Constantinou, 1/3/95, (PB95-266599, A09, MF-A02).

NCEER-95-0002 "Experimental and Analytical Study of Low-Cycle Fatigue Behavior of Semi-Rigid Top-And-Seat Angle Connections," by G. Pekcan, J.B. Mander and S.S. Chen, 1/5/95, (PB95-220042, A07, MF-A02).

NCEER-95-0003 "NCEER-ATC Joint Study on Fragility of Buildings," by T. Anagnos, C. Rojahn and A.S. Kiremidjian, 1/20/95, (PB95-220026, A06, MF-A02).

NCEER-95-0004 "Nonlinear Control Algorithms for Peak Response Reduction," by Z. Wu, T.T. Soong, V. Gattulli and R.C. Lin, 2/16/95, (PB95-220349, A05, MF-A01).

NCEER-95-0005 "Pipeline Replacement Feasibility Study: A Methodology for Minimizing Seismic and Corrosion Risks to Underground Natural Gas Pipelines," by R.T. Eguchi, H.A. Seligson and D.G. Honegger, 3/2/95, (PB95-252326, A06, MF-A02).

NCEER-95-0006 "Evaluation of Seismic Performance of an 11-Story Frame Building During the 1994 Northridge Earthquake," by F. Naeim, R. DiSulio, K. Benuska, A. Reinhorn and C. Li, to be published.

NCEER-95-0007 "Prioritization of Bridges for Seismic Retrofitting," by N. Basöz and A.S. Kiremidjian, 4/24/95, (PB95-252300, A08, MF-A02).

NCEER-95-0008 "Method for Developing Motion Damage Relationships for Reinforced Concrete Frames," by A. Singhal and A.S. Kiremidjian, 5/11/95, (PB95-266607, A06, MF-A02).

NCEER-95-0009 "Experimental and Analytical Investigation of Seismic Retrofit of Structures with Supplemental Damping: Part II - Friction Devices," by C. Li and A.M. Reinhorn, 7/6/95, (PB96-128087, A11, MF-A03).

NCEER-95-0010 "Experimental Performance and Analytical Study of a Non-Ductile Reinforced Concrete Frame Structure Retrofitted with Elastomeric Spring Dampers," by G. Pekcan, J.B. Mander and S.S. Chen, 7/14/95, (PB96-137161, A08, MF-A02).

NCEER-95-0011 "Development and Experimental Study of Semi-Active Fluid Damping Devices for Seismic Protection of Structures," by M.D. Symans and M.C. Constantinou, 8/3/95, (PB96-136940, A23, MF-A04).

NCEER-95-0012 "Real-Time Structural Parameter Modification (RSPM): Development of Innervated Structures," by Z. Liang, M. Tong and G.C. Lee, 4/11/95, (PB96-137153, A06, MF-A01).

NCEER-95-0013 "Experimental and Analytical Investigation of Seismic Retrofit of Structures with Supplemental Damping: Part III - Viscous Damping Walls," by A.M. Reinhorn and C. Li, 10/1/95, (PB96-176409, A11, MF-A03).

NCEER-95-0014 "Seismic Fragility Analysis of Equipment and Structures in a Memphis Electric Substation," by J-R. Huo and H.H.M. Hwang, 8/10/95, (PB96-128087, A09, MF-A02).

NCEER-95-0015 "The Hanshin-Awaji Earthquake of January 17, 1995: Performance of Lifelines," Edited by M. Shinozuka, 11/3/95, (PB96-176383, A15, MF-A03).

NCEER-95-0016 "Highway Culvert Performance During Earthquakes," by T.L. Youd and C.J. Beckman, available as NCEER-96-0015.

NCEER-95-0017 "The Hanshin-Awaji Earthquake of January 17, 1995: Performance of Highway Bridges," Edited by I.G. Buckle, 12/1/95, to be published.

NCEER-95-0018 "Modeling of Masonry Infill Panels for Structural Analysis," by A.M. Reinhorn, A. Madan, R.E. Valles, Y. Reichmann and J.B. Mander, 12/8/95, (PB97-110886, MF-A01, A06).

NCEER-95-0019 "Optimal Polynomial Control for Linear and Nonlinear Structures," by A.K. Agrawal and J.N. Yang, 12/11/95, (PB96-168737, A07, MF-A02).

NCEER-95-0020 "Retrofit of Non-Ductile Reinforced Concrete Frames Using Friction Dampers," by R.S. Rao, P. Gergely and R.N. White, 12/22/95, (PB97-133508, A10, MF-A02).

NCEER-95-0021 "Parametric Results for Seismic Response of Pile-Supported Bridge Bents," by G. Mylonakis, A. Nikolaou and G. Gazetas, 12/22/95, (PB97-100242, A12, MF-A03).

NCEER-95-0022 "Kinematic Bending Moments in Seismically Stressed Piles," by A. Nikolaou, G. Mylonakis and G. Gazetas, 12/23/95, (PB97-113914, MF-A03, A13).

NCEER-96-0001 "Dynamic Response of Unreinforced Masonry Buildings with Flexible Diaphragms," by A.C. Costley and D.P. Abrams," 10/10/96, (PB97-133573, MF-A03, A15).

NCEER-96-0002 "State of the Art Review: Foundations and Retaining Structures," by I. Po Lam, to be published.

NCEER-96-0003 "Ductility of Rectangular Reinforced Concrete Bridge Columns with Moderate Confinement," by N. Wehbe, M. Saiidi, D. Sanders and B. Douglas, 11/7/96, (PB97-133557, A06, MF-A02).

NCEER-96-0004 "Proceedings of the Long-Span Bridge Seismic Research Workshop," edited by I.G. Buckle and I.M. Friedland, to be published.

NCEER-96-0005 "Establish Representative Pier Types for Comprehensive Study: Eastern United States," by J. Kulicki and Z. Prucz, 5/28/96, (PB98-119217, A07, MF-A02).

NCEER-96-0006 "Establish Representative Pier Types for Comprehensive Study: Western United States," by R. Imbsen, R.A. Schamber and T.A. Osterkamp, 5/28/96, (PB98-118607, A07, MF-A02).

NCEER-96-0007 "Nonlinear Control Techniques for Dynamical Systems with Uncertain Parameters," by R.G. Ghanem and M.I. Bujakov, 5/27/96, (PB97-100259, A17, MF-A03).

NCEER-96-0008 "Seismic Evaluation of a 30-Year Old Non-Ductile Highway Bridge Pier and Its Retrofit," by J.B. Mander, B. Mahmoodzadegan, S. Bhadra and S.S. Chen, 5/31/96, (PB97-110902, MF-A03, A10).

NCEER-96-0009 "Seismic Performance of a Model Reinforced Concrete Bridge Pier Before and After Retrofit," by J.B. Mander, J.H. Kim and C.A. Ligozio, 5/31/96, (PB97-110910, MF-A02, A10).

NCEER-96-0010 "IDARC2D Version 4.0: A Computer Program for the Inelastic Damage Analysis of Buildings," by R.E. Valles, A.M. Reinhorn, S.K. Kunnath, C. Li and A. Madan, 6/3/96, (PB97-100234, A17, MF-A03).

NCEER-96-0011 "Estimation of the Economic Impact of Multiple Lifeline Disruption: Memphis Light, Gas and Water Division Case Study," by S.E. Chang, H.A. Seligson and R.T. Eguchi, 8/16/96, (PB97-133490, A11, MF-A03).

NCEER-96-0012 "Proceedings from the Sixth Japan-U.S. Workshop on Earthquake Resistant Design of Lifeline Facilities and Countermeasures Against Soil Liquefaction, Edited by M. Hamada and T. O'Rourke, 9/11/96, (PB97-133581, A99, MF-A06).

NCEER-96-0013 "Chemical Hazards, Mitigation and Preparedness in Areas of High Seismic Risk: A Methodology for Estimating the Risk of Post-Earthquake Hazardous Materials Release," by H.A. Seligson, R.T. Eguchi, K.J. Tierney and K. Richmond, 11/7/96, (PB97-133565, MF-A02, A08).

NCEER-96-0014 "Response of Steel Bridge Bearings to Reversed Cyclic Loading," by J.B. Mander, D-K. Kim, S.S. Chen and G.J. Premus, 11/13/96, (PB97-140735, A12, MF-A03).

NCEER-96-0015 "Highway Culvert Performance During Past Earthquakes," by T.L. Youd and C.J. Beckman, 11/25/96, (PB97-133532, A06, MF-A01).

NCEER-97-0001 "Evaluation, Prevention and Mitigation of Pounding Effects in Building Structures," by R.E. Valles and A.M. Reinhorn, 2/20/97, (PB97-159552, A14, MF-A03).

NCEER-97-0002 "Seismic Design Criteria for Bridges and Other Highway Structures," by C. Rojahn, R. Mayes, D.G. Anderson, J. Clark, J.H. Hom, R.V. Nutt and M.J. O'Rourke, 4/30/97, (PB97-194658, A06, MF-A03).

NCEER-97-0003 “Proceedings of the U.S.-Italian Workshop on Seismic Evaluation and Retrofit,” Edited by D.P. Abrams and G.M. Calvi, 3/19/97, (PB97-194666, A13, MF-A03).

NCEER-97-0004 "Investigation of Seismic Response of Buildings with Linear and Nonlinear Fluid Viscous Dampers," by A.A. Seleemah and M.C. Constantinou, 5/21/97, (PB98-109002, A15, MF-A03).

NCEER-97-0005 "Proceedings of the Workshop on Earthquake Engineering Frontiers in Transportation Facilities," edited by G.C. Lee and I.M. Friedland, 8/29/97, (PB98-128911, A25, MR-A04).

NCEER-97-0006 "Cumulative Seismic Damage of Reinforced Concrete Bridge Piers," by S.K. Kunnath, A. El-Bahy, A. Taylor and W. Stone, 9/2/97, (PB98-108814, A11, MF-A03).

NCEER-97-0007 "Structural Details to Accommodate Seismic Movements of Highway Bridges and Retaining Walls," by R.A. Imbsen, R.A. Schamber, E. Thorkildsen, A. Kartoum, B.T. Martin, T.N. Rosser and J.M. Kulicki, 9/3/97, (PB98-108996, A09, MF-A02).

NCEER-97-0008 "A Method for Earthquake Motion-Damage Relationships with Application to Reinforced Concrete Frames," by A. Singhal and A.S. Kiremidjian, 9/10/97, (PB98-108988, A13, MF-A03).

NCEER-97-0009 "Seismic Analysis and Design of Bridge Abutments Considering Sliding and Rotation," by K. Fishman and R. Richards, Jr., 9/15/97, (PB98-108897, A06, MF-A02).

NCEER-97-0010 "Proceedings of the FHWA/NCEER Workshop on the National Representation of Seismic Ground Motion for New and Existing Highway Facilities," edited by I.M. Friedland, M.S. Power and R.L. Mayes, 9/22/97, (PB98-128903, A21, MF-A04).

NCEER-97-0011 "Seismic Analysis for Design or Retrofit of Gravity Bridge Abutments," by K.L. Fishman, R. Richards, Jr. and R.C. Divito, 10/2/97, (PB98-128937, A08, MF-A02).

NCEER-97-0012 "Evaluation of Simplified Methods of Analysis for Yielding Structures," by P. Tsopelas, M.C. Constantinou, C.A. Kircher and A.S. Whittaker, 10/31/97, (PB98-128929, A10, MF-A03).

NCEER-97-0013 "Seismic Design of Bridge Columns Based on Control and Repairability of Damage," by C-T. Cheng and J.B. Mander, 12/8/97, (PB98-144249, A11, MF-A03).

NCEER-97-0014 "Seismic Resistance of Bridge Piers Based on Damage Avoidance Design," by J.B. Mander and C-T. Cheng, 12/10/97, (PB98-144223, A09, MF-A02).

NCEER-97-0015 “Seismic Response of Nominally Symmetric Systems with Strength Uncertainty,” by S. Balopoulou and M. Grigoriu, 12/23/97, (PB98-153422, A11, MF-A03).

NCEER-97-0016 “Evaluation of Seismic Retrofit Methods for Reinforced Concrete Bridge Columns,” by T.J. Wipf, F.W. Klaiber and F.M. Russo, 12/28/97, (PB98-144215, A12, MF-A03).

NCEER-97-0017 “Seismic Fragility of Existing Conventional Reinforced Concrete Highway Bridges,” by C.L. Mullen and A.S. Cakmak, 12/30/97, (PB98-153406, A08, MF-A02).

NCEER-97-0018 “Loss Asssessment of Memphis Buildings,” edited by D.P. Abrams and M. Shinozuka, 12/31/97, (PB98-144231, A13, MF-A03).

NCEER-97-0019 “Seismic Evaluation of Frames with Infill Walls Using Quasi-static Experiments,” by K.M. Mosalam, R.N. White and P. Gergely, 12/31/97, (PB98-153455, A07, MF-A02).

NCEER-97-0020 “Seismic Evaluation of Frames with Infill Walls Using Pseudo-dynamic Experiments,” by K.M. Mosalam, R.N. White and P. Gergely, 12/31/97, (PB98-153430, A07, MF-A02).

NCEER-97-0021 “Computational Strategies for Frames with Infill Walls: Discrete and Smeared Crack Analyses and Seismic Fragility,” by K.M. Mosalam, R.N. White and P. Gergely, 12/31/97, (PB98-153414, A10, MF-A02).

NCEER-97-0022 "Proceedings of the NCEER Workshop on Evaluation of Liquefaction Resistance of Soils," edited by T.L. Youd and I.M. Idriss, 12/31/97, (PB98-155617, A15, MF-A03).

MCEER-98-0001 "Extraction of Nonlinear Hysteretic Properties of Seismically Isolated Bridges from Quick-Release Field Tests," by Q. Chen, B.M. Douglas, E.M. Maragakis and I.G. Buckle, 5/26/98, (PB99-118838, A06, MF-A01).

MCEER-98-0002 "Methodologies for Evaluating the Importance of Highway Bridges," by A. Thomas, S. Eshenaur and J. Kulicki, 5/29/98, (PB99-118846, A10, MF-A02).

MCEER-98-0003 "Capacity Design of Bridge Piers and the Analysis of Overstrength," by J.B. Mander, A. Dutta and P. Goel, 6/1/98, (PB99-118853, A09, MF-A02).

MCEER-98-0004 "Evaluation of Bridge Damage Data from the Loma Prieta and Northridge, California Earthquakes," by N. Basoz and A. Kiremidjian, 6/2/98, (PB99-118861, A15, MF-A03).

MCEER-98-0005 "Screening Guide for Rapid Assessment of Liquefaction Hazard at Highway Bridge Sites," by T. L. Youd, 6/16/98, (PB99-118879, A06, not available on microfiche).

MCEER-98-0006 "Structural Steel and Steel/Concrete Interface Details for Bridges," by P. Ritchie, N. Kauhl and J. Kulicki, 7/13/98, (PB99-118945, A06, MF-A01).

MCEER-98-0007 "Capacity Design and Fatigue Analysis of Confined Concrete Columns," by A. Dutta and J.B. Mander, 7/14/98, (PB99-118960, A14, MF-A03).

MCEER-98-0008 "Proceedings of the Workshop on Performance Criteria for Telecommunication Services Under Earthquake Conditions," edited by A.J. Schiff, 7/15/98, (PB99-118952, A08, MF-A02).

MCEER-98-0009 "Fatigue Analysis of Unconfined Concrete Columns," by J.B. Mander, A. Dutta and J.H. Kim, 9/12/98, (PB99-123655, A10, MF-A02).

MCEER-98-0010 "Centrifuge Modeling of Cyclic Lateral Response of Pile-Cap Systems and Seat-Type Abutments in Dry Sands," by A.D. Gadre and R. Dobry, 10/2/98, (PB99-123606, A13, MF-A03).

MCEER-98-0011 "IDARC-BRIDGE: A Computational Platform for Seismic Damage Assessment of Bridge Structures," by A.M. Reinhorn, V. Simeonov, G. Mylonakis and Y. Reichman, 10/2/98, (PB99-162919, A15, MF-A03).

MCEER-98-0012 "Experimental Investigation of the Dynamic Response of Two Bridges Before and After Retrofitting with Elastomeric Bearings," by D.A. Wendichansky, S.S. Chen and J.B. Mander, 10/2/98, (PB99-162927, A15, MF-A03).

MCEER-98-0013 "Design Procedures for Hinge Restrainers and Hinge Sear Width for Multiple-Frame Bridges," by R. Des Roches and G.L. Fenves, 11/3/98, (PB99-140477, A13, MF-A03).

MCEER-98-0014 "Response Modification Factors for Seismically Isolated Bridges," by M.C. Constantinou and J.K. Quarshie, 11/3/98, (PB99-140485, A14, MF-A03).

MCEER-98-0015 "Proceedings of the U.S.-Italy Workshop on Seismic Protective Systems for Bridges," edited by I.M. Friedland and M.C. Constantinou, 11/3/98, (PB2000-101711, A22, MF-A04).

MCEER-98-0016 "Appropriate Seismic Reliability for Critical Equipment Systems: Recommendations Based on Regional Analysis of Financial and Life Loss," by K. Porter, C. Scawthorn, C. Taylor and N. Blais, 11/10/98, (PB99-157265, A08, MF-A02).

MCEER-98-0017 "Proceedings of the U.S. Japan Joint Seminar on Civil Infrastructure Systems Research," edited by M. Shinozuka and A. Rose, 11/12/98, (PB99-156713, A16, MF-A03).

MCEER-98-0018 "Modeling of Pile Footings and Drilled Shafts for Seismic Design," by I. PoLam, M. Kapuskar and D. Chaudhuri, 12/21/98, (PB99-157257, A09, MF-A02).

MCEER-99-0001 "Seismic Evaluation of a Masonry Infilled Reinforced Concrete Frame by Pseudodynamic Testing," by S.G. Buonopane and R.N. White, 2/16/99, (PB99-162851, A09, MF-A02).

MCEER-99-0002 "Response History Analysis of Structures with Seismic Isolation and Energy Dissipation Systems: Verification Examples for Program SAP2000," by J. Scheller and M.C. Constantinou, 2/22/99, (PB99-162869, A08, MF-A02).

MCEER-99-0003 "Experimental Study on the Seismic Design and Retrofit of Bridge Columns Including Axial Load Effects," by A. Dutta, T. Kokorina and J.B. Mander, 2/22/99, (PB99-162877, A09, MF-A02).

MCEER-99-0004 "Experimental Study of Bridge Elastomeric and Other Isolation and Energy Dissipation Systems with Emphasis on Uplift Prevention and High Velocity Near-source Seismic Excitation," by A. Kasalanati and M. C. Constantinou, 2/26/99, (PB99-162885, A12, MF-A03).

MCEER-99-0005 "Truss Modeling of Reinforced Concrete Shear-flexure Behavior," by J.H. Kim and J.B. Mander, 3/8/99, (PB99-163693, A12, MF-A03).

MCEER-99-0006 "Experimental Investigation and Computational Modeling of Seismic Response of a 1:4 Scale Model Steel Structure with a Load Balancing Supplemental Damping System," by G. Pekcan, J.B. Mander and S.S. Chen, 4/2/99, (PB99-162893, A11, MF-A03).

MCEER-99-0007 "Effect of Vertical Ground Motions on the Structural Response of Highway Bridges," by M.R. Button, C.J. Cronin and R.L. Mayes, 4/10/99, (PB2000-101411, A10, MF-A03).

MCEER-99-0008 "Seismic Reliability Assessment of Critical Facilities: A Handbook, Supporting Documentation, and Model Code Provisions," by G.S. Johnson, R.E. Sheppard, M.D. Quilici, S.J. Eder and C.R. Scawthorn, 4/12/99, (PB2000-101701, A18, MF-A04).

MCEER-99-0009 "Impact Assessment of Selected MCEER Highway Project Research on the Seismic Design of Highway Structures," by C. Rojahn, R. Mayes, D.G. Anderson, J.H. Clark, D'Appolonia Engineering, S. Gloyd and R.V. Nutt, 4/14/99, (PB99-162901, A10, MF-A02).

MCEER-99-0010 "Site Factors and Site Categories in Seismic Codes," by R. Dobry, R. Ramos and M.S. Power, 7/19/99, (PB2000-101705, A08, MF-A02).

MCEER-99-0011 "Restrainer Design Procedures for Multi-Span Simply-Supported Bridges," by M.J. Randall, M. Saiidi, E. Maragakis and T. Isakovic, 7/20/99, (PB2000-101702, A10, MF-A02).

MCEER-99-0012 "Property Modification Factors for Seismic Isolation Bearings," by M.C. Constantinou, P. Tsopelas, A. Kasalanati and E. Wolff, 7/20/99, (PB2000-103387, A11, MF-A03).

MCEER-99-0013 "Critical Seismic Issues for Existing Steel Bridges," by P. Ritchie, N. Kauhl and J. Kulicki, 7/20/99, (PB2000-101697, A09, MF-A02).

MCEER-99-0014 "Nonstructural Damage Database," by A. Kao, T.T. Soong and A. Vender, 7/24/99, (PB2000-101407, A06, MF-A01).

MCEER-99-0015 "Guide to Remedial Measures for Liquefaction Mitigation at Existing Highway Bridge Sites," by H.G. Cooke and J. K. Mitchell, 7/26/99, (PB2000-101703, A11, MF-A03).

MCEER-99-0016 "Proceedings of the MCEER Workshop on Ground Motion Methodologies for the Eastern United States," edited by N. Abrahamson and A. Becker, 8/11/99, (PB2000-103385, A07, MF-A02).

MCEER-99-0017 "Quindío, Colombia Earthquake of January 25, 1999: Reconnaissance Report," by A.P. Asfura and P.J. Flores, 10/4/99, (PB2000-106893, A06, MF-A01).

MCEER-99-0018 "Hysteretic Models for Cyclic Behavior of Deteriorating Inelastic Structures," by M.V. Sivaselvan and A.M. Reinhorn, 11/5/99, (PB2000-103386, A08, MF-A02).

MCEER-99-0019 "Proceedings of the 7th U.S.- Japan Workshop on Earthquake Resistant Design of Lifeline Facilities and Countermeasures Against Soil Liquefaction," edited by T.D. O'Rourke, J.P. Bardet and M. Hamada, 11/19/99, (PB2000-103354, A99, MF-A06).

MCEER-99-0020 "Development of Measurement Capability for Micro-Vibration Evaluations with Application to Chip Fabrication Facilities," by G.C. Lee, Z. Liang, J.W. Song, J.D. Shen and W.C. Liu, 12/1/99, (PB2000-105993, A08, MF-A02).

MCEER-99-0021 "Design and Retrofit Methodology for Building Structures with Supplemental Energy Dissipating Systems," by G. Pekcan, J.B. Mander and S.S. Chen, 12/31/99, (PB2000-105994, A11, MF-A03).

MCEER-00-0001 "The Marmara, Turkey Earthquake of August 17, 1999: Reconnaissance Report," edited by C. Scawthorn; with major contributions by M. Bruneau, R. Eguchi, T. Holzer, G. Johnson, J. Mander, J. Mitchell, W. Mitchell, A. Papageorgiou, C. Scaethorn, and G. Webb, 3/23/00, (PB2000-106200, A11, MF-A03).

MCEER-00-0002 "Proceedings of the MCEER Workshop for Seismic Hazard Mitigation of Health Care Facilities," edited by G.C. Lee, M. Ettouney, M. Grigoriu, J. Hauer and J. Nigg, 3/29/00, (PB2000-106892, A08, MF-A02).

MCEER-00-0003 "The Chi-Chi, Taiwan Earthquake of September 21, 1999: Reconnaissance Report," edited by G.C. Lee and C.H. Loh, with major contributions by G.C. Lee, M. Bruneau, I.G. Buckle, S.E. Chang, P.J. Flores, T.D. O'Rourke, M. Shinozuka, T.T. Soong, C-H. Loh, K-C. Chang, Z-J. Chen, J-S. Hwang, M-L. Lin, G-Y. Liu, K-C. Tsai, G.C. Yao and C-L. Yen, 4/30/00, (PB2001-100980, A10, MF-A02).

MCEER-00-0004 "Seismic Retrofit of End-Sway Frames of Steel Deck-Truss Bridges with a Supplemental Tendon System: Experimental and Analytical Investigation," by G. Pekcan, J.B. Mander and S.S. Chen, 7/1/00, (PB2001-100982, A10, MF-A02).

MCEER-00-0005 "Sliding Fragility of Unrestrained Equipment in Critical Facilities," by W.H. Chong and T.T. Soong, 7/5/00, (PB2001-100983, A08, MF-A02).

MCEER-00-0006 "Seismic Response of Reinforced Concrete Bridge Pier Walls in the Weak Direction," by N. Abo-Shadi, M. Saiidi and D. Sanders, 7/17/00, (PB2001-100981, A17, MF-A03).

MCEER-00-0007 "Low-Cycle Fatigue Behavior of Longitudinal Reinforcement in Reinforced Concrete Bridge Columns," by J. Brown and S.K. Kunnath, 7/23/00, (PB2001-104392, A08, MF-A02).

MCEER-00-0008 "Soil Structure Interaction of Bridges for Seismic Analysis," I. PoLam and H. Law, 9/25/00, (PB2001-105397, A08, MF-A02).

MCEER-00-0009 "Proceedings of the First MCEER Workshop on Mitigation of Earthquake Disaster by Advanced Technologies (MEDAT-1), edited by M. Shinozuka, D.J. Inman and T.D. O'Rourke, 11/10/00, (PB2001-105399, A14, MF-A03).

MCEER-00-0010 "Development and Evaluation of Simplified Procedures for Analysis and Design of Buildings with Passive Energy Dissipation Systems, Revision 01," by O.M. Ramirez, M.C. Constantinou, C.A. Kircher, A.S. Whittaker, M.W. Johnson, J.D. Gomez and C. Chrysostomou, 11/16/01, (PB2001-105523, A23, MF-A04).

MCEER-00-0011 "Dynamic Soil-Foundation-Structure Interaction Analyses of Large Caissons," by C-Y. Chang, C-M. Mok, Z-L. Wang, R. Settgast, F. Waggoner, M.A. Ketchum, H.M. Gonnermann and C-C. Chin, 12/30/00, (PB2001-104373, A07, MF-A02).

MCEER-00-0012 "Experimental Evaluation of Seismic Performance of Bridge Restrainers," by A.G. Vlassis, E.M. Maragakis and M. Saiid Saiidi, 12/30/00, (PB2001-104354, A09, MF-A02).

MCEER-00-0013 "Effect of Spatial Variation of Ground Motion on Highway Structures," by M. Shinozuka, V. Saxena and G. Deodatis, 12/31/00, (PB2001-108755, A13, MF-A03).

MCEER-00-0014 "A Risk-Based Methodology for Assessing the Seismic Performance of Highway Systems," by S.D. Werner, C.E. Taylor, J.E. Moore, II, J.S. Walton and S. Cho, 12/31/00, (PB2001-108756, A14, MF-A03).

MCEER-01-0001 "Experimental Investigation of P-Delta Effects to Collapse During Earthquakes," by D. Vian and M. Bruneau, 6/25/01, (PB2002-100534, A17, MF-A03).

MCEER-01-0002 "Proceedings of the Second MCEER Workshop on Mitigation of Earthquake Disaster by Advanced Technologies (MEDAT-2)," edited by M. Bruneau and D.J. Inman, 7/23/01, (PB2002-100434, A16, MF-A03).

MCEER-01-0003 "Sensitivity Analysis of Dynamic Systems Subjected to Seismic Loads," by C. Roth and M. Grigoriu, 9/18/01, (PB2003-100884, A12, MF-A03).

MCEER-01-0004 "Overcoming Obstacles to Implementing Earthquake Hazard Mitigation Policies: Stage 1 Report," by D.J. Alesch and W.J. Petak, 12/17/01, (PB2002-107949, A07, MF-A02).

MCEER-01-0005 "Updating Real-Time Earthquake Loss Estimates: Methods, Problems and Insights," by C.E. Taylor, S.E. Chang and R.T. Eguchi, 12/17/01, (PB2002-107948, A05, MF-A01).

MCEER-01-0006 "Experimental Investigation and Retrofit of Steel Pile Foundations and Pile Bents Under Cyclic Lateral Loadings," by A. Shama, J. Mander, B. Blabac and S. Chen, 12/31/01, (PB2002-107950, A13, MF-A03).

MCEER-02-0001 "Assessment of Performance of Bolu Viaduct in the 1999 Duzce Earthquake in Turkey" by P.C. Roussis, M.C. Constantinou, M. Erdik, E. Durukal and M. Dicleli, 5/8/02, (PB2003-100883, A08, MF-A02).

MCEER-02-0002 "Seismic Behavior of Rail Counterweight Systems of Elevators in Buildings," by M.P. Singh, Rildova and L.E. Suarez, 5/27/02. (PB2003-100882, A11, MF-A03).

MCEER-02-0003 "Development of Analysis and Design Procedures for Spread Footings," by G. Mylonakis, G. Gazetas, S. Nikolaou and A. Chauncey, 10/02/02, (PB2004-101636, A13, MF-A03, CD-A13).

MCEER-02-0004 "Bare-Earth Algorithms for Use with SAR and LIDAR Digital Elevation Models," by C.K. Huyck, R.T. Eguchi and B. Houshmand, 10/16/02, (PB2004-101637, A07, CD-A07).

MCEER-02-0005 "Review of Energy Dissipation of Compression Members in Concentrically Braced Frames," by K.Lee and M. Bruneau, 10/18/02, (PB2004-101638, A10, CD-A10).

MCEER-03-0001 "Experimental Investigation of Light-Gauge Steel Plate Shear Walls for the Seismic Retrofit of Buildings" by J. Berman and M. Bruneau, 5/2/03, (PB2004-101622, A10, MF-A03, CD-A10).

MCEER-03-0002 "Statistical Analysis of Fragility Curves," by M. Shinozuka, M.Q. Feng, H. Kim, T. Uzawa and T. Ueda, 6/16/03, (PB2004-101849, A09, CD-A09).

MCEER-03-0003 "Proceedings of the Eighth U.S.-Japan Workshop on Earthquake Resistant Design f Lifeline Facilities and Countermeasures Against Liquefaction," edited by M. Hamada, J.P. Bardet and T.D. O'Rourke, 6/30/03, (PB2004-104386, A99, CD-A99).

MCEER-03-0004 "Proceedings of the PRC-US Workshop on Seismic Analysis and Design of Special Bridges," edited by L.C. Fan and G.C. Lee, 7/15/03, (PB2004-104387, A14, CD-A14).

MCEER-03-0005 "Urban Disaster Recovery: A Framework and Simulation Model," by S.B. Miles and S.E. Chang, 7/25/03, (PB2004-104388, A07, CD-A07).

MCEER-03-0006 "Behavior of Underground Piping Joints Due to Static and Dynamic Loading," by R.D. Meis, M. Maragakis and R. Siddharthan, 11/17/03, (PB2005-102194, A13, MF-A03, CD-A00).

MCEER-04-0001 "Experimental Study of Seismic Isolation Systems with Emphasis on Secondary System Response and Verification of Accuracy of Dynamic Response History Analysis Methods," by E. Wolff and M. Constantinou, 1/16/04 (PB2005-102195, A99, MF-E08, CD-A00).

MCEER-04-0002 "Tension, Compression and Cyclic Testing of Engineered Cementitious Composite Materials," by K. Kesner and S.L. Billington, 3/1/04, (PB2005-102196, A08, CD-A08).

MCEER-04-0003 "Cyclic Testing of Braces Laterally Restrained by Steel Studs to Enhance Performance During Earthquakes," by O.C. Celik, J.W. Berman and M. Bruneau, 3/16/04, (PB2005-102197, A13, MF-A03, CD-A00).

MCEER-04-0004 "Methodologies for Post Earthquake Building Damage Detection Using SAR and Optical Remote Sensing: Application to the August 17, 1999 Marmara, Turkey Earthquake," by C.K. Huyck, B.J. Adams, S. Cho, R.T. Eguchi, B. Mansouri and B. Houshmand, 6/15/04, (PB2005-104888, A10, CD-A00).

MCEER-04-0005 "Nonlinear Structural Analysis Towards Collapse Simulation: A Dynamical Systems Approach," by M.V. Sivaselvan and A.M. Reinhorn, 6/16/04, (PB2005-104889, A11, MF-A03, CD-A00).

MCEER-04-0006 "Proceedings of the Second PRC-US Workshop on Seismic Analysis and Design of Special Bridges," edited by G.C. Lee and L.C. Fan, 6/25/04, (PB2005-104890, A16, CD-A00).

MCEER-04-0007 "Seismic Vulnerability Evaluation of Axially Loaded Steel Built-up Laced Members," by K. Lee and M. Bruneau, 6/30/04, (PB2005-104891, A16, CD-A00).

MCEER-04-0008 "Evaluation of Accuracy of Simplified Methods of Analysis and Design of Buildings with Damping Systems for Near-Fault and for Soft-Soil Seismic Motions," by E.A. Pavlou and M.C. Constantinou, 8/16/04, (PB2005-104892, A08, MF-A02, CD-A00).

MCEER-04-0009 "Assessment of Geotechnical Issues in Acute Care Facilities in California," by M. Lew, T.D. O'Rourke, R. Dobry and M. Koch, 9/15/04, (PB2005-104893, A08, CD-A00).

MCEER-04-0010 "Scissor-Jack-Damper Energy Dissipation System," by A.N. Sigaher-Boyle and M.C. Constantinou, 12/1/04 (PB2005-108221).

MCEER-04-0011 "Seismic Retrofit of Bridge Steel Truss Piers Using a Controlled Rocking Approach," by M. Pollino and M. Bruneau, 12/20/04 (PB2006-105795).

MCEER-05-0001 "Experimental and Analytical Studies of Structures Seismically Isolated with an Uplift-Restraint Isolation System," by P.C. Roussis and M.C. Constantinou, 1/10/05 (PB2005-108222).

MCEER-05-0002 "A Versatile Experimentation Model for Study of Structures Near Collapse Applied to Seismic Evaluation of Irregular Structures," by D. Kusumastuti, A.M. Reinhorn and A. Rutenberg, 3/31/05 (PB2006-101523).

MCEER-05-0003 "Proceedings of the Third PRC-US Workshop on Seismic Analysis and Design of Special Bridges," edited by L.C. Fan and G.C. Lee, 4/20/05, (PB2006-105796).

MCEER-05-0004 "Approaches for the Seismic Retrofit of Braced Steel Bridge Piers and Proof-of-Concept Testing of an Eccentrically Braced Frame with Tubular Link," by J.W. Berman and M. Bruneau, 4/21/05 (PB2006-101524).

MCEER-05-0005 "Simulation of Strong Ground Motions for Seismic Fragility Evaluation of Nonstructural Components in Hospitals," by A. Wanitkorkul and A. Filiatrault, 5/26/05 (PB2006-500027).

MCEER-05-0006 "Seismic Safety in California Hospitals: Assessing an Attempt to Accelerate the Replacement or Seismic Retrofit of Older Hospital Facilities," by D.J. Alesch, L.A. Arendt and W.J. Petak, 6/6/05 (PB2006-105794).

MCEER-05-0007 "Development of Seismic Strengthening and Retrofit Strategies for Critical Facilities Using Engineered Cementitious Composite Materials," by K. Kesner and S.L. Billington, 8/29/05 (PB2006-111701).

MCEER-05-0008 "Experimental and Analytical Studies of Base Isolation Systems for Seismic Protection of Power Transformers," by N. Murota, M.Q. Feng and G-Y. Liu, 9/30/05 (PB2006-111702).

MCEER-05-0009 "3D-BASIS-ME-MB: Computer Program for Nonlinear Dynamic Analysis of Seismically Isolated Structures," by P.C. Tsopelas, P.C. Roussis, M.C. Constantinou, R. Buchanan and A.M. Reinhorn, 10/3/05 (PB2006-111703).

MCEER-05-0010 "Steel Plate Shear Walls for Seismic Design and Retrofit of Building Structures," by D. Vian and M. Bruneau, 12/15/05 (PB2006-111704).

MCEER-05-0011 "The Performance-Based Design Paradigm," by M.J. Astrella and A. Whittaker, 12/15/05 (PB2006-111705).

MCEER-06-0001 "Seismic Fragility of Suspended Ceiling Systems," H. Badillo-Almaraz, A.S. Whittaker, A.M. Reinhorn and G.P. Cimellaro, 2/4/06 (PB2006-111706).

MCEER-06-0002 "Multi-Dimensional Fragility of Structures," by G.P. Cimellaro, A.M. Reinhorn and M. Bruneau, 3/1/06 (PB2007-106974, A09, MF-A02, CD A00).

MCEER-06-0003 "Built-Up Shear Links as Energy Dissipators for Seismic Protection of Bridges," by P. Dusicka, A.M. Itani and I.G. Buckle, 3/15/06 (PB2006-111708).

MCEER-06-0004 "Analytical Investigation of the Structural Fuse Concept," by R.E. Vargas and M. Bruneau, 3/16/06 (PB2006-111709).

MCEER-06-0005 "Experimental Investigation of the Structural Fuse Concept," by R.E. Vargas and M. Bruneau, 3/17/06 (PB2006-111710).

MCEER-06-0006 "Further Development of Tubular Eccentrically Braced Frame Links for the Seismic Retrofit of Braced Steel Truss Bridge Piers," by J.W. Berman and M. Bruneau, 3/27/06 (PB2007-105147).

MCEER-06-0007 "REDARS Validation Report," by S. Cho, C.K. Huyck, S. Ghosh and R.T. Eguchi, 8/8/06 (PB2007-106983).

MCEER-06-0008 "Review of Current NDE Technologies for Post-Earthquake Assessment of Retrofitted Bridge Columns," by J.W. Song, Z. Liang and G.C. Lee, 8/21/06 (PB2007-106984).

MCEER-06-0009 "Liquefaction Remediation in Silty Soils Using Dynamic Compaction and Stone Columns," by S. Thevanayagam, G.R. Martin, R. Nashed, T. Shenthan, T. Kanagalingam and N. Ecemis, 8/28/06 (PB2007-106985).

MCEER-06-0010 "Conceptual Design and Experimental Investigation of Polymer Matrix Composite Infill Panels for Seismic Retrofitting," by W. Jung, M. Chiewanichakorn and A.J. Aref, 9/21/06 (PB2007-106986).

MCEER-06-0011 "A Study of the Coupled Horizontal-Vertical Behavior of Elastomeric and Lead-Rubber Seismic Isolation Bearings," by G.P. Warn and A.S. Whittaker, 9/22/06 (PB2007-108679).

MCEER-06-0012 "Proceedings of the Fourth PRC-US Workshop on Seismic Analysis and Design of Special Bridges: Advancing Bridge Technologies in Research, Design, Construction and Preservation," Edited by L.C. Fan, G.C. Lee and L. Ziang, 10/12/06 (PB2007-109042).

MCEER-06-0013 "Cyclic Response and Low Cycle Fatigue Characteristics of Plate Steels," by P. Dusicka, A.M. Itani and I.G. Buckle, 11/1/06 06 (PB2007-106987).

MCEER-06-0014 "Proceedings of the Second US-Taiwan Bridge Engineering Workshop," edited by W.P. Yen, J. Shen, J-Y. Chen and M. Wang, 11/15/06 (PB2008-500041).

MCEER-06-0015 "User Manual and Technical Documentation for the REDARS^{TM} Import Wizard," by S. Cho, S. Ghosh, C.K. Huyck and S.D. Werner, 11/30/06 (PB2007-114766).

MCEER-06-0016 "Hazard Mitigation Strategy and Monitoring Technologies for Urban and Infrastructure Public Buildings: Proceedings of the China-US Workshops," edited by X.Y. Zhou, A.L. Zhang, G.C. Lee and M. Tong, 12/12/06 (PB2008-500018).

MCEER-07-0001 "Static and Kinetic Coefficients of Friction for Rigid Blocks," by C. Kafali, S. Fathali, M. Grigoriu and A.S. Whittaker, 3/20/07 (PB2007-114767).

MCEER-07-0002 "Hazard Mitigation Investment Decision Making: Organizational Response to Legislative Mandate," by L.A. Arendt, D.J. Alesch and W.J. Petak, 4/9/07 (PB2007-114768).

MCEER-07-0003 "Seismic Behavior of Bidirectional-Resistant Ductile End Diaphragms with Unbonded Braces in Straight or Skewed Steel Bridges," by O. Celik and M. Bruneau, 4/11/07 (PB2008-105141).

MCEER-07-0004 “Modeling Pile Behavior in Large Pile Groups Under Lateral Loading,” by A.M. Dodds and G.R. Martin, 4/16/07(PB2008-105142).

MCEER-07-0005 “Experimental Investigation of Blast Performance of Seismically Resistant Concrete-Filled Steel Tube Bridge Piers,” by S. Fujikura, M. Bruneau and D. Lopez-Garcia, 4/20/07 (PB2008-105143).

MCEER-07-0006 “Seismic Analysis of Conventional and Isolated Liquefied Natural Gas Tanks Using Mechanical Analogs,” by I.P. Christovasilis and A.S. Whittaker, 5/1/07.

MCEER-07-0007 “Experimental Seismic Performance Evaluation of Isolation/Restraint Systems for Mechanical Equipment – Part 1: Heavy Equipment Study,” by S. Fathali and A. Filiatrault, 6/6/07 (PB2008-105144).

MCEER-07-0008 “Seismic Vulnerability of Timber Bridges and Timber Substructures,” by A.A. Sharma, J.B. Mander, I.M. Friedland and D.R. Allicock, 6/7/07 (PB2008-105145).

MCEER-07-0009 “Experimental and Analytical Study of the XY-Friction Pendulum (XY-FP) Bearing for Bridge Applications,” by C.C. Marin-Artieda, A.S. Whittaker and M.C. Constantinou, 6/7/07 (PB2008-105191).

MCEER-07-0010 “Proceedings of the PRC-US Earthquake Engineering Forum for Young Researchers,” Edited by G.C. Lee and X.Z. Qi, 6/8/07 (PB2008-500058).

MCEER-07-0011 “Design Recommendations for Perforated Steel Plate Shear Walls,” by R. Purba and M. Bruneau, 6/18/07, (PB2008-105192).

MCEER-07-0012 “Performance of Seismic Isolation Hardware Under Service and Seismic Loading,” by M.C. Constantinou, A.S. Whittaker, Y. Kalpakidis, D.M. Fenz and G.P. Warn, 8/27/07, (PB2008-105193).

MCEER-07-0013 “Experimental Evaluation of the Seismic Performance of Hospital Piping Subassemblies,” by E.R. Goodwin, E. Maragakis and A.M. Itani, 9/4/07, (PB2008-105194).

MCEER-07-0014 “A Simulation Model of Urban Disaster Recovery and Resilience: Implementation for the 1994 Northridge Earthquake,” by S. Miles and S.E. Chang, 9/7/07, (PB2008-106426).

MCEER-07-0015 “Statistical and Mechanistic Fragility Analysis of Concrete Bridges,” by M. Shinozuka, S. Banerjee and S-H. Kim, 9/10/07, (PB2008-106427).

MCEER-07-0016 “Three-Dimensional Modeling of Inelastic Buckling in Frame Structures,” by M. Schachter and AM. Reinhorn, 9/13/07, (PB2008-108125).

MCEER-07-0017 “Modeling of Seismic Wave Scattering on Pile Groups and Caissons,” by I. Po Lam, H. Law and C.T. Yang, 9/17/07 (PB2008-108150).

MCEER-07-0018 “Bridge Foundations: Modeling Large Pile Groups and Caissons for Seismic Design,” by I. Po Lam, H. Law and G.R. Martin (Coordinating Author), 12/1/07 (PB2008-111190).

MCEER-07-0019 “Principles and Performance of Roller Seismic Isolation Bearings for Highway Bridges,” by G.C. Lee, Y.C. Ou, Z. Liang, T.C. Niu and J. Song, 12/10/07 (PB2009-110466).

MCEER-07-0020 “Centrifuge Modeling of Permeability and Pinning Reinforcement Effects on Pile Response to Lateral Spreading,” by L.L Gonzalez-Lagos, T. Abdoun and R. Dobry, 12/10/07 (PB2008-111191).

MCEER-07-0021 “Damage to the Highway System from the Pisco, Perú Earthquake of August 15, 2007,” by J.S. O’Connor, L. Mesa and M. Nykamp, 12/10/07, (PB2008-108126).

MCEER-07-0022 “Experimental Seismic Performance Evaluation of Isolation/Restraint Systems for Mechanical Equipment – Part 2: Light Equipment Study,” by S. Fathali and A. Filiatrault, 12/13/07 (PB2008-111192).

MCEER-07-0023 “Fragility Considerations in Highway Bridge Design,” by M. Shinozuka, S. Banerjee and S.H. Kim, 12/14/07 (PB2008-111193).

MCEER-07-0024 "Performance Estimates for Seismically Isolated Bridges," by G.P. Warn and A.S. Whittaker, 12/30/07 (PB2008-112230).

MCEER-08-0001 "Seismic Performance of Steel Girder Bridge Superstructures with Conventional Cross Frames," by L.P. Carden, A.M. Itani and I.G. Buckle, 1/7/08, (PB2008-112231).

MCEER-08-0002 "Seismic Performance of Steel Girder Bridge Superstructures with Ductile End Cross Frames with Seismic Isolators," by L.P. Carden, A.M. Itani and I.G. Buckle, 1/7/08 (PB2008-112232).

MCEER-08-0003 "Analytical and Experimental Investigation of a Controlled Rocking Approach for Seismic Protection of Bridge Steel Truss Piers," by M. Pollino and M. Bruneau, 1/21/08 (PB2008-112233).

MCEER-08-0004 "Linking Lifeline Infrastructure Performance and Community Disaster Resilience: Models and Multi-Stakeholder Processes," by S.E. Chang, C. Pasion, K. Tatebe and R. Ahmad, 3/3/08 (PB2008-112234).

MCEER-08-0005 "Modal Analysis of Generally Damped Linear Structures Subjected to Seismic Excitations," by J. Song, Y-L. Chu, Z. Liang and G.C. Lee, 3/4/08 (PB2009-102311).

MCEER-08-0006 "System Performance Under Multi-Hazard Environments," by C. Kafali and M. Grigoriu, 3/4/08 (PB2008-112235).

MCEER-08-0007 "Mechanical Behavior of Multi-Spherical Sliding Bearings," by D.M. Fenz and M.C. Constantinou, 3/6/08 (PB2008-112236).

MCEER-08-0008 "Post-Earthquake Restoration of the Los Angeles Water Supply System," by T.H.P. Tabucchi and R.A. Davidson, 3/7/08 (PB2008-112237).

MCEER-08-0009 "Fragility Analysis of Water Supply Systems," by A. Jacobson and M. Grigoriu, 3/10/08 (PB2009-105545).

MCEER-08-0010 "Experimental Investigation of Full-Scale Two-Story Steel Plate Shear Walls with Reduced Beam Section Connections," by B. Qu, M. Bruneau, C-H. Lin and K-C. Tsai, 3/17/08 (PB2009-106368).

MCEER-08-0011 "Seismic Evaluation and Rehabilitation of Critical Components of Electrical Power Systems," S. Ersoy, B. Feizi, A. Ashrafi and M. Ala Saadeghvaziri, 3/17/08 (PB2009-105546).

MCEER-08-0012 "Seismic Behavior and Design of Boundary Frame Members of Steel Plate Shear Walls," by B. Qu and M. Bruneau, 4/26/08 . (PB2009-106744).

MCEER-08-0013 "Development and Appraisal of a Numerical Cyclic Loading Protocol for Quantifying Building System Performance," by A. Filiatrault, A. Wanitkorkul and M. Constantinou, 4/27/08 (PB2009-107906).

MCEER-08-0014 "Structural and Nonstructural Earthquake Design: The Challenge of Integrating Specialty Areas in Designing Complex, Critical Facilities," by W.J. Petak and D.J. Alesch, 4/30/08 (PB2009-107907).

MCEER-08-0015 "Seismic Performance Evaluation of Water Systems," by Y. Wang and T.D. O'Rourke, 5/5/08 (PB2009-107908).

MCEER-08-0016 "Seismic Response Modeling of Water Supply Systems," by P. Shi and T.D. O'Rourke, 5/5/08 (PB2009-107910).

MCEER-08-0017 "Numerical and Experimental Studies of Self-Centering Post-Tensioned Steel Frames," by D. Wang and A. Filiatrault, 5/12/08 (PB2009-110479).

MCEER-08-0018 "Development, Implementation and Verification of Dynamic Analysis Models for Multi-Spherical Sliding Bearings," by D.M. Fenz and M.C. Constantinou, 8/15/08 (PB2009-107911).

MCEER-08-0019 "Performance Assessment of Conventional and Base Isolated Nuclear Power Plants for Earthquake Blast Loadings," by Y.N. Huang, A.S. Whittaker and N. Luco, 10/28/08 (PB2009-107912).

MCEER-08-0020 "Remote Sensing for Resilient Multi-Hazard Disaster Response – Volume I: Introduction to Damage Assessment Methodologies," by B.J. Adams and R.T. Eguchi, 11/17/08 (PB2010-102695).

MCEER-08-0021 "Remote Sensing for Resilient Multi-Hazard Disaster Response – Volume II: Counting the Number of Collapsed Buildings Using an Object-Oriented Analysis: Case Study of the 2003 Bam Earthquake," by L. Gusella, C.K. Huyck and B.J. Adams, 11/17/08 (PB2010-100925).

MCEER-08-0022 "Remote Sensing for Resilient Multi-Hazard Disaster Response – Volume III: Multi-Sensor Image Fusion Techniques for Robust Neighborhood-Scale Urban Damage Assessment," by B.J. Adams and A. McMillan, 11/17/08 (PB2010-100926).

MCEER-08-0023 "Remote Sensing for Resilient Multi-Hazard Disaster Response – Volume IV: A Study of Multi-Temporal and Multi-Resolution SAR Imagery for Post-Katrina Flood Monitoring in New Orleans," by A. McMillan, J.G. Morley, B.J. Adams and S. Chesworth, 11/17/08 (PB2010-100927).

MCEER-08-0024 "Remote Sensing for Resilient Multi-Hazard Disaster Response – Volume V: Integration of Remote Sensing Imagery and VIEWS™ Field Data for Post-Hurricane Charley Building Damage Assessment," by J.A. Womble, K. Mehta and B.J. Adams, 11/17/08 (PB2009-115532).

MCEER-08-0025 "Building Inventory Compilation for Disaster Management: Application of Remote Sensing and Statistical Modeling," by P. Sarabandi, A.S. Kiremidjian, R.T. Eguchi and B. J. Adams, 11/20/08 (PB2009-110484).

MCEER-08-0026 "New Experimental Capabilities and Loading Protocols for Seismic Qualification and Fragility Assessment of Nonstructural Systems," by R. Retamales, G. Mosqueda, A. Filiatrault and A. Reinhorn, 11/24/08 (PB2009-110485).

MCEER-08-0027 "Effects of Heating and Load History on the Behavior of Lead-Rubber Bearings," by I.V. Kalpakidis and M.C. Constantinou, 12/1/08 (PB2009-115533).

MCEER-08-0028 "Experimental and Analytical Investigation of Blast Performance of Seismically Resistant Bridge Piers," by S.Fujikura and M. Bruneau, 12/8/08 (PB2009-115534).

MCEER-08-0029 "Evolutionary Methodology for Aseismic Decision Support," by Y. Hu and G. Dargush, 12/15/08.

MCEER-08-0030 "Development of a Steel Plate Shear Wall Bridge Pier System Conceived from a Multi-Hazard Perspective," by D. Keller and M. Bruneau, 12/19/08 (PB2010-102696).

MCEER-09-0001 "Modal Analysis of Arbitrarily Damped Three-Dimensional Linear Structures Subjected to Seismic Excitations," by Y.L. Chu, J. Song and G.C. Lee, 1/31/09 (PB2010-100922).

MCEER-09-0002 "Air-Blast Effects on Structural Shapes," by G. Ballantyne, A.S. Whittaker, A.J. Aref and G.F. Dargush, 2/2/09 (PB2010-102697).

MCEER-09-0003 "Water Supply Performance During Earthquakes and Extreme Events," by A.L. Bonneau and T.D. O'Rourke, 2/16/09 (PB2010-100923).

MCEER-09-0004 "Generalized Linear (Mixed) Models of Post-Earthquake Ignitions," by R.A. Davidson, 7/20/09 (PB2010-102698).

MCEER-09-0005 "Seismic Testing of a Full-Scale Two-Story Light-Frame Wood Building: NEESWood Benchmark Test," by I.P. Christovasilis, A. Filiatrault and A. Wanitkorkul, 7/22/09.

MCEER-09-0006 "IDARC2D Version 7.0: A Program for the Inelastic Damage Analysis of Structures," by A.M. Reinhorn, H. Roh, M. Sivaselvan, S.K. Kunnath, R.E. Valles, A. Madan, C. Li, R. Lobo and Y.J. Park, 7/28/09 (PB2010-103199).

MCEER-09-0007 "Enhancements to Hospital Resiliency: Improving Emergency Planning for and Response to Hurricanes," by D.B. Hess and L.A. Arendt, 7/30/09 (PB2010-100924).

MCEER-09-0008 "Assessment of Base-Isolated Nuclear Structures for Design and Beyond-Design Basis Earthquake Shaking," by Y.N. Huang, A.S. Whittaker, R.P. Kennedy and R.L. Mayes, 8/20/09 (PB2010-102699).

MCEER-09-0009 "Quantification of Disaster Resilience of Health Care Facilities," by G.P. Cimellaro, C. Fumo, A.M Reinhorn and M. Bruneau, 9/14/09.

MCEER-09-0010 "Performance-Based Assessment and Design of Squat Reinforced Concrete Shear Walls," by C.K. Gulec and A.S. Whittaker, 9/15/09 (PB2010-102700).

MCEER-09-0011 "Proceedings of the Fourth US-Taiwan Bridge Engineering Workshop," edited by W.P. Yen, J.J. Shen, T.M. Lee and R.B. Zheng, 10/27/09 (PB2010-500009).

MCEER-09-0012 "Proceedings of the Special International Workshop on Seismic Connection Details for Segmental Bridge Construction," edited by W. Phillip Yen and George C. Lee, 12/21/09.

MCEER-10-0001 "Direct Displacement Procedure for Performance-Based Seismic Design of Multistory Woodframe Structures," by W. Pang and D. Rosowsky, 4/26/10.

MCEER-10-0002 "Simplified Direct Displacement Design of Six-Story NEESWood Capstone Building and Pre-Test Seismic Performance Assessment," by W. Pang, D. Rosowsky, J. van de Lindt and S. Pei, 5/28/10.

MCEER-10-0003 "Integration of Seismic Protection Systems in Performance-Based Seismic Design of Woodframed Structures," by J.K. Shinde and M.D. Symans, 6/18/10.

MCEER-10-0004 "Modeling and Seismic Evaluation of Nonstructural Components: Testing Frame for Experimental Evaluation of Suspended Ceiling Systems," by A.M. Reinhorn, K.P. Ryu and G. Maddaloni, 6/30/10.

MCEER-10-0005 "Analytical Development and Experimental Validation of a Structural-Fuse Bridge Pier Concept," by S. El-Bahey and M. Bruneau, 10/1/2010.

MCEER
EARTHQUAKE ENGINEERING TO EXTREME EVENTS
University at Buffalo, The State University of New York
Red Jacket Quadrangle ▪ Buffalo, New York 14261
Phone: (716) 645-3391 ▪ Fax: (716) 645-3399
E-mail: *mceer@buffalo.edu* ▪ WWW Site *http://mceer.buffalo.edu*
University at Buffalo *The State University of New York*

ISSN 1520-295X